



UNIVERSITAT DE  
BARCELONA

## Development and applications of photoswitchable ligands for G protein-coupled receptors

Rosalba Sortino



Aquesta tesi doctoral està subjecta a la llicència **Reconeixement- NoComercial – SenseObraDerivada 4.0. Espanya de Creative Commons.**

Esta tesis doctoral está sujeta a la licencia **Reconocimiento - NoComercial – SinObraDerivada 4.0. España de Creative Commons.**

This doctoral thesis is licensed under the **Creative Commons Attribution-NonCommercial-NoDerivs 4.0. Spain License.**

# Development and applications of photoswitchable ligands for G protein-coupled receptors



Rosalba Sortino



UNIVERSITAT DE  
BARCELONA



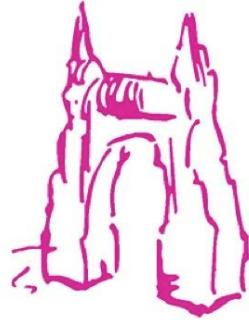
Development and applications of photoswitchable ligands for G protein-coupled receptors



UNIVERSITAT DE BARCELONA

FACULTAT DE FARMÀCIA I CIÈNCIES DE L'ALIMENTACIÓ

DOCTORAT EN BIOTECNOLOGIA



FACULTAT DE FARMÀCIA I  
CIÈNCIES DE L'ALIMENTACIÓ

# Development and applications of photoswitchable ligands for G protein-coupled receptors

*Doctoral Thesis*

Rosalba Sortino

Director and Tutor: Dr. Pau Goristiza Langa  
ICREA Researcher Professor at the  
Institute for Bioengineering of Catalonia

Barcelona, June 2023



## Copyright

The author and promoter give authorization to consult and copy parts of this thesis for personal use only. Any other use is limited by the laws of copyright, especially concerning the obligation to refer to the source whenever results are cited from this thesis.

Barcelona, Spain, the 9<sup>th</sup> of June 2023,

Promoter,

Prof. Dr. Pau Gorostiza Langa

Author,

Rosalba Sortino





Alla mia famiglia



# Table of contents

## List of abbreviations

XIII-XIX

## Chapter 1:

### Outline and objectives

1

## Chapter 2:

### General introduction

5

### 2.1 G protein-coupled receptors

7

2.1.1 Intracellular signaling

9

2.1.2 Modulation of GPCRs activity

12

### 2.2 Neurotransmission

17

2.2.1 Acetylcholine

17

2.2.1.1 Muscarinic acetylcholine receptors

18

2.2.1.1.1 *M<sub>1</sub>-like receptors*

19

2.2.1.1.2 *M<sub>2</sub>-like receptors*

21

2.2.1.2 Muscarinic ligands

22

2.2.2 Dopamine

26

2.2.2.1 Dopamine receptors

28

2.2.2.1.1 *D<sub>1</sub>-class receptors*

29

2.2.2.1.2 *D<sub>2</sub>-class receptors*

30

2.2.2.2 Dopaminergic ligands

31

2.2.3 Glutamate

34

2.2.3.1 Metabotropic glutamate receptors

35

2.2.3.2 Metabotropic glutamatergic ligands

39

### 2.3. G protein-coupled receptors photopharmacology

41

2.3.1 Irreversible photouncaging

43

2.3.2 Reversible ligands

44

2.3.3 Photoswitchable tethered ligands

47

2.3.4 Photochromic ligands

49

2.3.5 Multiphoton excitation techniques

53

### References

56

## Chapter 3:

### Rational design of photochromic analogues of tricyclic drugs

75

### 3.1 Introduction

79

### 3.2 Results and discussion

81

3.2.1 Rational design and chemical synthesis

81

3.2.2 Photochemical characterization

83

3.2.3 Competition binding assay

84

3.2.4 *In vitro* calcium imaging

85

3.2.5 *Ex vivo* experiments in mouse isolated atrium

88

### 3.3 Conclusions

89

### References

90

### Supporting Information of Chapter 3

94

<b>Chapter 4:</b>	
<b>Control of cortical slow oscillations and epileptiform discharges by photoswitchable muscarinic acetylcholine receptor subtype 1 ligands</b>	<b>129</b>
<b>4.1 Introduction</b>	<b>133</b>
<b>4.2 Results</b>	<b>134</b>
4.2.1 <i>In vitro</i> calcium imaging	134
4.2.2 <i>Ex vivo</i> photocontrol of the frequency of slow waves with BAI in ferret slices	136
4.2.3 <i>In vivo</i> photocontrol of the frequency of slow waves with BAI in mice	138
4.2.4 <i>Ex vivo</i> photocontrol of the frequency of slow waves with cryptozepine in ferret slices	139
4.2.5 <i>Ex vivo</i> experiment of seizure-like activity blockage with cryptozepine in ferret slices	141
<b>4.3 Discussion and conclusions</b>	<b>143</b>
<b>References</b>	<b>147</b>
<b>Supporting Information of Chapter 4</b>	<b>151</b>
<b>Chapter 5:</b>	
<b>Photoreversible modulation of brain activity with infrared light</b>	<b>159</b>
<b>5.1 Introduction</b>	<b>163</b>
<b>5.2 Results</b>	<b>165</b>
5.2.1 Rational design and chemical synthesis	165
5.2.2 Photochemical characterization	167
5.2.3 Split luciferase complementation assay	168
5.2.4 Molecular docking	170
5.2.5 <i>In vitro</i> calcium imaging	171
5.2.6 <i>In vitro</i> neuronal photocontrol in hippocampal neurons	173
5.2.7 <i>In vivo</i> neuronal photocontrol in mice	174
<b>5.3 Discussion</b>	<b>176</b>
<b>5.4 Conclusions</b>	<b>178</b>
<b>References</b>	<b>179</b>
<b>Supporting Information of Chapter 5</b>	<b>184</b>
<b>Chapter 6:</b>	
<b>Reversible photocontrol of muscarinic signaling using red-shifted azobenzenes</b>	<b>205</b>
<b>6.1 Introduction</b>	<b>209</b>
<b>6.2 Results</b>	<b>210</b>
6.2.1 Rational design and chemical synthesis	210
6.2.2 Photochemical characterization	215
6.2.3 Split luciferase complementation assay	215
6.2.4 <i>In vitro</i> calcium imaging	217
6.2.5 <i>In vivo</i> photocontrol of locomotor activity in zebrafish larvae	218
<b>6.3 Discussion</b>	<b>220</b>
<b>6.4 Conclusions</b>	<b>222</b>
<b>References</b>	<b>223</b>
<b>Supporting Information of Chapter 6</b>	<b>228</b>

<b>Chapter 7:</b>	
<b>Photo-BQCA:</b>	
<b>Positive allosteric modulators enabling optical control of the M<sub>1</sub> receptor</b>	<b>249</b>
<b>7.1 Introduction</b>	<b>253</b>
<b>7.2 Results and discussion</b>	<b>254</b>
7.2.1 Rational design and chemical synthesis	254
7.2.2 Photochemical characterization	258
7.2.3 Split luciferase complementation assay	258
7.2.4 Fluorescence-based plate reader assay	261
7.2.5 <i>In vitro</i> calcium imaging	262
7.2.6 Molecular docking	263
<b>7.3 Conclusions</b>	<b>264</b>
<b>References</b>	<b>266</b>
<b>Supporting Information of Chapter 7</b>	<b>269</b>
<b>Chapter 8:</b>	
<b>Optical control of cardiac function with a photoswitchable muscarinic agonist</b>	<b>283</b>
<b>8.1 Introduction</b>	<b>287</b>
<b>8.2 Results and discussion</b>	<b>288</b>
8.2.1 Rational design and chemical synthesis	288
8.2.2 Photochemical characterization	290
8.2.3 <i>In vitro</i> calcium imaging	291
8.2.4 Molecular docking	292
8.2.5 <i>In vivo</i> photocontrol of cardiac activity in rats	293
8.2.6 <i>In vivo</i> photocontrol of cardiac activity in frog tadpoles	294
8.2.7 <i>In vitro</i> calcium imaging and two-photon stimulation	295
<b>8.3 Conclusions</b>	<b>297</b>
<b>References</b>	<b>298</b>
<b>Supporting Information of Chapter 8</b>	<b>301</b>
<b>Chapter 9:</b>	
<b>Three-photon infrared stimulation of endogenous neuroreceptors <i>in vivo</i></b>	<b>327</b>
<b>9.1 Introduction</b>	<b>331</b>
<b>9.2 Results and discussion</b>	<b>332</b>
9.2.1 Theoretical calculations	333
9.2.2 <i>In vitro</i> calcium imaging and three-photon stimulation	334
9.2.3 <i>In vivo</i> neuronal photocontrol in zebrafish larvae and three-photon stimulation	337
<b>9.3 Conclusions</b>	<b>341</b>
<b>References</b>	<b>342</b>
<b>Supporting Information of Chapter 9</b>	<b>346</b>

<b>Chapter 10:</b>	
<b>Reversible photocontrol of dopaminergic transmission in wild-type animals</b>	<b>363</b>
<b>10.1 Introduction</b>	<b>367</b>
<b>10.2 Results</b>	<b>370</b>
10.2.1 Rational design and chemical synthesis	370
10.2.2 Photochemical characterization	371
10.2.3 <i>In vitro</i> pharmacological characterization	372
10.2.4 Behavioral effects in zebrafish larvae	375
10.2.5 Electrophysiological recordings in anesthetized mice	380
<b>10.3 Discussion and conclusions</b>	<b>384</b>
<b>References</b>	<b>387</b>
<b>Supporting Information of Chapter 10</b>	<b>391</b>
<b>Chapter 11:</b>	
<b>Restoration of visual acuity with upstream-targeted photopharmacology</b>	<b>415</b>
<b>11.1 Introduction</b>	<b>419</b>
<b>11.2 Results</b>	<b>422</b>
11.2.1 <i>In vitro</i> calcium imaging	422
11.2.2 <i>In vivo</i> optokinetic reflex assay in zebrafish larvae and behavioral assay in mice with prosthe6	424
11.2.3 Fluorescence-based plate reader assay	427
11.2.4 <i>In vivo</i> optokinetic reflex assay in zebrafish larvae and behavioral assay in mice with 1492 and 1495	428
<b>11.3 Discussion</b>	<b>430</b>
<b>11.4 Conclusions</b>	<b>432</b>
<b>References</b>	<b>433</b>
<b>Supporting Information of Chapter 11</b>	<b>437</b>
<b>Chapter 12:</b>	
<b>Discussion</b>	<b>453</b>
<b>Chapter 13:</b>	
<b>Conclusions</b>	<b>481</b>
<b>Summary</b>	<b>485</b>
<b>Resumen</b>	<b>485</b>
<b>Acknowledgements</b>	<b>497</b>

## List of abbreviations

1/2/3P	One/Two/Three-photon
1/2/3PE	One/Two/Three-photon excitation
3-MT	3-methoxytyramine
3PP	Three-photon pharmacology
5-HT	5-hydroxytryptamine, serotonin
7TM	Seven transmembrane
<b>A</b>	
AAD	Antiarrhythmic drugs
AADC	L-amino acid decarboxylase
AC	Adenylate cyclase
Acetyl-CoA	Acetyl coenzyme A
ACh	Acetylcholine
aCSF	Artificial cerebrospinal fluid
ACTM	Allosteric ternary complex model
AD	Alzheimer's disease
ADH	Alcohol dehydrogenase
ALDH	Aldehyde dehydrogenase
AMPA	Alpha-amino-3-hydroxy-5-methyl-4-isoxazolepropionic acid receptor
ANOVA	Analysis of variance
ATCC	American type culture collection
ATP	Adenosine triphosphate
a.u.	Atomic units
AU	Arbitrary units
AUC	Area under the curve
<b>B</b>	
BQCAAI or BAI	Benzyl quinolone carboxylic acid-azo-iperoxo
BBB	Blood brain barrier
BCA	Bicinchoninic acid assay
BQCA	Benzyl quinolone carboxylic acid
BSA	Bovine serum albumin
<b>C</b>	
C57BL/6	C57 black 6
cAMP	3',5'-cyclic adenosine monophosphate
Cb	Cerebellum
CCh	Carbachol
CDCl <sub>3</sub>	Deuterated chloroform



cGMP	Cyclic 3',5'-guanosine monophosphate
cGMP-PDE	Cyclic 3',5'-guanosine monophosphate phosphodiesterase
CH <sub>2</sub> Cl <sub>2</sub>	Dichloromethane
ChAT	Choline acetyltransferase
ChR	Channelrhodopsin
CHT1	Choline transporter 1
CNS	Central nervous system
COMT	Catechol-O-methyl transferase
CPCCoEt	(E)-ethyl 1,1a,7,7a-tetrahydro-7-(hydroxyimino)cyclopropa[b]chromene-1a-carboxylate
CRC	Concentration-response-curve
CRD	Cysteine-rich domain
CREB	cAMP response element-binding protein
Cryo-EM	Cryogenic electron microscopy
CTD	C-terminal domain
CYP2D6	Cytochrome P450 2D6

## D

D <sub>1-5</sub> R	Dopamine D <sub>1-5</sub> receptor
D <sub>2L</sub> R	Dopamine D <sub>2</sub> -long receptor
D <sub>2S</sub> R	Dopamine D <sub>2</sub> -short receptor
D <sub>2</sub> O	Deuterium oxide
DA	Dopamine
DAG	Diacylglycerol
DAR	Dopamine receptor
DARPP-32	32-kDa dopamine and cAMP-regulated phosphoprotein
DAT	Dopamine transporter
DIV	Days <i>in vitro</i>
DMEM	Dulbecco's modified Eagle's medium
DMF	Dimethylformamide
DMSO	Dimethyl sulfoxide
DOPAC	3,4-dihydroxyphenylacetic acid
DOPAL	3,4-dihydroxyphenylacetaldehyde
DOPET	3,4-dihydroxyphenylethanol
Dpf	Days post-fertilization
Dpm	Disintegrations per minute

## **E**

EAAT	Excitatory amino acid transporter
ECD	Extracellular domain
ECF	Extracellular fluid
ECL	Extracellular loop
ECV	Extracellular vestibule
ER	Endoplasmic reticulum
ERK1-2	Extracellular-signal regulated kinases 1-2
ESI	Electrospray ionization
Et <sub>2</sub> O	Diethyl ether
EtOAc	Ethyl acetate
EtOH	Ethanol
EYFP	Enhanced yellow fluorescent protein

## **F**

FBS	Fetal bovine serum
FCS	Fetal calf serum
FDA	Food and Drug Administration
FRET	Förster resonant energy transfer
FWHM	Full width at half maximum

## **G**

GABA	Gamma-aminobutyric acid
GABA <sub>A/B</sub> R	Gamma-aminobutyric acid type A/B receptor
GAIN	GPCR autoproteolysis-inducing
GDP	Guanidine diphosphate
GIRK	G protein-coupled inwardly-rectifying potassium
GluK2	Glutamate ionotropic receptors type subunit 2
GM	Goeppert-Mayer
GP	Globus pallidus
GPCR	G protein-coupled receptor
GPS	GPCR proteolytic site
GRK	GPCR kinase
GTP	Guanidine triphosphate
GTPase	Guanosine triphosphatase

## **H**

HEPES	<i>N</i> -(2-hydroxyethyl)piperazine- <i>N'</i> -(2-ethanesulfonic acid)
HEK 293T	Human embryonic kidney 293T cell line
HEK tsA201	Human embryonic kidney tsA201 cell line

HPLC	High-performance liquid chromatography
HSP90	Heat shock protein 90
HTRF	Homogeneous time-resolved fluorescence energy transfer
HTS	High-throughput screening
HVA	Homovanillic acid
Hz	Hertz
<b>I</b>	
i.p.	Intraperitoneal
ICL	Intracellular loop
iGlu receptor	Ionotropic glutamate receptor
iNOS	Inducible nitric oxide synthase
IP <sub>3</sub>	Inositol-1,4,5-trisphosphate
IPX	Iperoxo
IR	Infrared
IUPHAR	International Union of Basic and Clinical Pharmacology
<b>J</b>	
<i>J</i>	Coupling constants
JNK	c-Jun N-terminal kinase
<b>K</b>	
KA	Kainic acid
KAR	Kainic acid receptor
K <sub>i</sub>	Binding affinity
<b>L</b>	
L-AP4	L-2-amino-4-phosphonobutyric acid
LARG	Leukaemia-associated RhoGEF
L-DOPA	L-3,4-dihydroxyphenylalanine
LED	Light emitting diode
LPF	Local field potential
LSD	Least significant differences
<b>M</b>	
M <sub>1-5</sub> R	M <sub>1-5</sub> Muscarinic acetylcholine receptor
M2	Secondary motor cortex
mAChR	Muscarinic acetylcholine receptor
MAG	Maleimide-azobenzene-glutamate
MAO	Monoamine oxidase
MAP	Maleimide-azobenzene-PPHT
MAPK	Mitogen-activated protein kinase

MCI	Mild cognitive impairment
MeCN	Acetonitrile
MeOH	Methanol
mGlu receptor	Metabotropic glutamate receptor
mGlu <sub>1-8</sub> receptor	Metabotropic glutamate 1-8 receptor
MPE	Multiphoton excitation
MPP	Multiphoton pharmacology
MS	Mass spectroscopy
MSN	Medium spiny neuron
MUA	Multiunit activity
<b>N</b>	
NAc	Nucleus accumbens
nAChR	Nicotinic acetylcholine receptor
NAI	Naphthalimide-azo-iperoxo
NAL	Neutral allosteric ligand
NAM	Negative allosteric modulator
NHE-1	Sodium/hydrogen exchanger 1
NIR	Near-infrared
NMDAR	N-methyl-D-aspartate receptor
NMJ	Neuromuscular junction
NMR	Nuclear magnetic resonance
NMS	N-methyl scopolamine
NTD	N-terminal domain
<b>O</b>	
OBC	ON bipolar cell
OGB-1 AM	Oregon Green BAPTA-1 AM
OT	Optic tectum
<b>P</b>	
PAI	Phthalimide-azo-iperoxo
PAM	Positive allosteric modulator
PCL	Photochromic ligand
PD	Parkinson's disease
PDA	Photodiode detector
PDB	Protein data bank
PEI	Polyethylenimine
PH	Phenylalanine hydroxylase
PHCCC	7,7a-dihydro-7-(hydroxyimino)-N-phenyl-benzo[b]cyclopropa[e]pyran-1a(1H)-carboxamide

PhR	Photoreceptor
PI3K	Phosphatidylinositol-3 kinase
PIP <sub>2</sub>	Phosphatidylinositol 4,5-bisphosphate
PKA/C/D	Protein kinase A/C/D
PLC-β/Cε/D	Phospholipase C-β/Cε/D
PNS	Peripheral nervous system
PNZ	Pirenzepine
PORTL	Photoswitchable orthogonal remotely tethered ligand
PP1	Protein phosphatase 1
PP5	Protein phosphatase 5
PPHT	2-( <i>N</i> -phenethyl- <i>N</i> -propyl)amino-5-hydroxytetralin
Ppm	Parts-per-million
P-Rex1	Phosphatidylinositol-3,4,5-trisphosphate dependent Rac exchange factor 1
PSD	Photostationary distributions
PSS	Photostationary state
PTL	Photoswitchable tethered ligand
<b>Q</b>	
QNB	3-quinuclidinyl benzilate
<b>R</b>	
Rap1GAP	Rap1 GTPase activating protein
RF	Relative fluorescence
RGC	Retinal ganglion cell
R-GECO1	Red-genetically encoded calcium 1
RhoGEF	Rho-guanine nucleotide exchange factor
RP	Retinitis pigmentosa
<b>S</b>	
SAM	Silent allosteric modulator
SAR	Structure-activity relationship
SD	Standard deviation
SEM	Standard error of the mean
SLCA	Split luciferase complementation assay
SN	Substantia nigra
SNAT	Sodium-coupled neutral amino acid transporter
SO	Slow oscillations
SZ	Schizophrenia

## T

TBI	Traumatic brain injury
TCA	Tricarboxyl acid
TCP	Targeted covalent photoswitches
TH	Tyrosine hydroxylase
Th	Thalamus
THF	Tetrahydrofuran
TLC	Thin layer chromatography
TM	Transmembrane
TMD	Transmembrane domain
TO	Tuberculum olfactorium
TR-FRET	Time-resolved fluorescence resonance energy transfer
TRMP1	Transient receptor potential cation channel subfamily M member 1

## U

UV	Ultraviolet
UV-Vis	Ultraviolet-visible

## V

V1	Primary visual cortex
VACht	Vesicular acetylcholine transporter
VFD	Venus flytrap domain
VGLUT	Vesicular glutamate transporter
VMAT1-2	Vesicular monoamine transporter 1-2
V.S.	Variability score
VTA	Ventral tegmental area
VU0364770	<i>N</i> -(3-Chlorophenyl)-2-pyridinecarboxamide
VU0415374	<i>N</i> -[4-[[[(2-chlorophenyl)-oxomethyl]amino]-3-methoxyphenyl]-2-pyridinecarboxamide

## W

WL	White light
w/o	Wash-out
WT	Wild-type



# Chapter 1

---

Outline and objectives

---





G protein-coupled receptors (GPCRs) modulate diverse cellular responses and are regulated by the majority of neurotransmitters and hormones within the human body. Given their widespread cellular and tissue distribution, the expression and activity of GPCRs have been involved in a myriad of human diseases (*e.g.*, cardiac disorders, central nervous system disorders and cancer). For this reason, GPCRs are the central focus of pharmaceutical drug discovery and development efforts towards clinical settings. The pace of discovery of novel GPCR-based drugs has been accelerated through the development of new assays for high-throughput screening of GPCR-interacting compounds as well as advancements in structural biology and *in silico* computational modeling. Approximately 40% of clinically approved drugs mediate their effect by fine-tuning GPCR signaling.

However, the ubiquity of GPCRs in different tissues and organs leads to unintended reactions by systemically administered drugs, producing adverse effects as their actions cannot be turned off. In addition, it is known that GPCR subtypes share high sequence identities in orthosteric binding sites with distinct distribution and downstream signaling profiles. Consequently, cross activity among subtypes could cause severe side effects. Thus, another challenge of conventional pharmacology is developing subtype-selective compounds.

The field of photopharmacology provides a solution to these limitations. This approach allows to manipulate endogenous receptors in their physiological context, along with a higher spatiotemporal precision than conventional pharmacological or genetic approaches. This offers potential benefits for new drug-based therapies. In fact, manipulating drug activity in space and time by using light, makes it location-specific and on demand. Moreover, the pharmacological selectivity of photoswitchable drugs can be improved with subtype-selective molecular scaffolds (*e.g.*, allosteric ligands), which offer a great potential for photopharmacology as well. The general introduction presented in **Chapter 2** provides background information about the topics relevant for this thesis: (a) GPCRs, (b) neurotransmission and (c) photopharmacology.

The first aim of this thesis is to develop photoswitchable GPCR ligands that integrate the standards of modern pharmacology (*e.g.*, allosteric action) with those of advanced photochromic properties (*e.g.*, infrared activation). Our study models are muscarinic acetylcholine receptors (mAChRs or MRs), dopamine receptors (DARs) and metabotropic glutamate (mGlu) receptors. Photoswitchable GPCR ligands are interesting for fundamental purposes, but they also offer the opportunity to demonstrate novel proof of concept applications, which constitute the second aim of the thesis.

The objectives of this thesis can be summed up as follows:

- 1) To develop and characterize M<sub>1</sub>R-selective photoswitchable agonists and antagonists (**Chapter 3** and **Chapter 4**).
- 2) To develop and characterize photoswitchable muscarinic ligands activated by red or infrared light, allowing deep penetration in tissue (**Chapter 5** and **Chapter 6**).
- 3) To develop and characterize the first light-regulated allosteric modulators of class A GPCRs (**Chapter 7**).
- 4) To develop and characterize new M<sub>2</sub>R-selective photoswitchable agonists (**Chapter 8**).
- 5) To demonstrate a proof of concept of two- and three-photon excitation of GPCRs photoswitchable ligands (**Chapter 8** and **Chapter 9**).
- 6) To develop and characterize the first photoswitchable agonist of endogenous dopaminergic receptors (**Chapter 10**).
- 7) To develop a library of photoswitchable allosteric modulators of mGlu receptors with optimized pharmacological and photochromic properties to be used as drugs for vision restoration therapy (**Chapter 11**).
- 8) To demonstrate a proof of concept for vision restoration based on photoswitchable allosteric modulators of mGlu receptors (**Chapter 11**).

# Chapter 2

---

## General introduction

G protein-coupled receptors, neurotransmission and photopharmacology

---



## 2.1 G protein-coupled receptors

The G protein-coupled receptors (GPCRs), also known as seven transmembrane (7TM) receptors, are the largest and most diverse class of cell surface receptors, encoded by about 4% of the human protein-coding genome<sup>1,2</sup>. More than 800 GPCRs have been identified, which are expressed throughout the human body and have distinct features in a plethora of physiological processes, including cell-cell communication, hormonal signaling, sensory transduction and neuronal transmission. Many ligands are able to activate these receptors, including ions, photons, odorant molecules, peptides, amino acids, nucleotides, small molecules and lipids<sup>2</sup>. Given their diverse functions and widespread tissue distribution, it is not surprising that the expression and activity of GPCRs have been implicated in multiple human diseases. Therefore, GPCRs have become a hot topic in scientific research and an important target in the development of pharmaceuticals. In 2012, the Nobel Prize in Chemistry was awarded jointly to Brian Kobilka and Robert Lefkowitz, for the achievements made in their “studies of G protein-coupled receptors”<sup>3</sup>. Impressively, about 34% of all approved drugs by the Food and Drug Administration (FDA) act at 108 unique GPCRs, covering a global market share of ~27%<sup>4,5</sup>. Since around 100 of the 370 human non-sensory GPCRs are orphan receptors (with unknown function), the number of GPCR targets, and the number of GPCR-targeted drugs will likely increase, thus furthering expanding the GPCR repertoire and the many roles of GPCR drugs in therapeutics<sup>6</sup>.

Human GPCRs are categorized based on their phylogenetic characteristics by the classification system “GRAFS” in 5 classes: Glutamate-, Rhodopsin-, Adhesion-, Frizzled/Taste2 and Secretin<sup>1,7-10</sup>. Alternatively, the A-F class covers all GPCRs in both vertebrates and invertebrates, although it does not include the Frizzled and Taste2 receptors<sup>1</sup>. The 7TM receptors share a common tertiary structure containing an N-terminal extracellular domain (NTD), an intracellular C-terminal domain (CTD) and a transmembrane domain (TMD) formed by seven hydrophobic transmembrane  $\alpha$ -helices which span the plasma membrane in a counter-clockwise manner<sup>11</sup>. These transmembrane  $\alpha$ -helices are connected by three extracellular loops (ECL1-ECL3) and three intracellular loops (ICL1-ICL3) (**Figure 2.1**)<sup>12,13</sup>. Two cysteines are often present in the ECL1 and ECL2, forming a disulfide bond to stabilize the structure and limit the number of conformations. The intracellular regions are more conserved, whereas the extracellular structures have a higher diversity among GPCRs. However, the varying lengths and angles of specific domains provide each 7TM receptor with unique properties<sup>14</sup>.

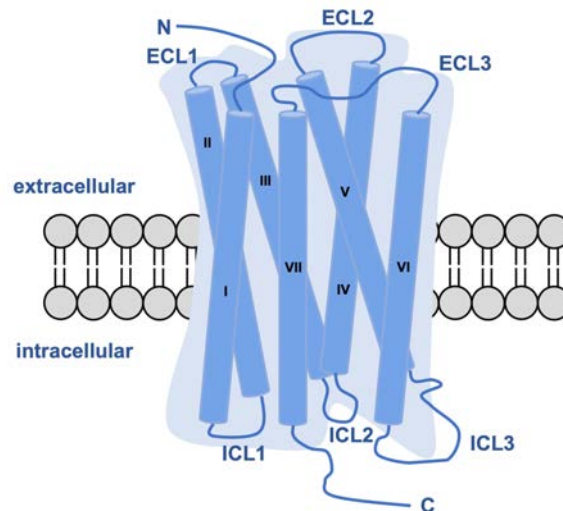


**Figure 2.1. Schematic structure of a G protein-coupled receptor.** The seven transmembrane domains (7TM) are shown with their typical three extracellular (ECL1-3), intracellular loops (ICL1-3) and N- and C-termini (NTD and CTD, respectively). Original figure by Rosalba Sortino.

Rhodopsin receptors (class A) are the most studied and largest subfamily, with 719 members (> 85% of all GPCRs) and the highest number of solved structures<sup>15</sup>. Given the wide range of their physiological function, this class of receptors is the most targeted therapeutically among all other classes. Most of this subfamily are olfactory receptors and ~350 are non-olfactory GPCRs. The class A has a short NTD and the conventional TMD forms the orthosteric ligand-binding pocket (**Figure 2.2**)<sup>1,7</sup>. The 15 Secretin family members (class B1) play key roles in the signal transduction of peptide hormones that are important for  $\text{Ca}^{2+}$  homeostasis and blood glucose regulation<sup>16</sup>. These receptors possess a long NTD which forms part of the orthosteric binding domain for their ligands, in addition to the ECLs and the TMD (**Figure 2.2**)<sup>17-19</sup>. The Glutamate receptor family (class C) consists of 22 members and includes the taste receptors, metabotropic glutamate (mGlu) receptors,  $\text{Ca}^{2+}$ -sensitive GPCRs, and  $\gamma$ -aminobutyric acid (GABA) subtype B ( $\text{GABA}_B$ ) receptor<sup>17,18</sup>. The class C members are twice as large as other GPCRs due to an extremely large, bi-lobed NTD containing the so called “Venus flytrap” domain (VFD) and a cysteine-rich domain (CRD)<sup>20,21</sup>. For the  $\text{GABA}_B$  receptors the VFD is directly linked to the TMD without the CRD. Noteworthy, class C receptors only function as dimers bound through their VFDs (**Figure 2.2**). Only a very few small molecules that target the class B1 or C GPCRs are currently on the market. Adhesion receptors or class B2 (33 members) are characterized by a large NTD containing various adhesion domains and a GPCR autoproteolysis-inducing (GAIN) domain that undergoes self-cleavage during receptor maturation (**Figure 2.2**)<sup>17,20,22</sup>. The Frizzled class F GPCRs consists of 11 Frizzled which exhibit a structure comprising a TMD and a CRD at the NTD<sup>23</sup>. Their ligands are known to

form a covalent bond with a palmitoyl group, which is located within the CRD (**Figure 2.2**)  
The transmembrane domains of the Taste2 receptors (25 members) most closely resemble those of the Frizzled family, but lack the analogous extracellular domains<sup>20</sup>.

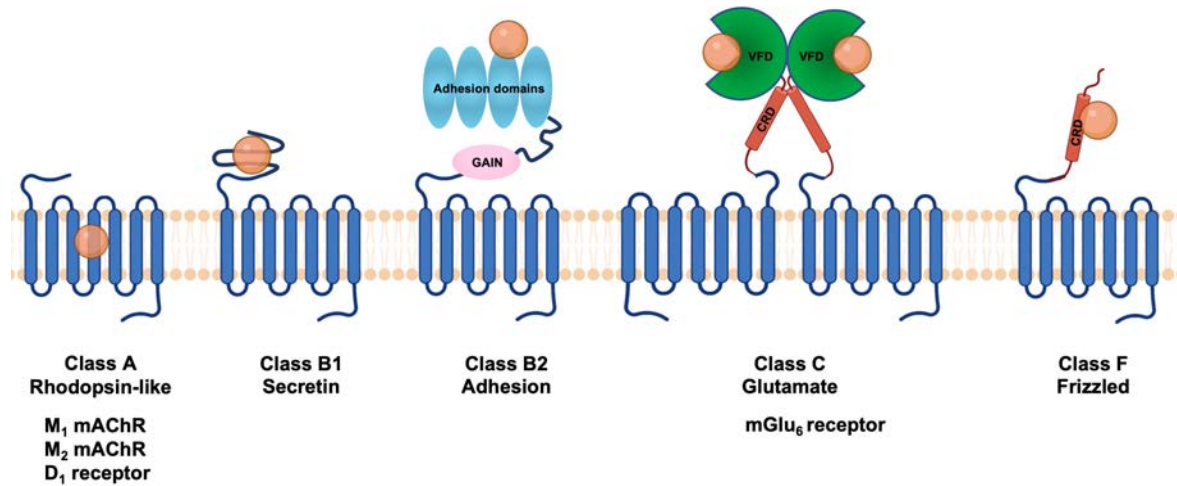


**Figure 2.2. Five classes of human G protein-coupled receptors and their respective orthosteric binding sites.**

Cartoon models displaying structural features of G protein-coupled receptors (GPCRs) from different classes. The canonical transmembrane hepta-helical bundle structure is shared by all GPCRs. Class A GPCRs possess a relatively short N-terminal extracellular domain (NTD). In contrast, class B1 GPCRs contains an extracellular domain (ECD) to accommodate hormone peptide binding with the transmembrane domain (TMD). The extremely large NTD of class B2 GPCRs consists of several cell adhesion domains and a GPCR autoproteolysis-inducing (GAIN) domain, which contains a conserved GPCR proteolytic site (GPS) motif that is associated with autoproteolysis. Responsible for endogenous ligand binding and dimer formation, the "Venus flytrap" domain (VFD) in class C GPCRs is connected to the TMD through a flexible cysteine-rich domain (CRD) linker. Class F GPCRs are characterized by a CRD at the NTD. Original figure by Rosalba Sortino.

### 2.1.1 Intracellular signaling

Upon receptor activation, the signal is amplified via intracellular transducers, such as the heterotrimeric G protein (composed of  $\alpha$ -,  $\beta$ -, and  $\gamma$ -subunits). First, the agonist binds at the core domain of the 7TM region, switching the receptor from an inactive to an active conformational state. In general, this affects the conformation of ECL1-2 and ECL1-3, which rotates the TM6 outwards to separate it from the TM3, unmasking the binding site for the C-terminal  $\alpha$ -helix of the G protein<sup>13,24</sup>. The G protein's active state provides the catalysis and exchange of a guanine diphosphate (GDP) for a guanine triphosphate (GTP) on the  $\alpha$ -subunit of the G proteins. Ultimately, this produces the dissociation of the  $G\alpha$  subunit from the  $G\beta\gamma$ -complex, with both the  $G\alpha$  subunit and the  $G\beta\gamma$ -complex activating downstream effectors<sup>25</sup>. The hydrolysis of GTP to GDP leads to a re-association of the subunits<sup>26</sup>.



The signaling cascade begins with the interaction of the  $G\alpha$  or  $G\beta\gamma$  subunits with their corresponding effectors, as summarized in **Table 2.1** and exemplified in **Figure 2.3**. Briefly, the G proteins are divided into  $G\alpha_s$ ,  $G\alpha_{i/o}$ ,  $G\alpha_{q/11}$  and  $G\alpha_{12/13}$ , based on primary sequence similarities<sup>27</sup>. GPCRs coupled to the  $G\alpha_{q/11}$  protein activate phospholipase C $\beta$  (PLC $\beta$ ), resulting in the formation of diacylglycerol (DAG) and inositol-1,4,5-trisphosphate (IP<sub>3</sub>). Subsequently, IP<sub>3</sub> binds to the endoplasmic IP<sub>3</sub>-gated Ca<sup>2+</sup> channel, which leads to an increase in cytoplasmic Ca<sup>2+</sup> concentrations, whereas DAG is associated with protein kinase C (PKC) recruitment. Coupling of  $G\alpha_s$  and  $G\alpha_{i/o}$  subunits with a GPCR activates or inhibits adenylyl cyclase (AC), respectively. This enzyme converts adenosine triphosphate (ATP) to 3',5'-cyclic adenosine monophosphate (cAMP), a second messenger activating protein kinase A (PKA) and other downstream effectors. The fourth class,  $G\alpha_{12/13}$ , couples with GPCRs to activate the Rho-guanine nucleotide exchange factor (RhoGEF), which in turn activates the small G protein RhoA. In addition, the dissociating  $G\beta\gamma$  subunits may recruit kinases or modulate ion channels, such as the G protein-coupled inwardly-rectifying potassium (GIRK) channels to produce hyperpolarization of the plasma membrane<sup>2</sup>.

Family	Subtypes	Effector molecules
$G\alpha_s$	$G\alpha_s$	Activates $\uparrow$ AC, Maxi K channel, Src tyrosine kinase and GTPase of tubulin
	$G\alpha_{olf}$	Activate $\uparrow$ AC
$G\alpha_{i/o}$	$G\alpha_i$ , $G\alpha_o$ , $G\alpha_z$	Inhibits $\downarrow$ AC and Ca <sup>2+</sup> channels; Activates $\uparrow$ K <sup>+</sup> channels, MAPK, GTPase of tubulin, Src tyrosine kinase, Rap1GAP and GRIN1-mediated activation of Cdc42
	$G\alpha_t$	Activate $\uparrow$ cGMP-PDE
	$G\alpha_{gust}$	?
$G\alpha_q$	$G\alpha_q$ , $G\alpha_{11}$ , $G\alpha_{14}$ , $G\alpha_{15}$ , $G\alpha_{16}$	Activates $\uparrow$ PLC $\beta$ isoforms, p63-RhoGEF, Bruton's tyrosine kinase and K <sup>+</sup> channels
$G\alpha_{12/13}$	$G\alpha_{12}$ , $G\alpha_{13}$	Activates $\uparrow$ PLD and PLC $\epsilon$ isoforms, p115-RhoGEF, PDZ-RhoGEF, NHE-1, iNOS, LARG, PP5, Radixin, AKAP110-mediated activation of PKA and HSP90
$G\beta\gamma$	$G\beta_{1-5}\gamma_{1-12}$	Inhibits $\downarrow$ AC I and Ca <sup>2+</sup> (N-, P/Q-, R-type) channels; Activates $\uparrow$ PLC $\beta$ isoforms, AC II, IV and VII, PI3K, K <sup>+</sup> channels, P-Rex1, JNK, Src kinases, GTPase of tubulin, PKD, Bruton's tyrosine kinase and p114-RhoGEF

**Table 2.1. Summary of mammalian heterotrimeric G protein subunits and functions of each family.**

Abbreviations: Adenylyl cyclase, AC; Guanosine triphosphatase, GTPase; Mitogen-activated protein kinase, MAPK; Rap1 GTPase activating protein, Rap1GAP; Cyclic 3',5'-guanosine monophosphate phosphodiesterase, cGMP-PDE; Phospholipase C $\beta$ /D/C $\epsilon$ , PLC $\beta$ /D/C $\epsilon$ ; Rho guanine nucleotide exchange factor, RhoGEF; Sodium/hydrogen exchanger 1, NHE-1; Inducible nitric oxide synthases, iNOS; Leukaemia-associated RhoGEF, LARG; Protein phosphatase 5, PP5; Heat shock protein 90, HSP90; Protein kinase A/D, PKA/D; Phosphatidylinositol-3 kinase, PI3K; Phosphatidylinositol-3,4,5-trisphosphate dependent Rac exchange factor 1, P-Rex1; c-Jun N-terminal kinase, JNK. Adapted from Milligan *et al.*, 2006<sup>28</sup>.

Continuous GPCR stimulation leads to desensitization, internalization and termination of the G protein signaling cascade. The recruitment of  $\beta$ -arrestin molecules is typically initiated via the phosphorylation of intracellular Thr/Ser residues of the receptor by GPCR kinases (GRKs)<sup>29</sup>. This multi-molecular complex triggers G protein signaling cessation and induces receptor endocytosis, thus desensitization. Then, the GPCR is either translocated back to the plasma membrane or degraded in the lysosome. In addition,  $\beta$ -arrestins function as scaffold adaptors in G protein-independent signaling pathways for receptor and non-receptor tyrosine kinases, mitogen-activated protein kinases (MAPKs), phosphatidylinositol-3 kinases (PI3Ks) and others<sup>30,31</sup>.

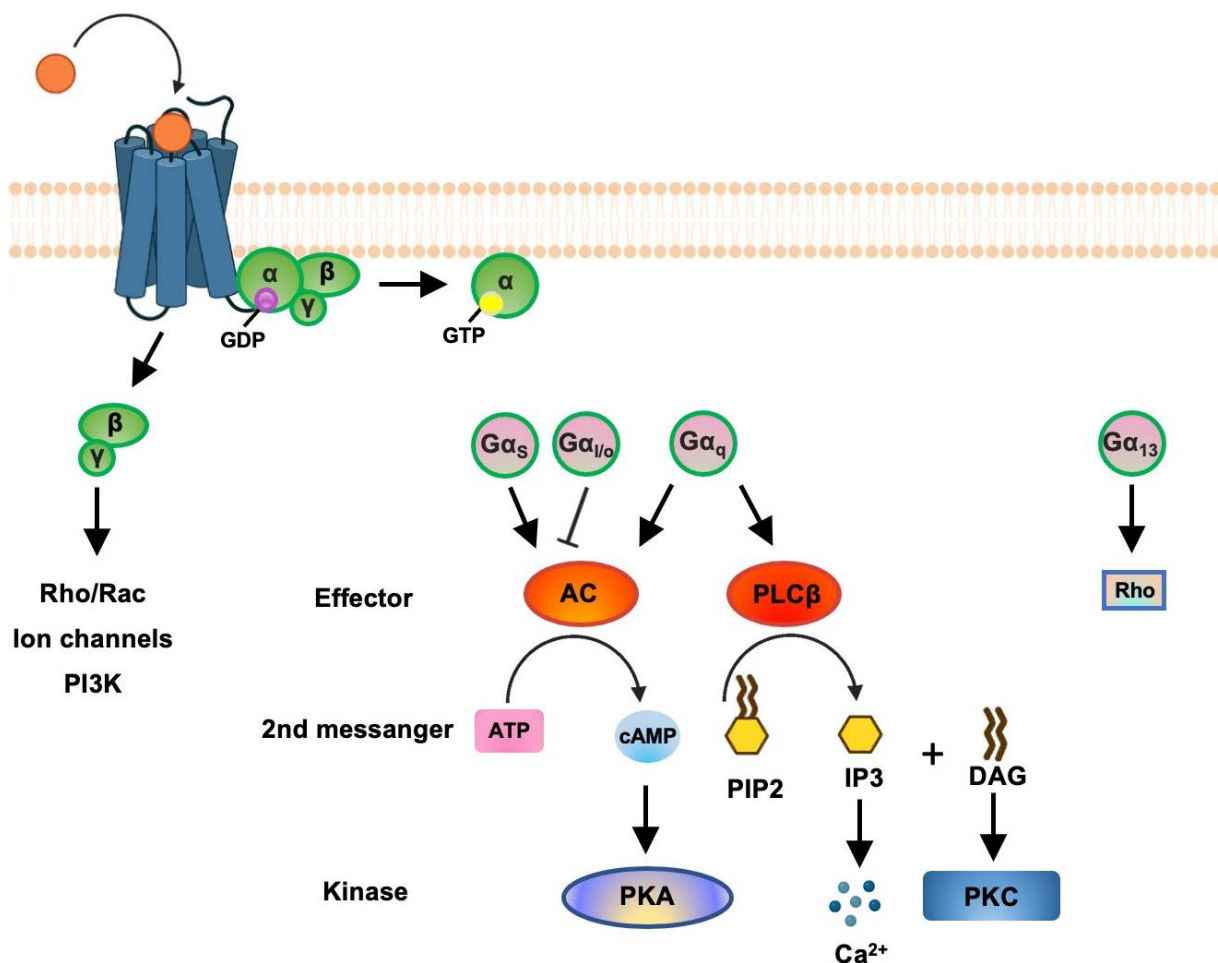


**Figure 2.3. G protein-coupled receptors ligand-gated signal through heterotrimeric G proteins.** Receptor activation catalyzes GDP dissociation that is bound to the  $G\alpha$  subunit. Subsequently,  $G\alpha$  can interact with GTP, which provokes the dissociation of  $\beta\gamma$  and  $\alpha$  subunits. Four families of  $G\alpha$  subunits ( $G\alpha_s$ ,  $G\alpha_{i/o}$ ,  $G\alpha_{q/11}$  and  $G\alpha_{12/13}$ ) exert different actions through multiple downstream effectors. Abbreviations: Guanosine diphosphate, GDP; Guanosine triphosphate, GTP; Adenosine triphosphate, ATP; Cyclic adenosine monophosphate, cAMP; Diacylglycerol, DAG; Phosphatidylinositol 4,5-bisphosphate, PIP<sub>2</sub>; Inositol 1,4,5-triphosphate, IP<sub>3</sub>; Protein kinase A/C, PKA/C; Phospholipase-C $\beta$ , PLC $\beta$ ; Adenylate cyclase, AC; Phosphatidylinositol-3 kinase, PI3K; Signal inhibition,  $\downarrow$ ; Signal activation,  $\downarrow$ . Original figure by Rosalba Sortino.

### 2.1.2 Modulation of GPCRs activity

Starting with the successful crystallization of the rhodopsin in 2000 and the  $\beta$ 2 adrenergic receptors in 2007, the breakthroughs in structural biology and crystallography contributed to unveil the precise structure of the receptors and understand the molecular basis of GPCR physiology, pharmacology and function<sup>32-34</sup>. Interestingly, GPCRs are highly dynamic structures rather than rigid entities, which is essential to fully understand the structural basis that underlies receptor activation<sup>35</sup>. These receptors pass through several three-dimensional arrangements, and thus, potentially inducing a different cellular response. Even in absence of an external stimulus, GPCRs are constantly in motion, including different active and inactive states. This results into the fact that they are constitutively active, which manifests in a basal level response. However, these conformational states can be characterized according to the signal each state transmits and the ligand responsible for the stabilization of that state. The advent of new techniques, such as the cryo-electron microscopy (cryo-EM), the advancements in nuclear magnetic resonance (NMR) spectroscopy together with the increasing of the computational power, help to deeper understand GPCR dynamics and function. The combination of these powerful methodologies promotes drug discovery towards the achievement of therapeutics depending on rational, structural based drug design<sup>36-39</sup>. In fact, the aim of modern chemical biology is to design new small molecules that selectively bind the target GPCR either as orthosteric, allosteric or as bitopic ligands, and modulate the pathway without side effects<sup>40</sup>.

Orthosteric ligands (either endogenous or exogenous, such as a substance or drug) bind to the endogenous ligand binding site, which is a pocket located on extracellular domain (ECD) or embedded within the TMD<sup>22</sup>. Full agonists bind to the receptors' orthosteric site with high affinity, causing a conformational change and subsequent receptor activation which leads to a cellular response. Partial agonists shift the receptor into its active conformation, but they have a lower efficacy and activate the receptor in a suboptimal manner. In contrast, the inverse agonists bind to the inactive state reducing the constitutive basal response. Although neutral antagonists bind to the receptor, they are not able to differentiate between an active or inactive conformation. Consequently, neutral antagonists do not change the cellular activity compared to basal levels (**Figure 2.4**)<sup>41-43</sup>.

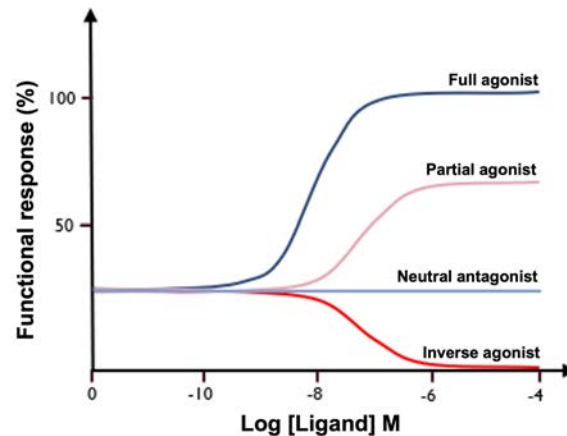


**Figure 2.4. Functional diversity of cellular response of a G protein-coupled receptors reflected by concentration-response-curves.** Full agonists induce a maximal response, while partial agonists mediate a submaximal activation at the receptor (< 100%) and their potency is also often reduced. Inverse agonists reduce the constitutive receptor activity. Neutral antagonists bind to the receptor blocking the binding site for other ligands, but do not differentiate between active or inactive state, thus leaving the basal level unchanged. Adapted from Ritter *et al.*, 2020<sup>44</sup>.

Traditionally, most drugs on the market are orthosteric ligands. However, the major problem of orthosteric drugs is their poor selectivity for specific GPCR subtypes. That is due to the high conservation of the orthosteric binding sites across homologous receptors<sup>45</sup>. In addition, these ligands mediate a persisting “all-or-nothing” response and are causing side effects, desensitization, and overdose risks.

In recent years, allosteric modulators have emerged as an alternative new approach of selectively modulating the GPCR activity<sup>46-49</sup>. These ligands bind to less highly conserved and topologically distinct (allosteric) sites from those utilized by orthosteric ligands, while they could influence the structure, dynamics, and function of GPCRs in multiple ways (**Figure 2.5A**)<sup>46,50-52</sup>. Allosterism is characterized by the underlying reciprocal effect between the two ligands, which is called cooperativity<sup>53-55</sup>. The allosteric ligands modulate the orthosteric signaling through the receptor by boosting or hampering affinity ( $\alpha$ ) and/or efficacy ( $\beta$ ) of the orthosteric ligand. The combined allosteric modulatory effects on the affinity and efficacy of the orthosteric ligand is named  $\alpha\beta$  or referred to as the functional cooperativity. In general, allosteric modulators are classified as: (a) positive allosteric modulator (PAM,  $\alpha\beta > 1$ ), (b) negative allosteric modulator (NAM,  $0 < \alpha\beta < 1$ ) or (c) neutral allosteric ligands (NAL,  $\alpha\beta = 1$ ), depending on their ability to increase, decrease, or not affect the affinity (**Figure 2.5AB**, red arrow/line) and/or efficacy (**Figure 2.5AB**, blue arrow/line) of the orthosteric ligand (**Figure 2.5AB**, black arrow/line)<sup>40,46,53,56</sup>. The magnitude and direction of an allosteric interaction may

vary with the nature of the orthosteric ligand, which is known as probe dependence<sup>51,57</sup>. Particularly, these modulators only exert a saturable effect in the presence of the orthoster, thereby providing a safer pharmacological profile than orthosteric ligands<sup>57,58</sup>. Moreover, several allosteric modulators possess an intrinsic efficacy ( $\tau_B$ ) and could perturb signaling even in absence of the orthosteric ligand in either a positive (ago-PAM) or negative (inverse agonists) way (**Figure 2.5AB**, green arrow/line)<sup>56,57</sup>. The  $\tau_A$  represents the intrinsic efficacy of a specific orthosteric ligand. This strategy of modulating GPCRs is hampered by the lack of knowledge regarding the location and structure of their allosteric sites<sup>48,54</sup>.

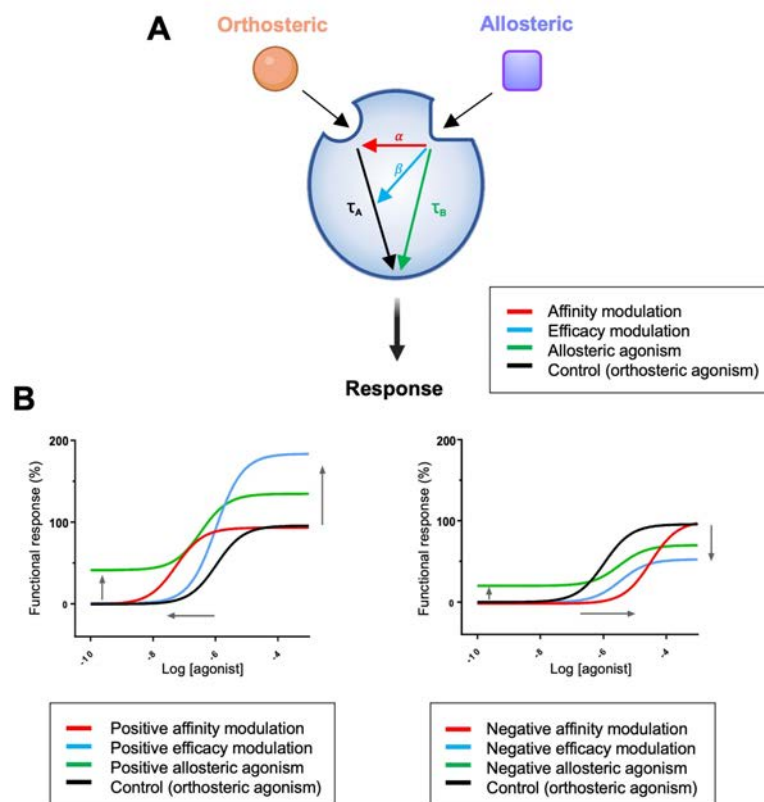
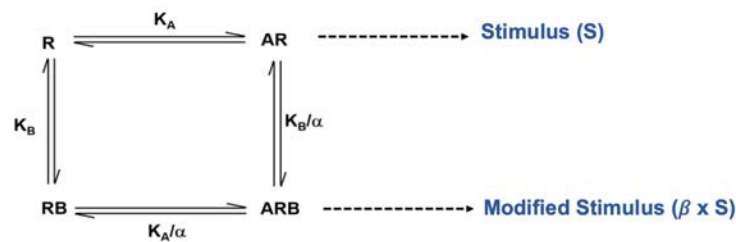


**Figure 2.5. The modes of action for allosteric modulators on G protein-coupled receptors.** (A) Allosteric ligands bind to the receptor at distinct binding sites than the orthosteric binding pocket. Although the allosteric binding sites are conformationally linked to the orthosteric pockets, they are structurally different. These ligands may either modulate the affinity ( $\alpha$ ) of the orthosteric ligand for the binding pocket (red arrow/line) or its efficacy ( $\beta$ ) by which it induces the receptor signaling (blue arrow/line). Several allosteric ligands directly induce a response ( $\tau_B$ ) (green arrow/line). (B) Simulations show the effects on the function of an orthosteric agonist mediated by six different allosteric modulators: the red ones increase (left) or decrease (right) orthosteric agonist affinity only; the blue ones increase (left) or decrease (right) orthosteric agonist efficacy only; the green ones modestly increase (left) or decrease (right) both affinity and efficacy, while displaying allosteric agonism. The positive cooperativity results in left shift of the concentration-response-curves (CRC) ( $\alpha\beta > 1$ ) and negative cooperativity is displayed by a right-shift of the CRC ( $0 < \alpha\beta < 1$ ). Adapted from Conn *et al.*, 2009<sup>59</sup>.

Studies of GPCR allosterism require analytical methods for application to experimental data to derive measures of modulator affinity and cooperativity<sup>46</sup>. The simplest model of GPCR allosteric interactions is the allosteric ternary complex model (ACTM) (**Figure 2.6A**), which assumes that the allosteric ligands modulate the affinity of the orthosteric ligand, with  $\alpha$  being the cooperativity factor and  $K_A$  and  $K_B$  the equilibrium dissociation constants of the orthosteric and allosteric ligands at the free receptor<sup>60-62</sup>. The operational model of allosterism and agonism describes the behavior of the allosteric modulators, in a more advanced way, including the allosteric agonism as well as the ability to modulate both affinity and efficacy (**Figure 2.6B**). In this model, two cooperativity parameters describe the cooperativity between the two interacting ligands,  $\alpha$  (affinity) and  $\beta$  (efficacy) and the parameters  $\tau_A$  and  $\tau_B$  denote the capacity of orthosteric and allosteric ligands, respectively, to exhibit agonism, and incorporate the intrinsic efficacy of each ligand<sup>56,57</sup>.

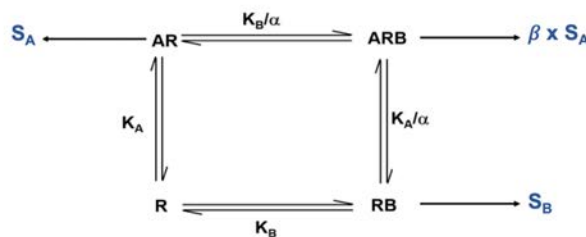
### A Allosteric ternary complex model



*Allosteric ternary complex model equation:*

$$E = \frac{[A] B_{\max}}{[A] + K_A \left( \frac{K_B + [B]}{K_B + \alpha[B]} \right)}$$

### B Operational model of allosterism and agonism



*Operational model of allosterism and agonism equation:*

$$E = \text{Basal} + \frac{(E_{\max} - \text{Basal})[A](K_B + \alpha\beta[B] + \tau_B[B]EC_{50})}{(EC_{50}(K_B + [B]) + ([A]K_B + \alpha\beta[B] + \tau_B[B]EC_{50}))}$$

**Figure 2.6. Allosteric G protein-coupled receptor-models.** (A) Allosteric ternary complex model in which  $K_A$  and  $K_B$  represent the equilibrium dissociation constants of an orthosteric ligand (A) and an allosteric ligand (B) for unoccupied receptors.  $S_A$  and  $S_B$  are the stimulus of the orthosteric and allosteric ligands, respectively. Cooperativity factor,  $\alpha$ , denotes the magnitude and direction of the allosteric effect on the ligand binding affinity.

$B_{\max}$  is the total number of receptors. **(B)** In the operational model of allosteric modulation and allosterism agonism  $K_A$  and  $K_B$  represent the equilibrium dissociation constants of an orthosteric ligand (A) and an allosteric ligand (B) for unoccupied receptors.  $S_A$  and  $S_B$  are the stimulus of the orthosteric and allosteric ligand, respectively.  $E_{\max}$  is the maximal possible response and Basal is the response in the absence of agonists.  $[A]$  and  $[B]$  are the concentrations of the orthosteric and allosteric ligands, respectively.  $EC_{50}$  is the concentration of orthosteric ligand required to achieve half maximal response. The  $\alpha$  and  $\beta$  denote the allosteric effect on the orthosteric ligand binding affinity and efficacy, respectively. The  $\tau_B$  denotes the efficacy of allosteric ligand on its own. Adapted from Lindsley *et al.*, 2016 and Leach *et al.*, 2007<sup>56,62</sup>.

Another class of ligands has been introduced to overcome the drawback of poor subtype selectivity that is represented by dualsteric ligands (*i.e.*, bitopic orthosteric/allosteric)<sup>58,63-65</sup>. These ligands contain two different pharmacophores that are connected by a linker, which allows simultaneous binding to both the orthosteric and the allosteric binding site. These ligands could be designed as (inverse) agonists or antagonist connected to PAMs or NAMs. Therefore, the dualsteric ligands benefit from the advantages of orthosteric and allosteric compounds by combining higher affinity and subtype selectivity, respectively (**Figure 2.7**)<sup>66,67</sup>.

In line with the concept that GPCRs can adopt multiple conformations, the orthosteric, allosteric or bitopic ligands could stabilize distinct receptor conformations. This may bias the resulting stimulus, thus selecting specific signaling pathways and the exclusion of others<sup>48,68</sup>. This phenomenon is called biased agonism, functional selectivity or stimulus bias, which is another mode to attain the selectivity of drug action at GPCRs<sup>69,70</sup>. The bias modulation provides a possibility of creating drugs that stimulate desirable signaling pathways without stimulating harmful ones and, thus, dramatically reducing drug side effects and safety issues<sup>71</sup>.

	Orthosteric	Allosteric	Bitopic
<i>Defined SAR</i>	✓	✗	✗
<i>High affinity</i>	✓	✗	✓
<i>Subtype selectivity</i>	✗	✓	✓
<i>Biased signaling</i>	✓	✓	✓

**Figure 2.7. General observed trends for orthosteric, allosteric and bitopic ligands.** Abbreviation: Structure-activity relationship, SAR. Adapted from Kruse *et al.*, 2014<sup>72</sup> and from Fronik *et al.*, 2017<sup>66</sup>.

## 2.2 Neurotransmission

The human brain is the most complex organ of the body. Comprehending the chemistry of the brain is a prerequisite for the understanding of its functions and their pathological alterations. All the operations carried by the billions of neuronal cells and synapses are bound together by chemical signals which mediate information processing in the brain from the molecular to the cognitive level<sup>73</sup>. This fundamental process that drives information transfer between neurons and their targets is called neurotransmission. Neurons produce and release molecules referred to as neurotransmitters, such as acetylcholine (ACh), glutamate and dopamine (DA), which control multiple vital functions<sup>74</sup>. These molecules are sent from one cell to another in small packages that deliver their cargo to the right place at the right time in the brain. The central nervous system (CNS) consists of the brain and the spinal cord, whereas the peripheral nervous system (PNS) refers to neurons and ganglia that are located outside the brain and the spinal cord. The PNS is divided in a somatic (*i.e.*, voluntary) and autonomic (*i.e.*, involuntary) nervous system. The latter is divided in the sympathetic, parasympathetic, and enteric nervous systems.

### 2.2.1 Acetylcholine

In 1936, ACh was demonstrated to be synthesized in the brain and was the first substance to be identified as a neurotransmitter<sup>75,76</sup>. This neurochemical is the most abundant neurotransmitters in CNS and PNS and is synthesized from choline and the precursor acetyl coenzyme A (acetyl-CoA) by choline acetyltransferase (ChAT), an enzyme primarily expressed in cholinergic neurons (**Figure 2.8**)<sup>77</sup>. Choline is present at high plasma concentrations (~10  $\mu$ M) and enters the nerve terminals via the choline transporter 1 (CHT1), whereas acetyl-CoA is derived from glucose<sup>78</sup>. The newly synthesized ACh is taken up into synaptic vesicles through the vesicular acetylcholine transporter (VAChT) and is released upon depolarization of the cholinergic neuron in the synaptic cleft. This neurotransmitter has been described to modulate important CNS functions, such as stress response, sleep, sensory processing, cognition, and motor control.

The postsynaptic actions are mediated through the activation of two receptor families, the muscarinic ACh receptors (mAChRs or MRs) or ionotropic nicotinic ACh receptors (nAChRs)<sup>79</sup>. Finally, the synaptic cleft contains acetylcholinesterase (AChE), which hydrolyses ACh to acetate and choline, thus terminating the postsynaptic actions of the neurotransmitter. Then, choline is transported back in the presynaptic nerve terminals and synthesized into ACh again<sup>78</sup>.



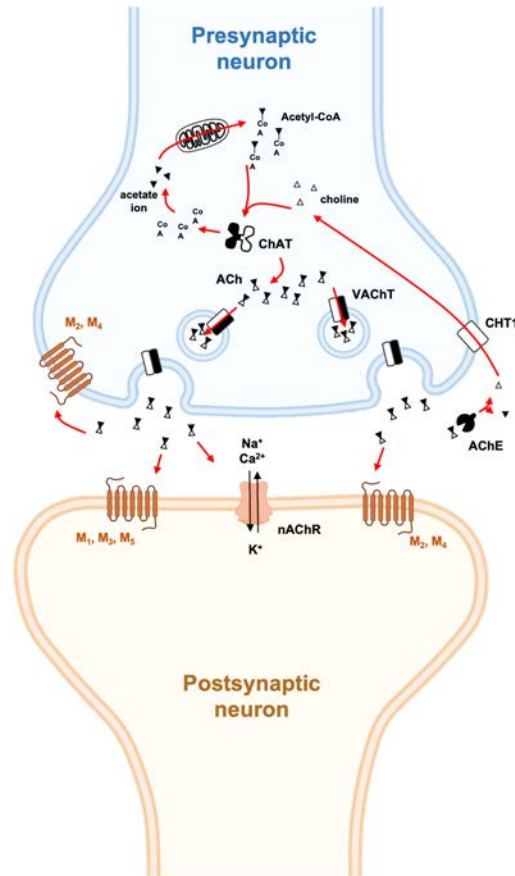


**Figure 2.8. Acetylcholine synthesis in the cholinergic nerve terminals.** The synthesis of acetylcholine (ACh) from choline and acetyl coenzyme A (acetyl-CoA) requires choline acetyltransferase (ChAT). Acetyl-CoA is derived from pyruvate generated by glycolysis, whereas choline is transported into the terminals via the choline transporter 1 (CHT1). ACh is taken up into synaptic vesicles by the vesicular ACh transporter (VAcHT). After release, ACh is metabolized by acetylcholinesterase (AChE) to choline and transported back in the presynaptic nerve terminal. Original figure by Rosalba Sortino.

### 2.2.1.1 Muscarinic acetylcholine receptors

In the synaptic cleft, ACh acts at neuronal cells expressing mAChRs and/or nAChRs. The latter are ligand-gated non-selective cation channels, which consist of a pentamer made by a combination of 12 subunits ( $\alpha_{2-10}$  and  $\beta_{2-4}$ ). The most abundant subtypes are the heteromeric  $\alpha_4\beta_2$  and homomeric  $\alpha_7$  nAChRs. These channels are predominantly located at presynaptic nerve terminals and their activation results in neuronal activity, followed by release of a neurotransmitter<sup>80</sup>. The mAChRs belong to the class A members of the GPCR superfamily (described in section 2.1) and are widely expressed through the CNS and PNS<sup>1,81</sup>. Together with nAChRs, they mediate many of the diverse effects of the endogenous agonist ACh. For instance, they control a plethora of physiological effects, such as neuronal, cardiac, and digestive functions, which bestow them with a highly relevant role as therapeutic drug targets<sup>72</sup>.

The name of these receptors refers to their specific sensitivity to muscarine, a poisonous alkaloid from certain mushrooms (**Figure 2.9**) which helped distinguishing them from nicotine-activated nAChRs. Based on molecular cloning and pharmacological studies, mAChRs are divided in five distinct subtypes ( $M_1R$ - $M_5R$ )<sup>82</sup>. All five subtypes have a central role in human physiology and defined functions in both CNS and PNS. Being expressed throughout the body in an overlapping fashion, their physiological effects are based on the location and the specific identity of these receptors (**Table 2.2**)<sup>81,83,84</sup>.

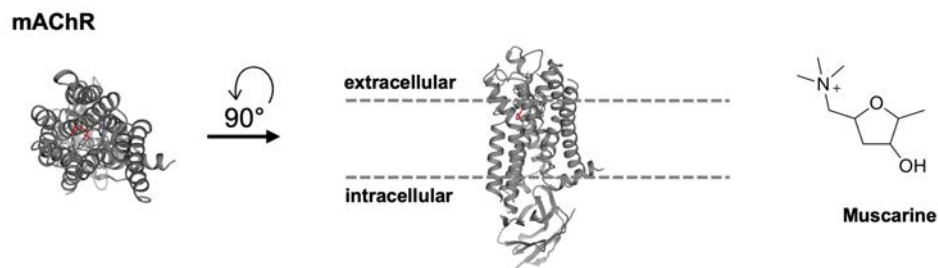


**Figure 2.9. Muscarinic acetylcholine receptors and the chemical structure of muscarine.** The mAChR (PDB ID: 4MQT) shown in side- and top-view (from the extracellular side) and structure of muscarine on the right.

### 2.2.1.1.1 $M_1$ -like receptors

Being expressed at the postsynaptic membrane, the  $M_1$ -like receptors ( $M_1R$ ,  $M_3R$  and  $M_5R$ ) are coupled to  $G_{\alpha_{q/11}}$  proteins, which lead to the activation of  $PLC\beta$  and  $Ca^{2+}$  influx following receptor stimulation (**Figure 2.10** and see section 2.1.1). In addition to the canonical pathway,  $M_1$ -like receptors can activate multiple signal transduction pathways, depending on the cell type. For instance, they can regulate phospholipase A2, phospholipase D2 and  $Ca^{2+}$  channels.

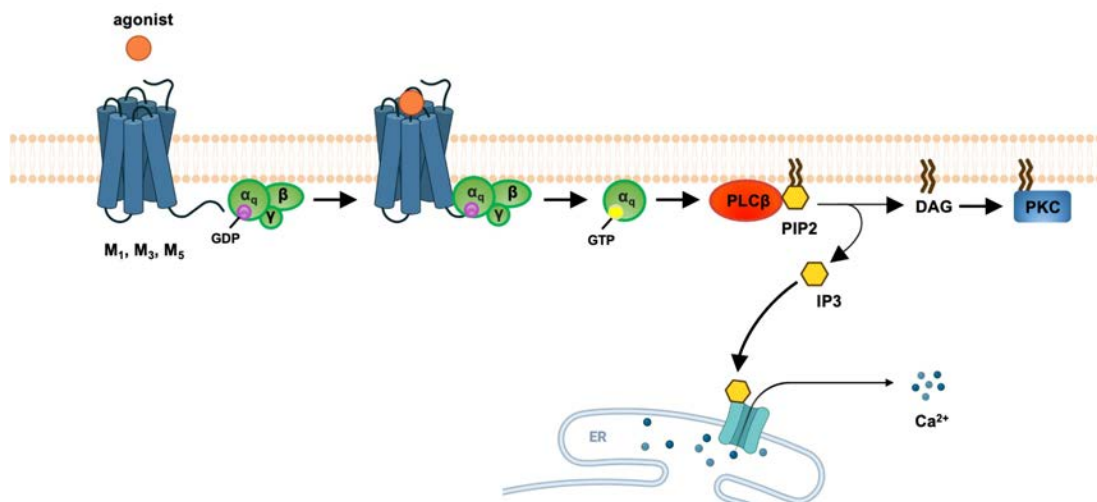


**Figure 2.10. Signaling specificity of the  $M_1$ -like receptors.**  $G_{\alpha_{q/11}}$  leading mainly to cytosolic calcium efflux specific for odd-membered receptors. Original figure by Rosalba Sortino.

Category	GPCR	CNS expression	Localization	G protein (main signaling)	PNS expression	Functions
<b>M<sub>1</sub>-like</b>	M <sub>1</sub> R	<u>High levels</u> Cortex, hippocampus <u>Levels</u> Striatum and thalamus	Postsynaptic	G $\alpha_q$ ( $\uparrow$ IP <sub>3</sub> , $\uparrow$ intracellular Ca <sup>2+</sup> , $\uparrow$ DAG, activation of PKC and MAPK pathway)	Autonomic ganglia, salivary glands, secretory glands, prostate and NMJ	Agonist-induced seizure, learning, memory, control of motor activity, indirect inhibition of N- and L-type calcium channels, MAPK pathway activation and modulate ACh release at the NMJ
	M <sub>3</sub> R	<u>Low levels</u> Cortex, hippocampus, and striatum			Gastrointestinal tract, glands, lung, pancreas, bladder, prostate, testis and NMJ	Papillary and urinary bladder contraction, salivary secretion, smooth muscle contraction, control of DA release and maintenance of body mass and food intake
	M <sub>5</sub> R	<u>Very low levels</u> Hippocampus, SN and VTA			Lung, bladder, and testis	Vasodilation of cerebral blood vessels and DA release
<b>M<sub>2</sub>-like</b>	M <sub>2</sub> R	<u>High levels</u> Nucleus basalis and occipital cortex <u>Lower levels</u> Hippocampus, striatum, thalamus, and other cortical regions	Presynaptic  (+ Postsynaptic)	G $\alpha_{i/o}$ ( $\downarrow$ cAMP, inhibition of Ca <sup>2+</sup> channels, activation of GIRK channels and MAPK pathway)	Heart, gastrointestinal tract, bladder, submandibular glands	Smooth muscle contraction, bradycardia, inhibition of N- and P/Q-type calcium channels, corticosterone release, modulate ACh release at the NMJ, pain perception and body temperature
	M <sub>4</sub> R	<u>High levels</u> Striatum <u>Lower levels</u> Cortex, hippocampus, thalamus, and midbrain	Bladder and testis		DA release, ACh release ( <i>i.e.</i> , in hippocampus), depression of motor control and analgesia	

**Table 2.2. Key features of muscarinic acetylcholine receptors in the central and peripheral nervous system.** Abbreviations: Substantia nigra, SN; Ventral tegmental area, VTA; 3',5'-cyclic adenosine monophosphate, cAMP; Mitogen-activated protein kinase, MAPK; Inositol 1,4,5-trisphosphate, IP<sub>3</sub>; G protein-coupled inwardly rectifying potassium channels, GIRK channels; Neuromuscular junction, NMJ; Acetylcholine, ACh; Dopamine, DA. Adapted from Langmead *et al.*, 2008, Scarr *et al.*, 2011 and Lebois *et al.*, 2018<sup>79,85,86</sup>.

The M<sub>1</sub>Rs constitute 50-60% of the total mAChRs in the brain and have pivotal roles in functions as motor control, attention, memory, and sleep-wake cycle regulation<sup>87,88</sup>. The M<sub>1</sub>R is predominantly expressed in the hippocampus and cortex. Moreover, substantial expression levels are found in the striatum and thalamus<sup>79,85</sup>. Therefore, the M<sub>1</sub> subtype has been identified as a key receptor for physiological brain functions such as neuronal excitability, synaptic plasticity, learning and memory processes and thereby holds immense therapeutic relevance for a variety of cognitive and neurodegenerative diseases such as schizophrenia (SZ), Parkinson's Disease (PD), and Alzheimer's Disease (AD)<sup>50,89-92</sup>. This receptor is also expressed peripherally in prostate, autonomic ganglia, and secretory glands. Importantly, M<sub>1</sub>R together with M<sub>2</sub>R act as presynaptic autoreceptors to regulate the ACh release at the neuromuscular junction<sup>93</sup>. The M<sub>3</sub>R is expressed in the cortex, striatum, and hippocampus, but at lower levels than the M<sub>1</sub>R and M<sub>2</sub>R<sup>79,85,89,94</sup>. This muscarinic subtype is found in gastrointestinal tract, lung, glands, pancreas, bladder, prostate, and testis as well<sup>86</sup>. The M<sub>5</sub>R represents less than 2% of the total mAChR population and is restricted to the substantia nigra (SN), ventral tegmental area (VTA) and hippocampus<sup>95</sup>. Additionally, this receptor is related to DA release and is located within the endothelium of the cerebral vasculature, where it modulates vasodilation<sup>96,97</sup>.

### 2.2.1.1.2 M<sub>2</sub>-like receptors

The M<sub>2</sub>-like receptors (M<sub>2</sub>R and M<sub>4</sub>R) are coupled to G $\alpha_{i/o}$  proteins and inhibit AC following receptor stimulation (**Figure 2.11**, see also section 2.1.1), but they could activate phospholipase A<sub>2</sub> as well.

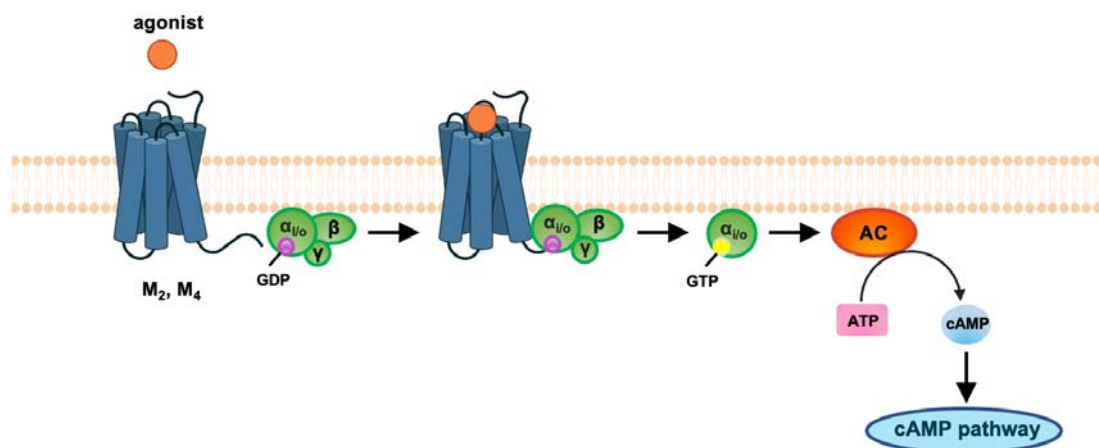


**Figure 2.11. Signaling specificity of the M<sub>2</sub>-like receptors.** G $\alpha_{i/o}$ -pathway leading mainly to a reduction of cAMP and related cellular responses. Original figure by Rosalba Sortino.

These GPCRs are cell type specifically located at the pre- and postsynaptic membranes<sup>85,98</sup>. M<sub>2</sub>R are abundantly distributed in both the CNS and the periphery<sup>99</sup>. In the CNS expression levels of M<sub>2</sub>R are present in the occipital cortex and nucleus basalis, striatum, hippocampus, and other cortical brain regions and are associated with body temperature regulation and pain perception. In the cortex, this subtype is expressed both pre- and postsynaptically<sup>100</sup>. In the axons of symmetric synapses, the M<sub>2</sub>R maintains a role as autoreceptor and is located at presynaptic nerve terminals. In the PNS, M<sub>2</sub> mAChRs are predominantly found in the myocardium, where they are proven to regulate heart rate, but also in the gastrointestinal tract, bladder and submandibular gland<sup>86</sup>. Together with M<sub>3</sub>R, the M<sub>2</sub>Rs are involved in muscle contractions, due to their presence in smooth muscle and skin tissues<sup>81,84</sup>. High concentrations of M<sub>4</sub>R are predominantly found in the striatum, where they are expressed at the dopaminergic-projecting neurons, as well as at GABAergic medium spiny neurons, thereby controlling the release of DA and locomotor activity<sup>101</sup>. In addition, these mAChRs are also present in brain regions as the cortex and hippocampus. In the periphery, the M<sub>4</sub>R has been found in bladder and testis<sup>86</sup>.

The last decades of research unraveled a lot of knowledge about the diverse functions of the mAChRs. However, the complex roles of muscarinic receptors need further studies to be completely understood.

### 2.2.1.2 Muscarinic ligands

Breakthroughs in X-ray crystallography and cryo-EM have led to determine the inactive state structures for all five mAChR subtypes. Moreover, those techniques have revealed the active state structures of the M<sub>1</sub>R and M<sub>2</sub>R associated with their G protein (*i.e.*, M<sub>1</sub> mAChR-G $\alpha_{11}$  and M<sub>2</sub> mAChR-G $\alpha_{o/A}$  complexes)<sup>96,102-105</sup>. The M<sub>2</sub> mAChRs have been solved in six different inactive states, including structures with this receptor bound to the non-selective ligands 3-quinuclidinyl benzilate (QNB), N-methyl scopolamine (NMS) and the selective ligand AF DX384<sup>96,106</sup>. In addition, the active co-bound conformation of M<sub>2</sub>R was presented with the high-affinity agonist iperoxo (IPX) and a PAM in a complex with a G protein mimetic nanobody and  $\beta$ -arrestin<sup>107,108</sup>. A recent NMR study at the M<sub>2</sub> mAChR revealed that each agonist stabilized different conformations of the M<sub>2</sub>R, providing new insights into the mechanism of ligand-receptor interaction<sup>109</sup>. The crystal structures of M<sub>1</sub>R, M<sub>3</sub>R, M<sub>4</sub>R, and M<sub>5</sub>R in their inactive-state with the antagonist tiotropium and the M<sub>2</sub> mAChR with NMS (*i.e.*, most similar to the tiotropium-bound in mAChR structures) allowed a complete subtype-wide

comparison and provided insights for the design of subtype selective mAChR ligands<sup>96,102-104</sup>. The confrontation of these crystal structures confirmed that the five mAChRs share similar features, including the 7TM topology and overall receptor fold, with the orthosteric binding pocket lying deep within the TM regions (**Figure 2.12A**). This revealed a high similarity of their orthosteric binding sites (**Figure 2.12A**, small rectangle). In particular, the amino acids that contact the antagonist are highly conserved across all the subtypes<sup>96,104</sup>. Therefore, the development of muscarinic subtype-specific agonists and antagonists that specifically target the mAChR orthosteric-binding site are extremely difficult<sup>104</sup>. Although the high degree of amino acid sequence conservation within the mAChR orthosteric binding site, several differences were observed in the ECL regions, which are the least conserved across these receptors and a major determinant in the ligand selectivity (*i.e.*, regarding the ligand being orthosteric or allosteric) (**Figure 2.12A**, big rectangle)<sup>96</sup>. Interestingly, mAChRs possess an extracellular vestibule (ECV) in their ligand-binding cavities together with an allosteric site (**Figure 2.12B**)<sup>51</sup>. This allosteric binding site is located  $\sim 15$  Å above the orthosteric binding site, defined by residues predominantly located at the top of TM2, TM7 and within ECL2<sup>110</sup>. Importantly, three tyrosine residues separate the ECV from the orthosteric-binding pocket, hindering the ligand to dissociate from the receptor and, thus, increasing the affinity for the orthosteric ligand<sup>102,108</sup>. The low degree of amino acid sequence conservation in the ECV shapes this location as an attractive target for the development of subtype selective allosteric modulators<sup>51</sup>. In fact, numerous PAMs and NAMs have been discovered that target the ECV, resulting in the ECV being labeled as a “common” allosteric site for mAChRs<sup>111-114</sup>. The majority of the first discovered mAChR allosteric modulators, (*e.g.*, gallamine and alcuronium) bind to this “common” allosteric site<sup>72,96,104,110</sup>.

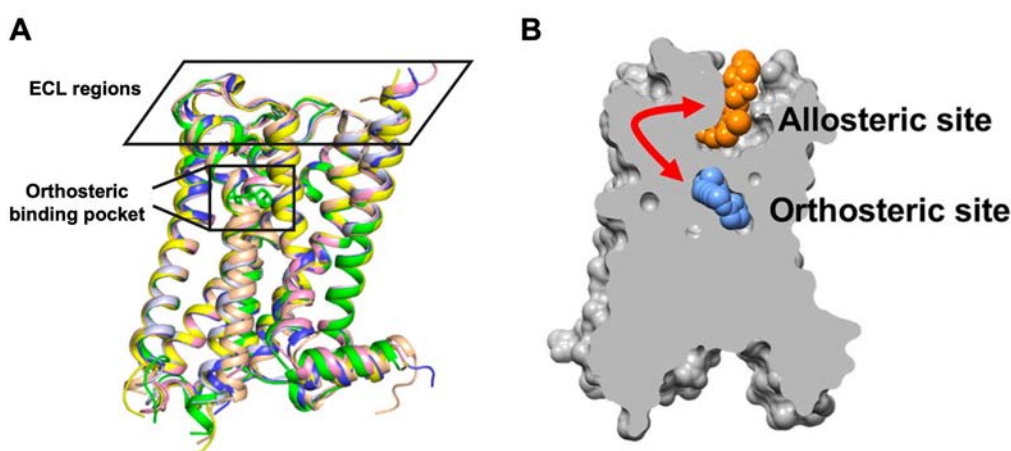


**Figure 2.12. Structural comparison of M<sub>1</sub>R to M<sub>5</sub>R and location of the orthosteric and allosteric binding sites.** (A) The overall view of the M<sub>1</sub>R to M<sub>5</sub>R structures aligned and shown as a cartoon. M<sub>1</sub>-tiotropium is colored

in peach (PDB ID: 5CXV), M<sub>2</sub>-NMS in dark blue (PDB ID: 5ZKC), M<sub>2</sub>-AF-DX384 in yellow (PDB ID: 5ZKB), M<sub>3</sub>-tiotropium in light blue (PDB ID: 4U15), M<sub>4</sub>-tiotropium in pink (PDB ID: 5DSG) and M<sub>5</sub>-tiotropium in green (PDB ID: 6OL9). The orthosteric binding pocket and the ECL regions are highlighted with rectangles. **(B)** Topology of the orthosteric binding site compared to the allosteric binding site. The orthosteric binding site is located more towards the inner core of the receptor, while the allosteric site is oriented outside being part of the extracellular vestibule (ECV). In the active conformation, the orthosteric site is separated from the allosteric binding site by the tyrosine lid. Adapted from Vuckovick *et al.*, 2019<sup>96</sup> and Burger *et al.*, 2018<sup>51</sup>.

Interestingly, recent studies have been focused on the identification of a second mAChRs allosteric site<sup>115,116</sup>. Although molecular docking studies suggest that the site may be in the intracellular domain of the M<sub>1</sub>R, its exact location and the residues involved remains still unknown<sup>117,118</sup>. Overall, these molecules exhibit pronounced selectivity upon a distinct subtype. The figures below display a selection of the most important allosteric modulators (**Figure 2.13**), agonists and antagonists (**Figure 2.14**) that are relevant for this thesis. Importantly, further knowledge on the underlying allosteric mechanisms may lead to significant breakthroughs regarding subtype selectivity and, hence, therapeutic relevant candidates, which may also be applied to other GPCRs<sup>57</sup>.

### Allosteric modulators

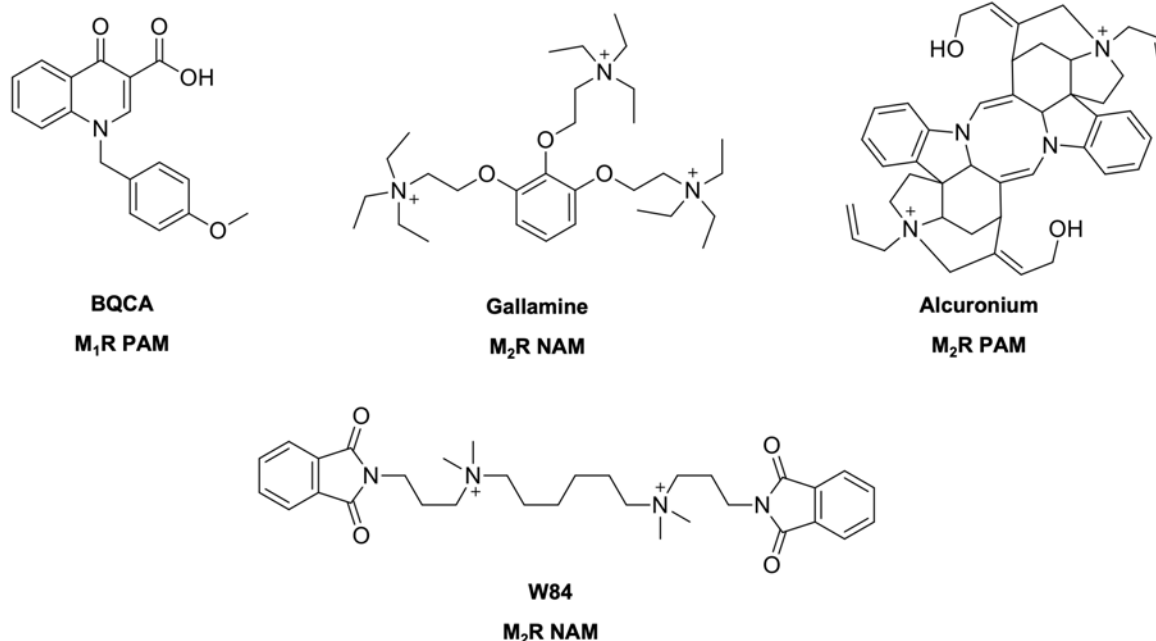
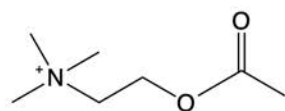
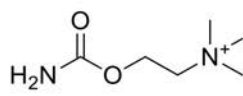


Figure 2.13. Selection of allosteric modulators of muscarinic receptors.

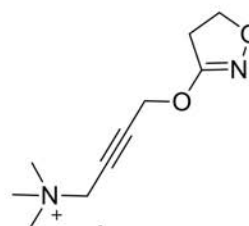
## agonists



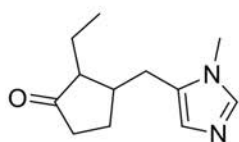
**Acetylcholine**  
Endogenous neurotransmitter



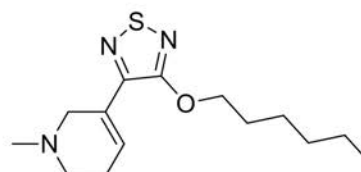
**Carbachol**  
non-selective agonist



**Iperoxo**  
 $M_2R$  superagonist

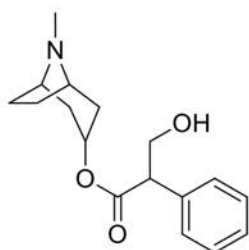


**Pilocarpine**  
non-selective partial agonist

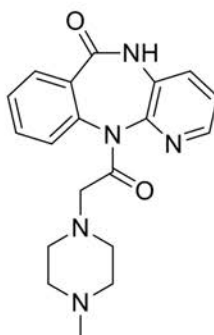


**Xanomeline**  
 $M_1R$  partial agonist

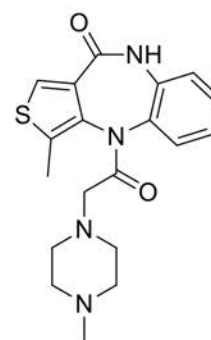
## antagonists



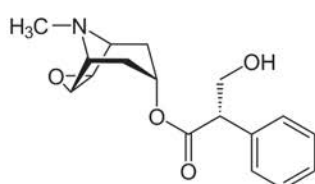
**Atropine**  
non-selective antagonist



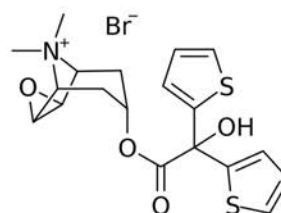
**Pirenzepine**  
 $M_1R$  antagonist



**Telenzepine**  
 $M_1R$  antagonist



**N.-metil scopolamine**  
non-selective antagonist



**Tiotropium bromide**  
non-selective antagonist

Figure 2.14. A selection of important agonists and antagonists for the muscarinic receptors.

Dualsteric ligands have mostly been investigated for  $M_1R$ s and  $M_2R$ s and each shows a notable preference for a receptor subtype, while preserving (partial) agonistic activity. It has also been observed that the length and nature of the linker must be taken under consideration, as these properties substantially contribute to the receptors binding mode<sup>119</sup>. For a complete list of allosteric modulators and dualsteric ligands see Bock *et al.*, 2018<sup>50</sup>.



### 2.2.2 Dopamine

DA was synthesized for the first time by George Barger and James Ewens at the Wellcome Laboratories in 1910. At about the same time, Henry Dale defined the biological activity of DA as a weak sympathomimetic<sup>120</sup>. Many years later, he suggested the name DA for 3,4-dihydroxyphenylethylamine, or shorter 3-hydroxytyramine, instead. Remarkably, DA was considered as an intermediate in the biosynthesis of adrenaline and noradrenaline until the mid-1950s. The perception about DA changed after this catecholamine showed vasodepressive effects and high concentrations were identified in the striatum<sup>121,122</sup>. In subsequent years, important findings in DA research followed and yielded great scientific rewards and clinical benefits<sup>123,124</sup>.

The catecholamine DA acts as a neurotransmitter in both the PNS as well as the CNS. DA is involved in many important brain functions, including reward, feeding, affection, sleep, attention, voluntary movement, learning, and working memory<sup>125</sup>. In the periphery, DA modulates cardiovascular function, hormonal regulation, renal functions, among others. The neurotransmitter is predominantly synthesized in DA-producing neurons because it is unable to cross the blood brain barrier (BBB). The biosynthesis of DA starts by L-tyrosine, a non-essential amino acid, which may be obtained by the conversion of L-phenylalanine an essential amino acid, into L-tyrosine in the liver through the action of phenylalanine hydroxylase (PH)<sup>126</sup>. The L-tyrosine is transported from the extracellular fluid (ECF) into dopaminergic neurons, producing DA via two enzymatic pathways (**Figure 2.15**).

In the first pathway, the L-tyrosine is converted into L-3,4-dihydroxyphenylalanine (L-DOPA) by cytosolic tyrosine hydroxylase (TH), which requires O<sub>2</sub>, Fe<sup>2+</sup> and tetrahydrobiopterin as cofactors<sup>127</sup>. After that rate-limiting step, L-DOPA is converted into DA by L-amino acid decarboxylase (AADC), which acts on all naturally occurring aromatic L-amino acids<sup>128</sup>. Alternatively, DA can be synthesized by a minor pathway: first the AADC converts L-tyrosine in tyramine, which is then hydroxylated to DA via Cytochrome P450 2D6 (CYP2D6), an enzyme expressed in the SN as well as in the liver<sup>129</sup>. After the synthesis, the neurotransmitter is taken up by storage vesicles by the vesicular monoamine transporters 1 and 2 (VMAT1 and VMAT2, respectively), which also transports serotonin (5-hydroxytryptamine; 5-HT), histamine, adrenaline, and noradrenaline<sup>130</sup>. VMAT1 is found in neuroendocrine cells, whereas VMAT2 is predominantly expressed in neurons.

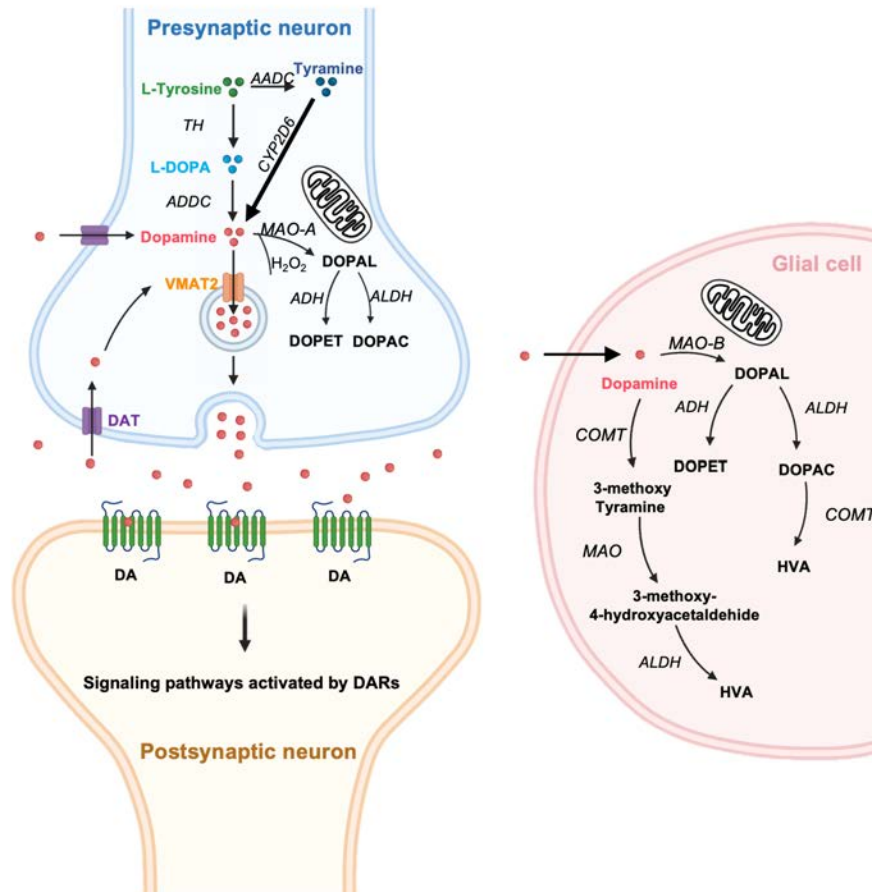


**Figure 2.15. Dopamine synthesis and degradation pathways.** The L-tyrosine is transported from the extracellular fluid into dopaminergic neurons, producing DA via two enzymatic pathways. In the first pathway, the L-tyrosine is converted into L-3,4-dihydroxyphenylalanine (L-DOPA) by cytosolic tyrosine hydroxylase (TH) and finally to DA by L-amino acid decarboxylase (ADDC). Alternatively, dopamine could be synthesized from tyramine by Cytochrome P450 2D6 (CYP2D6). The newly synthesized or taken up by DA transporter (DAT) is stored in vesicles with the aid of vesicular monoaminergic transporter 2 (VMAT2). Following an action potential to a synaptic neuron, DA in synaptic vesicles is released into the synaptic cleft and bind to DA receptors. Finally, the neurotransmitter DA is degraded into the inactive metabolites homovanillic acid (HVA), 3,4-dihydroxyphenylacetic acid (DOPAC) and 3,4-dihydroxyphenylethanol (DOPET) via enzymatic reactions mediated by predominantly monoamine oxidase (MAO), catechol-O-methyl transferase (COMT), aldehyde dehydrogenase (ALDH) and alcohol dehydrogenase (ADH). Original figure by Rosalba Sortino.

Upon arrival of the action potential generated from the soma at the presynaptic terminals, the vesicles are fused with the membrane and DA is released in the synaptic cleft<sup>131</sup>. The exocytosis is initiated by an influx of  $\text{Ca}^{2+}$  ions into the cytosol via voltage-gated  $\text{Ca}^{2+}$  channels, or in dopaminergic terminals through  $\text{Ca}^{2+}$  N- and P/Q-type channels. The amount of DA release appears to be dependent on the burst of action potentials and varies between low frequency “tonic” firing and higher frequency “phasic” firing, encoding for different behavioral information<sup>132</sup>. Once DA is in the synaptic cleft, it activates various DA receptors (DARs, see

section 2.2.2.1). At the end, the neurotransmitter is actively pumped back into the neurons by DA transporters (DATs) and DA is sequestered by VMAT2 into synaptic vesicles<sup>133</sup>. Of note, DA reuptake is fundamental for terminating its actions and maintaining a homeostasis. The DA leaking from synaptic vesicles accumulates in the cytosol and is degraded by monoamine oxidase (MAO). Interestingly, MAO has two subunits (*i.e.*, MAO-A and MAO-B), while glial cells contain MAO-B, MAO-A is present in catecholaminergic neurons<sup>134,135</sup>. However, DA in the synaptic cleft could be taken up by surrounding glial cells and degraded by two pathways, both having homovanillic acid (HVA) as a major end product (**Figure 2.15**). In one pathway, MAO catalyzes oxidative deamination and produces hydrogen peroxide and 3,4-dihydroxyphenylacetaldehyde (DOPAL)<sup>136</sup>. Then, DOPAL is reduced to inactive 3,4-dihydroxyphenylethanol (DOPET) by alcohol dehydrogenase (ADH) or further oxidized to 3,4-dihydroxyphenylacetic acid (DOPAC) by aldehyde dehydrogenase (ALDH)<sup>134,137</sup>. Finally, DOPAC is degraded to HVA via catechol-O-methyl transferase (COMT), which is secreted by glial cells. However, catecholaminergic neurons may have very low levels of this enzyme or even lack them<sup>135</sup>. Alternatively, COMT converts DA to 3-methoxytyramine (3-MT), which is converted by MAO to 3-methoxy-4-hydroxyacetaldehyde and later reduced to HVA<sup>127</sup>. In both pathways, HVA is excreted through the urine<sup>128</sup>.

### 2.2.2.1 Dopamine receptors

In the synaptic cleft, DA elicits its effect by the activation of five distinct DA receptors (D<sub>1</sub>R-D<sub>5</sub>R), which are class A GPCRs (see section 2.1). Based on structural, biochemical, physiological, and pharmacological characteristics, these receptors are categorized in D<sub>1</sub>-class receptors (*i.e.*, D<sub>1</sub>R and D<sub>5</sub>R) and D<sub>2</sub>-class receptors (*i.e.*, D<sub>2</sub>R, D<sub>3</sub>R and D<sub>4</sub>R), see **Table 2.3**<sup>138,139</sup>. Although within both classes there is a high degree of similarity in the primary amino acid sequences of their TMDs, each DAR has specific pharmacological properties. Overall, the D<sub>1</sub>R and D<sub>5</sub>R are 80% homologous, whereas the D<sub>3</sub>R and D<sub>4</sub>R are 75% and 53% homologous with D<sub>2</sub>R, respectively. Structurally, the DARs have similar numbers of amino acids at the extracellular NTD, whereas the intracellular CTD is about seven times larger in D<sub>1</sub>-class receptors than in D<sub>2</sub>-class receptors<sup>140,141</sup>.

Category	GPCR	CNS expression	Localization	G protein (main signaling)
<b>D<sub>1</sub>-class</b>	D <sub>1</sub> R	<u>High levels</u> SN, NAc, striatum, amygdala, TO and cortex	Postsynaptic	G $\alpha_{s/olf}$ ( $\uparrow$ cAMP, activation of ion channels, MAPK and DARPP-32, inhibition of PP1) +
		<u>Lower levels</u> Thalamus, hippocampus, hypothalamus, and cerebellum		
<b>D<sub>2</sub>-class</b>	D <sub>2</sub> R	<u>Low levels</u> SN, hypothalamus, cortex, and hippocampus	Presynaptic and postsynaptic	G $\alpha_q$ ( $\uparrow$ IP <sub>3</sub> , $\uparrow$ intracellular Ca <sup>2+</sup> , $\uparrow$ DAG, PKC activation)
		<u>Very low levels</u> NAc, dorsal striatum and TO		
	D <sub>3</sub> R	<u>Highest levels</u> TO, NAc and islands of Calleja	G $\alpha_{i/o}$ ( $\downarrow$ cAMP, inhibition of DARPP-32, activation of PP1)	
<b>D<sub>4</sub>-class</b>	D <sub>4</sub> R	<u>Low levels</u> VTA, SNpc, striatum, hippocampus, septum and cortex	Presynaptic and postsynaptic	G $\beta\gamma$ ( $\uparrow$ intracellular Ca <sup>2+</sup> , inhibition of L/N type Ca <sup>2+</sup> channels, activation of GIRK channels)
		<u>Low levels</u> Amygdala, cortex, hippocampus, hypothalamus, GP, SNpr and thalamus		

**Table 2.3. Key features of dopamine receptors in the central nervous system.** Abbreviations: Nucleus accumbens, NAc; Substantia nigra, SN; Substantia nigra pars compacta, SNpc; Substantia nigra pars reticulata, SNpr; Ventral tegmental area, VTA; tuberculum olfactorium, TO; Globus pallidus, GP; 3',5'-cyclic adenosine monophosphate, cAMP; Mitogen-activated protein kinase, MAPK; 32-kDa dopamine and cAMP-regulated phosphoprotein, DARPP-32; protein phosphatase-1, PP1; Inositol 1,4,5-trisphosphate, IP<sub>3</sub>; G protein-coupled inwardly rectifying potassium channels, GIRK channels. Adapted from Beaulieu *et al.*, 2011 and Hisahara *et al.*, 2011<sup>125,139</sup>.

### 2.2.2.1.1 D<sub>1</sub>-like receptors

The D<sub>1</sub>-class receptors are exclusively found at postsynaptic membranes and are typically coupled to G $\alpha_{s/olf}$  proteins. Thus, as main pathway they activate AC and stimulate the production of the second messenger cAMP, which results in the activation of PKA<sup>140</sup>. Many targets of PKA have been reported to be affected by DA stimulation, such as ionotropic Glu receptors (*N*-methyl-D-aspartate receptor; NMDAR or GluN, and  $\alpha$ -amino-3-hydroxy-5-methyl-4-isoxazole propionic acid receptor; AMPAR or GluA), cAMP response element-binding protein (CREB), ion channels and the 32-kDa DA and cAMP-regulated multifunctional phosphoprotein (DARPP-32)<sup>142</sup>. Alternatively, the D<sub>1</sub>-class receptors can increase intracellular Ca<sup>2+</sup> via the G $\alpha_q$  protein<sup>143</sup>. The D<sub>1</sub>R is the focus of **Chapter 10**, where we suggest that its activation is linked to the G $\alpha_q$ /Phospholipase C pathway.

In the brain, the expression pattern of D<sub>1</sub>R is the most widespread, with higher levels of expression compared to other DARs. D<sub>1</sub>Rs are expressed at a high level of density in the striatum, nucleus accumbens (NAc), SN, tuberculum olfactorium (TO), amygdala, and cortex, as well as at lower levels in the hippocampus, cerebellum, thalamic and hypothalamic areas<sup>125</sup>. D<sub>5</sub>Rs are expressed at low levels in multiple brain regions, including SN, hypothalamus, the hippocampus, and cerebellum. A very low level of expression has also been observed in the nucleus accumbens, dorsal striatum, and TO<sup>125</sup>.

### 2.2.2.1.2 D<sub>2</sub>-like receptors

The D<sub>2</sub>-class receptors are located both at the postsynaptic neurons, which are targeted by dopaminergic afferents, and at presynaptic membranes of dopaminergic neurons. Moreover, the D<sub>2</sub>R consists of two major isoforms, generated by alternative splicing, the D<sub>2</sub>-short and D<sub>2</sub>-long receptor (D<sub>2S</sub>R and D<sub>2L</sub>R, respectively). These two alternatively spliced variants differ from each other by 29 amino acids in the ICL3 and have distinct physiological, pharmacological, signaling, and anatomical characteristics<sup>144</sup>. For instance, the activation of D<sub>2S</sub>R causes a decrease in DA release and a reduction in locomotor activity, whereas induction of D<sub>2L</sub>R increases locomotion<sup>125</sup>. The long isoform is predominantly expressed postsynaptically, whereas D<sub>2S</sub>R mainly functions as an autoreceptor at presynaptic membranes by regulating the firing rate, synthesis, and release of DA<sup>145,146</sup>. In addition, two shorter D<sub>3</sub>R splice variants and various polymorphic variants of D<sub>4</sub>R have been reported<sup>147-149</sup>.

All the D<sub>2</sub>-class receptors are mainly coupled to G $\alpha_{i/o}$  proteins, preventing cAMP production and PKA activation through the inhibition of AC<sup>125,140</sup>. Interestingly, differences are observed between D<sub>2</sub>-class receptors or receptor isoforms in inhibiting AC. For instance, AC is more potently inhibited by the D<sub>2S</sub>R than by the D<sub>2L</sub>R. Despite the lack of G $\alpha_q$  activation through the D<sub>2</sub>-class receptors, it has been reported that Ca<sup>2+</sup> is mobilized through the G $\beta\gamma$  subunit which activates the PLC signaling. Alternatively, the G $\beta\gamma$  subunits inhibit the L-type and N-type Ca<sup>2+</sup> channels at MSNs and striatal interneurons, respectively, or may induce neuronal inhibition due to the activation of GIRK channels<sup>125</sup>.

The expression patterns of the D<sub>2</sub>-class receptors highly overlap with those of the D<sub>1</sub>-class receptors, although this does not directly result in a co-expression at the same neuron. D<sub>2</sub>R is very highly expressed in the NAc, striatum and TO, but is also significantly expressed in the VTA, SN, cortex, hippocampus, hypothalamus, septum, and amygdala. High expression levels of D<sub>1</sub>R and D<sub>2</sub>R are found in the striatum, but these GPCRs are only co-expressed in 5% of the

MSNs, a neuronal population covering around 95% of all the striatal cells<sup>150</sup>. Other D<sub>2</sub>-class receptors are only expressed in selected brain regions (D<sub>3</sub>R) or only at low levels (D<sub>4</sub>R). The highest expression levels of D<sub>3</sub>R are found in the TO, NAc and the islands of Calleja. In addition, significantly lower levels of D<sub>3</sub>R are observed in the SNpc, striatum, hippocampus, etc. The D<sub>4</sub>R has the lowest expression levels of DARs in the brain, but has been observed in the cortex, SN pars reticulata (SNpr) and other regions<sup>125,140</sup>.

### 2.2.2.2 Dopaminergic ligands

Crystal structures have given an in-depth insight of the structural differences between the DARs. The structures of (a) antagonists-bound to D<sub>2</sub>R, D<sub>3</sub>R, D<sub>4</sub>R and (b) a recent crystal structure of D<sub>1</sub>R complexed with a G protein and a non-catechol agonist have been obtained<sup>151-155</sup>. Furthermore, a tremendous progress has been made by cryo-EM to comprehend the basis for agonist selectivity, G protein selectivity and receptor activation of the D<sub>1</sub>R and D<sub>2</sub>R<sup>156-158</sup>. Structures of the human D<sub>1</sub>R-G $\alpha_s$  have been reported with a non-selective dopamine receptors agonist, such as apomorphine and highly selective catechol agonists SKF81297, A77636, SKF83959 and fenoldopam (**Figure 2.16A**) or non-catechol agonist PW0464 and a PAM (**Figure 2.16B**)<sup>157,158</sup>. Moreover, the structure of the human D<sub>2</sub>R-G $\alpha_i$  in a lipid membrane has been solved<sup>156,158</sup>. The D<sub>1</sub>R-G $\alpha_s$  complex displays a global architecture like that of the previously reported class A GPCR-G<sub>s</sub> complexes<sup>159,160</sup>. The orthosteric binding pocket is located within the core of the TMD and is “capped” by the ECL2. All the D<sub>1</sub>R complexes show a nearly identical orthosteric binding pocket with the most conformational structural differences concentrated at the ECL2 region, which probably contributes to the recognition of different D<sub>1</sub>R ligands. The ECL2 of D<sub>1</sub>R has completely diverged from that of D<sub>2</sub>R, which accounts for the agonist’s selectivity against those receptors<sup>156</sup>. A key conserved motif is responsible for the recognitions of agonists harboring catecholamine groups (*e.g.*, DA in DARs, **Figure 2.16B**). Apart from this, specific motifs in the extended binding pocket were responsible for discriminating D<sub>1</sub>-like from D<sub>2</sub>-like receptors<sup>157</sup>. Moreover, a network of aromatic interactions is involved in the activation of D<sub>1</sub>R by non-catechol agonists<sup>152,157</sup>. The PAM binding pocket is localized at the membrane-embedded binding site created by ICL2, where this is mainly composed of hydrophobic residues in the D<sub>1</sub>R<sup>152,157,161,162</sup>. Furthermore, additional PAM allosteric binding sites in the D<sub>1</sub>R have been identified.<sup>163</sup>

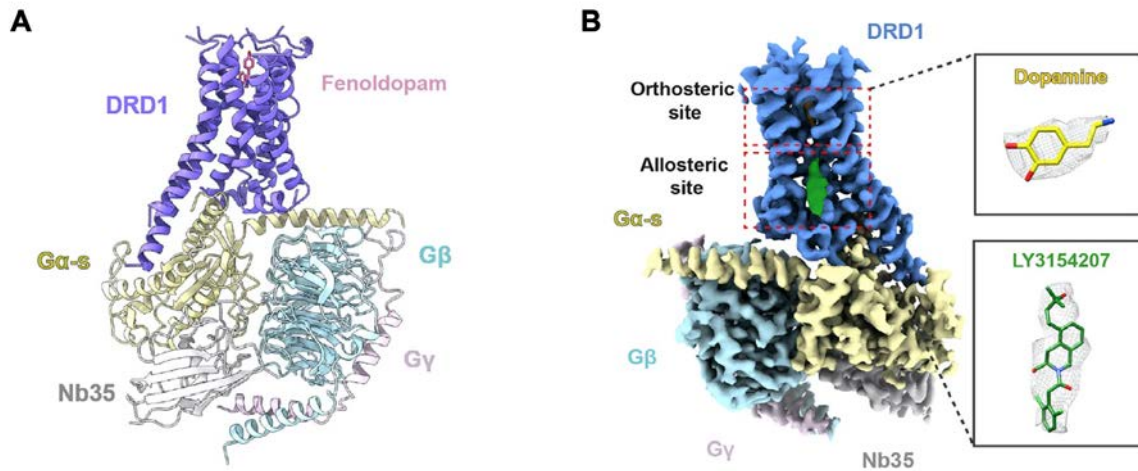


**Figure 2.16. Cryo-electron microscopy structure of dopamine D<sub>1</sub> receptor.** (A) cartoon representation of the D<sub>1</sub>R-Gα<sub>s</sub>-Nb35 complex with the antihypertensive drug fenoldopam. D<sub>1</sub>R; pink, fenoldopam; yellow, Gα<sub>s</sub>; cyan, Gβ; light pink, Gγ; and gray, Nb35. (B) Cryo-EM map of the D<sub>1</sub>R-Gα<sub>s</sub>-Nb35 with dopamine (yellow stick) and positive allosteric modulator LY3154207 (green stick). Adapted from Xiao *et al.*, 2021<sup>157</sup>.

Dopaminergic signaling pathways are crucial to the maintenance of physiological processes, whereas impairments of these mechanisms may lead to dysfunctions that are related to many diseases. More specific, D<sub>1</sub>R is an important drug target for a variety of disorders including SZ, PD and related movement disorders, AD and mild cognitive impairment (MCI). Currently, dopaminergic drugs on the market mainly target D<sub>2</sub>/D<sub>3</sub> receptors, although some potentially have D<sub>1</sub>R activity (*e.g.*, apomorphine and rotigotine, **Figure 2.17**)<sup>164</sup>. Many orthosteric D<sub>1</sub>R agonists display lack of selectivity with consequent side effects, potentially mediated by D<sub>1</sub>R<sub>s</sub> expressed in the periphery. Several steps have recently been made in the development of PAMs, which culminated with the evaluation of the first D<sub>1</sub>R PAM (*i.e.*, LY3154207) that entered a phase II clinical trial to ameliorate cognitive deficits associated with Lewy body dementias<sup>152,158,164-169</sup>.

**Figure 2.17** displays several agonists, antagonists, and modulators that have been mentioned and/or are relevant for **Chapter 10**, where a strategy is described to control dopaminergic neurotransmission with spatiotemporal resolution.

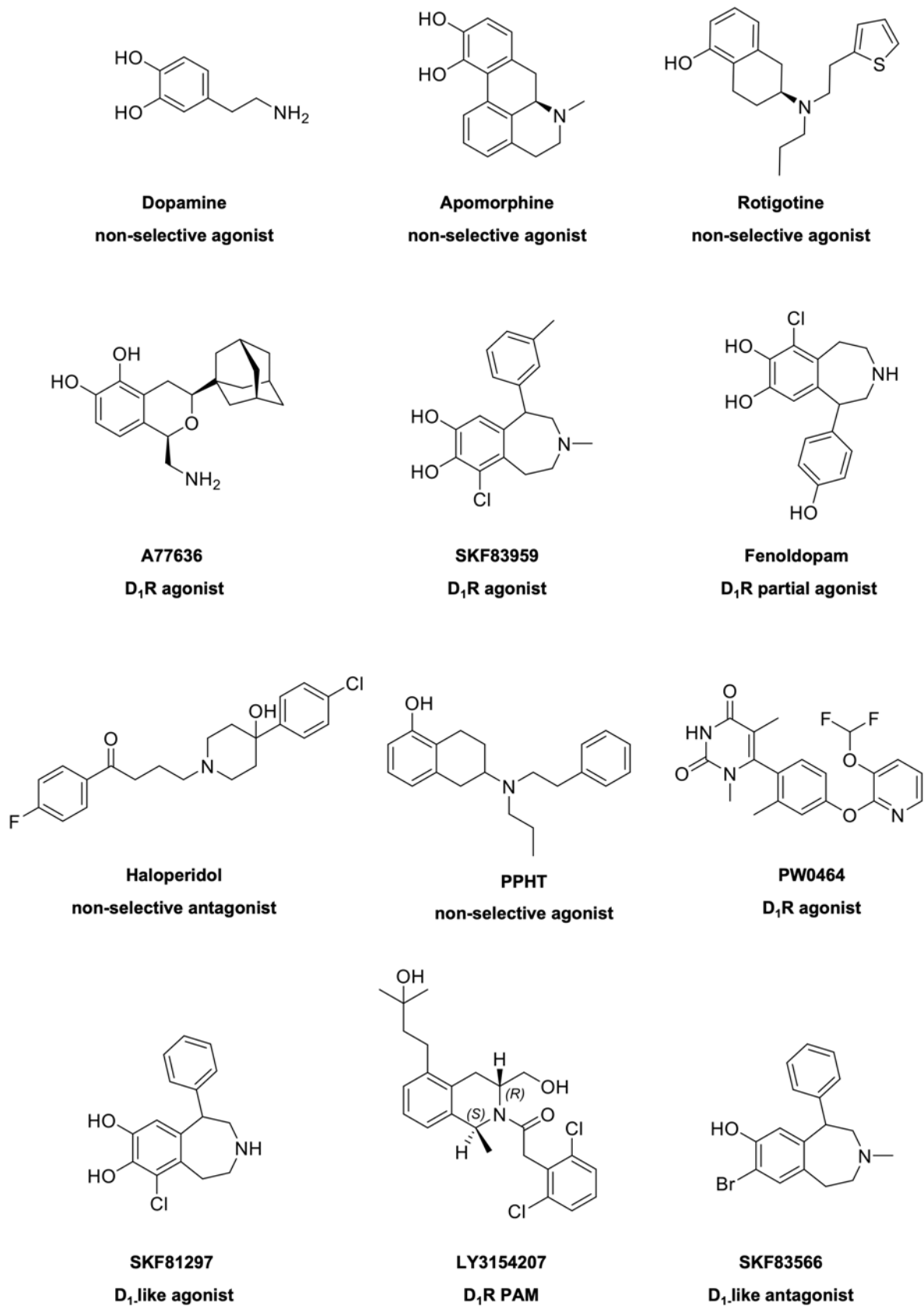
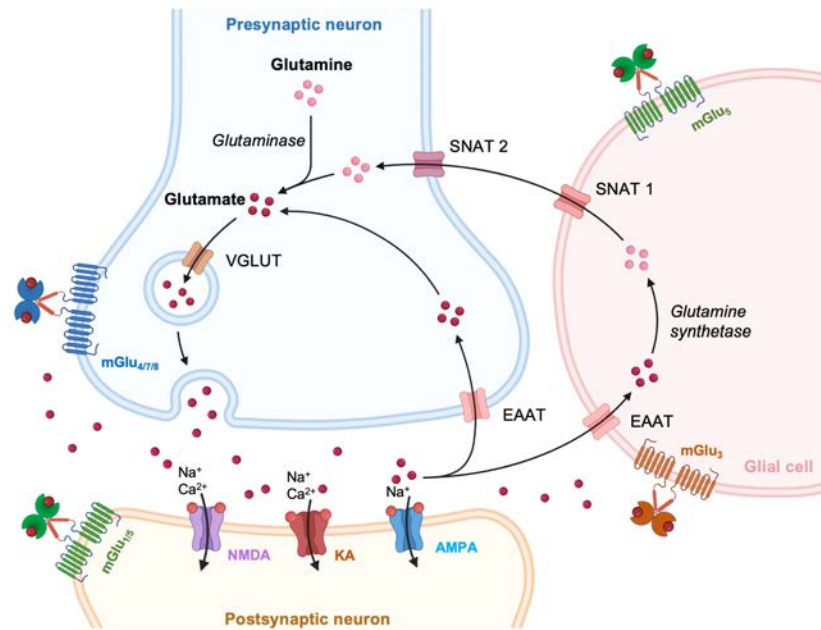


Figure 2.17. Selection of ligands for dopamine receptors.



### 2.2.3 Glutamate

Glutamate serves as the primary neurotransmitter at most excitatory synapses in mammals. This chemical messenger transmits a signal across the synapse from a neuron to a target cell, which can be a different neuron, muscle cell or gland cell. It is responsible for a plethora of physiological processes, including sensory processing and cognitive functions. Its levels should be tightly controlled, as elevated concentrations of extracellular glutamate might result in excitotoxicity and neuronal injury or death<sup>170-172</sup>. Glutamatergic neurons load the newly synthesized neurotransmitter into synaptic vesicles via the vesicular glutamate transporters (VGLUTs). In general, these vesicles are pooled in proximity of the active zone and docked to the plasma membrane. The synaptic vesicles are primed, a process that converts them into putative secretory vesicles<sup>173</sup>. An action potential propagated to the presynaptic terminal triggers a  $\text{Ca}^{2+}$  influx, resulting in the release of glutamate and the activation of glutamate receptors at synaptic membranes. Then, glutamate activates ionotropic receptors (AMPA, NMDAR and kainic acid receptor; KAR) and metabotropic receptors located in the postsynaptic terminal of a new cell, triggering a signaling cascade. Glutamate is removed from the synaptic cleft by excitatory amino acid transporters (EAATs) to prevent excitotoxicity caused by an excess of glutamate receptor activation, which has been associated with stroke, hypoxia and epilepsy. Once transported into glia, the glutamate is converted by glutamine synthetase into glutamine<sup>174</sup>. Finally, the glutamine is transported by the  $\text{Na}^+$ -coupled neutral amino acid transporters (SNATs) from astrocytes to neurons. In the presynaptic terminal, glutamine is metabolized via the action of mitochondrial phosphate-dependent glutaminase into glutamate<sup>174</sup>. In short, this process is known as the glutamate-glutamine cycle, a cooperation between glial cells and nerve terminals to sufficiently maintain the proper amount of the neurotransmitter (**Figure 2.18**). Glutamate does not cross the BBB and this nonessential amino acid could be synthesized from branched-chain amino acids (Leu, Ile, Val), which rapidly cross the BBB<sup>174</sup>. An alternative source is from the glucose metabolism, where glutamate is synthesized from 2-oxo-glutarate, an intermediate of the tricarboxylic acid (TCA) cycle, by transamination<sup>78,175</sup>.



**Figure 2.18. The glutamate-glutamine cycle.** The interplay between glial and neuronal cells prevents excitotoxicity. First, the neurotransmitter is released into the synaptic cleft via the activation of the presynaptic terminal. Then glutamate activates the two types of glutamate receptors, ionotropic and metabotropic at the postsynaptic terminal. The uptake of glutamate into the neurons and glial cells via excitatory amino acid transporters (EAATs) terminates the signaling. In the glial cells the glutamate is converted into glutamine by the glutamine synthetase and exported to neurons by  $\text{Na}^+$ -coupled neutral amino acid transporters (SNATs). The glutamine is converted into glutamate via glutaminase and loaded into vesicles via vesicular glutamate transporters (VGLUTs). Original figure by Rosalba Sortino.

### 2.2.3.1 Metabotropic glutamate receptors

The glutamate receptors consist of ionotropic glutamate (iGlu) receptors and mGlu receptors, both expressed in neuronal and glial cells. The iGlu receptors are cationic ligand-gated channels which mediate rapid excitatory synaptic neurotransmission and are divided in three families: the NMDAR, AMPAR, and KAR (GluN, GluA, and GluK, respectively). The mGlu receptors belong to class C of the GPCRs superfamily, in which glutamate activates downstream effectors via heterotrimeric G proteins (see section 2.1). The term metabotropic was coined to refer to receptors that indirectly induce responses by modulating the intracellular metabolism of neurons, which contrasts with the ionotropic receptors that directly alter the gating properties of integral ion channels<sup>176</sup>. The mGlu receptors participate in many different CNS processes and are attractive therapeutic targets for several neurological and psychiatric disorders.

Since 2000, many crystal and cryo-EM structures of class C GPCR dimeric VFDs have been solved in open and closed conformations (*i.e.*, with and without glutamate)<sup>177-180</sup>. Recent studies solved the related structures of mGlu<sub>5</sub>, mGlu<sub>2</sub>, mGlu<sub>4</sub>, and mGlu<sub>7</sub> receptors, but lacked

interpretable electron density especially in the TMD. This was complemented by the structure of the full length of mGlu receptors obtained through cryo-EM, starting with the full length of mGlu<sub>5</sub> receptor in 2019<sup>181,182</sup> (**Figure 2.19**). These structures elevated our knowledge about the activation of this GPCR class, although the mechanism is not yet fully understood. However, these studies confirmed and explained that the dimeric structure is obligatory for their activation<sup>178,181</sup>.

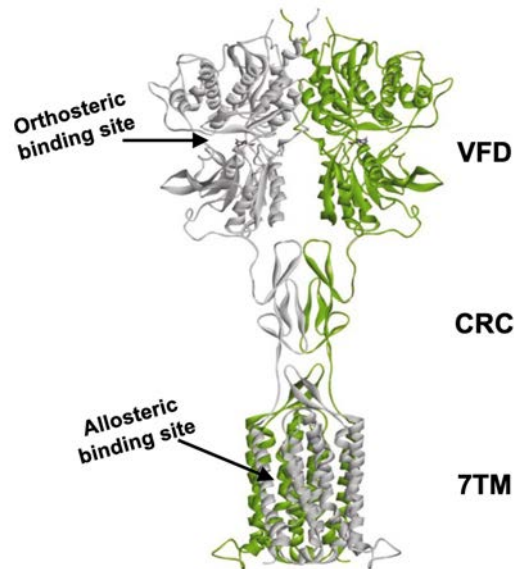


**Figure 2.19.** Cryo-electron microscopy structure of full-length mGlu<sub>5</sub> receptor dimer in the active conformation (PDB ID: 6N51). Orthosteric ligands bind to the “Venus flytrap” domain (VFD), while allosteric modulators bind to the transmembrane domain (TMD). Adapted from Acher *et al.*, 2022<sup>183</sup>.

In fact, all mGlu receptors form constitutive dimers, cross-linked by a disulfide bridge, and have equivalent architectures. The N-terminus of each protomer contains a VFD, which forms a cleft that functions as the orthosteric binding site for glutamate. The binding of glutamate to the dimer (**Figure 2.20**) inactive resting state (*i.e.*, both VFDs open) promotes the shift to the active state (*i.e.*, both VFDs closed) through an intermediate state (one VFD open and one closed)<sup>184,185</sup>. Glutamate binding to both VFDs is required for efficient signaling (*i.e.*, full activation), but only one of 7TM receptors activates the G protein<sup>184,186</sup>. The conformational changes upon ligand activation are propagated from the VFD through the CRD, which forms a disulfide bridge with the VFD and is involved in the intracellular signaling. The CTD of mGlu receptors plays a very important role for intracellular signaling, as this domain has many alternative splice variants and multiple phosphorylation sites. In addition to their G protein coupling, these 7TM receptors directly interact with a plethora of proteins at their CTD, which may play diversity of roles in the regulation of mGlu receptors.

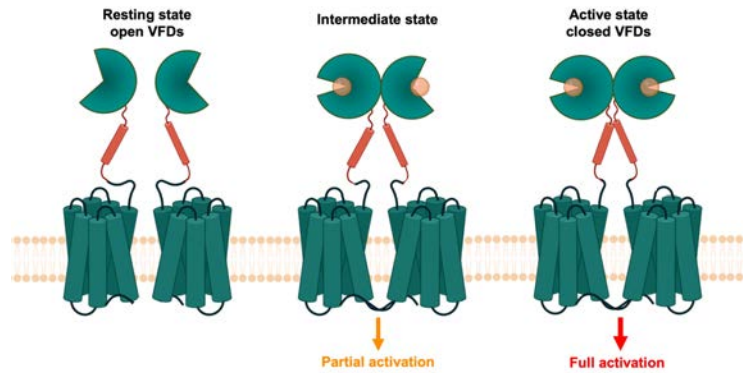


**Figure 2.20. Schematic representation of the activation mechanism for metabotropic glutamate receptors.** Upon binding of an agonist (*e.g.*, glutamate), the equilibrium of the receptor shifts from a resting to an intermediate state and subsequently to an active state. The “Venus flytrap” domains (VFDs) are both open in the closed state, while one is open and one is closed in the intermediate state and both VFDs are closed in the active state. Original figure by Rosalba Sortino.

The mGlu receptors comprise eight receptor subtypes (mGlu<sub>1</sub>-mGlu<sub>8</sub> receptors) that are classified into three groups based on sequence homology, ligand selectivity and cell signaling properties (**Table 2.4**). Group I subtypes (*i.e.*, mGlu<sub>1</sub> and mGlu<sub>5</sub> receptors) are mainly coupled to G $\alpha_q$  subunits and are predominantly localized at postsynaptic membranes surrounding the iGlu receptors, where they function to modulate neuronal excitability. They are expressed in neurons and glial cells, when these receptors are found on presynaptic membranes, they could modulate neurotransmitter release<sup>61,187</sup>. Both group II (*i.e.*, mGlu<sub>2</sub> and mGlu<sub>3</sub> receptors) and group III (*i.e.*, mGlu<sub>4</sub>, mGlu<sub>6</sub>, mGlu<sub>7</sub> and mGlu<sub>8</sub> receptors) predominantly bind to G $\alpha_{i/o}$  subunits, acting as autoreceptors by inhibiting glutamate or GABA release<sup>170-172</sup>. Group II subtypes are widely distributed in the CNS and PNS. In general, this subtype is located at the presynaptic membrane far from active zones of neurotransmitter release. The mGlu<sub>3</sub> receptor is found both pre- and postsynaptically as well as in glial cells<sup>188</sup>. Members of group III are mostly located on presynaptic membranes and quite widely spread throughout the CNS, with the exception of mGlu<sub>6</sub> receptors. The mGlu<sub>6</sub> receptor is exclusively found in the retina and expressed postsynaptically at the dendrites of ON bipolar cells (OBCs)<sup>189</sup>. **Figure 2.21A** displays the glutamate synapse for glutamatergic neurons. mGlu<sub>6</sub> receptor is involved in mediating a sign inversing neurotransmission from photoreceptors (PhRs) to OBCs (**Figure 2.21BC**). In the dark, glutamate is tonically released by PhRs and the activation of mGlu<sub>6</sub> receptors by glutamate leads to the closure of a non-selective cation channel, the transient receptor potential melanoma-related 1 (TRPM-1), via G $\alpha_o$ -mediated signaling<sup>190</sup>. Overall, the mGlu<sub>6</sub> receptors converts the depolarization of the PhRs, resulting in the hyperpolarization of OBCs. (**Figure 2.21B**)<sup>191-198</sup>.

Category	Subtype	CNS expression	Localization	G protein (main signaling)	Orthosteric agonist
I	mGlu <sub>1</sub>	Widespread in neurons	Predominantly postsynaptic	G $\alpha_q$ ( $\uparrow$ IP <sub>3</sub> , $\uparrow$ intracellular Ca <sup>2+</sup> , $\uparrow$ DAG, PKC activation)	Quisqualic acid
	mGlu <sub>5</sub>	Widespread in neurons, astrocytes			
II	mGlu <sub>2</sub>	Widespread in neurons	Presynaptic and postsynaptic	G $\alpha_{i/o}$ ( $\downarrow$ cAMP, inhibition of Ca <sup>2+</sup> channels, activation of K <sup>+</sup> channels and MAPK)	LY 354740
	mGlu <sub>3</sub>	Neurons and astrocytes			
III	mGlu <sub>4</sub>	Widespread in neurons (high in cerebellum)	Predominantly presynaptic	G $\alpha_{i/o}$ ( $\downarrow$ cAMP, inhibition of Ca <sup>2+</sup> channels, activation of K <sup>+</sup> channels and MAPK pathway)	L-AP4
	mGlu <sub>7</sub>	Widespread in neurons	Active zone of presynaptic terminals		
	mGlu <sub>8</sub>	Lower and more restricted expression than mGlu <sub>4</sub> and mGlu <sub>7</sub>	Predominantly presynaptic		
	mGlu <sub>6</sub>	Retina	Postsynaptic in ON-bipolar retinal cells		

**Table 2.4. Key features of the mGlu<sub>1-8</sub> receptors in the central nervous system.** Abbreviations: Inositol 1,4,5-trisphosphate, IP<sub>3</sub>; Diacylglycerol, DAG; Protein kinase C, PKC; 3',5'-cyclic adenosine monophosphate, cAMP; Mitogen-activated protein kinase, MAPK; Cyclic 3',5'-guanosine monophosphate phosphodiesterase, cGMP; Transient receptor potential cation channel subfamily M member 1, TRPM1. Adapted from Niswender *et al.*, 2017 and Nicoletti *et al.*, 2011<sup>172,187</sup>.

However, it is unclear whether the G $\alpha_o$  subunit, G $\beta\gamma$  dimer or both are necessary for the closure of TRPM1, which may be the result of a direct interaction<sup>194-196,199,200</sup>. In light conditions, mGlu<sub>6</sub> receptors convert the light-evoked hyperpolarization of the PhRs into depolarized OBCs<sup>189,191,192,195,196,201,202</sup>. In fact, light-induced reduction in glutamate release from the PhRs results in the opening of TRPM1 and the subsequent depolarization of the OBCs. This will activate ON-type retinal ganglion cells projecting to the brain (**Figure 2.21C**). In contrast, in the dark glutamate also induces the depolarization of the OFF bipolar cells through the activation of AMPARs and KARs, whereas in response to light it promotes the hyperpolarization of these cells<sup>195,197,202</sup>. In retinal degenerative diseases, like retinitis pigmentosa (RP), photoreceptor cells (*i.e.*, rods and cones) are progressively lost, leading to blindness. However, downstream neurons of the inner retina (*e.g.*, OBCs) are spared, providing a potential target for vision restoration therapy. One of the strategies used to introduce light sensitivity to the surviving cells of the retina will be described in **Chapter 11**.

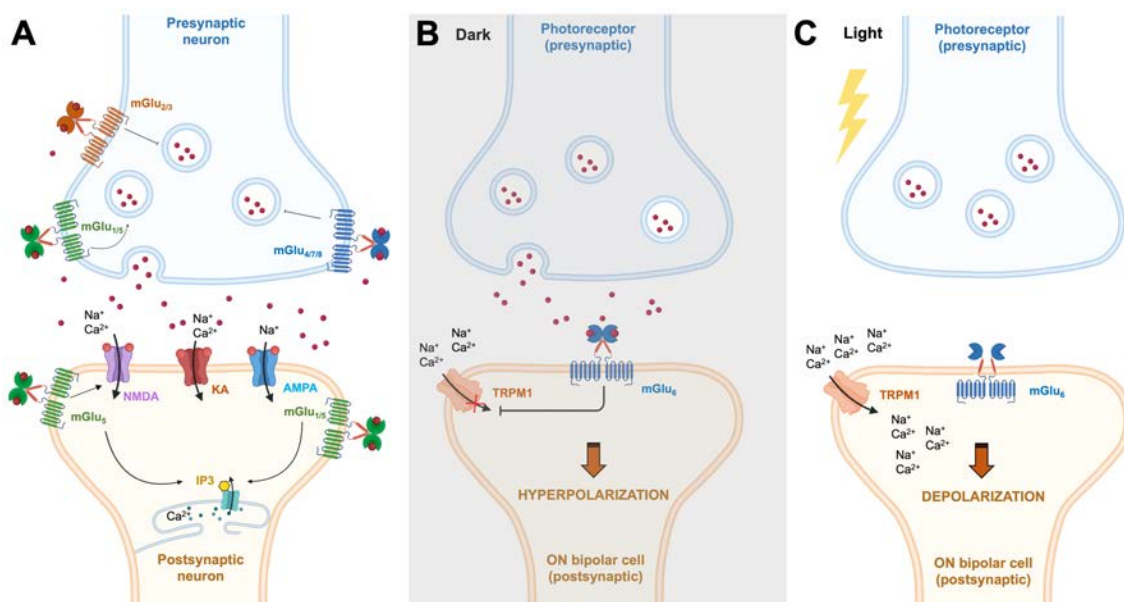


**Figure 2.21. The glutamate synapse for glutamatergic neuron (A) and for photoreceptors/ON bipolar cells in darkness (B) and under light condition (C).** (A) On presynaptic terminals, the group II and III mGlu receptors often function to inhibit neurotransmitter release, whereas group I promote release when present. Group I are generally localized at postsynaptic membranes, while their signal via  $G\alpha_q$  proteins induce the release of calcium from the endoplasmic reticulum (ER). The mGlu<sub>5</sub> receptor can potentiate *N*-methyl-D-aspartate receptor (NMDAR) currents. In addition to NMDAR, the  $\alpha$ -amino-3-hydroxy-5-methyl-4-isoxazole propionic acid receptors (AMPA) and kainic acid receptors (KARs) respond to glutamate through increasing the intracellular levels of sodium or calcium, thus, promoting cell excitability. (B) Glutamate released in darkness from photoreceptors activates mGlu<sub>6</sub> receptor, which is negatively associated with a membrane non-selective cation channel, the transient receptor potential melanoma-related 1 (TRPM1) and results in cell hyperpolarization. (C) In response to light, the photoreceptors are hyperpolarized. Thereby, the rate of glutamate release is reduced with the consequent deactivation of mGlu<sub>6</sub> receptor and opening of the TRPM1 channel. This leads to the depolarization of the ON bipolar cells. Original figure by Rosalba Sortino.

### 2.2.3.2 Metabotropic glutamatergic ligands

A plethora of orthosteric compounds against mGlu receptors have been designed and screened, including agonists, partial agonists, antagonists, or inverse agonists<sup>203,204</sup>. Group selective agonists such as quisqualate for group I, LY354740 for group II and L-2-amino-4-phosphonobutyric acid (L-AP4) for group III mGlu receptors are shown in **Figure 2.22**. In general, competitive antagonists have been less developed compared to agonists. Some of the agonists have been turned into the antagonist with high or moderate activity, such as L-AP4 into (*S*)-2-Amino-2-methyl-4-phosphonobutanoic acid<sup>183</sup>. Those orthosteric ligands are polar compounds and contain commonly charged amino acids analogs, allowing them to bind the

highly hydrophilic VFD. This property confers excellent aqueous solubility, although it makes these molecules less favorable drugs with low predicted bioavailabilities.

As we previously discussed (see section 2.1.2), the allosteric modulators offer an opportunity to “fine-tune” endogenous signaling in a more spatiotemporal manner, which is believed to confer a better and more controllable therapeutic profile. Several studies, by using the chimeric and truncated receptors constructs, have shown that the orthosteric and the allosteric binding sites in mGlu receptors are located in highly distinctive domains, whereas the TMD domain being the binding site of various non-endogenous allosteric ligands (**Figure 2.1**)<sup>61,62,205-210</sup>. These allosteric ligands modulate signaling either on their own or in conjunction with orthosteric ligands.

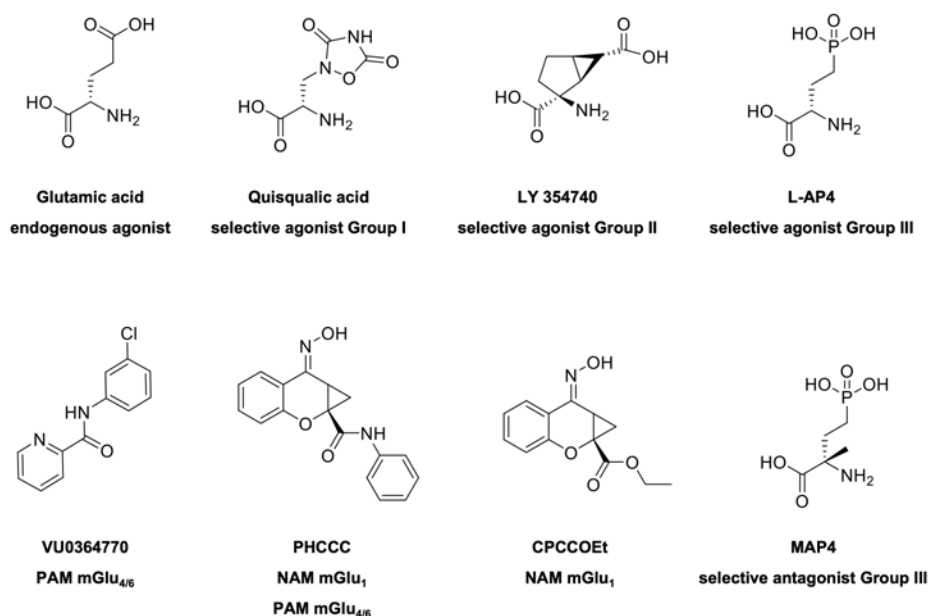


**Figure 2.22.** Selection of mGlu receptor orthosteric agonists, antagonists and allosteric modulators.

Of note, the entire class C of GPCRs has no endogenous allosteric modulators. For this reason, the allosteric binding site remained more hydrophobic than for class A or B of GPCRs. Hence, the polarity of the allosteric modulators is much lower than that of orthosteric ligands due to their hydrophobic environment. Since the discovery of the first mGlu<sub>1</sub> receptor NAM CPCCoEt in the late nineties, research was mostly focused on allosteric modulators. Some of them interact with more than one subtype from a different group (*e.g.*, PHCCC) or within the same group (*e.g.*, VU0364770), suggesting similarities within the allosteric binding pocket<sup>208,211-215</sup>. Moreover, allosteric ligands that do not compete with common allosteric sites have been described<sup>61</sup>. In **Figure 2.22**, a few structures are displayed of agonists, antagonists, or allosteric modulators, which are relevant for this thesis or have previously been mentioned in this chapter.

## 2.3 G protein-coupled receptors photopharmacology

GPCRs represent the largest family of membrane receptors and account for a total of 800, or 4%, genes in humans. These 7TM receptors are involved in the regulation of many physiological functions, such as senses, metabolism, neurotransmission, and cell growth. Their relevance in the treatment of various diseases makes them attractive drug targets. In fact, nearly one-third of all drugs on the market targets GPCRs (see section 2.1). One of the major challenges of the drug discovery is the high percentage of failure of the clinical drug development. Between 2013-2017, the success rate for phase III was about 25-30%, starting from 80% in phase I<sup>4</sup>. The main limitations of the candidate compound are the poor-selectivity and the poor pharmacokinetic properties. Moreover, the poor drug selectivity is related to an uncontrolled drug activity in time and space that results in toxicity-related side effects, as well as drug resistance<sup>216-218</sup>. To overcome these limitations, several approaches are emerging that employ light to control GPCR activity. The use of light in biological applications is highly advantageous, because it combines remote action, reversibility, speed, safety, easy delivery, and high spatial and temporal resolution. In addition, light can be controlled in a qualitative and quantitative manner by adjusting wavelength and intensity<sup>216,219,220</sup>. These are only few of the advantages that render light a suitable external and noninvasive stimulus. The use of light to manipulate biological processes has allowed important progresses in the fields of neuroscience and pharmacology.

In the last 20 years, a new field called optogenetics has risen, revolutionizing modern biology with a special impact on neurobiology<sup>221,222</sup>. This strategy combines the use of optical and genetic methods<sup>221,223,224</sup>. In fact, it utilizes light to control the activity of specific cell types, typically neurons, that have been genetically modified to express exogenous light-sensitive proteins from algae and bacteria<sup>225</sup>. The type of control achieved (excitatory vs. inhibitory) depends on the biological function of the light-sensitive protein introduced<sup>225</sup>. Since its inception, optogenetic tools were applied for vision restoration purposes. In 2005, a naturally light-sensitive microbial opsins (*i.e.*, channelrhodopsin-2; ChR2) derived from algae was virally introduced to bestow light-sensitivity on retinal neurons in blind animal models<sup>226,227</sup>. Later, red shifted variants of the light-gated ion channel ChR2 were developed, such as ReaChR and Chrimson<sup>228,229</sup>. Altogether, ion-channel-based optogenetic therapies have shown promising results for restoring visual functions, but these are irreversible interventions that introduce hurdles to further development as a therapeutic approach<sup>230</sup>. A recently developed tool to optogenetically control GPCRs is opto-XRs<sup>231</sup>. This tool is based on chimeric GPCRs,



where the intracellular domains of a light-sensitive GPCR opsin are replaced with the ones specific from another GPCR. In a recent study, the Opto-mGlu<sub>6</sub> receptor chimera was developed, which had the intracellular loops of the melanopsin substituted by those of the mGlu<sub>6</sub> receptor. The transgenic expression of this chimeric protein restored vision in blind mice<sup>232</sup>. Other receptor chimeras have been developed and coupled to Gα<sub>q</sub> and Gα<sub>i</sub><sup>231,233-236</sup>. This strategy allows to develop light sensitive GPCRs, allowing to mimic the spatiotemporal dynamics of neurotransmission pathways *in vivo*. However, they are not native proteins and, therefore, lack of crucial characteristics including the endogenous binding site which may provide an incomplete and inaccurate view of the GPCR function *in vivo*.

In current optogenetic approaches, they include a wider variety of biological processes in neuroscience<sup>221,222</sup>. Despite the enormous success of this technique, it presents several drawbacks<sup>237,238</sup>. A major limitation of optogenetics is the necessity to integrate exogenous genes into living organisms and cells using genetic manipulation, giving rise to safety and regulatory concerns. Therefore, optogenetics faces significant hurdles for clinical advancement.

Another method that utilizes light is photodynamic therapy, where light combined with a photosensitizer agent is used to produce reactive oxygen species locally that kill malignant cells. Despite its clinical application, the method is not pharmacologically selective and is not further discussed in this thesis<sup>239,240</sup>.

Photopharmacology is a light-based strategy that overcomes several of the main shortcomings presented in the abovementioned methods. This approach strictly interconnects the fields of photochromism and modern pharmacology, while it does not require any genetic manipulation. The term photopharmacology has become the dominant nomenclature, but optopharmacology and optochemical genetics have been used as well. Different modalities of photopharmacology have emerged and multiple strategies have been developed, including (a) irreversibly photoreleased ligands (*e.g.*, photocaged compounds, **Figure 2.23A**), (b) reversible ligands that comprise photoswitchable tethered ligands, PTLs (**Figure 2.23B**); PTLs variants named photoswitchable orthogonal remotely tethered ligands, PORTLs (**Figure 2.23C**) and photochromic ligands, PCLs (**Figure 2.23D**).

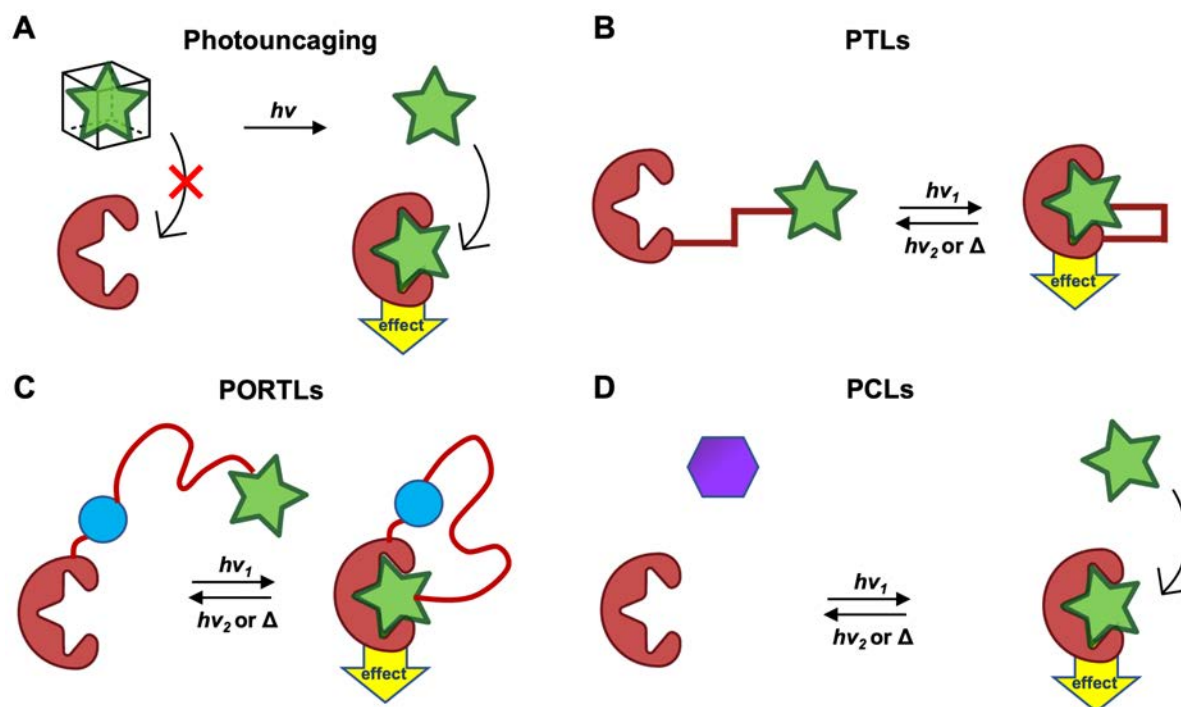


**Figure 2.23. Modalities of photopharmacology.** (A) Irreversible photouncaging; (B) Photoswitchable tethered ligands (PTLs); (C) Photoswitchable orthogonal remotely tethered ligands (PORTLs) and (D) Photocromic ligands (PCLs). Original figure by Rosalba Sortino.

### 2.3.1 Irreversible photouncaging

In the case of photocaged compounds, the ligand is attached to a photocleavable cage that prevents the ligand's activity. However, irradiation of a selected wavelength promotes a reaction that causes the removal of the photocage (*i.e.*, irreversible), triggering the release of the biologically active molecule and activating (or inhibiting) the targeted process of interest (**Figure 2.24A**)<sup>241-243</sup>. This allows great control over the delivery and activity of the drug at its site of action, reducing the risk of adverse side effects<sup>244</sup>. Since it was described in the 1970s, this has been the most widely used strategy in photopharmacology and photoactivatable neurotransmitters, which target different classes of GPCRs (especially class A and C) have been extensively developed (*e.g.*, caged carbachol derivatives and caged glutamate derivatives (**Figure 2.24AB**)). More specifically, caged glutamate derivatives allowed the mapping of neuronal circuits and to study the function of mGlu receptors<sup>245-247</sup>. Caged compounds can be designed to be uncaged by two-photon excitation (2PE) (**Figure 2.24BC**)<sup>248,249</sup>. However, the major drawback of this modality is that the photouncaging process is irreversible, restricting to control the properties of a pharmacological compound and its effects only once. Thus, it relies on (and is limited by) ligand diffusion for receptor unbinding and on the continuous supply of

the caged species, which can be problematic and costly to deliver in biological preparations. Furthermore, the proteolysis of the caging group can generate by-products, which may be toxic or present several disadvantages.

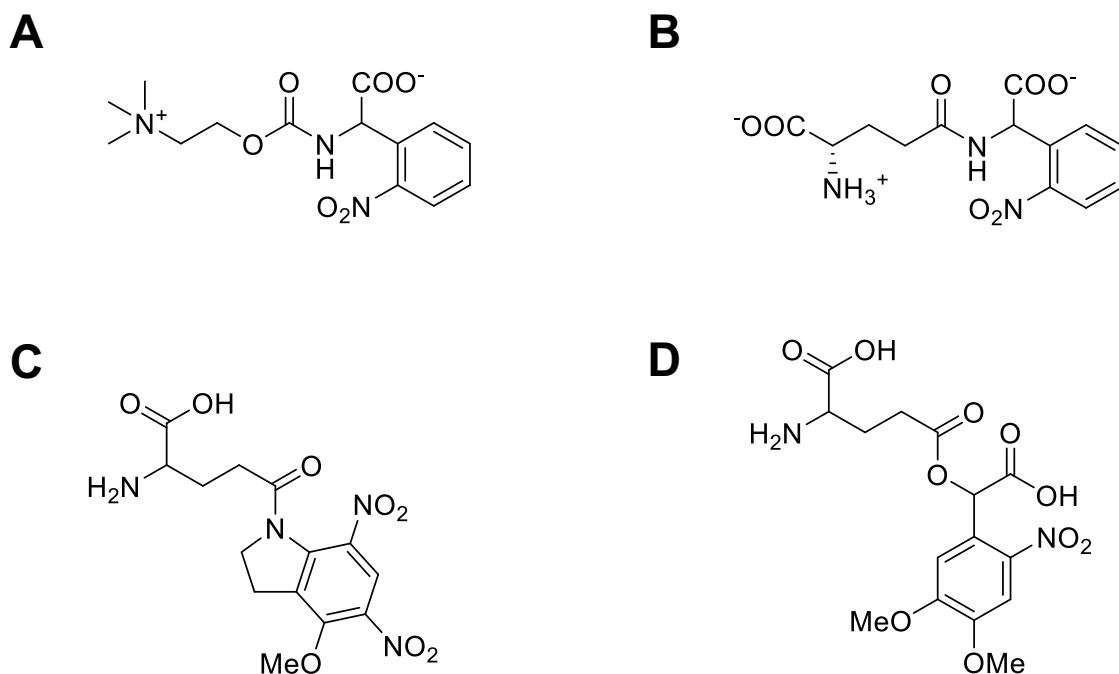


**Figure 2.24. Selection of photocaged ligands.** (A) Photocaged glutamate, (B) Photocaged carbachol, (C) MDNI Glu and (D) DMCNB-Glu.

### 2.3.2 Reversible ligands

Reversible photopharmacological tools are based on the ability of photoswitchable (photoisomerizable) moieties to undergo a conformational change upon light exposure with consequent modification of their chemical and physical properties<sup>250,251</sup>. These photochromic groups can be introduced into the molecular structure of the bioactive compound. Interestingly, photoswitchable drugs not only modulate in a light-dependent manner GPCRs, but also ion channels, transporters, pumps, enzymes, cytoskeleton elements, and lipids as well<sup>250</sup>. Many classes of photoswitchable moieties have been developed, such as azobenzenes, stilbenes, fulgimide, diarylethene, hemithioindigo, and spyropyran. These compounds can be classified in two groups, which is (a) a P-type (photochemically reversible) or (b) a T-type (thermally reversible) system<sup>60,252-254</sup>. P-type systems are driven by the absorption of light, while T-type systems could thermally relax to a more stable isomer over time. Nevertheless, many reversible photoswitchable tools are belonging to both these groups.

Azobenzenes are the most widely used for biological applications due to their versatility, efficiency, reversibility, and repeatability<sup>60,255</sup>. Moreover, azobenzenes are relatively small and easy to introduce into bioactive compounds using extensively documented synthetic strategies<sup>60</sup>. An azobenzene consists of two phenyl rings, linked by a -N=N- group, also called azo-bond or azo-bridge (**Figure 2.25**). “Regular” azobenzenes are thermodynamically stable in their elongated and planar *trans* conformation combined with a negligible dipolar moment. The *trans*-to-*cis* isomerization is obtained under illumination with ultraviolet light (UV), resulting in a large change in geometry and polarity. The *cis* conformation is shorter than the *trans* form, whereas the *cis* form is “bent” with a dipolar moment of  $\sim 3$  Debye (**Figure 2.25A**)<sup>216,245</sup>. The back isomerization to the *trans* form can be realized thermally or upon irradiation with visible light. The UV-Vis absorption spectra of the *trans*- and *cis*-isomers of an unsubstituted azobenzene overlap to a certain degree, but present noticeable differences (**Figure 2.25B**). The *trans* form shows a strong  $\pi$ - $\pi^*$  band around 320 nm and a very weak n- $\pi^*$  band near 440 nm, as a result of its symmetric geometry. In contrast, the *cis* form displays less intense  $\pi$ - $\pi^*$  bands around 300 nm and a stronger n- $\pi^*$  band near 440 nm than the *trans* one. The photostationary state (PSS) provides a measure of the percentage of *cis*- and *trans*-isomers at the photochemical equilibrium for a given wavelength. For instance, in the case of azobenzene, the isomeric ratio at the thermally relaxed state can be approximately 99:1 *trans/cis*. Usually, lower ratios can be obtained at the PSS under illumination if the absorption spectra are very well separated (e.g., 80:20). On the other hand, thermal isomerization rates depend on the chemical and electronic structure of the azobenzene and its local environment. These characteristics affect the half-life of the less-stable *cis*-isomer, which may vary between photoswitchable compounds from milliseconds to days, weeks or even months.

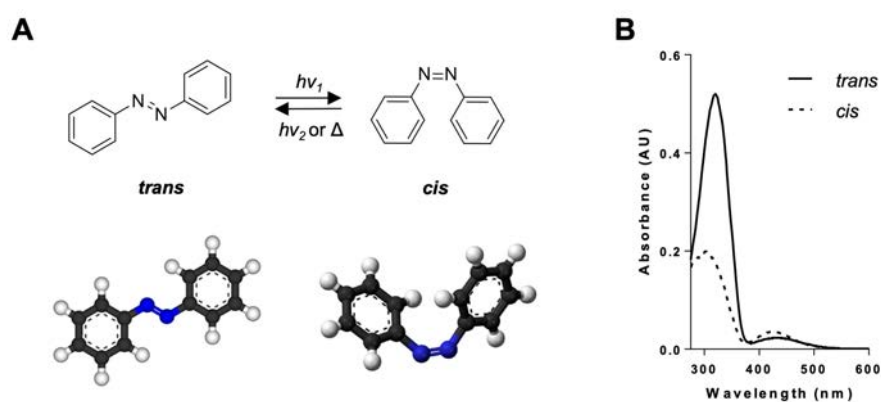


**Figure 2.25. Photoisomerization of azobenzene.** (A) Azobenzene 2D and 3D structures. (B) UV-Vis absorption spectra of the *trans* and *cis* azobenzene isomers. Adapted from Fuchter *et al.*, 2020<sup>256</sup>.

Several parameters, such as the thermal relaxation and the sensitivity to different wavelengths could be tuned by changing the *ortho*- and *para*- substituents of the azobenzene<sup>60,253,257</sup>. These adjustments may be important for the use of photoswitchable compounds to overcome potential limitations in physiological systems. For instance, appropriate substitutions in the aromatic ring of the azobenzene may red-shift the absorption wavelengths to the visible light range, which is less harmful and more suitable for biological application than UV light, or may make the drug more soluble in water<sup>252</sup>. Therefore, the chemical groups of the substitutions determine the photochemical properties of the compound. Based on these chemical groups, the azobenzenes are classified in several families: (a) aminoazobenzene family, (b) push-pull azobenzenes, (c) tetra-*ortho* substituted azobenzenes and (d) diazocines.

The aminoazobenzene family includes all the azobenzenes bearing amino or hydroxy substituents in the *ortho* or *para* positions. In this case, the thermal relaxation time of the *cis*-isomer is usually fast, although it could be slowed down by the introduction of sterically hindering di-*ortho* substitutions (*i.e.*, stabilizing the *cis*-isomer).

Push-pull azobenzenes are generally characterized by the presence of a strong electron-donor and a strong electron acceptor group in opposite rings of the azobenzene scaffold at the *ortho* or *para* positions (*i.e.*, creating a “push-pull” system). This allows a strong red-shift in the absorption wavelength range, whereas thermal relaxation occurs generally fast (*i.e.*, within seconds). Moreover, the bidirectional fast isomerization, high polarizability and large dipole make these azobenzenes useful as non-linear optical and photo-refractive compounds<sup>258,259</sup>.

Tetra-*ortho* substituted azobenzene derivatives strongly stabilize the thermal relaxation time of the *cis*-isomers (*e.g.*, their half-life may vary from hours to days in water)<sup>260,261</sup>. Furthermore, these derivatives could be isomerized from *trans*-to-*cis* with green light ( $\lambda = 500\text{-}540$  nm) and back isomerization to *trans* with a blue light ( $\lambda = 420\text{-}450$  nm). Tetra-*ortho*-methoxy-substituted azobenzene derivatives are often sterically too large to fit in the small binding pockets of the 7TM receptors, limiting their photobiological applications. Differently, tetra-*ortho*-substitutions with chlorine and fluorine have widely been applied for various biological applications<sup>262-265</sup>. Of note, asymmetric *ortho*-fluorinated azobenzenes, which are also less sterically demanding in comparison to the chlorinated derivatives, show a high two-photon absorption cross-section<sup>266</sup>. This characteristic allows their photoisomerization by using near-infrared light (*i.e.*, NIR, less toxic and more penetrant wavelengths)<sup>266</sup>.

For the diazocines, also called “bridged” azobenzenes, the *cis*-isomer is thermodynamically more stable and predominates in the dark, while irradiation with 370-400 nm light promotes

the formation of the less stable *trans*-isomer. Thus, diazocines provide “reversed functionality” compared to linear azobenzenes. The back-isomerization from the *trans*-to-*cis* form is realized with 450-500 nm light. Upon isomerization, the diazocines undergo a huge change in dipole moment, which probably allows for an inversion of the intrinsic dark activity of the photoswitch. Their limited synthetic accessibility restricts the use for biological application. However, attempts to produce larger yields have recently been reported<sup>253,267</sup>. According to the requirements of each application, thermal relaxation and/or photoswitch wavelengths can be adjusted<sup>216</sup>. Altogether, the azobenzene-based photoswitches must be evaluated for their metabolic stability and potential toxicity prior to clinical studies<sup>250,268</sup>.

Furthermore, other photoisomerizable groups such as hemithioindigos, like azobenzene, interconvert between *trans*- and *cis*-isomers with consequent change in shape and polarity (**Figure 2.26AB**). Other photoswitchable moieties, such as spiropyrans and fulgides have a distinct photoswitching mechanism. These compounds switch upon irradiation between an open and a closed ring conformation with change in flexibility and electron properties (**Figure 2.26CD**)<sup>254,269</sup>.

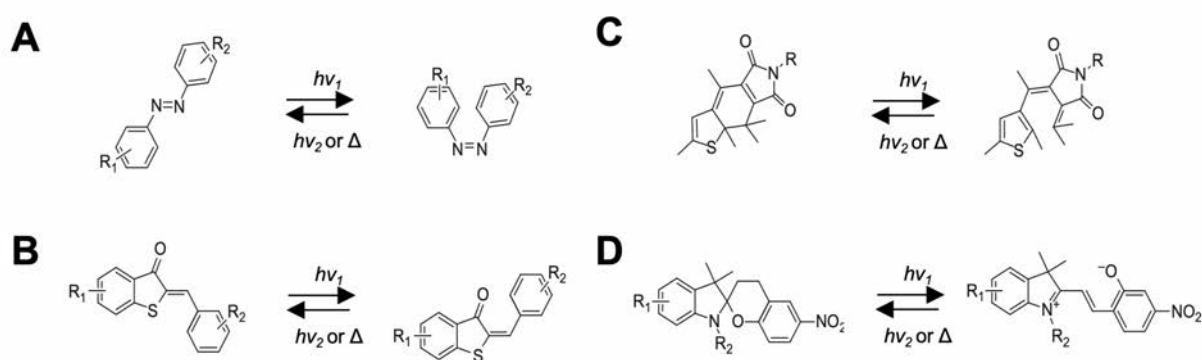


**Figure 2.26. Photoswitchable moieties that can interconvert between *trans* and *cis* or closed and open forms.** (A) Azobenzene, (B) hemithioindigos, (C) fulgides, (D) spiropyrans. Adapted from Berizzi *et al.*, 2020<sup>270</sup>.

### 2.3.3 Photoswitchable tethered ligands

Reversible photoswitches can be classified by the mechanism of interaction with the target in (a) photoswitchable tethered ligands (PTLs) that interact through a covalent bond or (b) photochromic ligands (PCLs) through noncovalent interactions. PTLs consist of a bioactive molecule for a specific receptor (*i.e.*, agonist or antagonist), a photoswitchable moiety (*e.g.*, an azobenzene) and a reactive group that is covalently linked to the receptor. Maleimides are one of the most common reactive groups and can selectively react with cysteine residues, within

the target receptor. Photoinduced conformation changes move the bioactive molecule close or further away from the binding site (**Figure 2.23B**). In this strategy, the PTL cannot diffuse away from the receptor, which leads to fast, reproducible, and spatially defined responses. This approach enables extremely selective optical modulation for the receptor of interest. Unfortunately, water accessible cysteines are rare in endogenous receptor (< 2%). Therefore, genetic modifications are needed to replace suitable residues with the required cysteines, allowing the conjugation of a reactive group *via* maleimide. This approach presents challenges that limit its usage. First, maleimide-based PTLs may not only react with the cysteine residues introduced at the intended target protein, but with cysteines in the same or in other proteins as well. This leads to non-specific cysteine conjugation and may give rise to off-target effects. Furthermore, the maleimide ring could be opened by hydrolysis in aqueous solution, which can limit their labeling efficiency. The MAQ family of K<sup>+</sup> blockers and the MAG (maleimide-azobenzene-glutamate) family of GluR agonists are examples of PTLs. MAGs target the glutamate ionotropic receptors type subunit 2 (GluK2) and mGlu receptor<sup>271-277</sup>. The compound D-MAG-0 in its *cis* configuration is a potent agonist of the mGlu<sub>2</sub> and mGlu<sub>3</sub> receptors and an antagonist of the mGlu<sub>6</sub> receptor. Moreover, a recently developed PTL (*i.e.*, D-MAG<sub>460</sub>) was able to photoswitch the mGlu<sub>3</sub> receptor under 2PE<sup>278</sup>. This approach has previously been implemented to control class A GPCRs in a light-dependent manner, including DARs (*e.g.*, maleimide-azobenzene-PPHT; MAP compound)<sup>279</sup>. This method, also called optogenetic pharmacology, requires genetic manipulation, thus, presenting the same virtues and shortcomings as optogenetics (see section 2.3)<sup>280</sup>.

Recently, a new family of PTLs has been developed (*i.e.*, tethered photopharmacology), overcoming this limitation. These compounds covalently tether the endogenous receptors at residues close to their binding site by means of more electrophilic groups than maleimide (*e.g.*, *N*-hydroxysuccinimide ester). They were dubbed targeted covalent photoswitches (TCPs) in analogy to targeted covalent drugs<sup>281</sup>. TCP-9 (**Figure 2.27**) was used to restore light-dependent electrical activity in a blind mouse retina<sup>282</sup>. However, this strategy has not been investigated for GPCRs yet.

Photoswitchable orthogonal remotely tethered ligands (*i.e.*, PORTL) are PTL variants that use self-labeling proteins (*e.g.*, SNAP, CLIP and HALO) for the covalent tether, which possess a much longer link (**Figure 2.23C**)<sup>283-285</sup>. This strategy is also described in GPCRs (*e.g.*, to specifically control mGlu receptors) and is meant to improve the photoisomerization efficiency and affinity of the PTLs. In fact, the addition of a long flexible linker facilitates PTL-receptor

binding. Interestingly, the PORTL (*i.e.*, BGAG) tethered to an engineered SNAG-mGlu<sub>2</sub> receptor enabled vision restoration in a mouse model for blindness<sup>286</sup>. Recently, a strategy using a PORTL and a genetically introduced membrane anchor (SNAP-tag and transmembrane segment) has been developed to precisely photocontrol D<sub>1</sub>R<sup>287</sup>.

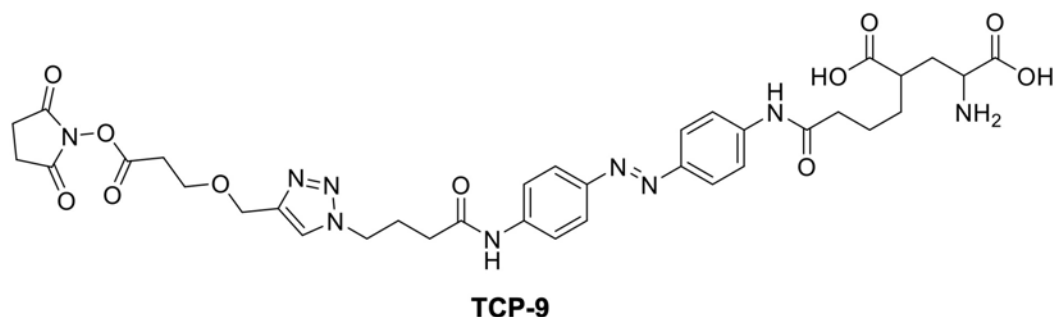


Figure 2.27. The structure of targeted covalent photoswitch-9 (TCP-9).

### 2.3.4 Photochromic ligands

PCLs are small molecules that can freely diffuse, like photo-uncaged ligands, but display the same reversibility of the PTLs and are the main focus of this thesis<sup>250</sup>. In fact, PCLs are composed of a pharmacologically active compound and a photoswitchable moiety, whose configuration can be changed upon irradiation. The significant change in configuration allows these two isomers (*i.e.*, *cis* and *trans* form) to show different affinity and potency or efficacy toward their target, which may be amplified with appropriate substitutions (**Figure 2.23D**)<sup>288</sup>. In most cases, azobenzene-based photoswitches turn out to be more active in the *trans*-isomer than in their *cis*-isomer. However, a drug that is pharmacologically inactive in the dark-adapted state is preferable<sup>216,289</sup>. The azobenzene is typically appended to the pharmacological scaffold, minimizing modification of the pharmacophore. This maintains the activity of the original compound in one configuration (*i.e.*, azoextension strategy). Alternatively, the azobenzene may be incorporated into the ligand itself in a strategy named “azologization” (see **Chapter 3**)<sup>268,290</sup>. In the latter case, a bridge between two aromatic rings into the chemical structure of the reference drug is replaced with an azo bond. This strategy is used to obtain new photoswitchable ligands libraries.

So far, PCLs have been synthesized to target all major GPCR classes through many different mechanisms of action. These mechanisms include orthosteric (see section 2.1.2 and **Chapters 3, 5, 6 and 10**), allosteric (see section 2.1.2 and **Chapters 7 and 11**) or bitopic interactions (see section 2.1.2 and **Chapters 4, 8 and 9**).



For instance, the PCL photoiperoxo is a photoswitchable mAChRs partial agonist that acts through an orthosteric interaction<sup>291</sup>. Moreover, AP (azobenzene-PPHT) is a PCL that is derived from a potent dopaminergic agonist 2-(*N*-phenethyl-*N*-propyl)amino-5-hydroxytetralin (PPHT), allowing reversible control of D<sub>1</sub>R and D<sub>2</sub>R<sup>279</sup>. Many photoswitchable allosteric modulators have been developed targeting the mGlu receptor family, such as Alloswitch-1 that was the first photoswitchable allosteric modulator of a GPCR and displayed high potency and selectivity as mGlu<sub>5</sub> receptor NAM<sup>292</sup>. Illumination with green light leads to the *trans*-isomer of Alloswitch-1, while illuminating it with violet light isomerizes it to the *cis* form. Moreover, reversible photoswitching of this compound was demonstrated in calcium imaging experiments within rat cortical astrocytes, and tadpole motility experiments<sup>289,293</sup>. In contrast, OPTOGluNAM4.1 is a NAM of mGlu<sub>4</sub> receptor, whereas protshe6 (*i.e.*, optogluram) is the first photoswitchable PAM for mGlu<sub>4</sub> receptor<sup>289,294,295</sup>. This ligand, like Alloswitch-1, is based on the structure of compound VU0415374, allowing optimal manipulation of mGlu<sub>4</sub> receptors' activities<sup>289,296</sup>. Optogluram isomerizes from *trans*-to-*cis* upon light with a wavelength of 380 nm and from *cis*-to-*trans* upon light with 500 nm, or by thermal relaxation (**Figure 2.28A**). The half-time of this photoswitchable compound is around 6.4 minutes (**Figure 2.28B**). The UV-Vis absorption spectra are shown in **Figure 2.28C**, where photoisomerization of optogluram is stable and reversible upon subsequent cycles of illumination (**Figure 2.87D**). Moreover, this compound enables photocontrol of mGlu<sub>4</sub> receptor activity *in vitro* (**Figure 2.28E**). The activity of the receptor is increased by *trans*-optogluram and reduced upon isomerization to the *cis* configuration after irradiation with violet light. In contrast, VU0364770, a classical PAM for the mGlu<sub>4</sub> receptor, is insensitive to light (**Figure 28E**)<sup>215</sup>. In addition, a murine model of persistent inflammatory pain showed that optogluram, delivered through a hybrid cannula (**Figure 2.27F**), optically controls mGlu<sub>4</sub> receptors, which were localized in the amygdala to produce analgesic, anxiolytic and anti-depressive effects in mice<sup>294</sup>. This compound also targets the mGlu<sub>6</sub> receptor and the characterization of protshe6 (*i.e.*, optogluram) by *in vitro* and *in vivo* studies is presented in **Chapter 11** of this thesis.

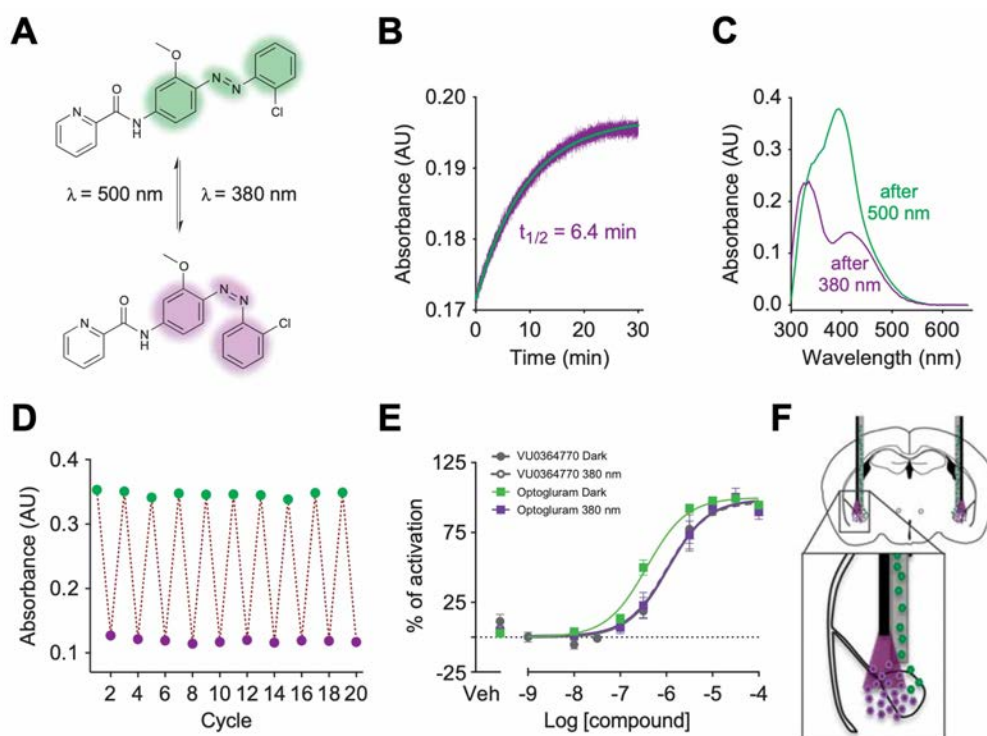


**Figure 2.27. Prosthe6 (*i.e.*, optogluram) is a positive allosteric modulator of mGlu<sub>4</sub> receptors.** (A) Structure and photoisomerization properties of the mGlu<sub>4</sub> receptor positive allosteric modulator (PAM) optogluram from *trans*-to-*cis* configuration after illumination with violet light ( $\lambda = 380$  nm) and from *cis*-to-*trans* with green light ( $\lambda = 500$  nm). (B) Thermal relaxation of *cis*-optogluram in aqueous solution ( $30 \mu\text{M}$  in PBS with 0.3% DMSO) after 3 min illumination with violet light. An exponential decay function was used to estimate relaxation half-life ( $t_{1/2} = 6.4$  min). Absorbance is shown as arbitrary units (AU). (C) The ultraviolet-visible absorption spectra of optogluram ( $30 \mu\text{M}$  in PBS with 0.3% DMSO) after 3 min illumination with either green or violet light. (D) Reversibility and stability of photoisomerization of optogluram ( $30 \mu\text{M}$  in PBS with 0.3% DMSO) after 3 min of illumination cycles with violet and green light. (E) Light-dependency of optogluram enhancing activity in a cell-based pharmacology assay. Dose-dependent enhancing activity of optogluram and VU0364770 (*i.e.*, a classical mGlu<sub>4</sub> receptor PAM) on a nominal concentration of agonist (*i.e.*, L-AP4, 3 nM) in dark conditions or under constant illumination with violet light (380 nm). Receptor activation was measured by inositol phosphate accumulation assay in mGlu<sub>4</sub> receptor-transfected HEK293 cells stimulated with a constant concentration of L-AP4 in presence of increasing concentrations of PAMs. Potency of optogluram was shifted from  $0.60 \pm 0.01 \mu\text{M}$  ( $n = 3$ ) in dark conditions to  $1.93 \pm 0.05 \mu\text{M}$  ( $n = 3$ ) under violet light, contrary to that of VU0364770 which is insensitive to light. (F) Diagram illustrating placement and design of the hybrid cannula for light and fluid delivery in the amygdala. Adapted from Zussy *et al.*, 2018<sup>294</sup>.

BQCAAI (BAI) is a bitopic photoswitchable ligand for M<sub>1</sub>Rs based on IPX (*i.e.*, a highly potent MR agonist) and BQCA (*i.e.*, an M<sub>1</sub>R PAM). BAI acts as a *cis*-antagonist and *trans*-agonist under illumination with 365 nm and 455 nm light in HEK cells overexpressing the M<sub>1</sub>R, respectively<sup>297</sup>. The chemical structures of all the compounds (as mentioned above) are presented in **Figure 2.28**, which only show a part of the repertoire of PCLs targeting GPCRs.

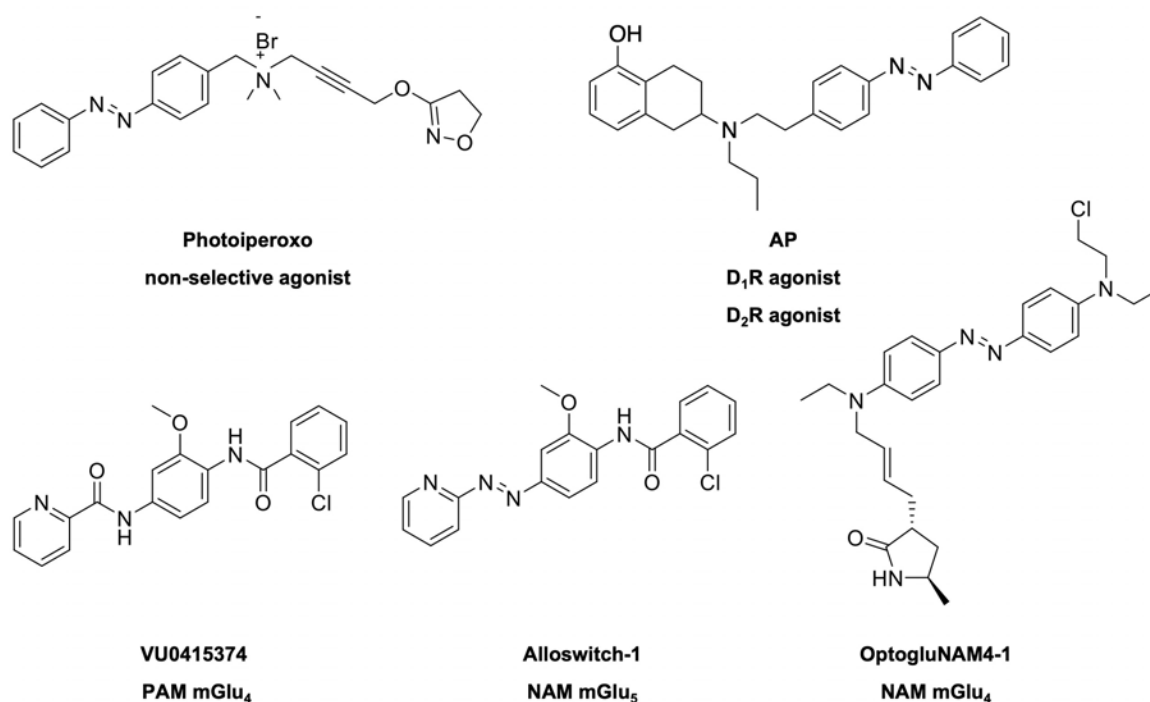


Figure 2.29. Selection of photoswitchable ligands.

Photopharmacology has yielded compounds that have the potential to be used for diverse applications including cancer chemotherapy, diabetes, or as antimicrobial agents, among others<sup>298-301</sup>. However, the preclinical and clinical development of photoswitches has progressed furthest for vision restoration in retinal degeneration disorders, such as RP. Many of the PCLs used in photopharmacological strategies are photoswitchable voltage-gated ion channel blockers, including AAQ, DENAQ, BENAQ<sup>302-306</sup>.

As previously mentioned, PCLs are freely diffusible small molecules that act directly on endogenous proteins. These compounds have the same advantages as small molecule drugs, including ease of application and the fast distribution into tissues. Moreover, a one-component system is simpler and potentially less toxic, than two-component systems used by photochemical approaches. This is due to the dosage that should be adjusted to maximize efficacy and minimize toxicity<sup>307</sup>. PCLs could be added, removed, or improved and do not require any irreversible or long-lasting modification. Equal to classical drugs, the selectivity between receptor subtype may be a challenge, but this could be overcome by a chemical functionalization of the molecule. Lastly, the pathway to their clinical approval resembles those of conventional drugs. When the efficacy and safety of a photoswitch are proven, they will be more affordable and widely applicable than other alternatives. Overall, PCLs may circumvent the limitations of caged ligands and optogenetic approaches.

### 2.3.5 Multiphoton excitation techniques

Multiphoton microscopy is a laser-scanning microscopy technique that implies localized nonlinear excitation and has become the method of choice for noninvasive imaging in thick tissue and live animals<sup>308</sup>. It has been applied for different purposes (*e.g.*, immunology, cancer, neuroscience)<sup>309-313</sup>.

The multiphoton excitation (MPE) is a relatively old concept theoretically proposed by Maria Goeppert-Mayer (*e.g.*, 2PE and three-photon excitations, 3PE) and was experimentally observed 30 years later, thanks to the invention of the laser. 2PE applies the simplest version of her predictions and provides more advantages than single photon excitation (1PE).

In 1PE processes, a high energy photon of a certain wavelength is absorbed by a molecule (*e.g.*, a fluorophore), which results in excitation of an electron in that molecule. The excited electron rapidly loses energy by non-radiative relaxation and eventually goes back to the ground state, emitting one photon of lower energy (fluorescence). The energy of a photon is inversely proportional to its wavelength ( $\lambda$ ), therefore, the emitted photon has a longer wavelength than the exciting photon (**Figure 2.30A**). Fluorescence emission occurs along the whole path of a laser beam crossing a fluorescent sample (**Figure 2.30B**).

In the 2PE process, the simultaneous absorption of two photons of low energy (*i.e.*, from a pulsed laser within  $\sim 10^{-18}$  seconds) by a molecule will excite it in a way equivalent to the absorption of a single photon carrying twice the energy (**Figure 2.30A**). The light emitted by the excited fluorophore will be of the same wavelength for both 1PE and 2PE, but with 2PE the fluorescence is only emitted at the focal point of the laser beam, where the photon density is high (**Figure 2.30B**). In fact, for the occurrence of 2PE, the photon density must be about a million times more than what is required to generate the same number of one-photon (1P) absorption events. The photon density increases at the focal plane, because of the spatial confinement of photons and declines away from this point. Consequently, the probability of coincident absorption of two photons in a single event is different from zero at the focal point, while it approaches to zero at distances less than  $1\mu\text{m}$  above and below the focal plane<sup>312</sup>. In 2PE, the relationship between excitation intensity and fluorescence intensity is quadratic, rather than the linear dependence of conventional fluorescence. This nonlinearity of excitation is quite advantageous for 2PE and for other MPE phenomena, as it allows three-dimensional submicrometric spatial resolution<sup>314-316</sup>. Using infrared (IR) light excitation to obtain visible fluorescence allows deep tissue penetration and lower scattering. Moreover, the power during

the peak of the pulse is high, but the average power is reasonably low. This means that generally there is neither background fluorescence, photobleaching nor light-induced damage, as the rest of the sample is exposed to low-energy NIR photons that fail to excite the fluorophore. The two-photon (2P) cross-section is a quantitative measure of the probability of a 2P absorption and characterizes an individual absorber. This parameter is usually expressed in units called GM (the abbreviation of Goeppert-Mayer) with  $1 \text{ GM} = 10^{-50} \text{ cm}^4 \text{ s per photon}$ .

MPE is related not only to the absorption of photons, but also to the subsequent physical and chemical effects (*e.g.*, fluorescence emission, dissociation of molecules, induced isomerization). In fact, following photon-absorption, an azobenzene undergo alterations in geometry or charge, which results to the modulation of the targeted molecule. While unsubstituted (symmetric) azobenzenes have low 2P absorption coefficient, chemical substitutions to the azobenzene core can increase the absorption coefficient and tune the excitation spectrum to longer wavelengths. However, these modifications may alter the photoswitch kinetic or isomerization yield<sup>250,317,318</sup>.

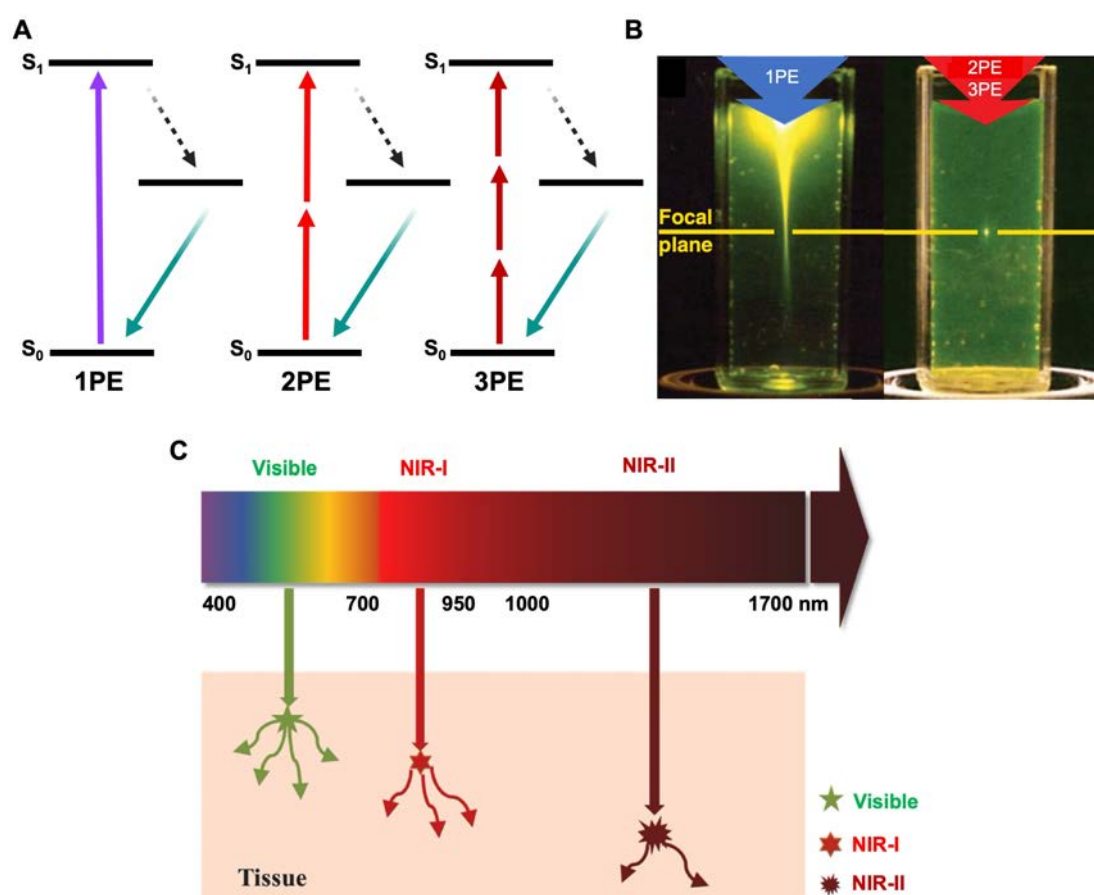


**Figure 2.30. Comparison between one-photon, two-photon, and three-photon excitation processes.** (A) Jablonski energy diagrams of single-photon (1P, left side), two-photon (2P, middle) and three-photon (3P, right side) excitation. In single-photon excitation (1PE) processes, a single photon of a UV or visible wavelength

(depicted as a violet upward arrow) is sufficient for the molecule to emit fluorescence (green downward arrow). In two-photon excitation (2PE) processes, two near-infrared (NIR) photons (depicted as red arrows) are needed to emit fluorescence of the same wavelength as emitted by 1PE. In three-photon excitation (3PE) three photons are needed for fluorescence emission. **(B)** Simultaneous single (1P, linear) and two-photon or three-photon (2P or 3P non-linear) excitation within a cuvette filled with a fluorescent molecule. When illuminating the cuvette with 1PE, light is absorbed throughout the entire optical path. When illuminating the cuvette with 2PE or 3PE, only molecules located at the focal point of the objective above can absorb multiple photons and emit fluorescence, as observed in the bright spot at the focal plane. **(C)** Light spectrum showing visible and near infrared (NIR) light, which is divided in two regions (NIR-I) and (NIR-II). When light enters in tissue, it can be reflected or absorbed by molecules within the medium or it can excite fluorophores to emit light at a different wavelength. Vertical arrow: penetration depth. Bent arrows: scattering. NIR-II exhibits the least scattering and deepest penetration depth compared with Vis and NIR-I. Adapted from Shen *et al.*, 2020 and Zipfel *et al.*, 2003<sup>308,319</sup>.

In 3PE, three photons (3Ps) simultaneously interact with a fluorescent molecule to excite it to a higher electronic state. The three photons exciting the fluorophore will have longer wavelengths and lower energy than those used to excite the same fluorophore in 1PE or 2PE. Since 3PE uses a broad range of wavelength (they have been reported up to 1700 nm for fluorescence activity imaging), this strategy provides increased tissue penetration and decreased light scattering<sup>320</sup>. Another advantage of 3P mechanism is that fluorescence has a higher order nonlinear dependency. The cubic laser power dependency, compared to quadratic one of two photon fluorescence interaction, confines the excitation target to an even smaller volume, thus providing a more targeted stimulation area known as optical sectioning<sup>321,322</sup>. This reduces the out-of-focus light as well as minimize photobleaching on the biological sample. These advantages of 3P microscopy gives it an edge for the visualization of the morphology and physiology within *in vivo* and *ex vivo* tissues, at a deep cellular level<sup>322</sup>. In the last 10 years, 3PE has especially been applied in neuroscience, allowing the imaging of the whole cortex and neuronal activities<sup>322-327</sup>. However, *in vivo* neuronal photostimulation has never been demonstrated with 3PE, neither with photopharmacology nor with optogenetics.

In this thesis we show the application of 2PE (**Chapters 5 and 8**) and 3PE (**Chapter 9**) of photoswitches *in vitro* and *in vivo*. In this way, we photocontrol endogenous receptors in a noninvasive manner. Continuous progress in light delivery methods, together with the development of new photoswitches optimized for MPE, will expand the photopharmacology field and its applications to control endogenous receptors with high temporal and spatial resolution.

## References

- 1 Fredriksson, R., Lagerstrom, M. C., Lundin, L. G. & Schioth, H. B. The G protein-coupled receptors in the human genome form five main families. Phylogenetic analysis, paralogon groups, and fingerprints. *Mol Pharmacol* **63**, 1256-1272, doi:10.1124/mol.63.6.1256 (2003).
- 2 Zhang, R. & Xie, X. Tools for GPCR drug discovery. *Acta Pharmacol Sin* **33**, 372-384, doi:10.1038/aps.2011.173 (2012).
- 3 Leftowitz, R. J. a. B. K. K. The Nobel prize in Chemistry 2012.
- 4 Hauser, A. S., Attwood, M. M., Rask-Andersen, M., Schioth, H. B. & Gloriam, D. E. Trends in GPCR drug discovery: New agents, targets and indications. *Nat Rev Drug Discov* **16**, 829-842, doi:10.1038/nrd.2017.178 (2017).
- 5 Hauser, A. S. *et al.* Pharmacogenomics of GPCR drug targets. *Cell* **172**, 41-54 e19, doi:10.1016/j.cell.2017.11.033 (2018).
- 6 Sriram, K. & Insel, P. A. G protein-coupled receptors as targets for approved drugs: How many targets and how many drugs? *Mol Pharmacol* **93**, 251-258, doi:10.1124/mol.117.111062 (2018).
- 7 Schioth, H. B. & Fredriksson, R. The GRAFS classification system of G protein-coupled receptors in comparative perspective. *Gen Comp Endocrinol* **142**, 94-101, doi:10.1016/j.ygcen.2004.12.018 (2005).
- 8 Attwood, T. K. & Findlay, J. B. Fingerprinting G protein-coupled receptors. *Protein Eng* **7**, 195-203, doi:10.1093/protein/7.2.195 (1994).
- 9 Kolakowski, L. F., Jr.,. GCRDb: A G-protein coupled receptor database. *Receptors Channels* **2**, 1-7 (1994).
- 10 Pandey-Szekeres, G. *et al.* GPCRdb in 2023: State-specific structure models using AlphaFold2 and new ligand resources. *Nucleic Acids Res* **51**, D395-D402, doi:10.1093/nar/gkac1013 (2023).
- 11 Moro, S. *et al.* Demystifying the three dimensional structure of G protein-coupled receptors (GPCRs) with the aid of molecular modeling. *Chem Commun (Camb)*, 2949-2956, doi:10.1039/b303439a (2003).
- 12 Venkatakrisnan, A. J. *et al.* Molecular signatures of G protein-coupled receptors. *Nature* **494**, 185-194, doi:10.1038/nature11896 (2013).
- 13 Kochman, K. Superfamily of G protein-coupled receptors (GPCRs)--extraordinary and outstanding success of evolution. *Postepy Hig Med Dosw (Online)* **68**, 1225-1237, doi:10.5604/17322693.1127326 (2014).
- 14 Bockaert, J. & Pin, J. P. Molecular tinkering of G protein-coupled receptors: An evolutionary success. *EMBO J* **18**, 1723-1729, doi:10.1093/emboj/18.7.1723 (1999).
- 15 Congreve, M., de Graaf, C., Swain, N. A. & Tate, C. G. Impact of GPCR structures on drug discovery. *Cell* **181**, 81-91, doi:10.1016/j.cell.2020.03.003 (2020).
- 16 Culhane, K. J., Liu, Y., Cai, Y. & Yan, E. C. Transmembrane signal transduction by peptide hormones via family B G protein-coupled receptors. *Front Pharmacol* **6**, 264, doi:10.3389/fphar.2015.00264 (2015).
- 17 Alexander, S. P. *et al.* The concise guide to pharmacology 2021/22: G protein-coupled receptors. *Br J Pharmacol* **178 Suppl 1**, S27-S156, doi:10.1111/bph.15538 (2021).
- 18 Yang, D. *et al.* G protein-coupled receptors: Structure- and function-based drug discovery. *Signal Transduct Target Ther* **6**, 7, doi:10.1038/s41392-020-00435-w (2021).
- 19 Zhao, L. H. *et al.* Differential requirement of the extracellular domain in activation of class B G protein-coupled receptors. *J Biol Chem* **291**, 15119-15130, doi:10.1074/jbc.M116.726620 (2016).

- 20 Tesmer, J. J. Hitchhiking on the heptahelical highway: Structure and function of 7TM receptor complexes. *Nat Rev Mol Cell Biol* **17**, 439-450, doi:10.1038/nrm.2016.36 (2016).
- 21 Qu, X., Wang, D. & Wu, B. in *GPCRs* (eds Beata Jastrzebska & Paul S. H. Park) 3-22 (Academic Press, 2020).
- 22 Hamann, J. *et al.* International union of basic and clinical pharmacology. XCIV. Adhesion G protein-coupled receptors. *Pharmacol Rev* **67**, 338-367, doi:10.1124/pr.114.009647 (2015).
- 23 Huang, H. C. & Klein, P. S. The Frizzled family: Receptors for multiple signal transduction pathways. *Genome Biol* **5**, 234, doi:10.1186/gb-2004-5-7-234 (2004).
- 24 Weis, W. I. & Kobilka, B. K. The molecular basis of G protein-coupled receptor activation. *Annu Rev Biochem* **87**, 897-919, doi:10.1146/annurev-biochem-060614-033910 (2018).
- 25 Bourne, H. R., Sanders, D. A. & McCormick, F. The GTPase superfamily: Conserved structure and molecular mechanism. *Nature* **349**, 117-127, doi:10.1038/349117a0 (1991).
- 26 Downes, G. B. & Gautam, N. The G protein subunit gene families. *Genomics* **62**, 544-552, doi:10.1006/geno.1999.5992 (1999).
- 27 Oldham, W. M. & Hamm, H. E. Heterotrimeric G protein activation by G protein-coupled receptors. *Nat Rev Mol Cell Biol* **9**, 60-71, doi:10.1038/nrm2299 (2008).
- 28 Milligan, G. & Kostenis, E. Heterotrimeric G proteins: A short history. *Br J Pharmacol* **147 Suppl 1**, S46-55, doi:10.1038/sj.bjp.0706405 (2006).
- 29 Kim, K. M. *et al.* Differential regulation of the dopamine D<sub>2</sub> and D<sub>3</sub> receptors by G protein-coupled receptor kinases and  $\beta$ -arrestins. *J Biol Chem* **276**, 37409-37414, doi:10.1074/jbc.M106728200 (2001).
- 30 Lefkowitz, R. J. & Shenoy, S. K. Transduction of receptor signals by  $\beta$ -arrestins. *Science* **308**, 512-517, doi:10.1126/science.1109237 (2005).
- 31 Tobin, A. B. G protein-coupled receptor phosphorylation: Where, when and by whom. *Br J Pharmacol* **153**, S167-176 (2008).
- 32 Palczewski, K. *et al.* Crystal structure of rhodopsin: A G protein-coupled receptor. *Science* **289**, 739-745, doi:10.1126/science.289.5480.739 (2000).
- 33 Cherezov, V. *et al.* High-resolution crystal structure of an engineered human  $\beta$ 2-adrenergic G protein-coupled receptor. *Science* **318**, 1258-1265, doi:10.1126/science.1150577 (2007).
- 34 Rosenbaum, D. M. *et al.* GPCR engineering yields high-resolution structural insights into  $\beta$ 2-adrenergic receptor function. *Science* **318**, 1266-1273, doi:10.1126/science.1150609 (2007).
- 35 Latorraca, N. R., Venkatakrishnan, A. J. & Dror, R. O. GPCR dynamics: Structures in motion. *Chem Rev* **117**, 139-155, doi:10.1021/acs.chemrev.6b00177 (2017).
- 36 Lee, Y., Basith, S. & Choi, S. Recent advances in structure-based drug design targeting class A G protein-coupled receptors utilizing crystal structures and computational simulations. *J Med Chem* **61**, 1-46, doi:10.1021/acs.jmedchem.6b01453 (2018).
- 37 Erlandson, S. C., McMahon, C. & Kruse, A. C. Structural basis for G protein-coupled receptor signaling. *Annu Rev Biophys* **47**, 1-18, doi:10.1146/annurev-biophys-070317-032931 (2018).
- 38 Renaud, J. P. *et al.* Cryo-EM in drug discovery: Achievements, limitations and prospects. *Nat Rev Drug Discov* **17**, 471-492, doi:10.1038/nrd.2018.77 (2018).
- 39 Basith, S. *et al.* Exploring G protein-coupled receptors (GPCRs) ligand space via cheminformatics approaches: Impact on rational drug design. *Front Pharmacol* **9**, 128, doi:10.3389/fphar.2018.00128 (2018).



- 40 Wacker, D., Stevens, R. C. & Roth, B. L. How ligands illuminate GPCR molecular pharmacology. *Cell* **170**, 414-427, doi:10.1016/j.cell.2017.07.009 (2017).
- 41 Kenakin, T. Inverse, protean, and ligand-selective agonism: Matters of receptor conformation. *FASEB J* **15**, 598-611, doi:10.1096/fj.00-0438rev (2001).
- 42 De Amici, M., Dallanoce, C., Holzgrabe, U., Trankle, C. & Mohr, K. Allosteric ligands for G protein-coupled receptors: A novel strategy with attractive therapeutic opportunities. *Med Res Rev* **30**, 463-549, doi:10.1002/med.20166 (2010).
- 43 Ritter, J., Flower, R.J., Henderson, G., Loke, Y.K., MacEwan, D.J., Rang H.P. *Rang & Dale's Pharmacology* (Elsevier, 2019).
- 44 Ritter, J., Flower, R.J., Henderson, G., Loke, Y.K., MacEwan, D.J., Rang, H.P. *Rang & Dale's Pharmacology* (Elsevier 2020).
- 45 Nussinov, R. & Tsai, C. J. The different ways through which specificity works in orthosteric and allosteric drugs. *Curr Pharm Des* **18**, 1311-1316, doi:10.2174/138161212799436377 (2012).
- 46 May, L. T., Leach, K., Sexton, P. M. & Christopoulos, A. Allosteric modulation of G protein-coupled receptors. *Annu Rev Pharmacol Toxicol* **47**, 1-51, doi:10.1146/annurev.pharmtox.47.120505.105159 (2007).
- 47 Wold, E. A. & Zhou, J. GPCR allosteric modulators: Mechanistic advantages and therapeutic applications. *Curr Top Med Chem* **18**, 2002-2006, doi:10.2174/1568026619999190101151837 (2018).
- 48 Lane, J. R., Abdul-Ridha, A. & Canals, M. Regulation of G protein-coupled receptors by allosteric ligands. *ACS Chem Neurosci* **4**, 527-534, doi:10.1021/cn400005t (2013).
- 49 Kenakin, T. P. Biased signalling and allosteric machines: New vistas and challenges for drug discovery. *Br J Pharmacol* **165**, 1659-1669, doi:10.1111/j.1476-5381.2011.01749.x (2012).
- 50 Bock, A., Schrage, R. & Mohr, K. Allosteric modulators targeting CNS muscarinic receptors. *Neuropharmacology* **136**, 427-437, doi:10.1016/j.neuropharm.2017.09.024 (2018).
- 51 Burger, W. A. C., Sexton, P. M., Christopoulos, A. & Thal, D. M. Toward an understanding of the structural basis of allostery in muscarinic acetylcholine receptors. *J Gen Physiol* **150**, 1360-1372, doi:10.1085/jgp.201711979 (2018).
- 52 Foster, D. J. & Conn, P. J. Allosteric modulation of GPCRs: New insights and potential utility for treatment of schizophrenia and other CNS disorders. *Neuron* **94**, 431-446, doi:10.1016/j.neuron.2017.03.016 (2017).
- 53 Christopoulos, A. Advances in G protein-coupled receptor allostery: From function to structure. *Mol Pharmacol* **86**, 463-478, doi:10.1124/mol.114.094342 (2014).
- 54 Wootten, D., Christopoulos, A. & Sexton, P. M. Emerging paradigms in GPCR allostery: implications for drug discovery. *Nat Rev Drug Discov* **12**, 630-644, doi:10.1038/nrd4052 (2013).
- 55 Gentry, P. R., Sexton, P. M. & Christopoulos, A. Novel allosteric modulators of G protein-coupled receptors. *J Biol Chem* **290**, 19478-19488, doi:10.1074/jbc.R115.662759 (2015).
- 56 Leach, K., Sexton, P. M. & Christopoulos, A. Allosteric GPCR modulators: Taking advantage of permissive receptor pharmacology. *Trends Pharmacol Sci* **28**, 382-389, doi:10.1016/j.tips.2007.06.004 (2007).
- 57 Keov, P., Sexton, P. M. & Christopoulos, A. Allosteric modulation of G protein-coupled receptors: A pharmacological perspective. *Neuropharmacology* **60**, 24-35, doi:10.1016/j.neuropharm.2010.07.010 (2011).
- 58 Valant, C., Sexton, P. M. & Christopoulos, A. Orthosteric/allosteric bitopic ligands: Going hybrid at GPCRs. *Mol Interv* **9**, 125-135, doi:10.1124/mi.9.3.6 (2009).

- 59 Conn, P. J., Christopoulos, A. & Lindsley, C. W. Allosteric modulators of GPCRs: A novel approach for the treatment of CNS disorders. *Nat Rev Drug Discov* **8**, 41-54, doi:10.1038/nrd2760 (2009).
- 60 Beharry, A. A. & Woolley, G. A. Azobenzene photoswitches for biomolecules. *Chem Soc Rev* **40**, 4422-4437, doi:10.1039/c1cs15023e (2011).
- 61 Sheffler, D. J., Gregory, K. J., Rook, J. M. & Conn, P. J. Allosteric modulation of metabotropic glutamate receptors. *Adv Pharmacol* **62**, 37-77, doi:10.1016/B978-0-12-385952-5.00010-5 (2011).
- 62 Lindsley, C. W. *et al.* Practical strategies and concepts in GPCR allosteric modulator discovery: Recent advances with metabotropic glutamate receptors. *Chem Rev* **116**, 6707-6741, doi:10.1021/acs.chemrev.5b00656 (2016).
- 63 Mohr, K. *et al.* Rational design of dualsteric GPCR ligands: Quests and promise. *Br J Pharmacol* **159**, 997-1008, doi:10.1111/j.1476-5381.2009.00601.x (2010).
- 64 Valant, C., Robert Lane, J., Sexton, P. M. & Christopoulos, A. The best of both worlds? Bitopic orthosteric/allosteric ligands of G protein-coupled receptors. *Annu Rev Pharmacol Toxicol* **52**, 153-178, doi:10.1146/annurev-pharmtox-010611-134514 (2012).
- 65 Mohr, K., Schmitz, J., Schrage, R., Trankle, C. & Holzgrabe, U. Molecular alliance- from orthosteric and allosteric ligands to dualsteric/bitopic agonists at G protein-coupled receptors. *Angew Chem Int Ed Engl* **52**, 508-516, doi:10.1002/anie.201205315 (2013).
- 66 Fronik, P., Gaiser, B. I. & Sejer Pedersen, D. Bitopic ligands and metastable binding sites: Opportunities for G protein-coupled receptor (GPCR) medicinal chemistry. *J Med Chem* **60**, 4126-4134, doi:10.1021/acs.jmedchem.6b01601 (2017).
- 67 Lane, J. R., Sexton, P. M. & Christopoulos, A. Bridging the gap: Bitopic ligands of G protein-coupled receptors. *Trends Pharmacol Sci* **34**, 59-66, doi:10.1016/j.tips.2012.10.003 (2013).
- 68 Kenakin, T. Biased signaling as allosteric probe dependence. *Cell Signal* **79**, 109844, doi:10.1016/j.cellsig.2020.109844 (2021).
- 69 Makita, N. & Iiri, T. Biased agonism: A novel paradigm in G protein-coupled receptor signaling observed in acquired hypocalciuric hypercalcemia. *Endocr J* **61**, 303-309, doi:10.1507/endocrj.ej13-0453 (2014).
- 70 Kenakin, T. & Christopoulos, A. Signalling bias in new drug discovery: Detection, quantification and therapeutic impact. *Nat Rev Drug Discov* **12**, 205-216, doi:10.1038/nrd3954 (2013).
- 71 Gundry, J., Glenn, R., Alagesan, P. & Rajagopal, S. A Practical guide to approaching biased agonism at G protein-coupled receptors. *Front Neurosci* **11**, 17, doi:10.3389/fnins.2017.00017 (2017).
- 72 Kruse, A. C. *et al.* Muscarinic acetylcholine receptors: Novel opportunities for drug development. *Nat Rev Drug Discov* **13**, 549-560, doi:10.1038/nrd4295 (2014).
- 73 Sankaranarayanan, S. & Ryan, T. A. in *Protein trafficking in neurons* (ed Andrew J. Bean) 97-124 (Academic Press, 2007).
- 74 Webster, R. in *Neurotransmitters, drugs and brain function* 1-32 (2001).
- 75 Cuello, A. in *Cholinergic pathways in CNS* 835-843 (2009).
- 76 Prado, M. A. M., Marchot, P. & Silman, I. Preface: Cholinergic mechanisms. *J Neurochem* **142 Suppl 2**, 3-6, doi:10.1111/jnc.14027 (2017).
- 77 Smythies, J. Section I. The cholinergic system. *Int Rev Neurobiol* **64**, 1-122, doi:10.1016/S0074-7742(05)64001-9 (2005).
- 78 *Neuroscience, 3rd ed.* (Sinauer Associates, 2004).

- 79 Scarr, E. Muscarinic receptors: Their roles in disorders of the central nervous system and potential as therapeutic targets. *CNS Neurosci Ther* **18**, 369-379, doi:10.1111/j.1755-5949.2011.00249.x (2012).
- 80 Zhou, F. M., Wilson, C. J. & Dani, J. A. Cholinergic interneuron characteristics and nicotinic properties in the striatum. *J Neurobiol* **53**, 590-605, doi:10.1002/neu.10150 (2002).
- 81 Caulfield, M. P. & Birdsall, N. J. International union of pharmacology. XVII. Classification of muscarinic acetylcholine receptors. *Pharmacol Rev* **50**, 279-290 (1998).
- 82 Wess, J. Molecular biology of muscarinic acetylcholine receptors. *Crit Rev Neurobiol* **10**, 69-99, doi:10.1615/critrevneurobiol.v10.i1.40 (1996).
- 83 Eglen, R. M. Muscarinic receptor subtype pharmacology and physiology. *Prog Med Chem* **43**, 105-136, doi:10.1016/S0079-6468(05)43004-0 (2005).
- 84 Caulfield, M. P. Muscarinic receptors-characterization, coupling and function. *Pharmacol Ther* **58**, 319-379, doi:10.1016/0163-7258(93)90027-b (1993).
- 85 Langmead, C. J., Watson, J. & Reavill, C. Muscarinic acetylcholine receptors as CNS drug targets. *Pharmacol Ther* **117**, 232-243, doi:10.1016/j.pharmthera.2007.09.009 (2008).
- 86 Lebois, E. P., Thorn, C., Edgerton, J. R., Popiolek, M. & Xi, S. Muscarinic receptor subtype distribution in the central nervous system and relevance to aging and Alzheimer's disease. *Neuropharmacology* **136**, 362-373, doi:10.1016/j.neuropharm.2017.11.018 (2018).
- 87 Felder, C. C., Bymaster, F. P., Ward, J. & DeLapp, N. Therapeutic opportunities for muscarinic receptors in the central nervous system. *J Med Chem* **43**, 4333-4353, doi:10.1021/jm990607u (2000).
- 88 Svoboda, J., Popelikova, A. & Stuchlik, A. Drugs interfering with muscarinic acetylcholine receptors and their effects on place navigation. *Front Psychiatry* **8**, 215, doi:10.3389/fpsy.2017.00215 (2017).
- 89 Ishii, M. & Kurachi, Y. Muscarinic acetylcholine receptors. *Curr Pharm Des* **12**, 3573-3581, doi:10.2174/138161206778522056 (2006).
- 90 Fisher, A. *et al.* M<sub>1</sub> muscarinic agonists can modulate some of the hallmarks in Alzheimer's disease: Implications in future therapy. *J Mol Neurosci* **20**, 349-356, doi:10.1385/JMN:20:3:349 (2003).
- 91 van Koppen, C. J. & Kaiser, B. Regulation of muscarinic acetylcholine receptor signaling. *Pharmacol Ther* **98**, 197-220, doi:10.1016/s0163-7258(03)00032-9 (2003).
- 92 Jiang, S. *et al.* M<sub>1</sub> muscarinic acetylcholine receptor in Alzheimer's disease. *Neurosci Bull* **30**, 295-307, doi:10.1007/s12264-013-1406-z (2014).
- 93 Cilleros-Mane, V. *et al.* The M<sub>2</sub> muscarinic receptor, in association to M<sub>1</sub>, regulates the neuromuscular PKA molecular dynamics. *FASEB J* **34**, 4934-4955, doi:10.1096/fj.201902113R (2020).
- 94 Thathiah, A. & De Strooper, B. The role of G protein-coupled receptors in the pathology of Alzheimer's disease. *Nat Rev Neurosci* **12**, 73-87, doi:10.1038/nrn2977 (2011).
- 95 Vilaro, M. T., Palacios, J. M. & Mengod, G. Localization of M<sub>5</sub> muscarinic receptor mRNA in rat brain examined by *in situ* hybridization histochemistry. *Neurosci Lett* **114**, 154-159, doi:10.1016/0304-3940(90)90064-g (1990).
- 96 Vuckovic, Z. *et al.* Crystal structure of the M<sub>5</sub> muscarinic acetylcholine receptor. *Proc Natl Acad Sci U S A* **116**, 26001-26007, doi:10.1073/pnas.1914446116 (2019).
- 97 Eglen, R. M. & Nahorski, S. R. The muscarinic M<sub>5</sub> receptor: A silent or emerging subtype? *Br J Pharmacol* **130**, 13-21, doi:10.1038/sj.bjp.0703276 (2000).

- 98 Felder, C. C. Muscarinic acetylcholine receptors: Signal transduction through multiple effectors. *FASEB J* **9**, 619-625 (1995).
- 99 Bubser, M., Byun, N., Wood, M. R. & Jones, C. K. Muscarinic receptor pharmacology and circuitry for the modulation of cognition. *Handb Exp Pharmacol*, 121-166, doi:10.1007/978-3-642-23274-9\_7 (2012).
- 100 Mrzljak, L., Levey, A. I. & Goldman-Rakic, P. S. Association of M<sub>1</sub> and M<sub>2</sub> muscarinic receptor proteins with asymmetric synapses in the primate cerebral cortex: Morphological evidence for cholinergic modulation of excitatory neurotransmission. *Proc Natl Acad Sci U S A* **90**, 5194-5198, doi:10.1073/pnas.90.11.5194 (1993).
- 101 Ztaou, S. *et al.* Involvement of striatal cholinergic interneurons and M<sub>1</sub> and M<sub>4</sub> muscarinic receptors in motor symptoms of Parkinson's disease. *J Neurosci* **36**, 9161-9172, doi:10.1523/JNEUROSCI.0873-16.2016 (2016).
- 102 Haga, K. *et al.* Structure of the human M<sub>2</sub> muscarinic acetylcholine receptor bound to an antagonist. *Nature* **482**, 547-551, doi:10.1038/nature10753 (2012).
- 103 Kruse, A. C. *et al.* Structure and dynamics of the M<sub>3</sub> muscarinic acetylcholine receptor. *Nature* **482**, 552-556, doi:10.1038/nature10867 (2012).
- 104 Thal, D. M. *et al.* Crystal structures of the M<sub>1</sub> and M<sub>4</sub> muscarinic acetylcholine receptors. *Nature* **531**, 335-340, doi:10.1038/nature17188 (2016).
- 105 Maeda, S., Qu, Q., Robertson, M. J., Skiniotis, G. & Kobilka, B. K. Structures of the M<sub>1</sub> and M<sub>2</sub> muscarinic acetylcholine receptor/G protein complexes. *Science* **364**, 552-557, doi:10.1126/science.aaw5188 (2019).
- 106 Suno, R. *et al.* Structural insights into the subtype-selective antagonist binding to the M<sub>2</sub> muscarinic receptor. *Nat Chem Biol* **14**, 1150-1158, doi:10.1038/s41589-018-0152-y (2018).
- 107 Staus, D. P. *et al.* Structure of the M<sub>2</sub> muscarinic receptor- $\beta$ -arrestin complex in a lipid nanodisc. *Nature* **579**, 297-302, doi:10.1038/s41586-020-1954-0 (2020).
- 108 Kruse, A. C. *et al.* Activation and allosteric modulation of a muscarinic acetylcholine receptor. *Nature* **504**, 101-106, doi:10.1038/nature12735 (2013).
- 109 Xu, J. *et al.* Conformational complexity and dynamics in a muscarinic receptor revealed by NMR spectroscopy. *Mol Cell* **75**, 53-65 e57, doi:10.1016/j.molcel.2019.04.028 (2019).
- 110 Dror, R. O. *et al.* Structural basis for modulation of a G protein-coupled receptor by allosteric drugs. *Nature* **503**, 295-299, doi:10.1038/nature12595 (2013).
- 111 Wess, J. Allosteric binding sites on muscarinic acetylcholine receptors. *Mol Pharmacol* **68**, 1506-1509, doi:10.1124/mol.105.019141 (2005).
- 112 Valant, C., Felder, C. C., Sexton, P. M. & Christopoulos, A. Probe dependence in the allosteric modulation of a G protein-coupled receptor: Implications for detection and validation of allosteric ligand effects. *Mol Pharmacol* **81**, 41-52, doi:10.1124/mol.111.074872 (2012).
- 113 Abdul-Ridha, A. *et al.* Molecular determinants of allosteric modulation at the M<sub>1</sub> muscarinic acetylcholine receptor. *J Biol Chem* **289**, 6067-6079, doi:10.1074/jbc.M113.539080 (2014).
- 114 Stahl, E. & Ellis, J. Novel allosteric effects of amiodarone at the muscarinic M<sub>5</sub> receptor. *J Pharmacol Exp Ther* **334**, 214-222, doi:10.1124/jpet.109.165316 (2010).
- 115 Lazareno, S., Popham, A. & Birdsall, N. J. Allosteric interactions of staurosporine and other indolocarbazoles with *N*-[methyl-(3)H]scopolamine and acetylcholine at muscarinic receptor subtypes: Identification of a second allosteric site. *Mol Pharmacol* **58**, 194-207, doi:10.1124/mol.58.1.194 (2000).

- 116 Lanzafame, A. A., Sexton, P. M. & Christopoulos, A. Interaction studies of multiple binding sites on M<sub>4</sub> muscarinic acetylcholine receptors. *Mol Pharmacol* **70**, 736-746, doi:10.1124/mol.106.024711 (2006).
- 117 Espinoza-Fonseca, L. M. & Trujillo-Ferrara, J. G. Identification of multiple allosteric sites on the M<sub>1</sub> muscarinic acetylcholine receptor. *FEBS Lett* **579**, 6726-6732, doi:10.1016/j.febslet.2005.10.069 (2005).
- 118 Espinoza-Fonseca, L. M. & Trujillo-Ferrara, J. G. The existence of a second allosteric site on the M<sub>1</sub> muscarinic acetylcholine receptor and its implications for drug design. *Bioorg Med Chem Lett* **16**, 1217-1220, doi:10.1016/j.bmcl.2005.11.097 (2006).
- 119 Bermudez, M. *et al.* Ligand-specific restriction of extracellular conformational dynamics constrains signaling of the M<sub>2</sub> muscarinic receptor. *ACS Chem Biol* **12**, 1743-1748, doi:10.1021/acscchembio.7b00275 (2017).
- 120 Barger, G. & Dale, H. H. Chemical structure and sympathomimetic action of amines. *J Physiol* **41**, 19-59, doi:10.1113/jphysiol.1910.sp001392 (1910).
- 121 Blaschko, H. Metabolism and storage of biogenic amines. *Experientia* **13**, 9-13, doi:10.1007/BF02156938 (1957).
- 122 Montagu, K. A. Catechol compounds in rat tissues and in brains of different animals. *Nature* **180**, 244-245, doi:10.1038/180244a0 (1957).
- 123 Hornykiewicz, O. Dopamine miracle: From brain homogenate to dopamine replacement. *Mov Disord* **17**, 501-508, doi:10.1002/mds.10115 (2002).
- 124 Marsden, C. A. Dopamine: The rewarding years. *Br J Pharmacol* **147 Suppl 1**, S136-144, doi:10.1038/sj.bjp.0706473 (2006).
- 125 Beaulieu, J. M. & Gainetdinov, R. R. The physiology, signaling, and pharmacology of dopamine receptors. *Pharmacol Rev* **63**, 182-217, doi:10.1124/pr.110.002642 (2011).
- 126 Elsworth, J. D. & Roth, R. H. Dopamine synthesis, uptake, metabolism, and receptors: Relevance to gene therapy of Parkinson's disease. *Exp Neurol* **144**, 4-9, doi:10.1006/exnr.1996.6379 (1997).
- 127 Klein, M. O. *et al.* Dopamine: Functions, signaling, and association with neurological diseases. *Cell Mol Neurobiol* **39**, 31-59, doi:10.1007/s10571-018-0632-3 (2019).
- 128 Zahoor, I., Shafi, A. & Haq, E. in *Parkinson's disease: Pathogenesis and clinical aspects* (eds T. B. Stoker & J. C. Greenland) (2018).
- 129 Wang, X., Li, J., Dong, G. & Yue, J. The endogenous substrates of brain CYP2D. *Eur J Pharmacol* **724**, 211-218, doi:10.1016/j.ejphar.2013.12.025 (2014).
- 130 Yaffe, D., Forrest, L. R. & Schuldiner, S. The ins and outs of vesicular monoamine transporters. *J Gen Physiol* **150**, 671-682, doi:10.1085/jgp.201711980 (2018).
- 131 Kelly, R. B. Storage and release of neurotransmitters. *Cell* **72 Suppl**, 43-53, doi:10.1016/s0092-8674(05)80027-3 (1993).
- 132 Rice, M. E., Patel, J. C. & Cragg, S. J. Dopamine release in the basal ganglia. *Neuroscience* **198**, 112-137, doi:10.1016/j.neuroscience.2011.08.066 (2011).
- 133 Lorang, D., Amara, S. G. & Simerly, R. B. Cell-type-specific expression of catecholamine transporters in the rat brain. *J Neurosci* **14**, 4903-4914, doi:10.1523/JNEUROSCI.14-08-04903.1994 (1994).
- 134 Latif, S. *et al.* Dopamine in Parkinson's disease. *Clin Chim Acta* **522**, 114-126, doi:10.1016/j.cca.2021.08.009 (2021).
- 135 Xu, H. & Yang, F. The interplay of dopamine metabolism abnormalities and mitochondrial defects in the pathogenesis of schizophrenia. *Transl Psychiatry* **12**, 464, doi:10.1038/s41398-022-02233-0 (2022).
- 136 Zhang, S., Wang, R. & Wang, G. Impact of dopamine oxidation on dopaminergic neurodegeneration. *ACS Chemical Neuroscience* **10**, 945-953, doi:10.1021/acscemneuro.8b00454 (2019).

- 137 Eisenhofer, G., Kopin, I. J. & Goldstein, D. S. Catecholamine metabolism: A contemporary view with implications for physiology and medicine. *Pharmacol Rev* **56**, 331-349, doi:10.1124/pr.56.3.1 (2004).
- 138 Vallone, D., Picetti, R. & Borrelli, E. Structure and function of dopamine receptors. *Neurosci Biobehav Rev* **24**, 125-132, doi:10.1016/s0149-7634(99)00063-9 (2000).
- 139 Hisahara, S. & Shimohama, S. Dopamine receptors and Parkinson's disease. *Int J Med Chem* **2011**, 403039, doi:10.1155/2011/403039 (2011).
- 140 Missale, C., Nash, S. R., Robinson, S. W., Jaber, M. & Caron, M. G. Dopamine receptors: From structure to function. *Physiol Rev* **78**, 189-225, doi:10.1152/physrev.1998.78.1.189 (1998).
- 141 Gingrich, J. A. & Caron, M. G. Recent advances in the molecular biology of dopamine receptors. *Annu Rev Neurosci* **16**, 299-321, doi:10.1146/annurev.ne.16.030193.001503 (1993).
- 142 Greengard, P. The neurobiology of slow synaptic transmission. *Science* **294**, 1024-1030, doi:10.1126/science.294.5544.1024 (2001).
- 143 Jin, L. Q., Wang, H. Y. & Friedman, E. Stimulated D<sub>1</sub> dopamine receptors couple to multiple G $\alpha$  proteins in different brain regions. *J Neurochem* **78**, 981-990, doi:10.1046/j.1471-4159.2001.00470.x (2001).
- 144 Monsma, F. J., Jr., McVittie, L. D., Gerfen, C. R., Mahan, L. C. & Sibley, D. R. Multiple D<sub>2</sub> dopamine receptors produced by alternative RNA splicing. *Nature* **342**, 926-929, doi:10.1038/342926a0 (1989).
- 145 De Mei, C., Ramos, M., Iitaka, C. & Borrelli, E. Getting specialized: Presynaptic and postsynaptic dopamine D<sub>2</sub> receptors. *Curr Opin Pharmacol* **9**, 53-58, doi:10.1016/j.coph.2008.12.002 (2009).
- 146 Usiello, A. *et al.* Distinct functions of the two isoforms of dopamine D<sub>2</sub> receptors. *Nature* **408**, 199-203, doi:10.1038/35041572 (2000).
- 147 Giros, B., Martres, M. P., Pilon, C., Sokoloff, P. & Schwartz, J. C. Shorter variants of the D<sub>3</sub> dopamine receptor produced through various patterns of alternative splicing. *Biochem Biophys Res Commun* **176**, 1584-1592, doi:10.1016/0006-291x(91)90469-n (1991).
- 148 Oak, J. N., Oldenhof, J. & Van Tol, H. H. The dopamine D<sub>4</sub> receptor: One decade of research. *Eur J Pharmacol* **405**, 303-327, doi:10.1016/s0014-2999(00)00562-8 (2000).
- 149 Van Tol, H. H. *et al.* Multiple dopamine D<sub>4</sub> receptor variants in the human population. *Nature* **358**, 149-152, doi:10.1038/358149a0 (1992).
- 150 Valjent, E., Bertran-Gonzalez, J., Herve, D., Fisone, G. & Girault, J. A. Looking BAC at striatal signaling: Cell-specific analysis in new transgenic mice. *Trends Neurosci* **32**, 538-547, doi:10.1016/j.tins.2009.06.005 (2009).
- 151 Fan, L. *et al.* Haloperidol bound D<sub>2</sub> dopamine receptor structure inspired the discovery of subtype selective ligands. *Nat Commun* **11**, 1074, doi:10.1038/s41467-020-14884-y (2020).
- 152 Sun, B. *et al.* Crystal structure of dopamine D<sub>1</sub> receptor in complex with G protein and a non-catechol agonist. *Nat Commun* **12**, 3305, doi:10.1038/s41467-021-23519-9 (2021).
- 153 Chien, E. Y. *et al.* Structure of the human dopamine D<sub>3</sub> receptor in complex with a D<sub>2</sub>/D<sub>3</sub> selective antagonist. *Science* **330**, 1091-1095, doi:10.1126/science.1197410 (2010).
- 154 Wang, S. *et al.* D<sub>4</sub> dopamine receptor high-resolution structures enable the discovery of selective agonists. *Science* **358**, 381-386, doi:10.1126/science.aan5468 (2017).
- 155 Wang, S. *et al.* Structure of the D<sub>2</sub> dopamine receptor bound to the atypical antipsychotic drug risperidone. *Nature* **555**, 269-273, doi:10.1038/nature25758 (2018).

- 156 Yin, J. *et al.* Structure of a D<sub>2</sub> dopamine receptor-G protein complex in a lipid membrane. *Nature* **584**, 125-129, doi:10.1038/s41586-020-2379-5 (2020).
- 157 Xiao, P. *et al.* Ligand recognition and allosteric regulation of D<sub>1</sub>R-Gα<sub>s</sub> signaling complexes. *Cell* **184**, 943-956 e918, doi:10.1016/j.cell.2021.01.028 (2021).
- 158 Zhuang, Y. *et al.* Structural insights into the human D<sub>1</sub> and D<sub>2</sub> dopamine receptor signaling complexes. *Cell* **184**, 931-942.e918, doi:10.1016/j.cell.2021.01.027 (2021).
- 159 Garcia-Nafria, J., Lee, Y., Bai, X., Carpenter, B. & Tate, C. G. Cryo-EM structure of the adenosine A<sub>2A</sub> receptor coupled to an engineered heterotrimeric G protein. *Elife* **7**, doi:10.7554/eLife.35946 (2018).
- 160 Rasmussen, S. G. *et al.* Crystal structure of the β<sub>2</sub> adrenergic receptor-Gα<sub>s</sub> protein complex. *Nature* **477**, 549-555, doi:10.1038/nature10361 (2011).
- 161 Lewis, M. A. *et al.* Discovery of D<sub>1</sub> dopamine receptor positive allosteric modulators: Characterization of pharmacology and identification of residues that regulate species selectivity. *J Pharmacol Exp Ther* **354**, 340-349, doi:10.1124/jpet.115.224071 (2015).
- 162 Wang, X. *et al.* Intracellular binding site for a positive allosteric modulator of the dopamine D<sub>1</sub> receptor. *Mol Pharmacol* **94**, 1232-1245, doi:10.1124/mol.118.112649 (2018).
- 163 Wang, X. *et al.* Mutual cooperativity of three allosteric sites on the dopamine D<sub>1</sub> receptor. *Mol Pharmacol* **103**, 176-187, doi:10.1124/molpharm.122.000605 (2023).
- 164 Hall, A., Provins, L. & Valade, A. Novel strategies to activate the dopamine D<sub>1</sub> receptor: Recent advances in orthosteric agonism and positive allosteric modulation. *J Med Chem* **62**, 128-140, doi:10.1021/acs.jmedchem.8b01767 (2019).
- 165 Sibley, D. R., Luderman, K. D., Free, R. B. & Shi, L. Novel Cryo-EM structures of the D<sub>1</sub> dopamine receptor unlock its therapeutic potential. *Signal Transduct Target Ther* **6**, 205, doi:10.1038/s41392-021-00630-3 (2021).
- 166 Luderman, K. D. *et al.* Development of pyrimidone D<sub>1</sub> dopamine receptor positive allosteric modulators. *Bioorg Med Chem Lett* **31**, 127696, doi:10.1016/j.bmcl.2020.127696 (2021).
- 167 Svensson, K. A., Hao, J. & Bruns, R. F. Positive allosteric modulators of the dopamine D<sub>1</sub> receptor: A new mechanism for the treatment of neuropsychiatric disorders. *Adv Pharmacol* **86**, 273-305, doi:10.1016/bs.apha.2019.06.001 (2019).
- 168 Luderman, K. D. *et al.* Identification of positive allosteric modulators of the D<sub>1</sub> dopamine receptor that act at diverse binding sites. *Mol Pharmacol* **94**, 1197-1209, doi:10.1124/mol.118.113175 (2018).
- 169 Svensson, K. A. *et al.* An allosteric potentiator of the dopamine D<sub>1</sub> receptor increases locomotor activity in human D<sub>1</sub> knock-in mice without causing stereotypy or tachyphylaxis. *J Pharmacol Exp Ther* **360**, 117-128, doi:10.1124/jpet.116.236372 (2017).
- 170 Romano, C., Yang, W. L. & O'Malley, K. L. Metabotropic glutamate receptor 5 is a disulfide-linked dimer. *J Biol Chem* **271**, 28612-28616, doi:10.1074/jbc.271.45.28612 (1996).
- 171 Ribeiro, F. M., Vieira, L. B., Pires, R. G., Olmo, R. P. & Ferguson, S. S. Metabotropic glutamate receptors and neurodegenerative diseases. *Pharmacol Res* **115**, 179-191, doi:10.1016/j.phrs.2016.11.013 (2017).
- 172 Niswender, C. M. & Conn, P. J. Metabotropic glutamate receptors: Physiology, pharmacology, and disease. *Annu Rev Pharmacol Toxicol* **50**, 295-322, doi:10.1146/annurev.pharmtox.011008.145533 (2010).
- 173 Sudhof, T. C. The synaptic vesicle cycle. *Annu Rev Neurosci* **27**, 509-547, doi:10.1146/annurev.neuro.26.041002.131412 (2004).

- 174 Daikhin, Y. & Yudkoff, M. Compartmentation of brain glutamate metabolism in neurons and glia. *J Nutr* **130**, 1026S-1031S, doi:10.1093/jn/130.4.1026S (2000).
- 175 Hayashi, M. K. Structure-function relationship of transporters in the glutamate-glutamine cycle of the central nervous system. *Int J Mol Sci* **19**, doi:10.3390/ijms19041177 (2018).
- 176 Eccles J.C., M. P. L. Ionotropic and metabotropic synaptic transmission. *Trend Neurosci* **2**, 39-40 (1978).
- 177 Rondard, P., Goudet, C., Kniazeff, J., Pin, J. P. & Prezeau, L. The complexity of their activation mechanism opens new possibilities for the modulation of mGlu and GABA<sub>B</sub> class C G protein-coupled receptors. *Neuropharmacology* **60**, 82-92, doi:10.1016/j.neuropharm.2010.08.009 (2011).
- 178 Kunishima, N. *et al.* Structural basis of glutamate recognition by a dimeric metabotropic glutamate receptor. *Nature* **407**, 971-977, doi:10.1038/35039564 (2000).
- 179 Muto, T., Tsuchiya, D., Morikawa, K. & Jingami, H. Structures of the extracellular regions of the group II/III metabotropic glutamate receptors. *Proc Natl Acad Sci U S A* **104**, 3759-3764, doi:10.1073/pnas.0611577104 (2007).
- 180 Tsuchiya, D., Kunishima, N., Kamiya, N., Jingami, H. & Morikawa, K. Structural views of the ligand-binding cores of a metabotropic glutamate receptor complexed with an antagonist and both glutamate and Gd<sup>3+</sup>. *Proc Natl Acad Sci U S A* **99**, 2660-2665, doi:10.1073/pnas.052708599 (2002).
- 181 Koehl, A. *et al.* Structural insights into the activation of metabotropic glutamate receptors. *Nature* **566**, 79-84, doi:10.1038/s41586-019-0881-4 (2019).
- 182 Lin, S. *et al.* Structures of Gα<sub>i</sub>-bound metabotropic glutamate receptors mGlu<sub>2</sub> and mGlu<sub>4</sub>. *Nature* **594**, 583-588, doi:10.1038/s41586-021-03495-2 (2021).
- 183 Acher, F. C., Cabaye, A., Eshak, F., Goupil-Lamy, A. & Pin, J. P. Metabotropic glutamate receptor orthosteric ligands and their binding sites. *Neuropharmacology* **204**, 108886, doi:10.1016/j.neuropharm.2021.108886 (2022).
- 184 Kniazeff, J. *et al.* Closed state of both binding domains of homodimeric mGlu receptors is required for full activity. *Nat Struct Mol Biol* **11**, 706-713, doi:10.1038/nsmb794 (2004).
- 185 Liauw, B. W., Afsari, H. S. & Vafabakhsh, R. Conformational rearrangement during activation of a metabotropic glutamate receptor. *Nat Chem Biol* **17**, 291-297, doi:10.1038/s41589-020-00702-5 (2021).
- 186 Hlavackova, V. *et al.* Sequential inter- and intrasubunit rearrangements during activation of dimeric metabotropic glutamate receptor 1. *Sci Signal* **5**, ra59, doi:10.1126/scisignal.2002720 (2012).
- 187 Nicoletti, F. *et al.* Metabotropic glutamate receptors: From the workbench to the bedside. *Neuropharmacology* **60**, 1017-1041, doi:10.1016/j.neuropharm.2010.10.022 (2011).
- 188 Petralia, R. S., Wang, Y. X., Niedzielski, A. S. & Wenthold, R. J. The metabotropic glutamate receptors, mGlu<sub>2</sub> and mGlu<sub>3</sub>, show unique postsynaptic, presynaptic and glial localizations. *Neuroscience* **71**, 949-976, doi:10.1016/0306-4522(95)00533-1 (1996).
- 189 Nakajima, Y. *et al.* Molecular characterization of a novel retinal metabotropic glutamate receptor mGlu<sub>6</sub> with a high agonist selectivity for L-2-amino-4-phosphonobutyrate. *J Biol Chem* **268**, 11868-11873 (1993).
- 190 Dhingra, A. *et al.* The light response of ON bipolar neurons requires Gα<sub>o</sub>. *J Neurosci* **20**, 9053-9058, doi:10.1523/JNEUROSCI.20-24-09053.2000 (2000).
- 191 Masu, M. *et al.* Specific deficit of the ON response in visual transmission by targeted disruption of the mGlu<sub>6</sub> gene. *Cell* **80**, 757-765, doi:10.1016/0092-8674(95)90354-2 (1995).



- 192 Nomura, A. *et al.* Developmentally regulated postsynaptic localization of a metabotropic glutamate receptor in rat rod bipolar cells. *Cell* **77**, 361-369, doi:10.1016/0092-8674(94)90151-1 (1994).
- 193 Vardi, N., Duvoisin, R., Wu, G. & Sterling, P. Localization of mGlu<sub>6</sub> to dendrites of ON bipolar cells in primate retina. *J Comp Neurol* **423**, 402-412, doi:10.1002/1096-9861(20000731)423:3<402::aid-cne4>3.0.co;2-e (2000).
- 194 Koike, C. *et al.* TRPM1 is a component of the retinal ON bipolar cell transduction channel in the mGlu<sub>6</sub> cascade. *Proc Natl Acad Sci U S A* **107**, 332-337, doi:10.1073/pnas.0912730107 (2010).
- 195 Morgans, C. W. *et al.* TRPM1 is required for the depolarizing light response in retinal ON bipolar cells. *Proc Natl Acad Sci U S A* **106**, 19174-19178, doi:10.1073/pnas.0908711106 (2009).
- 196 Shen, Y., Rampino, M. A., Carroll, R. C. & Nawy, S. G protein-mediated inhibition of the Trp channel TRPM1 requires the G $\beta\gamma$  dimer. *Proc Natl Acad Sci U S A* **109**, 8752-8757, doi:10.1073/pnas.1117433109 (2012).
- 197 Gerber, U. Metabotropic glutamate receptors in vertebrate retina. *Doc Ophthalmol* **106**, 83-87, doi:10.1023/a:1022477203420 (2003).
- 198 Palazzo, E. *et al.* The cold case of metabotropic glutamate receptor 6: Unjust detention in the retina? *Curr Neuropharmacol* **18**, 120-125, doi:10.2174/1570159X17666191001141849 (2020).
- 199 Xu, Y. *et al.* The TRPM1 channel in ON bipolar cells is gated by both the  $\alpha$  and the  $\beta\gamma$  subunits of the G protein G $\alpha_o$ . *Sci Rep* **6**, 20940, doi:10.1038/srep20940 (2016).
- 200 Koike, C., Numata, T., Ueda, H., Mori, Y. & Furukawa, T. TRPM1: A vertebrate TRP channel responsible for retinal ON bipolar function. *Cell Calcium* **48**, 95-101, doi:10.1016/j.ceca.2010.08.004 (2010).
- 201 Agosto, M. A. *et al.* Oligomeric state of purified transient receptor potential melastatin-1 (TRPM1), a protein essential for dim light vision. *J Biol Chem* **289**, 27019-27033, doi:10.1074/jbc.M114.593780 (2014).
- 202 Morgans, C. W., Brown, R. L. & Duvoisin, R. M. TRPM1: The endpoint of the mGlu<sub>6</sub> receptor signal transduction cascade in retinal ON bipolar cells. *Bioessays* **32**, 609-614, doi:10.1002/bies.200900198 (2010).
- 203 Flor, P. J. & Acher, F. C. Orthosteric *versus* allosteric GPCR activation: The great challenge of group-III mGluRs. *Biochem Pharmacol* **84**, 414-424, doi:10.1016/j.bcp.2012.04.013 (2012).
- 204 Schkeryantz, J. M. *et al.* Determination of L-AP4-bound human mGlu<sub>8</sub> receptor amino terminal domain structure and the molecular basis for L-AP4's group III mGlu receptor functional potency and selectivity. *Bioorg Med Chem Lett* **28**, 612-617, doi:10.1016/j.bmcl.2018.01.037 (2018).
- 205 Gasparini, F. *et al.* Discovery and characterization of non-competitive antagonists of group I metabotropic glutamate receptors. *Farmacologia* **56**, 95-99, doi:10.1016/s0014-827x(01)01008-4 (2001).
- 206 Pagano, A. *et al.* The non-competitive antagonists 2-methyl-6-(phenylethynyl)pyridine and 7-hydroxyiminocyclopropan[b]chromen-1a-carboxylic acid ethyl ester interact with overlapping binding pockets in the transmembrane region of group I metabotropic glutamate receptors. *J Biol Chem* **275**, 33750-33758, doi:10.1074/jbc.M006230200 (2000).
- 207 Brauner-Osborne, H., Jensen, A. A. & Krosgaard-Larsen, P. Interaction of CPCCOEt with a chimeric mGlu<sub>1b</sub> and calcium sensing receptor. *Neuroreport* **10**, 3923-3925, doi:10.1097/00001756-199912160-00036 (1999).

- 208 Maj, M. *et al.* (-)-PHCCC, a positive allosteric modulator of mGlu<sub>4</sub>: Characterization, mechanism of action, and neuroprotection. *Neuropharmacology* **45**, 895-906, doi:10.1016/s0028-3908(03)00271-5 (2003).
- 209 Mitsukawa, K. *et al.* A selective metabotropic glutamate receptor 7 agonist: Activation of receptor signaling via an allosteric site modulates stress parameters *in vivo*. *Proc Natl Acad Sci U S A* **102**, 18712-18717, doi:10.1073/pnas.0508063102 (2005).
- 210 Knoflach, F. *et al.* Positive allosteric modulators of metabotropic glutamate 1 receptor: Characterization, mechanism of action, and binding site. *Proc Natl Acad Sci U S A* **98**, 13402-13407, doi:10.1073/pnas.231358298 (2001).
- 211 O'Brien, J. A. *et al.* A family of highly selective allosteric modulators of the metabotropic glutamate receptor subtype 5. *Mol Pharmacol* **64**, 731-740, doi:10.1124/mol.64.3.731 (2003).
- 212 Annoura, H., Fukunaga, A., Uesugi, M., Tatsuoka, T. & Horikawa, Y. A novel class of antagonists for metabotropic glutamate receptors, 7-(Hydroxyimino)cyclopropa[b]chromen-1a-carboxylates. *Bioorganic & Medicinal Chemistry Letters* **6**, 763-766, doi:10.1016/0960-894X(96)00104-7 (1996).
- 213 O'Brien, J. A. *et al.* A novel selective allosteric modulator potentiates the activity of native metabotropic glutamate receptor subtype 5 in rat forebrain. *J Pharmacol Exp Ther* **309**, 568-577, doi:10.1124/jpet.103.061747 (2004).
- 214 Mathiesen, J. M., Svendsen, N., Brauner-Osborne, H., Thomsen, C. & Ramirez, M. T. Positive allosteric modulation of the human metabotropic glutamate receptor 4 (hmGlu<sub>4</sub>) by SIB-1893 and MPEP. *Br J Pharmacol* **138**, 1026-1030, doi:10.1038/sj.bjp.0705159 (2003).
- 215 Jones, C. K. *et al.* The metabotropic glutamate receptor 4-positive allosteric modulator VU0364770 produces efficacy alone and in combination with L-DOPA or an adenosine 2A antagonist in preclinical rodent models of Parkinson's disease. *J Pharmacol Exp Ther* **340**, 404-421, doi:10.1124/jpet.111.187443 (2012).
- 216 Velema, W. A., Szymanski, W. & Feringa, B. L. Photopharmacology: Beyond proof of principle. *J Am Chem Soc* **136**, 2178-2191, doi:10.1021/ja413063e (2014).
- 217 Edwards, I. R. & Aronson, J. K. Adverse drug reactions: Definitions, diagnosis, and management. *Lancet* **356**, 1255-1259, doi:10.1016/s0140-6736(00)02799-9 (2000).
- 218 Longley, D. B. & Johnston, P. G. Molecular mechanisms of drug resistance. *J Pathol* **205**, 275-292, doi:10.1002/path.1706 (2005).
- 219 Gorostiza, P. & Isacoff, E. Y. Optical switches for remote and noninvasive control of cell signaling. *Science* **322**, 395-399, doi:10.1126/science.1166022 (2008).
- 220 Lehar, J. *et al.* Synergistic drug combinations tend to improve therapeutically relevant selectivity. *Nat Biotechnol* **27**, 659-666, doi:10.1038/nbt.1549 (2009).
- 221 Deisseroth, K. Optogenetics: 10 years of microbial opsins in neuroscience. *Nat Neurosci* **18**, 1213-1225, doi:10.1038/nn.4091 (2015).
- 222 Weitzman, M. & Hahn, K. M. Optogenetic approaches to cell migration and beyond. *Curr Opin Cell Biol* **30**, 112-120, doi:10.1016/j.ceb.2014.08.004 (2014).
- 223 Hausser, M. Optogenetics: The age of light. *Nat Methods* **11**, 1012-1014, doi:10.1038/nmeth.3111 (2014).
- 224 Dwijayanti, A., Zhang, C., Poh, C. L. & Lautier, T. Toward multiplexed optogenetic circuits. *Front Bioeng Biotechnol* **9**, 804563, doi:10.3389/fbioe.2021.804563 (2021).
- 225 Deisseroth, K. Optogenetics. *Nat Methods* **8**, 26-29, doi:10.1038/nmeth.f.324 (2011).
- 226 Nagel, G. *et al.* Channelrhodopsin-2, a directly light-gated cation-selective membrane channel. *Proc Natl Acad Sci U S A* **100**, 13940-13945, doi:10.1073/pnas.1936192100 (2003).

- 227 Boyden, E. S., Zhang, F., Bamberg, E., Nagel, G. & Deisseroth, K. Millisecond-timescale, genetically targeted optical control of neural activity. *Nat Neurosci* **8**, 1263-1268, doi:10.1038/nn1525 (2005).
- 228 Sengupta, A. *et al.* Red-shifted channelrhodopsin stimulation restores light responses in blind mice, macaque retina, and human retina. *EMBO Mol Med* **8**, 1248-1264, doi:10.15252/emmm.201505699 (2016).
- 229 Klapoetke, N. C. *et al.* Independent optical excitation of distinct neural populations. *Nat Methods* **11**, 338-346, doi:10.1038/nmeth.2836 (2014).
- 230 Kleinlogel, S., Vogl, C., Jeschke, M., Neef, J. & Moser, T. Emerging approaches for restoration of hearing and vision. *Physiol Rev* **100**, 1467-1525, doi:10.1152/physrev.00035.2019 (2020).
- 231 Airan, R. D., Thompson, K. R., Fenno, L. E., Bernstein, H. & Deisseroth, K. Temporally precise *in vivo* control of intracellular signalling. *Nature* **458**, 1025-1029, doi:10.1038/nature07926 (2009).
- 232 van Wyk, M., Pielecka-Fortuna, J., Löwel, S. & Kleinlogel, S. Restoring the ON switch in blind retinas: Opto-mGlu<sub>6</sub>, a next-generation, cell-tailored optogenetic tool. *PLoS Biol* **13**, e1002143, doi:10.1371/journal.pbio.1002143 (2015).
- 233 Siuda, E. R. *et al.* Optodynamic simulation of  $\beta$ -adrenergic receptor signalling. *Nat Commun* **6**, 8480, doi:10.1038/ncomms9480 (2015).
- 234 Zheng, W. *et al.* Spatiotemporal control of GPR37 signaling and its behavioral effects by optogenetics. *Front Mol Neurosci* **11**, 95, doi:10.3389/fnmol.2018.00095 (2018).
- 235 Kim, J. M. *et al.* Light-driven activation of  $\beta_2$ -adrenergic receptor signaling by a chimeric rhodopsin containing the  $\beta_2$ -adrenergic receptor cytoplasmic loops. *Biochemistry* **44**, 2284-2292, doi:10.1021/bi048328i (2005).
- 236 Gunaydin, L. A. *et al.* Natural neural projection dynamics underlying social behavior. *Cell* **157**, 1535-1551, doi:10.1016/j.cell.2014.05.017 (2014).
- 237 Packer, A. M., Roska, B. & Hausser, M. Targeting neurons and photons for optogenetics. *Nat Neurosci* **16**, 805-815, doi:10.1038/nn.3427 (2013).
- 238 Allen, B. D., Singer, A. C. & Boyden, E. S. Principles of designing interpretable optogenetic behavior experiments. *Learn Mem* **22**, 232-238, doi:10.1101/lm.038026.114 (2015).
- 239 Chilakamarthi, U. & Giribabu, L. Photodynamic therapy: Past, present and future. *Chem Rec* **17**, 775-802, doi:10.1002/tcr.201600121 (2017).
- 240 Yanovsky, R. L., Bartenstein, D. W., Rogers, G. S., Isakoff, S. J. & Chen, S. T. Photodynamic therapy for solid tumors: A review of the literature. *Photodermatol Photoimmunol Photomed* **35**, 295-303, doi:10.1111/phpp.12489 (2019).
- 241 Hansen, M. J., Velema, W. A., Lerch, M. M., Szymanski, W. & Feringa, B. L. Wavelength-selective cleavage of photoprotecting groups: Strategies and applications in dynamic systems. *Chem Soc Rev* **44**, 3358-3377, doi:10.1039/c5cs00118h (2015).
- 242 Ellis-Davies, G. C. Caged compounds: Photorelease technology for control of cellular chemistry and physiology. *Nat Methods* **4**, 619-628, doi:10.1038/nmeth1072 (2007).
- 243 Klan, P. *et al.* Photoremovable protecting groups in chemistry and biology: Reaction mechanisms and efficacy. *Chem Rev* **113**, 119-191, doi:10.1021/cr300177k (2013).
- 244 Silva, J. M., Silva, E. & Reis, R. L. Light-triggered release of photocaged therapeutics - Where are we now? *J Control Release* **298**, 154-176, doi:10.1016/j.jconrel.2019.02.006 (2019).
- 245 Ricart-Ortega, M., Font, J. & Llebaria, A. GPCR photopharmacology. *Mol Cell Endocrinol* **488**, 36-51, doi:10.1016/j.mce.2019.03.003 (2019).

- 246 Callaway, E. M. & Katz, L. C. Photostimulation using caged glutamate reveals functional circuitry in living brain slices. *Proc Natl Acad Sci U S A* **90**, 7661-7665, doi:10.1073/pnas.90.16.7661 (1993).
- 247 Wieboldt, R. *et al.* Photolabile precursors of glutamate: synthesis, photochemical properties, and activation of glutamate receptors on a microsecond time scale. *Proc Natl Acad Sci U S A* **91**, 8752-8756, doi:10.1073/pnas.91.19.8752 (1994).
- 248 Brieke, C., Rohrbach, F., Gottschalk, A., Mayer, G. & Heckel, A. Light-controlled tools. *Angew Chem Int Ed Engl* **51**, 8446-8476, doi:10.1002/anie.201202134 (2012).
- 249 Passlick, S. & Ellis-Davies, G. C. R. Chromatically independent, two-color uncaging of glutamate and GABA with one- or two-photon excitation. *Methods Enzymol* **624**, 167-196, doi:10.1016/bs.mie.2019.05.003 (2019).
- 250 Hull, K., Morstein, J. & Trauner, D. *In vivo* photopharmacology. *Chem Rev* **118**, 10710-10747, doi:10.1021/acs.chemrev.8b00037 (2018).
- 251 Paoletti, P., Ellis-Davies, G. C. R. & Mourot, A. Optical control of neuronal ion channels and receptors. *Nat Rev Neurosci* **20**, 514-532, doi:10.1038/s41583-019-0197-2 (2019).
- 252 Castagna, R., Kolarski, D., Durand-de Cuttoli, R. & Maleeva, G. Orthogonal control of neuronal circuits and behavior using photopharmacology. *J Mol Neurosci* **72**, 1433-1442, doi:10.1007/s12031-022-02037-3 (2022).
- 253 Trads, J. B. *et al.* Sign inversion in photopharmacology: Incorporation of cyclic azobenzenes in photoswitchable potassium channel blockers and openers. *Angew Chem Int Ed Engl* **58**, 15421-15428, doi:10.1002/anie.201905790 (2019).
- 254 Szymanski, W., Beierle, J. M., Kistemaker, H. A., Velema, W. A. & Feringa, B. L. Reversible photocontrol of biological systems by the incorporation of molecular photoswitches. *Chem Rev* **113**, 6114-6178, doi:10.1021/cr300179f (2013).
- 255 Wijtmans, M., Josimovic, I., Vischer, H. F. & Leurs, R. Optical control of class A G protein-coupled receptors with photoswitchable ligands. *Curr Opin Pharmacol* **63**, 102192, doi:10.1016/j.coph.2022.102192 (2022).
- 256 Fuchter, M. J. On the promise of photopharmacology using photoswitches: A medicinal chemist's perspective. *J Med Chem* **63**, 11436-11447, doi:10.1021/acs.jmedchem.0c00629 (2020).
- 257 Dong, M. *et al.* Near-infrared photoswitching of azobenzenes under physiological conditions. *J Am Chem Soc* **139**, 13483-13486, doi:10.1021/jacs.7b06471 (2017).
- 258 Marder, S. R., Kippelen, B., Jen, A. K. Y. & Peyghambarian, N. Design and synthesis of chromophores and polymers for electro-optic and photorefractive applications. *Nature* **388**, 845-851, doi:10.1038/42190 (1997).
- 259 Meerholz, K., Volodin, B. L., Sandalphon, Kippelen, B. & Peyghambarian, N. A photorefractive polymer with high optical gain and diffraction efficiency near 100%. *Nature* **371**, 497-500, doi:10.1038/371497a0 (1994).
- 260 Beharry, A. A., Sadovski, O. & Woolley, G. A. Azobenzene photoswitching without ultraviolet light. *J Am Chem Soc* **133**, 19684-19687, doi:10.1021/ja209239m (2011).
- 261 Samanta, S., Qin, C., Lough, A. J. & Woolley, G. A. Bidirectional photocontrol of peptide conformation with a bridged azobenzene derivative. *Angew Chem Int Ed Engl* **51**, 6452-6455, doi:10.1002/anie.201202383 (2012).
- 262 Konrad, D. B., Frank, J. A. & Trauner, D. Synthesis of redshifted azobenzene photoswitches by late-stage functionalization. *Chemistry* **22**, 4364-4368, doi:10.1002/chem.201505061 (2016).
- 263 Rullo, A. *et al.* Long wavelength optical control of glutamate receptor ion channels using a tetra-*ortho*-substituted azobenzene derivative. *Chem Commun (Camb)* **50**, 14613-14615, doi:10.1039/c4cc06612j (2014).

- 264 Wegener, M., Hansen, M. J., Driessen, A. J. M., Szymanski, W. & Feringa, B. L. Photocontrol of antibacterial activity: Shifting from UV to red light activation. *J Am Chem Soc* **139**, 17979-17986, doi:10.1021/jacs.7b09281 (2017).
- 265 Volaric, J. *et al.* Design and synthesis of visible-light-responsive azobenzene building blocks for chemical biology. *J Org Chem* **87**, 14319-14333, doi:10.1021/acs.joc.2c01777 (2022).
- 266 Cabre, G. *et al.* Rationally designed azobenzene photoswitches for efficient two-photon neuronal excitation. *Nat Commun* **10**, 907, doi:10.1038/s41467-019-08796-9 (2019).
- 267 Cabre, G. *et al.* Synthetic photoswitchable neurotransmitters based on bridged azobenzenes. *Org Lett* **21**, 3780-3784, doi:10.1021/acs.orglett.9b01222 (2019).
- 268 Broichhagen, J., Frank, J. A. & Trauner, D. A roadmap to success in photopharmacology. *Acc Chem Res* **48**, 1947-1960, doi:10.1021/acs.accounts.5b00129 (2015).
- 269 Simeth, N. A., Crespi, S., Fagnoni, M. & Konig, B. Tuning the thermal isomerization of phenylazoindeole photoswitches from days to nanoseconds. *J Am Chem Soc* **140**, 2940-2946, doi:10.1021/jacs.7b12871 (2018).
- 270 Berizzi, A. E. & Goudet, C. Strategies and considerations of G protein-coupled receptor photopharmacology. *Adv Pharmacol* **88**, 143-172, doi:10.1016/bs.apha.2019.12.001 (2020).
- 271 Banghart, M., Borges, K., Isacoff, E., Trauner, D. & Kramer, R. H. Light-activated ion channels for remote control of neuronal firing. *Nat Neurosci* **7**, 1381-1386, doi:10.1038/nn1356 (2004).
- 272 Chambers, J. J., Banghart, M. R., Trauner, D. & Kramer, R. H. Light-induced depolarization of neurons using a modified Shaker K<sup>+</sup> channel and a molecular photoswitch. *J Neurophysiol* **96**, 2792-2796, doi:10.1152/jn.00318.2006 (2006).
- 273 Fortin, D. L. *et al.* Optogenetic photochemical control of designer K<sup>+</sup> channels in mammalian neurons. *J Neurophysiol* **106**, 488-496, doi:10.1152/jn.00251.2011 (2011).
- 274 Sandoz, G., Levitz, J., Kramer, R. H. & Isacoff, E. Y. Optical control of endogenous proteins with a photoswitchable conditional subunit reveals a role for TREK1 in GABA<sub>B</sub> signaling. *Neuron* **74**, 1005-1014, doi:10.1016/j.neuron.2012.04.026 (2012).
- 275 Izquierdo-Serra, M. *et al.* Two-photon neuronal and astrocytic stimulation with azobenzene-based photoswitches. *J Am Chem Soc* **136**, 8693-8701, doi:10.1021/ja5026326 (2014).
- 276 Volgraf, M. *et al.* Allosteric control of an ionotropic glutamate receptor with an optical switch. *Nat Chem Biol* **2**, 47-52, doi:10.1038/nchembio756 (2006).
- 277 Levitz, J. *et al.* Optical control of metabotropic glutamate receptors. *Nat Neurosci* **16**, 507-516, doi:10.1038/nn.3346 (2013).
- 278 Carroll, E. C. *et al.* Two-photon brightness of azobenzene photoswitches designed for glutamate receptor optogenetics. *Proc Natl Acad Sci U S A* **112**, E776-785, doi:10.1073/pnas.1416942112 (2015).
- 279 Donthamsetti, P. C. *et al.* Optical control of dopamine receptors using a photoswitchable tethered inverse agonist. *J Am Chem Soc* **139**, 18522-18535, doi:10.1021/jacs.7b07659 (2017).
- 280 Kramer, R. H., Mourot, A. & Adesnik, H. Optogenetic pharmacology for control of native neuronal signaling proteins. *Nat Neurosci* **16**, 816-823, doi:10.1038/nn.3424 (2013).
- 281 Singh, J., Petter, R. C., Baillie, T. A. & Whitty, A. The resurgence of covalent drugs. *Nature Reviews Drug Discovery* **10**, 307-317, doi:10.1038/nrd3410 (2011).

- 282 Izquierdo-Serra, M. *et al.* Optical control of endogenous receptors and cellular excitability using targeted covalent photoswitches. *Nat Commun* **7**, 12221, doi:10.1038/ncomms12221 (2016).
- 283 Gautier, A. *et al.* An engineered protein tag for multiprotein labeling in living cells. *Chem Biol* **15**, 128-136, doi:10.1016/j.chembiol.2008.01.007 (2008).
- 284 Hinner, M. J. & Johnsson, K. How to obtain labeled proteins and what to do with them. *Curr Opin Biotechnol* **21**, 766-776, doi:10.1016/j.copbio.2010.09.011 (2010).
- 285 Xue, L., Karpenko, I. A., Hiblot, J. & Johnsson, K. Imaging and manipulating proteins in live cells through covalent labeling. *Nat Chem Biol* **11**, 917-923, doi:10.1038/nchembio.1959 (2015).
- 286 Berry, M. H. *et al.* Restoration of patterned vision with an engineered photoactivatable G protein-coupled receptor. *Nat Commun* **8**, 1862, doi:10.1038/s41467-017-01990-7 (2017).
- 287 Donthamsetti, P. *et al.* Cell specific photoswitchable agonist for reversible control of endogenous dopamine receptors. *Nat Commun* **12**, 4775, doi:10.1038/s41467-021-25003-w (2021).
- 288 Bregestovski, P., Maleeva, G. & Gorostiza, P. Light-induced regulation of ligand-gated channel activity. *Br J Pharmacol* **175**, 1892-1902, doi:10.1111/bph.14022 (2018).
- 289 Pittolo, S. *et al.* An allosteric modulator to control endogenous G protein-coupled receptors with light. *Nat Chem Biol* **10**, 813-815, doi:10.1038/nchembio.1612 (2014).
- 290 Morstein, J., Awale, M., Reymond, J. L. & Trauner, D. Mapping the azolog space enables the optical control of new biological targets. *ACS Cent Sci* **5**, 607-618, doi:10.1021/acscentsci.8b00881 (2019).
- 291 Agnetta, L. *et al.* Fluorination of photoswitchable muscarinic agonists tunes receptor pharmacology and photochromic properties. *J Med Chem* **62**, 3009-3020, doi:10.1021/acs.jmedchem.8b01822 (2019).
- 292 Gomez-Santacana, X., Panarello, S., Rovira, X. & Llebaria, A. Photoswitchable allosteric modulators for metabotropic glutamate receptors. *Curr Opin Pharmacol* **66**, 102266, doi:10.1016/j.coph.2022.102266 (2022).
- 293 Gomez-Santacana, X. *et al.* Illuminating phenylazopyridines to photoswitch metabotropic glutamate receptors: From the flask to the animals. *ACS Cent Sci* **3**, 81-91, doi:10.1021/acscentsci.6b00353 (2017).
- 294 Zussy, C. *et al.* Dynamic modulation of inflammatory pain-related affective and sensory symptoms by optical control of amygdala metabotropic glutamate receptor 4. *Mol Psychiatry* **23**, 509-520, doi:10.1038/mp.2016.223 (2018).
- 295 Rovira, X. *et al.* OptoGluNAM4.1, a photoswitchable allosteric antagonist for real-time control of mGlu<sub>4</sub> receptor activity. *Cell chemical biology* **23** **8**, 929-934 (2016).
- 296 Goudet, C., Rovira, X. & Llebaria, A. Shedding light on metabotropic glutamate receptors using optogenetics and photopharmacology. *Curr Opin Pharmacol* **38**, 8-15, doi:10.1016/j.coph.2018.01.007 (2018).
- 297 Agnetta, L. *et al.* A photoswitchable dualsteric ligand controlling receptor efficacy. *Angew Chem Int Ed Engl* **56**, 7282-7287, doi:10.1002/anie.201701524 (2017).
- 298 Matera, C. *et al.* Photoswitchable antimetabolite for targeted photoactivated chemotherapy. *J Am Chem Soc* **140**, 15764-15773, doi:10.1021/jacs.8b08249 (2018).
- 299 Weston, C. E. *et al.* Toward photopharmacological antimicrobial chemotherapy using photoswitchable amidohydrolase inhibitors. *ACS Infect Dis* **3**, 152-161, doi:10.1021/acsinfectdis.6b00148 (2017).
- 300 Eikemo, V., Holmelid, B., Sydnes, L. K. & Sydnes, M. O. Photodegradable antimicrobial agents: Synthesis and mechanism of degradation. *J Org Chem* **87**, 8034-8047, doi:10.1021/acs.joc.2c00681 (2022).

- 301 Mehta, Z. B. *et al.* Remote control of glucose homeostasis *in vivo* using photopharmacology. *Sci Rep* **7**, 291, doi:10.1038/s41598-017-00397-0 (2017).
- 302 Tochitsky, I. *et al.* Restoring visual function to blind mice with a photoswitch that exploits electrophysiological remodeling of retinal ganglion cells. *Neuron* **81**, 800-813, doi:10.1016/j.neuron.2014.01.003 (2014).
- 303 Polosukhina, A. *et al.* Photochemical restoration of visual responses in blind mice. *Neuron* **75**, 271-282, doi:10.1016/j.neuron.2012.05.022 (2012).
- 304 Mourot, A. *et al.* Tuning photochromic ion channel blockers. *ACS Chem Neurosci* **2**, 536-543, doi:10.1021/cn200037p (2011).
- 305 Tochitsky, I., Trautman, J., Gallerani, N., Malis, J. G. & Kramer, R. H. Restoring visual function to the blind retina with a potent, safe and long-lasting photoswitch. *Sci Rep* **7**, 45487, doi:10.1038/srep45487 (2017).
- 306 Tochitsky, I., Kienzler, M. A., Isacoff, E. & Kramer, R. H. Restoring vision to the blind with chemical photoswitches. *Chem Rev* **118**, 10748-10773, doi:10.1021/acs.chemrev.7b00723 (2018).
- 307 Van Gelder, R. N. Photochemical approaches to vision restoration. *Vision Res* **111**, 134-141, doi:10.1016/j.visres.2015.02.001 (2015).
- 308 Zipfel, W. R., Williams, R. M. & Webb, W. W. Nonlinear magic: Multiphoton microscopy in the biosciences. *Nature Biotechnology* **21**, 1369-1377, doi:10.1038/nbt899 (2003).
- 309 Dzhagalov, I. L., Melichar, H. J., Ross, J. O., Herzmark, P. & Robey, E. A. Two-photon imaging of the immune system. *Curr Protoc Cytom* **Chapter 12**, Unit12 26, doi:10.1002/0471142956.cy1226s60 (2012).
- 310 Sun, T. Y., Haberman, A. M. & Greco, V. Preclinical advances with multiphoton microscopy in live imaging of skin cancers. *J Invest Dermatol* **137**, 282-287, doi:10.1016/j.jid.2016.08.033 (2017).
- 311 Stosiek, C., Garaschuk, O., Holthoff, K. & Konnerth, A. *In vivo* two-photon calcium imaging of neuronal networks. *Proc Natl Acad Sci U S A* **100**, 7319-7324, doi:10.1073/pnas.1232232100 (2003).
- 312 Cahalan, M. D., Parker, I., Wei, S. H. & Miller, M. J. Two-photon tissue imaging: Seeing the immune system in a fresh light. *Nat Rev Immunol* **2**, 872-880, doi:10.1038/nri935 (2002).
- 313 D'Amore, J. D. *et al.* *In vivo* multiphoton imaging of a transgenic mouse model of Alzheimer disease reveals marked thioflavine-S-associated alterations in neurite trajectories. *J Neuropathol Exp Neurol* **62**, 137-145, doi:10.1093/jnen/62.2.137 (2003).
- 314 Denk, W., Strickler, J. H. & Webb, W. W. Two-photon laser scanning fluorescence microscopy. *Science* **248**, 73-76, doi:10.1126/science.2321027 (1990).
- 315 Papagiakoumou, E., Ronzitti, E. & Emiliani, V. Scanless two-photon excitation with temporal focusing. *Nature Methods* **17**, 571-581, doi:10.1038/s41592-020-0795-y (2020).
- 316 Papagiakoumou, E. *et al.* Functional patterned multiphoton excitation deep inside scattering tissue. *Nature Photonics* **7**, 274-278, doi:10.1038/nphoton.2013.9 (2013).
- 317 Dudek, M. *et al.* Two-photon absorption and two-photon-induced isomerization of azobenzene compounds. *RSC Advances* **10**, 40489-40507, doi:10.1039/D0RA07693G (2020).
- 318 Dong, M., Babalhavaeji, A., Samanta, S., Beharry, A. A. & Woolley, G. A. Red-shifting azobenzene photoswitches for *in vivo* use. *Accounts of Chemical Research* **48**, 2662-2670, doi:10.1021/acs.accounts.5b00270 (2015).

- 319 Shen, Q. *et al.* Recent development of small-molecule organic fluorophores for multifunctional bioimaging in the second near-infrared window. *Journal of Luminescence* **225**, 117338, doi:10.1016/j.jlumin.2020.117338 (2020).
- 320 Wang, T. *et al.* Three-photon imaging of mouse brain structure and function through the intact skull. *Nat Methods* **15**, 789-792, doi:10.1038/s41592-018-0115-y (2018).
- 321 Wokosin, D. L., Centonze, V. E., Crittenden, S. & White, J. Three-photon excitation fluorescence imaging of biological specimens using an all-solid-state laser. *Bioimaging* **4**, 208-214 (1996).
- 322 Horton, N. G. *et al.* *In vivo* three-photon microscopy of subcortical structures within an intact mouse brain. *Nature Photonics* **7**, 205-209, doi:10.1038/nphoton.2012.336 (2013).
- 323 Guesmi, K. *et al.* Dual-color deep-tissue three-photon microscopy with a multiband infrared laser. *Light Sci Appl* **7**, 12, doi:10.1038/s41377-018-0012-2 (2018).
- 324 Ouzounov, D. G. *et al.* *In vivo* three-photon imaging of activity of GCaMP6-labeled neurons deep in intact mouse brain. *Nat Methods* **14**, 388-390, doi:10.1038/nmeth.4183 (2017).
- 325 Klioutchnikov, A. *et al.* Three-photon head-mounted microscope for imaging deep cortical layers in freely moving rats. *Nat Methods* **17**, 509-513, doi:10.1038/s41592-020-0817-9 (2020).
- 326 Klioutchnikov, A. *et al.* A three-photon head-mounted microscope for imaging all layers of visual cortex in freely moving mice. *Nat Methods*, doi:10.1038/s41592-022-01688-9 (2022).
- 327 Xiao, Y., Deng, P., Zhao, Y., Yang, S. & Li, B. Three-photon excited fluorescence imaging in neuroscience: From principles to applications. *Frontiers in Neuroscience* **17**, doi:10.3389/fnins.2023.1085682 (2023).





# Chapter 3

---

## Rational design of photochromic analogues of tricyclic drugs

---

---

Fabio Riefolo, **Rosalba Sortino**<sup>¶</sup>, Carlo Matera<sup>¶</sup>, Enrique Claro, Beatrice Preda, Simone Vitiello, Sara Traserra, Marcel Jiménez and Pau Gorostiza. **Rational design of photochromic analogues of tricyclic drugs.** *J. Am. Chem.* 2021, 64, 9259-9270. <sup>¶</sup>These authors contributed equally.



## Abstract

Tricyclic chemical structures are the core of many important drugs targeting all neurotransmitter pathways. These medicines enable effective therapies to treat from peptic ulcer disease to psychiatric disorders. However, when administered systemically, they cause serious adverse effects that limit their use. To obtain localized and on-demand pharmacological action using light, we have designed photoisomerizable ligands based on azobenzene that mimic the tricyclic chemical structure and display reversibly controlled activity. Pseudo-analogues of the tricyclic antagonist pirenzepine (PNZ) demonstrate that this is an effective strategy in muscarinic acetylcholine receptors (mAChR or MR), showing stronger inhibition upon illumination both *in vitro* and in cardiac atria *ex vivo*. Despite the applied chemical modifications to make PNZ derivatives sensitive to light stimuli, the most potent candidate of the set, cryptozepine-**2**, maintained a moderate but promising M<sub>1</sub>R vs. M<sub>2</sub>R subtype selectivity. These photoswitchable “crypto-azologs” of tricyclic drugs might open a general way to spatiotemporally target their therapeutic action while reducing their systemic toxicity and adverse effects.



### 3.1 Introduction

Photopharmacology is a modern branch of pharmacology that aims to improve the efficacy and safety of drugs by directing their action to target organs and controlling their doses using light. It deals with molecular strategies to photoregulate drug activity<sup>1,2</sup>. Most photoswitchable small molecule ligands developed in recent years have exploited the reduced size and robust photochromism of azobenzene, which allows two design approaches: (1) tailoring compounds through the extension of the drug core (“azo-extension” approach) and (2) introducing an isosteric azobenzene photoswitch in the core (“azologization” approach)<sup>3,4</sup>. The latter is the most straightforward design strategy and is generally preferred because it requires minimal modifications of the original structure, thus maintaining the drug-likeness of the parent compound and largely preserving its pharmacokinetic and pharmacodynamic properties<sup>5,6</sup>. If azologization motifs are not present, in some cases, the drug structure can be extended with a photoswitchable moiety while retaining the drug activity<sup>3,7</sup>. However, these versatile and complementary strategies are not applicable to all drugs. This is often the case when azobenzene-like motifs are absent from a parent molecule that can only tolerate minor variations in size (*i.e.*, nonazologizable and nonazo-extendable drugs), thus hampering the reach of photopharmacology. An important class of drugs that have not been endowed with photoregulation is characterized by the general formula, shown in **Figure 3.1A**, *i.e.*, those fused tricyclic compounds, which are known as “privileged structures” in medicinal chemistry<sup>8</sup>. This term was coined by Ben Evans in 1988 to recognize the potential of certain structural motifs as templates for the derivatization and discovery of novel biological ligands<sup>9</sup>. A great diversity of tricyclic derivatives has been developed and are marketed for different clinical conditions. They include central nervous system agents such as tricyclic antidepressants used to treat psychiatric disorders<sup>10</sup> but also for other therapeutic indications such as loratadine (an antihistamine drug used to treat the symptoms of allergies), nevirapine (a noncompetitive HIV-1 reverse transcriptase inhibitor), lonafarnib (a farnesyl transferase inhibitor used as anticancer), and pirenzepine (PNZ) (an antimuscarinic drug to treat peptic ulcers)<sup>11</sup>.

An arylazo moiety (*e.g.*, an azobenzene) in its *cis* configuration can quite resemble (at least in some of its conformations) the geometry of the tricyclic scaffold, whereas the corresponding *trans*-isomer cannot. This is illustrated by the three-dimensional alignment of conformers in **Figure 3.1B**. Thus, we devised a way to mimic the tricyclic system of these drugs with a photochromic arylazo unit by means of two modifications: (1) the isosteric substitution of the two-atom bridge connecting the aryl rings with a  $-N=N-$  group to confer photochromic

behavior and (2) the cleavage (ring opening) of one of the two single bonds forming the one-atom bridge to increase the flexibility and to enable greater changes in geometry upon photoisomerization. In this way, the photochromic pseudo-analogue of the tricyclic drug should be able to maintain the pharmacological properties of the parent compound upon photoisomerization to the *cis* configuration. Conversely, the most thermodynamically stable *trans*-isomer should display a reduced capacity to modulate its biological target. This situation would be particularly favorable to apply the inactive drug in the absence of illumination and to photoactivate it at the desired locations and times. We named this novel procedure to design photoswitchable small molecules “crypto-azologization” (where the prefix “crypto-” comes from the Ancient Greek word κρυπτός [kruptós], meaning “hidden”) because it expands the azologization strategy to compounds in which the potential photochromic scaffold is buried and must be sculpted out of the parent structure by a ring opening in addition to the canonical azosteric replacement.

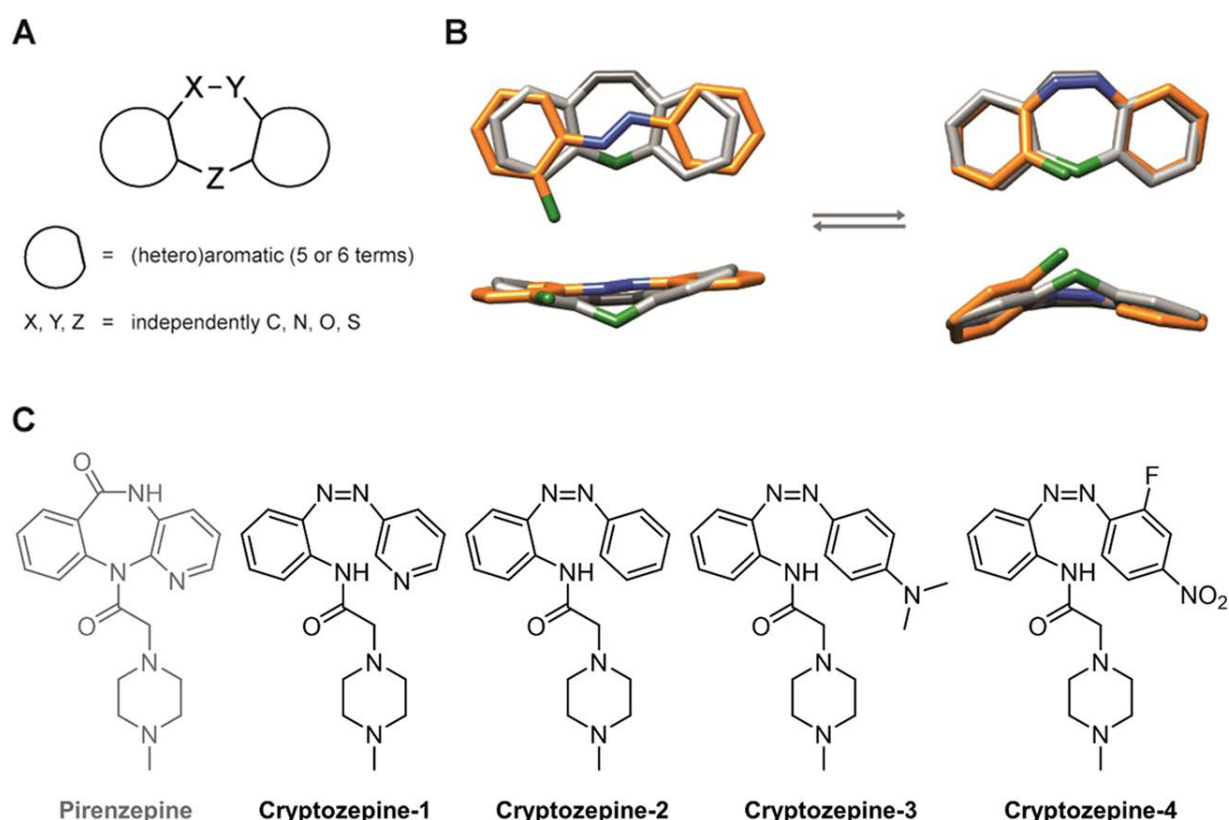


**Figure 3.1. Design strategy and structure of crypto-azologs.** (A) General scaffold of fused tricyclic drugs. (B) Best three-dimensional alignment of an azobenzene scaffold (*trans* on the left and *cis* on the right, both in orange) over a generic fused tricyclic system (in gray). For the sake of comparison, the carbon atom of the 1-atom bridge of the tricyclic system and the corresponding carbon atom of the azobenzene are indicated in green. Nitrogen atoms are in blue. (C) Chemical structure of the muscarinic M<sub>1</sub>R antagonist pirenzepine and the cryptozepines, the photochromic derivatives discussed in this work.

As a test bed for our design strategy, we chose the muscarinic acetylcholine receptor (mAChR or MR) antagonist PNZ (**Figure 3.1C**), both because of its tricyclic structure and therapeutic importance. Muscarinic receptors belong to the class A family of G protein-coupled receptors (GPCRs) and are classified into five distinct subtypes<sup>12,13</sup>. The wide distribution of mAChRs in the body and the limited subtype selectivity of muscarinic drugs are the cause of their adverse effects, which have made these receptors an attractive target in photopharmacology<sup>14-16</sup>. PNZ (Gastrozepine) is an M<sub>1</sub>R-selective muscarinic antagonist marketed to treat peptic ulcers. More specific, it inhibits the parasympathetic nervous system “rest-and-digest” response, reducing gastric acid secretion and muscle spasm<sup>17-20</sup>. Other potential applications have been considered, like slowing down myopia progression<sup>21</sup> and reducing the risk of lethal events in the ischemic heart disease<sup>22</sup>. The wide expression of M<sub>1</sub> mAChRs in the hippocampus and medial prefrontal cortex suggests that M<sub>1</sub>R-mediated signaling is important for cognitive and learning functions and plays a key role in several neurological disorders<sup>12,13</sup>. The development of photoswitchable M<sub>1</sub>R ligands is thus of great interest for both therapeutic and research purposes. Here, we report the synthesis of photoswitchable M<sub>1</sub> mAChR antagonists designed by crypto-azologization of PNZ and the characterization of their photopharmacological effects *in vitro* and *ex vivo*.

## 3.2 Results and discussion

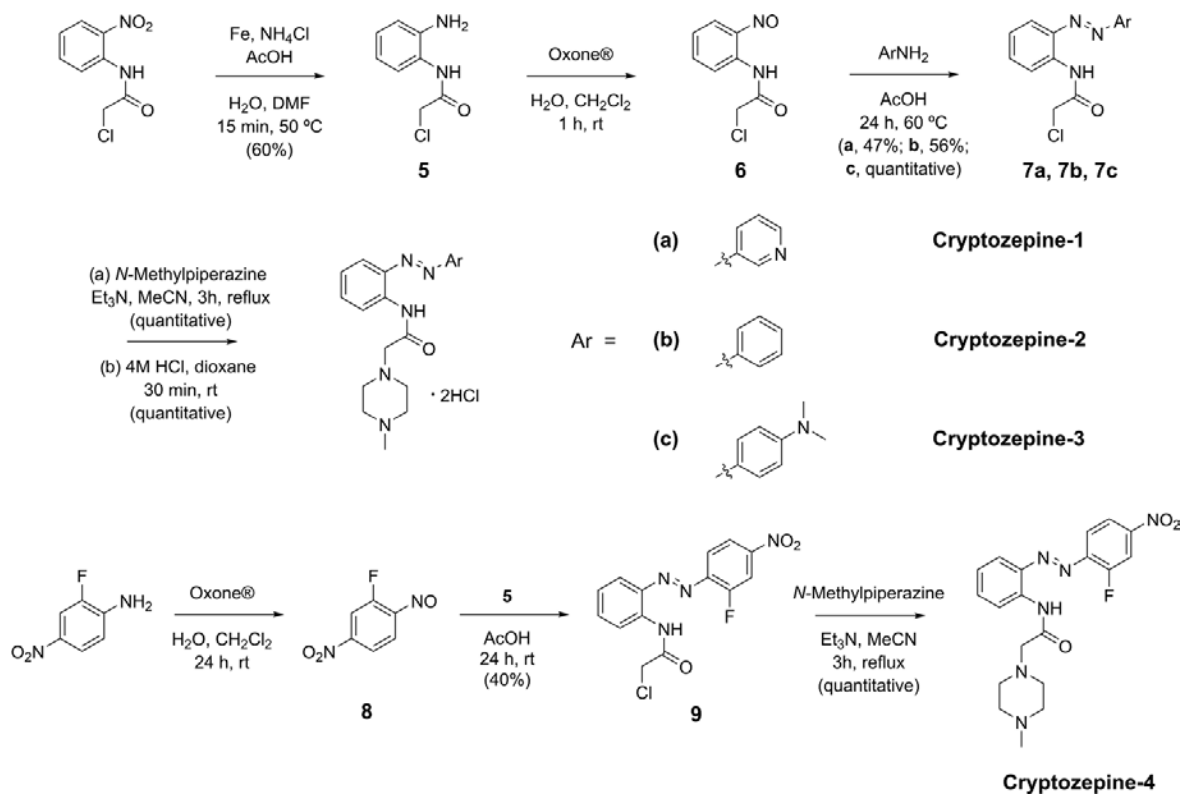
### 3.2.1 Rational design and chemical synthesis

As an initial control for our design strategy, we performed docking simulations of a representative structure at the M<sub>1</sub> mAChR<sup>23</sup>. The results supported our hypothesis (see the **Supplementary Information; SI** for details) and encouraged us to pursue the synthesis of a small set of PNZ crypto-azologs that were named “cryptozepines” (**Figure 3.1C**). Previous studies on PNZ congeners have shown how the nature and placement of accessory groups on the central core of the molecule determine the differences in receptor recognition and the binding process at mAChRs<sup>19</sup>. In particular, the positioning of the protonated nitrogen atom at the end of the piperazine, which is affected by the geometry of the whole structure, is crucial for the receptor recognition and the binding processes in M<sub>1</sub> mAChRs<sup>19,23,24</sup>. On the other hand, certain structural modifications at the tricyclic core are tolerated. The endocyclic amide group is thought to participate in polar interactions at the binding site; therefore, its replacement with a lipophilic function such as an ethylene bridge would likely produce a loss of affinity, whereas an azo group could be better accepted. The exocyclic amide group and the nitrogen atom in one of the two aromatic rings seem to have only a minor effect in terms of affinity and selectivity<sup>19</sup>.



As such, we decided to conserve the essential 2-(4-methylpiperazin-1-yl)acetamide side chain in all of the novel derivatives, while the endocyclic amide group was replaced with an azo group and the central seven-membered ring was “opened” to generate a fully unconstrained photochromic unit. In addition, structural variations at this unit were rationally designed to obtain analogues endowed with different photochemical properties. Cryptozepine-1 and cryptozepine-2 are straightforward crypto-azologs of PNZ and differ from one another in the presence of the nitrogen atom in one of the two aromatic rings of cryptozepine-1. This feature should significantly reduce the half-life of thermal relaxation of the *cis*-isomer, as well as increase the aqueous solubility of this derivative. We expected, though, that these two derivatives would need ultraviolet (UV) light to undergo *trans*-to-*cis* isomerization, which is generally not convenient in biology<sup>25</sup>. Cryptozepine-3 was designed to overcome this limitation by introducing an electron-donating group (-NMe<sub>2</sub>) at the para position of the benzene ring, which is not directly connected to the side chain, to produce a red-shifting “push-pull” effect (**Figure 3.1C**)<sup>26</sup>. A fourth compound, cryptozepine-4, characterized by a different “push-pull” system, was designed and prepared, but because of its very low aqueous solubility at neutral pH, we could not test its pharmacological properties. However, its physicochemical characterization is reported in the **SI**.

As mentioned above, we hypothesized that the M<sub>1</sub> mAChR should be able to properly accommodate the new ligands in their *cis* configuration, while the *trans* geometry should hinder the rest of the molecule from entering the binding pocket. Cryptozepines **1**, **2**, and **3** were synthesized as illustrated in **Scheme 3.1**. *N*-Chloroacetyl-2-nitroaniline was reduced to the corresponding amine (**5**) by treating with iron in ammonium chloride and acetic acid. Oxidation with Oxone gave the nitroso derivative (**6**), which was then coupled to the chosen arylamine under Mills conditions to yield the arylazo intermediates (**7a**, **7b**, **7c**). Nucleophilic substitution of chlorine with 1-methylpiperazine and subsequent treatment with hydrochloric acid afforded the three final compounds as dihydrochloride salts (**1**, **2**, and **3**). To synthesize cryptozepine-4 (Scheme 3.1), 2-fluoro-4-nitroaniline was oxidized with Oxone to give the nitroso derivative (**8**), which was then coupled to the corresponding amine (**5**) under Mills conditions to yield the arylazo intermediate (**9**). Nucleophilic substitution of chlorine with 1-methylpiperazine afforded cryptozepine-4.



Scheme 3.1. Chemical synthesis of cryptozepines.

### 3.2.2 Photochemical characterization

We then tested the ability of our photoswitchable compounds to respond effectively to light. First, we characterized the three cryptozepines by UV-Vis spectroscopy. Cryptozepines-**1** and -**2** displayed a clear photochromic behavior and the typical absorption bands of azobenzenes in water, with maxima at 318 and 433 nm due to  $\pi-\pi^*$  and  $n-\pi^*$  transitions, respectively (**Figure 3.2** and see the **SI** for details). As expected, the presence of an electron-donating group in cryptozepine-**3** resulted in a strong red-shift of the  $\pi-\pi^*$  transition band, with an absorption maximum at 465 nm in an aqueous solution. In this case, it was not possible to observe any change in the absorption spectrum with steady-state spectroscopy in an aqueous solution since the thermal isomerization of this kind of azobenzenes in protic solvents occurs extremely fast and generally completes within milli-seconds<sup>27</sup>. However, we proved the capacity of compound **3** to photoisomerize in a dry organic solvent (**Figure 3.2** and see the **SI** for details). We then determined the photostationary distribution of cryptozepines **1** and **2** by <sup>1</sup>H NMR analysis. The distribution changed from about 90% in favor of the *trans* form in the dark to about 10% (90% in favor of the *cis* form) after illumination with UV light (365 nm) for both compounds. Compounds **1** and **2** also showed a good thermal stability, with a half-life of thermal relaxation of 71 and 182 min, respectively (**Figure 3.2** and see the **SI** for details).

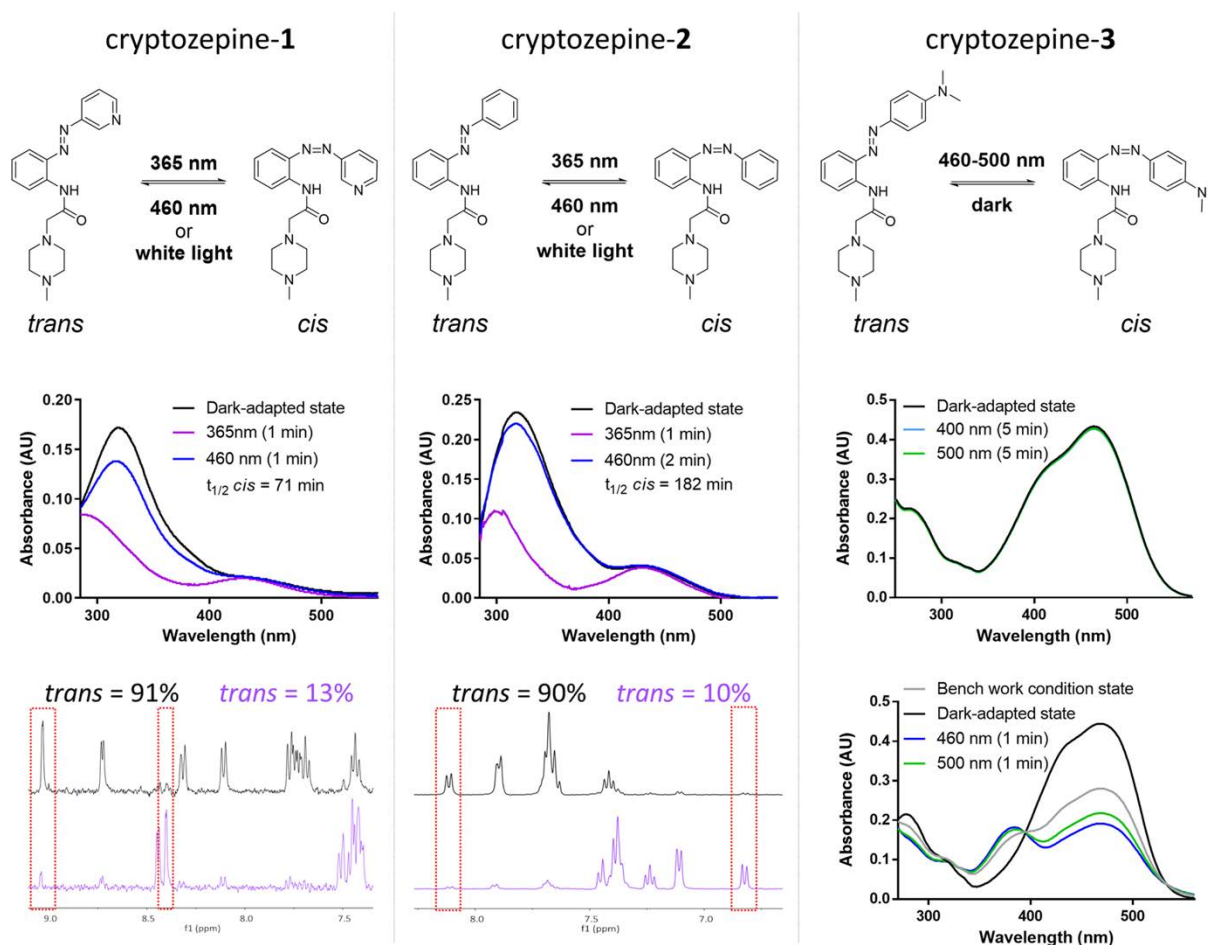


**Figure 3.2. Photochemical characterization.** Left column: absorption spectra (30  $\mu$ M in H<sub>2</sub>O) and quantification of the cryptozepine-1 photostationary state (PSS) by <sup>1</sup>H NMR analysis (1 mM in D<sub>2</sub>O), showing the ratio between the two isomers in the dark-adapted state (*trans* = 91%) and after illumination with 365 nm light for 5 min (*trans* = 13%). Middle column: absorption spectra (30  $\mu$ M in H<sub>2</sub>O) and quantification of cryptozepine-2 PSS by <sup>1</sup>H NMR analysis (1 mM in D<sub>2</sub>O), showing the ratio between the two isomers in the dark-adapted state (*trans* = 90%) and after illumination with 365 nm light for 5 min (*trans* = 10%). Right column: absorption spectra in water (30  $\mu$ M, spectra above) and absorption spectra in anhydrous dimethyl sulfoxide (DMSO) (30  $\mu$ M, spectra below) of cryptozepine-3. The switching of the red-shifted compound cryptozepine-3 can be observed by UV-Vis spectrophotometer analysis only in an anhydrous solvent.

### 3.2.3 Competition binding assay

We determined the affinity of PNZs and cryptozepines for the mAChRs by radioligand competition binding assays. For this purpose, we used Wistar rat brain membranes (whole cortex), which contain a high density of mAChRs<sup>28</sup>, and the nonselective muscarinic orthosteric antagonist [<sup>3</sup>H]quinclidinyl benzilate ([<sup>3</sup>H]QNB) as a competitive radioligand (see the SI for details)<sup>28-31</sup>. In this assay, PNZ has a good binding affinity in the nanomolar range, with an IC<sub>50</sub> of about 50 nM (Table 3.1 and Figure S3.17), and all cryptozepines showed a moderate binding

affinity in the low micromolar range, with cryptozepine-2 emerging as the best ligand with an  $IC_{50}$  of about 9  $\mu$ M (Table 3.1 and Figure S3.17).

Ligand	$K_i$ (M)	$IC_{50}$ (M)
Pirenzepine	$8.4 (\pm 1.4) \times 10^{-9}$	$5.0 \times 10^{-8}$
Cryptozepine-1 ( <i>trans</i> )	$6.4 (\pm 1.4) \times 10^{-6}$	$3.8 \times 10^{-5}$
Cryptozepine-1 ( <i>cis</i> )	$7.0 (\pm 2.2) \times 10^{-6}$	$4.2 \times 10^{-5}$
Cryptozepine-2 ( <i>trans</i> )	$1.7 (\pm 0.3) \times 10^{-6}$	$9.9 \times 10^{-6}$
Cryptozepine-2 ( <i>cis</i> )	$1.5 (\pm 0.5) \times 10^{-6}$	$9.2 \times 10^{-6}$
Cryptozepine-3 ( <i>trans</i> )	$5.3 (\pm 0.1) \times 10^{-6}$	$3.3 \times 10^{-5}$
Cryptozepine-3 ( <i>cis</i> )	$5.3 (\pm 0.1) \times 10^{-6}$	$3.2 \times 10^{-5}$

**Table 3.1.** <sup>a</sup>The parameters shown in the table were calculated using the “Binding-Competitive-one site-Fit  $K_i$ ” for  $K_i$  values and “Binding- Competitive-one site-Fit  $\log IC_{50}$ ” for the  $IC_{50}$ , which are functions in GraphPad Prism 6. Values are mean  $\pm$  SEM.

No significant differences in affinity were observed between the *trans*- and the *cis*-enriched forms (named “*trans*” and “*cis*” hereafter for the sake of simplicity) for the three cryptozepines in these experimental conditions. However, the fact that the compounds maintain the muscarinic binding despite the cleavage of the original tricyclic core encouraged us to further investigate their photopharmacological behavior through activity assays where differences between the *trans* and *cis* forms might be detected. In particular, our data suggested retaining cryptozepine-2 (best binding affinity) and cryptozepine-3 (best photochromic behavior) for further studies.

### 3.2.4 *In vitro* calcium imaging

We performed real-time calcium imaging experiments in transiently transfected human embryonic kidney (HEK) cells expressing  $M_1$  mAChR to study the antagonist behavior of our compounds (Figure 3.3). The calcium indicator Oregon Green BAPTA-1 AM (OGB-1 AM; excitation at 494 nm and emission at 523 nm) was suitable for cryptozepine-2, while Red Genetically Encoded Calcium 1 (R-GECO1; excitation at 561 nm and emission at 589 nm) was used for cryptozepine-3 to avoid artifacts due to unwanted emission of fluorescence from OGB-1 AM upon illumination at 460 nm. The natural orthosteric agonist acetylcholine (ACh, 0.5  $\mu$ M) was applied or coapplied to induce receptor activation. ACh alone induced reproducible cytosolic calcium oscillations, indicative of  $M_1$  mAChR agonism. Both cryptozepines-2 and -3 at 100  $\mu$ M showed antagonistic behavior. Importantly, a complete recovery of ACh-induced activity was observed after the complete wash-out of the two antagonists. At 100  $\mu$ M, cryptozepine-2 reduced the total cell response by 64% (mean) ( $\pm 2.1$ ; standard error of the mean [SEM]) in *trans* and by 73% ( $\pm 1.6$ ) in *cis*. Cryptozepine-3 did not antagonize the ACh-induced

response at 100  $\mu\text{M}$  in *trans*, and it reduced the cell response by 14% ( $\pm 2.6$ ) under continuous illumination (*cis*-enriched form) with blue light (460 nm) (Figure 3.3).

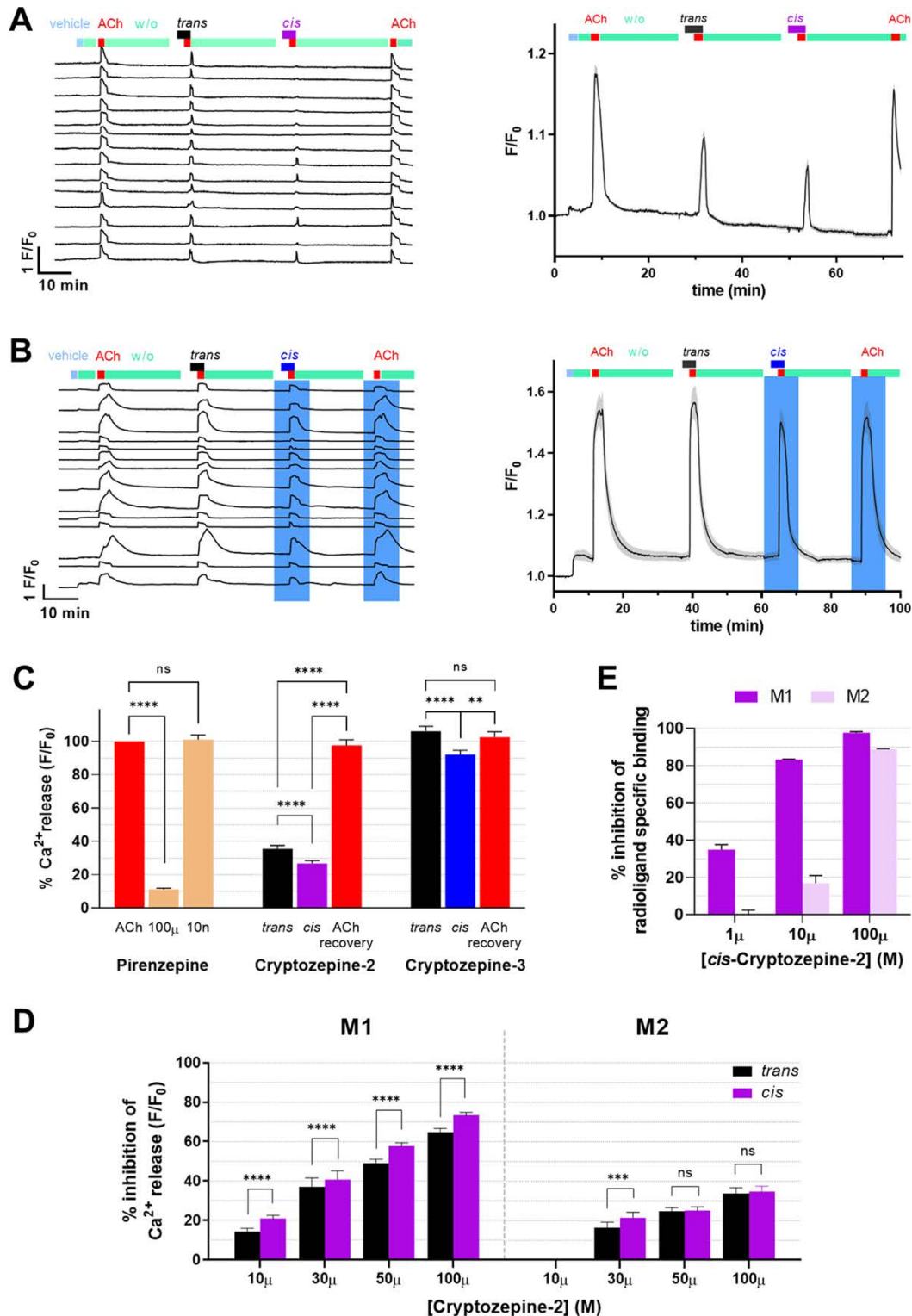


**Figure 3.3. Cryptozepine-2 and -3 antagonism on  $M_1$  mAChRs and cryptozepine-2 subtype selectivity.** (A) Cryptozepine-2 and (B) cryptozepine-3 real-time calcium imaging response from HEK cells expressing  $M_1$  mAChRs, loaded with 10  $\mu\text{M}$  calcium indicator OGB-1 AM (representative single traces,  $n = 14$  cells, on the left;

average,  $n = 67$  cells, on the right), and co-expressing R-GECO1 as a calcium indicator (representative single traces,  $n = 14$  cells, on the left; average,  $n = 48$  cells, on the right), respectively. After 365 nm illumination, 100  $\mu\text{M}$  cryptozepine-2 reduced 0.5  $\mu\text{M}$  ACh responses stronger than before UV light application. Under 460 nm illumination, 100  $\mu\text{M}$  cryptozepine-3 reduced 0.5  $\mu\text{M}$  ACh responses. The gray band indicates the standard error of the mean (SEM). (C) Quantification of the calcium imaging responses. ACh-induced calcium release was significantly reduced by 100  $\mu\text{M}$  pirenzepine and cryptozepine-2. *cis*-Cryptozepine-2 shows a significantly stronger inhibition than its *trans*-isomer. Cryptozepine-3 (100  $\mu\text{M}$ ) partially and significantly reduced ACh-induced calcium release only under 460 nm illumination (*cis*). Data were analyzed by paired-sample Wilcoxon signed-rank test ( $p$ -value (\*\*) $< 0.01$ ,  $p$ -value (\*\*\*) $< 0.001$ ,  $p$ -value (\*\*\*\*) $< 0.0001$ ; GraphPad Prism 6). Error bars are  $\pm$  SEM. (D) Calcium imaging studies of M<sub>1</sub>R vs. M<sub>2</sub>R-G $\alpha_{\text{qTOP}}$  selectivity with 10 (M<sub>1</sub>R,  $n = 183$ ; M<sub>2</sub>R,  $n = 99$ ), 30 (M<sub>1</sub>R,  $n = 58$ ; M<sub>2</sub>R,  $n = 106$ ), 50 (M<sub>1</sub>R,  $n = 262$ ; M<sub>2</sub>R,  $n = 191$ ), and 100 (M<sub>1</sub>R,  $n = 194$ ; M<sub>2</sub>R,  $n = 165$ )  $\mu\text{M}$  cryptozepine-2. On M<sub>1</sub>R-expressing cells, cryptozepine-2 significantly showed its stronger and photoswitchable antagonism than on M<sub>2</sub>R cells. The data were normalized over the maximum response obtained with 0.5  $\mu\text{M}$  ACh and analyzed by the paired-sample Wilcoxon signed-rank test ( $p$ -value (\*\*\*) $< 0.001$ ,  $p$ -value (\*\*\*\*) $< 0.0001$ ; GraphPad Prism 6). Error bars are  $\pm$  SEM. (E) Selective M<sub>1</sub> vs. M<sub>2</sub> mAChR radioligand binding inhibition of the more active *cis*-cryptozepine-2 isomers.

The antagonist activity and the significant differences observed between the *trans* and *cis* states for both compounds are in agreement with the design, where a higher inhibitory activity was intended upon illumination. The stronger inhibition displayed by cryptozepine-2 compared to cryptozepine-3 at 100  $\mu\text{M}$  is probably due to the three-fold tighter binding of the former (**Figure S3.17**). The activity of *trans*-cryptozepine-2 can also be attributed to its proximity to saturation at this concentration and could be reduced at lower concentrations. Correspondingly, cryptozepine-3 is inactive in the dark and a (weak) inhibitor under illumination with blue light at the same concentration. We hypothesized that the electronic and/or steric properties of the additional group ( $-\text{NMe}_2$ ) on the terminal aromatic ring in cryptozepine-3 might account for its reduction of efficacy in comparison with cryptozepine-2. However, the efficiency of cryptozepine-3 may also be limited by the relatively smaller population of the *cis*-isomer that is achieved upon irradiation as a consequence of its faster relaxation. Before using our most potent antagonist, cryptozepine-2, for physiologically more complex experiments, we studied whether it also retained the M<sub>1</sub>R vs. M<sub>2</sub>R subtype selectivity of PNZ. First, we measured calcium responses in HEK cells expressing M<sub>2</sub> mAChR and observed that the antagonist behavior of cryptozepine-2 was only partial (100  $\mu\text{M}$ ) or undetectable (10  $\mu\text{M}$ ) for this receptor subtype (**Figure 3.3D**). We also tested the M<sub>1</sub>R/M<sub>2</sub>R specific affinity of the more active *cis*-cryptozepine-2 in radioligand competition binding studies. These results also confirmed the M<sub>1</sub>R selectivity in the  $\mu\text{M}$  range of concentrations (1, 10, and 100  $\mu\text{M}$ ), with a quite negligible M<sub>2</sub>R affinity at 1 and 10  $\mu\text{M}$  (**Figure 3.3E**) and estimated IC<sub>50</sub> values of 1.9  $\mu\text{M}$  for M<sub>1</sub>R and

28  $\mu\text{M}$  for  $\text{M}_2\text{R}$  (**Figure S3.21**). These data altogether demonstrate that the crypto-azologization design yields *cis*-active light-sensitive derivatives that retain not only the original activity of the parent compound but also its selectivity.

### 3.2.5 *Ex vivo* experiments in mouse isolated atrium

To validate crypto-azologs in a physiologically relevant scenario (*i.e.*, in tissue expressing a diversity of endogenous receptors), we tested the effect of cryptozepine-2 on the mouse isolated atrium. Here, the excitation of muscarinic receptors induces arrest of the heartbeat<sup>32-34</sup>. This negative chronotropic effect in the atria is primarily mediated by mAChR activation, including  $\text{M}_1\text{R}$ , and the anticholinergic activity of PNZ resumes the heart rate and rhythm<sup>32-35</sup>. We isolated the right atria from male mice and measured their spontaneous frequency of contraction (control), which was about 360 beats/min (see the **SI** for details). Application of the muscarinic agonist carbachol (CCh, 1  $\mu\text{M}$ ) strongly reduces the frequency to around 200 beats/min (**Figure 3.4**), and the addition of PNZ (1  $\mu\text{M}$ ) to the bath restores the frequency almost to control values (**Figure 3.4**). We used this robust assay to test the antagonist behavior of cryptozepine-2 isomers. At a concentration of 100  $\mu\text{M}$ , the *trans*-isomer was unable to antagonize CCh-induced bradycardia and was seemingly inert, whereas *cis*-cryptozepine-2 readily induced the partial recovery of the atrium contraction frequency (**Figure 3.4** and see the **SI** for details). This effect is in accord with the  $\text{M}_1\text{R}$  anticholinergic activity of PNZ in the atria<sup>32-35</sup> and, considering the partial  $\text{M}_1\text{R}$  vs.  $\text{M}_2\text{R}$  selectivity of our ligand at 100  $\mu\text{M}$  (**Figure 3.3**), can be attributed mainly to  $\text{M}_1\text{R}$ , further highlighting the pharmacological potential of the crypto-azologization design.

Regarding future applications, the photopharmacological properties of cryptozepines should be enhanced by improving the potency of the active forms and avoiding the need for UV light, which is not optimal for biological applications. Although it is remarkable that crypto-azologs retain the activity and selectivity of the parent tricyclic compound, the actual potency achieved in our pilot study is almost 200-fold lower (see **Table 3.1**), which prompts subsequent rounds of lead optimization and safety testing as usually carried out in drug development processes. An option for improving the optical and pharmacological properties at once might be inserting fluorine in the ortho position(s) of the azobenzene. These modifications should preserve or even improve the antagonist potency by adding lipophilic contacts in the binding pocket<sup>16</sup> while providing favorable photochromic properties like slow thermal back-isomerization and high two-photon cross-section<sup>36</sup>. Furthermore, substitutions of the piperazine tail allow tuning subtype selectivity, *e.g.*, diethyl[(piperidin-2-yl)methyl]amine yields nanomolar,  $\text{M}_2\text{R}$  selective antagonists<sup>37,38</sup>.

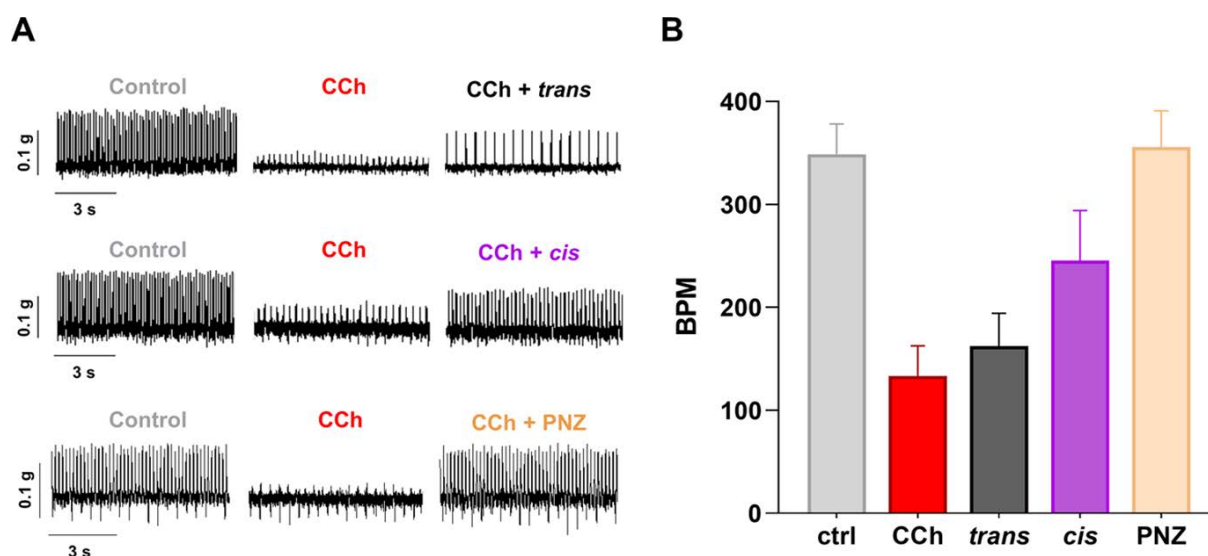


**Figure 3.4. Pirenzepine and cryptozepine-2 can antagonize CCh-induced bradycardia in mouse atria through M<sub>1</sub>Rs.** (A) Representative traces and (B) quantification of mouse right atrium heart rate treated with carbachol (CCh), pirenzepine (PNZ), and *trans/cis*-cryptozepine-2. Spontaneous mechanical contractions of the mouse atria were recorded as control (ctrl) and defined as the heartbeat frequency in beats/min (BPM). CCh (1  $\mu$ M) decreased both the amplitude and BPM. The presence of PNZ (n = 6) and *cis*-cryptozepine-2 (*cis*) (n = 2) reversed the CCh-induced bradycardia. In contrast, *trans*-cryptozepine-2 (*trans*) (n = 2) did not reverse the effect of CCh in terms of the heartbeat frequency (n = 2).

Overall, the photopharmacological properties of cryptozepines set the stage for interesting assays *in vivo*. If they can be enterically administered in the inactive form (*trans*), these drugs could be remotely photoactivated at the desired location and time using the built-in light-emitting diode (LED) of an endoscopy capsule<sup>39</sup>, potentially allowing to treat gastro-intestinal tract diseases without producing (adverse) effects in other regions or organs. More invasive applications include the manipulation of cardiac function *in vivo* using optoelectronic devices coupled to cardiac patches<sup>14,40</sup>. In any case, to test the feasibility of future therapies based on photoswitchable drugs, both isomers must be pharmacologically characterized.

### 3.3 Conclusions

In summary, we have expanded the rational design of photochromic ligands to the important class of tricyclic drugs. The proposed strategy involves two concomitant structural modifications to afford azobenzene derivatives that can mimic the tricyclic motif: (1) an isosteric replacement with a  $-N=N-$  group and (2) a ring cleavage. We have demonstrated a proof of concept with a set of photoswitchable derivatives of the muscarinic antagonist PNZ that we named cryptozepines. These novel compounds retain micromolar binding and antagonist character despite the structural dissimilarity with the parent compound. The most



potent photoswitchable compound (cryptozepine-2) displays negligible activity in mouse atrium in *trans* and M<sub>1</sub>R antagonism in *cis*, indicating that the crypto-azologization strategy has the potential to produce photoswitchable derivatives of tricyclic drugs that are inactive in their thermally stable *trans*-isomer, which is desirable in photopharmacology. Further optimization of photochromism and the potency of the active form might yield photopharmacological drug candidates, displaying high safety and localized therapeutic action. Interestingly, cryptozepine-2 already maintains a moderate selectivity for M<sub>1</sub> over M<sub>2</sub> mAChRs, similar to its parent compound. The proof of concept demonstrated with this strategy opens the way to use it in many other targets bearing the tricyclic motif. This work provides a new toolbox to design photochromic drugs that significantly expands the scope of photopharmacology and its applications.

## References

- 1 Lerch, M. M., Hansen, M. J., van Dam, G. M., Szymanski, W. & Feringa, B. L. Emerging targets in photopharmacology. *Angew Chem Int Ed Engl* **55**, 10978-10999, doi:10.1002/anie.201601931 (2016).
- 2 Hull, K., Morstein, J. & Trauner, D. *In vivo* photopharmacology. *Chem Rev* **118**, 10710-10747, doi:10.1021/acs.chemrev.8b00037 (2018).
- 3 Morstein, J., Awale, M., Reymond, J. L. & Trauner, D. Mapping the azolog space enables the optical control of new biological targets. *ACS Cent Sci* **5**, 607-618, doi:10.1021/acscentsci.8b00881 (2019).
- 4 Pittolo, S. *et al.* An allosteric modulator to control endogenous G protein-coupled receptors with light. *Nat Chem Biol* **10**, 813-815, doi:10.1038/nchembio.1612 (2014).
- 5 Schoenberger, M., Damijonaitis, A., Zhang, Z., Nagel, D. & Trauner, D. Development of a new photochromic ion channel blocker via azologization of fomocaine. *ACS Chem Neurosci* **5**, 514-518, doi:10.1021/cn500070w (2014).
- 6 Matera, C. *et al.* Photoswitchable antimetabolite for targeted photoactivated chemotherapy. *J Am Chem Soc* **140**, 15764-15773, doi:10.1021/jacs.8b08249 (2018).
- 7 Agnetta, L. D., M. Photoresponsive hybrid compounds. In design of hybrid molecules for drug development. *Elsevier Inc.*, 279-315 (2017).
- 8 Yet, L. Privileged structures in drug discovery. *Inc.: Hoboken, NJ* (2018).
- 9 Evans, B. E. *et al.* Methods for drug discovery: Development of potent, selective, orally effective cholecystokinin antagonists. *J Med Chem* **31**, 2235-2246, doi:10.1021/jm00120a002 (1988).
- 10 Marsh, W. Tricyclic antidepressants. In xPharm: The comprehensive pharmacology reference. *Elsevier Inc.*, 1-3 (2007).
- 11 Fedi, V., Guidi, A. & Altamura, M. Tricyclic structures in medicinal chemistry: An overview of their recent uses in non-CNS pathologies. *Mini Rev Med Chem* **8**, 1464-1484, doi:10.2174/138955708786786453 (2008).
- 12 Matera, C. & Tata, A. M. Pharmacological approaches to targeting muscarinic acetylcholine receptors. *Recent Pat CNS Drug Discov* **9**, 85-100, doi:10.2174/1574889809666141120131238 (2014).
- 13 Kruse, A. C. *et al.* Muscarinic acetylcholine receptors: Novel opportunities for drug development. *Nat Rev Drug Discov* **13**, 549-560, doi:10.1038/nrd4295 (2014).
- 14 Riefolo, F. *et al.* Optical control of cardiac function with a photoswitchable muscarinic agonist. *J Am Chem Soc* **141**, 7628-7636, doi:10.1021/jacs.9b03505 (2019).
- 15 Agnetta, L. *et al.* A photoswitchable dualsteric ligand controlling receptor efficacy. *Angew Chem Int Ed Engl* **56**, 7282-7287, doi:10.1002/anie.201701524 (2017).
- 16 Agnetta, L. *et al.* Fluorination of photoswitchable muscarinic agonists tunes receptor pharmacology and photochromic properties. *J Med Chem* **62**, 3009-3020, doi:10.1021/acs.jmedchem.8b01822 (2019).
- 17 Hammer, R., Berrie, C. P., Birdsall, N. J., Burgen, A. S. & Hulme, E. C. Pirenzepine distinguishes between different subclasses of muscarinic receptors. *Nature* **283**, 90-92, doi:10.1038/283090a0 (1980).
- 18 El-Obeid, H. A. B., S. A.; Al-Badr, A. A. Pirenzepine dihydrochloride. *Anal. Profiles Drug Subst. Excipients* **16**, 445-506 (1987).
- 19 Eberlein, W. G., Engel, W. W., Trummlitz, G., Schmidt, G. & Hammer, R. Tricyclic compounds as selective antimuscarinics. 2. Structure-activity relationships of M<sub>1</sub>R-selective antimuscarinics related to pirenzepine. *J Med Chem* **31**, 1169-1174, doi:10.1021/jm00401a016 (1988).
- 20 Stolerman, I. P. *Encyclopedia of Psychopharmacology*.

- 21 Walline, J. J. *et al.* Interventions to slow progression of myopia in children. *Cochrane Database Syst Rev*, CD004916, doi:10.1002/14651858.CD004916.pub3 (2011).
- 22 Pedretti, R. F., Prete, G., Foreman, R. D., Adamson, P. B. & Vanoli, E. Autonomic modulation during acute myocardial ischemia by low-dose pirenzepine in conscious dogs with a healed myocardial infarction: a comparison with beta-adrenergic blockade. *J Cardiovasc Pharmacol* **41**, 671-677, doi:10.1097/00005344-200305000-00002 (2003).
- 23 Thal, D. M. *et al.* Crystal structures of the M<sub>1</sub> and M<sub>4</sub> muscarinic acetylcholine receptors. *Nature* **531**, 335-340, doi:10.1038/nature17188 (2016).
- 24 Murgolo, N. J. K., J.; Tice, M. A. B.; Hollinger, F. P.; Brown, J. E.; Zhou, G.; Taylor, L. A.; McQuade, R. D. The N<sub>4</sub> nitrogen of pirenzepine is responsible for selective binding of the M<sub>1</sub> subtype human muscarinic receptor. *Bioorg. Med. Chem. Lett.* **6**, 785-788 (1996).
- 25 Dong, M., Babalhavaeji, A., Samanta, S., Beharry, A. A. & Woolley, G. A. Red-shifting azobenzene photoswitches for *in vivo* use. *Acc Chem Res* **48**, 2662-2670, doi:10.1021/acs.accounts.5b00270 (2015).
- 26 Ghetti, F. G., A. G.; Oelgemöller, M. (CRC Press, 2012).
- 27 Bandara, H. M. & Burdette, S. C. Photoisomerization in different classes of azobenzene. *Chem Soc Rev* **41**, 1809-1825, doi:10.1039/c1cs15179g (2012).
- 28 Claro, E. Analyzing ligand depletion in a saturation equilibrium binding experiment. *Biochem Mol Biol Educ* **34**, 428-431, doi:10.1002/bmb.2006.494034062677 (2006).
- 29 Yamamura, H. I. & Snyder, S. H. Muscarinic cholinergic binding in rat brain. *Proc Natl Acad Sci U S A* **71**, 1725-1729, doi:10.1073/pnas.71.5.1725 (1974).
- 30 Salles, J., Wallace, M. A. & Fain, J. N. Differential effects of alkylating agents on the multiple muscarinic receptor subtypes linked to activation of phospholipase C by carbachol in rat brain cortical membranes. *J Pharmacol Exp Ther* **264**, 521-529 (1993).
- 31 Massoulie, J., Carson, S. & Kato, G. Biochemical characterization of muscarinic receptors: Multiplicity of binding components. *Prog Brain Res* **49**, 303-311, doi:10.1016/S0079-6123(08)64642-7 (1979).
- 32 Heijman, J. *et al.* Muscarinic type-1 receptors contribute to I (K,ACh) in human atrial cardiomyocytes and are upregulated in patients with chronic atrial fibrillation. *Int J Cardiol* **255**, 61-68, doi:10.1016/j.ijcard.2017.12.050 (2018).
- 33 Susskand, K. & Sewing, K. F. Anticholinergic effects of pirenzepine on the guinea-pig isolated atrium. *Pharmacology* **19**, 163-164, doi:10.1159/000137304 (1979).
- 34 Woo, S. H., Lee, B. H., Kwon, K. I. & Lee, C. O. Excitatory effect of M<sub>1</sub> muscarinic acetylcholine receptor on automaticity of mouse heart. *Arch Pharm Res* **28**, 930-935, doi:10.1007/BF02973879 (2005).
- 35 Hogan, K. & Markos, F. Muscarinic type 1 receptors mediate part of nitric oxide's vagal facilitatory effect in the isolated innervated rat right atrium. *Nitric Oxide* **16**, 110-117, doi:10.1016/j.niox.2006.05.005 (2007).
- 36 Cabre, G. *et al.* Rationally designed azobenzene photoswitches for efficient two-photon neuronal excitation. *Nat Commun* **10**, 907, doi:10.1038/s41467-019-08796-9 (2019).
- 37 Araujo, D. M., Lapchak, P. A., Regenold, W. & Quirion, R. Characterization of [3H]AF-DX 116 binding sites in the rat brain: Evidence for heterogeneity of muscarinic-M<sub>2</sub> receptor sites. *Synapse* **4**, 106-114, doi:10.1002/syn.890040204 (1989).
- 38 Giachetti, A., Micheletti, R. & Montagna, E. Cardiosselective profile of AF-DX 116, a muscarine M<sub>2</sub> receptor antagonist. *Life Sci* **38**, 1663-1672, doi:10.1016/0024-3205(86)90410-8 (1986).
- 39 Shrestha, R., Mohammed, S. K., Hasan, M. M., Zhang, X. & Wahid, K. A. Automated adaptive brightness in wireless capsule endoscopy using image segmentation and

- sigmoid function. *IEEE Trans Biomed Circuits Syst* **10**, 884-892, doi:10.1109/TBCAS.2016.2546838 (2016).
- 40 Feiner, R. *et al.* Engineered hybrid cardiac patches with multifunctional electronics for online monitoring and regulation of tissue function. *Nat Mater* **15**, 679-685, doi:10.1038/nmat4590 (2016).

## Supporting Information (SI) of Chapter 3

### SI3.1 Molecular docking

#### SI3.1.1 Materials and methods

Molecular docking simulations were performed using the crystal structure of the human M<sub>1</sub> muscarinic acetylcholine receptor (M<sub>1</sub> mAChR or M<sub>1</sub>R) retrieved from the Protein Data Bank (PDB) bound to the antagonist tiotropium (PDB ID: 5CXV)<sup>1</sup>. The protein pdb file was prepared for docking by removing co-crystallized ligands, non-complexed ions and water molecules, and finally applying the Dock Prep tool available in the free software package UCSF Chimera. This involved the addition of hydrogens and assigning partial charges (AMBER ff14SB method). The cryptozepine-2, *trans* and *cis*, structures were built with standard bond length and angles using ChemDraw and then energy minimized with Chem3D by the MM2 method. The minimized compounds were further prepared for docking studies with UCSF Chimera by adding hydrogens and assigning partial charges (AMBER ff14SB method). The necessary pdbqt files of ligands and receptor were prepared using AutoDock 4.2 software. The docking studies were carried out using the standard docking protocol applied for AutoDock Vina in PyRx 0.8 virtual screening software. Autodock Vina has been reported to be an effective tool capable of quickly and accurately predicting bound conformations and binding energies of ligands with macromolecular targets<sup>2,3</sup>. A grid box of size 18.68 × 17.35 × 13.64 Å, with x, y and z coordinates of -11.52, -12.61 and 37.05, respectively, was fixed to cover the entire orthosteric binding sites and accommodate the ligands to move freely. Docking studies were performed using an exhaustiveness value of 8 while all other parameters were maintained as defaults. All rotatable bonds within the ligands were allowed to rotate freely, and the receptor was considered rigid. The docking simulations were repeated three times for each ligand. The obtained poses were then ranked based on the predicted affinity docking scores (kcal/mol) and the best pose for each experiment was selected. The results were then analyzed using UCSF Chimera. Both isomers of the cryptozepine-2 and pirenzepine (PNZ) were docked into the orthosteric binding sites of the human M<sub>1</sub> mAChR in its inactive conformation, bound to the antagonist tiotropium (PDB ID: 5CXV). All the ligands were docked at this receptor model using a standard docking protocol with AutoDock Vina in the PyRx 0.8 software with a suitable grid box. We ran three/five simulations for each ligand isomer and selected the best pose obtained in each experiment based on the predicted binding affinity scores (kcal/mol).

### SI3.1.2 Molecular docking simulations of cryptozepine isomers

In order to examine if the “crypto-azologization” concept was a reasonable strategy for developing light-sensitive crypto-azologs of PNZ, we firstly used molecular docking calculations. We docked cryptozepine-2, the crypto-azolog of PNZ with the simplest unsubstituted azobenzene as molecular switch, into the orthosteric binding site of the human M<sub>1</sub> mAChR (inactive conformation bound to the antagonist tiotropium, PDB ID: 5CXV)<sup>1</sup>. We first validated the docking protocol with the parent compound PNZ. The obtained best poses and their average binding affinity (-8.3 kcal/mol) were in agreement with the results previously published for the same ligand (**Figure S3.1D**)<sup>1</sup>. The key elements for antagonist binding at the M<sub>1</sub>R reside in the methylpiperazine amines<sup>1,4-6</sup>. This group must face and interact with the orthosteric site residues D105 and Y404 (transmembrane helices (TM) 3 and 7, respectively; residues are numbered according to the human M<sub>1</sub>R, PDB ID: 5CXV) (**Figure S3.1**). Additional confirmation that PNZ adopts the correct orientation in our calculations is provided by the tricyclic core oriented as the aromatic portions of tiotropium, which is free to create hydrophobic contacts with Y106 (TM3), W157 (TM4) and Y381 (TM6) (**Figure S3.1**)<sup>1</sup>. We next studied cryptozepine-2 (**Figure S3.1**). Our calculations showed that the best poses of the *cis*-isomer fit in the M<sub>1</sub>R orthosteric site in a similar way to PNZ (**Figure S3.1**), with favorable binding affinity values (-9.1 kcal/mol) (**Figure S3.1E**). In contrast, a flipped orientation was favored for the majority of the *trans*-isomer poses (**Figure S3.1F**), which are likely incompatible with antagonism activity<sup>1,4-6</sup>. The planar *trans* geometry of cryptozepine-2 covers a larger space with the aromatic portions (8.7 Å) than its bent *cis*-isomer (6.9 Å) and PNZ (7.1 Å) (**Figure S3.1**). This may hinder the correct placing into the binding pocket of the rest of the ligand and result in loss of antagonist behavior. Thus, computational results were in agreement with the “crypto-azologization” concept and encouraged to pursue the synthesis of a small library of cryptozepines.

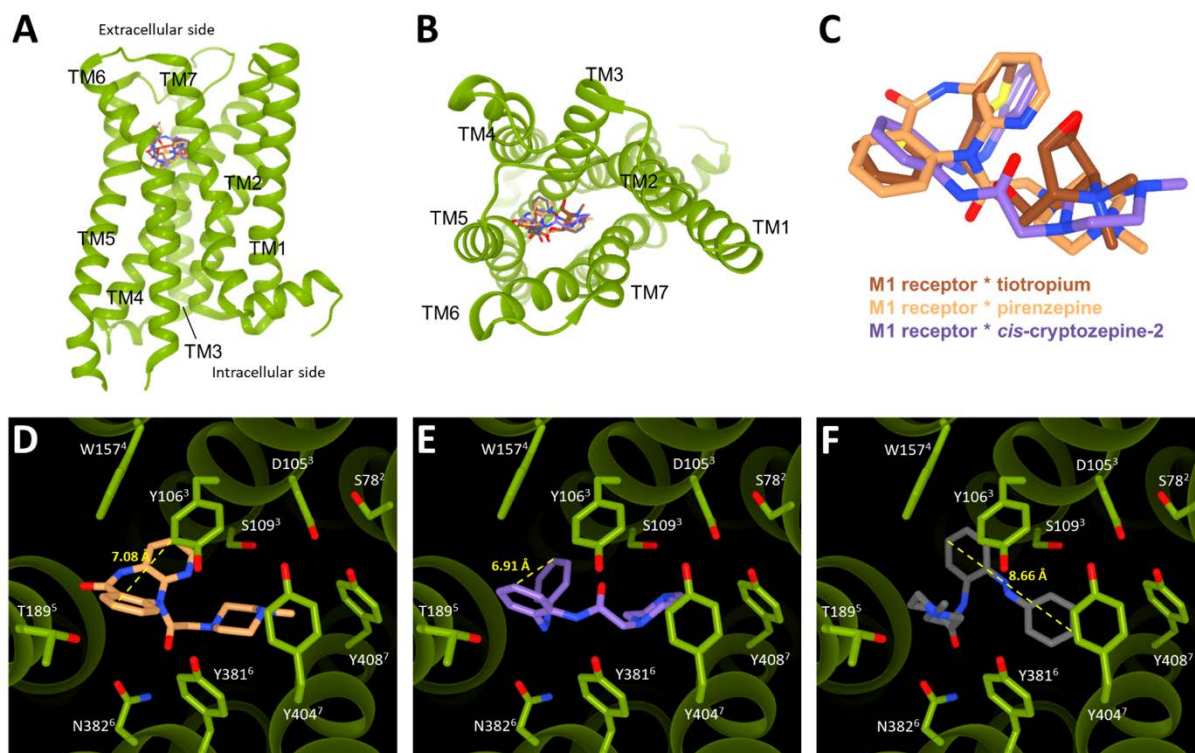


**Figure S3.1. Hypothetical binding mode of cryptozepine-2 (*trans*- and *cis*-isomers) in M<sub>1</sub> mAChR.** (A) Full view and (B) extracellular side view of the M<sub>1</sub>R muscarinic structure (PDB ID: 5CXV) colored in green, with our antagonists bound into the orthosteric site. (C) Superimposition of binding poses of tiotropium from the M<sub>1</sub>R structure (PDB ID: 5CXV), pirenzepine (PNZ), and the *cis*-cryptozepine-2 from our simulations using the same receptor. (D) PNZ, (E) *cis*- and (F) *trans*-cryptozepine-2 poses in the M<sub>1</sub>R with the fundamental residues that contribute to the orthosteric binding site (several residues are omitted for clarity). The ligands are shown as sticks and colored according to element: carbon, beige for PNZ, brown for tiotropium, purple for *cis*-cryptozepine-2, dark grey for *trans*-cryptozepine-2; oxygen, red; nitrogen, dark blue; sulfur, yellow. Residues are numbered according to the human M<sub>1</sub>R sequence (PDB ID: 5CXV). Superscript numbers indicate the transmembrane (TM) helices of the M<sub>1</sub>R. The yellow line and values indicate the length of the tricyclic core of PNZ, and the aromatic portions of *trans*- and *cis*-cryptozepine-2. PNZ and cryptozepine-2 can antagonize CCh-induced bradycardia in mouse atria through M<sub>1</sub>R.

## SI3.2 Chemical synthesis

### SI3.2.1 Materials and methods

All reagents and solvents were purchased from Sigma-Aldrich, Cymit Química, and ServiQuimia and were used without any further purification. Thin layer chromatography (TLC) analyses were performed on commercial silica gel 60 F<sub>254</sub> aluminum foils (Merck); spots were further evidenced by spraying with a dilute alkaline potassium permanganate solution or a 5% phosphomolybdic acid solution in ethanol and, for tertiary amines and quaternary ammonium compounds, with the Dragendorff reagent. Flash chromatography was performed on PanReac

AppliChem silica gel 60 (40-63  $\mu\text{m}$ ), Biotage SNAP KP-C18-HS 12 g or Biotage SNAP KP-SIL 25 gas stationary phases; mobile phases are specified for each compound. Ultraviolet-Visible (UV-Vis) spectra and experiments were recorded with a Shimadzu UV-1800 UV-Vis Spectrophotometer with standard quartz cuvettes (10 mm light path).  $^1\text{H}$  NMR and  $^{13}\text{C}$  NMR spectra were registered with a Varian Mercury 400 MHz (400 MHz for  $^1\text{H}$  NMR and 101 MHz for  $^{13}\text{C}$  NMR) and a Varian VNMRS 500 MHz instrument (500 MHz for  $^1\text{H}$  NMR and 126 MHz for  $^{13}\text{C}$  NMR) in  $\text{DMSO-}d_6$ ,  $\text{CDCl}_3$ , and  $\text{D}_2\text{O}$ . Residual signals of the deuterated solvents were used as an internal standard ( $\text{DMSO-}d_6$ :  $^1\text{H}$  2.50 ppm,  $^{13}\text{C}$  39.52 ppm;  $\text{CDCl}_3$ :  $^1\text{H}$  7.26 ppm,  $^{13}\text{C}$  77.16 ppm;  $\text{D}_2\text{O}$ :  $^1\text{H}$  4.79 ppm). Chemical shifts ( $\delta$ ) are expressed as parts-per-million (ppm) and coupling constants ( $J$ ) as hertz (Hz). High-performance liquid chromatography (HPLC) analyses were performed with a Waters Alliance 2795 separation module (RP column: XSelect CSH C18,  $50 \times 4.6 \text{ mm}^2$ , S-3.5  $\mu\text{m}$ , 1.6 ml/min; eluent: from 5% B to 100% B in 3.5 min using a linear gradient, A:  $\text{H}_2\text{O}$  0.1% formic acid, B: acetonitrile 0.1% formic acid) coupled to a Waters 2996 photodiode detector and a Waters 3100 mass spectrometer. High-resolution mass spectroscopy measurements (ionization: NanoESI, positive ionization) were performed at the mass spectrometry core facility of the Institute for Research in Biomedicine (IRB, Barcelona, Spain) with an LTQ-FT Ultra (ThermoFisher Scientific) for direct infusion (Automated Nanoelectrospray) of the sample. The NanoMate (Advion BioSciences) aspirated the samples from a 384-well plate (protein LoBind) with disposable, conductive pipette tips and infused the samples through the NanoESI Chip (which consists of 400 nozzles in a  $20 \times 20$  array) toward the mass spectrometer. Spray voltage was 1.70 kV and delivery pressure was 0.50 psi. Data are reported as a mass-to-charge ratio ( $m/z$ ) of the corresponding positively charged molecular ions.

### SI3.2.2 Abbreviations

**Solvents:** EtOAc, ethyl acetate;  $\text{CH}_2\text{Cl}_2$ , dichloromethane; MeCN, acetonitrile; MeOH, methanol; EtOH, ethanol; THF, tetrahydrofuran;  $\text{Et}_2\text{O}$ , diethyl ether; DMSO, dimethyl sulfoxide.

**Analytical characterizations:** NMR: d, doublet; dd, double doublet; ddd, double double doublet; dddd, doublet of doublet of doublet of doublets; dt, double triplet; m, multiplet; q, quartet; quin, quintet; s, singlet; t, triplet; m.p., melting point;  $R_f$ , retention factor; rt, room temperature; RT, retention time.



### SI3.2.3 Synthetic routes

***N*-(2-Aminophenyl)-2-chloroacetamide (5):** Fe (1.30 g, 23.30 mmol), NH<sub>4</sub>Cl (124.63 mg, 2.33 mmol), and glacial acetic acid (0.270 ml, 4.66 mmol) were added into 10 ml of H<sub>2</sub>O and stirred at 50°C for 15 min. A solution of 2-chloro-*N*-(2-nitrophenyl)acetamide (0.5 g, 2.33 mmol) in dimethylformamide (DMF) (5 ml) was added into the above solution quickly, and stirring was continued at 50°C for 15 min. Then, the reaction solution was alkalized to pH 9 with aqueous Na<sub>2</sub>CO<sub>3</sub>. Subsequently, the mixture was filtered, and the cake was washed with H<sub>2</sub>O and EtOAc. The combined filtrate was extracted with EtOAc. Then, the combined organic layers were washed with brine, dried over anhydrous MgSO<sub>4</sub>, filtered, and concentrated under reduced pressure. Purification of the crude product by chromatography on silica gel (cyclohexane/EtOAc, 4:6) afforded *N*-(2-aminophenyl)-2-chloroacetamide (**5**) as a white solid (260 mg, 60%).

<sup>1</sup>H NMR (400 MHz, CDCl<sub>3</sub>) δ 8.19 (s, <sup>1</sup>H), 7.31 (dd, *J* = 7.8, 1.5 Hz, 1H), 7.10 (td, *J* = 7.7, 1.5 Hz, 1H), 6.87 – 6.80 (m, 2H), 4.24 (s, 2H), 3.77 (s, 2H).

**2-Chloro-*N*-(2-nitrosophenyl)acetamide (6):** *N*-(2-Aminophenyl)-2-chloroacetamide (**5**) (250 mg, 1.35 mmol) was suspended in 5 ml of CH<sub>2</sub>Cl<sub>2</sub>. Oxone (630 mg, 2.05 mmol) in 20 ml of water was added, and the resulting mixture was stirred vigorously for 1 h at room temperature. The organic phase was separated, and the aqueous phase was extracted with 10 ml of CH<sub>2</sub>Cl<sub>2</sub>. The combined organic phases were washed with 1 M HCl (50 ml), saturated aqueous NaHCO<sub>3</sub> (50 ml), and water (50 ml). Finally, it was dried over MgSO<sub>4</sub> and evaporated under reduced pressure to afford the nitroso derivative (**6**), which was used in the next step without further purification.

**2-Chloro-*N*-(2-(pyridin-3-yl-diazenyl)phenyl)acetamide (7a):** Compound **6** (155 mg, 0.78 mmol) and 3-aminopyridine (147 mg, 1.56 mmol) were dissolved in glacial acetic acid (30 ml) and stirred for 24 h at 60°C. The solution was diluted with water and extracted with EtOAc. The organic phase was washed four times with water and once with brine and dried over MgSO<sub>4</sub>. The crude product was purified by chromatography (eluent: cyclohexane/EtOAc, 9:1) to yield **7a** (100 mg, 47%) as an orange solid.

<sup>1</sup>H NMR (400 MHz, CDCl<sub>3</sub>) δ 10.96 (s, 1H), 9.23 (dd, *J* = 2.4, 0.8 Hz, 1H), 8.73 (dd, *J* = 4.7, 1.6 Hz, 1H), 8.68 (dd, *J* = 8.4, 1.3 Hz, 1H), 8.15 (ddd, *J* = 8.2, 2.4, 1.6 Hz, 1H), 7.92 (dd, *J* = 8.1, 1.6 Hz, 1H), 7.55 (ddd, *J* = 8.7, 7.2, 1.6 Hz, 1H), 7.48 (ddd, *J* = 8.2, 4.8, 0.8 Hz, 1H), 7.29

– 7.22 (m, 1H), 4.29 (s, 2H).  $^{13}\text{C}$  NMR (101 MHz,  $\text{CDCl}_3$ )  $\delta$  164.33, 152.27, 147.88, 147.31, 139.79, 135.65, 133.91, 127.05, 124.63, 124.31, 120.30, 120.05, 43.58.

**2-Chloro-*N*-(2-(phenyldiazenyl)phenyl)acetamide (7b):** Compound **6** (170 mg, 0.86 mmol) and aniline (159 mg, 1.71 mmol) were dissolved in glacial acetic acid (30 ml) and stirred for 4 days at room temperature. The solution was diluted with water and extracted with EtOAc. The organic phase was washed four times with water and once with brine and dried over  $\text{MgSO}_4$ . The crude product was purified by chromatography (eluent: cyclohexane/EtOAc, 9:1) to yield **7b** (130 mg, 56%) as an orange solid.

$^1\text{H}$  NMR (400 MHz,  $\text{CDCl}_3$ )  $\delta$  11.03 (s, 1H), 8.66 (dd,  $J = 8.3, 1.3$  Hz, 1H), 7.97 – 7.91 (m, 2H), 7.89 (ddd,  $J = 8.2, 1.6, 0.5$  Hz, 1H), 7.56 – 7.46 (m, 4H), 7.22 (ddd,  $J = 8.2, 7.3, 1.3$  Hz, 1H), 4.27 (s, 2H).  $^{13}\text{C}$  NMR (101 MHz,  $\text{CDCl}_3$ )  $\delta$  164.28, 152.51, 139.63, 135.29, 132.90, 131.66, 129.39, 124.46, 123.01, 120.08, 119.98, 43.52.

**2-Chloro-*N*-(2-((4-(dimethylamino)phenyl)diazenyl)phenyl)-acetamide (7c):** Compound **6** (500 mg, 2.52 mmol) and 4-amino-*N,N*-dimethylaniline (514 mg, 3.78 mmol) were dissolved in glacial acetic acid (20 ml) and stirred for 30 min at room temperature. The solution was concentrated under reduced pressure and the crude product was purified by chromatography (eluent: cyclohexane/AcOEt, 8:2) to afford **7c** as a red solid in quantitative yield.

$^1\text{H}$  NMR (400 MHz,  $\text{CDCl}_3$ )  $\delta$  11.00 (s, 1H), 8.59 (dd,  $J = 8.3, 1.4$  Hz, 1H), 7.94 – 7.87 (m, 2H), 7.83 (ddd,  $J = 8.1, 1.6, 0.5$  Hz, 1H), 7.39 (dddd,  $J = 8.3, 7.3, 1.6, 0.5$  Hz, 1H), 7.19 (dddd,  $J = 8.0, 7.3, 1.3, 0.5$  Hz, 1H), 6.81 – 6.72 (m, 2H), 4.27 (s, 2H), 3.11 (s, 6H).  $^{13}\text{C}$  NMR (101 MHz,  $\text{CDCl}_3$ )  $\delta$  164.04, 152.87, 143.71, 140.36, 134.62, 130.79, 125.35, 124.46, 119.78, 118.42, 111.73, 43.61, 40.43.

**(E)-2-(4-Methylpiperazin-1-yl)-*N*-(2-(pyridin-3-yl)diazenyl)-phenylacetamide**

**(Cryptozepine-1):** Compound **7a** (100 mg, 0.364 mmol) was dissolved in 20 ml of MeCN. 1-Methylpiperazine (55 mg, 0.547 mmol) and triethylamine (55.3 mg, 0.546 mmol) were then slowly added to the solution. The mixture was stirred under reflux for 3 h. Upon completion, MeCN was removed under reduced pressure and the obtained oil was dissolved in EtOAc. The resulting organic solution was washed 4 times using 30 ml of saturated aqueous  $\text{NaHCO}_3$ . The organic layer was dried over  $\text{MgSO}_4$  and evaporated under reduced pressure to afford the final product (**1**) as a yellow solid (quantitative yield).

$^1\text{H}$  NMR (400 MHz,  $\text{CDCl}_3$ )  $\delta$  10.97 (s, 1H), 9.25 (dd,  $J = 2.4, 0.8$  Hz, 1H), 8.78 (dd,  $J = 8.4, 1.3$  Hz, 1H), 8.74 (dd,  $J = 4.8, 1.6$  Hz, 1H), 8.26 (ddd,  $J = 8.2, 2.4, 1.6$  Hz, 1H), 7.81 (dd,  $J =$

8.2, 1.5 Hz, 1H), 7.58 – 7.44 (m, 2H), 7.15 (ddd,  $J = 8.4, 7.3, 1.3$  Hz, 1H), 3.25 (s, 2H), 2.73 – 2.39 (m, 8H), 2.23 (s, 3H).  $^{13}\text{C}$  NMR (101 MHz,  $\text{CDCl}_3$ )  $\delta$  168.84, 151.95, 146.57, 139.99, 137.85, 134.10, 129.63, 128.23, 124.11, 123.65, 120.35, 116.24, 63.03, 55.04, 53.71, 45.95.

**(E)-1-Methyl-4-(2-oxo-2-((2-(pyridin-3-yl)diazenyl)phenyl)-amino)ethyl)piperazine-1,4-dium chloride** (Cryptozepine-1 dihydrochloride): A total of 5 ml of 4 M HCl in dioxane were added slowly to compound **1** (10 mg, 0.03 mmol) at 0°C. The mixture was stirred for 30 min at room temperature, then the solvent and excess of HCl were evaporated under reduced pressure, and the resulting solid was washed 3 times with  $\text{Et}_2\text{O}$  (30 ml). The so obtained orange solid was dried under vacuum to afford cryptozepine-1 dihydrochloride (quantitative yield).

$^1\text{H}$  NMR (500 MHz,  $\text{D}_2\text{O}$ )  $\delta$  9.23 (s, 1H), 8.88 (s, 1H), 8.70 (d,  $J = 8.4, 1.7$  Hz, 1H), 8.09 (dd,  $J = 8.3, 5.4$  Hz, 1H), 8.03 (d,  $J = 8.2$  Hz, 1H), 7.82 (d,  $J = 8.2, 1.5$  Hz, 1H), 7.72 (t, 1H), 7.44 (t, 1H), 3.61 (s, 2H), 3.58 – 3.00 (m, 8H), 2.88 (s, 3H).  $^{13}\text{C}$  NMR (126 MHz,  $\text{D}_2\text{O}$ )  $\delta$  170.19, 149.25, 145.58, 143.06, 140.05, 135.59, 134.71, 134.43, 127.04, 126.49, 124.01, 116.79, 59.48, 52.94, 49.49, 42.71.

MS (ESI, positive): calculated for  $\text{C}_{18}\text{H}_{23}\text{N}_6\text{O}^+$ : 339.19, found 339.1930  $[\text{M} + \text{H}]^+$ .

**(E)-2-(4-Methylpiperazin-1-yl)-N-(2-(phenyldiazenyl)phenyl)-acetamide** (Cryptozepine-2): Compound **7b** (100 mg, 0.364 mmol) was dissolved in 20 ml of MeCN. 1-Methylpiperazine (55 mg, 0.547 mmol) and triethylamine (55.3 mg, 0.546 mmol) were then slowly added to the solution. The mixture was stirred under reflux for 3 h. Upon completion, MeCN was removed under reduced pressure and the obtained oil was dissolved in EtOAc. The resulting organic solution was washed 4 times using 30 ml of saturated aqueous  $\text{NaHCO}_3$ . The organic layer was dried over  $\text{MgSO}_4$  and evaporated under reduced pressure to afford the final product (**2**) as a yellow solid (quantitative yield).

$^1\text{H}$  NMR (400 MHz,  $\text{CDCl}_3$ )  $\delta$  10.94 (s, 1H), 8.77 (dd,  $J = 8.4, 1.3$  Hz, 1H), 8.07 – 7.97 (m, 2H), 7.78 (dd,  $J = 8.2, 1.6$  Hz, 1H), 7.58 – 7.44 (m, 4H), 7.12 (ddd,  $J = 8.3, 7.2, 1.3$  Hz, 1H), 3.23 (s, 2H), 2.82 – 2.30 (m, 8H), 2.22 (s, 3H).  $^{13}\text{C}$  NMR (101 MHz,  $\text{CDCl}_3$ )  $\delta$  168.74, 152.75, 139.91, 137.41, 133.04, 131.31, 129.29, 123.49, 123.29, 120.09, 116.01, 63.02, 54.92, 53.73, 45.95.

**(E)-1-Methyl-4-(2-oxo-2-((2-(phenyldiazenyl)phenyl)amino)-ethyl)piperazine-1,4-dium chloride** (Cryptozepine-2 dihydrochloride): A total of 6 ml of 4 M HCl in dioxane was added slowly to compound **2** (50 mg, 0.15 mmol) at 0°C. The mixture was stirred for 30 min at room temperature, then the solvent and excess of HCl were evaporated under reduced pressure, and

the resulting solid was washed 3 times with Et<sub>2</sub>O (30 ml). The so obtained orange solid was dried under vacuum to afford cryptozepine-2 dihydrochloride (quantitative yield).

<sup>1</sup>H NMR (400 MHz, DMSO-*d*<sub>6</sub>) δ 10.74 (s, 1H), 8.41 (d, *J* = 8.3 Hz, 1H), 8.06 – 7.91 (m, 2H), 7.84 – 7.55 (m, 5H), 7.32 – 7.25 (m, 1H), 3.52 – 2.87 (m, 10H), 2.69 (s, 3H). <sup>13</sup>C NMR (126 MHz, DMSO-*d*<sub>6</sub>) δ 153.28, 152.26, 136.30, 132.77, 131.81, 129.58, 128.87, 124.48, 122.98, 120.02, 116.13, 58.52, 50.68, 48.77, 41.88.

MS (ESI, positive): calculated for C<sub>19</sub>H<sub>24</sub>N<sub>5</sub>O<sup>+</sup>: 338.20, found 338.1968 [M + H]<sup>+</sup>.

**(E)-N-(2-((4-(Dimethylamino)phenyl)diazenyl)phenyl)-2-(4-methylpiperazin-1-yl)acetamide (Cryptozepine-3):** Compound **7c** (20 mg, 0.063 mmol) was dissolved in 20 ml of MeCN. 1-Methylpiperazine (9.5 mg, 0.095 mmol) and triethylamine (9.58 mg, 0.095 mmol) were then slowly added to the solution. The mixture was stirred under reflux for 3 h. Upon completion, MeCN was removed under reduced pressure and the obtained oil was dissolved in EtOAc. The resulting organic solution was washed 4 times using 30 ml of saturated aqueous NaHCO<sub>3</sub>. The organic layer was dried over MgSO<sub>4</sub> and evaporated under reduced pressure to afford the final product (**3**) as a yellow solid (quantitative yield).

<sup>1</sup>H NMR (400 MHz, CDCl<sub>3</sub>) δ 10.90 (s, 1H), 8.72 (dd, *J* = 8.4, 1.3 Hz, 1H), 8.03 – 7.98 (m, 2H), 7.75 (dd, *J* = 8.1, 1.6 Hz, 1H), 7.38 (ddd, *J* = 8.6, 7.3, 1.6 Hz, 1H), 7.11 (ddd, *J* = 8.3, 7.3, 1.4 Hz, 1H), 6.82 – 6.74 (m, 2H), 3.24 (s, 2H), 3.11 (s, 6H), 2.83 – 2.43 (m, 8H), 2.29 (s, 3H). <sup>13</sup>C NMR (101 MHz, CDCl<sub>3</sub>) δ 168.61, 152.65, 143.93, 140.49, 136.28, 131.02, 125.61, 123.56, 119.80, 115.65, 111.67, 63.13, 54.97, 53.78, 45.98, 40.43.

**(E)-1-(2-((2-((4-(Dimethylamino)phenyl)diazenyl)phenyl)amino)-2-oxoethyl)-4-methylpiperazine-1,4-diium (Cryptozepine-3 dihydrochloride):** A total of 6 ml of 4 M HCl in dioxane was added slowly to compound **3** (10 mg, 0.026 mmol) at 0°C. The mixture was stirred for 30 min at room temperature, then the solvent and excess of HCl were evaporated under reduced pressure, and the resulting solid was washed 3 times with Et<sub>2</sub>O (30 ml). The so obtained orange solid was dried under vacuum to afford cryptozepine-3 dihydrochloride (quantitative yield).

<sup>1</sup>H NMR (400 MHz, D<sub>2</sub>O) δ 8.01 (d, *J* = 8.2 Hz, 1H), 7.91 – 7.77 (m, 2H), 7.65 – 7.53 (m, 2H), 7.36 (d, 3H), 3.82 – 2.61 (m, 19H). <sup>13</sup>C NMR (101 MHz, D<sub>2</sub>O) δ <sup>13</sup>C NMR (101 MHz, D<sub>2</sub>O) δ 168.82, 149.08, 147.06, 141.60, 133.70, 131.88, 125.79, 125.00, 122.23, 116.67, 116.55, 59.48, 52.67, 49.44, 42.72, 42.67.

MS (ESI, positive): calculated for C<sub>21</sub>H<sub>29</sub>N<sub>6</sub>O<sup>+</sup>: 381.24, found 381.2387 [M + H]<sup>+</sup>.

**2-Fluoro-4-nitro-1-nitrosobenzene (8):** 2-Fluoro-4-nitroaniline (500 mg, 3.20 mmol) was suspended in 10 ml of CH<sub>2</sub>Cl<sub>2</sub>. Oxone<sup>®</sup> (2.46 g, 8.00 mmol) in 20 ml of water was then added, and the resulting mixture was stirred vigorously for 24 h at room temperature. The organic phase was separated, and the aqueous phase was further extracted with 10 ml of CH<sub>2</sub>Cl<sub>2</sub> 3 times. The combined organic phases were washed with 1 M HCl (50 ml), saturated aqueous NaHCO<sub>3</sub> (50 ml), and water (50 ml). Finally, it was dried over MgSO<sub>4</sub>, concentrated under reduced pressure, and purified by chromatography (eluent: cyclohexane/EtOAc, 9:1) to yield **8** as a green solid (300 mg, 55%), which was immediately used in the following step without further purification.

**2-Chloro-N-(2-((2-fluoro-4-nitrophenyl)diazenyl)phenyl)-acetamide (9):** Compounds **5** (500 mg, 2.71 mmol) and **8** (250 mg, 1.47 mmol) were dissolved in glacial acetic acid (20 ml), and the resulting solution was stirred for 24 h at room temperature. The solution was then concentrated under reduced pressure, and the crude material was purified by chromatography (eluent: cyclohexane/EtOAc, 9:1). The so obtained solid was further purified by crystallization from methanol to yield **9** as an orange solid (200 mg, 40%).

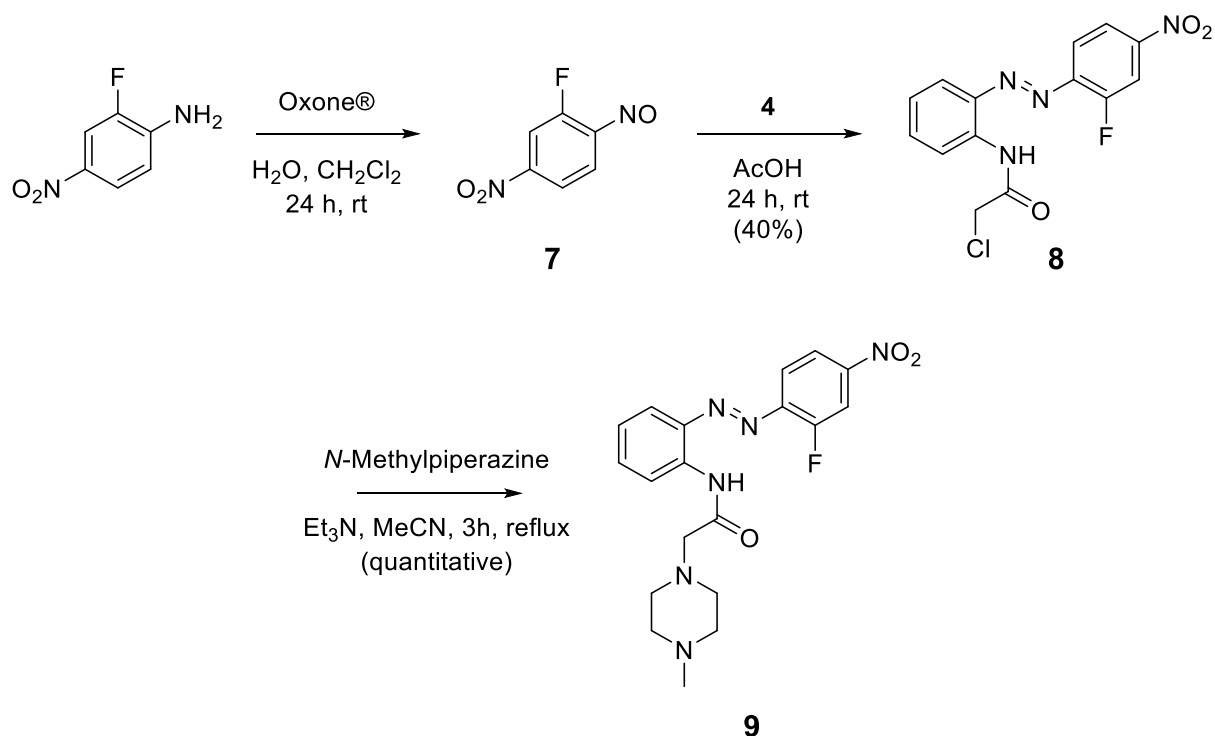
<sup>1</sup>H NMR (400 MHz, CDCl<sub>3</sub>) δ 10.83 (s, 1H), 8.70 (dd, *J* = 8.5, 1.3 Hz, 1H), 8.33 – 8.08 (m, 2H), 7.95 (dd, *J* = 8.2, 1.6 Hz, 1H), 7.90 – 7.84 (m, 1H), 7.61 (ddd, *J* = 8.7, 7.4, 1.6 Hz, 1H), 7.30 – 7.24 (m, 1H), 4.29 (s, 2H). <sup>13</sup>C NMR (101 MHz, CDCl<sub>3</sub>) δ 164.35, 144.45, 140.28, 136.53, 135.36, 126.98, 124.83, 124.75, 120.49, 120.07, 119.85, 119.81, 119.23, 43.56.

**(E)-N-(2-((2-Fluoro-4-nitrophenyl)diazenyl)phenyl)-2-(4-methyl-piperazin-1-yl)acetamide (Cryptozepine-4):** Compound **9** (200 mg, 0.594 mmol) was dissolved in 20 ml of MeCN. 1-Methylpiperazine (89.24 mg, 0.891 mmol) and triethylamine (90.16 mg, 0.891 mmol) were then slowly added to the solution. The mixture was stirred under reflux for 3 h. Upon completion, MeCN was removed under reduced pressure and the obtained oil was dissolved in EtOAc. The resulting organic solution was washed 4 times using 30 ml of saturated aqueous NaHCO<sub>3</sub>. The organic layer was dried over MgSO<sub>4</sub> and evaporated under reduced pressure to afford the desired final compound (**4**) as an orange solid (quantitative yield).

<sup>1</sup>H NMR (400 MHz, CDCl<sub>3</sub>) δ 10.94 (s, 1H), 8.80 (dd, *J* = 8.5, 1.3 Hz, 1H), 8.27 – 8.11 (m, 2H), 8.04 – 7.93 (m, 1H), 7.85 (dd, *J* = 8.3, 1.6 Hz, 1H), 7.58 (ddd, *J* = 8.6, 7.2, 1.6 Hz, 1H), 7.16 (ddd, *J* = 8.4, 7.2, 1.3 Hz, 1H), 3.26 (s, 2H), 2.80 – 2.30 (m, 8H), 2.21 (s, 3H). <sup>13</sup>C NMR (101 MHz, CDCl<sub>3</sub>) δ 168.86, 160.09, 157.48, 140.43, 138.63, 135.52, 123.79, 120.55, 119.88, 119.43, 116.84, 113.78, 113.53, 62.93, 55.17, 53.63, 46.07.

MS (ESI, positive): calculated for  $C_{19}H_{22}FN_6O_3^+$ : 401.17, found 401.1732  $[M + H]^+$ .

Compound **9** was synthesized as reported in **Scheme S3.1**. 2-fluoro-4-nitroaniline was oxidized with Oxone<sup>®</sup> to give the nitroso derivative (**7**), which was then coupled to the corresponding amine (**4**) under Mills conditions to yield the arylazo intermediate (**8**). Nucleophilic substitution of the chlorine with 1-methylpiperazine and subsequent treatment with hydrochloric acid afforded the compounds **9**.

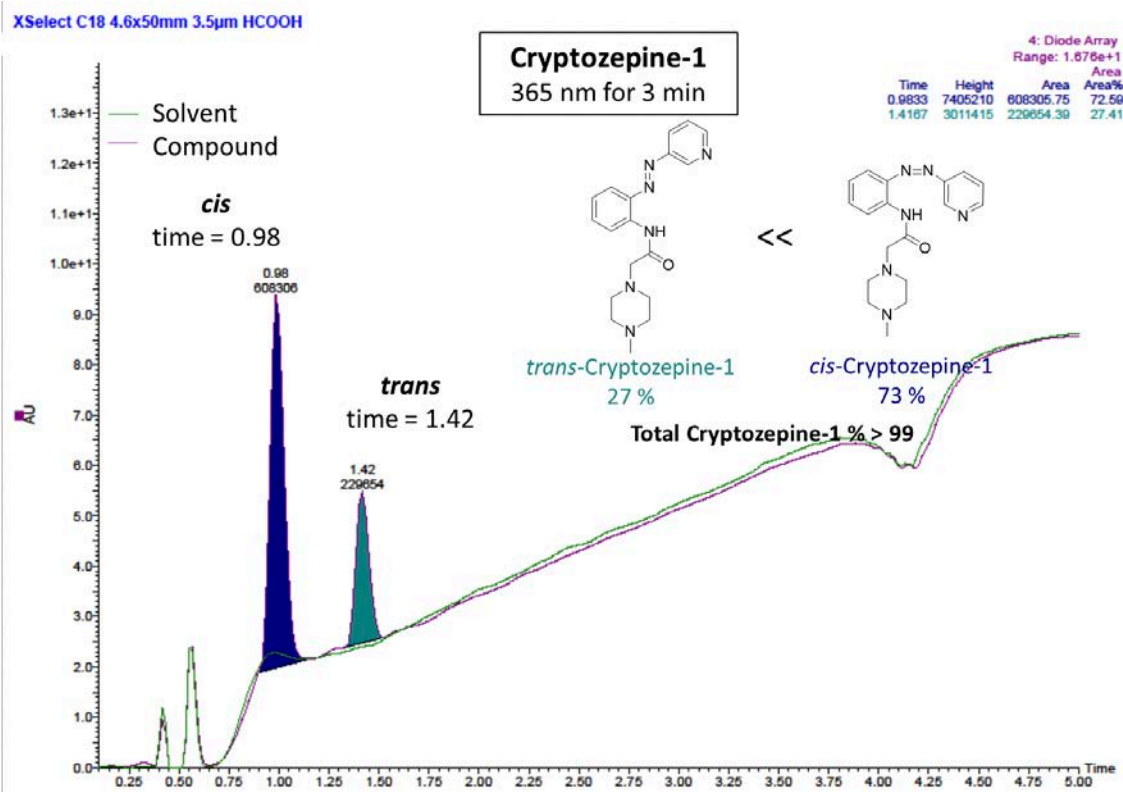
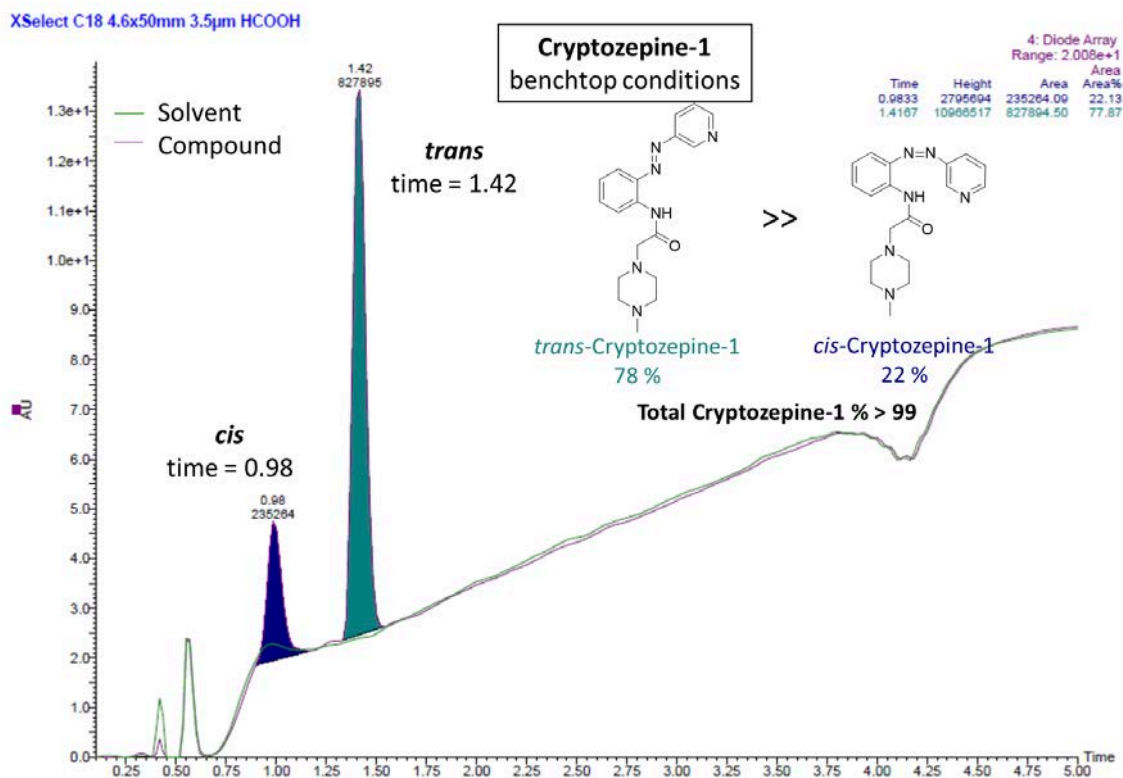


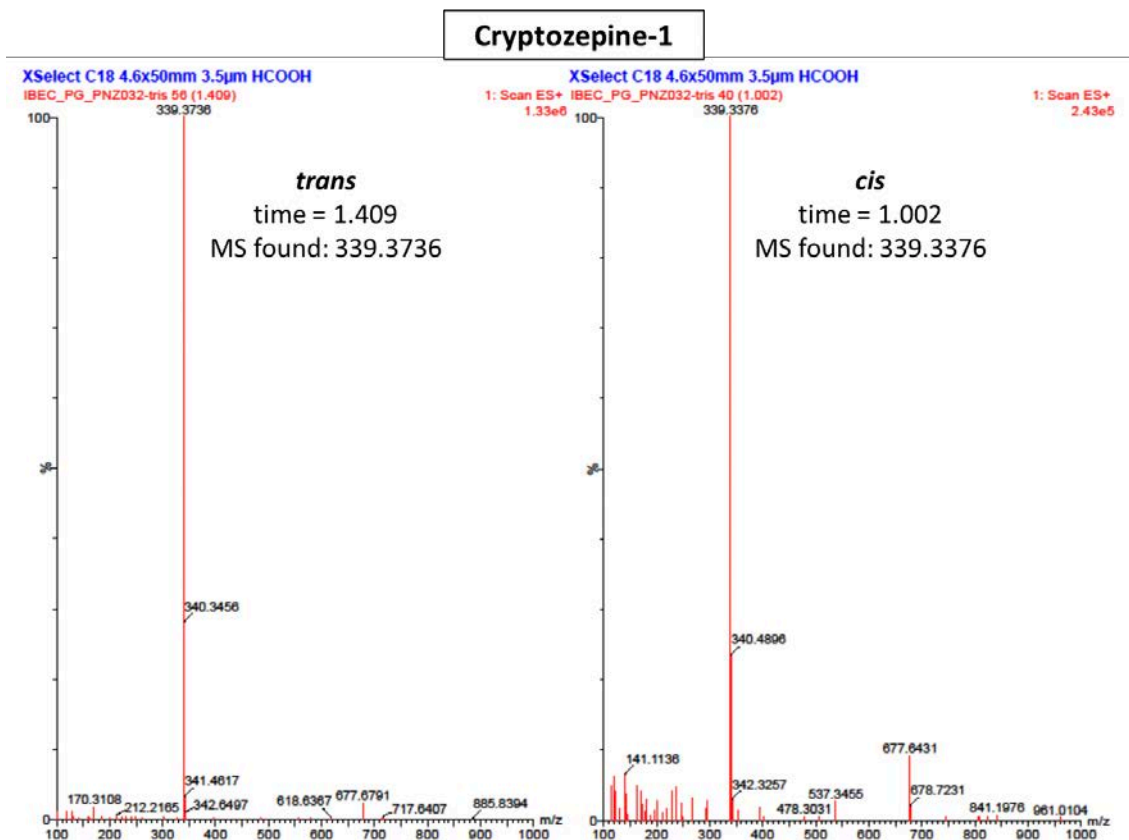
**Scheme S3.1.** Chemical synthesis of compound **9**.

### SI3.3 HPLC analyses and mass spectra

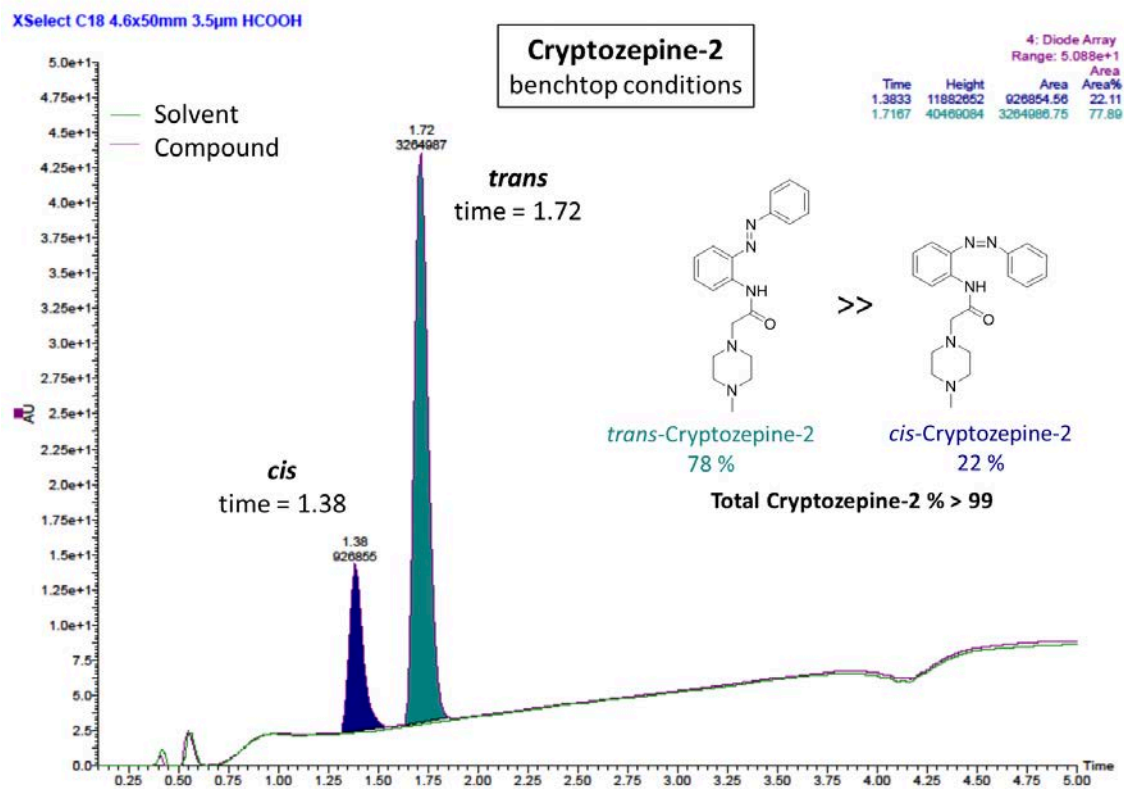
HPLC analyses were performed with a Waters Alliance 2795 separation module (RP column: XSelect CSH C18, 50 x 4.6 mm, S-3.5  $\mu$ m, 1.6 ml/min; eluent: from 5% B to 100% B in 3.5 min using a linear gradient, A: H<sub>2</sub>O 0.1% formic acid, B: acetonitrile 0.1% formic acid) coupled to a Waters 2996 photodiode detector and a Waters 3100 mass spectrometer (positive ionization analyses). PDA detector from 210 to 800 nm. Each HPLC analysis has been superimposed to the corresponding blank analysis. All the compound purities are  $\geq 95\%$ .

## SI3.3.1 Cryptozepine-1

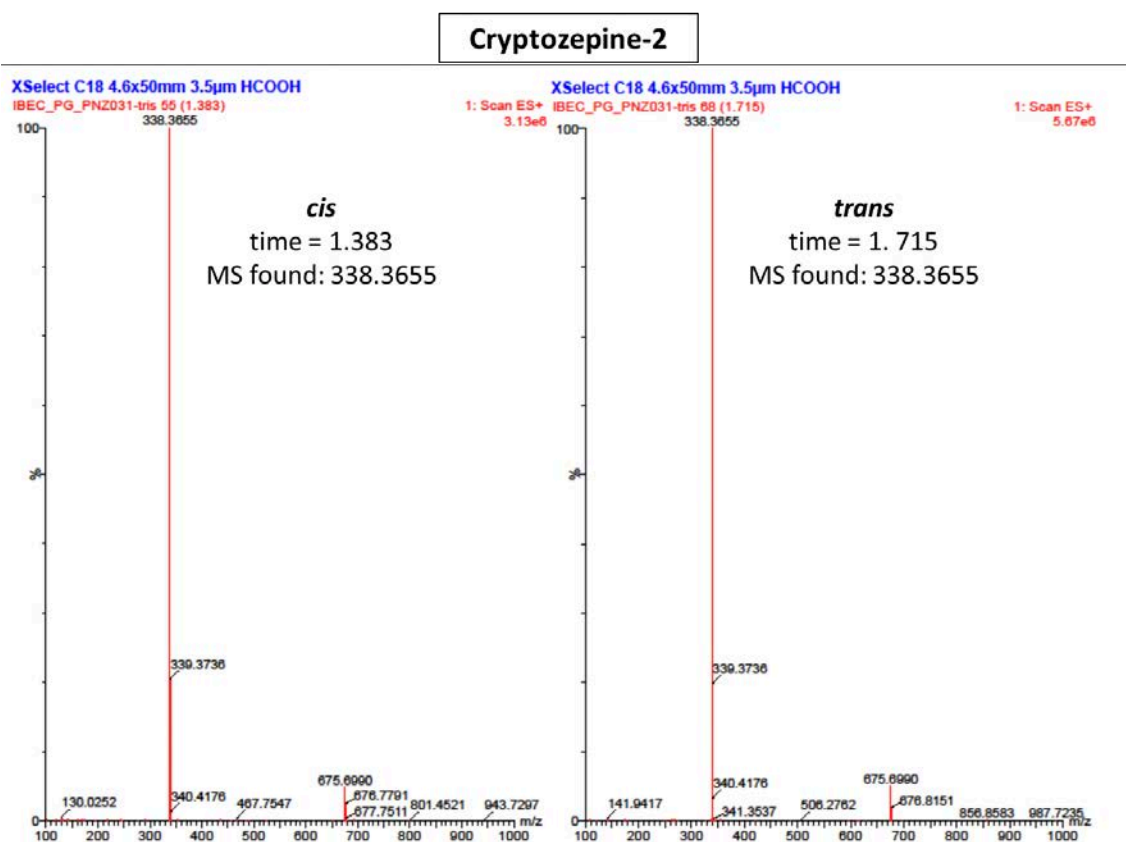
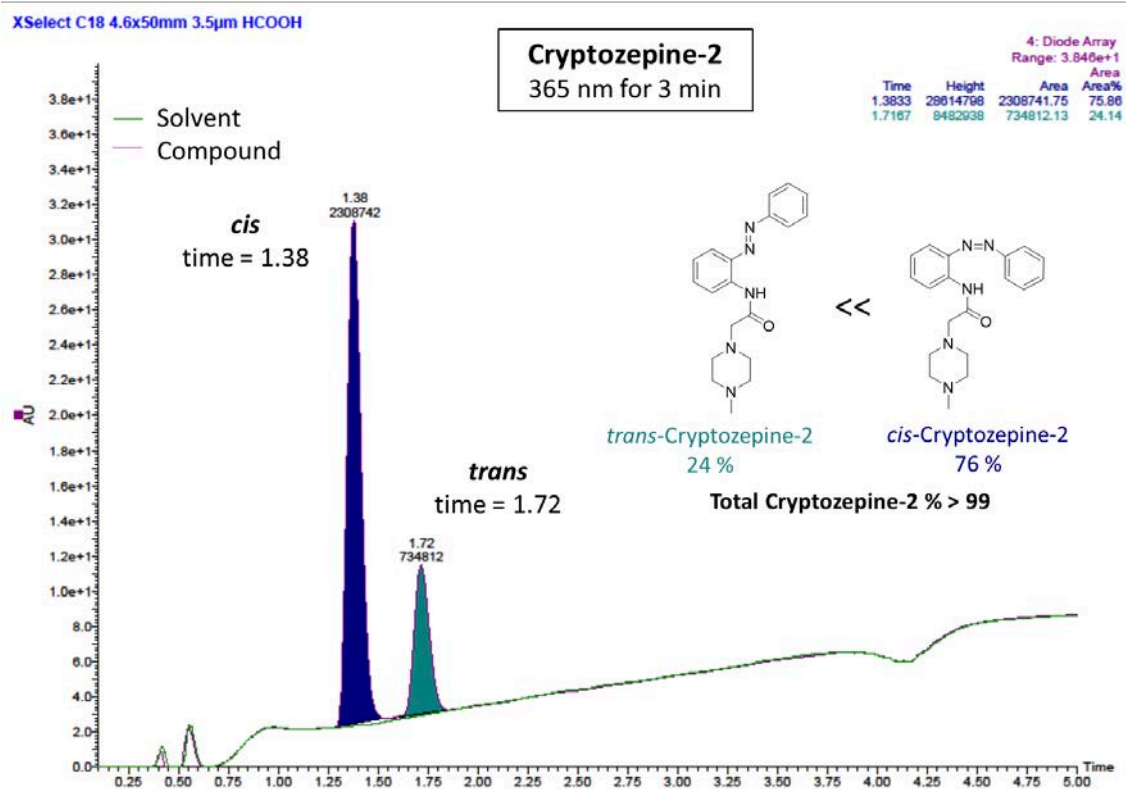




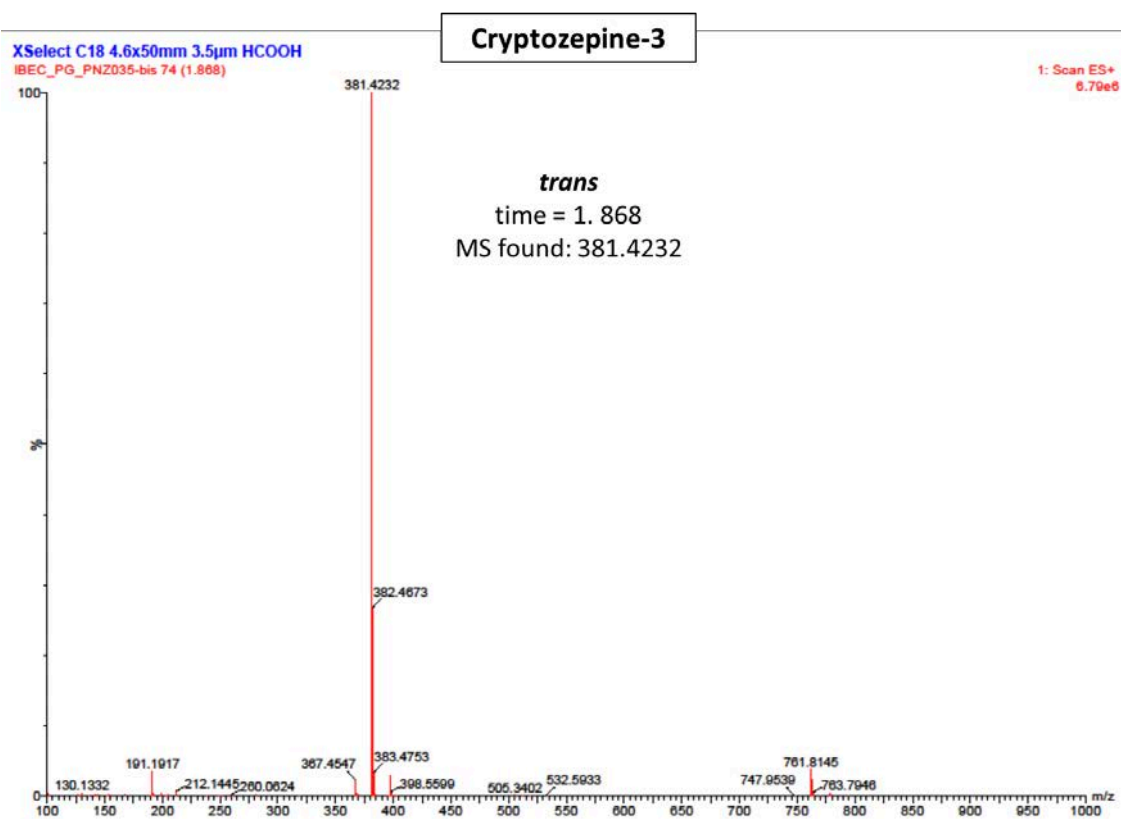
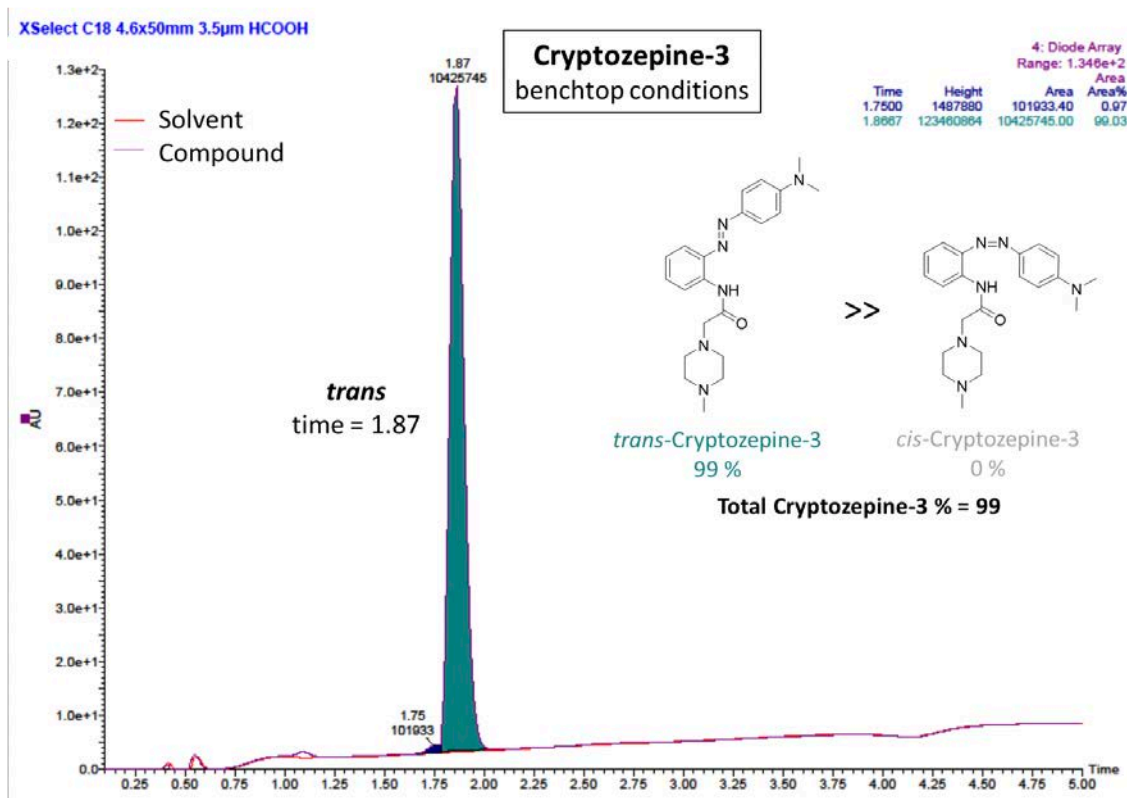
### SI3.3.2 Cryptozepine-2



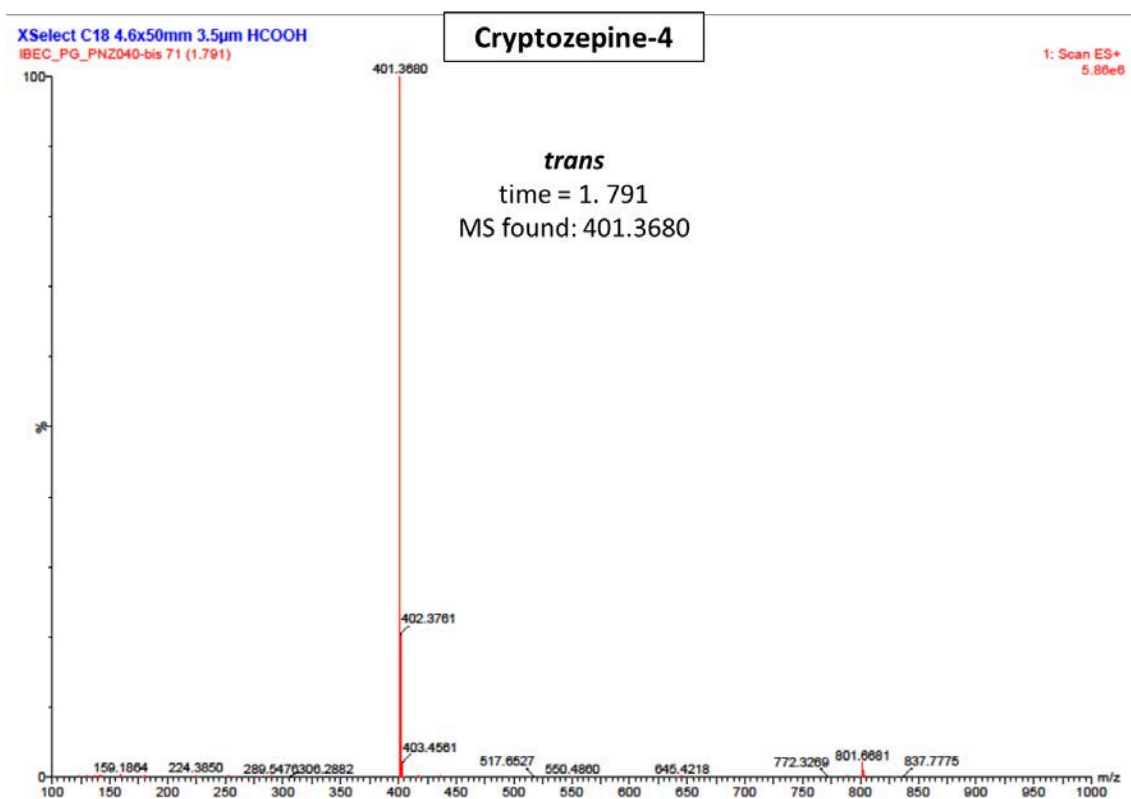
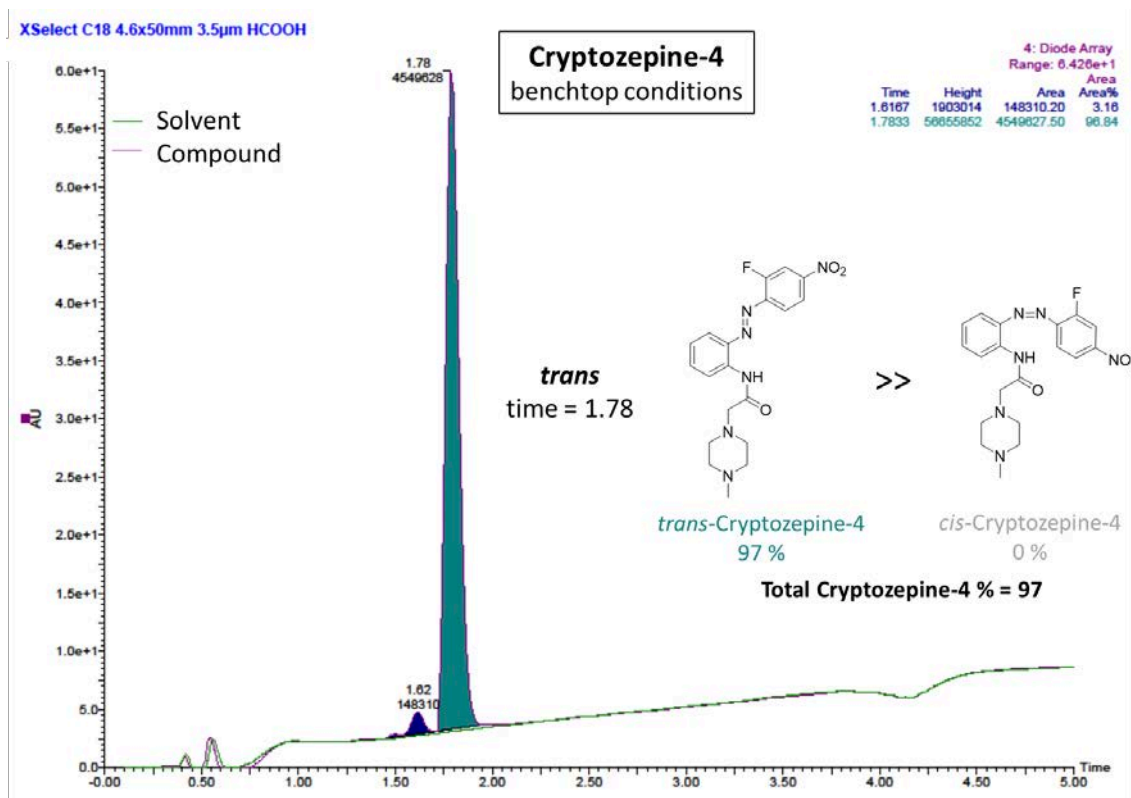




### SI3.3.3 Cryptozepine-3



## SI3.3.4 Cryptozepine-4



### SI3.4 Photochemical characterization

An essential requirement for using our compounds as light regulated  $M_1$  mAChRs antagonists is that they can effectively respond to light, which means that they can be quickly photoisomerized (from *trans*-to-*cis* and *vice versa*) between two different configurations with a relatively high degree of photoconversion (*trans/cis* ratio). We used UV-Vis spectroscopy and  $^1\text{H-NMR}$  to characterize their photochromic behavior.

#### SI3.4.1 Cryptozepine-1

Cryptozepine-1 revealed a clear photochromic behavior with the typical absorption bands of azobenzenes. Maximum absorption peaks in aqueous solution were observed at around 315 nm and 430 nm ( $\pi\text{-}\pi^*$  and  $n\text{-}\pi^*$  transitions, respectively) (**Figure S3.2B**). Cryptozepine-1 can be effectively isomerized from *trans*-to-*cis* with UV light (365 nm), and back-isomerized from *cis*-to-*trans* with white (WL) or blue (460 nm) light. The process is reversible and can be repeated several times without any noticeable loss of photochromic behavior (**Figure S3.2D**). We estimated a half-life of thermal relaxation of about 71 min at 37°C in the dark for the *cis*-isomer (30  $\mu\text{M}$  in water) obtained after illumination with 365 nm light (**Figure S3.2C**).

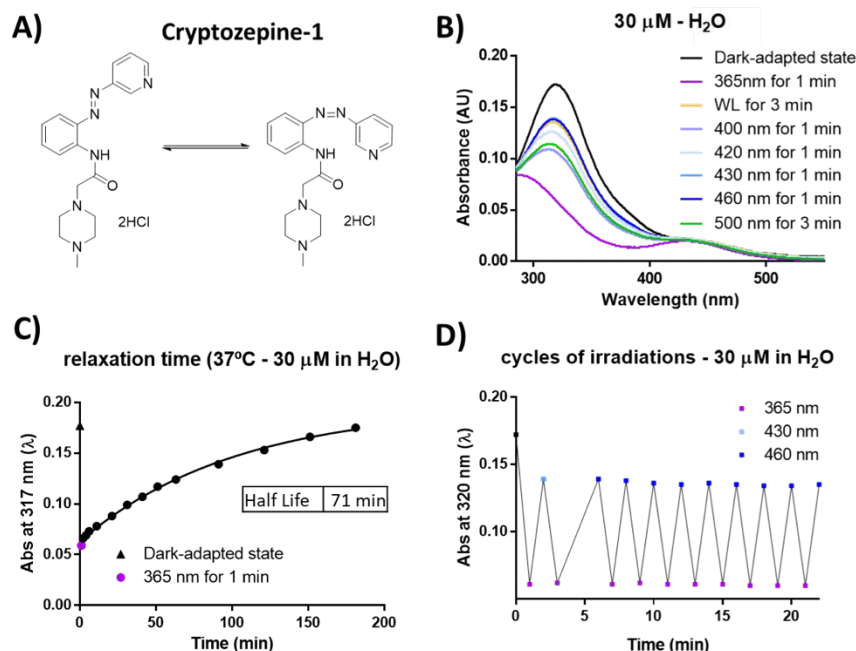


**Figure S3.2. Photochemical characterization of cryptozepine-1.** (A) Chemical structure of cryptozepine-1. (B) Absorption spectra in  $\text{H}_2\text{O}$  (30  $\mu\text{M}$ ). (C) Thermal stability: the photostationary state achieved after irradiation with 365 nm light in aqueous solution (30  $\mu\text{M}$ ) at 37°C in the dark reverts to its dark-adapted state in less than 200 min. (D) Reversibility and stability of the photochromic behavior over several cycles of isomerization.

We next quantified by  $^1\text{H-NMR}$  the extent of photoisomerization for cryptozepine-1 (1 mM in  $\text{D}_2\text{O}$ ) (**Figure S3.3**). The amount of the thermodynamically less stable *cis*-isomer shifted from an initial value of 19% (as obtained under benchtop conditions) to 87% upon irradiation with 365 nm light for 5 min. After irradiation at 460 nm (10 min), the *trans* form reverted to a 58%. In the dark-adapted state the amount of *trans*-isomer was 91%.

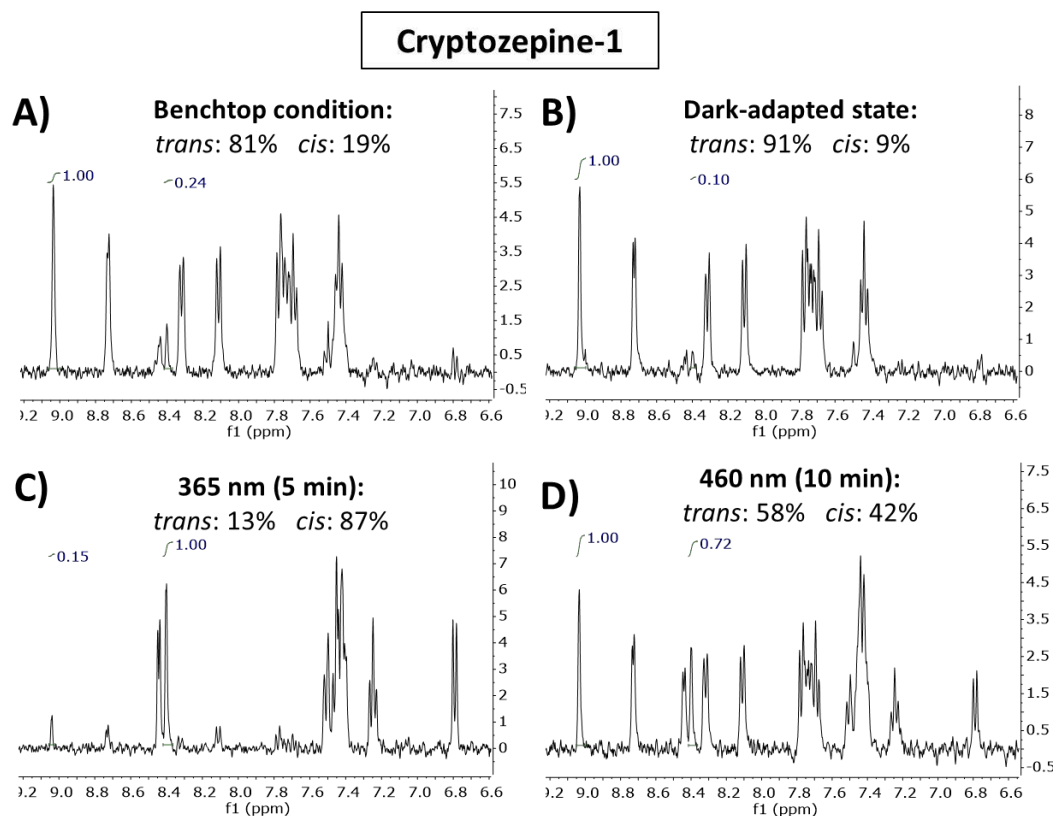


**Figure S3.3. Quantification of the photostationary state of cryptozepine-1.** (A) benchtop conditions, (B) dark-adapted state, (C) after 5 min of illumination with 365 nm light, and (D) after 10 min of illumination with 460 nm light.

### SI3.4.2 Cryptozepine-2

Cryptozepine-2 revealed a clear photochromic behavior with the typical absorption bands of azobenzenes. Maximum absorption peaks in aqueous solution were observed at around 315 nm and 430 nm ( $\pi-\pi^*$  and  $n-\pi^*$  transitions, respectively) (**Figure S3.4B**). Cryptozepine-2 can be effectively isomerized from *trans*-to-*cis* with UV light (365 nm), and completely back-isomerized from *cis*-to-*trans* with WL, blue (400-460 nm) or green (500 nm) light. The process is reversible and can be repeated several times without any noticeable loss of photochromic behavior (**Figure S3.4D**). We estimated a half-life of thermal relaxation of about 180 min at 37°C in the dark for the *cis*-isomer (30  $\mu\text{M}$  in water) obtained after illumination with 365 nm light (**Figure S3.4C**).

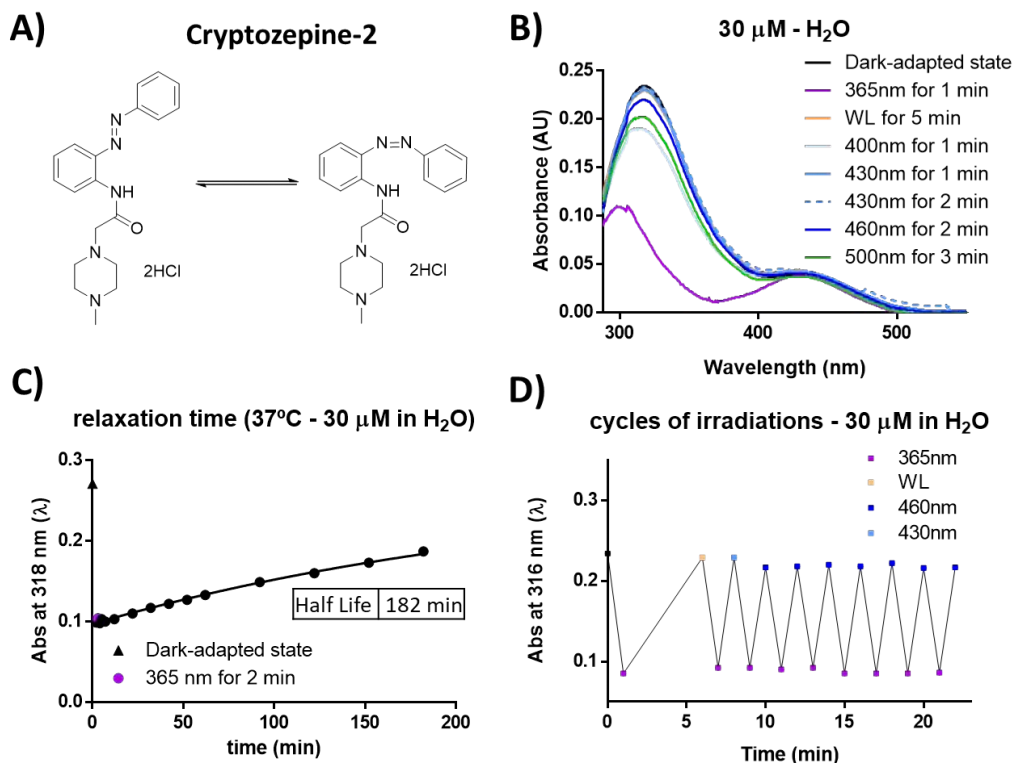


**Figure S3.4. Photochemical characterization of cryptozepine-2.** (A) Chemical structure of cryptozepine-2. (B) Absorption spectra in  $\text{H}_2\text{O}$  (30  $\mu\text{M}$ ). (C) Thermal stability: the photostationary state achieved after irradiation with 365 nm light in aqueous solution (30  $\mu\text{M}$ ) at 37°C in the dark has a half-life of 182 min. (D) Reversibility and stability of the photochromic behavior over several cycles of isomerization.

We next quantified by  $^1\text{H-NMR}$  the extent of photoisomerization for cryptozepine-2 (1 mM in  $\text{D}_2\text{O}$ ) (**Figure S3.5**). The amount of the thermodynamically less stable *cis*-isomer shifted from an initial value of 7% (as obtained under benchtop conditions) to 90% upon irradiation with 365 nm light for 5 minutes.

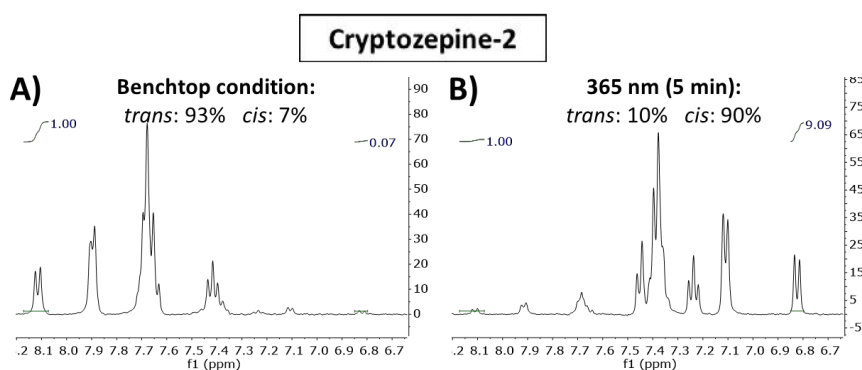


**Figure S3.5. Quantification of the photostationary state of cryptozepine-2.** (A) benchtop conditions, and (B) after 5 min of irradiation with 365 nm light.

### SI3.4.3 Cryptozepine-3

Cryptozepine-3 revealed a clear photochromic behavior with the typical absorption bands of push-pull azobenzenes. The absorbance of the *trans*-isomer is red shifted by ~100 nm and greatly decreases the thermal stability of the *cis*-isomer, so its photoisomerization cannot be observed by steady-state UV-Vis spectroscopy in aqueous solution. Maximum absorption peak in anhydrous DMSO (30  $\mu$ M) was observed at around 465 nm (**Figure S3.6B**). Cryptozepine-3 can be effectively isomerized from *trans*-to-*cis* with blue (420-460 nm) and green (500 nm) light. The photostationary state achieved after irradiation with red lights reverts in 20 min at 37°C in anhydrous DMSO in the dark (**Figure S3.6B**).

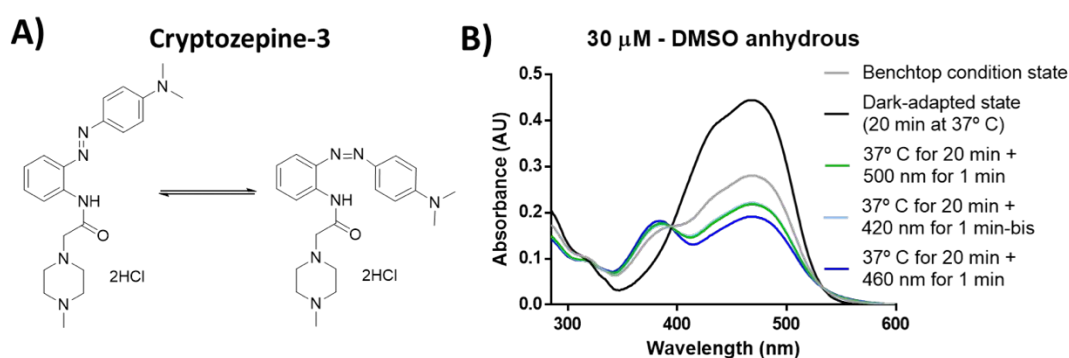


**Figure S3.6. Photochemical characterization of cryptozepine-3.** (A) Chemical structure of cryptozepine-3. (B) Absorption spectra in anhydrous DMSO (30  $\mu$ M).

### SI3.4.4 Cryptozepine-4

Cryptozepine-4 revealed a clear photochromic behavior with the typical absorption bands of azobenzenes. Maximum absorption peaks in acidic water solution (pH 2) were observed at around 335 nm and 450 nm ( $\pi$ - $\pi^*$  and  $n$ - $\pi^*$  transitions, respectively) (**Figure S3.7B**). Cryptozepine-4 can be effectively isomerized from *trans*-to-*cis* with UV (365-380 nm), and back-isomerized from *cis*-to-*trans* with blue light (420- 460 nm). The process is reversible and can be repeated several times without any noticeable loss of photochromic behavior (**Figure S3.7D**). We estimated a half-life of thermal relaxation of about 68 min at 37°C in the dark for the *cis*-isomer (30  $\mu$ M, pH 2) obtained after illumination with 380 nm light (**Figure S3.7C**).

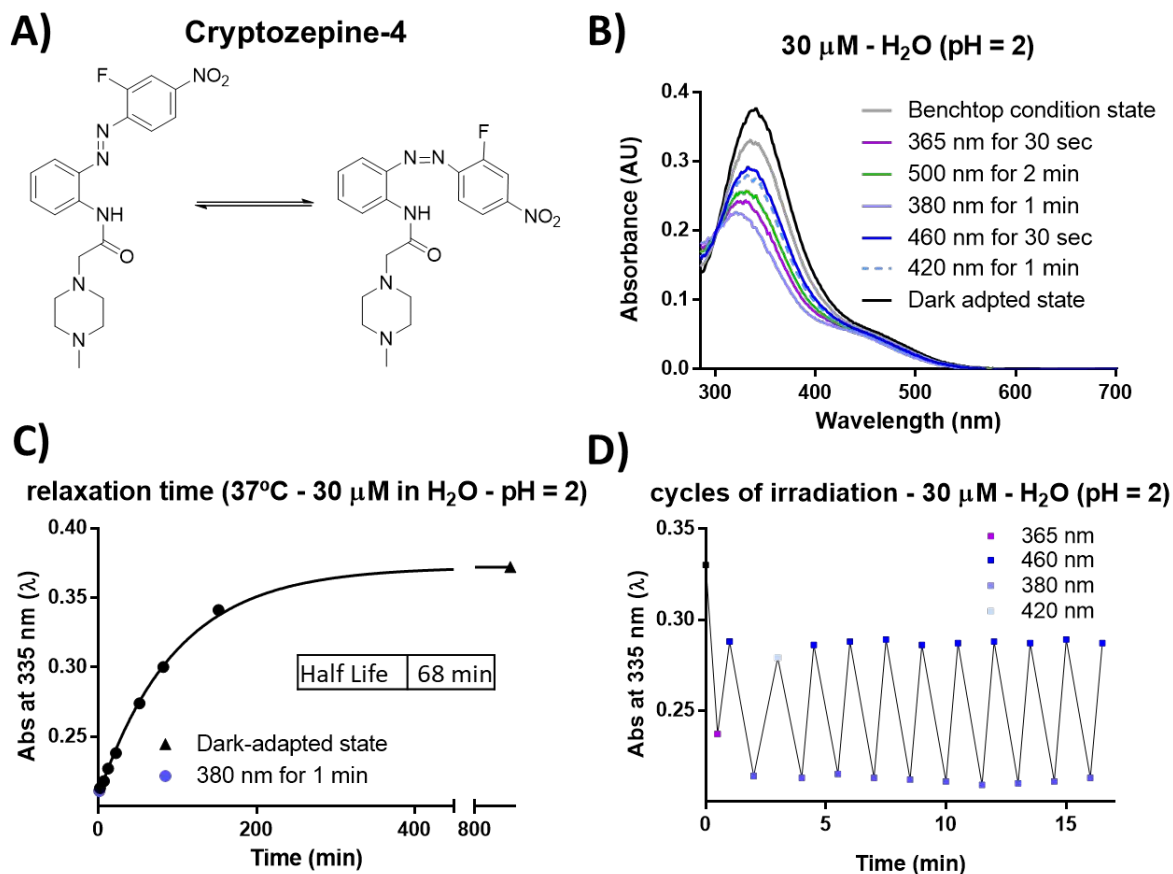


**Figure S3.7. Photochemical characterization of cryptozepine-4.** (A) Chemical structure of Cryptozepine-4. (B) Absorption spectra in aqueous solution (30  $\mu\text{M}$ , pH 2). (C) Thermal stability: the photostationary state achieved after irradiation with 380 nm light in aqueous solution (30  $\mu\text{M}$ , pH 2) at 37°C in the dark has a half-life of 68 min. (D) Reversibility and stability of the photochromic behavior over several cycles of isomerization.

We next quantified by  $^1\text{H-NMR}$  the extent of photoisomerization for cryptozepine-4 (1.5 mM in  $\text{D}_2\text{O} + \text{HCl}$ , pH 2) (**Figure S3.8**). The amount of the *cis*-isomer shifted from an initial value of 18% (benchtop conditions) to 61% upon irradiation with 380 nm light (10 min). After irradiation with 460 nm (10 min), the *trans* form reverted to a 67%. In the dark-adapted state the amount of the *trans*-isomer was about 93%.



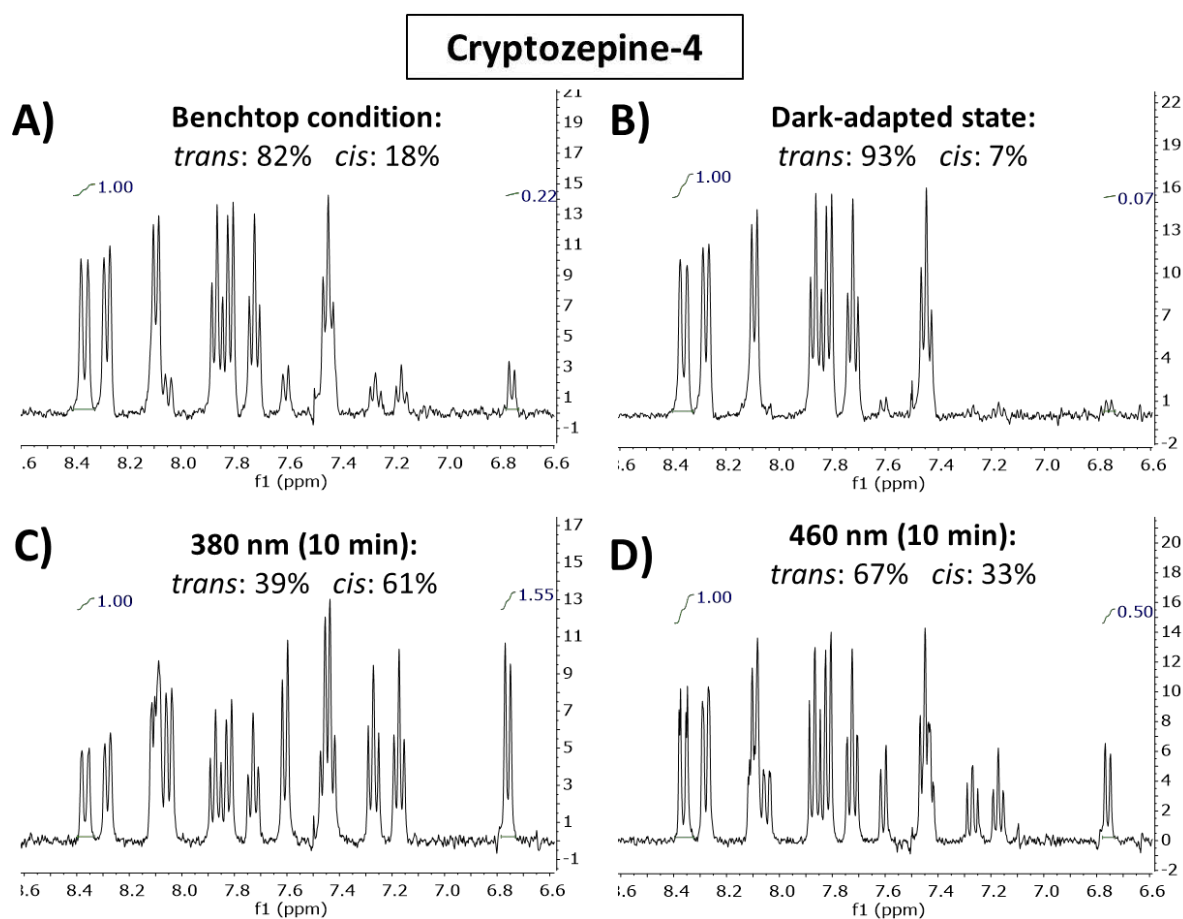


**Figure S3.8. Quantification of the photostationary state of cryptozepine-4.** (A) benchtop conditions, (B) dark-adapted state, (C) after 10 min of irradiation with 380 nm light, and (D) after 10 min of irradiation with 460 nm light.

## SI3.5 NMR spectroscopy

### SI3.5.1 NMR spectra of cryptozepine-1

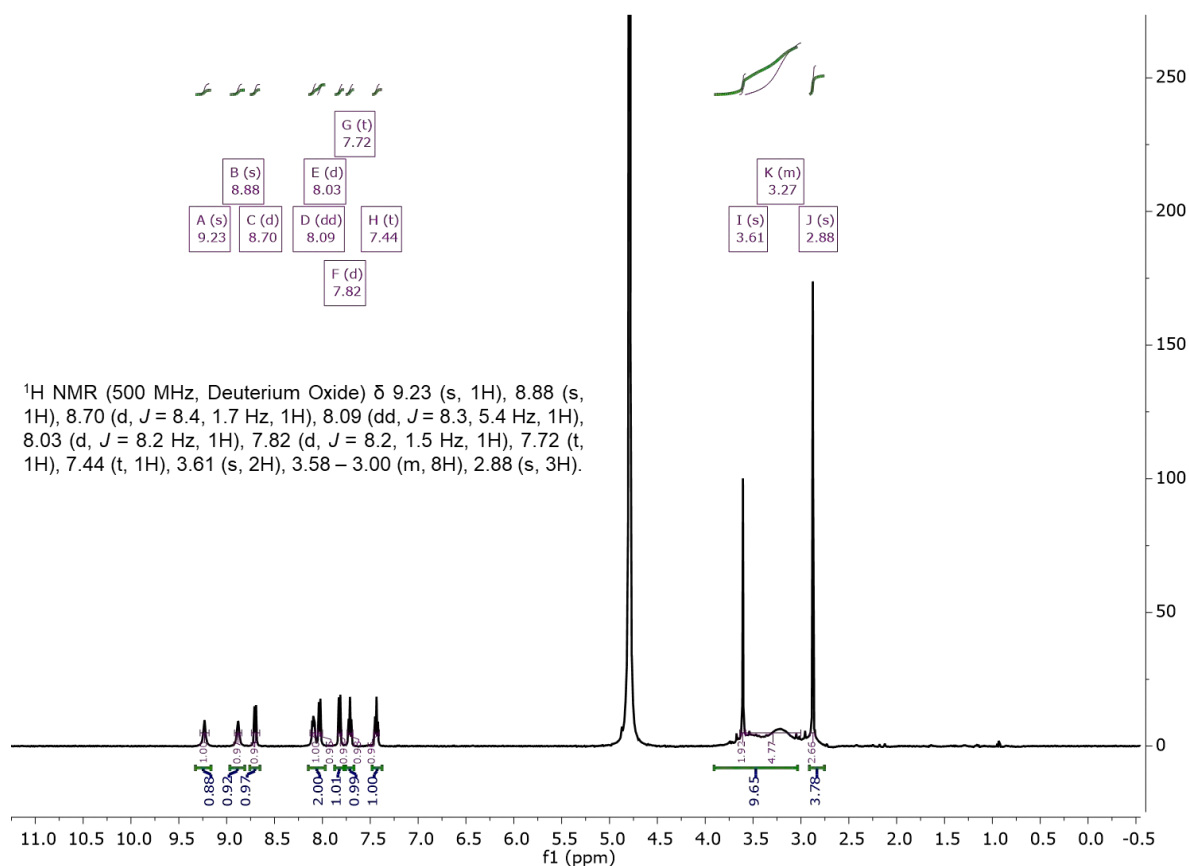


Figure S3.9. <sup>1</sup>H-NMR of cryptozepine-1 as obtained under benchtop conditions.

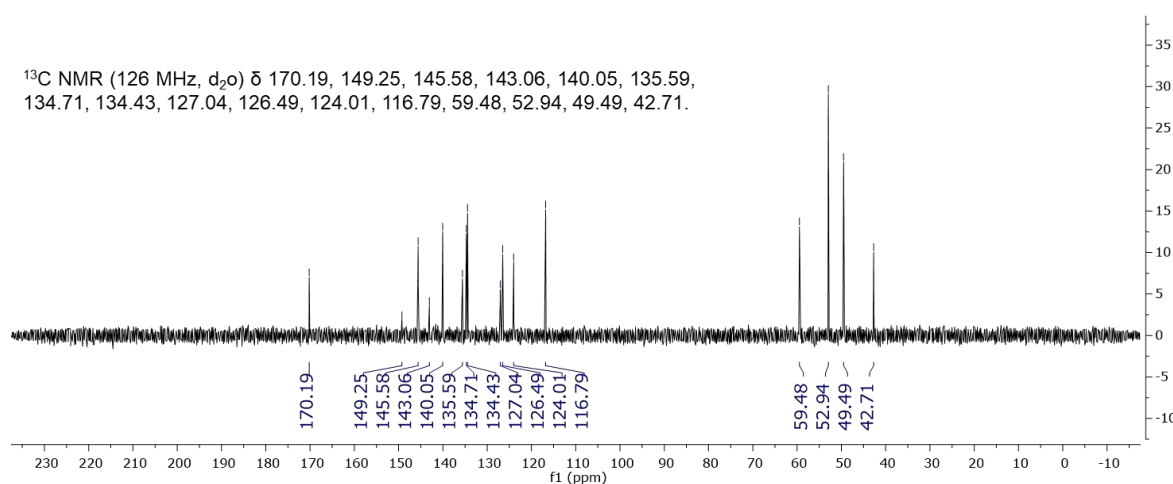
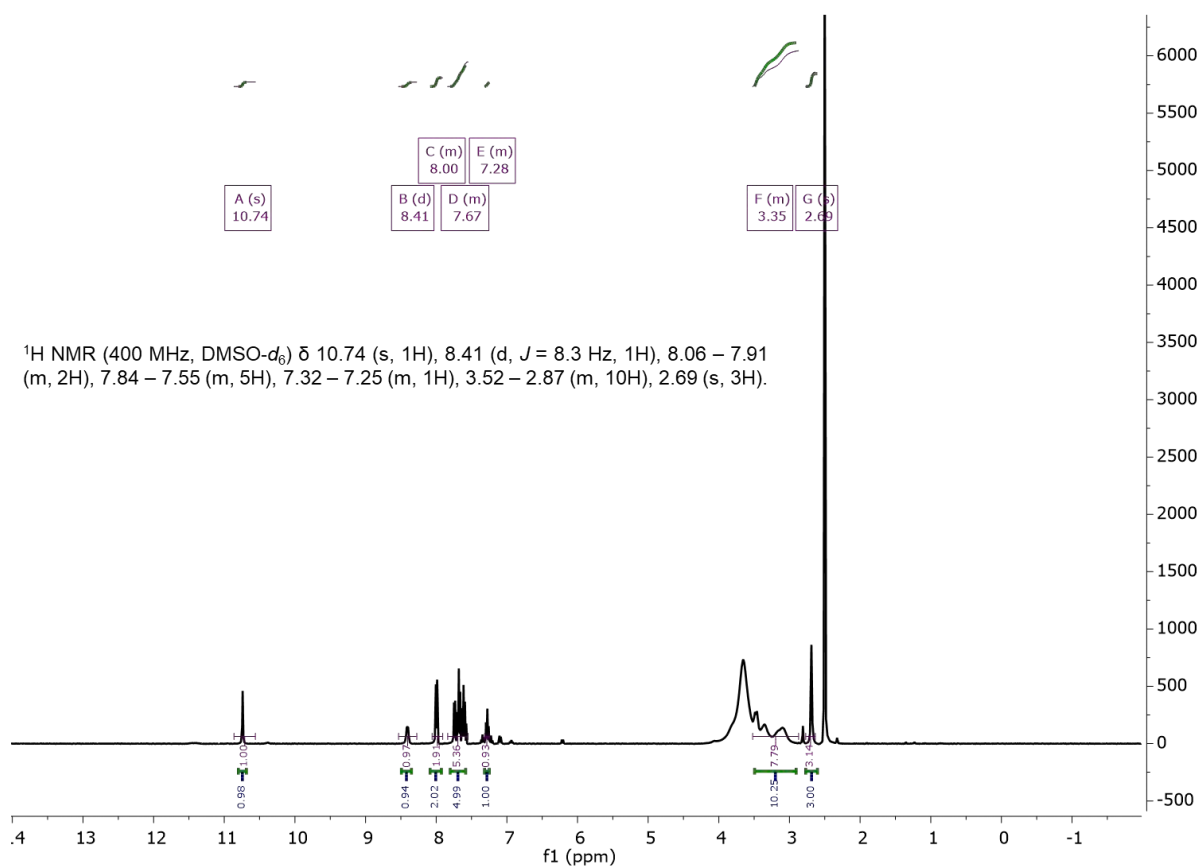
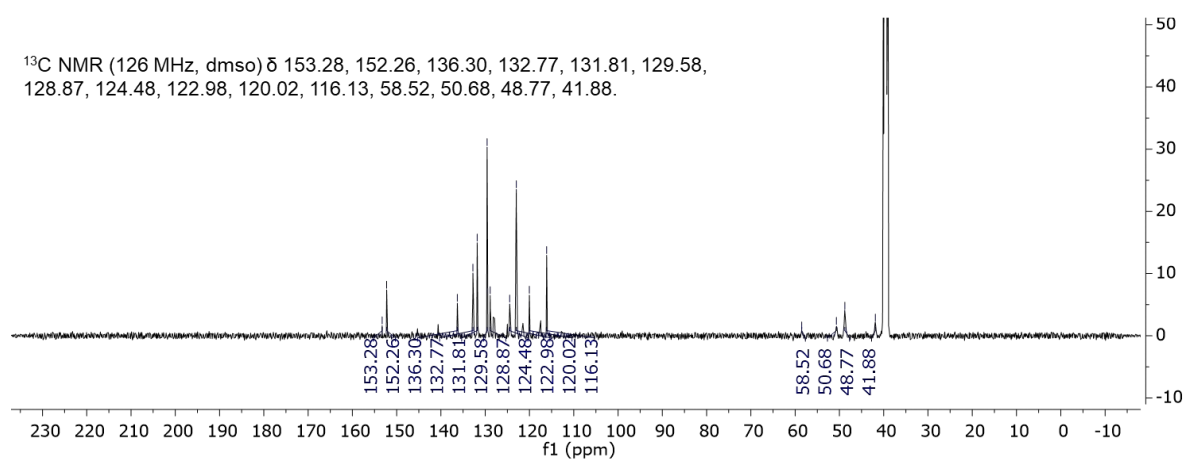
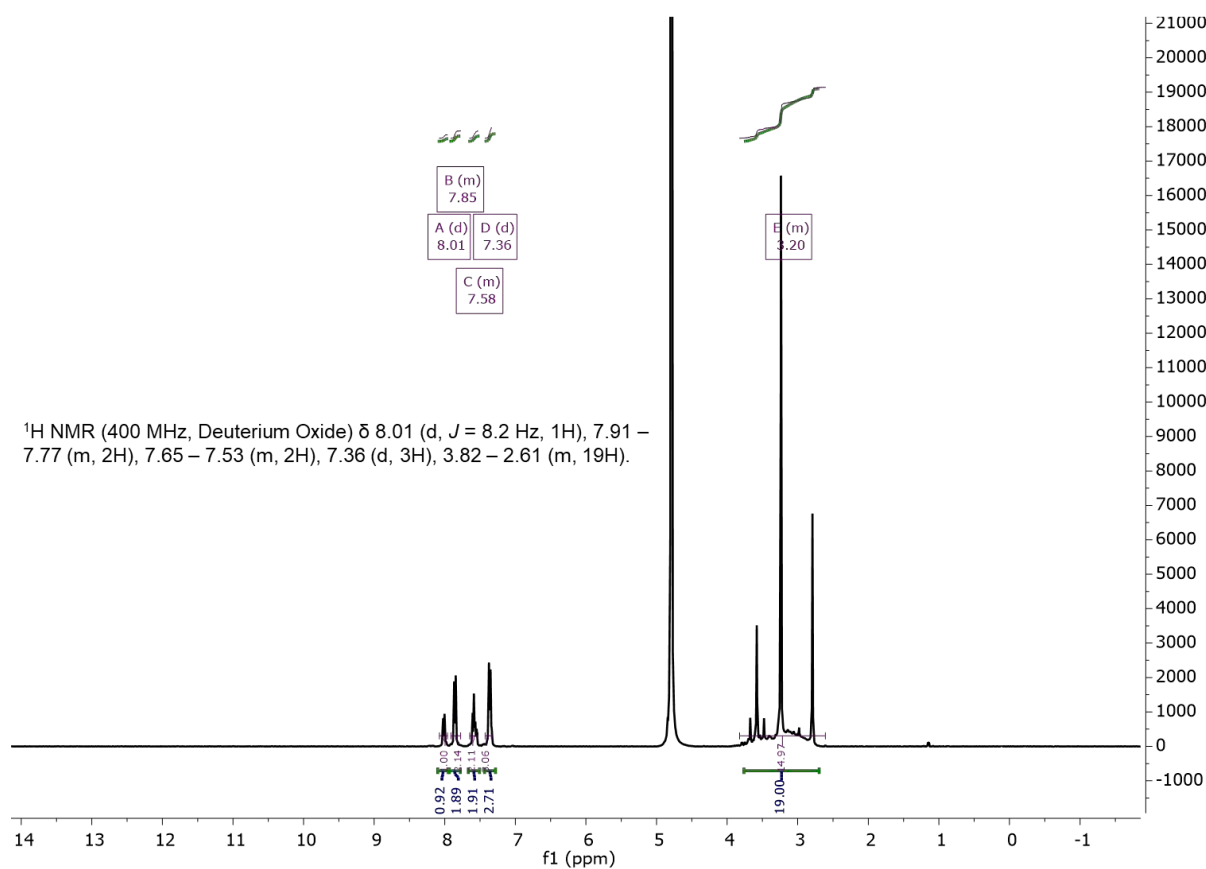
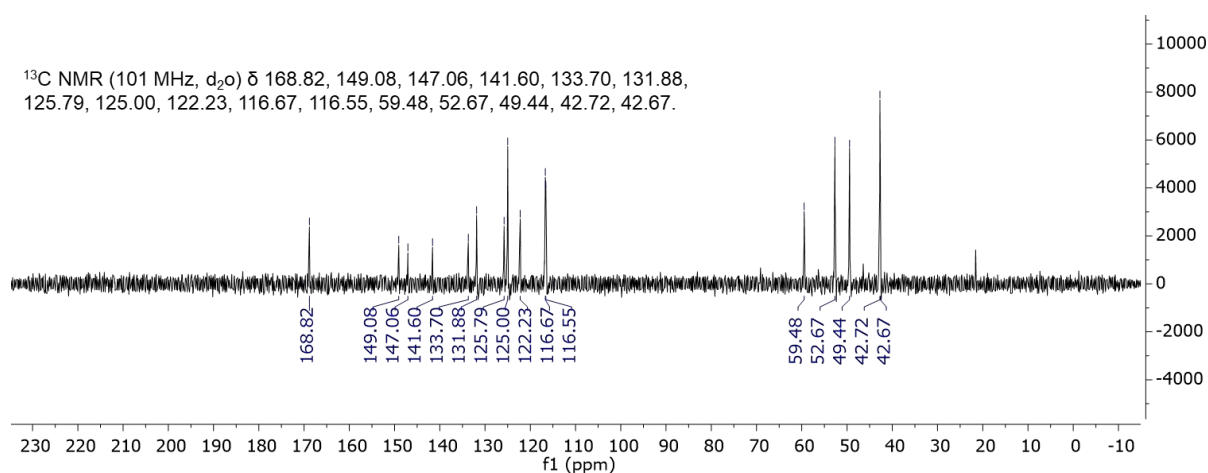


Figure S3.10. <sup>13</sup>C-NMR of cryptozepine-1 as obtained under benchtop conditions.

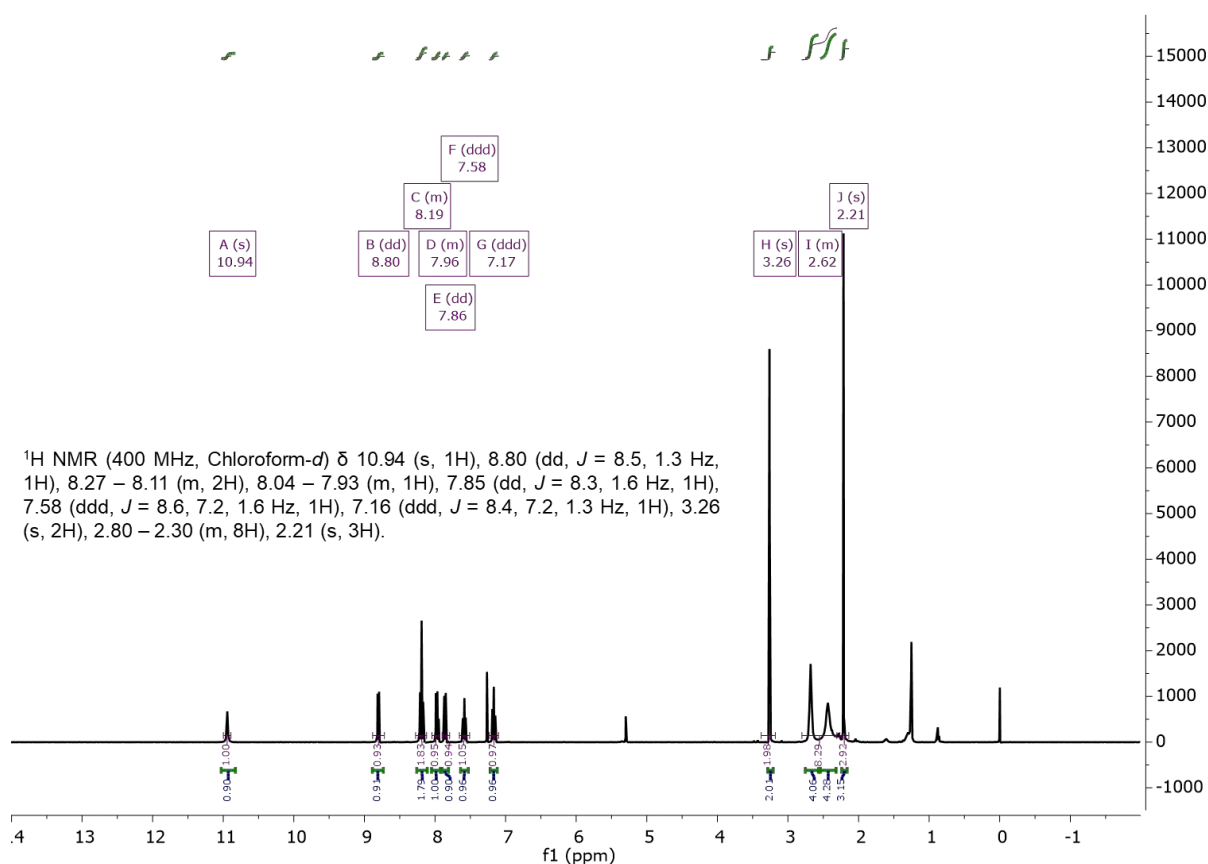
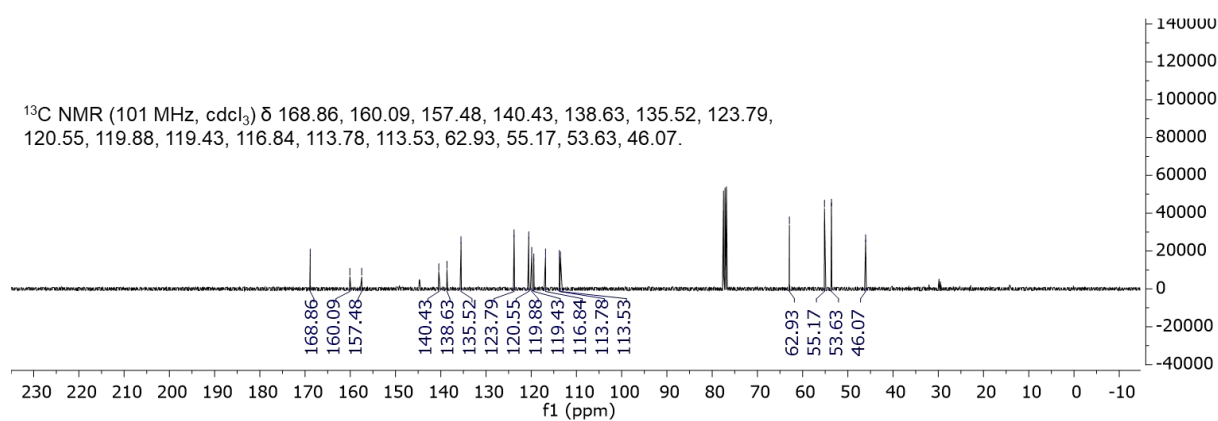
## SI3.5.2 NMR spectra of cryptozepine-2

Figure S3.11  $^1\text{H}$ -NMR of cryptozepine-2 as obtained under benchtop conditions.Figure S3.12.  $^{13}\text{C}$ -NMR of cryptozepine-2 as obtained under benchtop conditions.

## SI3.5.3 NMR spectra of cryptozepine-3

Figure S3.13. <sup>1</sup>H-NMR of cryptozepine-3 as obtained under benchtop conditions.Figure S3.14. <sup>13</sup>C-NMR of cryptozepine-3 as obtained under benchtop conditions.

## SI3.5.4 NMR spectra of cryptozepine-4

Figure S3.15. <sup>1</sup>H-NMR of cryptozepine-4 as obtained under benchtop conditions.Figure S3.16. <sup>13</sup>C-NMR of cryptozepine-4 as obtained under benchtop conditions.

### SI3.6 *In vitro* radioligand competition binding experiments

The affinity of our compounds and PNZ for mAChRs was studied by radioligand competition binding experiments (see Table 3.1 and Figure S3.17).

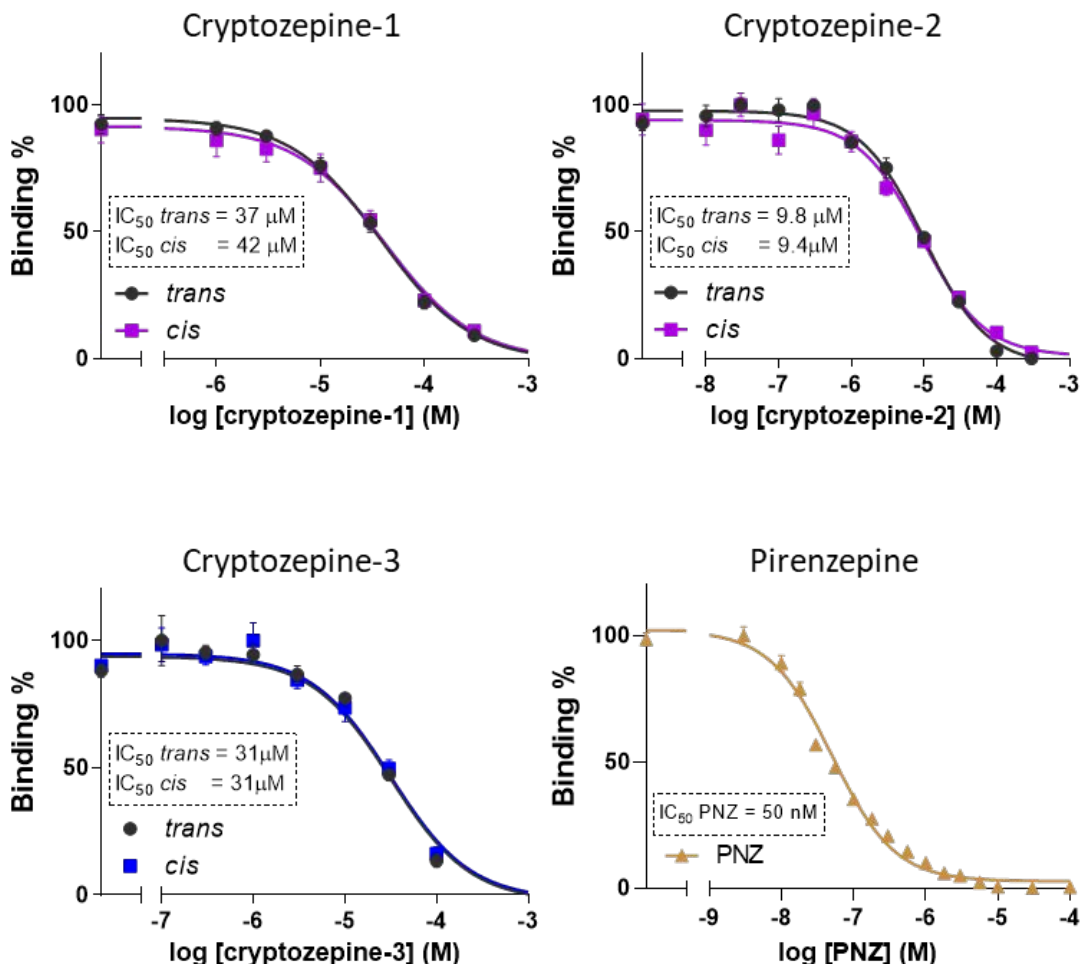


**Figure S3.17. Competitive displacement of specific radioligand binding from mAChRs.** Competition for specific binding of 200 pM [<sup>3</sup>H]QNB to 3-4 months-old female Wistar rats brain membranes (whole cortex) containing high density of all five mAChRs by cryptozepines-1, -2, -3 and pirenzepine (PNZ; n = 4 for each isomer of cryptozepines and n = 2 for PNZ). Data points were fitted using the “Binding – Competitive – one site - Fit K<sub>i</sub>” for K<sub>i</sub> values, and “Binding – Competitive – one site - Fit logIC<sub>50</sub>” for the IC<sub>50</sub>, which are functions in GraphPad Prism 6. Values are means ± SEM.

The Wistar rat brain membranes (whole cortex), which contain a high density of mAChRs, were used for this assay<sup>7</sup>. The muscarinic antagonist [<sup>3</sup>H]quinuclidinyl benzilate ([<sup>3</sup>H]QNB) in ethanol solution from Amersham Biosciences (catalog number TRK 604, 42 Ci/mmol, 1 mCi/ml) was used as a competitive radioligand<sup>8,9</sup>. Specific binding was defined with the new ligands at total nominal concentrations ranging from 1 or 10 nM to 300 μM, and derivatizing the raw disintegrations per minute (dpm) data from the scintillation counter to show the total

radioactivity<sup>7</sup>. Binding assays were carried out as already reported by Claro *et al.*, 2006<sup>7</sup>. Brain membranes were prepared from 2/3-month-old female rats. The meninges were cleaned with buffer-soaked filter paper, cortices were dissected, and white matter was trimmed off. The tissues were homogenized in 40 ml of Tris-HCl buffer using a Potter homogenizer with a motor-driven Teflon pestle. The homogenate was centrifuged (30 min at 50000g). The resulting pellet was homogenized and centrifuged again under the same conditions. The Bradford assay was used for protein determination. The final pellet was resuspended at 1 mg protein/ml, transferred to 1 ml microcentrifuge tubes, and centrifuged again. After discarding the supernatant, membrane pellets were kept at -80°C until use. During the assay, in 5 ml tubes (24 tubes in each experiment repetition), a total volume of 2 ml of Tris-HCl buffer with 6 mM MgCl<sub>2</sub> was used, containing 30 µg of mAChR proteins, 200 pM [<sup>3</sup>H]QNB concentration ([<sup>3</sup>H]QNB K<sub>d</sub> = 40 pM), and the correct amount of our ligands. These conditions ensure less than 10% ligand depletion at equilibrium, which was reached with 30 min at 37°C incubation. The unbound ligand and radioligand were separated from the membrane samples by rapid filtration through Whatman GF/C glass microfiber filters using a manifold Brandel device. Nonspecific binding was independent of protein concentration and defined with 2 µM atropine. It resulted to be lower than 5% of total binding.

### **SI3.7 *In vitro* calcium imaging**

Human Embryonic Kidney tsA201 (HEK tsA201) cells were purchased from the European Collection of Authenticated Cell Culture. The cells were maintained at 37°C in a humidified atmosphere with 5% CO<sub>2</sub> and grown in Dulbecco's modified Eagle's medium/Nutrient Mixture F-12 Ham (DMEM/F12 1:1, Life Technologies) medium, supplemented with 10% fetal bovine serum (FBS, Life Technologies) and antibiotics (1% penicillin/streptomycin, Sigma-Aldrich). The cells were transiently transfected with the human M<sub>1</sub>R (Addgene), co-transfected with M<sub>1</sub>R and R-GECO1 (ratio: 1:1), or human M<sub>2</sub>R (Addgene), and chimeric Gα<sub>i</sub>/αG<sub>q</sub> protein (Gα<sub>qTOP</sub>) (ratio: 1:1), using X-tremeGENE 9 DNA Transfection Reagent (Roche Applied Science) following the manufacturer's instructions. As generally known, M<sub>1</sub> mAChRs prevalently activate Gα<sub>q</sub> proteins and lead to the activation of the phospholipase C pathway, resulting in the production of inositol 1,4,5-trisphosphate (IP<sub>3</sub>) and the subsequent release of intracellular calcium from the endoplasmic reticulum. In contrast, the M<sub>2</sub> mAChR prevalently activates the Gα<sub>i</sub> protein; therefore, we co-transfected the cells with a chimeric Gα<sub>q</sub>/Gα<sub>i</sub>-protein, which couples M<sub>2</sub>R activation with the phospholipase C pathway. After 24 h, the cells were harvested with Accutase (Sigma-Aldrich) and plated onto 16 mm glass coverslips (ThermoFisher

Scientific) pretreated with poly-L-lysine (Sigma-Aldrich) to allow cell adhesion. Pre-confluent cultures were used for experiments between 48 and 72 h after transfection.

The bath solution used for single-cell intracellular calcium recordings contained 140 mM NaCl, 5.4 mM KCl, 1 mM MgCl<sub>2</sub>, 10 mM HEPES, 10 mM glucose, and 2 mM CaCl<sub>2</sub> (pH 7.4). The calcium indicator used to test cryptozepine-2 was Oregon Green BAPTA-1 AM (OGB-1 AM; Life Technologies). Before each experiment, the cells were mounted on the recording chamber (Open Diamond Bath Imaging Chamber for Round Coverslips from Warner Instruments) and loaded with OGB-1 AM for 30 min at 37°C with 5% CO<sub>2</sub> at a final concentration of 10 μM in Ca<sup>2+</sup>-free bath solution. The cells were rinsed with fresh solution, and the recording chamber was filled with 1 ml of recording solution and placed on an IX71 inverted microscope (Olympus) with an XLUMPLFLN 20XW x20/1 water immersion objective (Olympus). OGB-1 AM was excited during 50 ms at 488 nm using a Polychrome V light source (Till Photonics) equipped with a Xenon Short-Arc lamp (Ushio Europe B.V.) and a 505 nm dichroic beam splitter (Chroma Technology). The emission at 510 nm was filtered by a D535/40 nm emission filter (Chroma Technology) and finally collected by a C9100-13 EM-CCD camera (Hamamatsu Photonics). R-GECO1 was used as a Ca<sup>2+</sup> fluorescent indicator because it absorbs less than OGB-1 AM at 460 nm, a wavelength used to photoisomerize the compound cryptozepine-3. R-GECO1 was excited during 50 ms at 562 nm using a Polychrome V light source (Till Photonics) equipped with a Xenon Short-Arc lamp (Ushio Europe B.V.) and a 585 nm dichroic beam splitter (Chroma Technology). The emission at 600 nm was filtered using an ET630/75 nm emission filter (Chroma Technology) and finally collected by a C9100-13 EM-CCD camera (Hamamatsu Photonics). Images were acquired at room temperature with an imaging interval of 2 s with SmartLux software (HEKA), and the imaging analysis was performed with Fiji (NIH, ImageJ). The agonist used to stimulate M<sub>1</sub>Rs and M<sub>2</sub>Rs in HEK tsA201 cells was acetylcholine (ACh, Sigma). The application of the compounds was carried out by manually pipetting a small volume during imaging acquisition into the accessory pool of the recording chamber for the final dilution of approximately 1:1000. Every application of 0.5 ACh μM was followed by the next application after a 20-min recovery time. The effect of these photoswitchable antagonists on the ACh-induced calcium signal was observed by applying each compound (100 μM) for 2 min in its *trans* or *cis* form prior to the ACh application. The subtype-selectivity study (M<sub>1</sub> vs. M<sub>2</sub> mAChRs) of cryptozepine-2 was performed by comparing the amplitude of calcium signal response of cells expressing M<sub>2</sub>R-Gα<sub>q</sub>TOP or M<sub>1</sub> mAChR in the presence of different concentrations of cryptozepine-2 (10, 30, 50, and 100 μM). Data were



normalized over the maximum response obtained with ACh at 0.5  $\mu\text{M}$ . In the case of PNZ, it was applied at decreasing concentrations ranging from 10 nM to 100  $\mu\text{M}$ , 2 min before ACh. Photoisomerization of cryptozepine-2 was achieved by pre-illuminating the compounds with a Vilber Lourmat UV Lamp (365 nm, 6 W) for 2 min before application. Photoisomerization of cryptozepine-3 was achieved by continuously illuminating the specimen with 460 nm light. Numerical data were imported to GraphPad Prism version 6.00 for Windows (GraphPad Software). Statistical analysis was performed using the paired-sample Wilcoxon signed-rank test.

### SI3.7.1 Control experiments

In order to assess the significance of cryptozepine-2 and -3 (photo)responses in  $M_1$  mAChR expressing cells, further control experiments were performed in tsA201 cells without the transfection with  $M_1R$ . No responses were observed after application of acetylcholine (ACh), cryptozepine-2 (Figure S3.18) and cryptozepine-3 (Figure S3.19), and under illumination at 460 nm, which excludes any response artifacts.

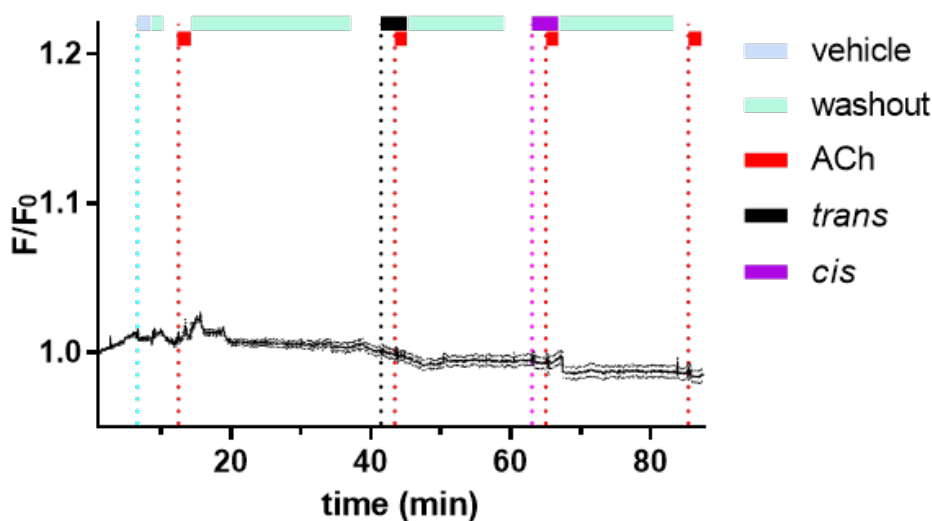


**Figure S3.18.** Control experiments for cryptozepine-2 with *in vitro* calcium imaging experiments in tsA201 cells without the presence of  $M_1R$ . No calcium oscillations were observed after application of ACh, cryptozepine-2 in the dark-adapted state (*trans*) and after 365 nm illumination (*cis*) ( $n = 50$  cells). Error bars are  $\pm$  SEM.

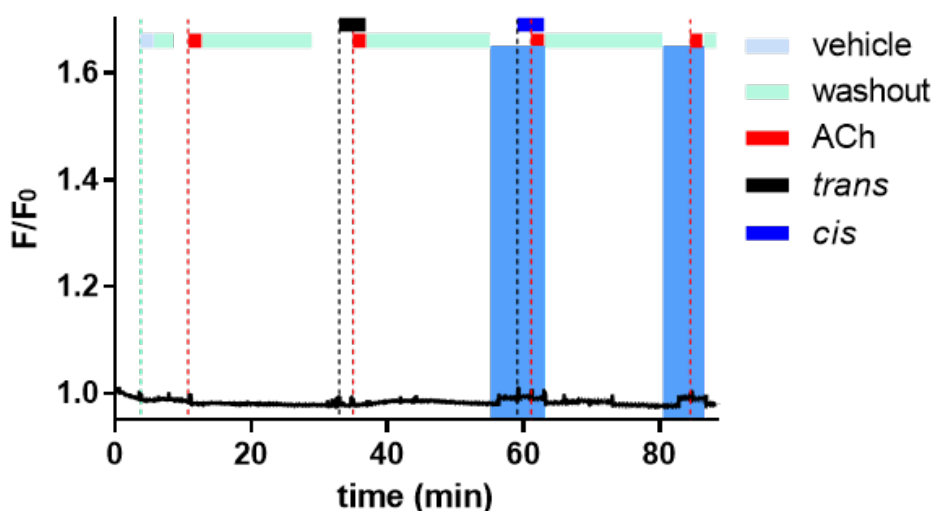


**Figure S3.19. Control experiments for cryptozepine-3 with *in vitro* calcium imaging experiments in tsA201 cells without the presence of  $M_1R$ .** No calcium oscillations were observed after application of ACh, cryptozepine-3 in the dark-adapted state (*trans*) and under 460 nm illumination (*cis*) ( $n = 50$  cells). Error bars are  $\pm$  SEM.

To validate our results, we performed calcium imaging recordings using the  $M_1R$  antagonist PNZ (Sigma-Aldrich). We used PNZ at decreasing concentrations ranging from 10 nM to 100  $\mu$ M, 2 min prior to ACh application (**Figure S3.20**). As expected, at concentrations of 100  $\mu$ M, 1  $\mu$ M and 100 nM, we observed a significant inhibition of 89%, 85% and 52% of ACh-mediated calcium response respectively. However, the lowest concentration of PNZ (10 nM) had no significant effect.

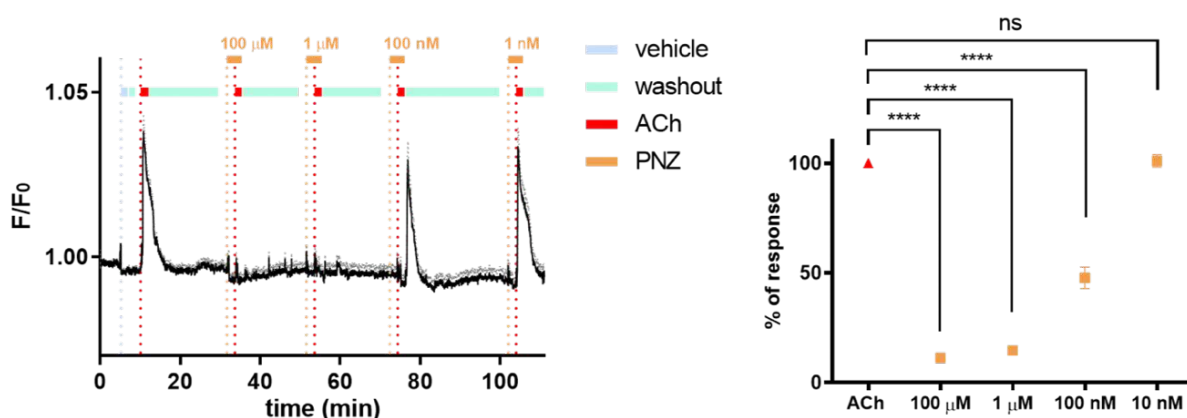


**Figure S3.20. Pirenzepine (PNZ) antagonizes ACh-induced activation of  $M_1$  mAChRs.** Real-time calcium imaging traces from HEK cells expressing  $M_1$  mAChRs, which were loaded with the calcium indicator OGB-1 AM (10  $\mu$ M). PNZ was used at concentrations ranging from 10 nM to 100  $\mu$ M. The cell responses to ACh (0.5  $\mu$ M) were significantly reduced in the presence of PNZ (100  $\mu$ M, 1  $\mu$ M and 100 nM). However, cell responses were recovered at lowest concentration (10 nM). Standard Error of the mean (SEM) is in gray. Quantification

results are presented in the right graph ( $n = 94$  cells). The data were normalized over the maximum response obtained with  $0.5 \mu\text{M}$  ACh and analyzed by the paired sample Wilcoxon signed rank test ( $p$ -value (\*\*\*)  $< 0.001$ ,  $p$ -value (\*\*\*\*)  $< 0.0001$ ; GraphPad Prism 6. Error bars are  $\pm$  SEM.

### SI3.8 *In vitro* specific M<sub>1</sub>R and M<sub>2</sub>R muscarinic binding assay study of *cis*-cryptozepine-2

The *in vitro* radioligand binding assay of 1, 10, and 100  $\mu\text{M}$  *cis*-cryptozepine-2 enriched form (active isomer) was assessed on recombinant human M<sub>1</sub>Rs and M<sub>2</sub>Rs expressed in Chinese hamster ovary (CHO) cells (Figure S3.21).

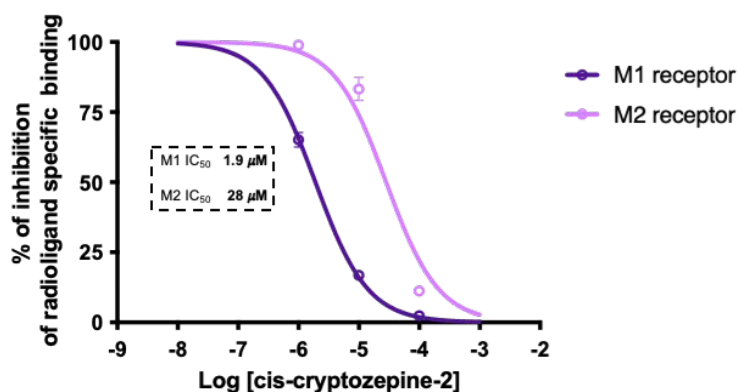


**Figure S3.21. Inhibitory dose-response curves of *cis*-cryptozepine-2 on M<sub>1</sub>Rs (purple line) and M<sub>2</sub>Rs (pink line).** The concentration-dependent inhibitory dose-curve data were plotted as percentage inhibition of radioligand specific binding (Figure 3.3E). The IC<sub>50</sub> values determined for *cis*-cryptozepine-2 on M<sub>1</sub>Rs and M<sub>2</sub>Rs are 1.9 and 28  $\mu\text{M}$ , respectively. The curves were obtained by nonlinear regression analysis using GraphPad Prism.

A 10 mM DMSO stock solution of the compound was used for the assay after 30 min irradiation with 365 nm light to work with a high percentage of the active *cis*-isomer ( $> 80\%$ ). The compound affinity was calculated as a percentage inhibition of the binding of a radioactively labeled antagonist specific for each target to assess the subtype-specific binding of cryptozepine-2. In particular, 2 nM [<sup>3</sup>H]PNZ for M<sub>1</sub>R and 2 nM [<sup>3</sup>H]AF-DX 384 for M<sub>2</sub>R were used as subtype-selective radioligand. The evaluation of the affinity of cryptozepine-2 for the human M<sub>1</sub>R was carried out using cell membrane homogenates (45  $\mu\text{g}$  of protein) incubated for 60 min at 22°C with 2 nM [<sup>3</sup>H]PNZ ( $K_d = 13$  nM) in the absence or presence of the test compound in a buffer containing 50 mM Tris-HCl (pH 7.4), 120 mM NaCl, 5 mM KCl, 5 mM MgCl<sub>2</sub>, and 1 mM EDTA. Nonspecific binding was determined in the presence of 1  $\mu\text{M}$  atropine. Following incubation, the samples were filtered rapidly under vacuum through glass fiber filters (GF/B, Packard) presoaked with 0.3% PEI and rinsed several times with ice-cold 50 mM Tris-HCl using a 96-sample cell harvester (Unifilter, Packard). The filters are dried and

then counted for radioactivity in a scintillation counter (Topcount, Packard) using a scintillation cocktail (MicroScint 0, Packard). The standard reference compound was PNZ, which was tested in each experiment at several concentrations to obtain a competition curve from which its IC<sub>50</sub> is calculated<sup>10</sup>.

For evaluating the affinity of cryptozepine-2 for the human M<sub>2</sub>R, cell membrane homogenates (60 µg protein) were incubated with 2 nM [<sup>3</sup>H]AF-DX 384 (K<sub>d</sub> = 4.6 nM) following the same procedure described for the M<sub>1</sub>Rs. The standard reference compound was methoctramine, which was tested in each experiment at several concentrations to obtain a competition curve from which its IC<sub>50</sub> is calculated<sup>10</sup>. The results showing an inhibition higher than 50% are considered to represent significant effects of the test compounds. The results showing an inhibition between 25 and 50% are indicative of weak to moderate effects. The results showing an inhibition lower than 25% are not considered significant. Experiments were performed in duplicate and accepted in accordance with Eurofins Cerep Quality Control Unit's validation standard operating procedure.

### **SI3.9 *Ex vivo* mice atria tissue experiments**

#### **SI3.9.1 Animals and tissue samples**

Ten CD-1 male mice (Charles River Laboratories) of 10-12 weeks old were used. Housing was under controlled conditions: constant temperature (22 ± 2°C) and humidity (55 ± 10%), a 12-h light/dark cycle, and *ad libitum* access to water and food. Before euthanasia, heparin (100 units/kg i.p.) was administered. Animals were sacrificed by cervical dislocation under sedation with ketamine (80 mg/kg i.p.) and xylazine (10 mg/kg i.p.). For functional studies, heart was quickly removed and placed in carbogenated (95% O<sub>2</sub> and 5% CO<sub>2</sub>) Krebs solution (composition in mmol/l: glucose 10.10, NaCl 115.48, NaHCO<sub>3</sub> 21.90, KCl 4.61, NaH<sub>2</sub>PO<sub>4</sub> 1.14, CaCl<sub>2</sub> 2.50, and MgSO<sub>4</sub> 1.16) (pH 7.4). Functional experiments were approved by the Ethics Committee of the Universitat Autònoma de Barcelona (code EUT-MJ001).

#### **SI3.9.2 Functional studies**

Right atrium was isolated and mounted in a 10 ml chamber using a compact organ bath (Panlab SL). The tissue was bathed in a carbogenated Krebs solution maintained at 37 ± 1°C using an external thermostat. The mechanical activity was measured with an isometric force transducer connected to a computer through an amplifier associated with PowerLab/800. LabChart software was used for data digitalization (1000 samples/s) and measurements. A tension of 0.2

g was applied, and the tissue was allowed to equilibrate for 5-10 min until spontaneous mechanical contractions were recorded. Carbachol (CCh;  $10^{-6}$  M) was added for 3 min and then  $10^{-6}$  and  $10^{-5}$  M PNZ,  $10^{-5}$ ,  $3 \times 10^{-5}$ , and  $10^{-4}$  M *trans*-cryptozepine-2 (*trans*), or  $10^{-5}$ ,  $3 \times 10^{-5}$ , and  $10^{-4}$  M *cis*-cryptozepine-2 (*cis*) were applied. Amplitude and beats per minute (beats/min, bpm) were calculated before and after the addition of the drug. Atrial contractions were recorded at a frequency of about 360 beats/min and a mean amplitude of 0.1 g. CCh concentration-dependently decreased both the amplitude and beats/ min ( $n = 6$ ) with an  $EC_{50}$  of about  $10^{-6}$  M. This concentration of CCh was used to activate muscarinic receptors in the bioassay and induces bradycardia. The presence of both PNZ ( $n = 6$ ) and *cis*-cryptozepine-2 (*cis*) ( $n = 2$ ) concentration-dependently reversed the effect of  $10^{-6}$  M CCh in terms of heartbeat frequency. In contrast, *trans*-cryptozepine-2 (*trans*) ( $n = 2$ ) did not reverse CCh-induced bradycardia ( $n = 2$ ) (Figures 3.4, Figure S3.22, and Figure S3.23).

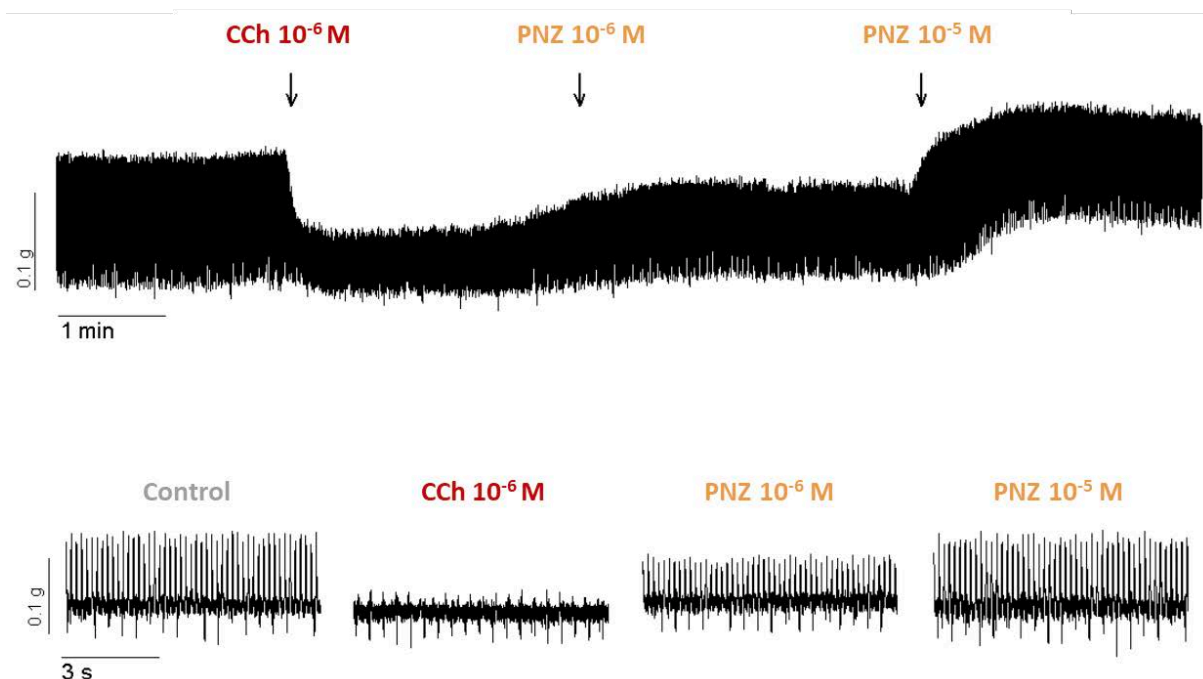


**Figure S3.22. Representative profile of the measured heart rate of a mouse right atrium treated with pirenzepine (PNZ).** Spontaneous mechanical contractions were recorded as control (ctrl). Carbachol (CCh)  $10^{-6}$  M decreased both the amplitude and beats/min (bpm). The presence of PNZ ( $n = 6$ ) concentration-dependently reversed the bradycardic effect of CCh  $10^{-6}$  M.

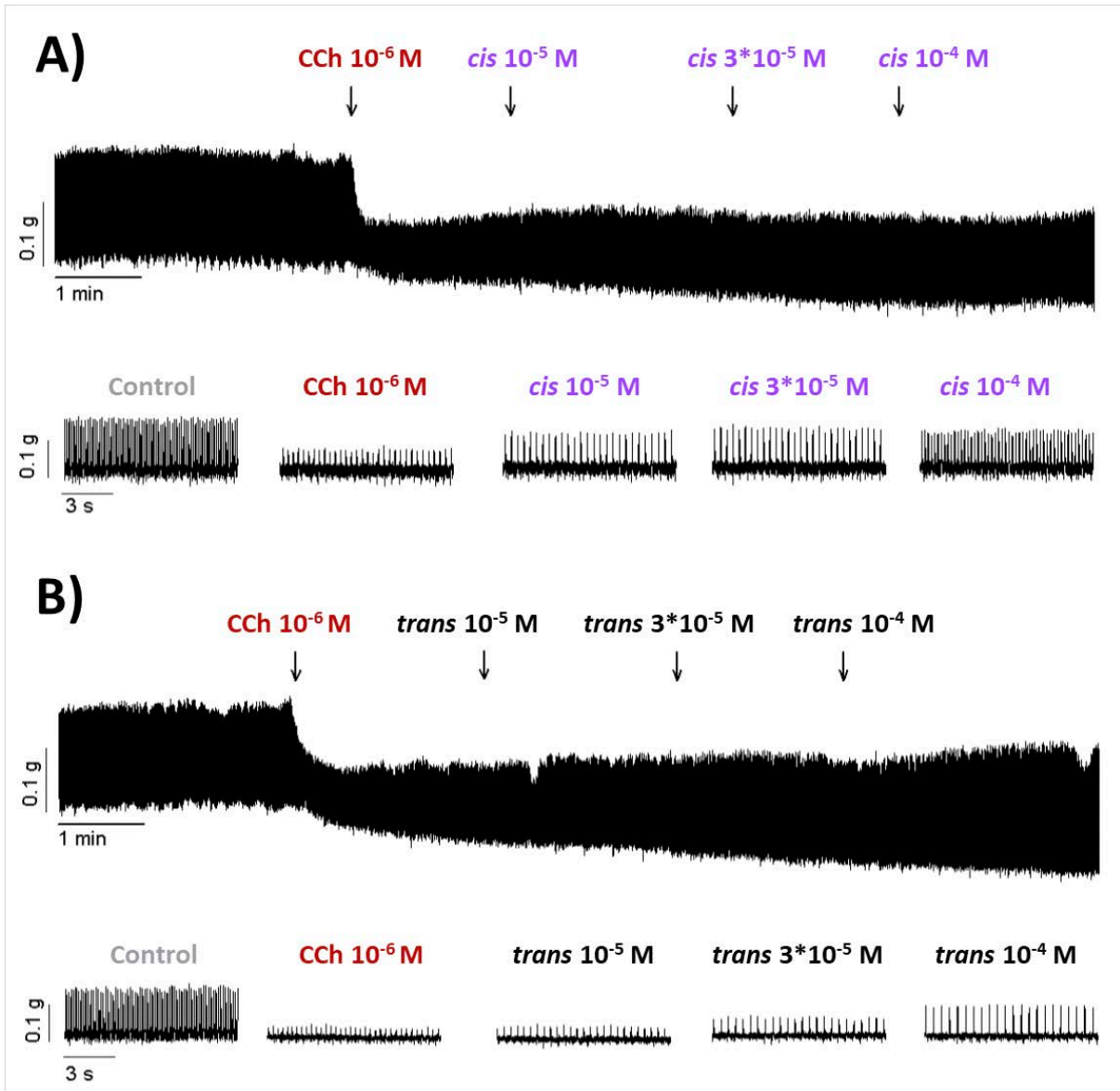


**Figure S3.23. Representative profile of the measured heart rate of a mouse right atrium treated with cryptozepine-2.** Spontaneous mechanical contractions were recorded as control (ctrl). Carbachol (CCh) 10<sup>-6</sup>M decreased both the amplitude and beats/min (bpm). (A) The presence of *cis*-cryptozepine-2 (*cis*) (n = 2) concentration-dependently reversed the bradycardia induced by CCh 10<sup>-6</sup> M, in line with the pirenzepine effect. (B) In contrast, *trans*-cryptozepine-2 (*trans*) (n = 2) did not reserve CCh effect in terms of heartbeat frequency (n = 2).

## Additional references

- 1 Thal, D. M. *et al.* Crystal structures of the M<sub>1</sub> and M<sub>4</sub> muscarinic acetylcholine receptors. *Nature* **531**, 335-340, doi:10.1038/nature17188 (2016).
- 2 Morris, G. M. *et al.* AutoDock4 and AutoDockTools4: Automated docking with selective receptor flexibility. *J Comput Chem* **30**, 2785-2791, doi:10.1002/jcc.21256 (2009).
- 3 Dallakyan, S. & Olson, A. J. Small-molecule library screening by docking with PyRx. *Methods Mol Biol* **1263**, 243-250, doi:10.1007/978-1-4939-2269-7\_19 (2015).
- 4 Lu, Z. L., Saldanha, J. W. & Hulme, E. C. Transmembrane domains 4 and 7 of the M<sub>1</sub> muscarinic acetylcholine receptor are critical for ligand binding and the receptor activation switch. *J Biol Chem* **276**, 34098-34104, doi:10.1074/jbc.M104217200 (2001).
- 5 Eberlein, W. G., Engel, W. W., Trummlitz, G., Schmidt, G. & Hammer, R. Tricyclic compounds as selective antimuscarinics. 2. Structure-activity relationships of M<sub>1</sub>-selective antimuscarinics related to pirenzepine. *J Med Chem* **31**, 1169-1174, doi:10.1021/jm00401a016 (1988).
- 6 Murgolo, N. J. K., J.; Tice, M. A. B.; Hollinger, F. P.; Brown, J. E.; Zhou, G.; Taylor, L. A.; McQuade, R. D. The N<sub>4</sub> nitrogen of pirenzepine is responsible for selective binding of the M<sub>1</sub> subtype human muscarinic receptor. *Bioorg. Med. Chem. Lett.* **6**, 785-788 (1996).
- 7 Claro, E. Analyzing ligand depletion in a saturation equilibrium binding experiment. *Biochem Mol Biol Educ* **34**, 428-431, doi:10.1002/bmb.2006.494034062677 (2006).
- 8 Salles, J., Wallace, M. A. & Fain, J. N. Differential effects of alkylating agents on the multiple muscarinic receptor subtypes linked to activation of phospholipase C by carbachol in rat brain cortical membranes. *J Pharmacol Exp Ther* **264**, 521-529 (1993).
- 9 Yamamura, H. I. & Snyder, S. H. Muscarinic cholinergic binding in rat brain. *Proc Natl Acad Sci U S A* **71**, 1725-1729, doi:10.1073/pnas.71.5.1725 (1974).
- 10 Dorje, F. *et al.* Antagonist binding profiles of five cloned human muscarinic receptor subtypes. *J Pharmacol Exp Ther* **256**, 727-733 (1991).

# Chapter 4

---

Control of cortical slow oscillations and  
epileptiform discharges by  
photoswitchable muscarinic acetylcholine  
receptor subtype 1 ligands

---

---

José M. Sanchez-Sanchez, Fabio Riefolo, Almudena Barbero-Castillo, **Rosalba Sortino**, Luca Agnetta, Arnau Manasanch, Carlo Matera, Miquel Bosch, Marta Forcella, Michael Decker, Pau Gorostiza and Maria V. Sanchez-Vives. **Control of cortical slow oscillations and epileptiform discharges by photoswitchable muscarinic acetylcholine receptor subtype 1 ligands.** *Under review.*





## Abstract

Acetylcholine is a key neurotransmitter in the peripheral and central nervous system, involved in cognitive and motor processes. Its dysregulation has been linked to several neurological disorders, including epilepsy. The remote control of cholinergic pathways could be of high importance for basic research and clinical neurology applications. Here, the neuronal activity was modulated by using photopharmacological tools based on selective subtype 1 muscarinic receptor (M<sub>1</sub>R) photoswitchable drugs. The agonist benzyl quinolone carboxylic acid-azo-iperoxo (**BAI**) and the antagonist cryptozepine-**2** were used to evaluate their light-mediated effects on the network activity in the cerebral cortex. In the first study, the M<sub>1</sub>R selectivity of **BAI** was confirmed *in vitro*. This was prior to demonstrating its ability to significantly increase the frequency of slow oscillatory activity in cortical networks, both *ex vivo* and *in vivo* under light activation. In addition, we found that cryptozepine-**2** suppressed M<sub>1</sub>R-mediated epileptiform seizures through illumination. These results provide new insights on the M<sub>1</sub>R cholinergic pathway in the cortical network and offer new opportunities for light-based pharmacological therapies with high specificity and spatiotemporal resolution, enabling precise modulation of brain networks in health and disease.



## 4.1 Introduction

Complex interactions among millions of neurons lead to the spontaneous emergent activity of the brain. Although spontaneous brain activity arises without external influence, the brain must adapt to the external environment to be functional. The cerebral cortex is critical in this adaptation: depending on the brain state (*e.g.*, wakefulness, slow wave sleep, etc.), they show different levels of synchronization, temporal patterns of neural firing and excitability<sup>1,2</sup>. This diversity of cortical activity patterns results in different levels of complexity and information processing<sup>3,4</sup>. Periods of low complexity are characterized by synchronous and high-voltage brain waves, including slow oscillations (SO) and epileptical discharges. SO is an activity pattern that dominates the cerebral cortex during periods of unconsciousness, such as deep sleep or during anesthesia<sup>5,6</sup>. Therefore, it has been proposed as the default mode of cerebral cortex activity<sup>7</sup>. In contrast, periods of high complexity such as wakefulness are characterized by desynchronized and low-voltage wave patterns<sup>8,9</sup>.

The transition between brain states is physiologically triggered by a combination of neurotransmitters from the ascending activating system, of which the cholinergic system is fundamental (for a review, see Lee *et al.*, 2012)<sup>10</sup>. Cholinergic action in the cerebral cortex takes place largely through muscarinic acetylcholine receptors (mAChRs or MRs), which are involved in a range of critical functions related to cognition, consciousness, and motor processing<sup>11-13</sup>.

The intracellular pathways of the 3 types of mAChRs predominant in the central nervous system (M<sub>1</sub>R, M<sub>2</sub>R and M<sub>4</sub>R) have been widely studied<sup>14</sup>. However, the role of each muscarinic pathway in cortical network dynamics remains unclear. Specific spatiotemporal modulation of the mAChRs' activity can contribute to the understanding of the role of the neurotransmitter acetylcholine (ACh) in the different cortical brain states and may provide new therapeutic opportunities<sup>15</sup>. This study assesses how the activity of M<sub>1</sub> mAChRs could be modulated in the cerebral cortex using photopharmacology, a technique that employs photoswitchable molecules to modulate the function of endogenous proteins and their downstream physiological pathways<sup>16</sup>. Specifically, we examine the impact of light-mediated activation and inhibition of M<sub>1</sub> mAChRs on SO and epileptiform discharges. Our goal is to better understand how M<sub>1</sub>Rs act as a bifurcation point, influencing brain states of transitions to high or low complexity (*e.g.*, those observed during wakefulness or epilepsy, respectively)<sup>17-19</sup>.

The value of photoswitchable molecules to modulate spontaneous cortical SO *ex vivo* and *in vivo* has previously been demonstrated by using phthalimide-azo-iperoxo (PAI), an agonist of M<sub>2</sub> mAChRs<sup>20,21</sup>. In this study, we use a photoswitchable M<sub>1</sub> mAChR agonist compound, benzylquinolone-carboxylic acid-azo-iperoxo (**BAI**)<sup>22</sup>, and the photoswitchable M<sub>1</sub> mAChR antagonist cryptozepine-2 (cryptozepine for simplicity)<sup>23</sup>. The different behaviors of the isomers of these two M<sub>1</sub> mAChR ligands (*cis*- and *trans*-) rely on azobenzene, which behaves as a light-dependent molecular switch (**Figure 4.1A**). The specificity and mode of action of **BAI** isomers was characterized for M<sub>1</sub> mAChRs in human embryonic kidney (HEK) cells by *in vitro* cultures and how M<sub>1</sub> mAChRs are modulated under different wavelengths. The effects of **BAI** were investigated on the cortical network *ex vivo* and *in vivo* as well as the capability of controlling spontaneous emergent cortical activity. In addition, we used the previous chemical characterization of the M<sub>1</sub> mAChR antagonist cryptozepine performed by Riefolo *et al.*, 2021<sup>23</sup> to investigate its ability to modulate spontaneous emergent cortical activity and muscarinic-induced seizure-like activity in the cerebral cortex *ex vivo*.

## 4.2 Results

### 4.2.1 *In vitro* calcium imaging

To study cell responses upon photopharmacological stimulation with **BQCAAI** (**BAI** for simplicity; **Figure 4.1A**), we performed real-time calcium imaging assay under continuous illumination (one-photon excitation, 1PE) in transiently transfected HEK cells with M<sub>1</sub>Rs and loaded with the fluorescent calcium indicator Oregon Green BAPTA-1 AM (OGB-1 AM). Neither the application of the vehicle (**Figure 4.1BC**, grey bar) nor the illumination alone evoked calcium responses (control experiments). Calcium oscillations characteristic of M<sub>1</sub>R activation (predominantly G $\alpha_q$ -coupled) were observed upon application of *trans*-**BAI** (orange bar, active isomer, dark-adapted state) and were terminated by photoconversion to *cis*-**BAI** (inactive isomer) under 365 nm illumination. Subsequent *cis*-to-*trans* isomerization under 460 nm light rapidly reactivated M<sub>1</sub> mAChR, triggering oscillatory calcium responses which are shown as both representative traces of individual cells (**Figure 4.1B**) and average trace of cell responses (**Figure 4.1C**). The neurotransmitter acetylcholine (ACh) was applied in each experiment as positive control (green bar).

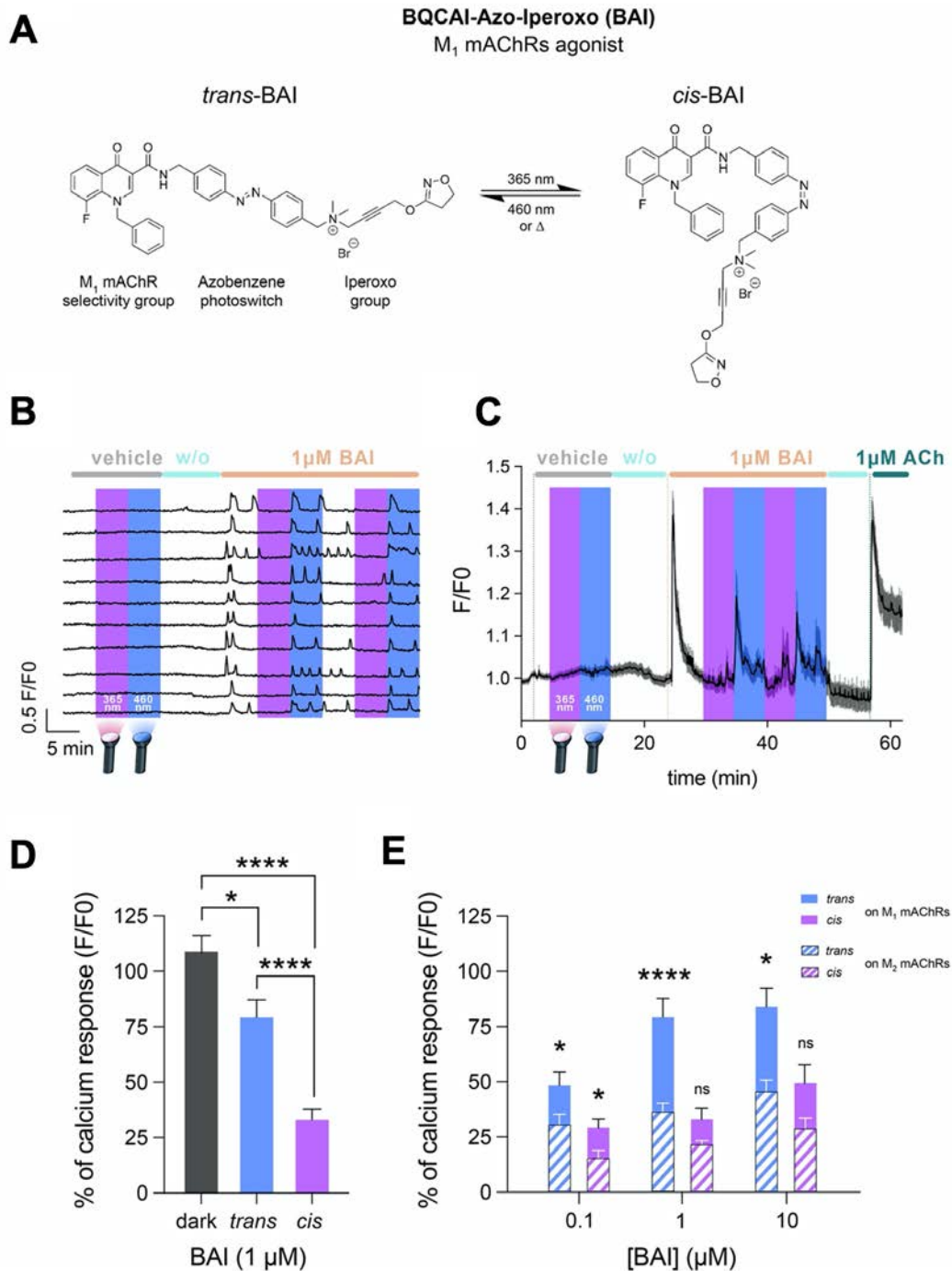


**Figure 4.1. *In vitro* pharmacological characterization of BAI in HEK cells.** (A) Structure of the *cis*- and *trans*-isomers of **BAI** and wavelength required for photoswitching. (B) Representative traces of intracellular calcium activity of individual cells expressing human M<sub>1</sub>R under 365/460 nm illumination in the presence of vehicle (grey bar) and after application of **BAI** (1 μM, orange bar). Light blue bars indicate wash-out periods (w/o). (C) Average trace (n = 15) of cell responses to 1 μM **BAI**. Green bar indicates the application of the reference agonist, acetylcholine (ACh, 1 μM). (D) Quantification of the calcium imaging responses (n = 53 cells from four independent experiments). A rapid increase of intracellular calcium in the presence of *trans*-**BAI** was observed, while calcium responses to the *cis* form were decreased by 46%. (E) Receptor-subtype selectivity studies of **BAI** (M<sub>1</sub> vs. M<sub>2</sub> mAChRs) at 0.1 (M<sub>1</sub>R, n = 34; M<sub>2</sub>R, n = 32); 1 (M<sub>1</sub>R, n = 53; M<sub>2</sub>R, n = 60) and 10 (M<sub>1</sub>R, n = 24; M<sub>2</sub>R, n = 10) μM.

The quantification of the response showed that *trans*-**BAI**, like ACh, significantly stimulated the release of intracellular calcium, while illumination with 365 nm (*trans*-to-*cis*) decreased calcium responses by 46% (from  $80 \pm 8$  % during *trans*-**BAI** to  $34 \pm 5$  % during *cis*-**BAI**,  $p$ -value = 0.000014), (**Figure 4.1D**). In addition, we measured **BAI**-mediated calcium responses in HEK cells co-expressing M<sub>2</sub> mAChR and G $\alpha_{qTOP}$  (the latter transduces G $\alpha_{i/o}$ -mediated receptor activation to calcium responses for the sake of comparison)<sup>24</sup> in order to study the selectivity of **BAI** for M<sub>1</sub> vs. M<sub>2</sub> mAChRs. In cells expressing M<sub>1</sub> mAChR, the photoconversion of **BAI** from *cis*-to-*trans* induced a stronger activation of calcium responses compared to the M<sub>2</sub> mAChR expressing cells for all the concentrations tested (**Figure 4.1E**), demonstrating the selectivity of **BAI** for M<sub>1</sub> vs. M<sub>2</sub> mAChRs. Furthermore, photoresponses were absent in cells not expressing M<sub>1</sub>R- or M<sub>2</sub>R-G $\alpha_{qTOP}$  mAChRs (**Figure S4.1**).

#### 4.2.2 *Ex vivo* photocontrol of the frequency of slow waves with **BAI** in ferret slices

Cerebral cortex slices *ex vivo* express spontaneous network activity as SO (**Figure 4.2A**)<sup>25</sup>. This is a rhythmic activity equivalent to that generated in the cortex *in vivo* during slow wave sleep and deep anesthesia<sup>26</sup> and it is an emergent activity of the cortical network that results from the integration of cellular and synaptic properties. These oscillations consist of periods of activity or Up states interspersed with periods of low activity or Down states (**Figure 4.2A**)<sup>25</sup>.

To identify the most suitable range of drug concentrations to achieve robust modulation of SO by light, we generated a dose-response curve under the effect of *cis*- and *trans*-**BAI** isomers in cortical slices *ex vivo*. The baseline characterized by SO was recorded as control. Then, three different concentrations of *trans*- and *cis*-**BAI** were applied to the bath in separated experiments, respectively (1  $\mu$ M, 2  $\mu$ M and 3  $\mu$ M, **Figure 4.2B**).

Compared to control conditions, the *trans*-**BAI** bath application led to an increase in the oscillatory frequency with reduction of the Down state duration, reaching the maximum effect at 3  $\mu$ M (from  $0.4 \pm 0.08$  Hz during control to  $0.92 \pm 0.05$  Hz with 3  $\mu$ M *trans*-**BAI**,  $p$ -value = 0.0286;). 1 and 2  $\mu$ M *cis*-**BAI** applications resulted in a lower increase in the oscillatory frequency compared to *trans*-**BAI** (from  $0.47 \pm 0.03$  Hz during control to  $0.66 \pm 0.04$  Hz with 2  $\mu$ M *cis*-**BAI**,  $p$ -value = 0.0079). Significant differences were observed in the oscillatory frequency values between the two isoforms at these concentrations (1  $\mu$ M  $p$ -value = 0.0317; 2  $\mu$ M  $p$ -value = 0.0079). In summary, both *trans*-**BAI** and *cis*-**BAI** were able to modulate SO in a dose-dependent manner at 1 and 2  $\mu$ M, but *cis*-**BAI** showed significantly weaker agonism.

The identification of this suitable concentration window allowed us to optimize the direct application of light to control M<sub>1</sub>R activity and to modulate cortical SO *ex vivo*.

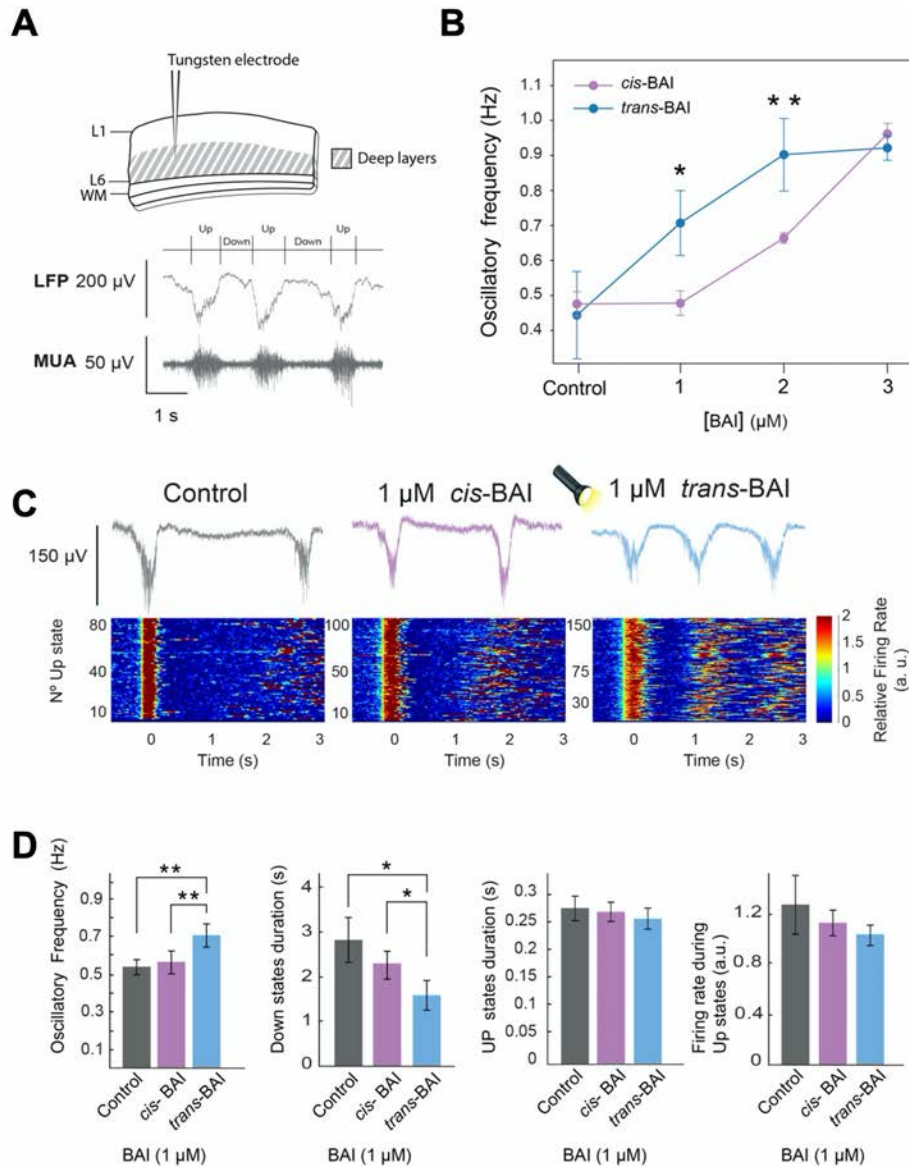


**Figure 4.2. Effect of BAI isomers and photocontrol of slow oscillations using BAI direct illumination with white light.** (A) Sectioned cortical slice scheme and recording point (top). Local field potential (LFP,  $\mu$ V) traces of slow oscillation and description of Up and Down states (middle). Multiunit activity (MUA,  $\mu$ V) during slow oscillation (bottom). (B) Oscillatory frequency (Hz) of the *cis*- (purple) and *trans*- (blue) BAI (for each isomer n = 4 ferret brain slices) at 1, 2 and 3  $\mu$ M. Significant differences between *cis*- and *trans*-BAI were found in the oscillatory frequency at 1  $\mu$ M and 2  $\mu$ M. Therefore 1  $\mu$ M was set as the concentration to modulate slow oscillations with light. (C) Representative local field potential (LFP,  $\mu$ V) traces (top) and raster plot of relative firing rate (bottom) under control condition, application of 1  $\mu$ M pre-illuminated with 365 nm light (*cis*-BAI) and photoconversion with white light 1  $\mu$ M BAI (*trans*-BAI). (D) Oscillatory frequency, firing rate during Up state (a.u.) and durations of Down and Up state (s) during previous conditions (n = 9 ferret slices). A significant increase in the oscillatory frequency and a decrease in Down state duration is shown after illumination of ferret slices with white light, containing 1  $\mu$ M of *cis*-BAI.



We then moved on to directly control **BAI**-mediated SO activity with light in cortical slices (**Figure 4.2CD**). We initially recorded SO as control condition and then applied 1  $\mu\text{M}$  of *cis*-**BAI** in dark conditions to not soil the quality of the recordings with the presence of *trans*-**BAI**<sup>20</sup>. Compared to control conditions, the frequency of oscillation under 1  $\mu\text{M}$  *cis*-**BAI** showed no significant changes (from  $0.53 \pm 0.04$  Hz during control to  $0.55 \pm 0.06$  Hz;  $p$ -value = 0.931), as expected. Subsequent illumination of the slices with white light produced the activation of **BAI** (**Figure 4.2CD**) and a significant increase in the oscillatory frequency (from  $0.53 \pm 0.04$  Hz during control to  $0.83 \pm 0.06$  Hz with 1  $\mu\text{M}$  of *trans*-**BAI**,  $p$ -value = 0.002). This increase was associated to a decrease in the duration of the Down state period (from  $2.81 \pm 0.5$  s during control to  $1.57 \pm 0.33$  s with 1  $\mu\text{M}$  *trans*-**BAI**,  $p$ -value = 0.018), while active periods or Up states duration did not significantly vary either in duration or firing rate. This evidence provides a mechanistic insight into the network dynamics and its modulation that points toward the network excitability during Down states<sup>27</sup>.

### 4.2.3 *In vivo* photocontrol of the frequency of slow waves with **BAI** in mice

To determine if the impact of the photoswitchable M<sub>1</sub>R agonist **BAI** on slow oscillatory activity was not only limited to cortical slices *ex vivo* but also evident in the intact brain *in vivo*, we conducted cortical activity recordings from the primary visual cortex (V1) of anesthetized mice. While in the cortical slices drug application was directly over and inside the cortical parenchyma, *in vivo* the drug application was done over the pia mater. Due to this different via of drug administration, we increased the concentration of the locally applied drug to 5  $\mu\text{M}$  (**Figure 4.3A**)<sup>21</sup>. Compared to control activity, application of *cis*-**BAI** did not show significant changes in the frequency of oscillation (from  $0.61 \pm 0.04$  Hz during control to  $0.63 \pm 0.04$  Hz under 5  $\mu\text{M}$  *cis*-**BAI**,  $p$ -value = 0.721). However, following direct white light illumination to the cortex, we were able to switch **BAI** *in situ* to its active *trans*-isomer, and observe a significant increase in the oscillatory frequency (from  $0.61 \pm 0.04$  Hz during control to  $0.78 \pm 0.05$  Hz with 5  $\mu\text{M}$  *trans*-**BAI**,  $p$ -value = 0.0379; **Figure 4.3B**). These results are aligned with what was empirically observed during our *ex vivo* demonstrations.

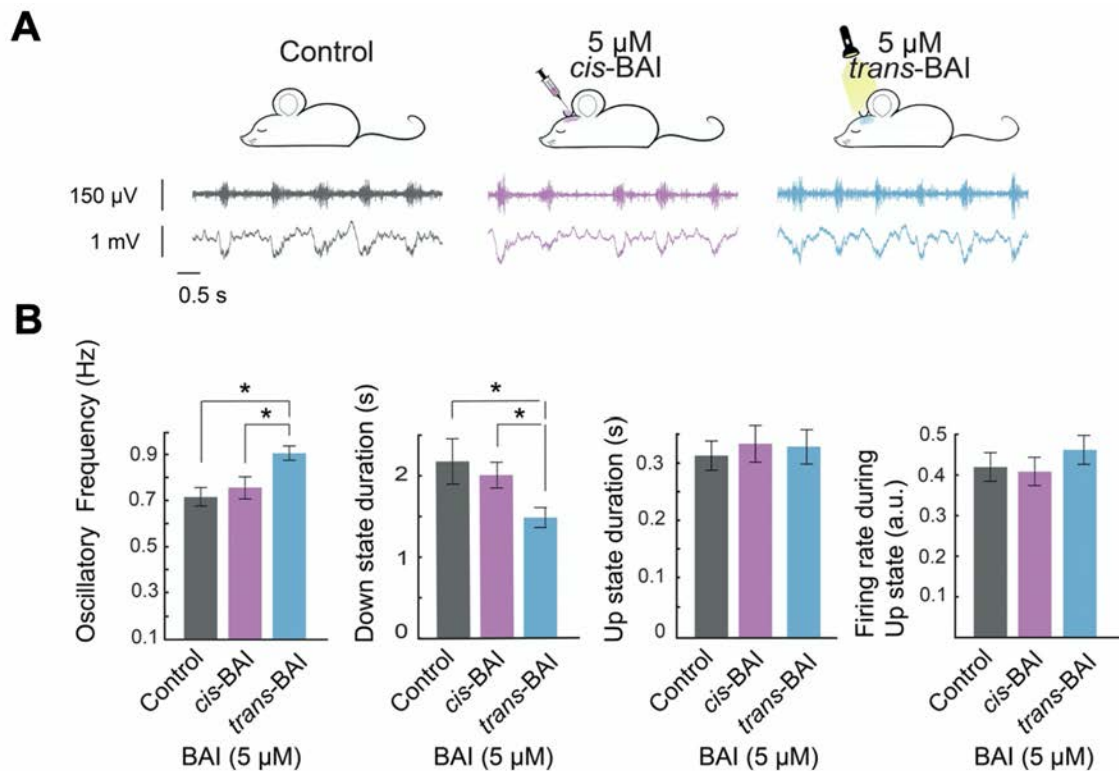


**Figure 4.3. Photocontrol of slow oscillations with BAI and direct illumination with white light *in vivo*.** (A) Steps of the *in vivo* photocontrol protocol (top). Representative multiunit activity (MUA,  $\mu$ V) (middle) and local field potential (LFP, mV) traces (bottom) of the *in vivo* recording during control condition, application of 5  $\mu$ M pre-illuminated with 365 nm light (*cis*-BAI) and photoconversion with white light 5  $\mu$ M BAI (*trans*-BAI). (B) Oscillatory frequency, firing rate during Up state (a.u.) and durations of Down and Up state (s) during previous conditions ( $n = 7$  mice). Illumination of the brain cortex containing 5  $\mu$ M *cis*-BAI with white light led to a significant increase in oscillatory frequency and a decrease in Down state duration.

#### 4.2.4 *Ex vivo* photocontrol of the frequency of slow waves with cryptozepine in ferret slices

To understanding about the broad and complex role of M<sub>1</sub>R on cortical dynamics, we also studied the effect of the recently reported photoswitchable M<sub>1</sub>R antagonist cryptozepine-2 (cryptozepine for simplicity) on SO<sup>23</sup>. We initially tested the light-dependent antagonism of *trans*- (inactive) and *cis*-cryptozepine (active) isomers at 1, 10, and 100  $\mu$ M concentrations in the presence of the muscarinic agonist carbachol (CCh) at 1  $\mu$ M (**Figure S4.2**).

The effects of 10 and 100  $\mu$ M *trans*-cryptozepine were strong enough to reduce oscillatory frequency values induced by CCh bath application. At 3  $\mu$ M, cryptozepine effectively blocked the effects of 500 nM CCh in a light-dependent manner (**Figure 4.4**). The SO activity (control condition) was initially recorded before the application of 500 nM CCh. Following the application of 500 nM CCh, the oscillatory frequency significantly increased (from  $0.75 \pm 0.06$

Hz in control condition to  $1.23 \pm 0.07$  Hz;  $p$ -value = 0.0022; **Figure 4.4B**). Next, 3  $\mu$ M *trans*-cryptozepine was added, without a significant reduction of the oscillatory frequency (from  $1.23 \pm 0.07$  Hz to  $1.13 \pm 0.06$  Hz,  $p$ -value = 0.2403), as expected. Illumination of the brain slices with 365 nm light produced *trans*-to-*cis* cryptozepine photoconversion *in situ*, causing a significant decrease in the frequency of oscillation (from  $1.13 \pm 0.06$  Hz to  $0.90 \pm 0.06$  Hz,  $p$ -value = 0.026). This change in activity was characterized by elongation of the Down state period (from  $0.61 \pm 0.05$  s during 500 nM CCh and 3  $\mu$ M *trans*-cryptozepine to  $0.93 \pm 0.09$  with 500 nM CCh and 3  $\mu$ M *cis*-cryptozepine,  $p$ -value = 0.0159). The isomerization of cryptozepine did not show any significant changes, neither in the duration of the Up state, nor in firing rate during the Up states (**Figure 4.4B**), suggesting a regulation of the membrane excitability during Down states<sup>27</sup>.

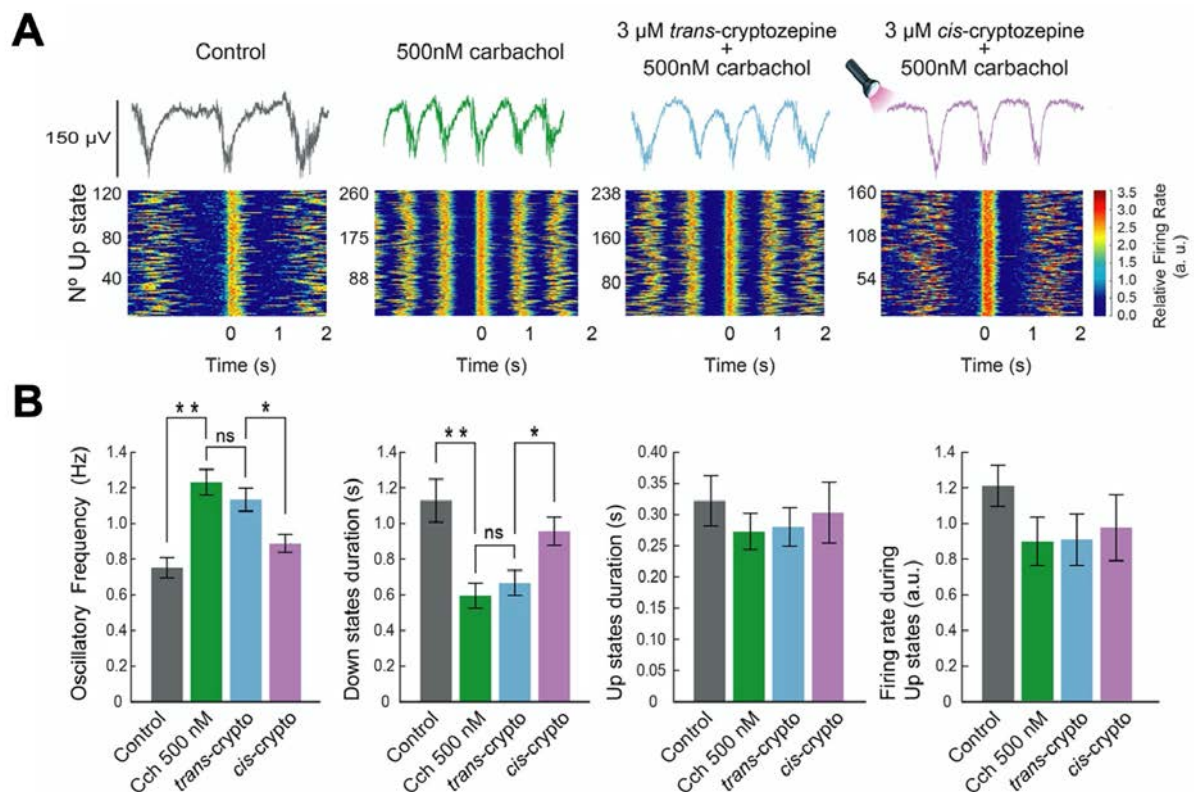


**Figure 4.4. Photocontrol of slow oscillations with cryptozepine and direct illumination with ultraviolet (UV) light in ferret slices.** (A) Representative local field potential (LFP) traces (top) and raster plot of relative firing rate (bottom) during control condition, at 500 nM of carbachol (CCh), 500 nM CCh + 3  $\mu$ M *trans*-cryptozepine (inactive isoform of the M<sub>1</sub> mAChR antagonist) and 500nM CCh + 3  $\mu$ M *cis*-cryptozepine (active isoform). (B) Oscillatory frequency (Hz), Down and Up state duration and firing rate during Up states during experiment conditions (n = 6 ferret slices). 500 nM CCh application in the bath led to a significant increase in oscillatory frequency. The increase was not reversed by the inactive isoform of cryptozepine, while photoconversion with 365 nm light (*trans*-to-*cis*) led to a significant decrease in oscillatory frequency.

### 4.2.5 *Ex vivo* experiment of seizure-like activity blockage with cryptozepine in ferret slices

Since we observed that the activation of mAChRs increases the excitability of the network in a seizure-like manner, we further analyzed the role of M<sub>1</sub>R on hyperexcitable states. As previously described<sup>21</sup>, the non-subtype selective mAChR superagonist iperoxo (IPX) induced seizure-like activity in cortical slices *ex vivo* (**Figure 4.5A**). We found that while 1-3  $\mu$ M concentrations of *trans*-**BAI** caused an increase in the physiological slow oscillatory frequency (**Figure 4.2B**), higher concentrations (*e.g.*, 30  $\mu$ M *trans*-**BAI**), induced cyclic periods of seizure-like activity (**Figure 4.5B**) mediated by M<sub>1</sub> mAChR. This activity was reminiscent of the initiation of seizure-like activity observed under the bath application of 150 nM of IPX (**Figure 4.5A**), characterized by highly synchronized discharges, due to mAChR activation. Before testing the photoswitchable M<sub>1</sub>R antagonist cryptozepine, we investigated whether (non-photoswitchable) pirenzepine (PNZ) can block the effect of IPX, suppressing the seizure-like activity (**Figure 4.5**)<sup>28,29</sup>.

**Figure 4.5C** illustrates the timeline of the network activity (spectrogram, local field potential and expanded traces) departing from spontaneous SO and transforming into highly synchronized seizure-like activity under the effect of 150 nM of IPX. Subsequent addition of 500 nM PNZ to the bath restored the SO regime.

To quantify the transition from SO to highly synchronized discharges during seizure-like activity, we measured the slope of multiunit activity (MUA) during the transition from Down state, and the firing rate to the next discharge event (which could be either Up states during SO or epileptogenic discharges during seizure-like activity). Both MUA slope and firing rate increase as previously reported for *ex vivo* cortical seizures<sup>30</sup>. The slope of the population discharge was increased when seizure-like activity was evoked (from  $8.26 \pm 4.27$  a.u. during control condition to  $15.96 \pm 5.29$  a.u. with 150 nM of IPX,  $p$ -value = 0.2000; **Figure 4.5D**). After PNZ blockade, the slope decreased (from  $15.96 \pm 5.29$  a.u. to  $7.69 \pm 5.00$  a.u.,  $p$ -value = 0.2000). (**Figure 4.5E**), returning to physiological slow oscillatory activity as the control values. As observed in **Figure 4.5F**, the firing rate was increased during seizure-like activity (from  $0.87 \pm 0.28$  a.u. during control condition to  $1.44 \pm 0.31$  a.u. with 150 nM IPX,  $p$ -value = 0.1000). In the presence of PNZ, the firing rate of the events decreased (from  $1.44 \pm 0.31$  a.u. with 150 nM IPX to  $0.90 \pm 0.27$  a.u. with 150 nM IPX + 500 nM PNZ,  $p$ -value = 0.1000)

(Figure 4.5F). Our results disclosed the fact that M<sub>1</sub> mAChRs act as the main contributor of muscarinic-induced seizure-like activity and can be blocked using M<sub>1</sub>R antagonists<sup>18</sup>.

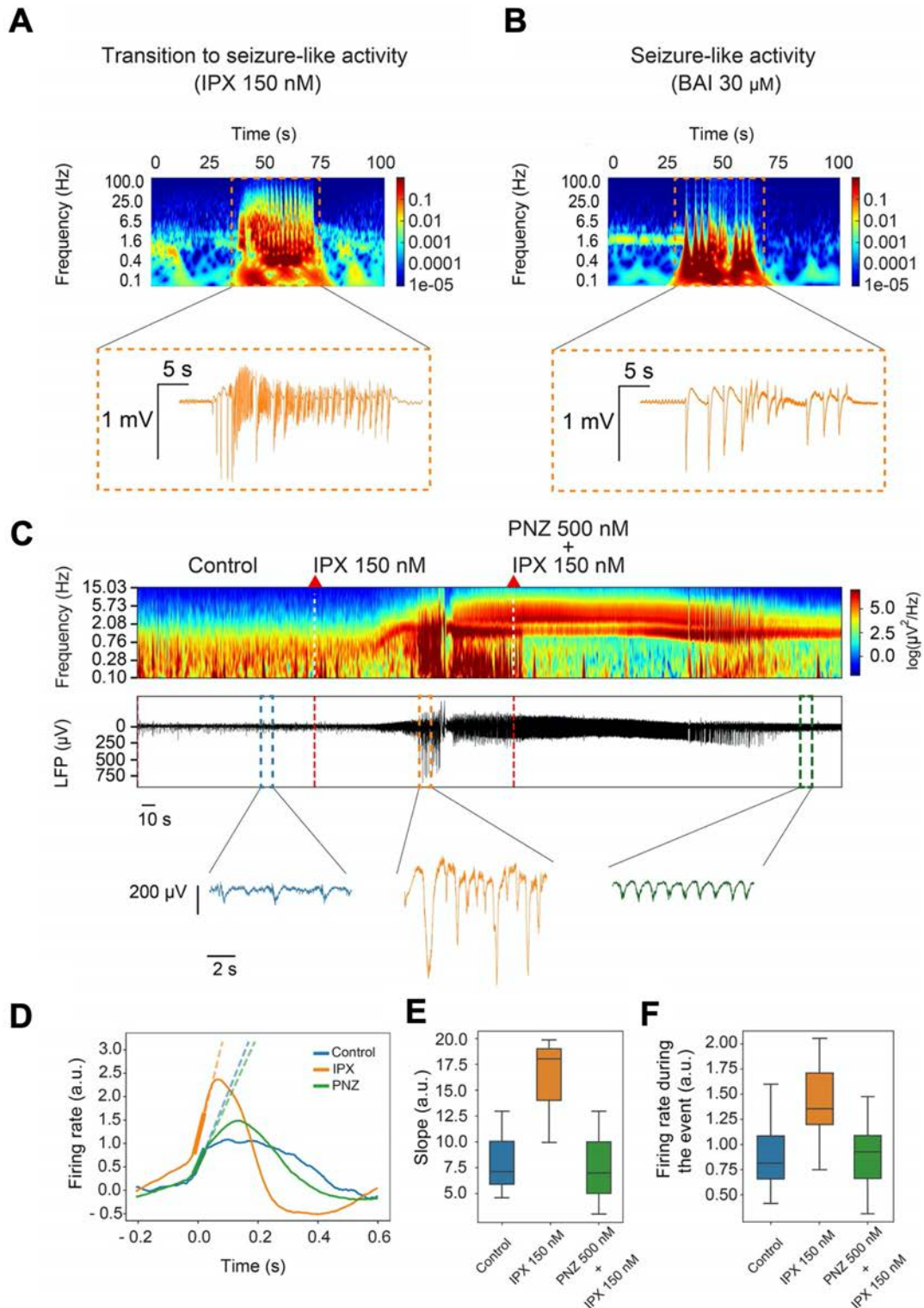


**Figure 4.5. Induction of seizure-like activity through M<sub>1</sub>R activation and blockage of seizure-like activity with pirenzepine.** (A) Representative spectrogram (top) and local field potential (LFP) traces (bottom) of the transition to seizure-like activity at 150 nM of iperoxo (IPX). (B) Representative spectrogram (top) and local field potential (LFP) traces (bottom) of seizure-like activity at 30 μM *trans*-BAI. (C) Representative spectrogram (top)

and LFP traces (bottom) during control condition, 150 nM IPX (seizure-like activity) and 150 nM IPX + 500 nM PNZ (reversing seizure-like activity). High-amplitude seizure-like activity appeared after bath application of IPX at 150 nM, this epileptogenic activity was blocked by application of 500 nM of PNZ. **(D)** Representative firing rate during Down to Up state transition (a.u.). The slope of the transition is represented by fitting the firing rate samples during -0.01 to 0.0025 seconds (dashed line) corresponding to the transition from down state and next discharge events. **(E)** Transition slope (a.u.). **(F)** Firing rate during the event (a.u.) (n = 3 ferret slices).

Subsequently, we tested the light-mediated effect of *trans*- (inactive isoform) and *cis*- (active isoform) cryptozepine at 35  $\mu$ M in the presence of 150 nM of IPX (**Figure 4.6A**). We initially recorded the SO as control condition and then applied 150 nM of IPX evoking high-amplitude seizure-like activity. First, the slope of MUA was significantly increased in the transition from Down to the next event with IPX (from  $21.33 \pm 3.20$  a.u. during control condition to  $35.03 \pm 3.80$  a.u. with IPX 150 nM,  $p$ -value = 0.0026; **Figure 4.6C**). Subsequent application of *trans*-cryptozepine had no evident effect on the seizure-like activity. *Trans*-to-*cis* photoconversion of cryptozepine from direct 365 nm illumination of the brain slices changed the pattern of discharge of the seizures to SO. Thus, the activity returned to the control baseline values following a SO activity pattern. The slope was significantly decreased (from  $34.03 \pm 3.20$  a.u. with 35  $\mu$ M *trans*-cryptozepine + 150 nM IPX to  $13.41 \pm 1.44$  a.u. with 35  $\mu$ M *cis*-cryptozepine + 150 nM IPX,  $p$ -value = 0.0022, **Figure 4.6D**) as well as the firing rate during the event (from  $1.72 \pm 0.09$  a.u. with 35  $\mu$ M *trans*-cryptozepine + 150 nM IPX to  $1.72 \pm 0.06$  a.u. 35  $\mu$ M *cis*-cryptozepine + 150 nM IPX,  $p$ -value = 0.0022, **Figure 4.6E**), which was an effect reported during M<sub>2</sub>R activation<sup>21</sup>. In summary, we demonstrate that a photoswitchable M<sub>1</sub>R antagonist (cryptozepine) can modulate muscarinic-induced seizure-like activity by means of illumination.

### 4.3 Discussion and conclusions

In this study, we have demonstrated that light-mediated activation of the photoswitchable M<sub>1</sub>R agonist **BAI** successfully modulates the emergent cerebral cortex network activity, significantly increasing the cortical SO frequency, both in the *ex vivo* isolated cortex and *in vivo* in the anesthetized animal. We also achieved light-mediated blockage of pharmacologically-induced seizure-like activity using the photoswitchable M<sub>1</sub>R antagonist cryptozepine, which antagonized a conventional muscarinic agonist such as CCh and reversed the seizure-like activity caused by the muscarinic superagonist IPX. Overall, we demonstrate that photoswitchable M<sub>1</sub>R ligands enable selectively modulating both physiological and pathological cortical activity with light. Furthermore, these results provide new insights into M<sub>1</sub>R role in cortical dynamics.

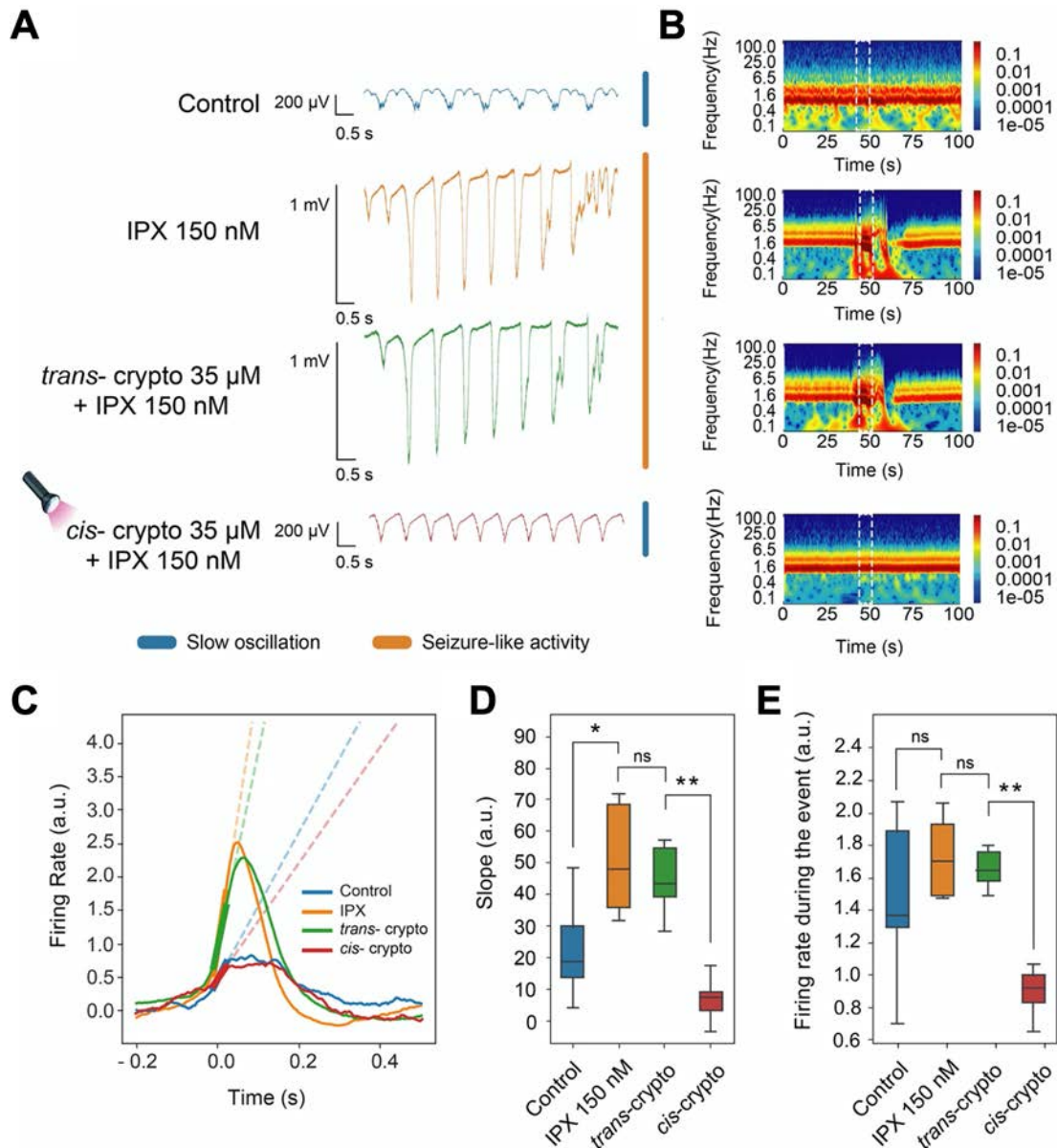


**Figure 4.6. Blockage of seizure-like activity with photoswitchable cryptozepine.** (A) Representative local field potential (LFP) traces during control condition (Control), 150 nM of iperoxo (IPX) (seizure-like activity), 150 nM of IPX + 35  $\mu$ M *trans*-cryptozepine (seizure-like activity, inactive isoform of cryptozepine) and 150 nM of IPX + 35  $\mu$ M of *cis*-cryptozepine. Seizure-like activity appeared after bath application of IPX at 150 nM and it was not blocked by application of 35  $\mu$ M *trans*-cryptozepine. Photoconversion from *trans*-to *cis* led to a total blockage of epileptiform discharges and recovery of the slow oscillation. (B) Representative spectrograms for previous conditions. (C) Firing rate during Down to Up state transition (a.u.) (second 0.0). Representative firing rate during Down to Up state transition (a.u.). The slope of the transition is represented by fitting the firing rate samples during -0.01 to 0.0025 seconds (dashed line) corresponding to the transition from down state and next discharge events transition slope (a.u.). (D) Maximum firing rate during the event (a.u.) (n = 6 ferret slices).

The SO constitute a physiological activity that dominates in slow wave sleep<sup>26</sup> and deep anesthesia<sup>5,31</sup>. SO patterns have been reported locally in pathological situations such stroke<sup>32</sup>, traumatic brain lesions<sup>33</sup> or focal lesions by thermo-coagulation<sup>34</sup>. Cholinergic innervation is a

driving force behind waking from sleep, contributing to the transition from synchronized (sleep) activity patterns to the desynchronized patterns that are associated with wakefulness and conscious processing<sup>35</sup>. Cholinergic drugs have been used to reverse the effects of anesthesia, an action attributed to nicotinic acetylcholine receptors (nAChRs) and M<sub>1</sub> and M<sub>4</sub> mAChRs<sup>36</sup>. Interestingly, an increase in SO frequency like that induced by light-activation of **BAI** was also found in the transition from deep anesthesia to light anesthesia<sup>37-39</sup>. The mechanism of this transition, along with a shortening of the Down state reported here, can be attributed to the blockage that M<sub>1</sub>R agonists exert over KCNQ potassium channels<sup>40</sup>, which results in enhanced excitability. This excitability has been attributed to a reduced medium after hyperpolarization and an enhanced after depolarization in pyramidal neurons<sup>41</sup>. Activation of M<sub>1</sub>R increases the excitability of the network. But to what extent can this increased excitability lead to epileptiform discharges or seizure activity? In a previous study, we demonstrated how a muscarinic super-agonist, IPX, induces epileptiform discharges in the cerebral cortex *ex vivo*<sup>21</sup>. Interestingly, PAI (an M<sub>2</sub>R selective IPX derivative) is not epileptogenic despite increasing excitability<sup>21</sup>. Here, we have found that high concentrations of **BAI** can replicate the epileptiform discharges described for the non-subtype selective IPX (**Figure 4.6A**) by inducing highly excitable and synchronized cortical activity states. This finding points to M<sub>1</sub>R as mediators of epilepsy and in agreement with the effect of the M<sub>1</sub>R antagonist PNZ. The role of M<sub>1</sub> mAChRs in epilepsy was proposed by Cruickshank *et al.*, 1994<sup>19</sup>, who found that CCh-induced seizures are inhibited by PNZ in rats. The differences in network excitability mediated by M<sub>1</sub> mAChR (seizures-like activity appearance) and M<sub>2</sub> mAChR (increase in SO frequency) could be explained by the different intracellular pathways between these two mAChR: while M<sub>2</sub>R activation is mediated by G $\alpha_{i/o}$ -coupled receptors, reducing the ACh level in the cortex as a postsynaptic autoreceptor and activating GABA terminals<sup>42</sup>, M<sub>1</sub>R activation is mediated by G $\alpha_q$ -coupled receptors, which has a suppressive effect on KCNQ channels by blocking membrane hyperpolarization<sup>43</sup> and increasing neuronal firing and epileptogenesis<sup>44,45</sup>.

Photopharmacology offers a direct way of modulating endogenous protein activity without requiring gene manipulation, making it a promising method for neuromodulation. This approach holds great potential for advancing our understanding of brain processes and for developing advanced light-based therapies<sup>21,46</sup>. This could be especially relevant in the treatment of disorders like Alzheimer's disease where M<sub>1</sub>R loss exacerbates cognitive decline<sup>47</sup> and activation of the M<sub>1</sub>R pathway has been suggested to inhibit the deposit of  $\beta$ -amyloid peptides and tau protein phosphorylation, improving cognition<sup>48-51</sup>. Light-mediated activation



of M<sub>1</sub>R could also be applied to treat pathological conditions like in perilesional regions<sup>52,53</sup>, where cortical tissue is "locked" in slow wave states and cannot process information, and in disorders of consciousness<sup>54</sup>.

While **BAI** has been shown promising in modulating SO, it is important to note that there are currently some limitations that must be addressed to fully realize this potential. One of the main limitations is that **BAI** effectiveness as a photoswitchable ligand can be limited since it is not photo-reversible in brain tissue. This is because of the reduced penetration of ultraviolet (UV) light. Nevertheless, this can be overcome with multiphoton excitation using pulsed infrared lasers<sup>55</sup>. For that purpose, the modification of the azobenzene structure is needed<sup>56</sup>, which allows using tissue-penetrating light to switch the drug once it is applied<sup>20,46</sup>. In addition, innovative illumination devices could be implanted in specific regions of the brain cortex with minimal invasiveness. Of course, many aspects need to be further evaluated for the clinical translation of **BAI**, as photoswitchable concentration ranges in humans, photosensitivity, toxicity levels, and blood-brain barrier permeability.

Cryptozepine allows to effectively reverse the effect of the muscarinic agonist CCh in SO by photoswitching its M<sub>1</sub>R antagonism. In addition, we have demonstrated the effectiveness of cryptozepine to block the epileptogenic effects of IPX. These results provide a photopharmacological technology for studying and controlling muscarinic-induced seizures. Moreover, the results further highlight the relevance of M<sub>1</sub>R in hypersynchronous events such as seizures. Cryptozepine photoswitching has the limitation of requiring UV light to operate, which allows limited tissue penetration and duration of light exposure due to potential damage to neuronal DNA<sup>57</sup>. Although we have not observed a significant decrease in the oscillatory frequency after UV light for 10 minutes exposure in ferret slices (**Figure S4.3**), this must be considered to assess the effect of the drug on brain tissue and encourages the design of new drugs susceptible to activation with red or infrared light.

In summary, our findings indicate that M<sub>1</sub>Rs can effectively regulate both physiological SO and pathological epileptic discharges in the cortex. By utilizing photoswitchable M<sub>1</sub>R ligands, we were able to achieve selective modulation of these neural patterns through light stimulation, without the need for gene manipulation. This approach offers a powerful tool for investigating cortical dynamics and exploring potential therapeutic approaches for patients who are unresponsive to conventional treatments.

## References

- 1 McCormick, D. A., Nestvogel, D. B. & He, B. J. Neuromodulation of brain state and behavior. *Annu Rev Neurosci* **43**, 391-415, doi:10.1146/annurev-neuro-100219-105424 (2020).
- 2 Li, C. Y., Poo, M. M. & Dan, Y. Burst spiking of a single cortical neuron modifies global brain state. *Science* **324**, 643-646, doi:10.1126/science.1169957 (2009).
- 3 Gervasoni, D. *et al.* Global forebrain dynamics predict rat behavioral states and their transitions. *J Neurosci* **24**, 11137-11147, doi:10.1523/JNEUROSCI.3524-04.2004 (2004).
- 4 Maloney, K. J., Cape, E. G., Gotman, J. & Jones, B. E. High-frequency gamma electroencephalogram activity in association with sleep-wake states and spontaneous behaviors in the rat. *Neuroscience* **76**, 541-555, doi:10.1016/s0306-4522(96)00298-9 (1997).
- 5 Ruiz-Mejias, M., Ciria-Suarez, L., Mattia, M. & Sanchez-Vives, M. V. Slow and fast rhythms generated in the cerebral cortex of the anesthetized mouse. *J Neurophysiol* **106**, 2910-2921, doi:10.1152/jn.00440.2011 (2011).
- 6 Sanchez-Vives, M. V. M., M. Slow wave activity as the default mode of the cerebral cortex. *Arch Ital Biol* **152**, 147-155, doi:10.12871/000298292014239. PMID: 25828686 (2014).
- 7 Sanchez-Vives, M. V., Massimini, M. & Mattia, M. Shaping the default activity pattern of the cortical network. *Neuron* **94**, 993-1001, doi:10.1016/j.neuron.2017.05.015 (2017).
- 8 Barbero-Castillo, A. *et al.* Impact of GABA<sub>A</sub> and GABA<sub>B</sub> inhibition on cortical dynamics and perturbational complexity during synchronous and desynchronized states. *J Neurosci* **41**, 5029-5044, doi:10.1523/JNEUROSCI.1837-20.2021 (2021).
- 9 D'Andola, M. *et al.* Bistability, causality, and complexity in cortical networks: An *in vitro* perturbational study. *Cereb Cortex* **28**, 2233-2242, doi:10.1093/cercor/bhx122 (2018).
- 10 Lee, S. H. & Dan, Y. Neuromodulation of brain states. *Neuron* **76**, 209-222, doi:10.1016/j.neuron.2012.09.012 (2012).
- 11 Caulfield, M. P. Muscarinic receptors-characterization, coupling and function. *Pharmacol Ther* **58**, 319-379, doi:10.1016/0163-7258(93)90027-b (1993).
- 12 Eglen, R. M. Muscarinic receptor subtype pharmacology and physiology. *Prog Med Chem* **43**, 105-136, doi:10.1016/S0079-6468(05)43004-0 (2005).
- 13 Herrero, J. L. *et al.* Acetylcholine contributes through muscarinic receptors to attentional modulation in V1. *Nature* **454**, 1110-1114, doi:10.1038/nature07141 (2008).
- 14 Volpicelli, L. A. & Levey, A. I. Muscarinic acetylcholine receptor subtypes in cerebral cortex and hippocampus. *Prog Brain Res* **145**, 59-66, doi:10.1016/S0079-6123(03)45003-6 (2004).
- 15 Kruse, A. C. *et al.* Muscarinic acetylcholine receptors: Novel opportunities for drug development. *Nat Rev Drug Discov* **13**, 549-560, doi:10.1038/nrd4295 (2014).
- 16 Bamberg, E., Gartner, W. & Trauner, D. Introduction: Optogenetics and photopharmacology. *Chem Rev* **118**, 10627-10628, doi:10.1021/acs.chemrev.8b00483 (2018).
- 17 Carrera-Canas, C., Garzon, M. & de Andres, I. The transition between slow-wave sleep and REM sleep constitutes an independent sleep stage organized by cholinergic mechanisms in the rostradorsal pontine tegmentum. *Front Neurosci* **13**, 748, doi:10.3389/fnins.2019.00748 (2019).

- 18 Hamilton, S. E. *et al.* Disruption of the M<sub>1</sub> receptor gene ablates muscarinic receptor-dependent M current regulation and seizure activity in mice. *Proc Natl Acad Sci U S A* **94**, 13311-13316, doi:10.1073/pnas.94.24.13311 (1997).
- 19 Cruickshank, J. W., Brudzynski, S. M. & McLachlan, R. S. Involvement of M<sub>1</sub> muscarinic receptors in the initiation of cholinergically induced epileptic seizures in the rat brain. *Brain Res* **643**, 125-129, doi:10.1016/0006-8993(94)90017-5 (1994).
- 20 Riefolo, F. *et al.* Optical control of cardiac function with a photoswitchable muscarinic agonist. *J Am Chem Soc* **141**, 7628-7636, doi:10.1021/jacs.9b03505 (2019).
- 21 Barbero-Castillo, A. *et al.* Control of brain state transitions with a photoswitchable muscarinic agonist. *Adv Sci (Weinh)* **8**, e2005027, doi:10.1002/advs.202005027 (2021).
- 22 Agnetta, L. *et al.* A Photoswitchable dualsteric ligand controlling receptor efficacy. *Angew Chem Int Ed Engl* **56**, 7282-7287, doi:10.1002/anie.201701524 (2017).
- 23 Riefolo, F. *et al.* Rational design of photochromic analogues of tricyclic drugs. *J Med Chem* **64**, 9259-9270, doi:10.1021/acs.jmedchem.1c00504 (2021).
- 24 Gomeza, J. *et al.* Coupling of metabotropic glutamate receptors 2 and 4 to G $\alpha_{15}$ , G $\alpha_{16}$ , and chimeric G $\alpha_{qi}$  proteins: Characterization of new antagonists. *Mol Pharmacol* **50**, 923-930 (1996).
- 25 Sanchez-Vives, M. V. & McCormick, D. A. Cellular and network mechanisms of rhythmic recurrent activity in neocortex. *Nat Neurosci* **3**, 1027-1034, doi:10.1038/79848 (2000).
- 26 Steriade, M., Nunez, A. & Amzica, F. A novel slow (< 1 Hz) oscillation of neocortical neurons *in vivo*: Depolarizing and hyperpolarizing components. *J Neurosci* **13**, 3252-3265, doi:10.1523/JNEUROSCI.13-08-03252.1993 (1993).
- 27 Camassa, A., Galluzzi, A., Mattia, M. & Sanchez-Vives, M. V. Deterministic and stochastic components of cortical down states: Dynamics and modulation. *J Neurosci* **42**, 9387-9400, doi:10.1523/JNEUROSCI.0914-22.2022 (2022).
- 28 Mohr, K. *et al.* Rational design of dualsteric GPCR ligands: Quests and promise. *Br J Pharmacol* **159**, 997-1008, doi:10.1111/j.1476-5381.2009.00601.x (2010).
- 29 Dallanoce, C. *et al.* Synthesis and functional characterization of novel derivatives related to oxotremorine and oxotremorine-M. *Bioorg Med Chem* **7**, 1539-1547, doi:10.1016/s0968-0896(99)00107-8 (1999).
- 30 Sanchez-Vives, M. V. *et al.* Inhibitory modulation of cortical up states. *J Neurophysiol* **104**, 1314-1324, doi:10.1152/jn.00178.2010 (2010).
- 31 Chauvette, S., Crochet, S., Volgushev, M. & Timofeev, I. Properties of slow oscillation during slow-wave sleep and anesthesia in cats. *J Neurosci* **31**, 14998-15008, doi:10.1523/JNEUROSCI.2339-11.2011 (2011).
- 32 Cassidy, J. M. *et al.* Low-frequency oscillations are a biomarker of injury and recovery after stroke. *Stroke* **51**, 1442-1450, doi:10.1161/STROKEAHA.120.028932 (2020).
- 33 Modarres, M. H., Kuzma, N. N., Kretzmer, T., Pack, A. I. & Lim, M. M. EEG slow waves in traumatic brain injury: Convergent findings in mouse and man. *Neurobiol Sleep Circadian Rhythms* **2**, 59-70, doi:10.1016/j.nbscr.2016.06.001 (2017).
- 34 Russo, S. *et al.* Focal lesions induce large-scale percolation of sleep-like intracerebral activity in awake humans. *Neuroimage* **234**, 117964, doi:10.1016/j.neuroimage.2021.117964 (2021).
- 35 Steriade, M., Amzica, F. & Nunez, A. Cholinergic and noradrenergic modulation of the slow (approximately 0.3 Hz) oscillation in neocortical cells. *J Neurophysiol* **70**, 1385-1400, doi:10.1152/jn.1993.70.4.1385 (1993).
- 36 Hudetz, A. G., Wood, J. D. & Kampine, J. P. Cholinergic reversal of isoflurane anesthesia in rats as measured by cross-approximate entropy of the

- electroencephalogram. *Anesthesiology* **99**, 1125-1131, doi:10.1097/00000542-200311000-00019 (2003).
- 37 Dasilva, M. *et al.* Modulation of cortical slow oscillations and complexity across anesthesia levels. *Neuroimage* **224**, 117415, doi:10.1016/j.neuroimage.2020.117415 (2021).
- 38 Torao-Angosto, M., Manasanch, A., Mattia, M. & Sanchez-Vives, M. V. Up and down states during slow oscillations in slow-wave sleep and different levels of anesthesia. *Front Syst Neurosci* **15**, 609645, doi:10.3389/fnsys.2021.609645 (2021).
- 39 Tort-Colet, N., Capone, C., Sanchez-Vives, M. V. & Mattia, M. Attractor competition enriches cortical dynamics during awakening from anesthesia. *Cell Rep* **35**, 109270, doi:10.1016/j.celrep.2021.109270 (2021).
- 40 Selyanko, A. A. *et al.* Inhibition of KCNQ1-4 potassium channels expressed in mammalian cells via M<sub>1</sub> muscarinic acetylcholine receptors. *J Physiol* **522 Pt 3**, 349-355, doi:10.1111/j.1469-7793.2000.t01-2-00349.x (2000).
- 41 Soh, H., Pant, R., LoTurco, J. J. & Tzingounis, A. V. Conditional deletions of epilepsy-associated KCNQ2 and KCNQ3 channels from cerebral cortex cause differential effects on neuronal excitability. *J Neurosci* **34**, 5311-5321, doi:10.1523/JNEUROSCI.3919-13.2014 (2014).
- 42 Douglas, C. L., Baghdoyan, H. A. & Lydic, R. Postsynaptic muscarinic M<sub>1</sub> receptors activate prefrontal cortical EEG of C57BL/6J mouse. *J Neurophysiol* **88**, 3003-3009, doi:10.1152/jn.00318.2002 (2002).
- 43 Brown, D. A. & Adams, P. R. Muscarinic suppression of a novel voltage-sensitive K<sup>+</sup> current in a vertebrate neurone. *Nature* **283**, 673-676, doi:10.1038/283673a0 (1980).
- 44 Jentsch, T. J. Neuronal KCNQ potassium channels: physiology and role in disease. *Nat Rev Neurosci* **1**, 21-30, doi:10.1038/35036198 (2000).
- 45 Schroeder, B. C., Kubisch, C., Stein, V. & Jentsch, T. J. Moderate loss of function of cyclic-AMP-modulated KCNQ2/KCNQ3 K<sup>+</sup> channels causes epilepsy. *Nature* **396**, 687-690, doi:10.1038/25367 (1998).
- 46 Pittolo, S. *et al.* Reversible silencing of endogenous receptors in intact brain tissue using 2-photon pharmacology. *Proc Natl Acad Sci U S A* **116**, 13680-13689, doi:10.1073/pnas.1900430116 (2019).
- 47 Medeiros, R., Baglietto-Vargas, D. & LaFerla, F. M. The role of tau in Alzheimer's disease and related disorders. *CNS Neurosci Ther* **17**, 514-524, doi:10.1111/j.1755-5949.2010.00177.x (2011).
- 48 Caccamo, A. *et al.* M<sub>1</sub> receptors play a central role in modulating AD-like pathology in transgenic mice. *Neuron* **49**, 671-682, doi:10.1016/j.neuron.2006.01.020 (2006).
- 49 Davis, A. A., Fritz, J. J., Wess, J., Lah, J. J. & Levey, A. I. Deletion of M<sub>1</sub> muscarinic acetylcholine receptors increases amyloid pathology *in vitro* and *in vivo*. *J Neurosci* **30**, 4190-4196, doi:10.1523/JNEUROSCI.6393-09.2010 (2010).
- 50 Fisher, A. Cholinergic treatments with emphasis on M<sub>1</sub> muscarinic agonists as potential disease-modifying agents for Alzheimer's disease. *Neurotherapeutics* **5**, 433-442, doi:10.1016/j.nurt.2008.05.002 (2008).
- 51 Melancon, B. J., Tarr, J. C., Panarese, J. D., Wood, M. R. & Lindsley, C. W. Allosteric modulation of the M<sub>1</sub> muscarinic acetylcholine receptor: Improving cognition and a potential treatment for schizophrenia and Alzheimer's disease. *Drug Discov Today* **18**, 1185-1199, doi:10.1016/j.drudis.2013.09.005 (2013).
- 52 Sarasso, S. *et al.* Local sleep-like cortical reactivity in the awake brain after focal injury. *Brain* **143**, 3672-3684, doi:10.1093/brain/awaa338 (2020).
- 53 Gloor, P., Ball, G. & Schaul, N. Brain lesions that produce delta waves in the EEG. *Neurology* **27**, 326-333, doi:10.1212/wnl.27.4.326 (1977).

- 54 Rosanova, M. *et al.* Sleep-like cortical OFF-periods disrupt causality and complexity in the brain of unresponsive wakefulness syndrome patients. *Nat Commun* **9**, 4427, doi:10.1038/s41467-018-06871-1 (2018).
- 55 Izquierdo-Serra, M. *et al.* Two-photon neuronal and astrocytic stimulation with azobenzene-based photoswitches. *J Am Chem Soc* **136**, 8693-8701, doi:10.1021/ja5026326 (2014).
- 56 Cabre, G. *et al.* Rationally designed azobenzene photoswitches for efficient two-photon neuronal excitation. *Nat Commun* **10**, 907, doi:10.1038/s41467-019-08796-9 (2019).
- 57 Kienzler, M. A. *et al.* A red-shifted, fast-relaxing azobenzene photoswitch for visible light control of an ionotropic glutamate receptor. *J Am Chem Soc* **135**, 17683-17686, doi:10.1021/ja408104w (2013).

## Supporting Information (SI) of Chapter 4

### SI4.1 Materials and methods

#### SI4.1.1 Cell culture and transient transfection

Human embryonic kidney tsA201 (HEK tsA201, American Type Culture Collection; ATCC) cells were maintained in Dulbecco's Modified Eagle's Medium/Nutrient Mixture F-12 Ham (DMEM/F12 1:1, Life Technologies) supplemented with 10% fetal bovine serum (FBS; Life Technologies), penicillin and streptomycin (1%, Sigma-Aldrich) in a controlled environment (37°C, 98% humidity and 5% CO<sub>2</sub>).

The cells were transiently transfected with the human M<sub>1</sub> muscarinic acetylcholine receptor (M<sub>1</sub> mAChR or M<sub>1</sub>R; Addgene) or co-transfected with human M<sub>2</sub> muscarinic acetylcholine receptor (M<sub>2</sub> mAChR or M<sub>2</sub>R; Addgene) and chimeric Gα<sub>i</sub>/Gα<sub>q</sub> protein (Gα<sub>qTOP</sub>) with a ratio of 1:1, using X-tremeGENE 9 DNA Transfection Reagent (Roche Applied Science) following the manufacturer's instructions. As generally known, M<sub>1</sub> mAChR prevalently activates the Gα<sub>q</sub> proteins and leads to the activation of the phospholipase C-β (PLC-β) pathway, resulting in the production of inositol 1,4,5-trisphosphate (IP<sub>3</sub>) and the subsequent release of intracellular calcium from the endoplasmic reticulum. In contrast, the M<sub>2</sub> mAChR prevalently activates the Gα<sub>i</sub> proteins, therefore we co-transfected the cells with a chimeric Gα<sub>q/i</sub>-protein (Gα<sub>qTOP</sub>), which couples M<sub>2</sub> mAChR activation with the PLC-β pathway<sup>24</sup>.

The day after, cells were harvested with accutase (Sigma-Aldrich) and seeded onto 16 mm glass coverslips (ThermoFisher Scientific) coated with poly-L-Lysine (Sigma-Aldrich) to allow cell adhesion. Finally, the seeded cells were used for the experiments after 24 h.

#### SI4.1.2 *In vitro* calcium imaging

The calcium imaging assay was performed in the HEK tsA201 cell line, using a calcium indicator Oregon Green BAPTA-1 AM (OGB-1 AM) to determine changes in intracellular calcium concentrations upon receptor activation.

The bath solution used for single-cell intracellular calcium recordings contained: 140 mM NaCl, 5.4 mM KCl, 1 mM MgCl<sub>2</sub>, 10 mM HEPES, 10 mM glucose and 2 mM CaCl<sub>2</sub> (pH 7.4). The calcium indicator used to test benzyl quinolone carboxylic acid-azo-iperoxo (**BAI**) was OGB-1 AM (Life Technologies). Prior to each experiment, cells were mounted on the recording chamber (Open Diamond Bath Imaging Chamber for Round Coverslips from Warner

Instruments) and loaded with OGB-1 AM for 30 min at 37°C with 5% CO<sub>2</sub>, at a final concentration of 10 μM in Ca<sup>2+</sup>-free bath solution. Cells were rinsed with fresh solution, and the recording chamber was filled with 1 ml recording solution and placed on an IX71 inverted microscope (Olympus) with a XLUMPLFLN 20XW 20× water immersion objective (Olympus).

The OGB-1 AM was excited for 50 ms at 488 nm by using a Polychrome V light source (Till Photonics) equipped with a Xenon Short Arc lamp (Ushio Europe B.V.) and a 505 nm dichroic beam splitter (Chroma Technology). Emission at 510 nm was filtered using a D535/40 nm emission filter (Chroma Technology) and finally collected with a C9100-13 EM-CCD camera (Hamamatsu Photonics). Images were acquired at room temperature with an imaging interval of 4 s with SmartLux software (HEKA), and the imaging analysis was executed with Fiji (NIH, ImageJ).

The agonist used to stimulate M<sub>1</sub>R and M<sub>2</sub>R in HEK tsA201 cells was acetylcholine (ACh; Sigma-Aldrich). Application of vehicle (0.1% DMSO), **BAI** and ACh was carried out by manually pipetting a small volume during imaging acquisition into the accessory pool of the recording chamber for the final dilution of approximately 1:1000.

Photostimulation under 1PE during recordings was done by illumination of the entire focused field using the Polychrome V connected to a PC. Shutter and wavelength were controlled using Patchmaster software (HEKA). For all the HEK cell experiments, the light intervals lasted a total of 5 min, with flashes of blue (460 nm, 3.5 s duration) and ultraviolet (UV; 365 nm, 3.5 s duration) light. The light power measured with a Newport 1916-C light meter placed after the objective was 16 W·m<sup>-2</sup> for 488 nm, 5 W·m<sup>-2</sup> for 365 nm, and 16 W·m<sup>-2</sup> for 460 nm.

Control experiments were performed in HEK tsA201 cells not expressing the M<sub>1</sub> mAChR (**Figure S4.1**).

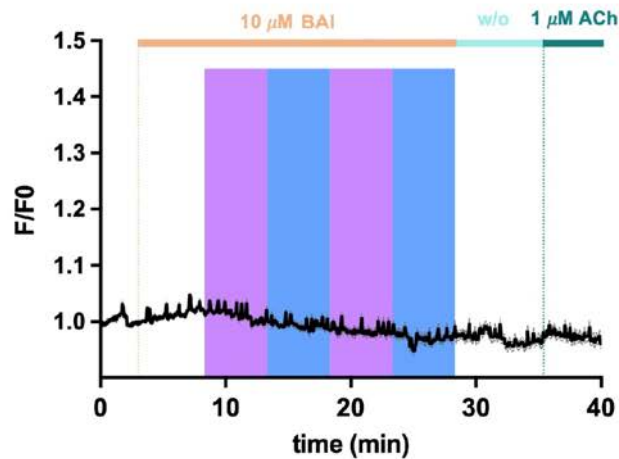


**Figure S4.1.** Control for BAI with *in vitro* calcium imaging experiments in HEK cells without the presence of M<sub>1</sub>R or M<sub>2</sub>R-Gα<sub>TOP</sub>. No calcium oscillations were observed after application of ACh, BAI in the dark-adapted state (*trans*) and under 365/460 nm illumination (n = 20 cells).

### SI4.1.3 Recording in cortical slices *ex vivo*

Isolated cortical slices of ferret fully reproduce slow oscillations compared with other species<sup>1</sup>. For this reason, cortical electrophysiology experiments were carried out in 3/7-month-old ferrets, either sex. All experiments were performed in accordance with protocols approved by the Animal Ethics Committee of the University of Barcelona, which comply with the European Union guidelines on the protection of vertebrates used for experimentation (Directive 2010/63/EU of the European Parliament and the Council of 22 September 2010).

Cortical slices were prepared as previously described<sup>1</sup>. Briefly, ferrets were anesthetized with sodium pentobarbital (40 mg/kg) and decapitated. The entire forebrain was rapidly removed to an oxygenated cold (4-10°C) bathing medium and cut into 400 μm-thick coronal slices (Microm HM 650 V, ThermoFisher Scientific) from the occipital cortex containing primary and secondary visual cortical areas (areas 17, 18, and 19). To increase tissue viability, a modification of the sucrose-substitution technique developed by Aghajanian and Rasmussen (1989)<sup>2</sup> was used during the preparation. Then, slices were placed in an interface-style recording chamber (Scientific Systems Design, Inc.), and bathed for 30 min in an equal mixture of the sucrose-substituted solution and artificial cerebrospinal fluid (aCSF). Afterward, slices were maintained for 2 h in aCSF for recovery. Extracellular local field potential (LFP) was recorded using tungsten electrodes (**Figure 4.2A**). The signal was amplified by 100 using a PGA16 from Multichannel System (Harvard Bioscience). LFP was acquired with Spike2 software (Cambridge Electronic Design) at a sampling rate of 5 kHz.



The effect of cryptozepine was characterized *ex vivo* in ferret slices and is shown in **Figure S4.2**.

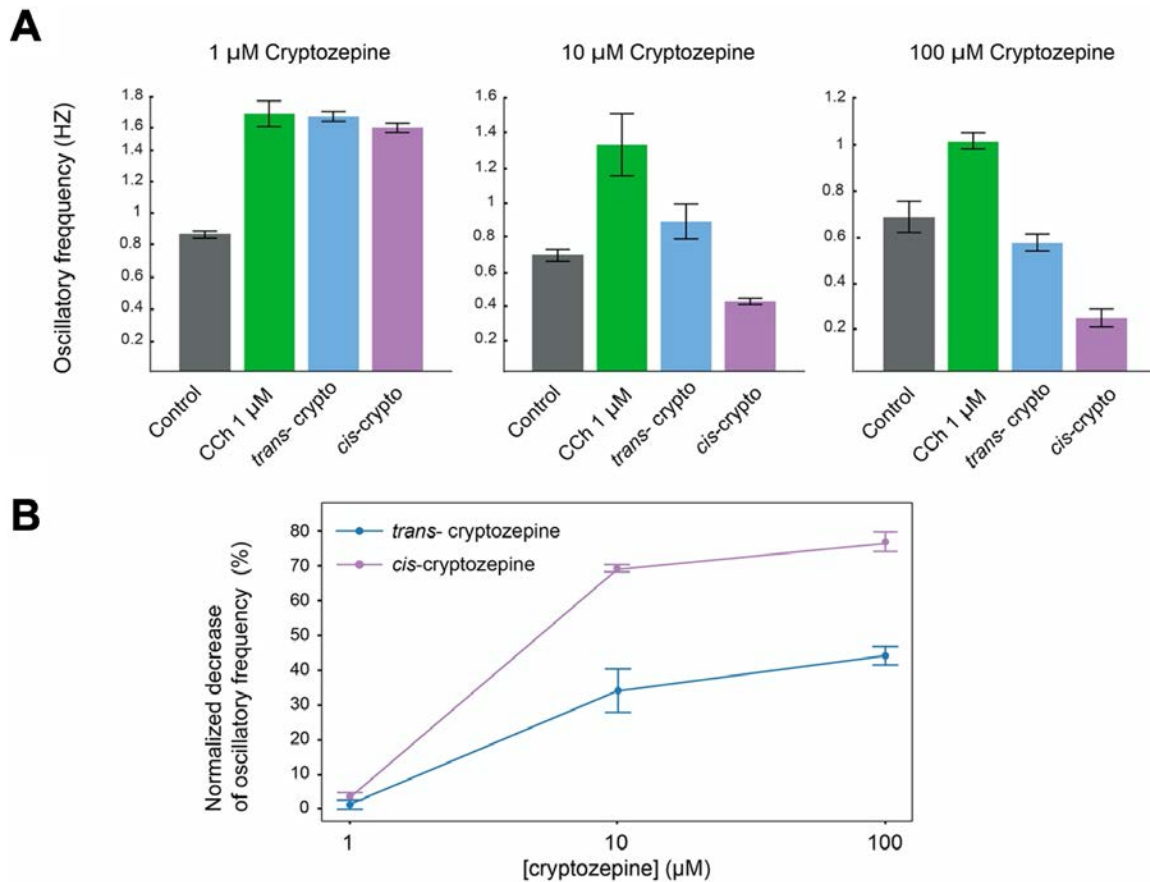


**Figure S4.2. Characterization of the effect of cryptozepine isomers in ferret slices.** (A) Oscillatory frequency (Hz) during control conditions, application of 1 μM carbachol (CCh; 1 μM), 1 μM CCh + *trans*-cryptozepine (*trans*-crypto) and 1 μM of CCh + *cis*-cryptozepine (*cis*-crypto) at different concentrations of cryptozepine (1, 10 and 100 μM, n = 2 ferret slices for each concentration). (B) Normalized decrease of oscillatory frequency (a.u.) of *cis*- (violet, n = 2) and *trans*- (blue, n = 2) cryptozepine for 1, 10 and 100 μM concentration over the effects of the muscarinic agonist 1 μM CCh. These experiments were aimed at estimating the concentration required to achieve effective photoswitching of cryptozepine. Inactive form of cryptozepine, *trans*-cryptozepine showed measurable effects at 10 μM. A lower concentration of cryptozepine and CCh (3 μM cryptozepine/500 nM CCh) was set to achieve effective modulation of slow oscillations by light.

#### SI4.1.4 Recording in mouse neocortex *in vivo*

Cortical electrophysiology experiments *in vivo* were carried out in 2/3-month-old C57Bl6/JR mice (Charles River Laboratories), following the European Union Directive 2010/63/EU, and approved by the local ethics committee. Mice were kept under standard conditions (room temperature, 12:12-h light dark cycle, lights on at 0:00 a.m.). Anesthesia was induced by intraperitoneal injection of ketamine (30 mg/kg) and medetomidine (100 mg/kg). The mice

were fixed in a stereotaxic frame and the body temperature was maintained at 37°C throughout the experiment. A craniotomy was performed in each mouse in the primary visual cortex, V1; coordinates: AP -2.5 mm, L 1.5 mm). Later, a well was made using dental cement and the *cis*-**BAI** was delivered in the craniotomy. LFP was recorded from infragranular layers using a 16-channel in-depth multielectrode array (ATLAS Neuroengineering), which was able to record complete cortical column. Amplification and digitalization hardware and software was equivalent as for the *ex vivo* recordings (see section **SI4.1.3**).

### **SI4.1.5 Drug application**

**BAI** is a dualsteric agonist composed of iperoxo (IPX; the orthosteric moiety), azobenzene (photoswitchable spacer chain), and the benzyl quinolone carboxylic acid (BQCA; allosteric moiety and a M<sub>1</sub> mAChR positive allosteric modulator, **Figure 4.1A**). **BAI** was developed and obtained from the Nanoswitchers research group (IBEC, Barcelona, Spain) and diluted in 98% DMSO (Sigma-Aldrich).

To study the effect of **BAI** on cortical dynamics *ex vivo*, first we obtained **BAI cis**-isomer, which has a lower affinity for M<sub>1</sub> mAChRs (inactive molecule). We applied UV light (365 nm) for 5 min to the stock dilution (100 μM **BAI**), then it was diluted to 1 μM **BAI** and added the interphase chamber bath in the dark. Finally, white light (WL) was applied to obtain the *trans*-isomer (active molecule, **Figure 4.2C**). We waited 1000 s in each condition (control, *cis*-**BAI** and *trans*-**BAI**) to observe the effects of the **BAI** isomers. In the *in vivo* experiments, **BAI** was delivered to the dental cement well following the same experimental sequence as *ex vivo*. The **BAI** concentration used *in vivo* was five times higher than that used *ex vivo*, as previously described<sup>3</sup> for this type of drug delivery. We applied drops of 5 μM of *cis*-**BAI** in dark conditions, and after exposure to 1000 s WL to obtain *trans*-**BAI**.

Cryptozepine is a modified PNZ (M<sub>1</sub> mAChR antagonist) with an azobenzene chain, which allows photoconversion from *trans*- (less active isomer) to *cis*-cryptozepine (isomer with stronger affinity for M<sub>1</sub> mAChRs) when exposed to UV light (365 nm) and in reverse when exposed to 460 nm light or WL.

To study the effect of cryptozepine on the cortical network, carbachol (CCh) was used, an agonist of the five types of mAChR. CCh was applied to the recording chamber at a concentration of 3 μM. Next, we added the lower-affinity *trans*-isomer and exposed the chamber to 10 minutes of UV light to obtain the more active *cis*-isomer. We waited for 1000 s in each condition to observe the effects of the cryptozepine isomers. The UV light lamp was

positioned with a 45°C tilt and 3/4 cm distance from the slices to achieve harmless long-lasting UV exposure providing enough photoconversion of cryptozepine from *trans*- to *cis*-isomers. A UV exposure test was performed under emergent slow oscillations to study the effect of UV light on the slice (**Figure S4.3**).

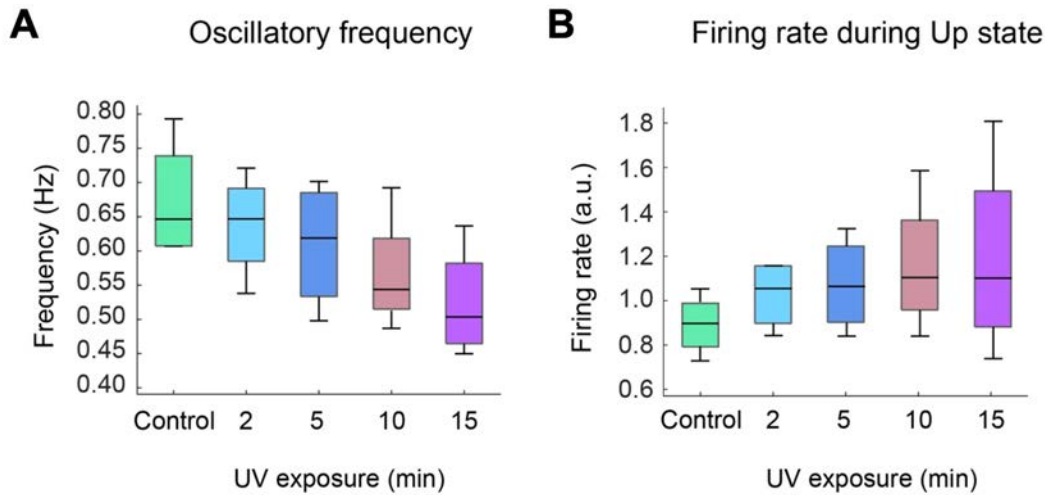


**Figure S4.3. Ultraviolet light exposure test in cerebral cortex slices.** (A) Oscillatory frequency (Hz) after the exposure of ferret slices to UV light (365 nm) for 2, 5, 10 and 15 min ( $n = 4$  ferret slices). No significant changes appeared after UV light exposure to slices although a tendency to decrease in oscillatory frequency is shown. (B) Firing rate during Up state (a.u.) during previous conditions. Experimental setting for cryptozepine photoconversion *trans*-to-*cis* form is not affecting slow oscillation properties. However, UV light could have negative effects for light exposures greater than 10 min.

#### SI4.1.6 Data analysis

Numerical data from calcium imaging experiments were imported to GraphPad Prism version 6.00 for Windows (GraphPad Software). Statistical analysis was performed using one-way ANOVA followed by Tukey's post-hoc test and the paired-sample Wilcoxon signed rank test. The data were normalized over the maximum response obtained with ACh at 1  $\mu$ M and analyzed and presented as mean  $\pm$  SEM.  $p$ -value (\*) < 0.05,  $p$ -value (\*\*) < 0.01,  $p$ -value (\*\*\*) < 0.001,  $p$ -value (\*\*\*\*) < 0.0001.

In the case of cortical electrophysiology recordings, we estimated the MUA from the LFP recordings and quantified Up and Down states, as previously described<sup>4,5</sup>. We obtained the oscillatory frequency (OF) and other variables such as Up and Down state duration, slopes from down to up transitions, which were used to estimate the effect of the photoswitchable drugs. The slope of the down to the next active event (epileptogenic discharge or Up state) was computed by fitting a line over the firing rate data samples surrounding the transition point (10 to 25 ms). A relative firing rate was calculated as previously described in Sanchez-Vives *et al.*,

2010<sup>6</sup> as the peak log(MUA) value during Up states normalized by the log(MUA) during Down states. This measure gives an estimation of the overall network firing rate. Statistical analysis for both *ex vivo* and *in vivo* electrophysiology data was performed using the Friedman test and the Wilcoxon post-hoc test corrected for multiple comparisons in MATLAB R2020b. Data are presented as mean ± SEM. *p*-value (\*) < 0.05, *p*-value (\*\*) < 0.01.

## Additional references

- 1 Sanchez-Vives, M. V. in *Isolated central nervous system circuits. Neuromethods* Vol. 73 (ed K. Ballanyi) (Humana Press, 2012).
- 2 Aghajanian, G. K. & Rasmussen, K. Intracellular studies in the facial nucleus illustrating a simple new method for obtaining viable motoneurons in adult rat brain slices. *Synapse* **3**, 331-338, doi:10.1002/syn.890030406 (1989).
- 3 Barbero-Castillo, A. *et al.* Control of brain state transitions with a photoswitchable muscarinic agonist. *Adv Sci (Weinh)* **8**, e2005027, doi:10.1002/advs.202005027 (2021).
- 4 D'Andola, M. *et al.* Bistability, Causality, and complexity in cortical networks: An *in vitro* perturbational study. *Cereb Cortex* **28**, 2233-2242, doi:10.1093/cercor/bhx122 (2018).
- 5 Reig, R., Mattia, M., Compte, A., Belmonte, C. & Sanchez-Vives, M. V. Temperature modulation of slow and fast cortical rhythms. *J Neurophysiol* **103**, 1253-1261, doi:10.1152/jn.00890.2009 (2010).
- 6 Sanchez-Vives, M. V. *et al.* Inhibitory modulation of cortical Up states. *J Neurophysiol* **104**, 1314-1324, doi:10.1152/jn.00178.2010 (2010).



# Chapter 5

---

## Photoreversible modulation of brain activity with infrared light

---

---

**Rosalba Sortino**<sup>¶</sup>, Hubert Gerwe<sup>¶</sup>, Galyna Maleeva, Maria Calvo, Carles Justicia, Fabio Riefolo, Ekin Opar, Marcel Bermudez, Anna Maria Planas, Carlo Matera, Michael Decker\* and Pau Gorostiza\*. **Photoreversible modulation of brain activity with infrared light.** *In prep.* <sup>¶</sup>These authors contributed equally. \*Corresponding authors: michael.decker@uni-wuerzburg.de (M.D.) and pau@icrea.cat (P.G.).



## Abstract

Photoswitchable ligands enable reversible control of receptor activity by light-dependent isomerization between an active or inactive isomer. Great progress has been made to shift the operating wavelengths of azobenzene based photoswitchable ligands towards the visible spectrum while maintaining thermodynamically stable isomers. However, bidirectional switching with red/near-infrared (NIR) light under physiological conditions remains a challenge and an important limitation *in vivo*. We have developed a set of bistable, photoswitchable xanomeline derivatives (“xanoswitches”) that are inactive in the dark and display agonist activity in muscarinic acetylcholine receptors (mAChRs or MRs) which can be toggled by conventional one-photon as well as by two-photon excitation (2PE). Xanoswitches can be operated bidirectionally with tissue-penetrating NIR wavelengths (730 nm, 800 nm and 910 nm) using 2PE and enable reversibly activating and deactivating mAChRs *in vitro* and *in vivo* in the mouse brain. These novel compounds offer the opportunity to study the role of endogenous mAChRs in intact tissue with unprecedented precision and open the way for noninvasive and pharmacologically-selective neuromodulation therapies.





## 5.1 Introduction

Controlling the activity of selected endogenous proteins using patterns of illumination would be key to understanding their physiological roles and molecular mechanisms, and to apply personalized interventions. Such is the stated purpose of photopharmacology<sup>1-3</sup>, a field that has considerably expanded in recent years based mostly on demonstrations *in vitro*, which are exemplified by the large number of reported photoswitchable ligands of G protein-coupled receptors (GPCRs; for reviews see Ricart-Ortega *et al.*, 2019 and Wijtmans *et al.*, 2022)<sup>4,5</sup>.

However, mechanistic insights and therapeutic demonstrations are most significant in experiments with animals, due in part to the higher usability and safety demands they pose to the technology. Most photoswitchable moieties are operated at ultraviolet-visible (UV-Vis) wavelengths (which are absorbed and scattered by biomolecules, leading to tissue penetration depth below ~100  $\mu\text{m}$ ) and using continuous wave illumination (whose excitation volume spans the entire light beam due to the linear dependence of one-photon absorption with intensity)<sup>6</sup>. Thus, the available photopharmacological drugs cannot deliver the promise of noninvasive, specific pharmacological action with spatiotemporal selectivity in three dimensions.

In principle, intensity attenuation and tissue damage could be reduced by shifting the drug photoswitching wavelengths into the low absorption “biological window” (650–1100 nm). However, despite the efforts in the field to red-shift the one-photon excitation (1PE) wavelengths<sup>7-12</sup>, only few reported compounds achieve photo-reversible red or near-infrared (NIR) switching and these are not soluble and/or not reversibly isomerizable<sup>13</sup> under physiological conditions<sup>7</sup>. Moreover, red light excitability is often accompanied by faster relaxation of the less thermodynamically stable photo-isoform<sup>8</sup>, which is disadvantageous in some applications. In general, many substituents required in red-shifted photoswitches become a liability to target sterically hindered binding pockets, such as those of most GPCRs. Thus, water-soluble, reversible, and red-shifted photoswitchable moieties are yet to be found for photopharmacology and the field is still dominated by photoswitches operated with light displaying low tissue penetration<sup>4,12</sup>.

Besides these chemical difficulties, the large excitation volume associated to continuous wave illumination mentioned above is an intrinsic limitation of 1PE regardless of wavelength and constitutes a major hurdle for basic and clinical photopharmacology. This is paradigmatic in the nervous system, whose intricate architecture of circuits, proximity between different neural cells and glia, and compartmentalization of intra- and extracellular signaling processes in

spines, boutons, and synaptic clefts are certain to blur the action of even the most target-selective photopharmacological drugs. While photopharmacology has already shown its value using continuous illumination of large brain structures<sup>14,15</sup>, arguably its greatest potential lies at controlling drug action at submicrometric cellular compartments. To meet both requirements of deep tissue penetration and focalized photoswitching, multiphoton pharmacology (MPP) takes advantage of NIR pulsed lasers and nonlinear absorption of certain photochromic moieties. In the case of two-photon excitation (2PE), the photoisomerization rate depends on the square of the intensity of light and thus, drug photoswitching by 2PE is constrained to the focal point of a femtosecond-pulsed laser beam wherein the photon flux is sufficiently high, while remaining negligible elsewhere in the optical path<sup>16</sup>. Hence, 2PE and MPP in general enable micrometric resolution in three dimensions<sup>17</sup> as well as patterned illumination<sup>18-20</sup>. In addition, 2PE allows isomerization to occur with half the energy per photon, which corresponds to twice the wavelength required for 1PE (typically, non-substituted azobenzenes that switch at 365 nm can also be switched by 2PE around 730 nm in the NIR range). Thus, in turn, 2PE provides deep penetration into tissue<sup>14,21-24</sup>.

The advantages of MPP come at the price of using relatively large laser equipment and optics for focusing and for pulse dispersion compensation, although miniscopes coupled to fiber lasers have been recently developed for 2PE brain activity imaging in freely moving mice<sup>25-28</sup>. Besides, photoswitches with significant 2PE cross section are required<sup>29</sup>. Electronically symmetric azobenzene is in principle not susceptible to isomerize by 2PE, but in practice some have been used for MPP<sup>21-23,29,30</sup>. Their 2PE cross section can be increased by introducing 2P-antennas which transfer energy to the photoswitch by Förster resonant energy transfer (FRET)<sup>21,31</sup>, or by increasing the 2PE absorption cross section of the azobenzene itself<sup>20</sup>. Since many 2PE antennae are large and poorly soluble in water<sup>21</sup>, a convenient option for azobenzenes is to increase their electronic asymmetry by introducing strong push-pull systems<sup>21,32,33</sup> or by a combination of a weak push-pull system together with asymmetric substitution of strong inductive electron-withdrawing groups<sup>22</sup>. These approaches achieve outstanding 2PE functional responses that may reach equivalent magnitude to 1PE responses.

Push-pull substitutions have been applied to photoswitchable tethered ligands in which the azobenzene is far from the ligand and is not involved in binding. However, this convenient approach is not directly transferable to freely diffusible photochromic ligands that fit snugly in the binding pocket of a GPCR. Such targets require small ligands with an intrinsic electronic

distribution that is part of their pharmacophore and that is generally not amenable to additional modifications for 2PE switching or other purposes<sup>23</sup>.

Here, we introduce isosteric, single atom modifications as the key last step to turn a potent photochromic ligand that is 2PE inactive into one that is fully 2PE-enabled. We show that a compound optimized in this way allows for the first time the photoreversible modulation of excitation with two different NIR wavelengths *in vivo*.

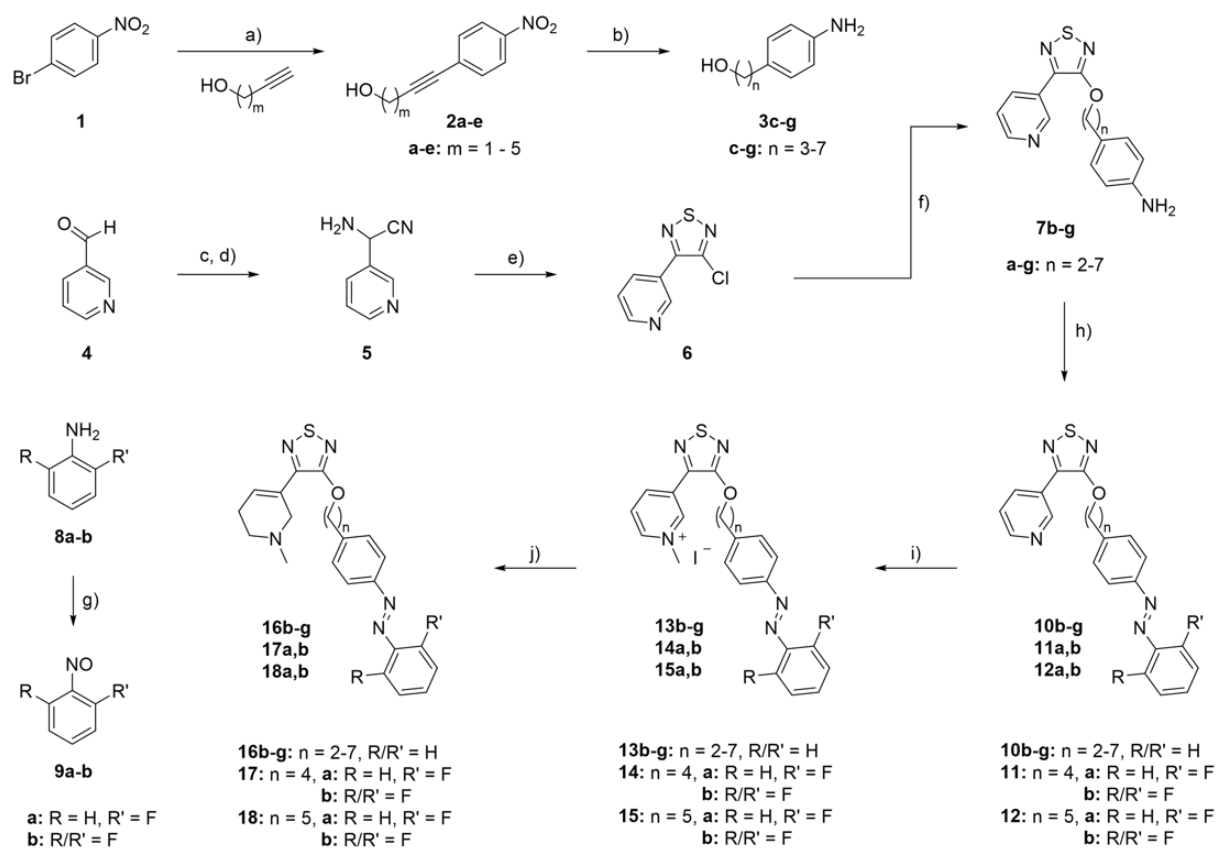
This achievement must be framed within an integral plan to design photoswitches optimized for MPP of the brain *in vivo*, which includes several steps: (a) selection of muscarinic acetylcholine receptor (mAChR or MR) targets (both M<sub>1</sub>R and M<sub>2</sub>R) as privileged neuromodulators of emergent brain activity<sup>14</sup>, (b) selection of xanomeline as parent compound to inherit at least some of the best-of-its-kind properties (including potency, efficacy, solubility, drug-likeness, bioavailability)<sup>34-38</sup>, (c) design of photoswitchable xanomeline derivatives (“xanoswitches”) by introduction and rational optimization of unmodified azobenzene photoswitches for dark-inactive operation at nanomolar concentrations, and finally (d) MPP optimization as mentioned above, while retaining all the other properties.

Using this method and the unique compounds that we have discovered, we can increase and decrease neuronal activity with NIR light in both directions *in vivo*, a milestone in the path towards noninvasive photopharmacology and an unprecedented tool both for brain neuromodulation and for dissecting the mechanisms of mAChR-mediated signaling at the scale of neuronal compartments.

## 5.2 Results

### 5.2.1 Rational design and chemical synthesis

Based on the thoroughly conducted structure-activity relationship (SAR) studies of the late 90s<sup>39,40</sup> and the experiences with M<sub>1</sub>R ligands of our research groups<sup>41-44</sup>, it was apparent that xanomeline would allow introduction of an azobenzene only at the aliphatic chain. Naturally, this raised the question on which linker length between the thiadiazole core and the azobenzene would not only fit in the receptor, but also result in a pronounced activity difference upon photoisomerization. To study the effect of the linker length, various xanoswitches (**16a-g**) with linker lengths ranging from one to seven carbon atoms were synthesized (**Scheme 5.1**).



**Scheme 5.1. Synthesis of one- and two-photon switchable xanomeline derivatives.** Reagents and conditions: (a) CuI, PdCl<sub>2</sub>(PPh<sub>3</sub>)<sub>2</sub>, PPh<sub>3</sub>, NEt<sub>3</sub>/THF, 70°C, 64-98%; (b) Pd/C, 10 bar H<sub>2</sub>, MeOH, RT, 80%, quant.); (c) KCN, H<sub>2</sub>O, HOAc, 0°C to RT, 80%; (d) NH<sub>4</sub>Cl/NH<sub>3</sub> (aq.), RT, 49%; (e) S<sub>2</sub>Cl<sub>2</sub>, DMF, 9N NaOH, 0°C, 63%; (f) 3c-g/2-(4-aminophenyl)ethan-1-ol (**3b**), NaH, THF, 70°C, 49-71%; (g) Oxone®, H<sub>2</sub>O/ CH<sub>2</sub>Cl<sub>2</sub>, RT; (h) nitrosobenzene (**9a-c**), HOAc, RT, 56-93%; (i) MeI, Acetone, RT, 77-99% and (j) NaBH<sub>4</sub>, MeOH, 0°C to RT, 30-78%.

Based on the results of this first set of xanoswitches (*vide infra*), we explored whether small functional modifications, which presumably would not affect 1PE photochemical properties including the thermodynamic stability of the *cis*-isomer, would enable 2PE switching. To introduce the required electronic asymmetry with minimal changes in overall geometry, fluorine as strongly inductive electron withdrawing group was introduced at the *ortho* position of the “best-in-class” compounds **16d** and **16e**. Starting with mono- and difluorination approaches the distal benzene ring of the azobenzene was chosen for modification since *ortho* substitution at the proximal ring was more likely to interfere with closing of the tyrosine lid (*vide infra*) and would thereby risk losing the functionality of the switch. Since introduction of fluorine at the proximal ring would require derivatization in the beginning of the synthesis (**Scheme 5.1**), this approach also allowed a more straightforward synthesis towards the potential 2PE ligands (**17a,b**; **18a,b**). For the synthesis of the linker lengths 3C-7C, a Sonogashira cross coupling reaction was employed to couple 1-bromo-4-nitrobenzene (**1**) to

the respective alkyne-alcohols. The resulting 4-nitrophenyl-alkyne-alcohols (**2a-e**) were reduced by palladium-catalyzed hydrogenation which gave the 4-aminophenyl-alkane-alcohols (**3c-g**). The corresponding C1 (**3a**) and C2 (**3b**) compounds were obtained from chemical suppliers. However, the C1 compound could not be used in the next reaction, as the strongly basic conditions lead to its decomposition. Hence, a slightly different route was chosen to obtain azobenzene **10a**. The thiadiazole core fragment (**6**) was synthesized according to literature<sup>40</sup>. Starting from nicotinaldehyde (**4**) a two-step Strecker-like synthesis was employed to form the aminonitrile (**5**). Subsequent cyclization of compound **5** using sulfur monochloride in DMF gave the desired 3-chloro-4-(pyridin-3-yl)-1,2,5-thiadiazole (**6**). In a nucleophilic aromatic substitution, employing Williamson ether synthesis reaction conditions, 4-aminophenyl-alkane-alcohols **3b-g** were coupled to the thiadiazole core (**6**), resulting in the thiadiazole-anilines (**7b-g**). Formation of the corresponding azobenzenes (**10b-g**; **11a,b**; **12a,b**) was achieved in a Baeyer-Mills reaction, condensing the anilines with the respective nitrosobenzene in acetic acid. Nitrosobenzenes (**9a,b**) were synthesized by partial oxidation of the corresponding anilines in a heterogeneous water/dichloromethane system using Oxone<sup>®</sup> and directly used without further purification. Quaternization of the pyridine by *N*-methylation with iodomethane in acetone was followed by reduction of the resulting pyridinium cations (**13a-g**; **14a,b**; **15a,b**) with sodium tetraborohydrid in methanol to regioselectively yield the desired 1-methyl-1,2,3,6-tetrahydropyridines (“xanoswitches”, **16a-g**; **17a,b**; **18a,b**).

### 5.2.2 Photochemical characterization

The 1PE photochemical properties of the azobenzenes were not altered by mono-fluorination. The most enriching wavelengths were conserved at 455 and 400 nm for maximal *trans*-enrichment and 365 nm for maximal *cis*-enrichment. Also, no decomposition upon irradiation and the typical thermal stability were observed (see the **Supplementary Information**; **SI**, for details). Difluorination, however, resulted in lower *cis*-enrichment upon irradiation with 365 nm (PSS<sub>365 nm</sub>: *cis/trans* = 70:30). Notably, it also resulted in a change of the most *trans*-enriching wavelengths (PSS<sub>455 nm</sub> < PSS<sub>400 nm</sub>), but without significant changes of the corresponding *cis/trans* ratio (~20:80). Like the non- and mono-fluorinated xanoswitches, the difluorinated xanoswitches showed no photobleaching and the thermal stability of the *cis*-isomer was not altered.

### 5.2.3 Split luciferase complementation assay

The whole set was tested under IPE conditions at their maximally *cis/trans*-enriched photostationary states (PSSs) for the ability to activate the human M<sub>1</sub>R *in vitro*. A split luciferase complementation assay (SLCA) which detects interactions between G $\alpha_q$  and its effector phospholipase C- $\beta_3$  (PLC- $\beta_3$ ) as a quantifiable parameter of receptor activation was employed (**Figure 5.1** and **Table S5.1**)<sup>45</sup>. The wavelength emitted by the modified luciferase from the click-beetle *Pyrophorus plagiophthalmus* ( $\lambda_{\text{max}} = 613$  nm) shows at the given intensity no interference with the compounds photoisomerization<sup>46</sup>.

All xanoswitches were shown to be “*cis*-on”, that means, more active in their thermodynamically less stable *cis* form, which is a desired feature for the majority of photopharmacological applications. This way, the photoswitch can on its own only turn itself inactive instead of spontaneously forming the bioactive isomer by thermal relaxation in the dark.

With exception of the almost inactive C1 derivative (**16a**), the whole set consists of highly potent agonists comparable in potency to the parent compound xanomeline itself ( $EC_{50}(\text{xanomeline}) = 83$  nM). However, while C2 (**16b**) and C3 (**16c**) linker lengths resulted in active molecules with an up to two-digit nanomolar potency, these compounds do not show a strong potency or efficacy shift upon irradiation. Useful functional photoswitching is only observed employing linker lengths of C4 (**16d**) and C5 (**16e**), both resulting in an approximately 3-fold increase of potency upon irradiation with ultraviolet (UV) light. Additionally, compound (**16e**) shows a 25% reduced maximal efficacy in its *trans* form. Further elongation of linker lengths leads to an overall reduced maximal efficacy ( $E_{\text{max}} = \sim 80\%$ ) and a decrease in functional photoswitching, rendering (**16d** and **16e**) the best leads for 2PE optimization. Previous work had shown that tetra-*ortho*-fluorination at orthosteric M<sub>1</sub>R ligands can have a significant effect on the biological properties of a photoswitchable ligand<sup>43</sup>. Therefore, potential 2PE xanoswitches (**17a,b** and **18a,b**) were characterized under IPE conditions in the SLCA to check whether their biological properties were altered by fluorination (**Figure 5.1**).

Activity and functional IPE switching were preserved for the mono-fluorinated xanoswitches (**17a**, **18a**), with **18a** showing even a slightly improved *cis/trans* activity difference ( $EC_{50\text{trans}}/EC_{50\text{cis}} = 3.3$ ) but at the cost of reduced efficacy switching. Interestingly, the di-fluorinated C4 compound **17b** showed a complete loss of functional photoswitching while maintaining its agonistic properties (**17b**: *cis* = *trans*:  $EC_{50} \sim 130$  nM,  $E_{\text{max}} \sim 96\%$ ).

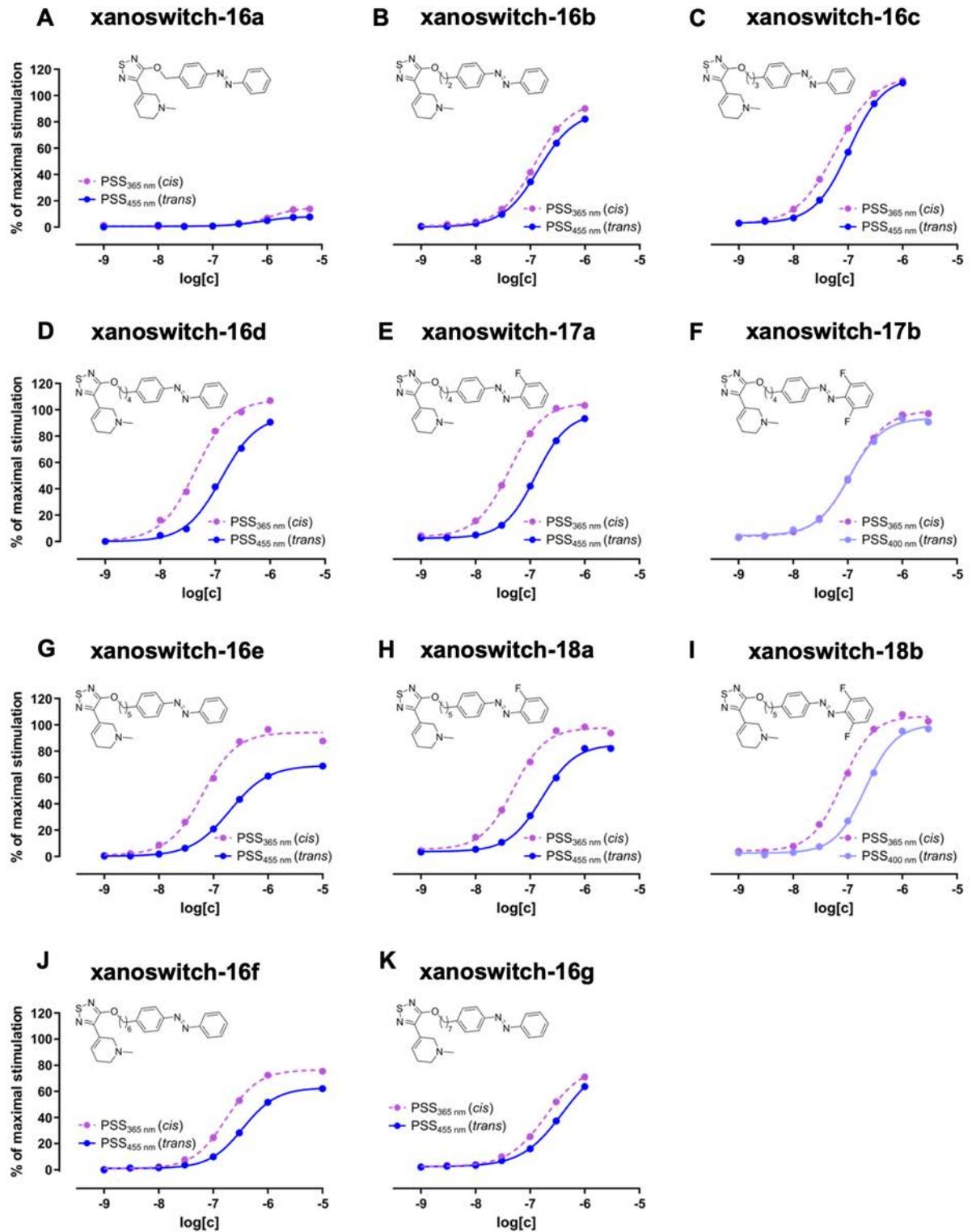


**Figure 5.1.** *In vitro* characterization of photoswitchable M<sub>1</sub> mAChR ligands using a split luciferase complementation assay. This assay detects the interaction between Gα<sub>q</sub> and its effector phospholipase C-β<sub>3</sub> (PLC-β<sub>3</sub>) as a quantifiable parameter of receptor activation. Dose response curves of best-in-class xanoswitches-**16d** and **-16e** and their 2PE derivatives (**17a,b**; **18a,b**) in their *cis*- and *trans*-enriched states, respectively.



The corresponding di-fluorinated C5 compound **18b** retained functional photoswitching, although with a significant reduction in its potency difference which might be due to the suboptimal *cis/trans* ratio in its *cis*-enriched state under 1PE conditions. As a whole, the fluorinated set demonstrates the sensitivity of the receptor to even smallest ligand modifications, underlining the importance to find minor modifications which enable 2PE switching<sup>2,8</sup>.

### 5.2.4 Molecular docking

Interestingly, the best linker length of four and five carbon atoms in combination with the azobenzene moiety results in a side-chain more than twice as long as the length of the parent compounds side-chain. To get a better understanding of the compounds and the obtained pharmacological effects, we performed molecular docking of xanoswitch-**16d** (Figure 5.2). Based on the cryo-electron microscopy structure of the active M<sub>1</sub>R (PDB ID: 6OIJ), docking of **16d** showed that the xanomeline substructure resembles the binding mode of orthosteric agonists, while the azobenzene scaffold protrudes in the extracellular loop region. The dynamic nature of the so-called tyrosine lid, which closes over the orthosteric binding site, provides a possibility for extended ligands to interact with residues in the extracellular loop region.

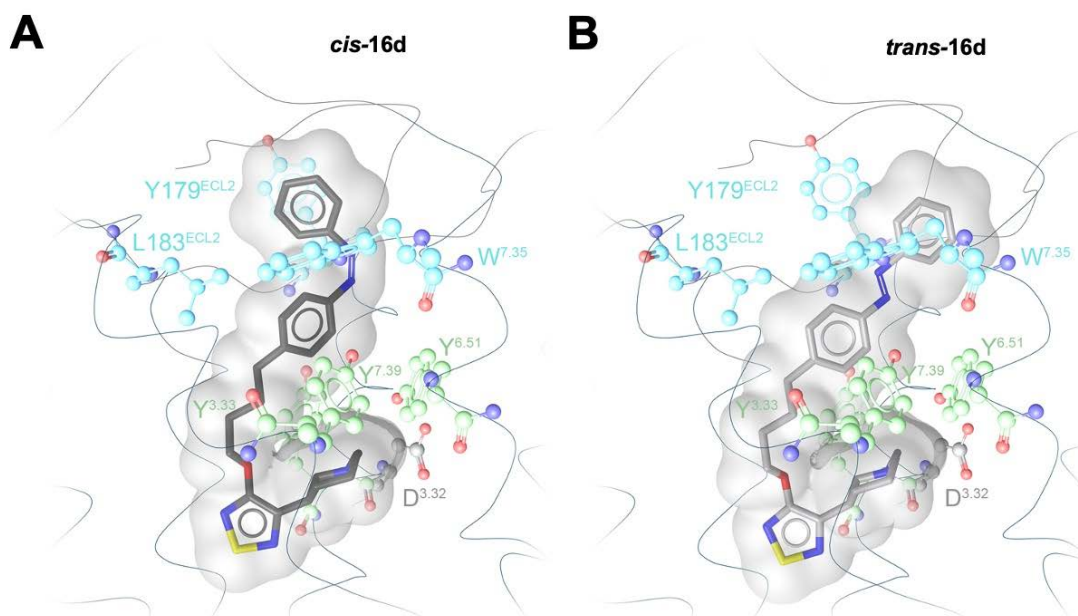


**Figure 5.2. Docking pose of *cis*- and *trans*-xanoswitch-16d.** In the *cis* configuration (A), the distal benzyl ring lays directly between two key residues of the allosteric binding site (Y179<sup>ECL2</sup>, L183<sup>ECL2</sup>, and W7.35). This binding mode is likely to be favorable when compared to (B) the *trans*-configuration of **16d** that is not directly engaged with these allosteric hotspots. The tyrosine lid which closes the orthosteric binding site is depicted in green and allosteric key residues are highlighted in blue.

The length of the linker is critical to enable closing of the tyrosine lid which is pivotal for receptor activation<sup>47</sup>. Spatial interference with the lid is linked to reduced receptor activation and in the latest consequence with antagonistic effects. A linker length of 4 carbon atoms results in a perfect positioning of the distal benzene ring which interacts with key residues of the allosteric vestibule (Y179<sup>ECL2</sup>, L183<sup>ECL2</sup>, and W<sup>7.35</sup>), avoiding steric obstruction between the azobenzene moiety with the tyrosine lid. While there is some flexibility in regard to the linker length, shorter linker would result in interference of the azobenzene with the tyrosine lid closure (**16a**) and longer linkers would result in a position of the azobenzene that is unfavorable to interact with residues of the allosteric vestibule (**16f,g**).

### 5.2.5 *In vitro* calcium imaging

The pharmacological properties of the “best-in-class” **16e** and its mono and di-ortho derivatives (**18a** and **18b**) were tested for their ability to induce cytosolic calcium oscillations *in vitro* under 1PE and 2PE conditions. (**Figure 5.3**)<sup>15</sup>. First, fluorescence imaging with genetically encoded calcium sensor GCaMP6s (excitation 488 nm, emission 510 nm) was performed before and after 1PE of the compounds with UV light of 365 nm (**Figure 5.3A-F**), which showed that the cytosolic calcium oscillations were induced by the *cis* form of the compounds but not by the *trans* form. Moreover, the photoresponses could be dynamically photomodulated. Converting the compounds to the *trans* configuration live on the cells, using 455 nm for **16e**, **18a** and 400 nm for **18b** (**Figure 5.3A-C**) resulted in significantly reduced responses which could be reverted by irradiation with 365 nm light. Neither the application of the compounds in *trans* (dark-adapted state) nor 1PE alone elicited fluorescence responses. The muscarinic agonist acetylcholine (ACh) served as positive control in all the experiments. The responses under the application of the *trans* forms and upon photoswitching with 1PE (*cis* forms) for the selected compounds were quantified by peak amplitude and the analysis showed a complete on/off switching at several concentrations (**Figure 5.3D-F**). Fluorescence photoresponses were only observed in cells expressing M<sub>1</sub> mAChRs (**Figure S5.14A-C**).

We further aimed to monitor and manipulate the activity of M<sub>1</sub> mAChR with 2PE of xanowitches-**18a** and -**18b** using calcium imaging in an inverted laser-scanning microscope equipped with a pulsed NIR laser (**Figure 5.3G-L**) and the described calcium imaging assay. The utilized wavelengths for 2PE experiments correspond to twice the wavelength used for 1PE. Dark adapted xanowitches-**18a** and -**18b** caused no fluorescence increase, but irradiation with 730 nm produced M<sub>1</sub> mAChR activation, indicating that *trans*-to-*cis* isomerization had occurred.

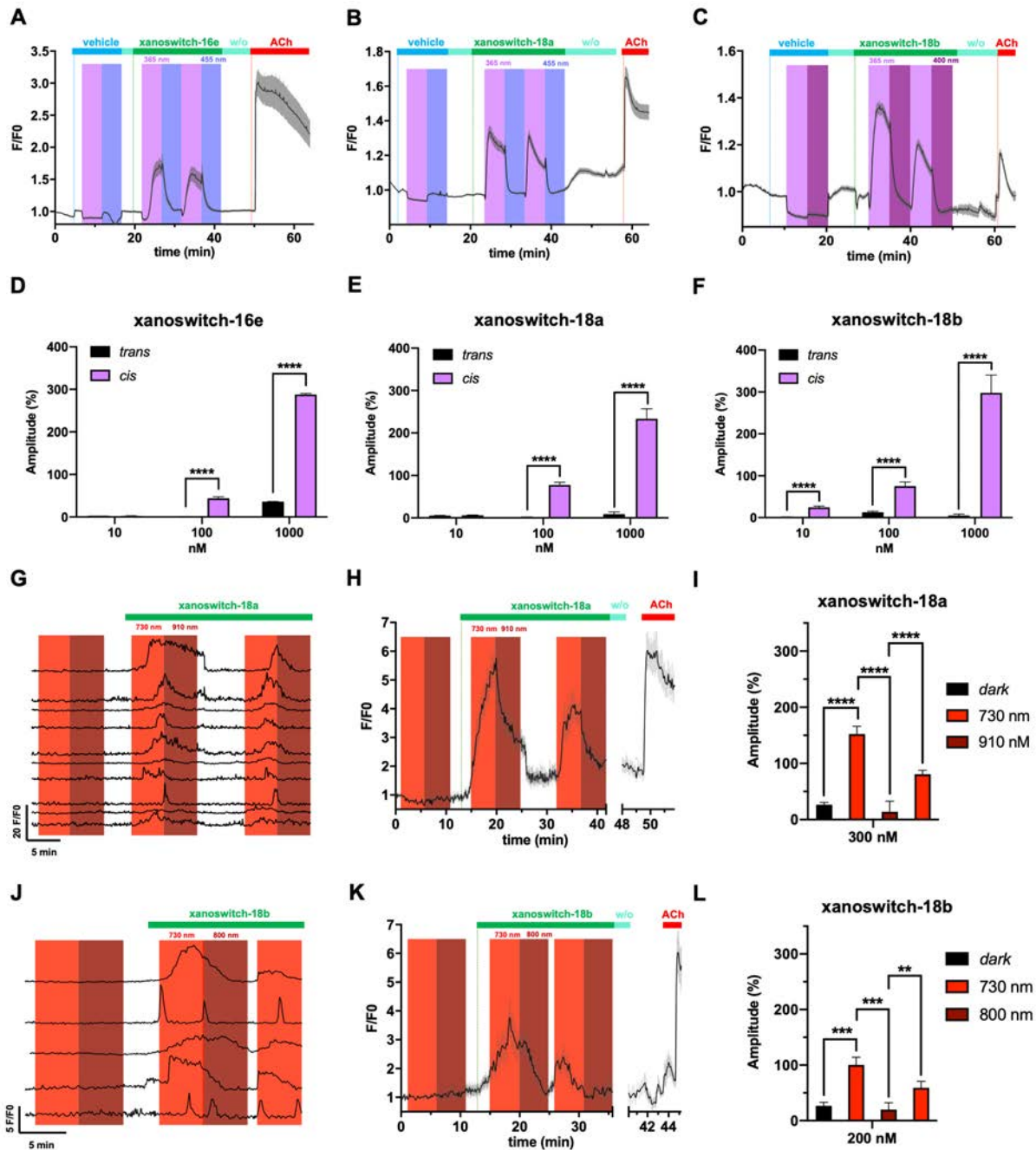


**Figure 5.3. *In vitro* characterization of photoswitchable M<sub>1</sub> mAChR ligands using calcium fluorescence imaging under one-photon excitation versus two-photon excitation.** (A, B and C) Time course of F/F<sub>0</sub> responses in cells overexpressing M<sub>1</sub> mAChR (black trace indicates the average and the grey band corresponds to the standard error of the mean; SEM) in the presence of vehicle, (A) 100 nM xanoswitch-16e (n = 37 cells), (B) 100 nM 18a (n = 62 cells) and (C) 100 nM 18b (n = 76 cells), where 500 nM ACh was used as a positive control for all compounds. Photoisomerization under one-photon excitation (1PE) occurred by alternating 365 nm and 455 nm for 16e and 18a and 365 nm and 400 nm for 18b. (D, E and F) Quantification of M<sub>1</sub> mAChR 1PE responses by (D) 16e, (E) 18a and (F) 18b. The compounds yielded significant differences between 365 nm and 455 nm or 400 nm illumination at different concentrations 10 nM (n = 51 cells for 16e; n = 65 cells for 18a; n = 43 cells for 18b); 100 nM (n = 37 cells for 16e; n = 94 cells for 18a; n = 48 cells for 18b); 1000 nM (n = 71 cells for 16e; n = 48 cells for 18a; n = 76 cells from 18b). (G and H) Example traces (G, n = 10 cells) and average (H, n = 70 cells)

of calcium activity ( $F/F_0$ ) under two-photon excitation (2PE) alternating 730 nm and 910 nm illumination alone (control) and in the presence of 300 nM **18a**. Responses are elicited upon photoconversion to *cis*-**18a** by 730 nm and are terminated by **18a** under 910 nm light. Subsequent *trans*-to-*cis* isomerization under 730 nm light rapidly reactivated  $M_1$  mAChRs. (**J** and **K**) Example traces (**J**,  $n = 5$  cells) and average (**K**,  $n = 15$  cells) of calcium activity ( $F/F_0$ ) under 2PE alternating 730 nm and 800 nm illumination alone (control) and in the presence of 200 nM **18b**. Responses were observed upon photoconversion to *cis*-**18b** by 730 nm and were inhibited by **18b** under 800 nm light. Subsequent *trans*-to-*cis* isomerization under 730 nm light rapidly reactivated  $M_1$  mAChRs. (**I** and **L**) Quantification of  $M_1$  mAChR photoresponses by 300 nM **18a** (**I**,  $n = 71$  cells) and 200 nM **18b** (**L**,  $n = 16$  cells) showed reversible and significant bidirectional photoswitching under 2PE. Statistical analysis of **panel D, E, F, I** and **L** were performed by the paired sample Wilcoxon signed rank test ( $p$ -value (\*\*\*\*)  $< 0.0001$ ;  $p$ -value (\*\*\*)  $< 0.001$ ;  $p$ -value (\*\*\*)  $< 0.01$ ) using GraphPad Prism 9. Error bars indicate  $\pm$  SEM.

Interestingly, the observed photoresponses could be completely inhibited under 2PE at longer wavelengths, suggesting that *cis*-to-*trans* photoisomerization is also viable. More specifically, we used 910 nm, for **18a** (*i.e.*, twice the optimal wavelength for 1PE, 455 nm, **Figure 5.3GH**) and 800 nm, for **18b** (*i.e.*, twice the optimal wavelength for 1PE, 400 nm, **Figure 5.3JK**). Again, the *trans* forms did not produce calcium responses, and 2PE alone did not produce any stimulation artefacts. Photoresponses required  $M_1$ R expression (**Figure S5.14D-F**). These results are quantified in **Figure 5.3IL** and demonstrate that both xanoswitch-**18a** and -**18b** can isomerize in both ways using 2PE, with **18a** showing better bidirectional switching.

### 5.2.6 *In vitro* neuronal photocontrol in hippocampal neurons

Compounds **18a** and **18b** were tested for their ability to reversibly photo-regulate the firing activity in cultured hippocampal neurons under 1PE (**Figure 5.4**). The membrane-permeable calcium indicator Oregon Green BAPTA-1 AM (OGB-1 AM; excitation 494 nm, emission 523 nm) was used for fluorescence imaging. The application of the vehicle, *trans*-**18a** or *trans*-**18b** did not produce any change in calcium fluorescence responses, whereas enriching the *cis* forms of both xanoswitches, by illumination of the preparation with UV light, triggered neuronal responses (**Figure 5.4AC**). Quantification of the results (**Figure 5.4BD**) showed an increase in neuronal firing frequency, induced by the *cis* forms of both compounds, compared to their *trans* forms. More specifically, xanoswitch-**18b** yielded significantly higher firing frequency at 365 than 400 nm illumination. These results indicate that neuronal activity can be controlled using xanoswitches.

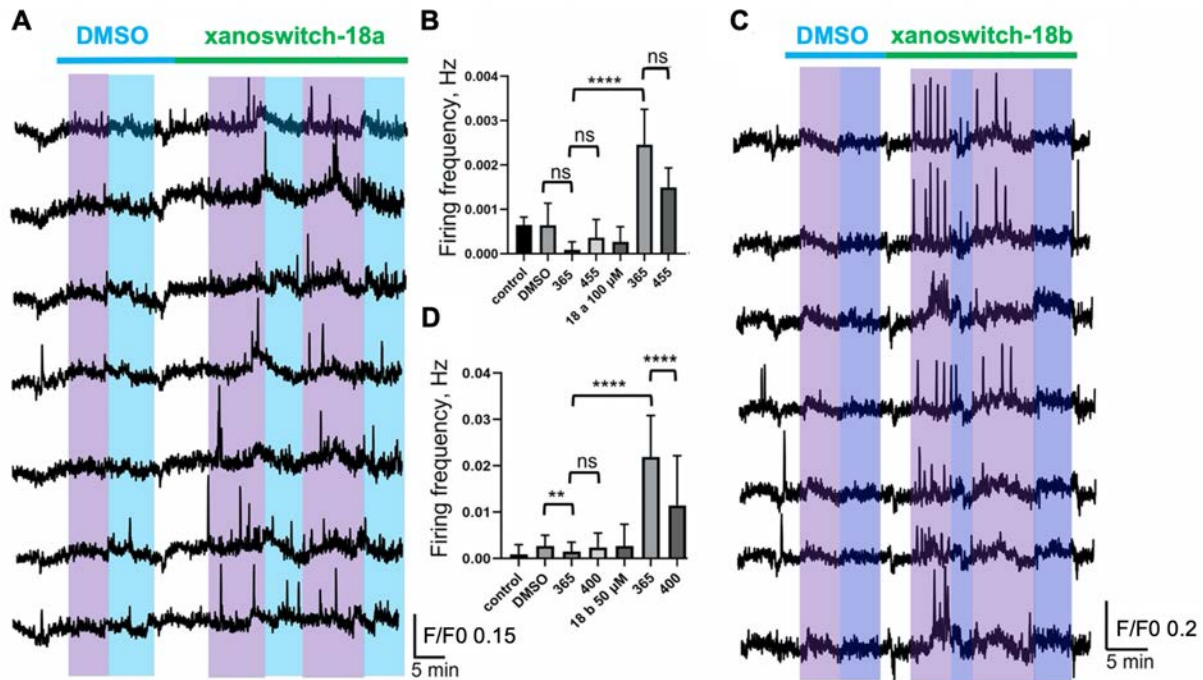


**Figure 5.4. Xanoswitches-18a and -18b modulate firing activity of cultured hippocampal neurons in a light-dependent manner.** (A) Live-cell imaging recordings of Oregon Green BAPTA-1 AM (OGB-1 AM) fluorescence. Calcium transients were induced by UV light (365 nm) during application of 100  $\mu$ M **18a**. Blue bar above the traces indicates application of vehicle (1% DMSO), green bar above the traces indicates application of 100  $\mu$ M **18a**. Violet and blue rectangles represent periods of 365 nm and 455 nm illumination, respectively. (B) Cumulative graph showing the effect of 365 nm and 455 nm light on the frequency of generation of calcium transients in the presence of DMSO or 100  $\mu$ M **18a**. Graph is created based on the data of 31 cells from 4 independent experiments. Each column represents mean  $\pm$  standard deviation (SD). Statistical analysis was performed with paired t-test, ( $p$ -value (\*\*\*\*)  $<$  0,0001, ns = not significant). (C) Live-cell imaging recording of calcium transients in culture hippocampal neurons triggered by 365 nm light during application of 50  $\mu$ M **18b**. Blue bar and green bar above the traces indicate application of DMSO and 50  $\mu$ M **18b**, respectively. Violet rectangles and blue rectangles represent periods of 365 nm and 400 nm illumination, respectively. (D) Cumulative graph demonstrating the effect of 365 nm and 400 nm light on the frequency of generation of calcium transients in the presence of DMSO or 50  $\mu$ M **18b**. Graph is based on the data of 28 cells from 4 independent experiments. Each column represents mean  $\pm$  SD. Statistical analysis was performed with paired t-test, ( $p$ -value (\*\*\*\*)  $<$  0.0001;  $p$ -value (\*\*)  $<$  0.01); ns = not significant.

### 5.2.7 *In vivo* neuronal photocontrol in mice

To test the ability of 2PE bidirectional switching *in vivo*, xanoswitch-**18a** was selected as most promising candidate. It had shown better results in the *in vitro* 2PE assay and had also shown its ability to photocontrol firing activity in cultured hippocampal neurons under 1PE. Consequently, control of spontaneous calcium activity in mice cortex using **18a** was tested. OGB-1 AM was pressure-injected through a glass pipette into the cortex of anesthetized mice.

This was possible thanks to the introduction of an opening in the cranial window<sup>48,49</sup> (see **SI**) which gives access directly to the cortex as well as allowing *in vivo* imaging to track calcium imaging changes (**Figure 5.5A**). Typically, 1h after dye injection, all cells within a radius of  $\sim 300\ \mu\text{m}$  were labeled with OGB-1 AM. We monitored spontaneous calcium transients (excitation 800 nm, emission 510 nm) at 100  $\mu\text{m}$  below the cortical surface for several minutes before and after 730 nm illumination (single plane scan), with or without the compound. Application of the *trans* compound did not alter cortical activity, which remains alike the control (**Figure S5.15A**). In contrast, photoconversion to the *cis* form upon 730 nm illumination increased cortical excitability (**Figure 5.5B**). These results were quantified by means of the response amplitude and the area under the curve (AUC) of the response time course.

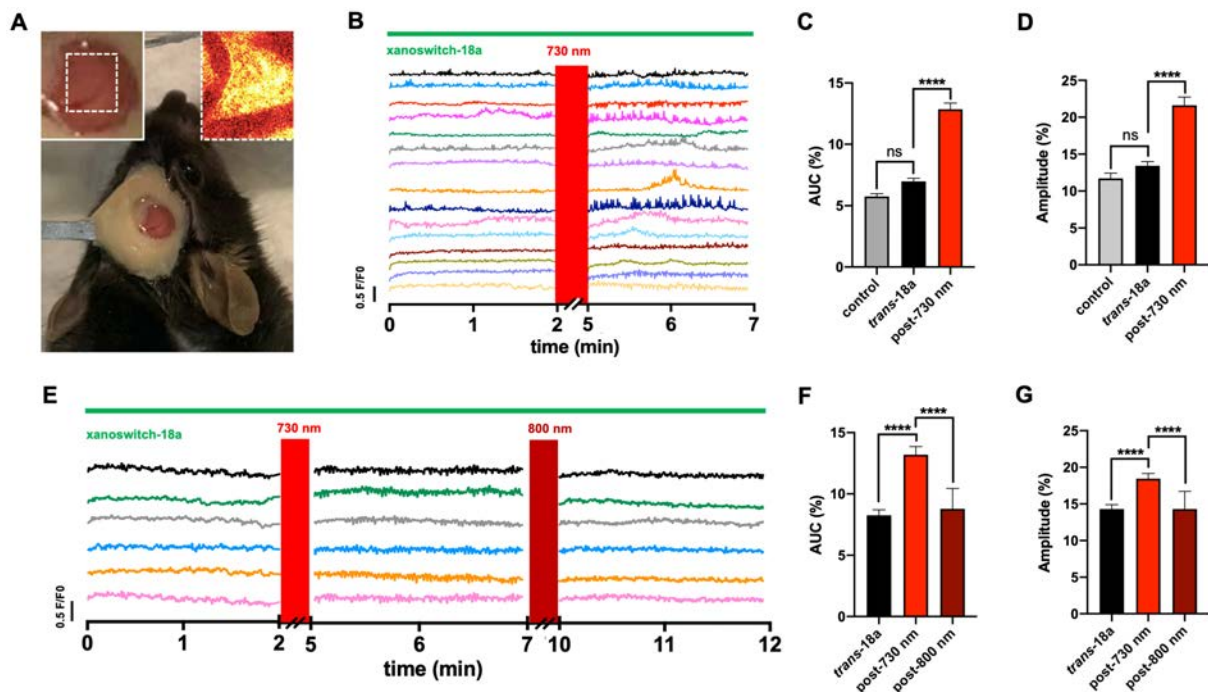


**Figure 5.5. *In vivo* photoinduced reversible calcium responses by two-photon excitation of xanoswitch-18a (100  $\mu\text{M}$ ) in mice.** (A) Image of the cranial window which enables to monitor the calcium activity and apply compounds through an opening. Left inset: window detail showing blood vessels and the cortical surface. Right inset: OGB-1 calcium image of the same region. (B) Representative traces ( $n = 15$  cells) of 2PE-induced photoactivation of endogenous muscarinic responses in animals treated with **18a** (green bar). (C and D) Quantification of photoresponses as area under the curve (AUC) and amplitude ( $n = 68$  cells from four different animals). (E) Representative traces ( $n = 6$  cells) showing the bidirectional photocontrol of the endogenous muscarinic receptors, in animals injected with **18a**. (F and G) Quantification of photoresponses as AUC and amplitude ( $n = 16$  cells from one animal). Red and dark red areas represent a period of 730 nm (maximum laser power), and 800 nm light illumination (at 50% of the maximum laser power, while 25% was used for imaging), respectively. Statistical analysis of **panel C, D, F and G** were performed by the paired sample Wilcoxon signed rank test ( $p$ -value (\*\*\*)  $< 0.0001$ ) using GraphPad Prism 9. Error bars indicate  $\pm$  SEM.

Both parameters showed that **18a** significantly altered firing activity upon photoactivation (**Figure 5.5CD**).

Subsequently, the potential of xanoswitch-**18a** to enable reversible photocontrol of cortical activity *in vivo* by 2PE was evaluated. After photoconversion of **18a** to the pharmacologically active *cis*-isomer, 800 nm light was applied (twice the power density used for imaging) to switch it back to its *trans* inactive form (**Figure 5.5E**). A decrease in firing activity back to control level (**Figure S5.15B**) was observed, suggesting that **18a** is effectively back isomerized by 2PE *in vivo*. The analysis of the response amplitude and AUC showed a significant reduction in cortical excitability upon deactivation of *cis*-**18a** by 2PE at 800 nm (**Figure 5.5FG**).

### 5.3 Discussion

Xanomeline received widespread attention after clinical studies showed promising efficacy in schizophrenia (SZ) and Alzheimer's disease (AD) patients<sup>35-37</sup>. However, due to its unselective binding to peripheral mAChRs, clinical development was at first thwarted. Administered as combination product with the peripherally restricted muscarinic antagonist tropium chloride to reduce adverse effects, xanomeline is back in the track of clinical trials (NCT03697252; NCT04659161) and is currently in phase 3<sup>38</sup>. This example suggests that any degree of spatiotemporal control of xanomeline activity may help increasing its safety.

Photopharmacology entails the manipulation of drug activity in space and time by using light, making it location-specific and, thereby, reducing the risk of adverse consequences in unwanted tissues<sup>12,50,51</sup>. In this work, we present a set of photoswitchable xanomeline derivatives, xanoswitches, which are dark-inactive, while retaining the nanomolar potency of their parent compound. In principle, these compounds could be administered systemically in their inactive conformation and be activated locally using light. However, a potential disadvantage of azobenzene derivatives of xanomeline is that unmodified azobenzene requires UV light for *trans*-to-*cis* isomerization. This wavelength is not optimal for biological applications because it can damage living cells and has a low penetration depth<sup>52-54</sup>. To solve these problems, longer wavelengths in the red to NIR range can be used.

In theory, this is possible by photoactivating the compounds with red light at 1PE, but to obtain compounds with this characteristic has proven difficult<sup>7</sup>. Alternatively, it has been shown<sup>21-23,30</sup> that simple azobenzene can be isomerized by 2PE with femtosecond pulsed lasers, enabling deep tissue penetration and subcellular resolution in three-dimensions. The non-linear properties of photoswitchable tethered ligands have been enhanced indirectly by linking a 2PE

antenna (*e.g.*, naphthalene<sup>21</sup> or pyrene<sup>31</sup> derivatives) to the molecular switch. Another strategy employs a push pull system to break the electronic symmetry of the azobenzene core<sup>21,22,33</sup>. Unfortunately, the first approach generally leads to reduced aqueous solubility and the second to low thermal stability of the *cis*-isomer. We have previously demonstrated that a photoswitchable dualsteric agonist (PAI) switches *in vitro* from the inactive *cis* to the active *trans* isoform under 840 nm light. However, *trans*-to-*cis* switching of PAI is not efficient under 2PE<sup>55</sup>. Other approaches such as neuroligand uncaging have been used with 2PE<sup>56-58</sup> but ligand release is intrinsically irreversible, which limits the experimental designs and *in vivo* applications. 2PE optogenetics has been recently optimized and is widely used to precisely control neural activity *in vitro* and *in vivo*<sup>59-65</sup>, however, the required genetic manipulation limits physiological relevance to genetically defined circuits and hampers therapeutic applications<sup>66,67</sup>.

In this work we have developed potent, water-soluble, dark-inactive muscarinic photoswitches and introduced single atom modifications that allow NIR operation by 2PE while retaining bistability. These photochromic ligands target endogenous receptors and allow reversibly controlling their activity in intact tissue with spatiotemporal precision and without genetic manipulation. Photoresponses of xanoswitches-**18a** and -**18b** appear faster under 1PE compared to 2PE (**Figure 5.3**) at the irradiation power densities used in our experiments, suggesting that further optimization of the 2PE wavelengths, pulse dispersion compensation, and illumination plane is possible. Since GPCR action is mediated by intracellular signaling, applying our molecular design strategy to ion channel ligands may also yield faster, more direct photoresponses.

Xanoswitches enables for the first time photoreversible (bidirectional) control *in vitro* and of neuronal activity in wild-type animals with NIR light and offer superior drug-likeness than other reported muscarinic photoswitchable ligands PAI<sup>30</sup> or BAI<sup>42</sup>. Therefore, xanoswitches constitute suitable candidates for animal research and potential clinical use. Muscarinic receptors are involved in neuronal excitability, plasticity and feedback regulation of ACh release among other functions<sup>68</sup>. Moreover, it has been demonstrated that PAI<sup>14</sup> and BAI<sup>15</sup> can reversibly modulate slow brain activity *in vivo*. Pathological conditions like AD, SZ or Parkinson's disease could benefit from the systemic administration of inactive muscarinic drug and the transcranial activation using tissue-penetrating NIR light from an external device. This technology could also allow reactivating brain regions displaying reduced activity as a result of stroke<sup>69</sup> or traumatic brain injury<sup>70,71</sup>; regulating brain activity associated with sleep disorders<sup>72</sup>;



inducing faster recovery from anesthesia<sup>73</sup> or the awakening from coma state<sup>74</sup>. The limited portability of pulsed lasers, optical set-ups and head-fixed devices currently restrains these applications but advances in fiber-coupled multiphoton miniscopes for freely moving mice<sup>25-28</sup> may soon make them a reality.

## 5.4 Conclusions

In conclusion, we have developed and characterized a set of photoswitchable xanomeline derivatives “xanoswitches” that are dark-inactive, light-activated agonists of muscarinic receptors. They are reversibly operated by UV and visible light and two of them are optimized for 2PE using NIR light. Since long wavelengths offer good tissue penetration and pulsed excitation affords subcellular resolution in three dimensions, the use of 2PE has great potential for biological applications. Xanoswitches enable reversible manipulation of endogenous muscarinic receptors in intact tissue that is unprecedented with other compounds at 1PE and 2PE<sup>14,15,30,42</sup>. Xanoswitch-**18a** stands out by its potency, efficacy, low activity in the dark, and most importantly by its ability to bidirectionally modulate cortical activity *in vivo* using wavelengths bearing deep tissue penetration and multiphoton focusing. The ensemble of these results allows envisaging a great diversity of basic and therapeutic applications of spatiotemporal selective muscarinic neuromodulation in neuroscience and in physiology at large.

## References

- 1 Kirchner, S. & Pianowski, Z. Photopharmacology of antimetabolic agents. *Int J Mol Sci* **23**, doi:10.3390/ijms23105657 (2022).
- 2 Castagna, R., Kolarski, D., Durand-de Cuttoli, R. & Maleeva, G. Orthogonal control of neuronal circuits and behavior using photopharmacology. *J Mol Neurosci* **72**, 1433-1442, doi:10.1007/s12031-022-02037-3 (2022).
- 3 Berry, M. H. *et al.* Photopharmacology for vision restoration. *Curr Opin Pharmacol* **65**, 102259, doi:10.1016/j.coph.2022.102259 (2022).
- 4 Ricart-Ortega, M., Font, J. & Llebaria, A. GPCR photopharmacology. *Mol Cell Endocrinol* **488**, 36-51, doi:10.1016/j.mce.2019.03.003 (2019).
- 5 Wijtmans, M., Josimovic, I., Vischer, H. F. & Leurs, R. Optical control of class A G protein-coupled receptors with photoswitchable ligands. *Curr Opin Pharmacol* **63**, 102192, doi:10.1016/j.coph.2022.102192 (2022).
- 6 Beharry, A. A., Sadovski, O. & Woolley, G. A. Azobenzene photoswitching without ultraviolet light. *J Am Chem Soc* **133**, 19684-19687, doi:10.1021/ja209239m (2011).
- 7 Dong, M., Babalhavaeji, A., Samanta, S., Beharry, A. A. & Woolley, G. A. Red-shifting azobenzene photoswitches for *in vivo* use. *Accounts of Chemical Research* **48**, 2662-2670, doi:10.1021/acs.accounts.5b00270 (2015).
- 8 Dong, M. *et al.* Near-infrared photoswitching of azobenzenes under physiological conditions. *J Am Chem Soc* **139**, 13483-13486, doi:10.1021/jacs.7b06471 (2017).
- 9 Hammerich, M. *et al.* Heterodiazocines: Synthesis and photochromic properties, trans-to-cis switching within the bio-optical window. *Journal of the American Chemical Society* **138**, 13111-13114, doi:10.1021/jacs.6b05846 (2016).
- 10 Konrad, D. B., Frank, J. A. & Trauner, D. Synthesis of redshifted azobenzene photoswitches by late-stage functionalization. *Chemistry* **22**, 4364-4368, doi:10.1002/chem.201505061 (2016).
- 11 Lentjes, P. *et al.* Nitrogen bridged diazocines: Photochromes switching within the near-infrared region with high quantum yields in organic solvents and in water. *Journal of the American Chemical Society* **141**, 13592-13600, doi:10.1021/jacs.9b06104 (2019).
- 12 Hull, K., Morstein, J. & Trauner, D. *In vivo* photopharmacology. *Chem Rev* **118**, 10710-10747, doi:10.1021/acs.chemrev.8b00037 (2018).
- 13 Castagna, R., Maleeva, G., Pirovano, D., Matera, C. & Gorostiza, P. Donor-acceptor stenhouse adduct displaying reversible photoswitching in water and neuronal activity. *J Am Chem Soc* **144**, 15595-15602, doi:10.1021/jacs.2c04920 (2022).
- 14 Barbero-Castillo, A. *et al.* Control of brain state transitions with a photoswitchable muscarinic agonist. *Adv Sci (Weinh)* **8**, e2005027, doi:10.1002/advs.202005027 (2021).
- 15 Sanchez-Sanchez J. M., R. F., Barbero-Castillo A., Sortino R., Agnetta L., Manasanch A., Matera C., Bosch M., Forcella M., Decker M., Gorostiza P., Sanchez- Vives M. V. Control of cortical slow oscillations and epileptiform discharges by photoswitchable muscarinic acetylcholine receptor subtype 1 ligands. *Submitted*.
- 16 Lakowicz, J. R. *Topics in fluorescence spectroscopy: Nonlinear and two-photon-induced fluorescence*. (Plenum Press, 1991).
- 17 Denk, W., Strickler, J. H. & Webb, W. W. Two-photon laser scanning fluorescence microscopy. *Science* **248**, 73-76, doi:10.1126/science.2321027 (1990).
- 18 Oron, D. P., E.; Anselmi, F.; Emiliani, V. in *Optogenetics: Tools for controlling and monitoring neuronal activity* (ed T.; Boyden Knöpfel, E.S.) Ch. 7, 119-143 (Progress in Brain Research, 2012).

- 19 Watson, E. E., Russo, F., Moreau, D. & Winssinger, N. Optochemical control of therapeutic agents through photocatalyzed isomerization. *Angew Chem Int Ed Engl* **61**, e202203390, doi:10.1002/anie.202203390 (2022).
- 20 Dudek, M. *et al.* Two-photon absorption and two-photon-induced isomerization of azobenzene compounds. *RSC Adv* **10**, 40489-40507, doi:10.1039/d0ra07693g (2020).
- 21 Izquierdo-Serra, M. *et al.* Two-photon neuronal and astrocytic stimulation with azobenzene-based photoswitches. *J Am Chem Soc* **136**, 8693-8701, doi:10.1021/ja5026326 (2014).
- 22 Cabre, G. *et al.* Rationally designed azobenzene photoswitches for efficient two-photon neuronal excitation. *Nat Commun* **10**, 907, doi:10.1038/s41467-019-08796-9 (2019).
- 23 Pittolo, S. *et al.* Reversible silencing of endogenous receptors in intact brain tissue using 2-photon pharmacology. *Proc Natl Acad Sci U S A* **116**, 13680-13689, doi:10.1073/pnas.1900430116 (2019).
- 24 Papagiakoumou, E. B., A.; Leshem, B.; Schwartz, O; Stell, B.M.; Bradley, J.; Oron, D.; Emiliani, V. Functional patterned multiphoton excitation deep inside scattering tissue. *Nature Photon* **7**, 274-278, doi:10.1038/nphoton.2013.9 (2013).
- 25 Zong, W. *et al.* Large-scale two-photon calcium imaging in freely moving mice. *Cell* **185**, 1240-1256.e1230, doi:https://doi.org/10.1016/j.cell.2022.02.017 (2022).
- 26 Zong, W. *et al.* Miniature two-photon microscopy for enlarged field-of-view, multi-plane and long-term brain imaging. *Nature Methods* **18**, 46-49, doi:10.1038/s41592-020-01024-z (2021).
- 27 Zong, W. *et al.* Fast high-resolution miniature two-photon microscopy for brain imaging in freely behaving mice. *Nature Methods* **14**, 713-719, doi:10.1038/nmeth.4305 (2017).
- 28 Klioutchnikov, A. *et al.* A three-photon head-mounted microscope for imaging all layers of visual cortex in freely moving mice. *Nature Methods* **20**, 610-616, doi:10.1038/s41592-022-01688-9 (2023).
- 29 Carroll, E. C. *et al.* Two-photon brightness of azobenzene photoswitches designed for glutamate receptor optogenetics. *Proc Natl Acad Sci U S A* **112**, E776-785, doi:10.1073/pnas.1416942112 (2015).
- 30 Riefolo, F. *et al.* Optical control of cardiac function with a photoswitchable muscarinic agonist. *J Am Chem Soc* **141**, 7628-7636, doi:10.1021/jacs.9b03505 (2019).
- 31 Gascón-Moya, M. *et al.* An optimized glutamate receptor photoswitch with sensitized azobenzene isomerization. *The Journal of Organic Chemistry* **80**, 9915-9925, doi:10.1021/acs.joc.5b01402 (2015).
- 32 Garrido-Charles, A. *et al.* Fast photoswitchable molecular prosthetics control neuronal activity in the cochlea. *J Am Chem Soc* **144**, 9229-9239, doi:10.1021/jacs.1c12314 (2022).
- 33 Kienzler, M. A. *et al.* A red-shifted, fast-relaxing azobenzene photoswitch for visible light control of an ionotropic glutamate receptor. *Journal of the American Chemical Society* **135**, 17683-17686, doi:10.1021/ja408104w (2013).
- 34 Bender, A. M., Jones, C. K. & Lindsley, C. W. Classics in chemical neuroscience: Xanomeline. *ACS Chemical Neuroscience* **8**, 435-443, doi:10.1021/acschemneuro.7b00001 (2017).
- 35 Bodick, N. C. *et al.* Effects of xanomeline, a selective muscarinic receptor agonist, on cognitive function and behavioral symptoms in Alzheimer disease. *Arch Neurol* **54**, 465-473, doi:10.1001/archneur.1997.00550160091022 (1997).
- 36 Shekhar, A. *et al.* Selective muscarinic receptor agonist xanomeline as a novel treatment approach for schizophrenia. *Am J Psychiatry* **165**, 1033-1039, doi:10.1176/appi.ajp.2008.06091591 (2008).

- 37 Bodick, N. C. *et al.* The selective muscarinic agonist xanomeline improves both the cognitive deficits and behavioral symptoms of Alzheimer disease. *Alzheimer Dis Assoc Disord* **11 Suppl 4**, S16-22 (1997).
- 38 Brannan, S. K. *et al.* Muscarinic cholinergic receptor agonist and peripheral antagonist for schizophrenia. *New England Journal of Medicine* **384**, 717-726, doi:10.1056/NEJMoa2017015 (2021).
- 39 Sauerberg, P. *et al.* Novel functional M<sub>1</sub> selective muscarinic agonists. Synthesis and structure-activity relationships of 3-(1,2,5-thiadiazolyl)-1,2,5,6-tetrahydro-1-methylpyridines. *J Med Chem* **35**, 2274-2283, doi:10.1021/jm00090a019 (1992).
- 40 Sauerberg, P. *et al.* Identification of side chains on 1,2,5-thiadiazole-azacycles optimal for muscarinic M<sub>1</sub> receptor activation. *Bioorg Med Chem Lett* **8**, 2897-2902, doi:10.1016/s0960-894x(98)00509-5 (1998).
- 41 Fang, L. *et al.* Hybrid molecules from xanomeline and tacrine: enhanced tacrine actions on cholinesterases and muscarinic M<sub>1</sub> receptors. *J Med Chem* **53**, 2094-2103, doi:10.1021/jm901616h (2010).
- 42 Agnetta, L. *et al.* A photoswitchable dualsteric ligand controlling receptor efficacy. *Angew Chem Int Ed Engl* **56**, 7282-7287, doi:10.1002/anie.201701524 (2017).
- 43 Agnetta, L. *et al.* Fluorination of photoswitchable muscarinic agonists tunes receptor pharmacology and photochromic properties. *J Med Chem* **62**, 3009-3020, doi:10.1021/acs.jmedchem.8b01822 (2019).
- 44 Schramm, S. *et al.* Novel BQCA- and TBPB-derived M<sub>1</sub> receptor hybrid ligands: Orthosteric carbachol differentially regulates partial agonism. *ChemMedChem* **14**, 1349-1358, doi:10.1002/cmdc.201900283 (2019).
- 45 Littmann, T., Ozawa, T., Hoffmann, C., Buschauer, A. & Bernhardt, G. A split luciferase-based probe for quantitative proximal determination of G $\alpha_q$  signalling in live cells. *Sci Rep* **8**, 17179, doi:10.1038/s41598-018-35615-w (2018).
- 46 Littmann, T., Ozawa, T., Hoffmann, C., Buschauer, A. & Bernhardt, G. A split luciferase-based probe for quantitative proximal determination of G $\alpha_q$  signalling in live cells. *Scientific Reports* **8**, 17179, doi:10.1038/s41598-018-35615-w (2018).
- 47 Kruse, A. C. *et al.* Muscarinic acetylcholine receptors: Novel opportunities for drug development. *Nat Rev Drug Discov* **13**, 549-560, doi:10.1038/nrd4295 (2014).
- 48 de la Rosa, X. *et al.* *In vivo* imaging of induction of heat-shock protein-70 gene expression with fluorescence reflectance imaging and intravital confocal microscopy following brain ischaemia in reporter mice. *European Journal of Nuclear Medicine and Molecular Imaging* **40**, 426-438, doi:10.1007/s00259-012-2277-7 (2013).
- 49 Roome, C. J. & Kuhn, B. Chronic cranial window with access port for repeated cellular manipulations, drug application, and electrophysiology. *Front Cell Neurosci* **8**, 379, doi:10.3389/fncel.2014.00379 (2014).
- 50 Velema, W. A., Szymanski, W. & Feringa, B. L. Photopharmacology: Beyond proof of principle. *J Am Chem Soc* **136**, 2178-2191, doi:10.1021/ja413063e (2014).
- 51 Broichhagen, J., Frank, J. A. & Trauner, D. A roadmap to success in photopharmacology. *Acc Chem Res* **48**, 1947-1960, doi:10.1021/acs.accounts.5b00129 (2015).
- 52 Banerjee, G., Gupta, N., Kapoor, A. & Raman, G. UV induced bystander signaling leading to apoptosis. *Cancer Lett* **223**, 275-284, doi:10.1016/j.canlet.2004.09.035 (2005).
- 53 Bachelor, M. A. & Bowden, G. T. UVA-mediated activation of signaling pathways involved in skin tumor promotion and progression. *Semin Cancer Biol* **14**, 131-138, doi:10.1016/j.semcancer.2003.09.017 (2004).

- 54 Kamarajan, P. & Chao, C. C. UV-induced apoptosis in resistant HeLa cells. *Biosci Rep* **20**, 99-108, doi:10.1023/a:1005515400285 (2000).
- 55 Sortino R., C. M., Castro-Olvera G., Gelabert R., Moreno M., Riefolo F., Matera C., Fernández-Castillo N., Lluc J.M., Hernando J., Loza-Alvarez P., Gorostiza P. Three-photon infrared stimulation of endogenous neuroreceptors *in vivo*. *In preparation*.
- 56 Ellis-Davies, G. C. R. Two-Photon Uncaging of Glutamate. *Front Synaptic Neurosci* **10**, 48, doi:10.3389/fnsyn.2018.00048 (2018).
- 57 Passlick, S. & Ellis-Davies, G. C. R. Comparative one- and two-photon uncaging of MNI-glutamate and MNI-kainate on hippocampal CA1 neurons. *J Neurosci Methods* **293**, 321-328, doi:10.1016/j.jneumeth.2017.10.013 (2018).
- 58 Denk, W. Two-photon scanning photochemical microscopy: Mapping ligand-gated ion channel distributions. *Proc Natl Acad Sci U S A* **91**, 6629-6633, doi:10.1073/pnas.91.14.6629 (1994).
- 59 Packer, A. M., Russell, L. E., Dalglish, H. W. & Hausser, M. Simultaneous all-optical manipulation and recording of neural circuit activity with cellular resolution *in vivo*. *Nat Methods* **12**, 140-146, doi:10.1038/nmeth.3217 (2015).
- 60 Chen, I. W., Papagiakoumou, E. & Emiliani, V. Towards circuit optogenetics. *Curr Opin Neurobiol* **50**, 179-189, doi:10.1016/j.conb.2018.03.008 (2018).
- 61 Adesnik, H. & Abdeladim, L. Probing neural codes with two-photon holographic optogenetics. *Nat Neurosci* **24**, 1356-1366, doi:10.1038/s41593-021-00902-9 (2021).
- 62 Yang, W., Carrillo-Reid, L., Bando, Y., Peterka, D. S. & Yuste, R. Simultaneous two-photon imaging and two-photon optogenetics of cortical circuits in three dimensions. *eLife* **7**, e32671, doi:10.7554/eLife.32671 (2018).
- 63 Rickgauer, J. P. & Tank, D. W. Two-photon excitation of channelrhodopsin-2 at saturation. *Proc Natl Acad Sci U S A* **106**, 15025-15030, doi:10.1073/pnas.0907084106 (2009).
- 64 Oron, D., Papagiakoumou, E., Anselmi, F. & Emiliani, V. Two-photon optogenetics. *Prog Brain Res* **196**, 119-143, doi:10.1016/b978-0-444-59426-6.00007-0 (2012).
- 65 Begue, A. *et al*. Two-photon excitation in scattering media by spatiotemporally shaped beams and their application in optogenetic stimulation. *Biomed Opt Express* **4**, 2869-2879, doi:10.1364/BOE.4.002869 (2013).
- 66 Packer, A. M., Roska, B. & Hausser, M. Targeting neurons and photons for optogenetics. *Nat Neurosci* **16**, 805-815, doi:10.1038/nn.3427 (2013).
- 67 Allen, B. D., Singer, A. C. & Boyden, E. S. Principles of designing interpretable optogenetic behavior experiments. *Learn Mem* **22**, 232-238, doi:10.1101/lm.038026.114 (2015).
- 68 Bubser, M., Byun, N., Wood, M. R. & Jones, C. K. Muscarinic receptor pharmacology and circuitry for the modulation of cognition. *Handb Exp Pharmacol*, 121-166, doi:10.1007/978-3-642-23274-9\_7 (2012).
- 69 Cassidy, J. M. *et al*. Low-frequency oscillations are a biomarker of injury and recovery after stroke. *Stroke* **51**, 1442-1450, doi:doi:10.1161/STROKEAHA.120.028932 (2020).
- 70 Modarres, M. H., Kuzma, N. N., Kretzmer, T., Pack, A. I. & Lim, M. M. EEG slow waves in traumatic brain injury: Convergent findings in mouse and man. *Neurobiol Sleep Circadian Rhythms* **2**, 59-70, doi:10.1016/j.nbscr.2016.06.001 (2017).
- 71 Kaltiainen, H., Helle, L., Liljeström, M., Renvall, H. & Forss, N. Theta-band oscillations as an indicator of mild traumatic brain injury. *Brain Topogr* **31**, 1037-1046, doi:10.1007/s10548-018-0667-2 (2018).
- 72 Hogan, S. E. *et al*. Slow-oscillation activity is reduced and high frequency activity is elevated in older adults with insomnia. *J Clin Sleep Med* **16**, 1445-1454, doi:10.5664/jcsm.8568 (2020).

- 73 Torao-Angosto, M., Manasanch, A., Mattia, M. & Sanchez-Vives, M. V. Up and Down states during slow oscillations in slow-wave sleep and different levels of anesthesia. *Front Syst Neurosci* **15**, 609645, doi:10.3389/fnsys.2021.609645 (2021).
- 74 Kaada, B. R., Harkmark, W. & Stokke, O. Deep coma associated with desynchronization in EEG. *Electroencephalography and Clinical Neurophysiology* **13**, 785-789, doi:https://doi.org/10.1016/0013-4694(61)90111-0 (1961).

## Supporting Information (SI) of Chapter 5

### SI5.1 Chemical synthesis

#### SI5.1.1 Materials and methods

Common reagents and solvents were purchased from the following commercial suppliers: ABCR, Alfa Aesar, BLD-Pharm, Sigma-Aldrich and used without further purification unless otherwise stated. Dry tetrahydrofuran (THF) was freshly distilled from sodium-benzophenone under an argon atmosphere. Reaction progress was monitored using analytical thin-layer chromatography (TLC) on precoated silica gel 60 GF254 plates (Macherey Nagel GmbH & Co). Detection was carried out by irradiation and consequent fluorescence quenching at 254 nm or excitation at 365 nm. Compounds were purified by column chromatography using silica gel 60 (60 Å pore size, 40–63 µm; Macherey Nagel GmbH & Co) as the stationary phase.

Reverse phase column chromatography was performed on an Interchim Puri Flash 430 (Ultra Performance Flash Purification) instrument connected to an Interchim Flash ELSD. FlashPure 4 g or 12 g C18 columns were used. Nuclear magnetic resonance spectra were measured on a Bruker AV-400 NMR instrument (Bruker) in deuterated solvents (DMSO-*d*<sub>6</sub>, CDCl<sub>3</sub>, MeOD-*d*<sub>4</sub>). Chemical shifts are expressed in ppm relative to DMSO-*d*<sub>6</sub>, CDCl<sub>3</sub>, MeOD-*d*<sub>4</sub> (2.50/7.26/3.31 for <sup>1</sup>H; 39.52/77.16/49.00 for <sup>13</sup>C).

Measurements for verification and purity of the compounds were performed with a Shimadzu LC/MS system, comprising a DGU-20A3R controller, pump LC-20AB, degasser DGU-20A, and SPD-20A UV-Vis detector. Compounds were dissolved in MeOH and filtered through syringe filters prior to measurement. As a stationary phase, a Synergi 4U fusion-RP 80 Å (150 × 4.6 mm) column was used (Phenomenex). As a mobile phase, a gradient of MeOH/water (both containing 0.1% formic acid) was used.

Method: flow rate: 1.0 ml/min; detection: 254 nm; scan range: 60–1000 *m/z*; gradient: A: H<sub>2</sub>O (0.1 % HCOOH); B: MeOH (0.1% HCOOH) 0–8 min 5%→90% B, 8–13 min 90% B, 13–14 min 90%→5% B, 14–18 min 5% B. The purity of all target compounds was found to be ≥ 95%. Purities were not tested at a particular PSS and therefore show an arbitrary *cis/trans* ratio (cf. chromatograms). ESI ionization was accomplished by a downstream Shimadzu LCMS-2020 mass spectrometer. Data are reported as mass-to-charge ratio (*m/z*) of the corresponding positively charged molecular ions.

### SI5.1.2 Abbreviations

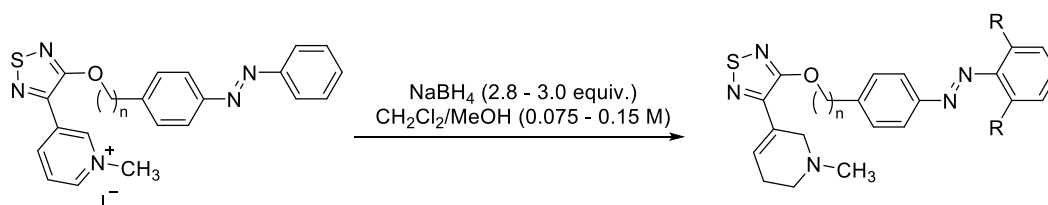
**Solvents:** EtOAc, ethyl acetate; CH<sub>2</sub>Cl<sub>2</sub>, dichloromethane; MeCN, acetonitrile; MeOH, methanol; EtOH, ethanol; THF, tetrahydrofuran; Et<sub>2</sub>O, diethyl ether; DMSO, dimethyl sulfoxide.

**Analytical characterizations:** NMR: d, doublet; dd, double doublet; ddd, double double doublet; dddd, doublet of doublet of doublet of doublets; dt, double triplet; m, multiplet; q, quartet; quin, quintet; s, singlet; t, triplet; m.p., melting point; R<sub>f</sub>, retention factor; rt, room temperature; RT, retention time.

### SI5.1.3 Synthetic routes

A solution of the respective pyridinium iodide (1.0 equiv.) in a 1:1 mixture of dichloromethane/methanol was cooled down to 0°C, sodium tetrahydroborate (2.8-3.0 equiv.) was added portion wise and the reaction mixture was allowed to warm up and stirred overnight at ambient temperature. Afterwards, the remaining sodium tetrahydroborate was quenched with an excess of water. The mixture was then extracted with dichloromethane. The combined organic layers were subsequently dried over Na<sub>2</sub>SO<sub>4</sub>, concentrated under reduced pressure and purified by silica gel column chromatography and reverse phase (C18) flash chromatography, yielding the photoswitchable xanomeline derivative (**16e**; **18a,b**) (30-78%).

#### Preparation of 1,2,5,6-tetrahydropyridinyl-phenyldiazenyl-1,2,5-thiadiazole **16e**; **18a,b**



**3-(1-methyl-1,2,5,6-tetrahydropyridin-3-yl)-4-((5-(4-(phenyldiazenyl)phenyl)pentyl)oxy)-1,2,5-thiadiazole (**16e**):** According to general method G 1-methyl-3-(4-((5-(4-(phenyldiazenyl)phenyl)pentyl)oxy)-1,2,5-thiadiazol-3-yl)pyridin-1-ium iodide (170 mg, 0.30 mmol, 1.0 equiv.) was reduced with sodium tetrahydroborate (32 mg, 0.83 mmol, 2.8 equiv.) in a mixture of CH<sub>2</sub>Cl<sub>2</sub>/MeOH (~2 ml). Purification by silica column chromatography (CH<sub>2</sub>Cl<sub>2</sub>/MeOH 20:1) and subsequent purification by reverse phase flash chromatography (H<sub>2</sub>O/MeOH) afforded 3-(1-methyl-1,2,5,6-tetrahydropyridin-3-yl)-4-((5-(4-(phenyldiazenyl)phenyl)pentyl)oxy)-1,2,5-thiadiazole (56 mg, 0.13 mmol, 42%) as an orange film.



$^1\text{H}$  NMR (400 MHz,  $\text{CDCl}_3$ ):  $\delta$  7.94 – 7.81 (m, 4H), 7.56 – 7.40 (m, 3H), 7.38 – 7.28 (m, 2H), 7.05 – 6.98 (m, 1H), 4.45 (t,  $J = 6.5$  Hz, 2H), 3.63 – 3.37 (m, 2H), 2.72 (t,  $J = 7.6$  Hz, 2H), 2.56 (t,  $J = 5.7$  Hz, 2H), 2.45 (s, 3H), 2.45 - 2.38 (m, 2H), 1.89 (p,  $J = 6.8$  Hz, 2H), 1.82 – 1.69 (m, 2H), 1.53 (qd,  $J = 9.6, 8.8, 5.7$  Hz, 2H).  $^{13}\text{C}$  NMR (101 MHz,  $\text{CDCl}_3$ ):  $\delta$  162.58, 152.85, 151.15, 146.84, 145.96, 130.86, 129.22, 129.19, 129.17, 128.41, 123.05, 122.84, 70.86, 54.99, 51.26, 45.89, 35.80, 30.92, 28.86, 26.57, 25.74.

MS (ESI, positive):  $m/z$  calculated for  $[\text{C}_{25}\text{H}_{30}\text{N}_5\text{OS}]^+$ : 448.22, found: 448.15  $[\text{M} + \text{H}]^+$ . Purity (HPLC<sub>254nm</sub>) = 96.5%.

**3-((5-(4-((2-fluorophenyl)diazenyl)phenyl)pentyl)oxy)-4-(1-methyl-1,2,5,6-**

**tetrahydropyridin-3-yl)-1,2,5-thiadiazole (18a):** According to general method A 3-(4-((5-(4-((2-fluorophenyl)diazenyl)phenyl)pentyl)oxy)-1,2,5-thiadiazol-3-yl)-1-methylpyridin-1-ium iodide (190 mg, 0.32 mmol, 1.0 equiv.) was reduced with sodium tetrahydroborate (37 mg, 0.97 mmol, 3.0 equiv.) in a mixture of  $\text{CH}_2\text{Cl}_2/\text{MeOH}$  (2 ml). Purification by silica column chromatography ( $\text{CH}_2\text{Cl}_2/\text{MeOH}$  20:1) and subsequent purification by reverse phase flash chromatography ( $\text{H}_2\text{O}/\text{MeOH}$ ) afforded 3-(4-(4-((2-fluorophenyl)diazenyl)phenyl)butoxy)-4-(1-methyl-1,2,5,6-tetrahydropyridin-3-yl)-1,2,5-thiadiazole (70 mg, 0.15 mmol, 47%) as an orange film.

$^1\text{H}$  NMR (400 MHz,  $\text{CDCl}_3$ ):  $\delta$  7.92 – 7.86 (m, 2H), 7.80 – 7.73 (m, 1H), 7.48 – 7.39 (m, 1H), 7.36 – 7.30 (m, 2H), 7.30 – 7.19 (m, 2H), 7.05 – 7.00 (m, 1H), 4.46 (t,  $J = 6.6$  Hz, 2H), 3.51 – 3.42 (m, 2H), 2.73 (t,  $J = 7.6$  Hz, 2H), 2.56 (t,  $J = 5.8$  Hz, 2H), 2.46 (s, 3H), 2.44 – 2.38 (m, 2H), 1.89 (p,  $J = 7.1$  Hz, 2H), 1.76 (p,  $J = 7.7$  Hz, 2H), 1.59 – 1.48 (m, 2H).  $^{13}\text{C}$  NMR (101 MHz,  $\text{CDCl}_3$ ):  $\delta$  162.53, 160.07 (d,  $J = 257.3$  Hz), 151.31, 146.91, 146.48, 140.83 (d,  $J = 6.9$  Hz), 132.23 (d,  $J = 8.2$  Hz), 129.40, 129.18, 128.43, 124.33 (d,  $J = 3.7$  Hz), 123.32, 117.84, 117.06 (d,  $J = 19.8$  Hz), 70.80, 55.11, 51.30, 45.98, 35.79, 30.84, 28.82, 26.70, 25.71.

MS (ESI, positive):  $m/z$  calculated for  $[\text{C}_{25}\text{H}_{29}\text{FN}_5\text{OS}]^+$ : 466.21, found: 466.20  $[\text{M} + \text{H}]^+$ . Purity (HPLC<sub>254nm</sub>) = 99.2%.

**3-((5-(4-((2,6-difluorophenyl)diazenyl)phenyl)pentyl)oxy)-4-(1-methyl-1,2,5,6-**

**tetrahydropyridin-3-yl)-1,2,5-thiadiazole (18b):** According to general method A 3-(4-((5-(4-((2,6-difluorophenyl)diazenyl)phenyl)pentyl)oxy)-1,2,5-thiadiazol-3-yl)-1-methylpyridin-1-ium iodide (93 mg, 0.153 mmol, 1.0 equiv.) was reduced with sodium tetrahydroborate (18 mg, 0.459 mmol, 3.0 equiv.) in a mixture of  $\text{CH}_2\text{Cl}_2/\text{MeOH}$  (2 ml). Purification by silica column chromatography ( $\text{CH}_2\text{Cl}_2/\text{MeOH}$  20:1) and subsequent purification by reverse phase flash

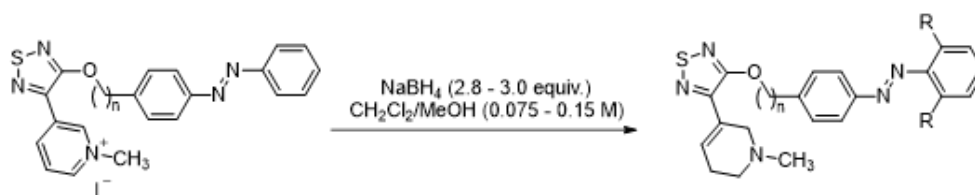
chromatography (H<sub>2</sub>O/MeOH) afforded 3-((5-(4-((2,6-difluorophenyl)diazenyl)phenyl)pentyl)oxy)-4-(1-methyl-1,2,5,6-tetrahydropyridin-3-yl)-1,2,5-thiadiazole as an orange film (38 mg, 0.120 mmol, 78%).

<sup>1</sup>H NMR (400 MHz, CDCl<sub>3</sub>): δ 7.81 – 7.75 (m, 2H), 7.27 – 7.16 (m, 2H), 7.06 – 6.89 (m, 3H), 4.37 (t, *J* = 6.5 Hz, 2H), 3.40 – 3.33 (m, 2H), 2.65 (t, *J* = 7.6 Hz, 2H), 2.47 (t, *J* = 5.7 Hz, 2H), 2.37 (s, 3H), 2.35 – 2.29 (m, 2H), 1.87 – 1.73 (m, 2H), 1.74 – 1.52 (m, 2H), 1.49 – 1.32 (m, 2H). <sup>13</sup>C NMR (101 MHz, CDCl<sub>3</sub>): δ 162.56, 155.80 (dd, *J* = 258.6, 4.5 Hz), 151.75, 147.14, 146.93, 131.66 (t, *J* = 10.4 Hz), 129.98 (t, *J* = 10.3 Hz), 129.23, 128.47, 123.19, 119.38, 112.88 – 112.27 (m), 70.83, 55.12, 51.31, 45.99, 35.84, 30.87, 28.85, 26.71, 25.74.

MS (ESI, positive): *m/z* calculated for [C<sub>25</sub>H<sub>28</sub>F<sub>2</sub>N<sub>5</sub>OS]<sup>+</sup>: 484.20, found: 484.20 [M + H]<sup>+</sup>. Purity (HPLC<sub>254nm</sub>) = 98.0%.

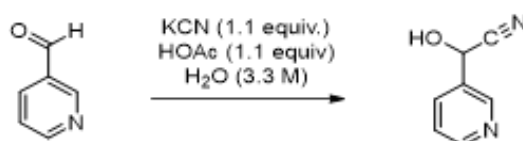
### SI5.1.3 General method

Preparation of 1,2,5,6-tetrahydropyridinyl-phenyldiazenyl-1,2,5-thiadiazole **16a-g**; **17a,b**; **18a,b**



A solution of the respective pyridinium iodide (1.0 equiv.) in a 1:1 mixture of dichloromethane/methanol was cooled down to 0°C, sodium tetrahydroborate (2.8 – 3.0 equiv.) was added portion wise and the reaction mixture was allowed to warm up and stirred overnight at ambient temperature. Afterwards, the remaining sodium tetrahydroborate was quenched with an excess of water. The mixture was then extracted with dichloromethane. The combined organic layers were subsequently dried over Na<sub>2</sub>SO<sub>4</sub>, concentrated under reduced pressure and purified by silica gel column chromatography and reverse phase (C18) flash chromatography, yielding the photoswitchable xanomeline derivative (**16a-g**; **17a,b**; **18a,b**)(30-78%).

#### 2-hydroxy-2-(pyridin-3-yl)acetonitrile

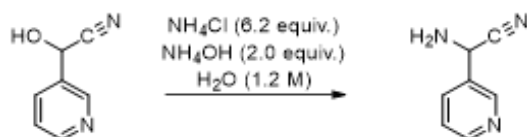


KCN (20.0 g, 0.31 mol, 1.1 equiv.) was dissolved in water (85 ml) and cooled down to 0°C. Nicotinaldehyde (26.3 ml, 0.28 mol, 1.0 equiv.) was added over a period of 25 min. Subsequently, acetic acid (17.6 ml, 0.31 mol, 1.1 equiv.) was added to the yellow reaction mixture over the next 15 min resulting in the formation of a precipitate. The reaction mixture was allowed to warm up and stirred for 12 h at ambient temperature. It was then cooled down to 0°C and the cyanohydrin product was filtered off as a white precipitate. The aqueous solution, still containing some amounts of the product, was extracted with ethyl acetate. The organic layers were combined, washed with water as well as brine and dried over Na<sub>2</sub>SO<sub>4</sub>. The solvent was removed under reduced pressure and the oily residue was purified by silica column chromatography (petroleum ether/ethyl acetate 3:4). Precipitated and chromatographed product were combined to yield 2-hydroxy-2-phenylacetonitrile as a white solid (24.0 g, 0.18 mol, 64%).

<sup>1</sup>H NMR (400 MHz, CDCl<sub>3</sub>): δ 8.66 – 8.59 (m, 1H), 8.59 – 8.52 (m, 1H), 8.05 – 7.90 (m, 1H), 7.49 – 7.39 (m, 1H), 5.65 (s, 1H). <sup>13</sup>C NMR (101 MHz, CDCl<sub>3</sub>): δ 149.99, 147.27, 135.49, 132.82, 124.47, 118.55, 61.28.

MS (ESI, positive): *m/z* calculated for [C<sub>7</sub>H<sub>7</sub>N<sub>2</sub>O]<sup>+</sup>: 135.06, found: 135.10 [M+H]<sup>+</sup>.

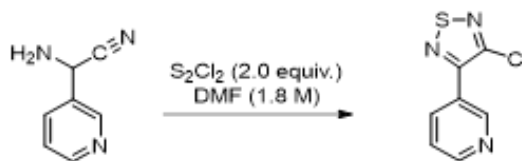
**2-amino-2-(pyridin-3-yl)acetonitrile (5)**



A suspension of 2-hydroxy-2-(pyridin-3-yl)acetonitrile (24.0 g, 0.18 mol, 1.0 equiv.) in water (50 ml) was stirred at ambient temperature, then a solution of NH<sub>4</sub>Cl (60 g, 1.12 mol, 6.2 equiv.) in water (50 ml) and NH<sub>3</sub> (25% aqueous) (57 ml, 0.36 mol, 2 equiv.) was added. The mixture was stirred vigorously at ambient temperature overnight. Afterwards, the mixture was exhaustingly extracted with EtOAc. The combined organic layers were dried with MgSO<sub>4</sub> and the solvent was removed under reduced pressure to yield a brown oil. The crude product was purified by silica column chromatography (dichloromethane/methanol 15:1) to give 2-amino-2-(pyridin-3-yl)acetonitrile as a yellow oil (17.5 g, 0.13 mol, 73%).

<sup>1</sup>H NMR (400 MHz, CDCl<sub>3</sub>): δ 8.84 – 8.79 (m, 1H), 8.67 – 8.63 (m, 1H), 7.92 – 7.88 (m, 1H), 7.40 – 7.34 (m, 1H), 4.98 (s, 1H), 1.89 (s, 2H). <sup>13</sup>C NMR (101 MHz, CDCl<sub>3</sub>): δ 150.58, 148.48, 134.51, 132.15, 123.86, 120.10, 45.40.

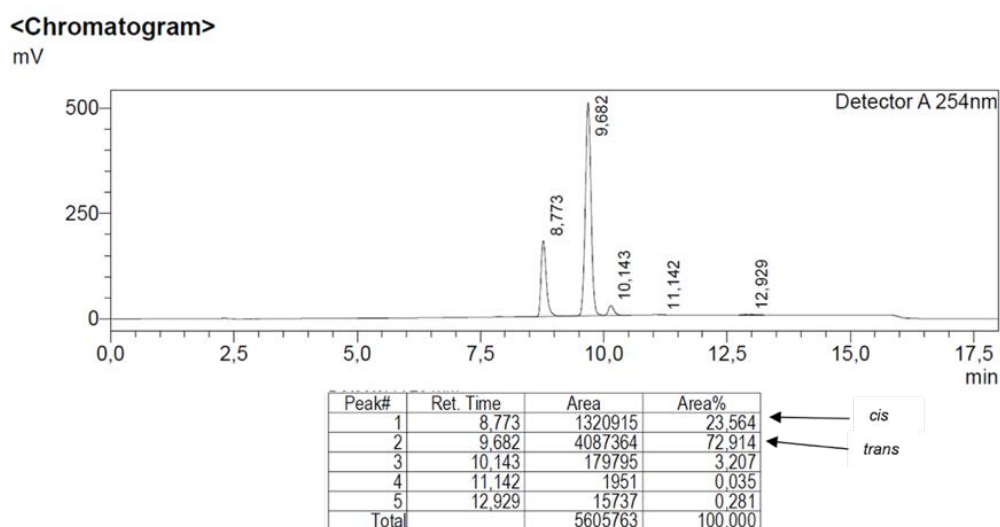
MS (ESI, positive): *m/z* calculated for [C<sub>7</sub>H<sub>8</sub>N<sub>3</sub>O]<sup>+</sup>: 134.07, found: 134.10 [M+H]<sup>+</sup>.

**3-chloro-4-(pyridin-3-yl)-1,2,5-thiadiazole (6)**

*N,N*-Dimethylformamide (6 ml) was cooled down to 0°C and S<sub>2</sub>Cl<sub>2</sub> (5.88 g, 3.48 ml, 43.6 mmol) was added slowly. Subsequently, a 3.5 M solution of 2-amino-2-(pyridin-3-yl)acetonitrile (2.90 g, 21.8 mmol) in *N,N*-Dimethylformamide (6 ml) was added over a period of 40 min. The reaction mixture was stirred at 0°C for 1 h, ice water was added, and the mixture was filtrated. The filtrate was cooled down to 0°C and 9M NaOH (~10 ml) was added until formation of a precipitate. The precipitate was collected, and the mother liquor was extracted with dichloromethane. The combined organic layers were washed with brine, dried over MgSO<sub>4</sub> and concentrated. The brown crude product was purified by column chromatography (petroleum ether/ethyl acetate 5:2). Precipitated and chromatographed product were combined to yield 3-chloro-4-(pyridin-3-yl)-1,2,5-thiadiazole as a yellowish solid (2.62 g, 13.3 mmol, 63%).

<sup>1</sup>H NMR (400 MHz, CDCl<sub>3</sub>): δ 9.33 – 9.16 (m, 1H), 8.81 – 8.68 (m, 1H), 8.35 – 8.24 (m, 1H), 7.51 – 7.42 (m, 1H). <sup>13</sup>C NMR (101 MHz, CDCl<sub>3</sub>): δ 155.30, 150.96, 149.36, 143.72, 136.03, 127.13, 123.57.

MS (ESI, positive): *m/z* calculated for [C<sub>7</sub>H<sub>5</sub>ClN<sub>3</sub>S]<sup>+</sup>: 197.99, found: 134.10 [M+H]<sup>+</sup>.

**SI5.2 HPLC analyses**

**Figure S5.1.** HPLC chromatogram of 3-(1-methyl-1,2,5,6-tetrahydropyridin-3-yl)-4-((5-(4-(phenyldiazenyl)phenyl)pentyl)oxy)-1,2,5-thiadiazole (16e).

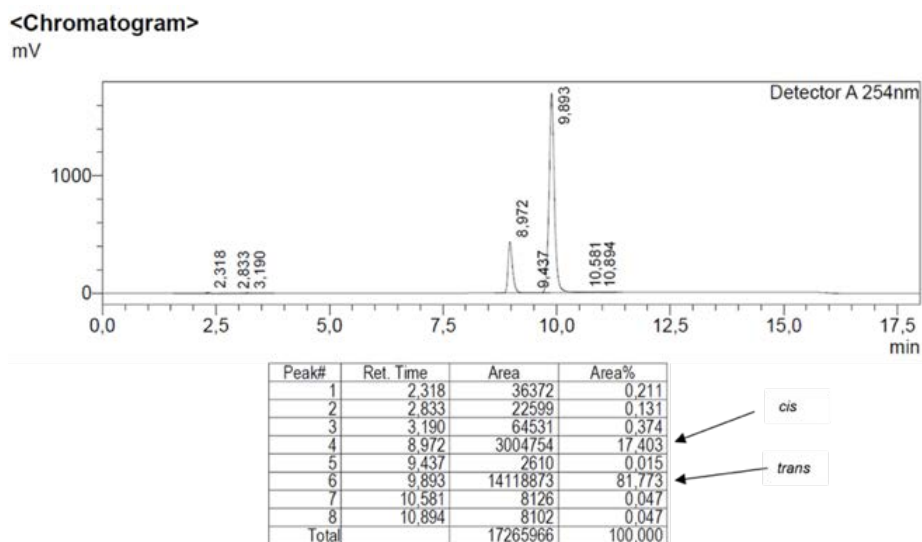


Figure S5.2. HPLC chromatogram of 3-((5-(4-((2-fluorophenyl)diazanyl)phenyl)pentyl)oxy)-4-(1-methyl-1,2,5,6-tetrahydropyridin-3-yl)-1,2,5-thiadiazole (18a).

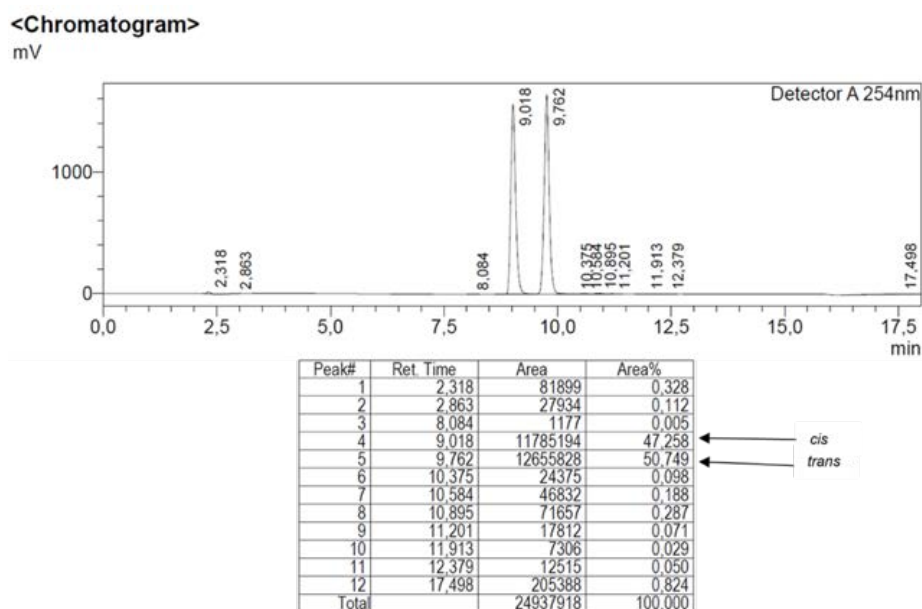


Figure S5.3. HPLC chromatogram of 3-((5-(4-((2,6-difluorophenyl)diazanyl)phenyl)pentyl)oxy)-4-(1-methyl-1,2,5,6-tetrahydropyridin-3-yl)-1,2,5-thiadiazole (18b).

### SI5.3 Photochemical characterization

UV-Vis spectra were recorded on a Varian Cary 50 Bio UV-Vis Spectrophotometer connected to a water bath for temperature control. Hellma (Type 100-QS) cuvettes (10mm light path) were used. Characterization was performed with 25  $\mu$ M/50  $\mu$ M solutions in DMSO/H<sub>2</sub>O 1:1 (v:v). Samples were irradiated using LEDs of Seoulviosys (UV Z5 series CUNx6A1B; 365nm), Roschwege (RSW-P01-385-2; 385 nm), LedEngin (LZ4-00UB00-U7, 405 nm), Osram (LD CQ7P-2U3U-W5-1-K, 451 nm; LT CP7P-KZLX-26, 528 nm; LY CP7P-JUKQ-36, 590 nm;

LA CP7P-KQKS-W3, 617 nm), Cree (XPeBBL-L1-0000-00205, 475 nm) and Lumileds (LXML-PE01, 505 nm). LED modules were combined to a rated power of 4W and used with a forward current of  $I_F = 350$  mA. Irradiation of the solutions with the respective wavelengths were performed until the corresponding photostationary state (PSS) had equilibrated (1-2 min).

Compound	Thermal relaxation @ 37°C (DMSO/H <sub>2</sub> O, 1:1)	<i>cis/trans</i> ratio (MeOH)	EC <sub>50</sub> [nM]	%E <sub>max</sub>
<b>16a</b>	2.1% (2 h)	PSS <sub>365</sub> : 93/7	1117	15.0 ± 0.6
		PSS <sub>455</sub> : 19/81	775	8.2 ± 0.5
<b>16b</b>	3.5% (2 h)	PSS <sub>365</sub> : 90/10	121	95.4 ± 1.1
		PSS <sub>455</sub> : 20/80	143	88.2 ± 1.5
<b>16c</b>	3.5% (2 h)	PSS <sub>365</sub> : 70/30	60.3	115 ± 1.4
		PSS <sub>455</sub> : 20/80	104	114 ± 1.4
<b>16d</b>	3.1% (2 h)	PSS <sub>365</sub> : 93/7	44.0	108 ± 1.2
		PSS <sub>455</sub> : 20/80	130	96.0 ± 1.5
<b>16e</b>	5.6% (2 h)	PSS <sub>365</sub> : 92/8	63.6	94.3 ± 0.8
		PSS <sub>455</sub> : 20/80	198	69.2 ± 1.1
<b>16f</b>	5.6% (2 h)	PSS <sub>365</sub> : 92/8	180	79.0 ± 0.6
		PSS <sub>455</sub> : 20/80	371	64.7 ± 0.6
<b>16g</b>	5.1% (2 h)	PSS <sub>365</sub> : 85/15	194	79.2 ± 1.8
		PSS <sub>455</sub> : 14/86	395	84.2 ± 4.4
<b>17a</b>	3.7% (2 h)	PSS <sub>365</sub> : 86/14	41.9	105 ± 1.0
		PSS <sub>455</sub> : 19/81	127	97.4 ± 1.6
<b>17b</b>	3.4% (2 h)	PSS <sub>365</sub> : 73/27	116	99.4 ± 0.9
		PSS <sub>400</sub> : 20/80	107	93.4 ± 0.7
<b>18a</b>	4.2% (2 h)	PSS <sub>365</sub> : 77/23	49.6	97.4 ± 0.2
		PSS <sub>455</sub> : 18/82	164	84.5 ± 0.9
<b>18b</b>	5.6% (2 h)	PSS <sub>365</sub> : 70/30	78.7	106 ± 0.7
		PSS <sub>400</sub> : 18/82	208	99.9 ± 0.8

**Table S5.1. Summary of thermal relaxation, *cis/trans* ratios and biological effects of the relevant photostationary states.**

Thermal relaxation was measured for a period over 2 h to determine whether the relaxation was significant with regards to the duration of the biological assays. For this purpose, the photochromic compounds were switched into the maximally *trans*-enriched photostationary state. The absorption at the wavelength were the spectrum of the *cis*- and *trans*-isomer showed maximal difference ( $I_{Dmax}$ ) was measured for 15 min. Subsequently, the solutions were switched to the thermodynamically less stable *cis*-isomer using 365 nm light. The relaxation was recorded by monitoring the change of absorption at  $\lambda_{\Delta max}$  for 2 h at 37°C. Afterwards, the solutions were switched to their maximally *trans* enriched PSS again to ensure that the previous

level of absorption could be restored. Percentage relaxation was calculated as  $\Delta = (A_{cis\text{-enriched } t=2\text{ h}} - A_{cis\text{-enriched } t=0}) * 100 / (A_{trans\text{-enriched}} - A_{cis\text{-enriched } t=0})$ . Absence of photo-fatigue was checked for all compounds of the same switching wavelengths simultaneously. Using a 96-well plate and a Spectramax 250 absorbance microplate reader (molecular devices), the compounds were irradiated alternately with the indicated wavelengths and their absorbance at  $\lambda_{\Delta\text{max}}$  was checked to be constant.

The photostationary distributions (PSD) of the PSSs of interests were determined by HPLC. The amount of *cis*- and *trans*-isomer was quantified by integration of the respective peak. Absorption was measured at the respective isosbestic point.

### SI5.3.1 Xanoswitch-16d (representative for the series 16a-g)

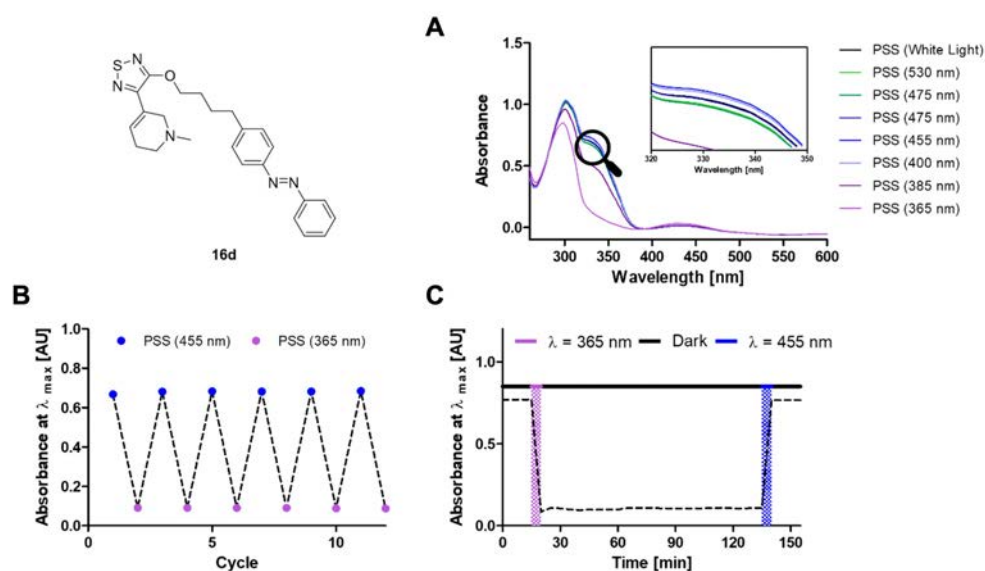


**Figure S5.4. Photochemical characterization of 16d (25  $\mu\text{M}$ , DMSO/H<sub>2</sub>O 1:1), representative for the non-fluorinated series 16a-g.** (A) Absorption spectra of PSSs after irradiation with corresponding lights for 2 min. Inlet: PSS of 400 nm and 455 nm are almost identical in their *trans*-isomer content, with 455 nm PSS having a slightly higher absorption (B) Cycles of 365/455 nm light irradiation showing no photodecomposition. (C) Thermal relaxation of the *cis*-isomer after irradiation with 365 nm LED light at 37°C.

## SI5.3.2 Xanoswitch-17a (representative for the compound 18a)

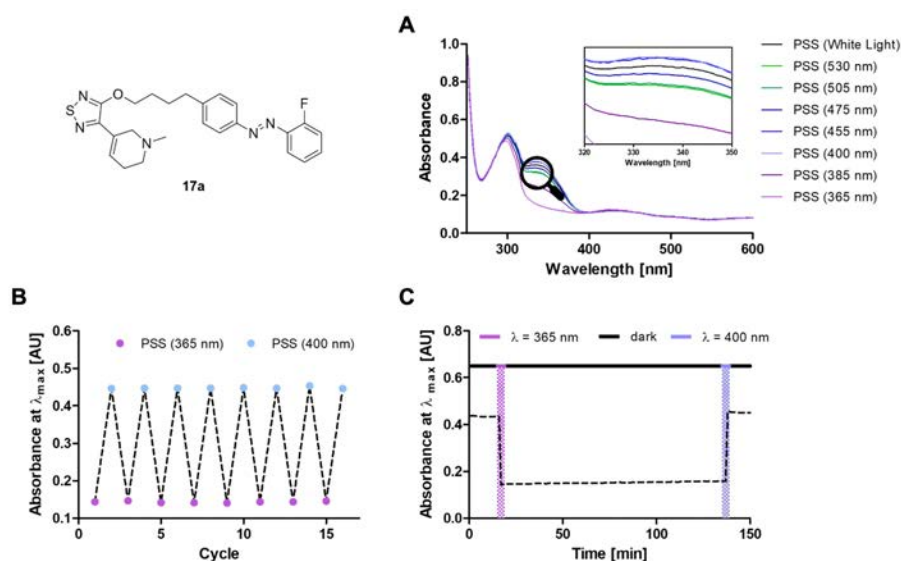


**Figure S5.5. Photochemical characterization of 17a (25  $\mu$ M, DMSO/H<sub>2</sub>O 1:1), representative for the mono-fluorinated compounds 17a, 18a.** (A) Absorption spectra of PSSs after irradiation with corresponding lights for 2 min. Inlet: PSS of 400 nm and 455 nm are almost identical in their *trans*-isomer content, with 400 nm PSS having a slightly higher absorption (B) Cycles of 365/400 nm light irradiation showing no photodecomposition. (C) Thermal relaxation of the *cis*-isomer after irradiation with 365 nm LED light at 37°C.

## SI5.3.2 Xanoswitch-17b (representative for the compound 18b)

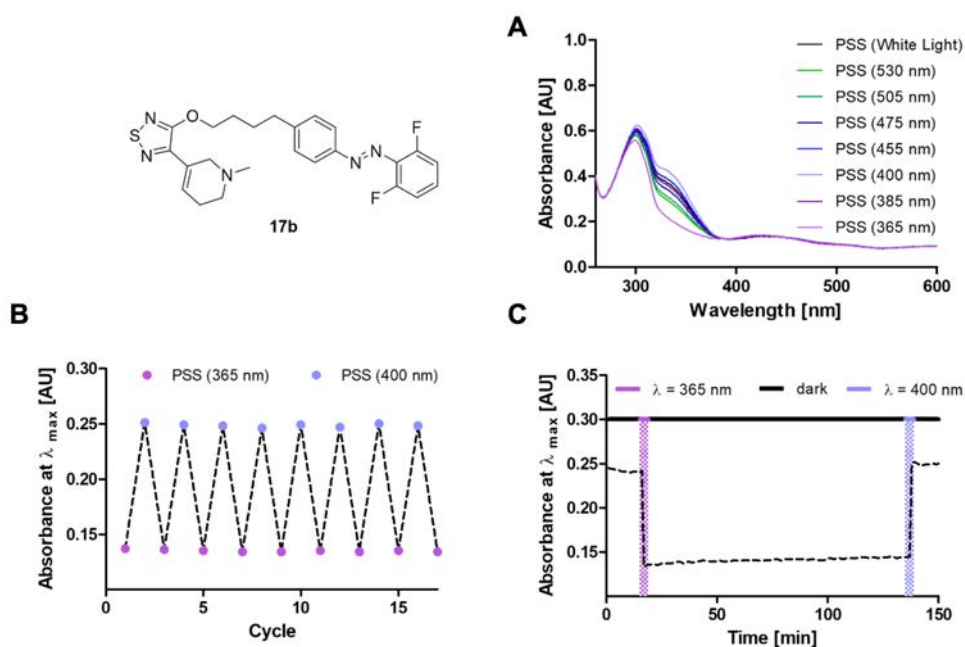


**Figure S5.6. Photochemical characterization of 17b (25  $\mu$ M, DMSO/H<sub>2</sub>O 1:1), representative for the di-fluorinated compounds 17b, 18b.** (A) Absorption spectra of PSSs after irradiation with corresponding lights for 2 min. Inlet: PSS of 400 nm and 455 nm are almost identical in their *trans*-isomer content, with 400 nm PSS having a slightly higher absorption (B) Cycles of 365/400 nm light irradiation showing no photodecomposition. (C) Thermal relaxation of the *cis*-isomer after irradiation with 365 nm LED light at 37°C.



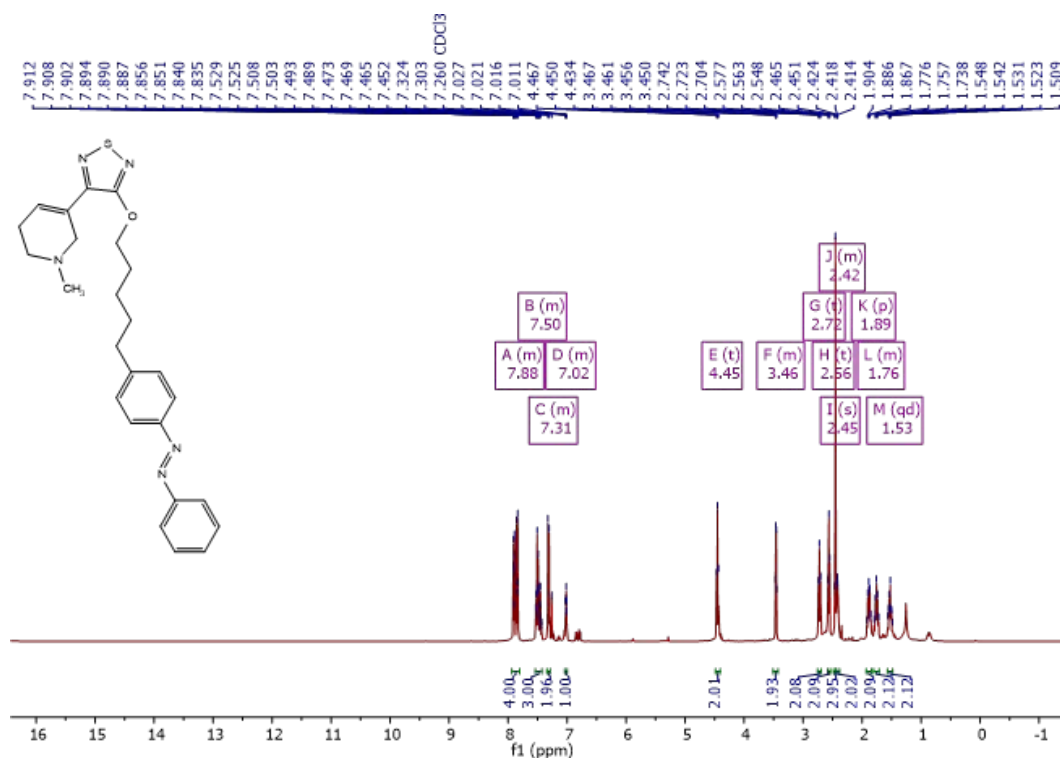
SI5.4  $^1\text{H-NMR}$  and  $^{13}\text{C-NMR}$  spectroscopy

Figure S5.7.  $^1\text{H-NMR}$  of 3-(1-methyl-1,2,5,6-tetrahydropyridin-3-yl)-4-((5-(4-(phenyldiazenyl)phenyl)pentyl)oxy)-1,2,5-thiadiazole (16e).

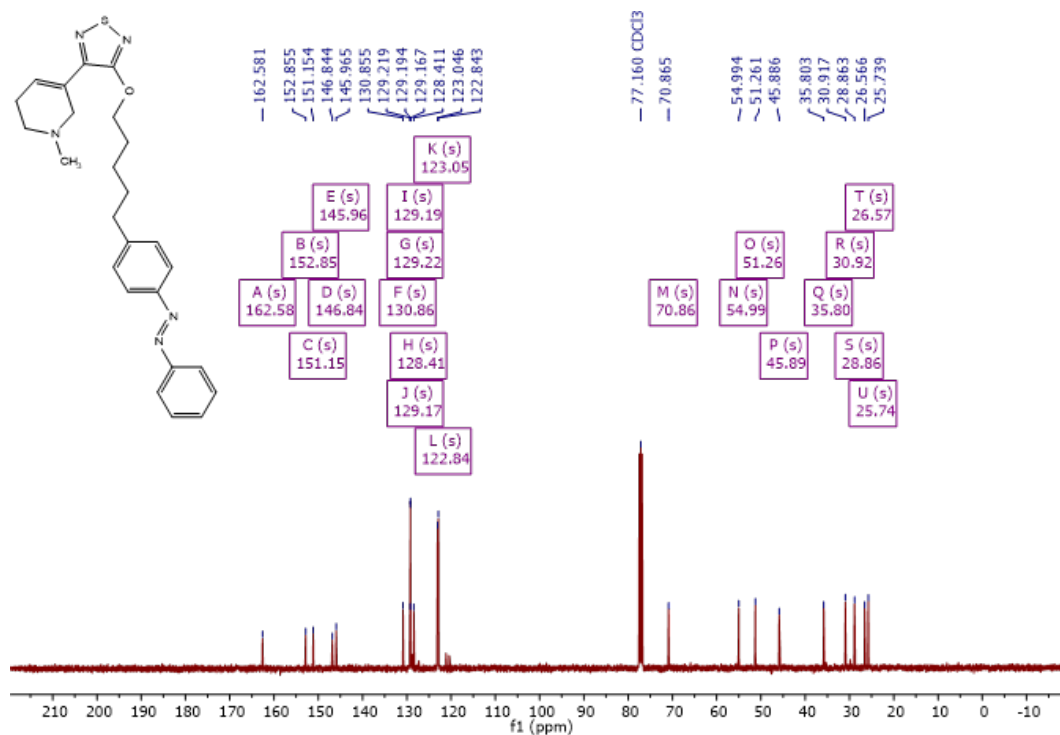


Figure S5.8.  $^{13}\text{C-NMR}$  of 3-(1-methyl-1,2,5,6-tetrahydropyridin-3-yl)-4-((5-(4-(phenyldiazenyl)phenyl)pentyl)oxy)-1,2,5-thiadiazole (16e).

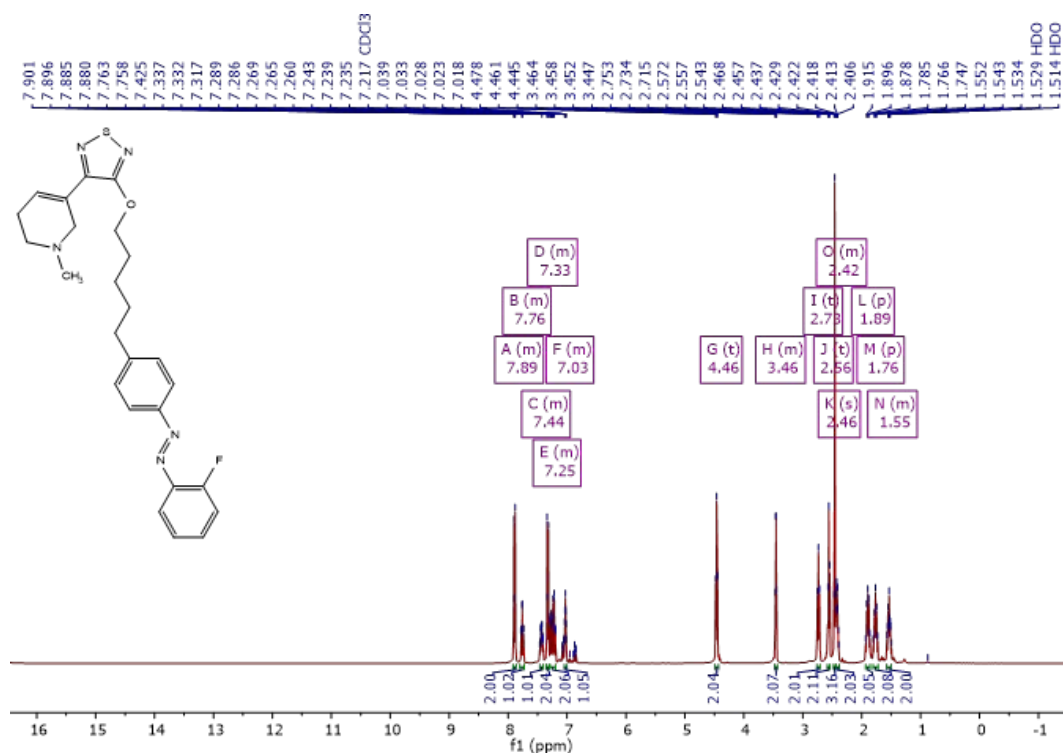


Figure S5.9. <sup>1</sup>H-NMR of 3-((5-(4-((2-fluorophenyl)diazenyl)phenyl)pentyl)oxy)-4-(1-methyl-1,2,5,6-tetrahydropyridin-3-yl)-1,2,5-thiadiazole (18a).

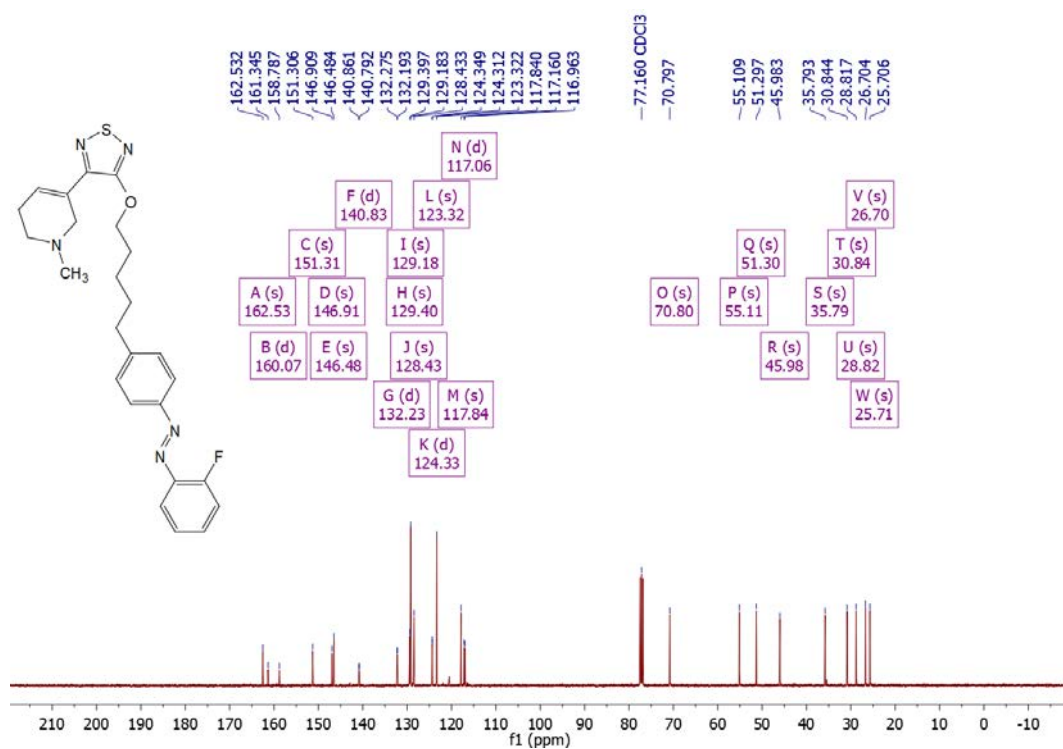


Figure S5.10. <sup>13</sup>C-NMR of 3-((5-(4-((2-fluorophenyl)diazenyl)phenyl)pentyl)oxy)-4-(1-methyl-1,2,5,6-tetrahydropyridin-3-yl)-1,2,5-thiadiazole (18a).

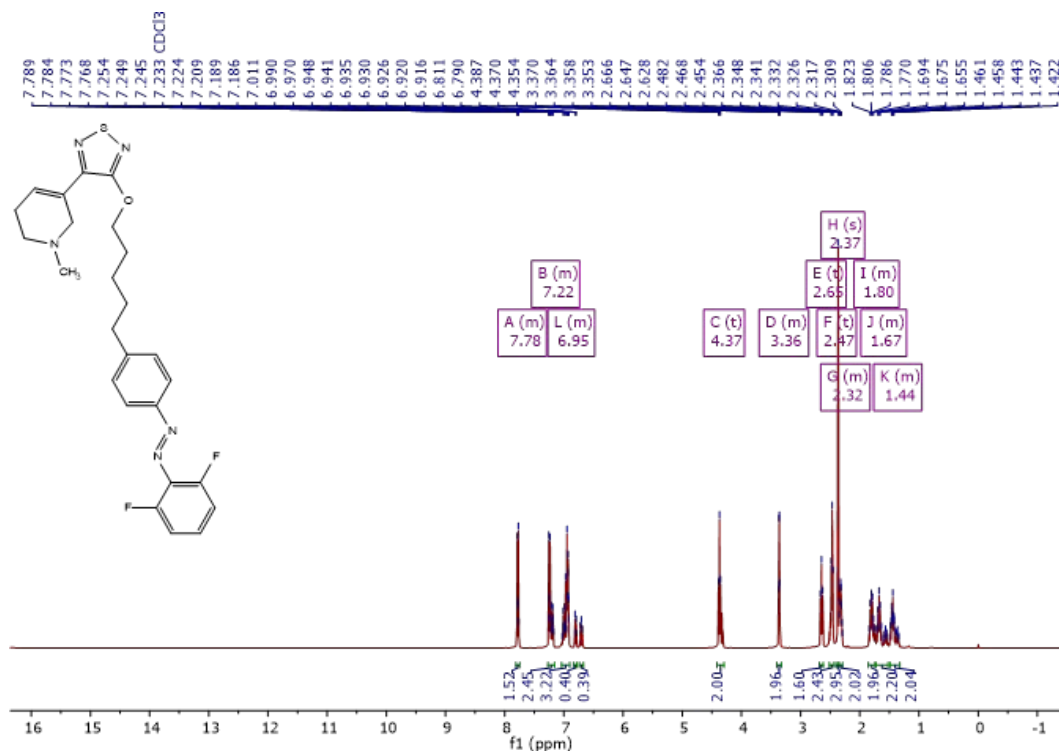


Figure S5.11. <sup>1</sup>H-NMR of 3-((5-(4-((2,6-difluorophenyl)diazenyl)phenyl)pentyl)oxy)-4-(1-methyl-1,2,5,6-tetrahydropyridin-3-yl)-1,2,5-thiadiazole (18b).

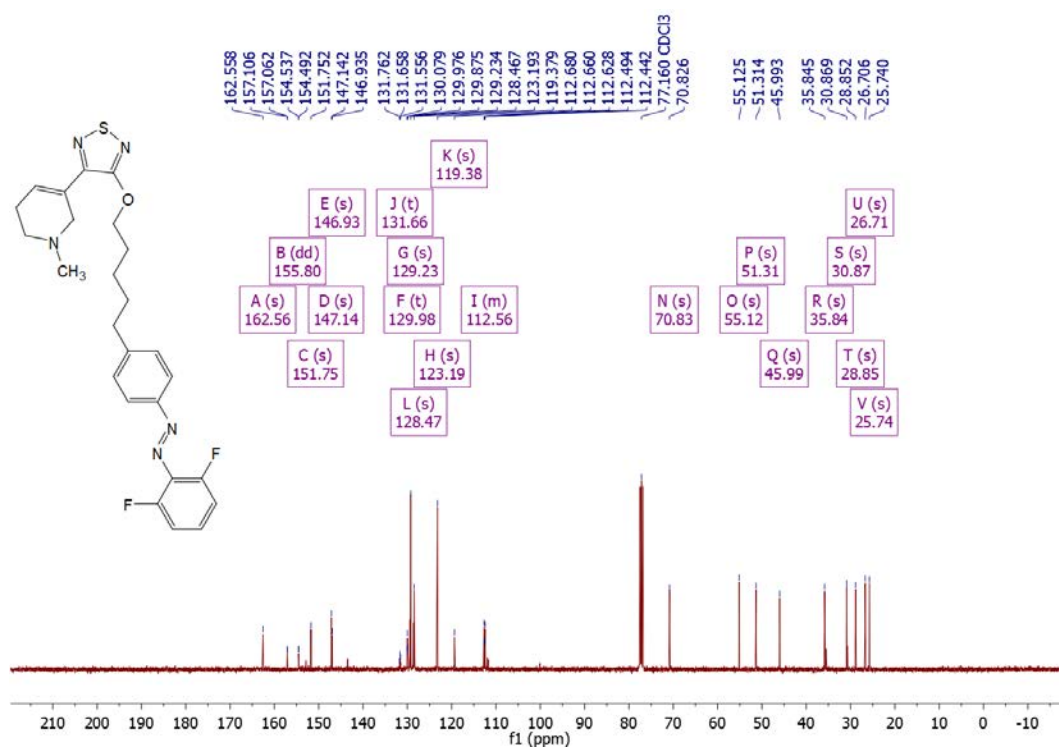
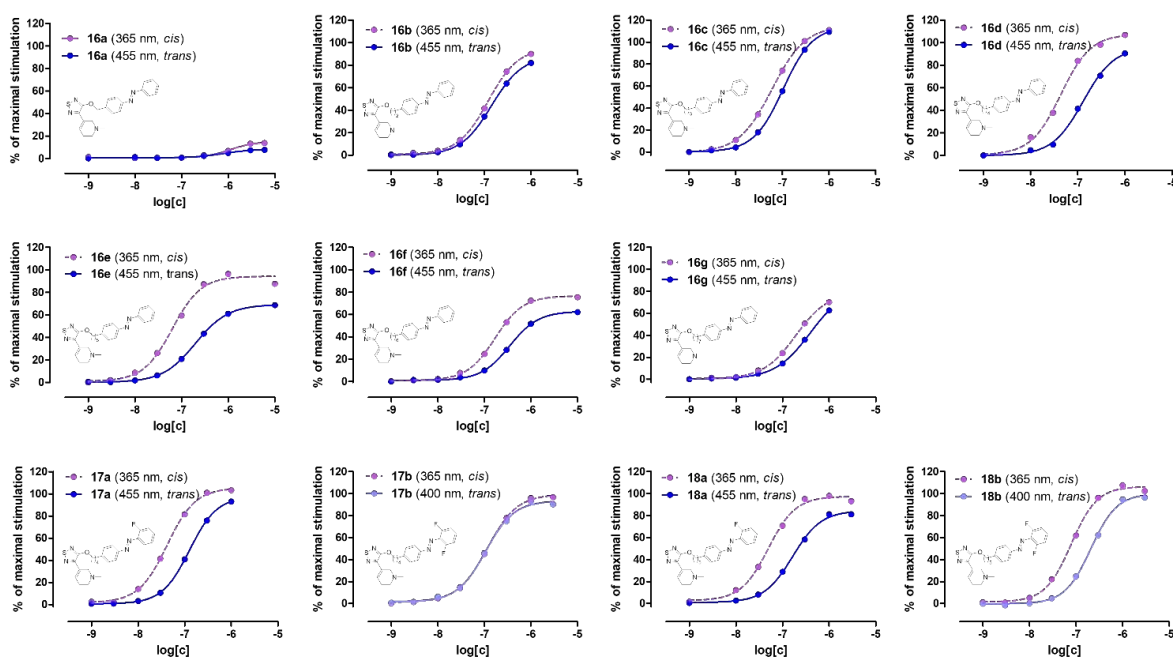


Figure S5.12. <sup>13</sup>C-NMR of 3-((5-(4-((2,6-difluorophenyl)diazenyl)phenyl)pentyl)oxy)-4-(1-methyl-1,2,5,6-tetrahydropyridin-3-yl)-1,2,5-thiadiazole (18b).

## SI5.5 Split luciferase complementation assay

The activity of the photoswitchable xanomeline derivatives was determined by means of a human embryonic kidney 293T (HEK 293T, American Type Culture Collection; ATCC) cell line, stably expressing the human M<sub>1</sub> muscarinic acetylcholine receptor (M<sub>1</sub> mAChR or M<sub>1</sub>R) and a split luciferase complementation system: The G $\alpha_q$  subunit fused to a click-beetle luciferase fragment and the phospholipase C- $\beta_3$  (PLC- $\beta_3$ ) fused to the corresponding fragment<sup>1</sup>. Cells were routinely monitored for mycoplasma contamination and were negative. The cells were cultivated in Dulbecco's modified Eagle's medium (DMEM) containing 10% fetal calf serum (FCS), 0.6 mg/ml G418 and 0.001 mg/ml puromycin, at 37°C in a water-saturated atmosphere containing 5% CO<sub>2</sub>. On the evening before the assay, the cells were detached from a 75-cm<sup>2</sup> flask by trypsinization and centrifuged. The pellet was resuspended in assay medium consisting of Leibovitz' L-15 (w/o phenol red) with 5% FCS and 10  $\mu$ M HEPES and the density of the suspension was adjusted to 1.25 x 10<sup>6</sup> cells/ml. Then, 80  $\mu$ l of the cells were seeded in Nunc™ MicroWell™ 96 well plates (ThermoFisher Scientific: 136101) and incubated overnight in a humidified atmosphere at 37°C without additional CO<sub>2</sub>. For the assay, 10  $\mu$ l of 10 mM luciferin (ThermoFisher Scientific: 88293) in L-15 were added to each well and the cells were allowed to equilibrate for 10 min at 37°C. Afterwards, 10  $\mu$ l per concentration of an irradiated ligand dilution series was added, yielding final in-well concentrations of (10  $\mu$ M) – (3  $\mu$ M) – 1  $\mu$ M – 300 nM – 100 nM – 30 nM – 10 nM – 1 nM). Afterwards the plate was read in a pre-warmed Berthold Mithras LB 940. Additionally, a duplicate of the reference substance carbachol (CCh) and a negative control (L-15) was included in each individual experiment. The luminescent signal was continuously monitored for 30 min after which a stable plateau had formed for every concentration. Each substance was measured in at least three independent experiments, in which each condition was tested in duplicate. Data were analyzed by taking the last 5 data points of each plateau and plotting them in GraphPad Prism 5. These values were normalized to the maximal response of reference agonist CCh (100%) and the negative control L-15 (0%). Afterwards, the values of the independent experiments were pooled to generate the overall concentration-response curves which were fitted using GraphPad Prisms built-in log(agonist) vs. response equation.



**Figure S5.13.** *In vitro* characterization of all compounds in their *cis*- and *trans*-enriched states respectively. Detection of  $G\alpha_q$  interaction with PLC- $\beta_3$  as a measure of receptor activation. Data points are given as the mean  $\pm$  SEM of 3 independent experiments conducted in duplicates.

## SI5.6 *In vitro* calcium imaging

Human embryonic kidney tsA201 (HEK tsA201, American Type Culture Collection; ATCC) cells were maintained in DMEM/Nutrient Mixture F-12 Ham (DMEM/F12 1:1, Life Technologies) supplemented with 10% fetal bovine serum (FBS, Life Technologies), penicillin and streptomycin (1%, Sigma-Aldrich) in a controlled environment (37°C, 98% humidity and 5% CO<sub>2</sub>). The cells were transiently co-transfected with the human M<sub>1</sub>R (Addgene) and GCaMP6s (ratio 1:1) using X-tremeGENE 9 DNA Transfection Reagent (Roche Applied Science) following the manufacturer's instructions. As generally known, M<sub>1</sub> mAChRs prevalently activate  $G\alpha_q$  proteins, leading to the activation of the phospholipase C pathway, which results in the production of inositol 1,4,5-trisphosphate (IP<sub>3</sub>) and the subsequent release of intracellular calcium from the endoplasmic reticulum. The day after, cells were harvested with accutase (Sigma-Aldrich) and seeded onto 16 mm or 25 mm (1PE or 2PE experiments) glass coverslips (ThermoFisher Scientific) coated with poly-L-Lysine (Sigma-Aldrich) to allow cell adhesion. Finally, the seeded cells were used for the experiments after 24 h.

The genetically encoded calcium indicator GCaMP6s was used in all the experiments to determine changes in intracellular calcium concentrations upon receptor activation. The bath solution used for single cell intracellular calcium recordings contained: 140 mM NaCl, 5.4 mM KCl, 1 mM MgCl<sub>2</sub>, 10 mM HEPES, 10 mM glucose and 2 mM CaCl<sub>2</sub>, with pH 7.40. Before

each experiment, cells were mounted on the recording chamber and rinsed with fresh solution. Then, the recording chamber was filled with 1 ml of the bath solution and placed on an IX71 inverted microscope (Olympus) with a XLUMPLFLN 20XW x20/1 water immersion objective (Olympus). GCaMP6s was excited during 50 ms at 488 nm by using a Polychrome V light source (Till Photonics) equipped with a Xenon Short Arc lamp (Ushio Europe B.V.) and a 505 nm dichroic beam splitter (Chroma Technology). Emission at 510 nm was filtered by a D535/540 nm emission filter (Chroma Technology) and finally collected by a C9100-13 EM-CCD camera (Hamamatsu Photonics). Images were acquired at room temperature with an imaging interval of 4 s with the SmartLux software (HEKA), and the imaging analysis was done with Fiji (NIH, ImageJ).

Photostimulation under 1PE during recordings was done by illumination of the entire focused field using the Polychrome V connected to a personal computer, and shutter and wavelengths were controlled using Patchmaster software (HEKA). Light intervals lasted a total of 5 min for all the HEK tsA201 cell experiments, with flashes of 455 nm (3.5 s duration) and 365 nm (3.5 s duration) light for the xanoswitches-**16e** and **-18a**. Furthermore, for the xanoswitch-**18b** flashes of 400 nm (3.5 s duration) and 365 nm (3.5 s duration) light were used.

2PE experiments were performed in the Advanced Digital Microscopy Core Facility of the Institute for Research in Biomedicine (IRB, Barcelona, Spain) with a confocal multiphoton microscope equipped with a pulsed broadband Ti:Sapphire laser (Mai Tai, Spectra- Physics) which can be tuned between 710-990 nm (80 MHz repetition rate, 80 fs pulse, light power  $2.8 \text{ mW} \cdot \mu\text{m}^{-2}$  at 720-840 nm). Images under 2PE were acquired at room temperature with an inverted laser-scanning confocal microscope (TCS SP5, Leica Microsystems) equipped with a HCX PL APO 40 $\times$ /1.25-0.75-NA oil objective for imaging cultured cells, and a HC PL APO 20 $\times$ /.0.7-NA CS air objective (Leica Microsystems). The imaging interval was 4 s. Acquired image sequences were stored in the Leica image format and stacks for offline analysis with Fiji (NIH, ImageJ).

These experiments were performed under dark conditions to keep the compounds in their *trans* conformation. Addition of agonists and vehicle was carried out by carefully pipetting directly into the recording chamber for the final dilution of approximately 1:1000. Stock solutions of the agonists were stored at -20°C in DMSO (Sigma-Aldrich) and diluted with the assay buffer to a 0.1% final concentration of DMSO. Acetylcholine (ACh; Sigma-Aldrich) was used as a positive control to stimulate M<sub>1</sub> mAChRs in HEK tsA201 cells. Data were normalized over the maximum response obtained with ACh at 500 nM.

Imaging data were extracted with Fiji (NIH, ImageJ). All data were analyzed by using Excel (Microsoft, version 16.62) and GraphPad Prism (GraphPad Software, version 9). Statistical differences were analyzed by paired-sample Wilcoxon signed-rank test, whereas a value of  $p$ -value (\*) < 0.05 was considered as significant. The data are expressed as the mean  $\pm$  SEM.

Further control experiments were performed in HEK cells not expressing the M<sub>1</sub> mAChR (Figure S5.14).

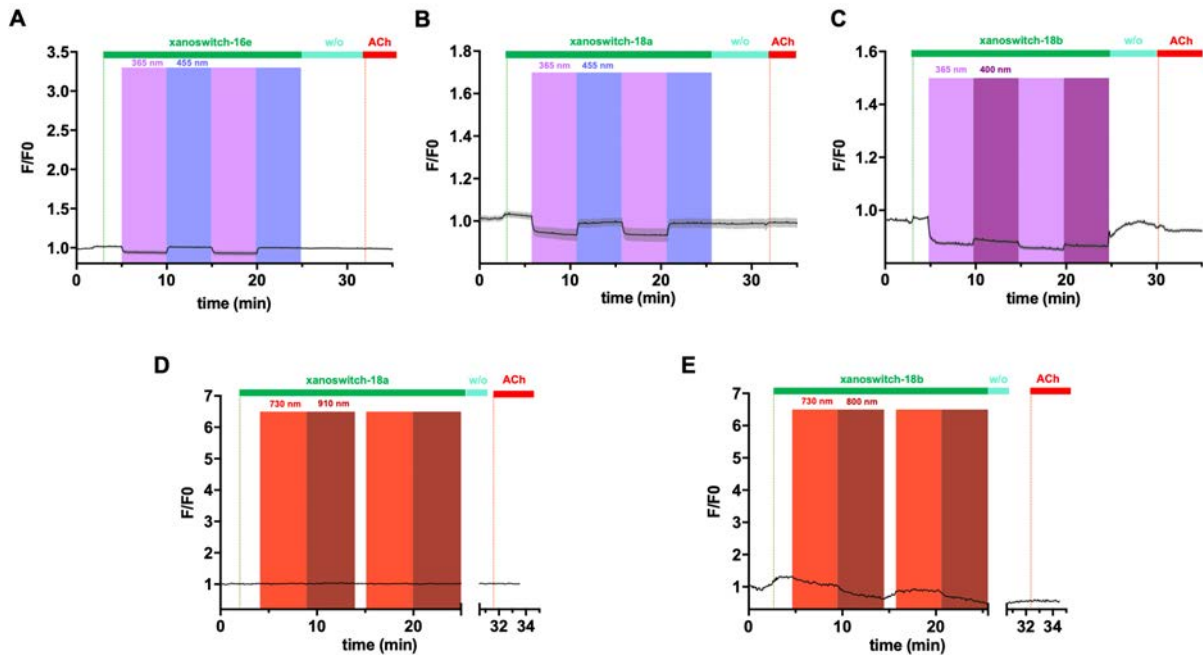


**Figure S5.14.** Control experiments in HEK cells without the presence of M<sub>1</sub> mAChR. No calcium oscillations were observed after application of ACh, xanoswitches-16e (A, n = 50 cells), -18a (B, n = 50 cells), -18b (C, n = 50 cells) and under 1PE at 365 nm and 455 nm (A and B) or 400 nm (C) light cycles. No calcium oscillations were observed after application of ACh, xanoswitches-18a (D, n = 50 cells), -18b (E, n = 50 cells) and under 2PE alternating 730 nm and 910 nm (D) or 800 nm (E) illumination.

## SI5.7 Calcium imaging of culture hippocampal neurons

Procedures were performed in accordance with the European guidelines for animal care and use in research and were approved by the Animal Experimentation Ethics Committee at the University of Barcelona.

Sprague-Dawley rat pups (P 1-5) were sacrificed by decapitation, hippocampi were isolated and treated with 0,1% trypsin in HBSS (10 min, 37°C). Neurons were plated on Poly-D-Lysine (PDL)-coated 16 mm coverslips (0.5-1 x 10<sup>5</sup> cells) and incubated at 37°C, 5% CO<sub>2</sub> for 1.5 h (to allow cells adhesion) in MEM supplemented with heat-inactivated FBS (5%), heat-inactivated HS (5%), penstrep (10 UI/ml), L-glutamine (2mM) and glucose (20mM). Neurons were

cultured in Neurobasal A medium, supplemented with B-27 (5%), penstrep (5 UI/ml), glutaMAX (0,5x) and glucose (15mM). After three days *in vitro* (DIV), cultured cells were treated with 1  $\mu$ M of Ara-C to prevent proliferation of non-neuronal cells. 50% of the maintenance medium was exchanged every 4 days.

Calcium imaging experiment were done using inverted IX71 Olympus microscope (Olympus) with XLUMPLFLN 20X Olympus water immersion objective (Japan). Polychrome V (Till Photonics) with Xenon Short-Arc lamp (Ushio Europe B.V.) was used as a light source. Excitation light was directed to the specimen by 505 nm dichroic beam splitter, emitted light was filtered by D535/540 nm emission filter (Chroma Technology) and collected by C9100-13 EM-CCD camera (Hamamatsu Photonics).

Before each experiment neurons were incubated in PBS solution containing 10  $\mu$ M of the calcium indicator Oregon Green BAPTA-1 AM (OGB-1 AM; ThermoFisher Scientific) for 30 min at 37°C and 5% CO<sub>2</sub>. During imaging experiment neurons were maintained in the solution containing: 150 NaCl, 3 KCl, 1 MgCl<sub>2</sub>, 2 CaCl<sub>2</sub>, 10 HEPES, 10 D-glucose; pH 7.40-7.42.

OGB-1 AM was excited with 488 nm light during 100 ms every 2 s. Switching of the molecules with 365/ 400/ 455 nm light was done through the optic path of the microscope using Polychrome (Till Photonics) during 1.5 s every 2 s.

## **SI5.8 *In vivo* calcium imaging**

Animal work was conducted according to the Spanish law (Real Decreto 53/2013) in compliance with the EU Directive 2010/63/EU for animal experiments, and with approval of the ethics committees: *Comite Etic d'Experimentacio Animal de la Universitat de Barcelona* (CEEA: 10702) and the local competent organs of the *Generalitat de Catalunya*. The study followed the ARRIVE guidelines.

Four C57Bl/6J mice (Charles River Laboratories), male and female of approximately 3 months of age, were used for two-photon (2P) *in vivo* imaging experiments.

The animals were anesthetized with isofluorane and were positioned in a stereotaxic apparatus for the insertion of a cranial window<sup>2</sup>. Briefly, using a surgical microdrill, a skull puncture, approximately 4.5 mm in diameter, was made at the coordinates AP: -1 mm; L: 3 mm of the right hemisphere, and covered with a glass coverslip modified to add an injection port sealed with medical grade silicone<sup>3</sup> (Sylgard-184, Sigma-Aldrich). The window was held in place with



cyanoacrylate and dental cement. In addition, a small metal bracket was attached for fixation to a stand adapted for the microscope.

24 h later, the 2P *in vivo* imaging experiment was performed. Stock solution of OGB-1 AM (Life Technologies) was prepared by dissolving it in PBS with 20% pluronic acid till the concentration of 10 mM. For tissue loading stock solution was diluted 20-fold into physiological saline containing (mM) 150 NaCl, 3 KCl, 1 MgCl<sub>2</sub>, 2 CaCl<sub>2</sub>, 10 HEPES, 10 D-glucose; pH 7.40-7.42. The loading solution was made immediately prior to the injection.

The animal was anesthetized by intraperitoneal injection of ketamine/xylazine (100mg/kg and 10mg/kg respectively), and an injection line was prepared to deliver additional doses as needed (approximately every 30 min). The mouse was positioned in the stereotaxic device.

Glass capillaries with the tip size of 2-3  $\mu\text{m}$  were used for injection of the OGB-1 AM solution into the cortex. The glass tip was submerged to a depth of around 100-200  $\mu\text{m}$  from the surface of the brain. OGB-1 AM was pressure-injected from the pipette with the pressure of 500 hPa for 15-20 s.

Imaging was performed after 1 h post injection. The mouse was placed on the microscope stand, fixed by the metal insert to minimize motion artifacts during image acquisition. After acquiring the baseline, the coordinates were recorded for subsequent re-positioning, and the microinjection process was repeated. A micropipette was filled with 3-4 ml of the compound **18a** at 100  $\mu\text{M}$  and 500 hPa pressure was applied for 15-20 s. The mouse was repositioned at the same coordinates and images were acquired at the same position after 1 h post injection. At the end of the experiment the animals were euthanized.

*In vivo* calcium imaging was performed using an inverted laser-scanning confocal microscope (TCS SP5, Leica Microsystems), coupled with a mode-locked Ti:Sapphire laser (720-990 nm) and resonant scanner. Excitation light was focused onto tissue using 25X, NA 0.95 water immersion objective working distance 2.5 mm with a water dispenser (manufactured in CCiTUB workshop). All the data were collected on the Leica system. Excitation wavelength was 800 nm at 25% of the maximum laser power.

Photoisomerization of the compound **18a** was achieved by illuminating the field with 730 nm (maximum laser power) at 1 X 64. line scan for 3 min and with 800 nm (50% of the maximum laser power) 1 X 64. line scan for 3 min.

Calcium transients were imaged using 512 x 512 pixels, 1 X 64. line scan and 8000 Hz frame rate. The imaging interval was of 0.5 s. Acquired image sequences were stored in the Leica

image format and stacks for offline analysis with Fiji (NIH, ImageJ). Fluorescence was expressed as relative fluorescence changes  $F/F_0$ . All data are presented as mean  $\pm$  SEM.

The firing activity was recorded also in absence of the compound to validate our results (Figure S5.15).

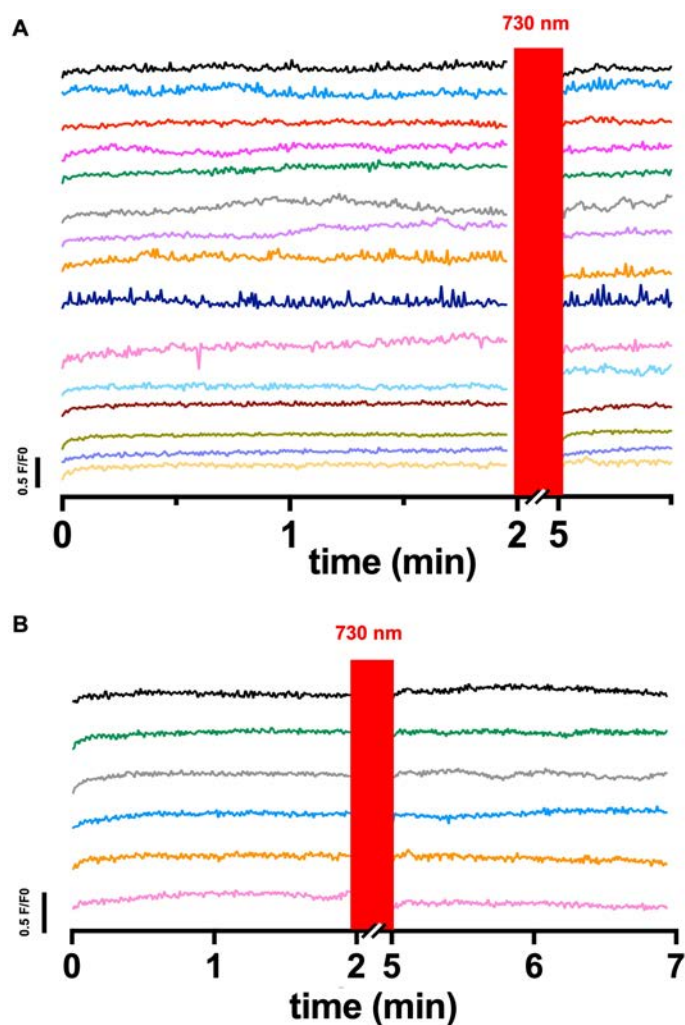


**Figure S5.15. *In vivo* control experiments.** (A) Representative control traces ( $n = 15$  cells) in absence of the compound **18a**. The firing activity in this figure is lower than what is observed after the activation of the compound **18a** which is subsequent to the 730 nm (red area) illumination (Figure 5.5B). (B) Representative control traces ( $n = 6$  cells) showing the cellular activity in absence of compound **18a**, which did not change after the activation of the compound **18a** with 730 nm (red area) illumination (Figure 5.5E).

## Additional references

- 1 Littmann, T., Ozawa, T., Hoffmann, C., Buschauer, A. & Bernhardt, G. A split luciferase-based probe for quantitative proximal determination of G $\alpha_q$  signalling in live cells. *Sci Rep* **8**, 17179, doi:10.1038/s41598-018-35615-w (2018).
- 2 de la Rosa, X. *et al.* *In vivo* imaging of induction of heat-shock protein-70 gene expression with fluorescence reflectance imaging and intravital confocal microscopy following brain ischaemia in reporter mice. *European Journal of Nuclear Medicine and Molecular Imaging* **40**, 426-438, doi:10.1007/s00259-012-2277-7 (2013).
- 3 Roome, C. J. & Kuhn, B. Chronic cranial window with access port for repeated cellular manipulations, drug application, and electrophysiology. *Front Cell Neurosci* **8**, 379, doi:10.3389/fncel.2014.00379 (2014).

# Chapter 6

---

## Reversible activation of muscarinic signaling using orange-red light

---

---

Hubert Gerwe<sup>¶</sup>, **Rosalba Sortino<sup>¶</sup>**, Nayeli Fernanda Pérez-Pérez, Carlo Matera, Fabio Riefolo, Michael Decker\* and Pau Gorostiza\*. **Reversible activation of muscarinic signaling using orange-red light.** *In prep.* <sup>¶</sup>These authors contributed equally. \*Corresponding authors: michael.decker@uni-wuerzburg.de (M.D.) and pau@icrea.cat (P.G.).



## Abstract

The lack of tissue selectivity of conventional systemic pharmacological agents has long sparked the desire for compounds that allow on demand, localized control. Even drugs displaying highly selective pharmacological profiles act on their target at unintended organs and locations, and they do so with pharmacokinetics that cannot be altered externally. Especially in the treatment of neurological disorders, the predominant unselective and fixed kinetics of action of conventional pharmacological agents has caused major challenges. Photopharmacology provides reversible control of endogenous receptor activity with high spatiotemporal resolution by photoswitching ligands between an active and an inactive isomer. Here, we report photoswitchable xanomeline derivatives including one compound (xanoswitch-5) that is inactive in the dark and allows activating M<sub>1</sub> muscarinic acetylcholine receptors with tissue-penetrating orange-red light. Muscarinic deactivation can be achieved with blue light and thermal relaxation. Xanoswitch-5 displays photoreversible efficacy *in vitro* and *in vivo* and no acute toxicity. In the context of ongoing clinical trials with xanomeline and tropium bromide to reduce the adverse effects of peripheral muscarinic activation, our findings have implications to control muscarinic neurotransmission at selected locations using noninvasive light patterns and systemic administration of a dark-inactive photoswitchable drug.



## 6.1 Introduction

Muscarinic acetylcholine receptors (mAChRs or MR) are members of the class A G protein-coupled receptor (GPCR) family and have a crucial role in the central nervous system (CNS) as well as the peripheral nervous system (PNS)<sup>1</sup>. The group comprises five receptor subtypes (M<sub>1</sub>R-M<sub>5</sub>R) of which the odd numbered receptors are excitatory by coupling to G $\alpha_{q/11}$ , while the even numbered receptors are inhibitory by predominantly coupling to G $\alpha_{i/o}$ . Altogether they are involved in a widespread range of functions, regulated by their endogenous ligand acetylcholine. In the CNS, mAChRs control vital functions (*e.g.*, learning, memory and cognition), while these receptors in the PNS prominently mediate negative chronotropic and inotropic effects in the heart, smooth muscle contraction, and glandular secretions<sup>2</sup>. Given the involvement of mAChRs in a broad range of tasks, the impairment of their function is associated with various chronic neurological and peripheral disorders. The disturbed functions of these receptors in the CNS are associated with Alzheimer's disease (AD), schizophrenia (SZ) and Parkinson's disease (PD)<sup>3</sup>, while in the periphery drugs targeting mAChRs are already used in urology, pulmonology, ophthalmology and gastroenterology<sup>4</sup>. Recently, MRs have been linked to potential therapeutic strategies in acute brain diseases, such as traumatic brain injury (TBI)<sup>5</sup> and stroke<sup>6</sup>.

Multiple therapeutic approaches targeting mAChRs have been developed to treat the above-mentioned neurological disorders, however, with limited success<sup>7-10</sup>. The abundant expression in almost all tissues combined with the highly conserved orthosteric binding site of the mAChR subtypes, has made selectively targeting the right receptor subtype in the desired tissue a paradigmatic challenge for medicinal chemists. Some experimental therapeutics (*e.g.*, the functional M<sub>1</sub>R/M<sub>4</sub>R selective orthosteric agonist xanomeline) have shown promising efficacy in clinical studies targeting AD and SZ, although those compounds were ultimately stopped due to severe side effects<sup>11,12</sup>. However, the initial efficacy was promising enough to further develop it into KarTX, a mixture of xanomeline and tiotropium bromide (a peripherally restricted muscarinic antagonist) to mitigate the adverse effects of xanomeline<sup>13</sup>. So far, KarTX has advanced to a phase III clinical study for the treatment of SZ (ClinicalTrials.gov; Identifier: NCT03697252 and NCT04659161)<sup>14,15</sup>. Even though the KarTX approach appears to constrain the agonist actions to the CNS, the conventional agonist xanomeline is not limited to a specific region of the brain or spinal cord. Therefore, this compound could potentially activate its target in multiple CNS regions simultaneously, thus unintentionally affecting other physiological functions. To overcome the limited spatiotemporal selectivity of conventional pharmacological



agents, other methods are required, allowing the controlled activation and deactivation of ligands.

Since 2014, various GPCR ligands have been developed, whose biological activity could be controlled with light as an external stimulus. These photopharmacological agents have been used to photo-modulate a variety of GPCRs with unprecedented spatiotemporal resolution *in vitro* and even *in vivo*<sup>16-38</sup>. Among the so far developed photoswitchable GPCR ligands, a considerable amount has targeted the muscarinic receptors, including the first ever reported photoswitchable ligand Bis-Q in 1971<sup>39</sup>. A great deal of work has been done on these receptors, such as photoswitchable dualsteric ligands<sup>37,40</sup>, optimization of the operational wavelengths<sup>41</sup> and *in vivo* photomodulation of the cardiac activity in rats<sup>37</sup> and brain waves<sup>28,42</sup>. However, each of those photoswitchable ligands share equivalent shortcomings, as these are more active in their thermodynamically stable *trans* form (*trans*-on) and operational with only poorly tissue penetrating wavelengths. The inherent disadvantage of *trans*-on compounds arise out of the thermodynamically driven relaxation from the *cis*- to the *trans*-isomer. This non-radiative process allows an inactive *cis*-isomer to spontaneously convert to its active *trans* form. Thereby, it uncontrollably (re)activates itself, reducing its spatiotemporal resolution in the process.

Here, we report the design, synthesis, and photopharmacological characterization of a series of *cis*-on photoswitchable derivatives of xanomeline, which we termed “xanoswitches”. Highly red-shifted functional photoswitches were developed, which allowed remotely and reversibly photocontrolling GPCR activity *in vitro* and *in vivo*.

## 6.2 Results

### 6.2.1 Rational design and chemical synthesis

We recently developed a set of azobenzene based *cis*-on xanomeline photoswitches, which operated with UV light (one-photon excitation, 1PE), and with near-infrared light using pulsed lasers and two-photon excitation (2PE)<sup>43</sup>. The natural complement of these 2PE xanoswitches is a 1PE-xanoswitch operational with tissue-penetrating light (*e.g.*, orange or red) that trades off the three-dimensional focalized excitation of 2PE photoswitches by the simplicity and portability of continuous 1PE light sources like light emitting diodes (LEDs).

To red-shift the 1PE photophysical properties of the azobenzene, we decided to use *ortho* substitutions rather than electronic push-pull-approaches. The latter affords ~500 nm switching at most with a concomitant decrease of thermal stability of the *cis*-isomer, leading to a fast

relaxation for the *trans* form that prevents highly enriched *cis* states and requires continuous irradiation. In contrast, non-push-pull modifications (*e.g.*, tetra-*ortho*-substitutions with respect to the azobond) yield stronger red-shifting while increasing the thermal stability, giving bistable photoswitches. However, to the best of our knowledge no red-light switchable ligand has been reported for class A GPCRs, probably due to the steric demands of these units.

Aiming at a red-shifted and thermally stable photoswitch (*i.e.*, suitable for a sterically limited orthosteric binding pocket), only a few of the known *ortho* substitutions were accessible. *Ortho*-alkoxyazobenzenes<sup>44-46</sup>, *ortho*-aminoazobenzenes<sup>47,48</sup> and *ortho*-*S*-ethyl-azobenzenes<sup>49</sup> were excluded for their steric demand. The same was true for some of the strongly red-shifted photoswitches based on more exotic scaffolds, including boron-azopyrrole complexes and delocalized cationic azo dyes<sup>50</sup>. Thus, tetra-*ortho*-halogenated azobenzenes were left as the most promising photoswitchable moieties for this target<sup>49,51-55</sup>.

Based on previous work of the research group<sup>40,41,56</sup> and the most recent development of 2PE xanoswitches<sup>43</sup>, we knew that the most suitable position for an azo-extension of xanomeline would be the hydrocarbon side chain. The resulting linker between the thiadiazole core and the azobenzene unit had proven to be optimal with a length of 4 to 5 carbon atoms to afford full agonist efficacy, micromolar potency, and *cis*-on switching<sup>43</sup>.

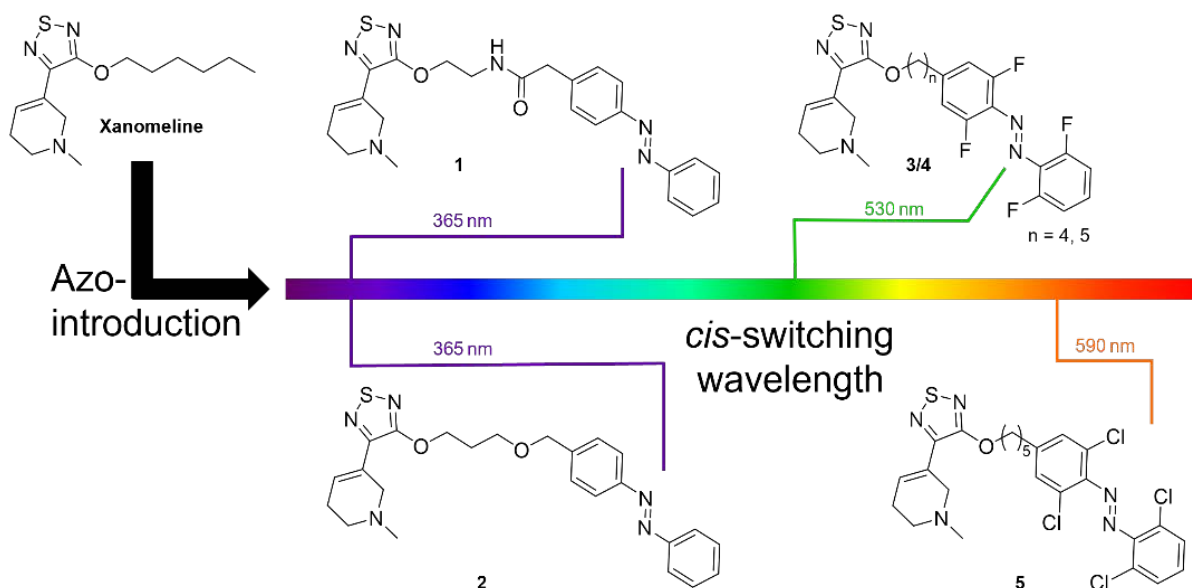
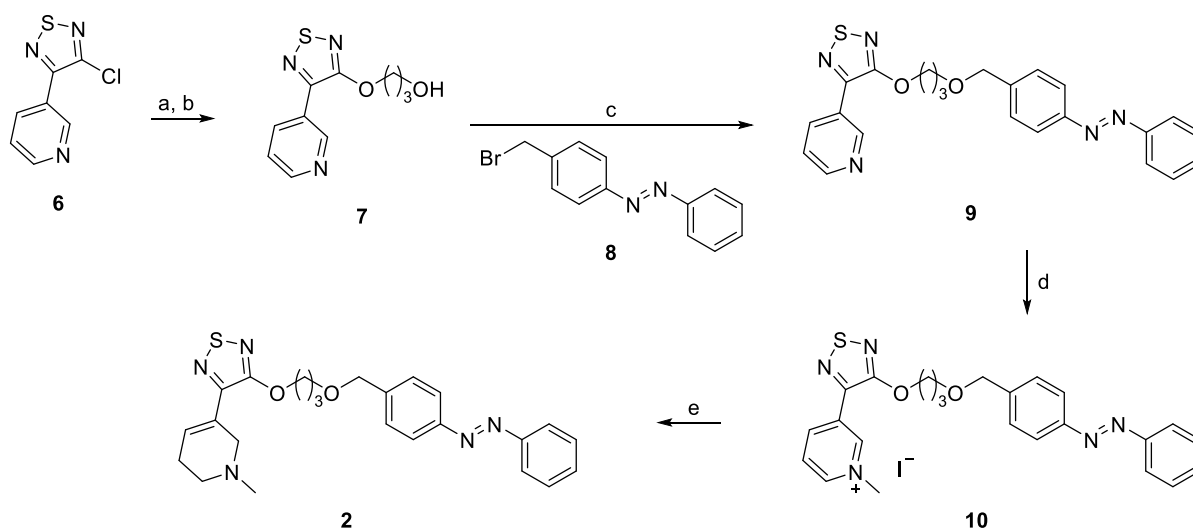


**Figure 6.1.** Diverse ways of introducing the photoswitchable moiety (*i.e.*, the azobenzene) into the structure of xanomeline. Unsubstituted azobenzenes could be switched to their *cis* form with UV light. Tetra-*ortho*-halogenation enables visible light switching, including orange-red light in the case of chloro substitution.

To simplify screening of suitable azobenzenes moieties, a synthetic route was needed which allowed late-stage derivatization. Based on the thoroughly conducted structure-activity

relationships (SARs) of the tetrahydropyridines<sup>57-61</sup>, we reasoned that incorporation of an amide into the linker would maintain activity and simultaneously give the desired access to fast derivatization. This led to amide-linked xanoswitch-1 (**Figure 6.1**), comprising an unsubstituted azobenzene to assess the effect of the amide on functional photoswitching. Although chemically advantageous (see **Supporting Information; SI** for the details), this approach did not prove to be successful (*vide infra*).

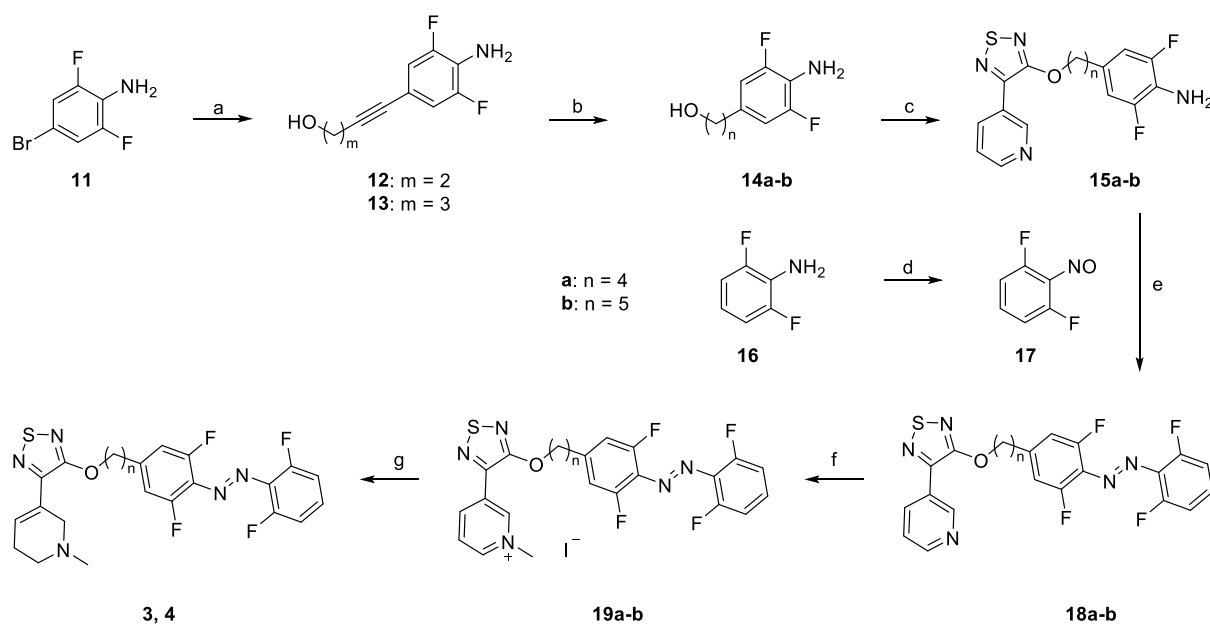
Next, we investigated whether an ether linker was accessible. As a less polar group, in comparison to the amide, the ether was supposed to maintain functional photoswitching and allow using a Williamson ether synthesis to connect various bromomethyl-azobenzenes moieties to the thiadiazole-fragment (**7**). This would also allow a convergent synthetic approach that facilitates derivatization (**Scheme 6.1**). Starting from 3-chloro-4-(pyridin-3-yl)-1,2,5-thiadiazole (**6**) which had been synthesized according to literature<sup>57</sup> a nucleophilic aromatic substitution using 3-((tert-butyldimethylsilyl)oxy)propan-1-ol with sodium hydride in tetrahydrofuran (THF) was conducted. Subsequent desilylation of the TBS protected alcohol using 2 N aqueous hydrochloric acid yielded the alcohol (**7**) which was coupled to 1-(4-(bromomethyl)phenyl)-2-phenyldiazene (**8**) in a Williamson ether synthesis. However, this step was hampered by a competing reaction which formed the symmetric dimer. Hence, the reaction conditions were carefully adjusted to favor the substitution at the bromoethyl-moiety of compound **8**. This was achieved by using KOtBu in dioxane, which yielded 3-(3-((4-(phenyldiazenyl)benzyl)oxy)propoxy)-4-(pyridin-3-yl)-1,2,5-thiadiazole (**9**) in sufficient yield.



**Scheme 6.1. Synthesis of ether-linked xanoswitch-2.** Reagents and conditions: (a) 3-((tert-butyldimethylsilyl)oxy)propan-1-ol, NaH, THF, 60°C, 89%; (b) 2 N HCl, MeOH, RT, 72%; (c) **8**, KOtBu, dioxane, 70°C, 30%; (d) MeI, acetone, RT, 98%; (e) NaBH<sub>4</sub>, MeOH/CH<sub>2</sub>Cl<sub>2</sub>, RT, 57%.

Quaternization of compound **9** by *N*-methylation of the pyridine with iodomethane in acetone was followed by reduction of the resulting pyridinium cation (**10**) with sodium tetra borohydride in methanol. This reaction region-selectively yielded the desired 1-methyl-1,2,3,6-tetrahydropyridine xanoswitch-**2**. This route was not repeated with any *ortho*-halogenated azobenzene as the *in vitro* evaluation proved the ether-linker unfavorable (for concentration-response curves see **Figure 6.2**). Thus, we ceased to focus on late-stage derivatization approaches and continued with the pure aliphatic linkers used for the 2PE-xanoswitches<sup>43</sup>.

Hence, tetra-*ortho*-fluorinated xanoswitches comprising an alkylene linker of 4 and 5 methylene units (**3,4**; cf. **Scheme 6.2**) were synthesized starting from 4-bromo-2,6-difluoroaniline (**11**). An alkynol with the desired length was introduced by Sonogashira cross coupling reaction yielding the corresponding amino-difluorophenyl-alkynols (**12,13**). Subsequent palladium-catalyzed hydrogenation of the alkynol gave the saturated amino-difluorophenyl-alcohols (**14a,b**). In a nucleophilic aromatic substitution, employing Williamson ether synthesis reaction conditions, these alcohols were coupled to the thiadiazole core (**6**), which resulted in thiadiazole-difluorophenyl anilines (**15a,b**).

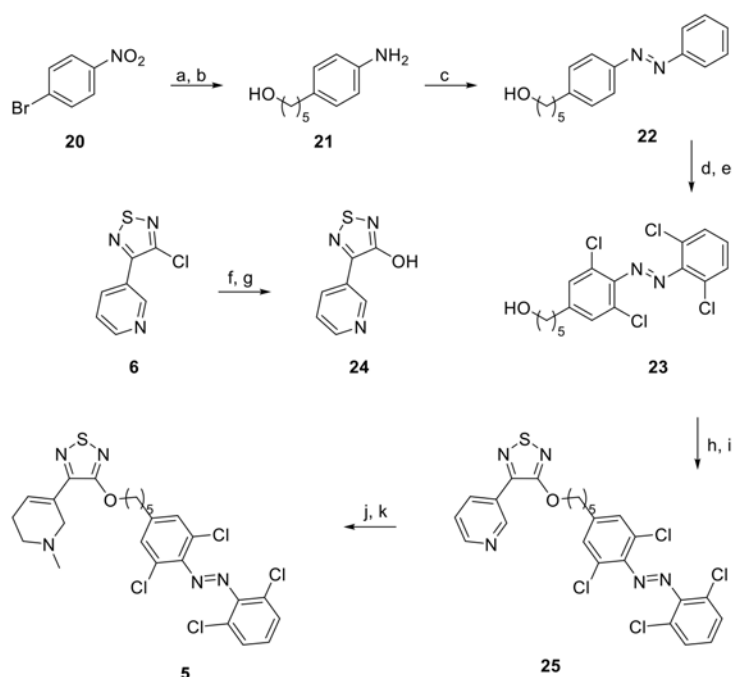


**Scheme 6.2** Synthetic route to tetra-*ortho*-fluorinated xanoswitches-**3** and -**4**. Reagents and conditions: (a) Alkynol, CuI, PdCl<sub>2</sub>(PPh<sub>3</sub>)<sub>2</sub>, PPh<sub>3</sub>, NEt<sub>3</sub>/THF, 90°C, 72-85%; (b) Pd/C, H<sub>2</sub>, MeOH, RT, 85-89%, t.); (c) **6**, NaH, THF, 70°C, 46-48%; (d) Oxone<sup>®</sup>, CH<sub>2</sub>Cl<sub>2</sub>, H<sub>2</sub>O, RT (e) 1,3-difluoro-2-nitrosobenzene, HOAc/Toluol/TFA 6:6:1, RT, 79-83%; (f) MeI, acetone, RT, 87%, quant.); (g) NaBH<sub>4</sub>, MeOH/CH<sub>2</sub>Cl<sub>2</sub>, 0°C to RT, 21-43%.

In a Baeyer-Mills reaction the tetra-*ortho*-fluorinated azobenzenes (**18a,b**) were formed, condensing the anilines with the respective difluorinated nitrosobenzene (**17**) in a mixture of acetic acid, THF and trifluoro acetic acid. Difluoronitrosobenzene (**17**) was synthesized by

partial oxidation of the corresponding aniline in a heterogeneous water/dichloromethane system by using Oxone<sup>®</sup> and directly proceeded without further purification. Quaternization and reduction of the pyridine to give fluorinated xanoswitches (**3,4**) were performed as described above.

The corresponding tetra-*ortho*-chlorinated compound could not be synthesized via the same route. The conditions upon which tetra-*ortho*-chlorinated azobenzenes are formed, are across-the-board incompatible with the thiadiazole moiety. Hence, the desired azobenzene had to be formed first (**Scheme 6.3**).



**Scheme 6.3. Synthetic route to tetra-*ortho*-chlorinated xanoswitch-5.** Reagents and conditions: (a) pent-4-yn-1-ol, CuI, PdCl<sub>2</sub>(PPh<sub>3</sub>)<sub>2</sub>, PPh<sub>3</sub>, NEt<sub>3</sub>/THF, 70°C, 98%; (b) Pd/C, 10 atm. H<sub>2</sub>, MeOH, RT, 95%; (c) nitrosobenzene, HOAc, RT, 79%; (d) NCS, Pd(OAc)<sub>2</sub>, HOAc, 140°C, 49%; (e) 6N HCl, THF, RT, quant.; (f) phenylmethanol, NaH, THF, 65°C, 78%; (g) CH<sub>2</sub>Cl<sub>2</sub>, HBr/AcOH, RT, 70%; (h) **24**, DEAD, PPh<sub>3</sub>, THF, 0°C to RT, 67%; (i) MeI, acetone, RT; (j) NaBH<sub>4</sub>, MeOH/CH<sub>2</sub>Cl<sub>2</sub>, 0°C to RT.

Using the Sonogashira cross coupling reaction, followed by catalytic hydrogenation, the 5-(4-aminophenyl)pentan-1-ol (**21**) was synthesized. In a Baeyer-Mills reaction compound **21** was reacted with commercially available nitrosobenzene, yielding 5-(4-(phenyldiazenyl)phenyl)pentan-1-ol (**22**). Functionalization by late-stage chlorination<sup>62</sup> followed by ester saponification of the resulting acetate was conducted to obtain the desired tetra-*ortho*-chlorinated azobenzene (**23**). Compound **23** could not be coupled to the thiadiazol core (**6**) through using the above-described nucleophilic aromatic substitution of the chlorine.

For tetra-*ortho*-halogenated azobenzenes, the nucleophilic aromatic substitution at the heterocyclic core is competing with the nucleophilic substitution at the halogenated azobenzenes, resulting in a red goo of discouraging composition. Therefore, a Mitsunobu reaction was employed. The necessary aromatic alcohol (**24**) was synthesized by nucleophilic aromatic substitution of **6** with benzyl alcohol followed by benzyl deprotection using HBr in AcOH. The resulting hydroxyarene was then coupled to compound **23** using standard Mitsunobu conditions to yield the desired compound **25**. Subsequent quaternization and reduction, as described above, yielded the tetra-*ortho*-chlorinated xanoswitch-**5**.

### 6.2.2 Photochemical characterization

By using ultraviolet-visible (UV-Vis) spectroscopy, the photochemical properties of the xanoswitches (see **SI**) were determined. Unsubstituted azobenzenes (**1,2**) could be operated with ultraviolet (UV) light (365 nm, *trans*-to-*cis*) and blue light (455 nm, *cis*-to-*trans*). Tetra-*ortho*-fluorinated xanoswitches (**3,4**) could be operated with blue (455 nm, *cis*-to-*trans*) and green light (530 nm, *trans*-to-*cis*). Finally, tetra-*ortho*-chlorinated xanoswitch-**5** could be switched with orange (590 nm, *trans*-to-*cis*) and blue light (455 nm, *cis*-to-*trans*), as intended by design. Thermostability and photobleaching behavior were in accordance with the prototypical photoswitchable moieties of each species, allowing for clear, reversible switching, highly enriched photostationary states and long thermal relaxation half-lives (see **SI**).

### 6.2.3 Split luciferase complementation assay

Next, we tested the compounds at their maximally *cis/trans*-enriched photostationary states for their ability to activate the human M<sub>1</sub>R using a split luciferase-based probe for quantitative proximal determination of G $\alpha_q$  signaling in live cells (**Figure 6.2**). The probe detects interactions between G $\alpha_q$  and its effector phospholipase C- $\beta_3$  (PLC- $\beta_3$ ) as a quantifiable parameter of receptor activation<sup>63</sup>. The wavelength emitted by the modified luciferase from the click-beetle *Pyrophorus plagiophthalmus* ( $\lambda_{\text{max}} = 613$  nm) shows at the given intensity no interference with the compounds photoisomerization<sup>63</sup>. Taken from the previous work on 2PE xanoswitches, an unmodified, photochemical sub-optimal but functional xanoswitch (**16e**, linker length  $n = 5$ , see **Scheme 5.1**) was included as *de facto* parent compound and served as benchmark of the newly developed xanoswitches (**Figure 6.2**)<sup>43</sup>. Incorporation of an amide into the linker was shown to be highly detrimental for functional photoswitching. The amide almost completely stripped off any significant potency difference between the two isoforms of xanoswitch-**1**, maintaining a merely weak (~10%) *cis*-on efficacy difference. Moreover, the

amide moiety decreased the maximal efficacy of xanoswitch-1 down to ~70%. Interestingly, both isoforms of compound **1** behaved like the *trans* form of reference compound **16e**, suggesting that the amide only affects the *cis* form. Considering that the introduction of the amide alone had removed all positive features of **16e**, hence a less polar group within the linker was supposed to retain functional photoswitching, consequently ether-linked xanoswitch-2 was developed. The effects of the ether linker were indeed less dramatic. Xanoswitch-2 remained a highly potent agonist with a noticeable separation between the *cis*- and *trans*-enriched states concentration-response curve. Nevertheless, xanoswitch-2 performed worse than reference xanoswitch-16e. In combination with the synthetic difficulties (*vide supra*), this ruled out any further investigation into ether-linked xanoswitches.

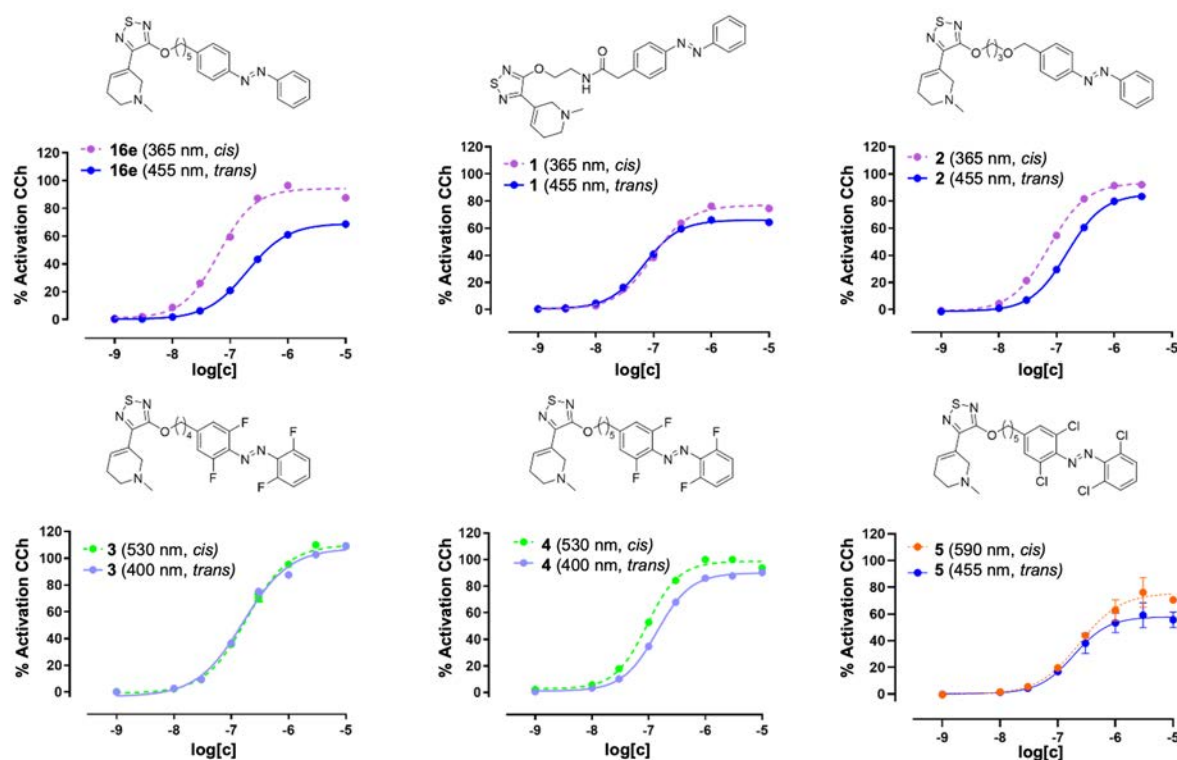


**Figure 6.2.** *In vitro* characterization of photoswitchable M<sub>1</sub> mAChR ligands using a split luciferase complementation assay. This assay detects the interaction between Gα<sub>q</sub> and its effector phospholipase C-β<sub>3</sub> (PLC-β<sub>3</sub>) as a quantifiable parameter of receptor activation. Concentration-response-curves of pre-illuminated xanoswitches in either *cis* or *trans* form. Data is given as the mean ± SEM of 3 independent experiments and normalized over the maximum response obtained with 10 μM carbachol.

Taking into consideration the results of the fluorination of 2PE xanoswitches, it was already suspected that *ortho* fluorination could have a detrimental effect on functional photoswitching. Indeed, the same trend was observed. The C4 linked tetra-*ortho*-fluorinated xanoswitch-3 showed complete elimination of any functional photoswitching. *Cis*- and *trans*-enriched states,

even though being almost quantitatively switched, showed identical activity, while acting as sub-micromolar agonists. This is in line with the observation on the difluorinated (2PE) xanoswitch of the same linker length<sup>43</sup>. Further following the observation on the difluorinated 2PE xanoswitches, some functional photoswitching could be recovered by elongation of the linker to five methylene units (xanoswitch-4). The same degree of functional photoswitching was also observed for the tetra-*ortho*-chlorinated xanoswitch-5. However, the sterically more demanding chloro substituents reduced the efficacy to ~78% in the *cis*-enriches state and ~62% in the *trans*-enriched state at identical potencies (**Table S6.1**).

We had previously observed that due to the nonlinear response of biological systems, slight differences (measured on the receptor level of signaling) can be amplified to significant differences in downstream responses reaching even full on/off switching<sup>64</sup>. Thus, out of this set of red-shifted 1PE xanoswitches, compounds **4** and **5** were selected to be further investigated for their ability to induce cytosolic calcium oscillations.

#### 6.2.4 *In vitro* calcium imaging

Xanoswitches-4 and -5 were tested for their ability to photocontrol the calcium influx in a fluorescence imaging assay in human embryonic kidney (HEK) cells co-expressing human M<sub>1</sub>R and R-GECO1, a red calcium indicator (excitation 562 nm, emission 600 nm). Here, carbachol (CCh) was used as control (**Figure 6.3** and **Figure S6.12**). When xanoswitch-4 or -5 were applied to the cells in their dark adapted *trans* form, it resulted in no significant responses. A robust increase of intracellular calcium was observed under illumination with 530 nm (**Figure 6.3AB**) and 590 nm (**Figure 6.3DE**), which induced the *trans*-to-*cis* isomerization of xanoswitch-4 and -5, respectively. Calcium responses were abolished under 400 nm illumination for xanoswitch-4 (**Figure 6.3AB**) and 455 nm for xanoswitch-5 (**Figure 6.3DE**), which photoisomerize back to their *trans*-enriched states. To further validate the *cis*-on activity of xanoswitch-5, we applied pre-illuminated *cis*-5. This resulted in a more evident effect. The quantification of the peak amplitude confirmed that *trans*-4 (**Figure 6.3C**) and *trans*-5 (**Figure 6.3D**) do not evoke any effect, while both *cis*-4 (**Figure 6.3C**) and *cis*-5 (**Figure 6.3D**) stimulated intracellular calcium release (similar or above CCh) at all the concentrations used (0.3, 1 and 10  $\mu$ M). No responses were observed in control experiments with HEK cells not expressing human M<sub>1</sub>R (**Figure S6.12**). Altogether, the *in vitro* data demonstrated that both compounds can be dynamically photomodulated with respect to their agonistic behavior and both are more active in their *cis* forms.



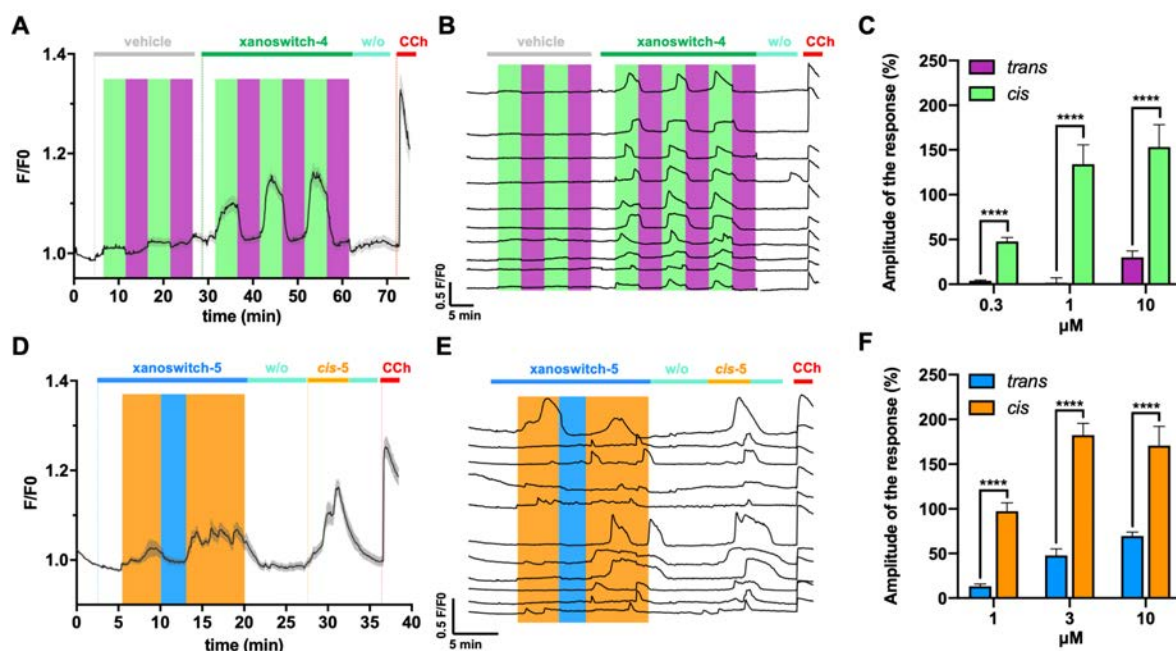


**Figure 6.3. *In vitro* characterization of xanoswitches-4 and -5 using calcium fluorescence imaging.** (A and D) Time course of  $M_1$  mAChR F/F0 responses (black trace indicates the average; grey band corresponds to the SEM) in the presence of (A) vehicle and  $0.3 \mu\text{M}$  xanoswitch-4 ( $n = 33$  cells), (D)  $1 \mu\text{M}$  xanoswitch-5 ( $n = 37$  cells). For both compounds,  $10 \mu\text{M}$  carbachol was used as positive control. Example traces (B,  $n = 10$  cells) and (E,  $n = 11$  cells) of calcium fluorescence photoresponses (F/F0) for compounds 4 and 5, respectively. Photoisomerization under one-photon excitation occurred by alternating 530 nm (green) and 400 nm (violet) for xanoswitch-4 (A and B) and 590 nm (orange) and 455 nm (blue) for xanoswitch-5 (D and E). (C and F) Quantification of  $M_1$  mAChR photoresponses elicited by (C) xanoswitch-4, and (F) xanoswitch-5, normalized to  $10 \mu\text{M}$  carbachol responses. (C) Xanoswitch-4 yielded significant differences between 530 nm and 400 nm at different concentrations:  $0.3 \mu\text{M}$  ( $n = 63$  cells),  $1 \mu\text{M}$  ( $n = 31$  cells), and  $10 \mu\text{M}$  ( $n = 65$  cells). (F) Xanoswitch-5 showed significant differences between 590 nm and 455 nm at  $1 \mu\text{M}$  ( $n = 102$  cells),  $3 \mu\text{M}$  ( $n = 102$  cells), and  $10 \mu\text{M}$  ( $n = 63$  cells). Statistical analysis of panels C and F were performed by the paired sample Wilcoxon signed rank test ( $p$ -value (\*\*\*\*)  $< 0.0001$ ).

### 6.2.5 *In vivo* photocontrol of locomotor activity in zebrafish larvae

The outstanding properties of xanoswitch-5 *in vitro* (Figure 6.3) prompted further characterization in an animal model to evaluate photocontrol of behavior and preliminary toxicity<sup>26,65</sup>. MRs play key roles in countless CNS processes, such as locomotion. To test xanoswitch-5, we recorded and quantified the locomotor activity of zebrafish larvae (*Danio rerio*), taking advantage of their small size and ease of manipulation (for high-throughput screening in multiwell plates), their transparency (for illumination), and their permeability to small molecules (to add xanoswitch-5 directly in water)<sup>66</sup>. Note that the zebrafish brain presents

a similar structural organization and a cellular morphology to higher vertebrates<sup>66</sup> and its genome comprises orthologs of 71% of human genes, including all five mAChR subtypes.

We performed behavioral experiments in blinded zebrafish larvae to isolate motility photoresponses due solely to the compound rather than mediated by visual behaviors. Zebrafish larval movements were tracked at 7 days post-fertilization (7 dpf) using a Viewpoint Zebrabox device for automated behavioral recordings as previously reported<sup>26,67</sup>.

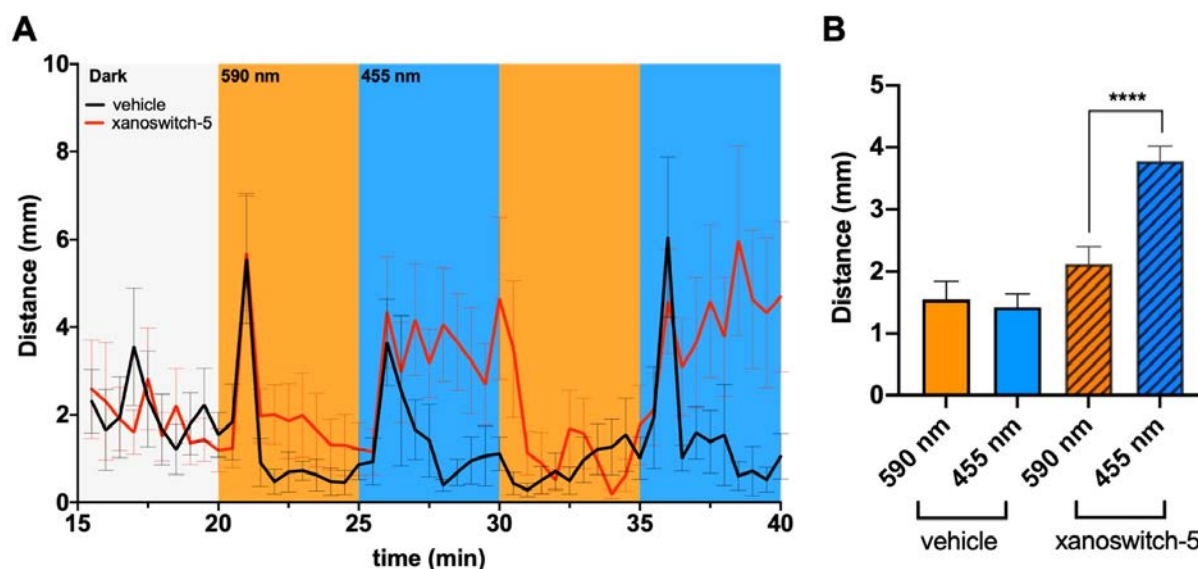


**Figure 6.4. Photocontrol of behavior by xanoswitch-5 in blinded zebrafish larvae.** (A) One-minute trajectories of average swimming distances (in mm integrated every half-min interval,  $n = 24$  larvae) are shown for vehicle (0.3% DMSO) and xanoswitch-5 (30  $\mu\text{M}$ ). In the first 20 min, larvae were undisturbed in complete darkness (relaxation period, RP). Following RP, larvae were illuminated with two consecutive cycles of orange (590 nm; 2 mW) and blue (455 nm; 7 mW) light for 5 min each cycle. Error bars represent standard error of the mean (SEM). (B) Quantification of the total distances swum by the control group (vehicle,  $n = 6$ ) and the treatment group (xanoswitch-5,  $n = 6$ ) during two consecutive cycles of 590 nm and 455 nm light. Data are mean  $\pm$  SEM and were analyzed by two-way ANOVA followed by Tukey's post hoc test ( $p$ -value (\*\*\*\*)  $< 0.0001$  for vehicle 590 nm vs. *trans*-5;  $p$ -value (\*\*\*\*)  $< 0.0001$  for vehicle 455 nm vs. *trans*-5;  $p$ -value (\*\*\*\*)  $< 0.0001$  for *cis*-5 vs. *trans*-5) using GraphPad Prism 9. Error bars indicate  $\pm$  SEM.

Blinded larvae were randomly divided into control (vehicle, 0.3% DMSO) and treatment groups (30  $\mu\text{M}$  xanoswitch-5 added to water) with each individual placed in a different well of a 96-well plate. After a relaxation period of 20 min, blinded larvae were exposed to two consecutive cycles of 590 nm and 455 nm light and the swum distances were measured over time for each individual and quantified for the treated and control groups (Figure 6.4A). Xanoswitch-5 produced clear and reversible differences in activity under 590 nm and 455 nm light, whereas no changes in locomotion were observed in the control group for the same illumination cycles (Figure 6.4A). The quantification and statistical analysis of locomotion of

the control and treated groups during the light cycles show that larvae swim significantly longer distances under 455 nm than under 590 nm light (**Figure 6.4B**). Remarkably, all larvae were alive 24 h after the experiments in presence of the xanoswitch-5, which demonstrates that this compound does not produce acute toxicity, neither alone nor under illumination.

### 6.3 Discussion

Understanding the role of the different muscarinic receptor subtypes among distinct tissues is fundamental in neurobiology. In fact, muscarinic signaling is extraordinarily complex with all five subtypes (*i.e.*, M<sub>1</sub>R-M<sub>5</sub>R) carrying out functions that depend on the identity and location of each receptor in the body<sup>2</sup>. Given their implication in the modulation of pivotal physiological functions in CNS and PNS, these receptors have been identified as potential therapeutical targets for several pathologies<sup>7,68</sup>. In particular, M<sub>1</sub>R holds immense therapeutic relevance, as it is involved in neuronal excitability, synaptic plasticity, learning, and memory. These processes are dysregulated in various cognitive and neurodegenerative diseases, such as SZ, PD and AD<sup>69-71</sup>. Many muscarinic agonists (*e.g.*, xanomeline) and antagonists have been developed for both basic research and clinical purpose<sup>12</sup>. However, they have limited subtype selectivity due to the high degree of homology of the transmembrane region among the different muscarinic receptors. Even if subtype-selective muscarinic ligands could be developed, MRs are expressed in multiple organs and tissues, where they play diverse roles. Therefore, the clinical use of systemically administered muscarinic drugs is quite limited due to their severe adverse effects.

Optogenetic approaches have been used to photocontrol the activity of specific cell types and organisms in a genetically targeted manner, allowing to dissect neuronal circuits<sup>72</sup>. Despite the valuable contributions of this method to address many central questions in neuroscience, it does not allow targeting the endogenous receptors and their physiological role, and it requires genetic manipulation. This raises several limitations to study the intact neurotransmitter pathways and for *in vivo* applications, both fundamental and therapeutic.

Photopharmacological strategies that employ photochromic ligands (PCLs) target endogenous receptors with light without requiring genetic manipulation, thus overcoming the limitations of optogenetics. In contrast to caged compounds, PCLs target the receptor in a reversible manner, allowing to fine-tune its activity<sup>73-75</sup>. This property also makes PCLs more suitable for potential clinical applications. At present, PCLs have been synthesized to target all major GPCRs classes, but most of them require UV light for photoisomerization<sup>26,29,36-38,40</sup>. Longer wavelengths can

penetrate deeper and do not damage tissue, like those in the red or infrared range. Red light photoswitching would be very convenient for clinical usage and great efforts have been devoted to this aim<sup>46,48-50</sup>. However, few usable photoswitches have been identified in this range. Another possibility is using IR light for 2PE of PCLs with femtosecond pulsed lasers, which combine even deeper tissue penetration and a lower toxicity and allow photostimulating at subcellular resolution in three dimensions<sup>37,76-79</sup>. In recent work<sup>43</sup>, we have developed xanoswitches that allow bidirectional control of the M<sub>1</sub>R *in vitro* and *in vivo* by 2PE processes. While 2PE photoswitches offer great promise to study neural circuits, for translational purposes this approach is hindered by the limited portability of the pulsed laser, optical setup, and head fixed device.

Thus, PCLs activated by continuous wave illumination with red light bear great interest, as suitable illumination devices could be portable and robust, built with inexpensive, lightweight, and commercially available light emitting diodes (LEDs). However, red-activated photoswitches are notably difficult to synthesize and the chemical substitutions to tune the spectrum to longer wavelengths often damage their pharmacological properties.

Here, we report xanoswitch-**5**, a dark-inactive (*cis*-on) PCL activated by orange-red light that allows reversible activation of M<sub>1</sub>R, both *in vitro* and *in vivo*. This compound could be noninvasively activated with external illumination devices to regulate muscarinic neurotransmission at selected locations. For instance, xanoswitch-**5** could be applied to activate specific neuronal pathways with high spatiotemporal precision as well as to potentially treat pathological conditions involving M<sub>1</sub>Rs, like SZ, PD<sup>3</sup>, AD, sleep disorders, and acute brain diseases, such as TBI<sup>4</sup> and stroke<sup>5</sup>. Localized, on-demand photoactivation of mAChRs may provide higher versatility and lower adverse effects than current approaches combining an agonist and an antagonist with different biodistribution to target the CNS (KarTX)<sup>13</sup>. Xanoswitches may also be useful for peripheral indications in urology, pulmonology, ophthalmology, and gastroenterology<sup>3</sup>, which are also validated for mAChRs drugs and might be more accessible to noninvasive or minimally invasive illumination than the CNS.

Both xanoswitches-**4** and -**5** display micromolar potency and full agonism *in vitro*, which can be reversibly photoswitched with different wavelengths of light. Remarkably, as derivatives of the clinical candidate compound xanomeline (ClinicalTrials.gov; Identifier: NCT03697252 and NCT04659161)<sup>14,15</sup>, xanoswitches (including xanoswitch-**5**) may inherit the drug-like properties of their parent compound<sup>65</sup>. Compared to other reported muscarinic photoswitchable agonists like BAI<sup>40</sup> and PAI<sup>37</sup>, xanoswitches are smaller, display good aqueous solubility,

intermediate potency (micromolar), and do not bear charges, which may allow the compounds to cross membranes.

Behavioral studies in zebrafish larvae demonstrate that xanoswitch-**5** allows reversibly controlling locomotory activity *in vivo*. We hypothesize that M<sub>1</sub>R activation by *cis-5* may account for the partial inhibition of locomotion. However, the mechanism underlying such outcome of a cholinergic input is overly complex. Published evidence reveals an interplay between the cholinergic and dopaminergic systems in the basal ganglia that is responsible for locomotion<sup>80</sup>. Different muscarinic receptor subtypes expressed at interneurons and medium spiny neurons could be activated or deactivated by xanoswitch-**5**, thereby producing diverse locomotor outcomes<sup>81,82</sup>. In fact, photoswitchable xanomelines offer unique opportunities to study these endogenous synaptic circuits *in vivo* in wildtype organisms.

## 6.4 Conclusions

We have developed novel photoswitchable xanomeline derivatives (xanoswitches) that are inactive in the dark (*cis-on*) and allow reversibly controlling M<sub>1</sub>Rs using visible wavelengths. Amongst those compounds, xanoswitch-**5** stands out by its full agonism, micromolar potency, and orange-red light activation *in vitro* and *in vivo*. Activation of endogenous M<sub>1</sub>Rs in spatiotemporal patterns will allow dissecting the pathophysiological roles of muscarinic subtypes in cholinergic neurotransmission. In combination with suitable illumination devices, xanoswitch-**5** gathers several favorable properties to support photopharmacological therapies for the PNS and CNS.

## References

- 1 Eglen, R. M. Overview of muscarinic receptor subtypes. *Handb Exp Pharmacol*, 3-28, doi:10.1007/978-3-642-23274-9\_1 (2012).
- 2 Eglen, R. M. Muscarinic receptor subtype pharmacology and physiology. *Prog Med Chem* **43**, 105-136, doi:10.1016/S0079-6468(05)43004-0 (2005).
- 3 Winek, K., Soreq, H. & Meisel, A. Regulators of cholinergic signaling in disorders of the central nervous system. *J Neurochem* **158**, 1425-1438, doi:10.1111/jnc.15332 (2021).
- 4 Kruse, A. C. *et al.* Muscarinic acetylcholine receptors: Novel opportunities for drug development. *Nat Rev Drug Discov* **13**, 549-560, doi:10.1038/nrd4295 (2014).
- 5 Shin, S. S. & Dixon, C. E. Alterations in cholinergic pathways and therapeutic strategies targeting cholinergic system after traumatic brain injury. *J Neurotrauma* **32**, 1429-1440, doi:10.1089/neu.2014.3445 (2015).
- 6 Martín, A., Domercq, M. & Matute, C. Inflammation in stroke: The role of cholinergic, purinergic and glutamatergic signaling. *Ther Adv Neurol Disord* **11**, 1756286418774267, doi:10.1177/1756286418774267 (2018).
- 7 Felder, C. C., Bymaster, F. P., Ward, J. & DeLapp, N. Therapeutic opportunities for muscarinic receptors in the central nervous system. *J Med Chem* **43**, 4333-4353, doi:10.1021/jm990607u (2000).
- 8 Erskine, D. *et al.* Cholinergic muscarinic M<sub>1</sub> and M<sub>4</sub> receptors as therapeutic targets for cognitive, behavioural, and psychological symptoms in psychiatric and neurological disorders. *Drug Discov Today* **24**, 2307-2314, doi:10.1016/j.drudis.2019.08.009 (2019).
- 9 Subramaniam, S., Blake, D. T. & Constantinidis, C. Cholinergic deep brain stimulation for memory and cognitive disorders. *J Alzheimers Dis* **83**, 491-503, doi:10.3233/jad-210425 (2021).
- 10 Brown, A. J. H. *et al.* From structure to clinic: Design of a muscarinic M<sub>1</sub> receptor agonist with potential to treatment of Alzheimer's disease. *Cell* **184**, 5886-5901.e5822, doi:10.1016/j.cell.2021.11.001 (2021).
- 11 Bodick, N. C. *et al.* Effects of xanomeline, a selective muscarinic receptor agonist, on cognitive function and behavioral symptoms in Alzheimer disease. *Arch Neurol* **54**, 465-473, doi:10.1001/archneur.1997.00550160091022 (1997).
- 12 Shekhar, A. *et al.* Selective muscarinic receptor agonist xanomeline as a novel treatment approach for schizophrenia. *Am J Psychiatry* **165**, 1033-1039, doi:10.1176/appi.ajp.2008.06091591 (2008).
- 13 Brannan, S. K. *et al.* Muscarinic cholinergic receptor agonist and peripheral antagonist for schizophrenia. *N Engl J Med* **384**, 717-726, doi:10.1056/NEJMoa2017015 (2021).
- 14 Correll, C. U., Angelov, A. S., Miller, A. C., Weiden, P. J. & Brannan, S. K. Safety and tolerability of KarXT (xanomeline-trospium) in a phase 2, randomized, double-blind, placebo-controlled study in patients with schizophrenia. *Schizophrenia (Heidelb)* **8**, 109, doi:10.1038/s41537-022-00320-1 (2022).
- 15 Sauder, C. *et al.* Effectiveness of KarXT (xanomeline-trospium) for cognitive impairment in schizophrenia: Post hoc analyses from a randomised, double-blind, placebo-controlled phase 2 study. *Translational Psychiatry* **12**, 491, doi:10.1038/s41398-022-02254-9 (2022).
- 16 Morstein, J. *et al.* Photoswitchable serotoninins for optical control of the 5-HT<sub>2A</sub> receptor\*\*. *Angewandte Chemie International Edition* **61**, e202117094, doi:https://doi.org/10.1002/anie.202117094 (2022).
- 17 Gerwe, H., He, F., Pottie, E., Stove, C. & Decker, M. Enlightening the “spirit molecule”: Photomodulation of the 5-HT<sub>2A</sub> receptor by a light-controllable *N,N*-

- dimethyltryptamine derivative. *Angewandte Chemie International Edition* **61**, e202203034, doi:https://doi.org/10.1002/anie.202203034 (2022).
- 18 Donthamsetti, P. *et al.* Cell specific photoswitchable agonist for reversible control of endogenous dopamine receptors. *Nat Commun* **12**, 4775, doi:10.1038/s41467-021-25003-w (2021).
- 19 Donthamsetti, P. *et al.* Selective photoswitchable allosteric agonist of a G protein-coupled receptor. *J Am Chem Soc* **143**, 8951-8956, doi:10.1021/jacs.1c02586 (2021).
- 20 Bosma, R. *et al.* Optical control of the  $\beta_2$ -adrenergic receptor with opto-prop-2: A *cis*-active azobenzene analog of propranolol. *iScience* **25**, 104882, doi:10.1016/j.isci.2022.104882 (2022).
- 21 Hauwert, N. J. *et al.* A Photoswitchable agonist for the histamine H<sub>3</sub> receptor, a prototypic family A G protein-coupled receptor. *Angewandte Chemie International Edition* **58**, 4531-4535, doi:https://doi.org/10.1002/anie.201813110 (2019).
- 22 Gómez-Santacana, X. *et al.* Photoswitching the efficacy of a small-molecule ligand for a peptidergic GPCR: From antagonism to agonism. *Angewandte Chemie International Edition* **57**, 11608-11612, doi:https://doi.org/10.1002/anie.201804875 (2018).
- 23 Lahmy, R. *et al.* Photochromic fentanyl derivatives for controlled  $\mu$ -opioid receptor activation. *Chemistry – A European Journal* **28**, e202201515, doi:https://doi.org/10.1002/chem.202201515 (2022).
- 24 Rustler, K., Pockes, S. & König, B. Light-switchable antagonists for the histamine H<sub>1</sub> receptor at the isolated guinea pig ileum. *ChemMedChem* **14**, 636-644, doi:https://doi.org/10.1002/cmdc.201800815 (2019).
- 25 Lachmann, D., Konieczny, A., Keller, M. & König, B. Photochromic peptidic NPY Y4 receptor ligands. *Organic & Biomolecular Chemistry* **17**, 2467-2478, doi:10.1039/C8OB03221A (2019).
- 26 Matera, C. *et al.* Reversible photocontrol of dopaminergic transmission in wild-type animals. *Int J Mol Sci* **23**, doi:10.3390/ijms231710114 (2022).
- 27 Garrido-Charles, A. *et al.* Fast photoswitchable molecular prosthetics control neuronal activity in the cochlea. *Journal of the American Chemical Society* **144**, 9229-9239, doi:10.1021/jacs.1c12314 (2022).
- 28 Barbero-Castillo, A. *et al.* Control of brain state transitions with a photoswitchable muscarinic agonist. *Adv Sci (Weinh)* **8**, e2005027, doi:10.1002/advs.202005027 (2021).
- 29 Riefolo, F. *et al.* Rational design of photochromic analogues of tricyclic drugs. *J Med Chem* **64**, 9259-9270, doi:10.1021/acs.jmedchem.1c00504 (2021).
- 30 Bossi, S. *et al.* A light-controlled allosteric modulator unveils a role for mGlu<sub>4</sub> receptors during early stages of ischemia in the rodent cerebellar cortex. *Frontiers in Cellular Neuroscience* **12**, doi:10.3389/fncel.2018.00449 (2018).
- 31 Morstein, J. *et al.* Optical control of lysophosphatidic acid signaling. *Journal of the American Chemical Society* **142**, 10612-10616, doi:10.1021/jacs.0c02154 (2020).
- 32 Acosta-Ruiz, A. *et al.* Branched photoswitchable tethered ligands enable ultra-efficient optical control and detection of G protein-coupled receptors *in vivo*. *Neuron* **105**, 446-463.e413, doi:https://doi.org/10.1016/j.neuron.2019.10.036 (2020).
- 33 Gutzeit, V. A. *et al.* A fine-tuned azobenzene for enhanced photopharmacology *in vivo*. *Cell Chem Biol* **28**, 1648-1663.e1616, doi:10.1016/j.chembiol.2021.02.020 (2021).
- 34 Ricart-Ortega, M., Font, J. & Llebaria, A. GPCR photopharmacology. *Mol Cell Endocrinol* **488**, 36-51, doi:10.1016/j.mce.2019.03.003 (2019).
- 35 Wijtmans, M., Josimovic, I., Vischer, H. F. & Leurs, R. Optical control of class A G protein-coupled receptors with photoswitchable ligands. *Curr Opin Pharmacol* **63**, 102192, doi:10.1016/j.coph.2022.102192 (2022).

- 36 Pittolo, S. *et al.* An allosteric modulator to control endogenous G protein-coupled receptors with light. *Nat Chem Biol* **10**, 813-815, doi:10.1038/nchembio.1612 (2014).
- 37 Riefolo, F. *et al.* Optical control of cardiac function with a photoswitchable muscarinic agonist. *J Am Chem Soc* **141**, 7628-7636, doi:10.1021/jacs.9b03505 (2019).
- 38 Prischich, D. *et al.* Adrenergic modulation with photochromic ligands. *Angew Chem Int Ed Engl* **60**, 3625-3631, doi:10.1002/anie.202010553 (2021).
- 39 Bartels, E., Wassermann, N. H. & Erlanger, B. F. Photochromic activators of the acetylcholine receptor. *Proc Natl Acad Sci U S A* **68**, 1820-1823, doi:10.1073/pnas.68.8.1820 (1971).
- 40 Agnetta, L. *et al.* A photoswitchable dualsteric ligand controlling receptor efficacy. *Angew Chem Int Ed Engl* **56**, 7282-7287, doi:10.1002/anie.201701524 (2017).
- 41 Agnetta, L. *et al.* Fluorination of photoswitchable muscarinic agonists tunes receptor pharmacology and photochromic properties. *J Med Chem* **62**, 3009-3020, doi:10.1021/acs.jmedchem.8b01822 (2019).
- 42 Sanchez-Sanchez J. M., R. F., Babero-Castillo A., Sortino R., Agnetta L., Manasanch A., Matera C., Bosch M., Forcella M., Decker M., Gorostiza P., Sanchez- Vives M. Control of cortical slow oscillations and epileptiform discharges by photoswitchable muscarinic acetylcholine receptor subtype 1 ligands.
- 43 Sortino R., G. H., Maleeva G., Calvo M., Justicia C., Riefolo F., Opar E., Bermudez M., Planas A.M., Matera C., Decker M., Gorostiza P. Photoreversible modulation of brain activity with infrared light. *In preparation*.
- 44 Martínez-López, D., Babalhavaeji, A., Sampedro, D. & Woolley, G. A. Synthesis and characterization of bis(4-amino-2-bromo-6-methoxy)azobenzene derivatives. *Beilstein J Org Chem* **15**, 3000-3008, doi:10.3762/bjoc.15.296 (2019).
- 45 Dong, M. *et al.* Near-infrared photoswitching of azobenzenes under physiological conditions. *J Am Chem Soc* **139**, 13483-13486, doi:10.1021/jacs.7b06471 (2017).
- 46 Beharry, A. A., Sadowski, O. & Woolley, G. A. Azobenzene photoswitching without ultraviolet light. *J Am Chem Soc* **133**, 19684-19687, doi:10.1021/ja209239m (2011).
- 47 Kuntze, K. *et al.* Towards low-energy-light-driven bistable photoswitches: *ortho*-Fluoroaminoazobenzenes. *Photochem Photobiol Sci* **21**, 159-173, doi:10.1007/s43630-021-00145-4 (2022).
- 48 Sadowski, O., Beharry, A. A., Zhang, F. & Woolley, G. A. Spectral tuning of azobenzene photoswitches for biological applications. *Angewandte Chemie International Edition* **48**, 1484-1486, doi:https://doi.org/10.1002/anie.200805013 (2009).
- 49 Samanta, S. *et al.* Photoswitching azo compounds *in vivo* with red Light. *Journal of the American Chemical Society* **135**, 9777-9784, doi:10.1021/ja402220t (2013).
- 50 Dong, M., Babalhavaeji, A., Samanta, S., Beharry, A. A. & Woolley, G. A. Red-shifting azobenzene photoswitches for *in vivo* use. *Accounts of Chemical Research* **48**, 2662-2670, doi:10.1021/acs.accounts.5b00270 (2015).
- 51 Rullo, A. *et al.* Long wavelength optical control of glutamate receptor ion channels using a tetra-*ortho*-substituted azobenzene derivative. *Chem Commun (Camb)* **50**, 14613-14615, doi:10.1039/c4cc06612j (2014).
- 52 Konrad, D. B., Frank, J. A. & Trauner, D. Synthesis of redshifted azobenzene photoswitches by late-stage functionalization. *Chemistry – A European Journal* **22**, 4364-4368, doi:https://doi.org/10.1002/chem.201505061 (2016).
- 53 Bléger, D. & Hecht, S. Visible-light-activated molecular switches. *Angewandte Chemie International Edition* **54**, 11338-11349, doi:https://doi.org/10.1002/anie.201500628 (2015).



- 54 Lameijer, L. N. *et al.* General principles for the design of visible-light-responsive photoswitches: Tetra-*ortho*-chloro-azobenzenes. *Angew Chem Int Ed Engl* **59**, 21663-21670, doi:10.1002/anie.202008700 (2020).
- 55 Knie, C. *et al.* *ortho*-Fluoroazobenzenes: Visible light switches with very long-lived *z* isomers. *Chemistry – A European Journal* **20**, 16492-16501, doi:https://doi.org/10.1002/chem.201404649 (2014).
- 56 Schramm, S. *et al.* Novel BQCA- and TBPB-derived M<sub>1</sub> receptor hybrid ligands: Orthosteric carbachol differentially regulates partial agonism. *ChemMedChem* **14**, 1349-1358, doi:https://doi.org/10.1002/cmdc.201900283 (2019).
- 57 Sauerberg, P. *et al.* Novel functional M<sub>1</sub> selective muscarinic agonists. Synthesis and structure-activity relationships of 3-(1,2,5-thiadiazolyl)-1,2,5,6-tetrahydro-1-methylpyridines. *J Med Chem* **35**, 2274-2283, doi:10.1021/jm00090a019 (1992).
- 58 Shannon, H. E. *et al.* Xanomeline: A novel muscarinic receptor agonist with functional selectivity for M<sub>1</sub> receptors. *J Pharmacol Exp Ther* **269**, 271-281 (1994).
- 59 Ward, J. S. *et al.* 1,2,5-Thiadiazole analogues of aceclidine as potent M<sub>1</sub> muscarinic agonists. *J Med Chem* **41**, 379-392, doi:10.1021/jm970125n (1998).
- 60 Bymaster, F. P. *et al.* Xanomeline compared to other muscarinic agents on stimulation of phosphoinositide hydrolysis *in vivo* and other cholinomimetic effects. *Brain Res* **795**, 179-190, doi:10.1016/s0006-8993(98)00267-4 (1998).
- 61 Sauerberg, P. *et al.* Identification of side chains on 1,2,5-thiadiazole-azacycles optimal for muscarinic M<sub>1</sub> receptor activation. *Bioorganic & Medicinal Chemistry Letters* **8**, 2897-2902, doi:https://doi.org/10.1016/S0960-894X(98)00509-5 (1998).
- 62 Konrad, D. B., Frank, J. A. & Trauner, D. Synthesis of redshifted azobenzene photoswitches by late-stage functionalization. *Chemistry* **22**, 4364-4368, doi:10.1002/chem.201505061 (2016).
- 63 Littmann, T., Ozawa, T., Hoffmann, C., Buschauer, A. & Bernhardt, G. A split luciferase-based probe for quantitative proximal determination of Gα<sub>q</sub> signalling in live cells. *Sci Rep* **8**, 17179, doi:10.1038/s41598-018-35615-w (2018).
- 64 Scheiner, M. *et al.* Photoswitchable pseudoirreversible butyrylcholinesterase inhibitors allow optical control of inhibition *in vitro* and enable restoration of cognition in an Alzheimer's disease mouse model upon irradiation. *Journal of the American Chemical Society* **144**, 3279-3284, doi:10.1021/jacs.1c13492 (2022).
- 65 Matera, C. *et al.* Photoswitchable antimetabolite for targeted photoactivated chemotherapy. *J Am Chem Soc* **140**, 15764-15773, doi:10.1021/jacs.8b08249 (2018).
- 66 Basnet, R. M., Zizioli, D., Taweedet, S., Finazzi, D. & Memo, M. Zebrafish larvae as a behavioral model in neuropharmacology. *Biomedicines* **7**, doi:10.3390/biomedicines7010023 (2019).
- 67 Gomila, A. M. J. *et al.* Photocontrol of endogenous glycine receptors *in vivo*. *Cell Chem Biol* **27**, 1425-1433 e1427, doi:10.1016/j.chembiol.2020.08.005 (2020).
- 68 Scarr, E. Muscarinic receptors: Their roles in disorders of the central nervous system and potential as therapeutic targets. *CNS Neurosci Ther* **18**, 369-379, doi:10.1111/j.1755-5949.2011.00249.x (2012).
- 69 Fisher, A. *et al.* M<sub>1</sub> muscarinic agonists can modulate some of the hallmarks in Alzheimer's disease: Implications in future therapy. *J Mol Neurosci* **20**, 349-356, doi:10.1385/JMN:20:3:349 (2003).
- 70 Jiang, S. *et al.* M<sub>1</sub> muscarinic acetylcholine receptor in Alzheimer's disease. *Neurosci Bull* **30**, 295-307, doi:10.1007/s12264-013-1406-z (2014).
- 71 Bock, A., Schrage, R. & Mohr, K. Allosteric modulators targeting CNS muscarinic receptors. *Neuropharmacology* **136**, 427-437, doi:10.1016/j.neuropharm.2017.09.024 (2018).

- 72 Deisseroth, K. Optogenetics. *Nat Methods* **8**, 26-29, doi:10.1038/nmeth.f.324 (2011).
- 73 Velema, W. A., Szymanski, W. & Feringa, B. L. Photopharmacology: Beyond proof of principle. *J Am Chem Soc* **136**, 2178-2191, doi:10.1021/ja413063e (2014).
- 74 Hull, K., Morstein, J. & Trauner, D. *In vivo* photopharmacology. *Chem Rev* **118**, 10710-10747, doi:10.1021/acs.chemrev.8b00037 (2018).
- 75 Broichhagen, J., Frank, J. A. & Trauner, D. A roadmap to success in photopharmacology. *Acc Chem Res* **48**, 1947-1960, doi:10.1021/acs.accounts.5b00129 (2015).
- 76 Pittolo, S. *et al.* Reversible silencing of endogenous receptors in intact brain tissue using 2-photon pharmacology. *Proc Natl Acad Sci U S A* **116**, 13680-13689, doi:10.1073/pnas.1900430116 (2019).
- 77 Carroll, E. C. *et al.* Two-photon brightness of azobenzene photoswitches designed for glutamate receptor optogenetics. *Proceedings of the National Academy of Sciences* **112**, E776-E785, doi:doi:10.1073/pnas.1416942112 (2015).
- 78 Cabre, G. *et al.* Rationally designed azobenzene photoswitches for efficient two-photon neuronal excitation. *Nat Commun* **10**, 907, doi:10.1038/s41467-019-08796-9 (2019).
- 79 Izquierdo-Serra, M. *et al.* Two-photon neuronal and astrocytic stimulation with azobenzene-based photoswitches. *J Am Chem Soc* **136**, 8693-8701, doi:10.1021/ja5026326 (2014).
- 80 Crans, R. A. J. *et al.* Striatal dopamine D<sub>2</sub>-muscarinic acetylcholine M<sub>1</sub> receptor-receptor interaction in a model of movement disorders. *Front Pharmacol* **11**, 194, doi:10.3389/fphar.2020.00194 (2020).
- 81 Gerber, D. J. *et al.* Hyperactivity, elevated dopaminergic transmission, and response to amphetamine in M<sub>1</sub> muscarinic acetylcholine receptor-deficient mice. *Proc Natl Acad Sci U S A* **98**, 15312-15317, doi:10.1073/pnas.261583798 (2001).
- 82 Crans, R. A. J. & Ciruela, F. Dopaminergic-cholinergic imbalance in movement disorders: A role for the novel striatal dopamine D<sub>2</sub>-muscarinic acetylcholine M<sub>1</sub> receptor heteromer. *Neural Regen Res* **16**, 1406-1408, doi:10.4103/1673-5374.300988 (2021).

## Supporting Information (SI) of Chapter 6

### SI6.1 Chemical synthesis

#### SI6.1.1 Materials and methods

Common reagents and solvents were purchased from the following commercial suppliers: ABCR, Alfa Aesar, BLD-Pharm, Sigma-Aldrich, Merck, TCI Chemicals and used without further purification unless otherwise stated. Dry tetrahydrofuran (THF) was freshly distilled from sodium-benzophenone under an argon atmosphere. Reaction progress was monitored using analytical thin-layer chromatography (TLC) on precoated silica gel 60 GF254 plates (Macherey Nagel GmbH & Co). Detection was carried out by irradiation and consequent fluorescence quenching at 254 nm or excitation at 365 nm. Compounds were purified by column chromatography using silica gel 60 (60 Å pore size, 40-63 µm; Macherey Nagel GmbH & Co. KG, Duren, Germany) as the stationary phase.

Reverse phase column chromatography was performed on an Interchim Puri Flash 430 (Ultra Performance Flash Purification) instrument connected to an Interchim Flash ELSD. FlashPure 4 g or 12 g C18 columns were used with gradients of H<sub>2</sub>O/MeOH as eluent systems. Nuclear magnetic resonance spectra were measured on a Bruker AV-400 NMR instrument (Bruker, Karlsruhe, Germany) in deuterated solvents (DMSO-*d*<sub>6</sub>, CDCl<sub>3</sub>, MeOD-*d*<sub>4</sub>, THF-*d*<sub>8</sub>). Chemical shifts are expressed in ppm relative to DMSO-*d*<sub>6</sub>, CDCl<sub>3</sub>, MeOD-*d*<sub>4</sub>, THF-*d*<sub>8</sub> (2.50; 7.26; 3.31; 3.58/1.73 for <sup>1</sup>H; 39.52; 77.16; 49.00; 67.57/25.37 for <sup>13</sup>C).

Measurements for verification and purity of the compounds were performed with a Shimadzu LC/MS system, comprising a DGU-20A3R controller, pump LC-20AB, degasser DGU-20A, and SPD-20A ultraviolet-visible (UV-Vis) detector. Compounds were dissolved in MeOH and filtered through syringe filters prior to measurement. As a stationary phase, a Synergi 4U fusion-RP 80 Å (150 × 4.6 mm) column was used (Phenomenex). As a mobile phase, a gradient of H<sub>2</sub>O/MeOH (both containing 0.1% formic acid) was used.

Method: flow rate: 1.0 ml/min; detection: 254 nm; scan range: 60–1000 *m/z*; gradient: A: H<sub>2</sub>O (0.1 % HCOOH); B: MeOH (0.1% HCOOH) 0–8 min 5%→90% B, 8–13 min 90% B, 13–14 min 90%→5% B, 14–18 min 5% B. The purity of all target compounds was found to be ≥ 95%. Purities were not tested at a particular photostationary state and therefore show an arbitrary *cis/trans* ratio (cf. chromatograms). ESI ionization was accomplished by a downstream

Shimadzu LCMS-2020 mass spectrometer. Data are reported as mass-to-charge ratio ( $m/z$ ) of the corresponding positively charged molecular ions.

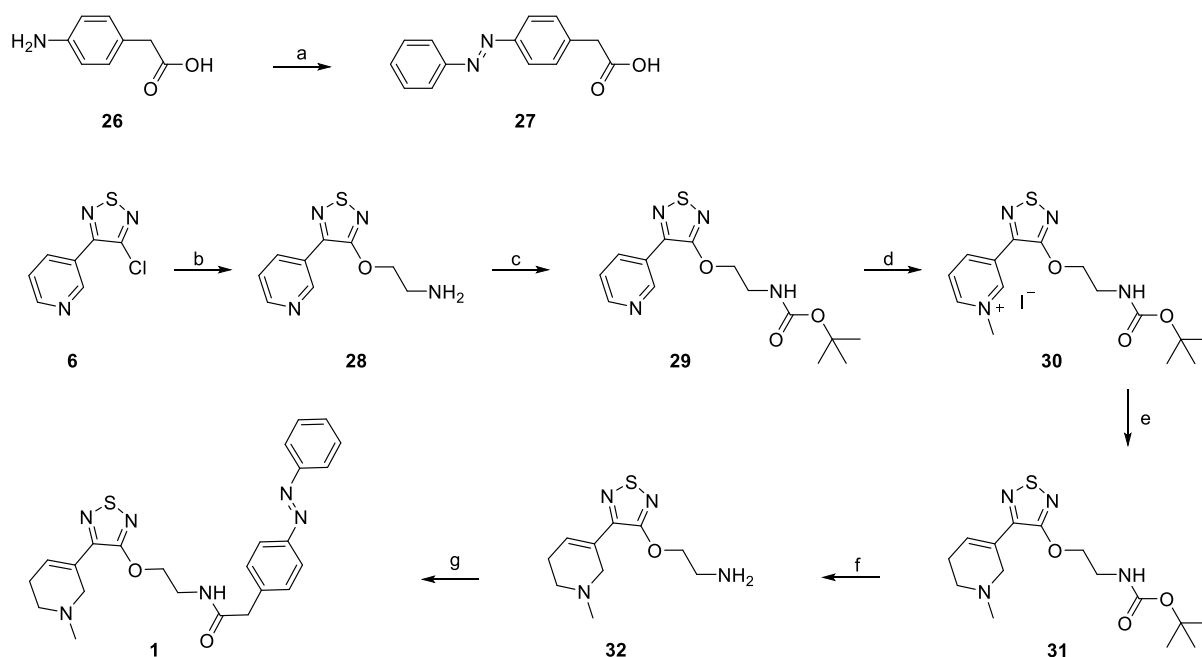
### SI6.1.2 Abbreviations

**Solvents:** EtOAc, ethyl acetate;  $\text{CH}_2\text{Cl}_2$ , dichloromethane; MeCN, acetonitrile; MeOH, methanol; EtOH, ethanol; THF, tetrahydrofuran;  $\text{Et}_2\text{O}$ , diethyl ether; DMSO, dimethyl sulfoxide.

**Analytical characterizations:** NMR: d, doublet; dd, double doublet; ddd, double double doublet; dddd, doublet of doublet of doublet of doublets; dt, double triplet; m, multiplet; q, quartet; quin, quintet; s, singlet; t, triplet; m.p., melting point;  $R_f$ , retention factor; rt, room temperature; RT, retention time.

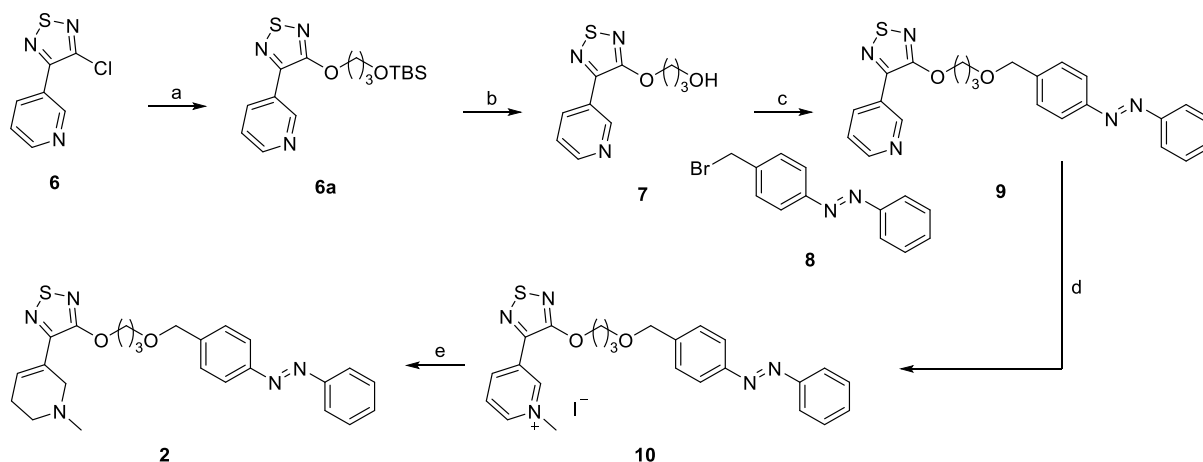
### SI6.1.3 Synthetic routes

The synthesis of *N*-(2-((4-(1-methyl-1,2,5,6-tetrahydropyridin-3-yl)-1,2,5-thiadiazol-3-yl)oxy)ethyl)-2-(4-(phenyldiazenyl)phenyl)acetamide (**1**) is shown in **Scheme S6.1**.



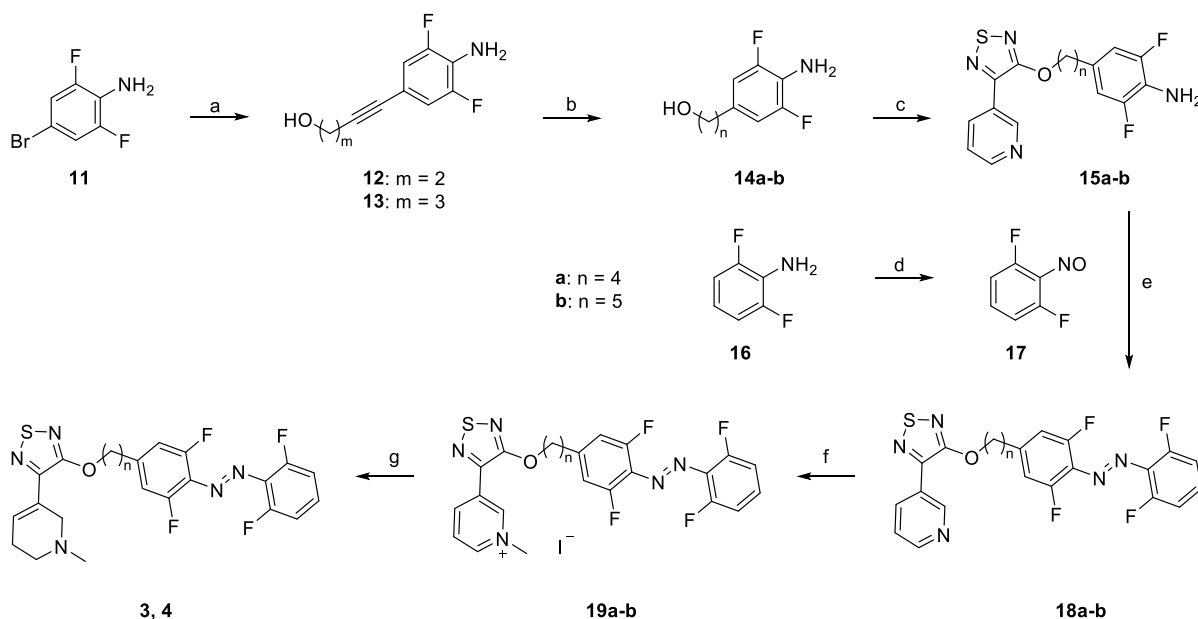
**Scheme S6.1.** The synthesis of *N*-(2-((4-(1-methyl-1,2,5,6-tetrahydropyridin-3-yl)-1,2,5-thiadiazol-3-yl)oxy)ethyl)-2-(4-(phenyldiazenyl)phenyl)acetamide (**1**). Reagents and conditions: (a) Nitrosobenzene, HOAc, rt (83%); (b) 2-aminoethan-1-ol, NaH, THF, 60°C, 27%; (c)  $\text{BOC}_2\text{O}$ ,  $\text{NEt}_3$ ,  $\text{CH}_2\text{Cl}_2$ , 0°C to RT, 97%; (d) MeI, acetone, RT, 87%; (e)  $\text{NaBH}_4$ , MeOH/ $\text{CH}_2\text{Cl}_2$ , 0°C to RT, 51%; (f) TFA,  $\text{CH}_2\text{Cl}_2$ , RT, 87%; (g) **27**, ECC x HCl, HOBT x  $\text{H}_2\text{O}$ , DIPEA, DMF, RT, 54%.

The synthesis of 3-(1-methyl-1,2,5,6-tetrahydropyridin-3-yl)-4-(3-((4-(phenyldiazenyl)benzyl)oxy)propoxy)-1,2,5-thiadiazole (**2**) is shown in **Scheme S6.2**.



**Scheme S6.2.** The synthesis of 3-(1-methyl-1,2,5,6-tetrahydropyridin-3-yl)-4-(3-((4-(phenyldiazenyl)benzyl)oxy)propoxy)-1,2,5-thiadiazole (**2**). Reagents and conditions: (a) 3-((*tert*-butyldimethylsilyloxy)propyl)propan-1-ol, NaH, THF, 60°C, 89%; (b) 2N HCl, MeOH, RT, 72%; (c) 1-(4-(bromomethyl)phenyl)-2-phenyldiazene (**8**), KOtBu, dioxane, 70°C, 30%; (d) MeI, acetone, RT, 98%; (e) NaBH<sub>4</sub>, MeOH/CH<sub>2</sub>Cl<sub>2</sub>, RT, 57%.

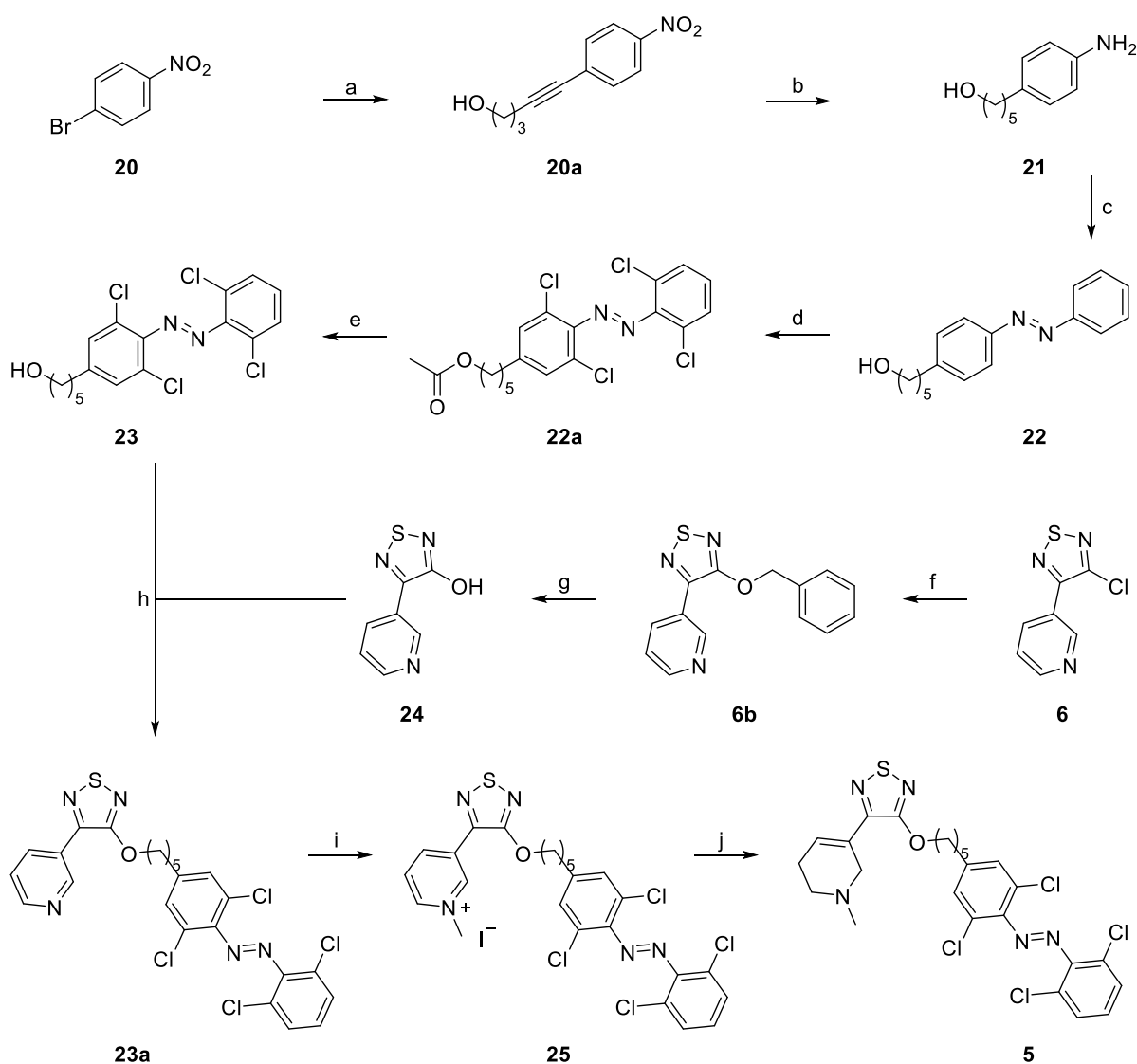
The synthesis of 3-(4-(4-((2,6-difluorophenyl)diazenyl)-3,5-difluorophenyl)butoxy)-4-(1-methyl-1,2,5,6-tetrahydropyridin-3-yl)-1,2,5-thiadiazole (**3**) and 3-((5-(4-((2,6-difluorophenyl)diazenyl)-3,5-difluorophenyl)pentyl)oxy)-4-(1-methyl-1,2,5,6-tetrahydropyridin-3-yl)-1,2,5-thiadiazole (**4**) are shown in **Scheme S6.3**.



**Scheme S6.3.** The synthesis of 3-(4-(4-((2,6-difluorophenyl)diazenyl)-3,5-difluorophenyl)butoxy)-4-(1-methyl-1,2,5,6-tetrahydropyridin-3-yl)-1,2,5-thiadiazole (**3**) and 3-((5-(4-((2,6-difluorophenyl)diazenyl)-3,5-difluorophenyl)pentyl)oxy)-4-(1-methyl-1,2,5,6-tetrahydropyridin-3-yl)-1,2,5-thiadiazole (**4**).

**difluorophenyl)pentyl)oxy)-4-(1-methyl-1,2,5,6-tetrahydropyridin-3-yl)-1,2,5-thiadiazole (4)**. Reagents and conditions: (a) Alkynol, CuI, PdCl<sub>2</sub>(PPh<sub>3</sub>)<sub>2</sub>, PPh<sub>3</sub>, NEt<sub>3</sub>/THF, 90°C, 72-85%; (b) Pd/C, H<sub>2</sub>, MeOH, RT, 85-89%; (c) **6**, NaH, THF, 70°C, 46-48%; (d) Oxone<sup>®</sup>, CH<sub>2</sub>Cl<sub>2</sub>, H<sub>2</sub>O, RT (e) **17**, HOAc/Toluol/TFA 6:6:1, RT, 79-83%; (f) MeI, acetone, RT, 87%, quant.); (g) NaBH<sub>4</sub>, MeOH/CH<sub>2</sub>Cl<sub>2</sub>, 0°C to RT, 21-43%.

The synthesis 3-((5-(3,5-dichloro-4-((2,6-dichlorophenyl)diazenyl)phenyl)pentyl)oxy)-4-(1-methyl-1,2,5,6-tetrahydropyridin-3-yl)-1,2,5-thiadiazole (**5**) is shown in **Scheme S6.4**.



**Scheme S6.4. The synthesis 3-((5-(3,5-dichloro-4-((2,6-dichlorophenyl)diazenyl)phenyl)pentyl)oxy)-4-(1-methyl-1,2,5,6-tetrahydropyridin-3-yl)-1,2,5-thiadiazole (5)**. Reagents and conditions: (a) CuI, PdCl<sub>2</sub>(PPh<sub>3</sub>)<sub>2</sub>, PPh<sub>3</sub>, NEt<sub>3</sub>/THF, 70°C, 98%; (b) Pd/C, 10 atm. H<sub>2</sub>, MeOH, RT, 95%; (c) Nitrosobenzene, HOAc, RT, 79%; (d) NCS, Pd(OAc)<sub>2</sub>, HOAc, 140°C, 49%; (e) 6N HCl, THF, RT, quant.; (f) phenylmethanol, NaH, THF, 65°C, 78%; (g) CH<sub>2</sub>Cl<sub>2</sub>, HBr/AcOH, RT, 70%; (h) DEAD, PPh<sub>3</sub>, THF, 0°C to RT, 67%; (i) MeI, acetone, RT, 56%, (j) NaBH<sub>4</sub>, MeOH/CH<sub>2</sub>Cl<sub>2</sub>, 0°C to RT, 19%.

### SI6.1.4 General methods

**General method A: Sonogashira Cross-Coupling (12; 13; 20b):** All steps were carried out under an argon atmosphere and every liquid was degassed before use. The respective aryl bromide (1.0 equiv.), PdCl<sub>2</sub>(PPh<sub>3</sub>)<sub>2</sub> (0.25 equiv.), copper(I)iodide (0.015 equiv.) and triphenylphosphine (0.25 equiv.) were dissolved in a solution of 60 vol.-% triethylamine in tetrahydrofuran. The respective alkyne (1.25-3.0 equiv.) was added and the solution was stirred at 70°C overnight. The reaction mixture was then diluted with water and ethyl acetate and washed with 1 M HCl. Subsequently, the organic layer was washed with sat. aq. NaHCO<sub>3</sub> and brine. The organic phase was dried over Na<sub>2</sub>SO<sub>4</sub>. And the solvent was removed under reduced pressure. Purification of the oily residue by silica column chromatography yielded the desired products.

**General method B: Nucleophilic Substitution at 3-chloro-4-(pyridin-3-yl)-1,2,5-thiadiazole (6a,b; 15a,b; 28):** A solution of the respective alcohol (1.0-2.5 equiv.) in anhydrous THF was prepared. NaH (60% dispersion in mineral oil, 3.0-9.0 equiv.) was added and the mixture was stirred at ambient temperature until gas development stopped. Subsequently, 3-chloro-4-(pyridin-3-yl)-1,2,5-thiadiazole (1.0-1.05 equiv.) dissolved in anhydrous THF was added and the reaction was stirred overnight at 70°C. The mixture was afterwards quenched with an excess of water and extracted with EtOAc. The combined organic layers were dried over Na<sub>2</sub>SO<sub>4</sub> and concentrated under reduced pressure. Purification by silica column chromatography yielded the desired products.

**General method C: Baeyer-Mills-Reaction (18a,b; 22):** The respective aniline (1.0 equiv.) and the respective nitrosobenzene (1.0-2.85 equiv.) were stirred in acetic acid or a mixture of acetic acid/toluene/TFA (6:6:1) overnight at ambient temperature. The reaction mixture was concentrated under reduced pressure, diluted in EtOAc and washed with sat. aq. NaHCO<sub>3</sub> and brine. The aqueous layers were extracted with ethyl acetate until no orange colour could be detected in the aqueous. The combined organic layers were then dried over Na<sub>2</sub>SO<sub>4</sub> and concentrated under reduced pressure. The crude was purified by silica column chromatography yielding the desired azobenzene.

**General method D: Preparation of pyridinium iodides (10; 19a,b; 24; 30):** The respective pyridinyl-thiadiazole (1.0 equiv.) was dissolved in acetone. After the addition of iodomethane (5.0-10 equiv.) the reaction mixture was stirred for 1 to 2 days at ambient temperature. Parts of the desired pyridinium iodide precipitated as an orange or yellow solid, which was filtered off

and washed with acetone (no further purification was performed). The filtrate was concentrated, the residue purified by silica column chromatography and combined with the precipitate yielding the desired pyridinium iodides.

**General method E: Reduction of pyridinium iodides to tetrahydropyridines (1-5):** A solution of the respective pyridinium iodide (1.0 equiv.) in a 1:1 mixture of dichloromethane/methanol was cooled down to 0°C, sodium tetrahydroborate (2.8-3.0 equiv.) was added portion wise and the reaction mixture was allowed to warm up and stirred overnight at ambient temperature. Afterwards, the remaining sodium tetrahydroborate was quenched with an excess of water. The mixture was then extracted with dichloromethane. The combined organic layers were subsequently dried over Na<sub>2</sub>SO<sub>4</sub>, concentrated under reduced pressure and purified by silica gel column chromatography and reverse phase (C18) flash chromatography, yielding the xanomeline derivative.

### SI6.1.5 Preparation of tetra-chloro-xanoswitch-5

**3-(benzyloxy)-4-(pyridin-3-yl)-1,2,5-thiadiazole (6b):** According to general procedure **B**, 3-chloro-4-(pyridin-3-yl)-1,2,5-thiadiazole (**6**; 309 mg, 1.73 mmol, 1.0 equiv.) was reacted with phenylmethanol (202 mg, 1.87 mmol, 1.1 equiv.) using NaH (207 mg, 5.18 mmol, 3.0 equiv.) in dry THF (7 ml) stirring the reaction for 16 h at 60°C. Purification by silica column chromatography (petroleum ether/ethyl acetate 10:1) yielded 3-(benzyloxy)-4-(pyridin-3-yl)-1,2,5-thiadiazole (**6b**; 378 mg, 1.26 mmol, 73%) as an off white solid.

<sup>1</sup>H NMR (400 MHz, CDCl<sub>3</sub>) δ 9.44 – 9.38 (m, 1H), 8.65 – 8.62 (m, 1H), 8.44 – 8.40 (m, 1H), 7.54 – 7.46 (m, 2H), 7.46 – 7.33 (m, 4H), 5.57 (s, 2H). <sup>13</sup>C NMR (101 MHz, CDCl<sub>3</sub>) δ 162.55, 150.24, 148.73, 145.17, 135.56, 134.95, 128.87, 128.77, 128.38, 127.72, 123.59, 73.05.

MS (ESI, positive): *m/z* calculated for [C<sub>14</sub>H<sub>12</sub>N<sub>3</sub>OS]<sup>+</sup>: 270.07, found: 270.05 [M + H]<sup>+</sup>.

**4-(pyridin-3-yl)-1,2,5-thiadiazol-3-ol (24):** A solution of 3-(benzyloxy)-4-(pyridin-3-yl)-1,2,5-thiadiazole (**6**; 316 mg, 1.17 mmol, 1.0 equiv.) in CH<sub>2</sub>Cl<sub>2</sub> (6 ml) was mixed with HBr in AcOH (189 mg, 2.35 mmol, 2.0 equiv.) at ambient temperature and the reaction was stirred overnight at ambient temperature. Subsequently, the reaction mixture was quenched with sat. NaHCO<sub>3</sub> and extracted with CH<sub>2</sub>Cl<sub>2</sub> at pH = 9 to remove the benzylic alcohol. After acidifying the mixture to pH = 5 the product could be extracted with EtOAc. The EtOAc was dried over Na<sub>2</sub>SO<sub>4</sub> and concentrated under reduced pressure to yield the pure product as a white solid (**24**; 193 mg, 1.08 mmol, 92%).



$^1\text{H}$  NMR (400 MHz,  $\text{DMSO-}d_6$ )  $\delta$  13.38 (s, 1H), 9.31 – 9.22 (m, 1H), 8.71 – 8.60 (m, 1H), 8.50 – 8.40 (m, 1H), 7.59 – 7.50 (m, 1H).  $^{13}\text{C}$  NMR (101 MHz,  $\text{DMSO-}d_6$ )  $\delta$  162.56, 150.01, 147.82, 144.77, 134.30, 127.44, 123.78.

MS (ESI, positive):  $m/z$  calculated for  $[\text{C}_7\text{H}_6\text{N}_3\text{OS}]^+$ : 180.02, found: 180.00  $[\text{M} + \text{H}]^+$ .

**5-(4-nitrophenyl)pent-4-yn-1-ol (20a):** According to general method A, 1-bromo-4-nitrobenzene (2000 mg, 9.90 mmol, 1.0 equiv.) was coupled with pent-4-yn-1-ol (1.15 ml, 1041 mg, 12.40 mmol, 1.25 equiv.) using dry THF (40 ml) and stirring the reaction for 14 h at  $70^\circ\text{C}$ . Purification by silica column chromatography (petroleum ether/ethyl acetate 7:2) afforded 5-(4-nitrophenyl)pent-4-yn-1-ol (**20a**; 1.98 g, 9.66 mmol, 98%) as an orange solid.

$^1\text{H}$  NMR (400 MHz,  $\text{CDCl}_3$ )  $\delta$  8.22 – 8.01 (m, 2H), 7.58 – 7.41 (m, 2H), 3.79 (dd,  $J = 6.7, 5.6$  Hz, 2H), 2.57 (t,  $J = 7.0$  Hz, 2H), 1.92 – 1.80 (m, 3H).  $^{13}\text{C}$  NMR (101 MHz,  $\text{CDCl}_3$ )  $\delta$  146.72, 132.34, 130.97, 123.56, 95.80, 79.71, 61.54, 31.20, 16.17.

**5-(4-aminophenyl)pentan-1-ol (21):** A solution of 5-(4-nitrophenyl)pent-4-yn-1-ol (**20a**; 1.90 g, 9.26 mmol, 1.0 equiv.) in methanol (30 ml) was flushed with argon and palladium on activated charcoal (150mg, 20 wt%) was added. The reaction was then stirred for four hours at room temperature under  $\text{H}_2$  (10 atm.). Since the reaction was not complete, another 75 mg of palladium on activated charcoal was added and the reaction was stirred overnight at room temperature under 1 atm. of  $\text{H}_2$ . The reaction mixture was subsequently filtrated over a paper filter the filtrate was evaporated and subsequently filtered through a syringe filter yielding 5-(4-aminophenyl)pentan-1-ol (**21**; 1.58 g, 8.80 mmol, 95%) as a brown solid.

$^1\text{H}$  NMR (400 MHz, chloroform- $d$ )  $\delta$  7.02 – 6.92 (m, 2H), 6.67 – 6.59 (m, 2H), 3.63 (t,  $J = 6.6$  Hz, 2H), 2.51 (t,  $J = 7.6$  Hz, 2H), 1.69 – 1.48 (m, 6H).  $^{13}\text{C}$  NMR (101 MHz, chloroform- $d$ )  $\delta$  143.87, 133.44, 129.30, 115.46, 63.15, 35.15, 32.84, 31.68, 25.47.

MS (ESI, positive):  $m/z$  calculated for  $[\text{C}_{11}\text{H}_{18}\text{NO}]^+$ : 180.14, found: 180.10  $[\text{M} + \text{H}]^+$ .

**5-(4-(phenyldiazenyl)phenyl)pentan-1-ol (22):** According to general procedure C, nitrosobenzene (313 mg, 0.293 mmol 1.2 equiv.) and 5-(4-aminophenyl)pentan-1-ol (**21**; 436 mg, 0.244 mmol, 1.0 equiv.) were reacted in acetic acid (2 ml). Purification by silica column chromatography (petroleum ether/ethyl acetate 5:2) yielded 5-(4-(phenyldiazenyl)phenyl)pentan-1-ol (**22**; 550 mg, 2.05 mmol, 84%) as an orange solid.

$^1\text{H}$  NMR (400 MHz,  $\text{CDCl}_3$ )  $\delta$  7.96 – 7.82 (m, 4H), 7.55 – 7.43 (m, 3H), 7.35 – 7.29 (m, 2H), 3.64 (t,  $J = 6.6$  Hz, 2H), 2.70 (t,  $J = 7.7$  Hz, 2H), 2.47 (s, 1H), 1.75 – 1.56 (m, 4H), 1.48 – 1.38

(m, 2H).  $^{13}\text{C}$  NMR (101 MHz,  $\text{CDCl}_3$ )  $\delta$  152.86, 151.11, 146.27, 130.83, 129.21, 129.16, 123.01, 122.83, 62.93, 35.93, 32.67, 31.16, 25.51.

MS (ESI, positive):  $m/z$  calculated for  $[\text{C}_{17}\text{H}_{21}\text{N}_2\text{O}]^+$ : 269.16, found: 269.15  $[\text{M} + \text{H}]^+$ .

**5-(3,5-dichloro-4-((2,6-dichlorophenyl)diazenyl)phenyl)pentyl acetate (22a):** In a sealed reaction vessel, a solution of 5-(4-(phenyldiazenyl)phenyl)pentan-1-ol (**22**; 250 mg, 0.93 mmol, 1.0 equiv) in degassed AcOH (9 ml) was mixed with  $\text{Pd}(\text{OAc})_2$  (21 mg, 93.2  $\mu\text{mol}$ ) and NCS (622 mg, 4.66 mmol, 5.0 equiv.). The reaction mixture was then heated to 140°C for 15 h. After cooling down to ambient temperature, the reaction mixture was diluted with EtOAc, washed with sat.  $\text{NaHCO}_3$ , dried over sodium sulfate and concentrated under reduced pressure. Purification by silica column chromatography yielded 5-(3,5-dichloro-4-((2,6-dichlorophenyl)diazenyl)phenyl)pentyl acetate (**22a**; 163 mg, 0.364 mmol, 39%) as a red oil.

$^1\text{H}$  NMR (400 MHz, chloroform-*d*)  $\delta$  7.43 – 7.02 (m, 5H), 4.05 (t,  $J = 6.6$  Hz, 2H), 2.60 (t,  $J = 7.7$  Hz, 2H), 2.03 (s, 3H), 1.71 – 1.59 (m, 4H), 1.44 – 1.34 (m, 2H).  $^{13}\text{C}$  NMR (101 MHz, chloroform-*d*)  $\delta$  171.09, 147.88, 145.40, 129.40, 129.33, 127.53, 127.08, 64.23, 34.98, 30.35, 28.37, 25.43, 21.00.

MS (ESI, positive):  $m/z$  calculated for  $[\text{C}_{19}\text{H}_{19}\text{Cl}_4\text{N}_2\text{O}_2]^+$ : 449.07, found: 449.00  $[\text{M} + \text{H}]^+$ .

**5-(3,5-dichloro-4-((2,6-dichlorophenyl)diazenyl)phenyl)pentan-1-ol (23):** A solution of 5-(3,5-dichloro-4-((2,6-dichlorophenyl)diazenyl)phenyl)pentyl acetate (**22a**; 110 mg, 0.245 mmol) in THF (6 ml) was mixed with 6N HCl (1.5 ml) at ambient temperature. The mixture was heated to 70°C for 3 hours and the reaction was afterwards quenched with  $\text{NaHCO}_3$  and extracted with EtOAc until the aqueous layer was colorless. The combined organic layers were dried over  $\text{NaHCO}_3$  and concentrated. Purification by silica column chromatography (petroleum ether/ethyl acetate 5:1) yielded 5-(3,5-dichloro-4-((2,6-dichlorophenyl)diazenyl)phenyl)pentan-1-ol (**23**; 100 mg, 0.245 mmol, quant.) as a dark red oil.

$^1\text{H}$  NMR (400 MHz,  $\text{CDCl}_3$ )  $\delta$  7.48 – 7.39 (m, 2H), 7.30 – 7.27 (m, 2H), 7.26 – 7.22 (m, 1H), 3.65 (t,  $J = 6.5$  Hz, 2H), 2.64 (t,  $J = 7.7$  Hz, 2H), 1.70 – 1.58 (m, 4H), 1.46 – 1.41 (m, 2H).  $^{13}\text{C}$  NMR (101 MHz,  $\text{CDCl}_3$ )  $\delta$  147.93, 145.64, 145.16, 129.45, 129.43, 129.36, 127.54, 127.10, 62.65, 35.18, 32.47, 30.64, 25.35.

MS (ESI, positive):  $m/z$  calculated for  $[\text{C}_{17}\text{H}_{17}\text{Cl}_4\text{N}_2\text{O}]^+$ : 407.01, found: 406.95  $[\text{M} + \text{H}]^+$ .

**3-((5-(3,5-dichloro-4-((2,6-dichlorophenyl)diazenyl)phenyl)pentyl)oxy)-4-(pyridin-3-yl)-1,2,5-thiadiazole (23a):** A solution of PPh<sub>3</sub> (152 mg, 0.579 mmol, 1.25 equiv.) was cooled down to 0°C before a solution of DEAD (91 µl, 0.579 mmol, 1.25 equiv.) in dry THF (1 ml) was added slowly. The mixture was stirred for 30 min before 4-(pyridin-3-yl)-1,2,5-thiadiazol-3-ol (104 mg, 0.579 mmol, 1.25 equiv.) and 5-(3,5-dichloro-4-((2,6-dichlorophenyl)diazenyl)phenyl)pentan-1-ol (188 mg, 0.463 mmol, 1.0 equiv.) dissolved in THF (1 ml) were added. The reaction was stirred overnight at room temperature. Afterwards the reaction was diluted with EtOAc and washed three times with sat. NaHCO<sub>3</sub> and brine. The organic layer was dried over Na<sub>2</sub>SO<sub>4</sub> and concentrated under reduced pressure. Purification by silica column chromatography (petroleum ether/ethyl acetate 5:2) yielded 3-((5-(3,5-dichloro-4-((2,6-dichlorophenyl)diazenyl)phenyl)pentyl)oxy)-4-(pyridin-3-yl)-1,2,5-thiadiazole (**23a**; 262 mg, 0.462 mmol, 99%) as an dark red oil.

<sup>1</sup>H NMR (400 MHz, CDCl<sub>3</sub>) δ 9.45 – 9.32 (m, 1H), 8.71 – 8.60 (m, 1H), 8.48 – 8.30 (m, 1H), 7.48 – 7.42 (m, 2H), 7.41 – 7.36 (m, 1H), 7.29 – 7.20 (m, 4H), 4.63 – 4.46 (m, 2H), 2.67 (t, *J* = 7.6 Hz, 2H), 2.03 – 1.87 (m, 2H), 1.85 – 1.66 (m, 3H), 1.64 – 1.50 (m, 2H). <sup>13</sup>C NMR (101 MHz, CDCl<sub>3</sub>) δ 162.84, 150.35, 148.74, 148.05, 145.40, 145.30, 145.12, 134.81, 129.52, 129.50, 129.46, 127.74, 127.71, 127.26, 123.57, 71.21, 35.17, 30.60, 28.86, 25.74.

MS (ESI, positive): *m/z* calculated for [C<sub>24</sub>H<sub>20</sub>Cl<sub>4</sub>N<sub>5</sub>OS]<sup>+</sup>: 568.01, found: 567.95 [M+H]<sup>+</sup>.

**3-(4-((5-(3,5-dichloro-4-((2,6-dichlorophenyl)diazenyl)phenyl)pentyl)oxy)-1,2,5-thiadiazol-3-yl)-1-methylpyridin-1-ium iodide (25):** A solution of 3-((5-(3,5-dichloro-4-((2,6-dichlorophenyl)diazenyl)phenyl)pentyl)oxy)-4-(pyridin-3-yl)-1,2,5-thiadiazole (**23a**; 263 mg, 0.463 mmol, 1.0 equiv.) in acetone was mixed with Iodomethane (289 µl, 4.64 mmol, 10 equiv.) and the reaction was stirred for two overnights at room temperature. Subsequently the solvent was removed and the crude product was purified by column chromatography (CH<sub>2</sub>Cl<sub>2</sub>/MeOH 20:1) yielding the pyridinium salt as an red oil (184 mg, 0.270 mmol, 56%).

<sup>1</sup>H NMR (400 MHz, CDCl<sub>3</sub>) δ 9.54 – 9.49 (m, 1H), 9.48 – 9.44 (m, 1H), 9.11 – 9.03 (m, 1H), 8.29 – 8.22 (m, 1H), 7.46 – 7.39 (m, 2H), 7.29 – 7.19 (m, 3H), 4.77 (s, 3H), 4.59 (t, *J* = 6.7 Hz, 2H), 2.67 (t, *J* = 7.6 Hz, 2H), 2.04 – 1.90 (m, 2H), 1.79 – 1.65 (m, 2H), 1.57 – 1.44 (m, 2H). <sup>13</sup>C NMR (101 MHz, CDCl<sub>3</sub>) δ 163.12, 147.88, 145.61, 145.40, 145.26, 143.09, 142.09, 139.62, 131.51, 129.60, 129.53, 129.47, 128.76, 127.49, 127.14, 72.20, 50.75, 34.97, 30.38, 28.64, 25.34.

MS (ESI, positive): *m/z* calculated for [C<sub>25</sub>H<sub>22</sub>Cl<sub>4</sub>N<sub>5</sub>OS]<sup>+</sup>: 582.03, found: 582.00 [M+H]<sup>+</sup>.

## SI6.2 HPLC analyses

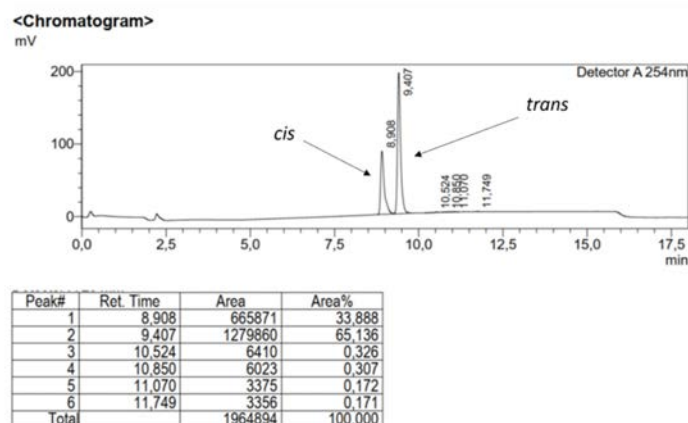


Figure S6.1. HPLC chromatogram of 3-((5-(4-((2,6-difluorophenyl)diazenyl)-3,5-difluorophenyl)pentyl)oxy)-4-(1-methyl-1,2,5,6-tetrahydropyridin-3-yl)-1,2,5-thiadiazole (4).

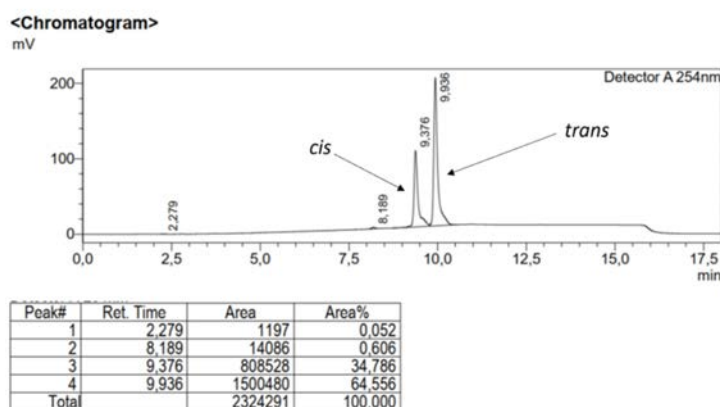


Figure S6.2. HPLC chromatogram of 3-((5-(3,5-dichloro-4-((2,6-dichlorophenyl)diazenyl)phenyl)pentyl)oxy)-4-(1-methyl-1,2,5,6-tetrahydropyridin-3-yl)-1,2,5-thiadiazole (5)

## SI6.3 Photochemical characterization

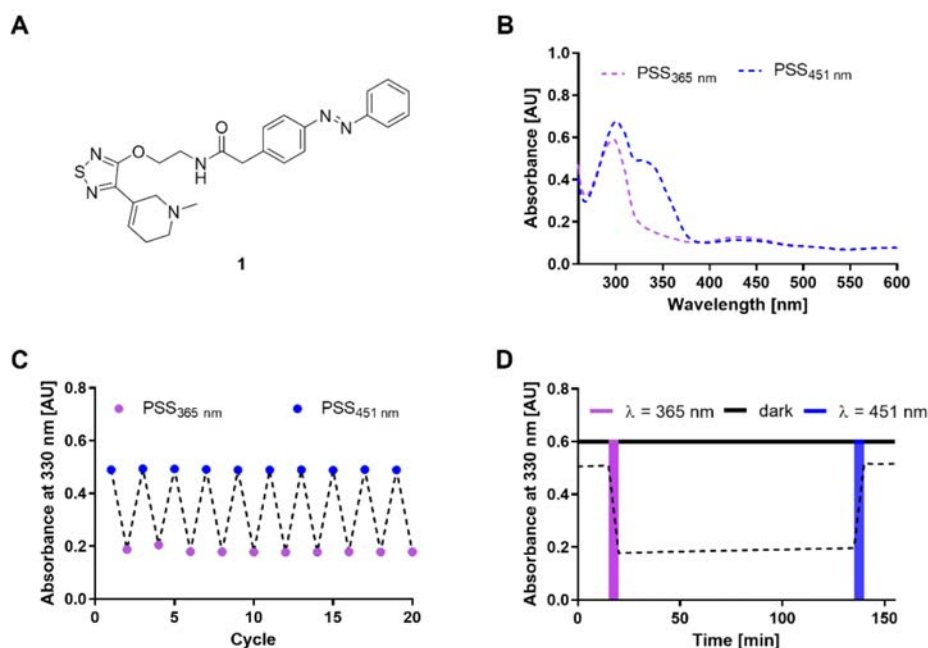
UV-Vis spectra were recorded on a Varian Cary 50 Bio UV-Vis Spectrophotometer connected to a water bath for temperature control. Hellma (Type 100-QS) cuvettes (10 mm light path) were used. Characterization was performed with 25  $\mu$ M/50  $\mu$ M solutions in DMSO/H<sub>2</sub>O 1:1 (V:V). Samples were irradiated using LEDs of Seoulviosys (UV Z5 series CUNx6A1B; 365nm), Roschwege (RSW-P01-385-2; 385 nm), LedEngin (LZ4-00UB00-U7, 405 nm), Osram (LD CQ7P-2U3U-W5-1-K, 451 nm; LT CP7P-KZLX-26, 528 nm; LY CP7P-JUKQ-36, 590 nm; LA CP7P-KQKS-W3, 617 nm), Cree (XPeBBL-L1-0000-00205, 475 nm) and Lumileds (LXML-PE01, 505 nm). LED modules were combined to a rated power of 4W and

used with a forward current of  $I_F = 350$  mA. Irradiation of the solutions with the respective wavelengths were performed until the corresponding photostationary state (PSS) had equilibrated (1-2 min). Thermal relaxation was measured for a period over 2 h to determine whether the relaxation was significant with regards to the duration of the biological assays. For this purpose, the photochromic compounds were switched into the maximally *trans* enriched photostationary state. The absorption at the wavelength were the spectrum of the *cis*- and *trans*-isomer showed maximal difference ( $\lambda_{\Delta_{\max}}$ ) was measured for 15 min. Subsequently, the solutions were switched to the thermodynamically less stable *cis*-isomer using 365 nm light. The relaxation was recorded by monitoring the change of absorption at  $\lambda_{\max}$  for 2 h at 37°C. Afterwards, the solutions were switched to their maximally *trans*-enriched PSS again. Percentage relaxation was calculated as  $\Delta = (A_{cis\text{-enriched } t = 2 \text{ h}} - A_{cis\text{-enriched } t = 0}) * 100 / (A_{trans\text{-enriched}} - A_{cis\text{-enriched } t = 0})$ . Absence of photo-fatigue was checked for all compounds of the same switching wavelengths simultaneously. Using a 96-well plate and a Spectramax 250 absorbance microplate reader (molecular devices) the compounds were irradiated alternatingly with the indicated wavelengths and their absorbance at  $\lambda_{\max}$  was checked to be constant. The photostationary distributions (PSD) of the PSSs of interests were determined by high-performance liquid chromatography (HPLC). The amount of *cis*- and *trans*-isomer was quantified by integration of the respective peak. Absorption was measured at the respective isosbestic point.

Compound	Thermal relaxation @ 37°C (DMSO/H <sub>2</sub> O, 1:1)	<i>cis/trans</i> ratio (MeOH)	EC <sub>50</sub> [nM]	%E <sub>max</sub>
1	5.7% (2 h)	PSS <sub>365</sub> : 93/07	95.4	76.2 ± 0.8
		PSS <sub>451</sub> : 19/81	69.1	66.0 ± 0.5
2	9% (2 h)	PSS <sub>365</sub> : 75/25	74.1	93.5 ± 0.7
		PSS <sub>451</sub> : 21/79	154	85.2 ± 0.7
3	1.7% (14 h)	PSS <sub>528</sub> : 91/9	186	110 ± 1.5
		PSS <sub>405</sub> : 11/89	163	108 ± 1.8
4	1.8% (16 h)	PSS <sub>528</sub> : 90/10	93.3	98.6 ± 0.7
		PSS <sub>405</sub> : 12/88	139	90.0 ± 0.5
5	1.8% (18 h)	PSS <sub>590</sub> : 89/11	199	77.8 ± 1.7
		PSS <sub>405</sub> : 10/90	205	62.0 ± 1.3

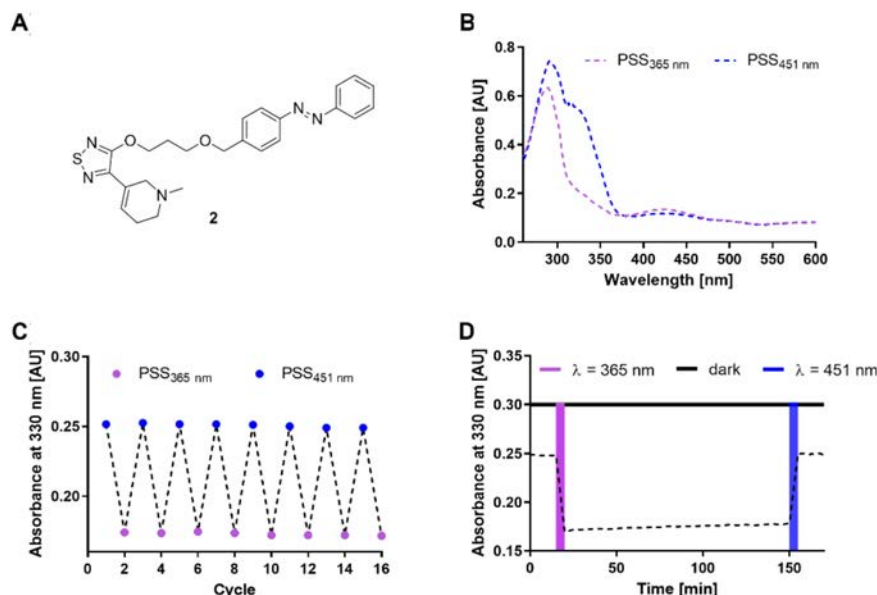
**Table S6.1. Summary of thermal relaxation, *cis/trans* ratios and biological effects of the relevant photostationary states.**

## SI6.3.1 Xanoswitch-1



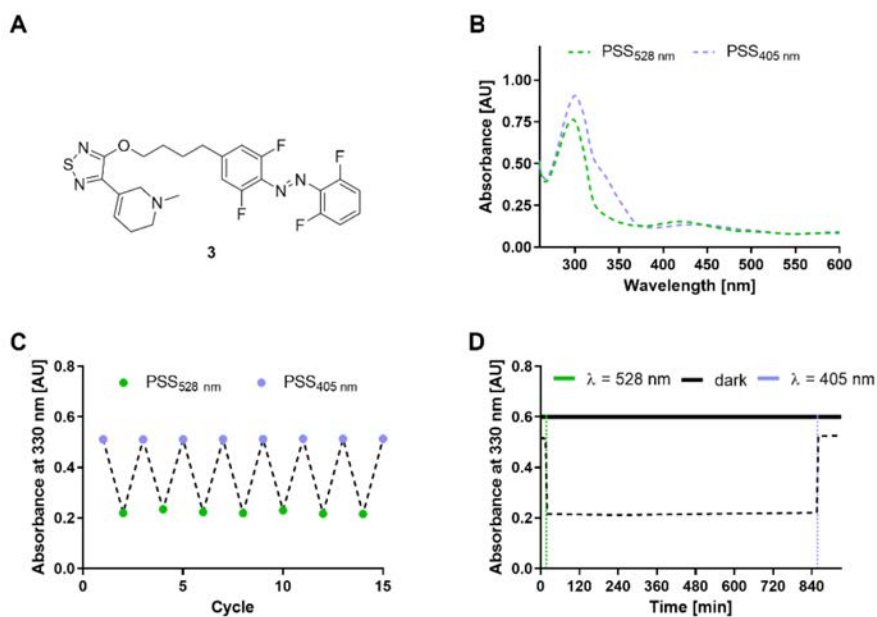
**Figure S6.3. Photochemical characterization of amide-xanoswitch-1 (25  $\mu$ M, DMSO/H<sub>2</sub>O 1:1).** (A) Structure of **1** in its *trans* configuration. (B) Absorption spectra of maximally *cis/trans* enriched PSSs after irradiation with corresponding lights for 2 min. (C) Cycles of 365/451 nm light irradiation showing no photodecomposition. (D) Thermal relaxation of the *cis*-isomer over a period of 2 h at 37°C.

## SI6.3.2 Xanoswitch-2



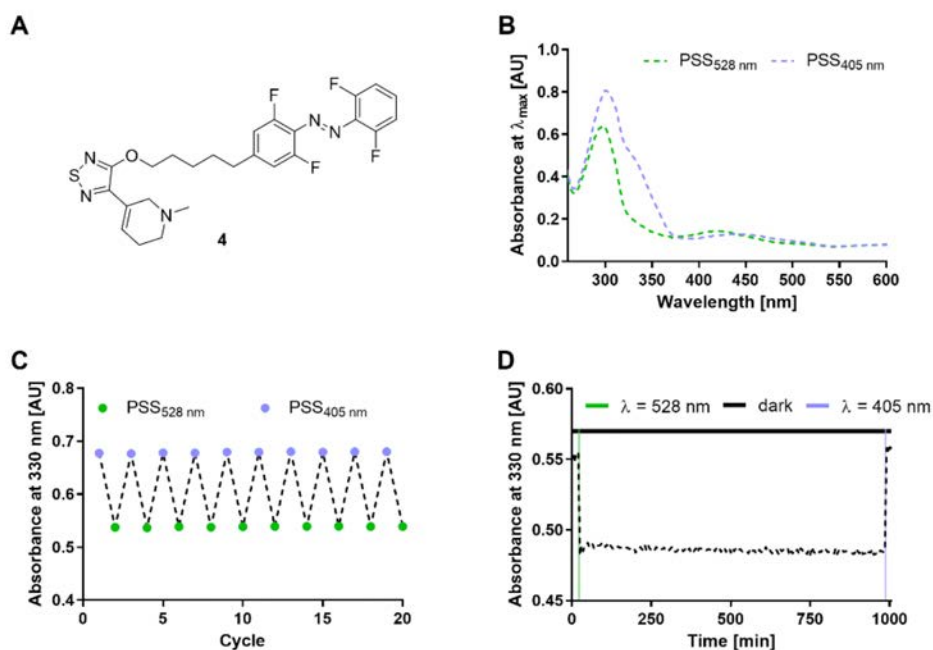
**Figure S6.4. Photochemical characterization of ether-xanoswitch-2 (25  $\mu$ M, DMSO/H<sub>2</sub>O 1:1).** (A) Structure of **2** in its *trans* configuration. (B) Absorption spectra of maximally *cis/trans* enriched PSSs after irradiation with corresponding lights for 2 min. (C) Cycles of 365/451 nm light irradiation showing no photodecomposition. (D) Thermal relaxation of the *cis*-isomer over a period of 2 h at 37°C.

## SI6.3.3 Xanoswitch-3



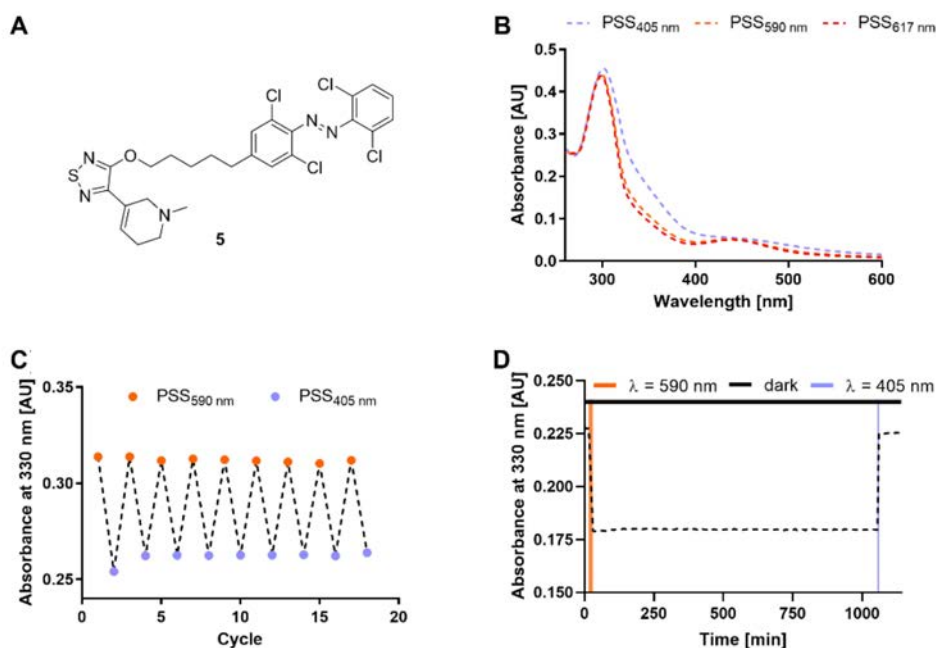
**Figure S6.5. Photochemical characterization of tetra-fluoro-C4-xanoswitch-3 (25  $\mu$ M, DMSO/H<sub>2</sub>O 1:1).** (A) Structure of **3** in its *trans* configuration. (B) Absorption spectra of maximally *cis/trans* enriched PSSs after irradiation with corresponding lights for 2 min. (C) Cycles of 528/405 nm light irradiation showing no photodecomposition. (D) Thermal relaxation of the *cis*-isomer over a period of 14 h at 37°C.

## SI6.3.4 Xanoswitch-4

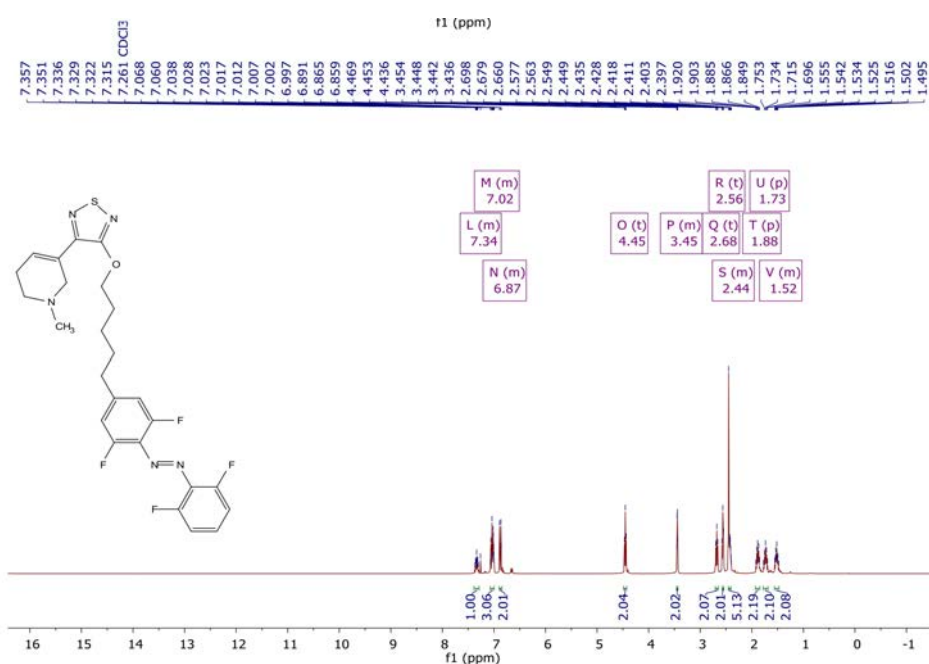


**Figure S6.6. Photochemical characterization of tetra-fluoro-C5-xanoswitch-4 (25  $\mu$ M, DMSO/H<sub>2</sub>O 1:1).** (A) Structure of **4** in its *trans* configuration. (B) Absorption spectra of maximally *cis/trans* enriched PSSs after irradiation with corresponding lights for 2 min. (C) Cycles of 528/405 nm light irradiation showing no photodecomposition. (D) Thermal relaxation of the *cis*-isomer over a period of 16 h at 37°C.

## SI6.3.5 Xanoswitch-5



**Figure S6.7. Photochemical characterization of tetra-chloro-C5-xanoswitch-5 (50  $\mu$ M, DMSO/H<sub>2</sub>O 1:1).** (A) Structure of **5** in its *trans* configuration. (B) Absorption spectra of maximally *cis/trans* enriched PSSs after irradiation with corresponding lights for 2 min (405 nm), 5 min (590 nm) and 20 min (617 nm). (C) Cycles of 405/590 nm light irradiation showing no photodecomposition. (D) Thermal relaxation (50  $\mu$ M, DMSO) of the *cis*-isomer over a period of 18 h at 37°C.

SI6.4 <sup>1</sup>H-NMR and <sup>13</sup>C-NMR spectroscopy

**Figure S6.8. <sup>1</sup>H-NMR of 3-((5-(4-((2,6-difluorophenyl)diazanyl)-3,5-difluorophenyl)pentyl)oxy)-4-(1-methyl-1,2,5,6-tetrahydropyridin-3-yl)-1,2,5-thiadiazole (4).**



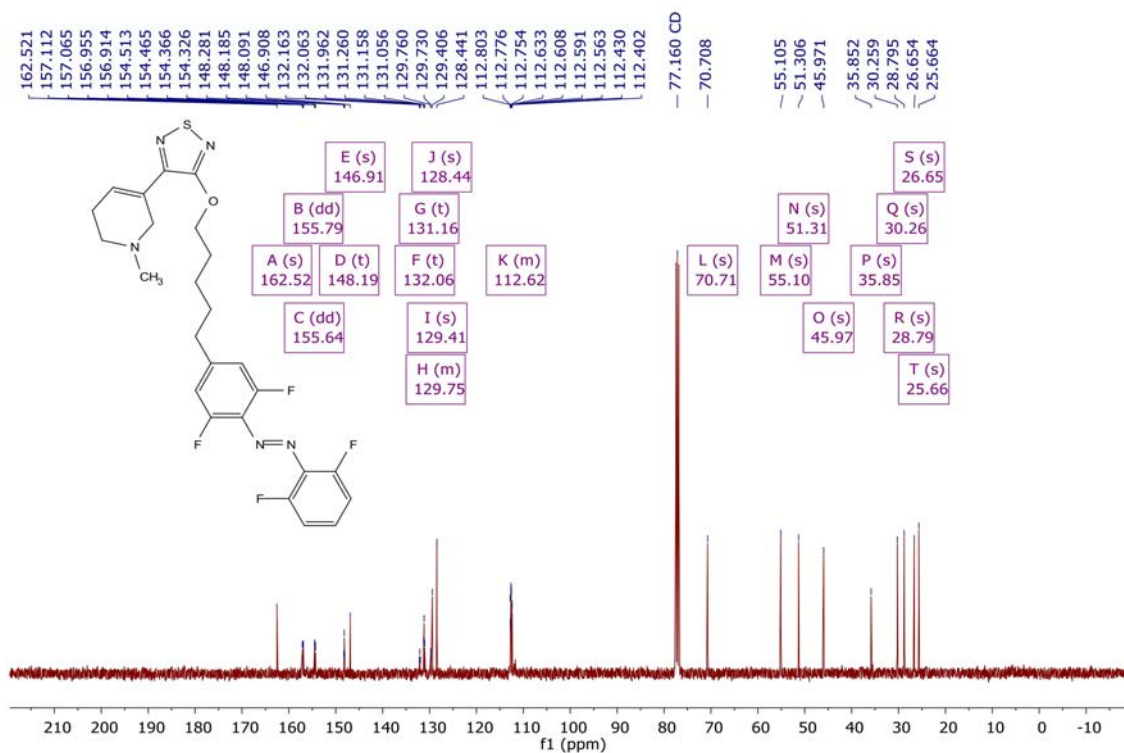


Figure S6.9.  $^{13}\text{C}$ -NMR of 3-((5-(4-((2,6-difluorophenyl)diazenyl)-3,5-difluorophenyl)pentyl)oxy)-4-(1-methyl-1,2,5,6-tetrahydropyridin-3-yl)-1,2,5-thiadiazole (4).

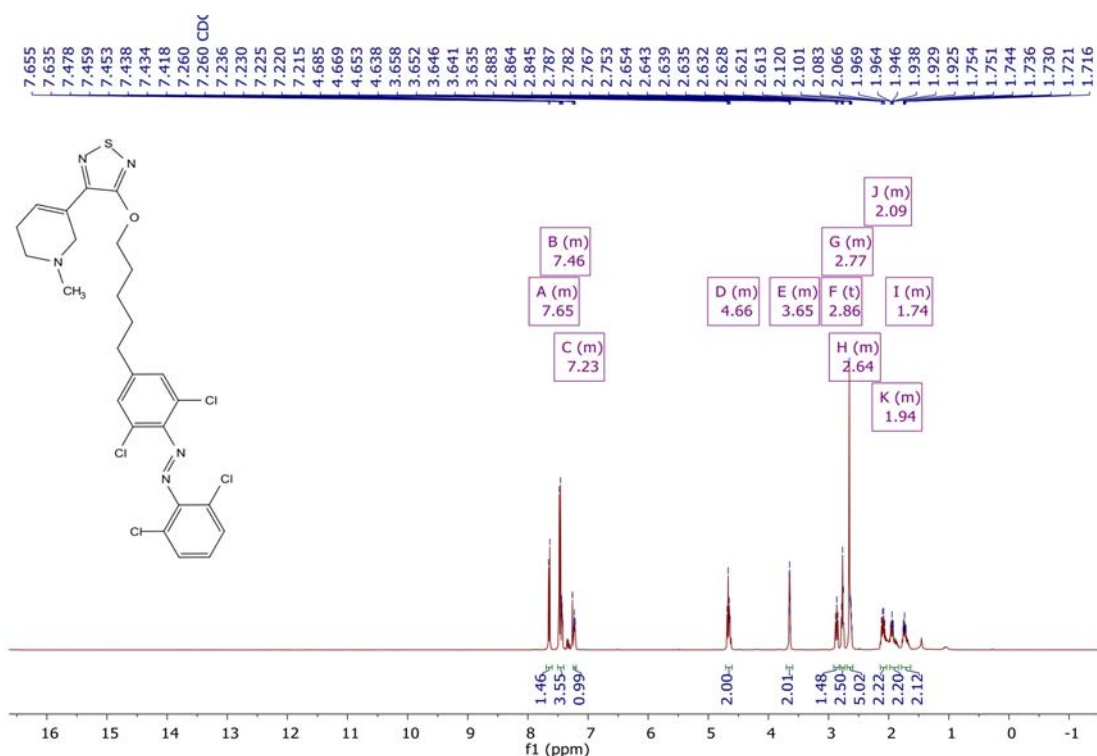
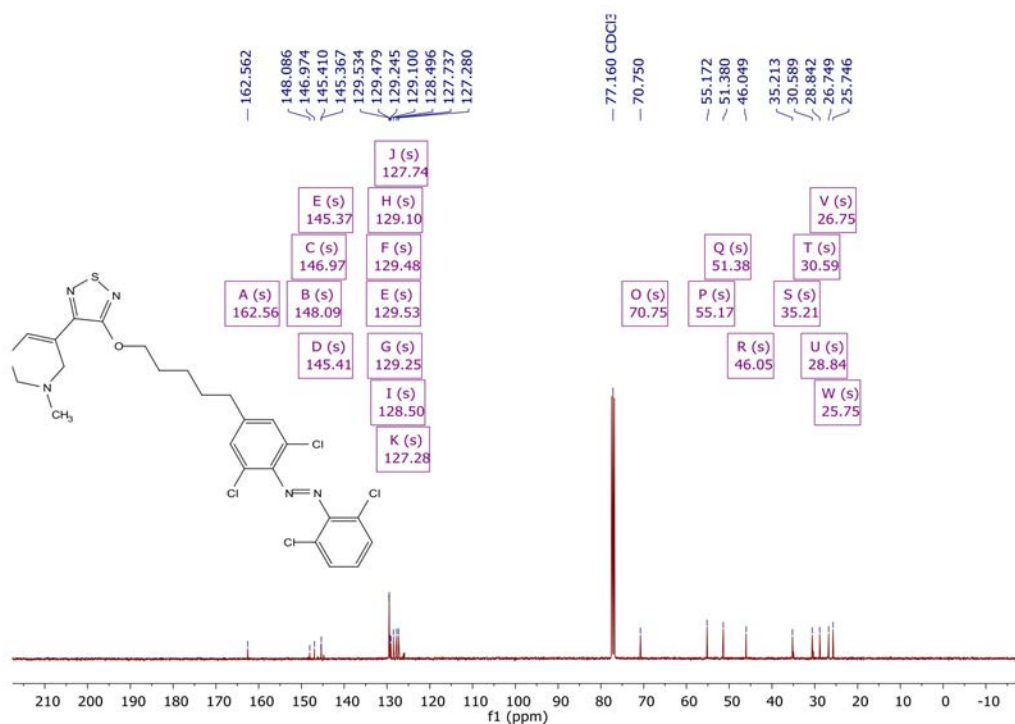


Figure S6.10.  $^1\text{H}$ -NMR of 3-((5-(3,5-dichloro-4-((2,6-dichlorophenyl)diazenyl)phenyl)pentyl)oxy)-4-(1-methyl-1,2,5,6-tetrahydropyridin-3-yl)-1,2,5-thiadiazole (5).



**Figure S6.11.**  $^{13}\text{C}$ -NMR of 3-((5-(3,5-dichloro-4-((2,6-dichlorophenyl)diazanyl)phenyl)pentyl)oxy)-4-(1-methyl-1,2,5,6-tetrahydropyridin-3-yl)-1,2,5-thiadiazole (5).

## SI6.5 Split luciferase complementation assay

The activity of the photoswitchable xanomeline derivatives was determined by means of a human embryonic kidney 293T (HEK 293T, American Type Culture Collection; ATCC) cell line, stably expressing the human  $M_1$  muscarinic acetylcholine receptor ( $M_1R$ ) and a split luciferase complementation system: the  $G\alpha_q$  subunit fused to a click-beetle luciferase fragment and the phospholipase C- $\beta_3$  (PLC- $\beta_3$ ) fused to the corresponding fragment<sup>1</sup>. Cells were routinely monitored for mycoplasma contamination and were negative. The cells were cultivated in Dulbecco's modified Eagle's medium (DMEM) containing 10% fetal calf serum (FCS), 0.6 mg/ml G418 and 0.001 mg/ml Puromycin, at 37°C in a water-saturated atmosphere containing 5%  $\text{CO}_2$ . On the evening before the assay, the cells were detached from a 75-cm<sup>2</sup> flask by trypsinization and centrifuged. The pellet was resuspended in assay medium consisting of Leibovitz' L-15 (w/o phenol red) with 5% FCS and 10  $\mu\text{M}$  HEPES and the density of the suspension was adjusted to  $1.25 \times 10^6$  cells/ml. Then, 80  $\mu\text{l}$  of the cells were seeded in Nunc<sup>TM</sup> MicroWell<sup>TM</sup> 96 well plates (ThermoFisher Scientific: 136101) and incubated overnight in a humidified atmosphere at 37°C without additional  $\text{CO}_2$ . For the assay, 10  $\mu\text{l}$  of 10 mM luciferin (ThermoFisher Scientific: 88293) in L-15 were added to each well and the cells were allowed to equilibrate for 10 min at 37°C. Afterwards, 10  $\mu\text{l}$  per concentration of a pre irradiated ligand

dilution series was added, yielding final in-well concentrations of (10  $\mu$ M) – (3  $\mu$ M) – (1  $\mu$ M) – (300 nM) – (100 nM) – (30 nM) – (10 nM) – (1 nM). Afterwards the plate was read in a pre-warmed Berthold Mithras LB 940. Additionally, a duplicate of the reference substance carbachol (CCh) and a negative control (L-15) was included in each individual experiment. The luminescent signal was continuously monitored for 30 min after which a stable plateau had formed for every concentration. Each substance was measured in at least three independent experiments, in which each condition was tested in duplicate. Data were analyzed by taking the last 5 data points of each plateau and plotting them in GraphPad Prism 5. These values were normalized to the maximal response of reference agonist CCh (100%) and the negative control L-15 (0%). Afterwards, the values of the independent experiments were pooled to generate the overall concentration-response curves which were fitted using GraphPad Prisms built-in log(agonist) vs. response equation.

### **SI6.6 *In vitro* calcium imaging**

Human embryonic kidney tsA201 (HEK tsA201, American Type Culture Collection; ATCC) cells were maintained in DMEM/Nutrient Mixture F-12 Ham (DMEM/F12 1:1, Life Technologies) supplemented with 10% fetal bovine serum (FBS; Life Technologies), penicillin and streptomycin (1%, Sigma-Aldrich) in a controlled environment (37°C, 98% humidity and 5% CO<sub>2</sub>). The cells were transiently co-transfected with the human M<sub>1</sub>R (Addgene) and Red-Genetically Encoded Calcium 1 (R-GECO1; ratio1:1) using X-tremeGENE 9 DNA Transfection Reagent (Roche Applied Science) following the manufacturer's instructions. The calcium indicator allows to determine changes in intracellular calcium concentrations upon receptor activation. As generally known, M<sub>1</sub> mAChRs prevalently activate G $\alpha_q$  proteins, leading to the activation of the phospholipase C pathway, which results in the production of inositol 1,4,5-trisphosphate (IP<sub>3</sub>) and the subsequent release of intracellular calcium from the endoplasmic reticulum. The day after, cells were harvested with accutase (Sigma-Aldrich) and seeded onto 16 mm or 25 mm (1PE or 2PE experiments) glass coverslips (ThermoFisher Scientific) coated with poly-L-Lysine (Sigma-Aldrich) to allow cell adhesion. Finally, the seeded cells were used for the experiments after 24 h.

The bath solution used for single cell intracellular calcium recordings contained: 140 mM NaCl, 5.4 mM KCl, 1 mM MgCl<sub>2</sub>, 10 mM HEPES, 10 mM glucose and 2 mM CaCl<sub>2</sub>, with pH 7.40. Before each experiment, cells were mounted on the recording chamber and rinsed with fresh solution. Then, the recording chamber was filled with 1 ml of the bath solution and placed on an IX71 inverted microscope (Olympus) with a XLUMPLFLN 20XW x20/1 water immersion

objective (Olympus). R-GECO1 was excited during 50 ms at 562 nm using a Polychrome V light source (Till Photonics) equipped with a Xenon Short-Arc lamp (Ushio) and a 585 nm dichroic beam splitter (Chroma Technology). The emission at 600 nm was filtered using an ET630/675 nm emission filter (Chroma Technology) and finally collected by a C9100-13 EM-CCD camera (Hamamatsu Photonics). Images were acquired at room temperature with an imaging interval of 4 s with the SmartLux software (HEKA), and the imaging analysis was done with Fiji (NIH, ImageJ).

Photostimulation under 1PE during recordings was done by illumination of the entire focused field using the Polychrome V connected to a personal computer, and shutter and wavelengths were controlled using Patchmaster software (HEKA). Light intervals lasted a total of 5 min for all the HEK tsA201 cell experiments, except for the illumination with 455 nm where it lasted 3 min. Xanoswitch-4 isomerizes from *trans*-to-*cis* with flashes of 530 nm (3.5 s duration) and 400 nm (3.5 s duration) light. Furthermore, for the compound xanoswitch-5 flashes of 580 nm (3.5 s duration) and 455 nm (3.5 s duration) light were used. An extra LED of continuous illumination with 460 nm light was used to guarantee an efficient photoswitching. The pre-illuminated *cis*-5 was applied to validate our results. The pre-irradiation was made with a LED from OSRAM Oslon (SSL 80-green, part number LT-2014, 590 nm). LED modules were combined to a rated power of 4W and used with a forward current of  $I_F = 350$  mA.

These experiments were performed under dark conditions to keep the compounds in their *trans* conformation. Further control experiments were performed in HEK tsA201 cells that do not express the  $M_1$  mAChRs (**Figure S6.12**).

Addition of agonists and vehicle was carried out by carefully pipetting directly into the recording chamber for the final dilution of approximately 1:1000. Stock solutions of the agonists were stored at -20°C in DMSO (Sigma-Aldrich) and diluted with the assay buffer to a 0.1% final concentration of DMSO. CCh (Sigma-Aldrich) was used as a positive control to stimulate  $M_1$  mAChRs in HEK tsA201 cells. Data were normalized over the maximum response obtained with CCh at 10  $\mu$ M.

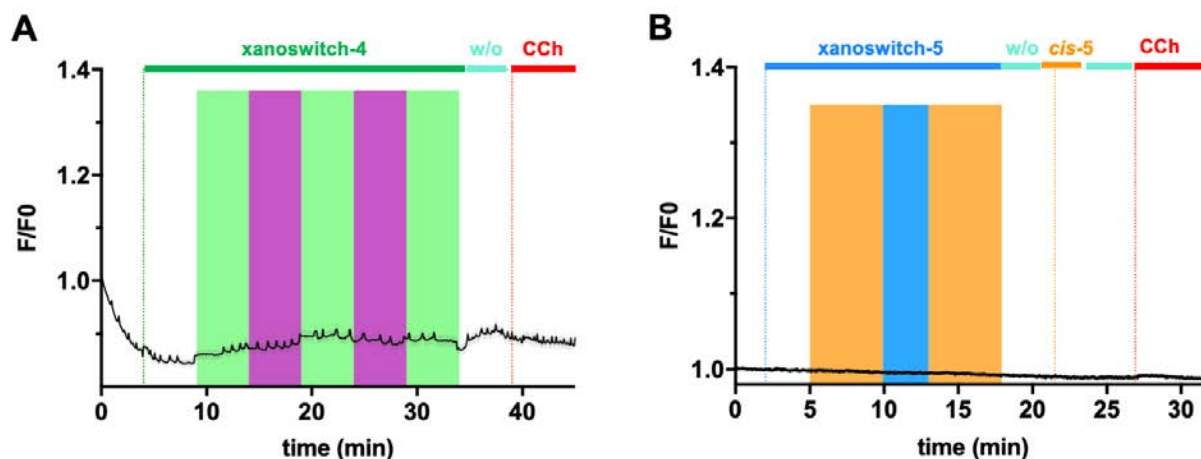


**Figure S6.12. Control experiments in HEK cells without the presence of M<sub>1</sub>R.** No calcium oscillations were observed after application of CCh, xanoswitches-4 (A, n = 50 cells) or -5 (B, n = 50 cells), and under 400 nm and 530 nm (A) or 580 nm and 455 nm (B) light cycles.

## SI6.7 Zebrafish larvae experiments

Wild-type zebrafish embryos (Tüpfel long-fin strain) were purchased from the animal facility of the Barcelona Biomedical Research Park (PRBB) and raised in darkness for 6 days at 28.5°C in UV filtered tap water in petri dishes (daily cleaned and refilled). Animal development<sup>2</sup> was checked every 24 h. Unhealthy or abnormal embryos and larvae were removed and euthanatized in tricaine methanesulfonate 0.02%. All experiments and procedures were conducted according to the European Directive 2010/63/EU.

For the experiments blinded zebrafish were used. The animals underwent a noninvasive and highly specific blinding technique that induces photoreceptor apoptosis in the dorsal and central retina<sup>2,3</sup>. The light-lesioning procedure was performed in a thermostatic and well-ventilated room equipped with small fans for air circulation and heat dissipation. Larvae at 7 days post-fertilization (dpf) were placed in a 25-mm petri dish containing 20 ml of UV filtered tap water, inserted in a closed mirrored chamber, and then exposed to 135.000 lux light emitted by a mercury lamp (model Olympus U-LH100HG) for 30 min. Temperature was monitored throughout the whole procedure.

The experiment was carried at 12 h after the induction of blindness. Each fish was randomly placed between vehicle (n = 6) and treatment group (n = 6) in a separate well of a 96-well plate, each containing 100 µl of fresh sterilized water. The animals were left undisturbed in the dark for 20 min to get acquainted with the new setting (habituation time). The compound (*i.e.*, 30 µM of xanoswitch-5) and vehicle (*i.e.*, 0.3% of DMSO) were prepared in fresh water. The application was made in darkness and with a multichannel pipette to exclude differences due to

delays in the application of each solution. At this point, the plate was inserted into the ZebraBox and movements were recorded and analysed using the ZebraBox tracking system and the ZebraLab software (ViewPoint Life Science).

After 20 min of dark adaptation, the animals were exposed to controlled cycles: 590 nm (ProLight 3W Power Led) at 2 mW for 5 min, 455 nm (ProLight 3W Power Led) at 7 mW for 5 min. The sources were placed at 8 cm of distance from the 96-well plate. The light intensity was measured with Optical Power Monitor, Power Meter Interface PM101, and the sensor S470C, Thermal Power Sensor Head (Thorlabs).

Alterations of locomotor activity were determined by monitoring and measuring fast movements, swimming distances and duration of high-speed swimming. Data were analyzed by two-way ANOVA (GraphPad Prism 9).

## Additional references

- 1 Littmann, T., Ozawa, T., Hoffmann, C., Buschauer, A. & Bernhardt, G. A split luciferase-based probe for quantitative proximal determination of G $\alpha_q$  signalling in live cells. *Sci Rep* **8**, 17179, doi:10.1038/s41598-018-35615-w (2018).
- 2 Matera, C. *et al.* Reversible Photocontrol of dopaminergic transmission in wild-type animals. *Int J Mol Sci* **23**, doi:10.3390/ijms231710114 (2022).
- 3 Taylor, S., Chen, J., Luo, J. & Hitchcock, P. Light-induced photoreceptor degeneration in the retina of the zebrafish. *Methods Mol Biol* **884**, 247-254, doi:10.1007/978-1-61779-848-1\_17 (2012).

# Chapter 7

---

## Photo-BQCA: Positive allosteric modulators enabling optical control of the M<sub>1</sub> receptor

---

---

Hubert Gerwe, **Rosalba Sortino**, Ekin Opar, Pau Gorostiza and Michael Decker. **Photo-BQCA: Positive allosteric modulators enabling optical control of the M<sub>1</sub> receptor.** *Submitted.*





## Abstract

The field of G protein-coupled receptor (GPCR) research has benefited greatly from the spatiotemporal resolution provided by light controllable, photoswitchable agents. Most of the developed tools have targeted the Rhodopsin like family (class A), the largest family of GPCRs. However, to date, all such class A photoswitchable ligands were designed to act at the orthosteric binding site of these receptors. Herein, we report the development of two novel photoswitchable allosteric modulators designed to target the M<sub>1</sub> muscarinic acetylcholine receptor (M<sub>1</sub> mAChR or M<sub>1</sub>R). The presented benzyl quinolone carboxylic acid (BQCA) derivatives, photo-BQCisA and photo-BQC*trAns* exhibit complementary photopharmacological behavior and allow reversible control over the receptor using light as an external stimulus. This makes them valuable tools to further investigate M<sub>1</sub>R signaling and a proof of concept for photoswitchable allosteric modulators at class A GPCR receptors.



## 7.1 Introduction

A major challenge of medicinal chemistry is the development of compounds selective to a receptor class, and especially to a specific subtype. A challenge which is particularly difficult in the development of G protein-coupled receptors (GPCRs) ligands. These receptors are of exceptional therapeutic value and make up for approximately one third of all FDA approved drugs<sup>1</sup>. However, some GPCR subfamilies have proven almost intractable in drug discovery as selectivity among their subtypes is infamously difficult to achieve. The five muscarinic acetylcholine receptor subtypes being prototypically difficult to target with selectivity. This is in essence caused by the high homology within the orthosteric binding site of these receptor subtypes. In contrast, the topographically distinct allosteric binding sites are often less conserved, thus enabling the development of subtype selective ligands with a diverse range of functions<sup>2,3</sup>.

Coincidentally, the development of photoswitchable ligands (*i.e.*, molecules that reversibly change their chemical structure and concomitantly their biological activity upon irradiation with light) has provided pharmacological and biomedical research with the ability to turn a given receptor into an artificial photoreceptor. A plethora of light controllable GPCR ligands was developed which found application in a variety of pharmacological settings<sup>4-19</sup>. Surprisingly, only a minority of these photoswitchable ligands has been developed to target allosteric binding sites. The few ligands developed, have successfully demonstrated the value of combining subtype selectivity of allosteric ligands with the unmatched spatiotemporal resolution of photoswitchable compounds<sup>20-26</sup>. However, none of them acts at the largest of the five major GPCR families, the Rhodopsin like family (class A). This is remarkable since class A GPCRs have so far received the highest interest in the development of photopharmacological tool compounds, primarily because they comprise many therapeutically important receptors subfamilies<sup>27-31</sup>.

To challenge this lack of photopharmacological know-how, we selected a class A GPCR subfamily prototypical for allosteric modulation: the muscarinic acetylcholine receptors (mAChR or MR). The closely related mAChRs (M<sub>1</sub>R-M<sub>5</sub>R) subtypes are therapeutically important targets, hence, various subtype selective positive allosteric modulators (PAMs) have been developed<sup>32,33</sup>. For this study, the first PAM reported for the muscarinic receptors, **benzyl quinolone carboxylic acid (BQCA)** was especially appealing since structure-activity relationships (SARs) are available<sup>34-37</sup>.

Here, the first two reversibly photoswitchable allosteric modulators for class A GPCRs are presented. Based on BQCA, an iterative generation-evaluation approach was used to find and enhance functional photoswitching at the M<sub>1</sub>R. This resulted in a *cis*-on PAM which was termed “photo-BQC*is*A”. In addition, a derivative with complementary photopharmacological properties (*trans*-on) termed “photo-BQC*tr*Ans” was also synthesized and pharmacologically characterized.

## 7.2 Results and discussion

### 7.2.1 Rational design and chemical synthesis

The design of the presented photoswitchable allosteric modulators was based on SARs available for a variety of BQCA derivatives<sup>36-40</sup>. In general, SARs of BQCA can be classified in three categories (**Figure 7.1**): top-moiety, quinolone-core and non-planar arm. While the acid function of the top-moiety is not essential for allosteric affinity, it is essential for binding cooperativity. If cooperativity is to be maintained, its substitution is only possible in exchange with a hydrogen bond donor in the correct orientation<sup>36</sup>.

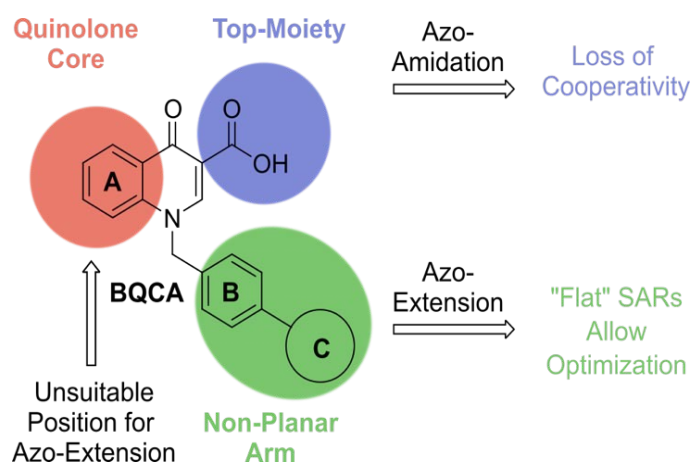
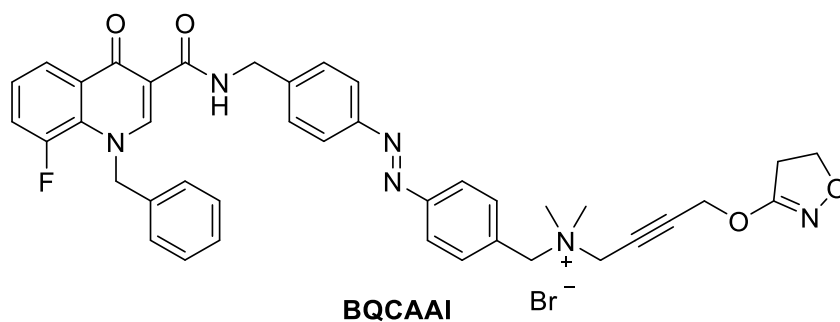


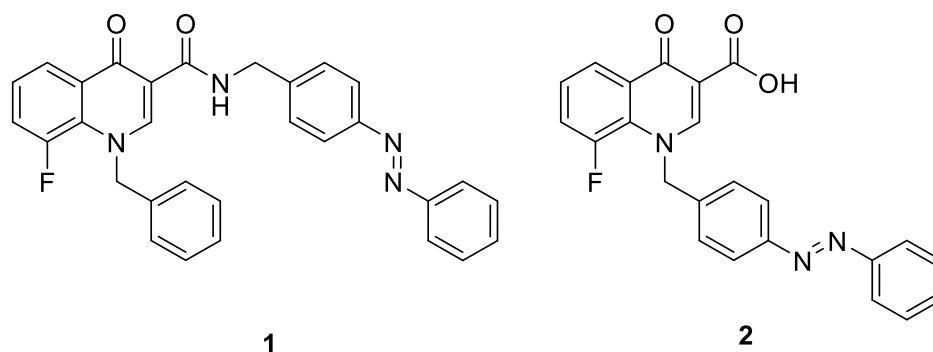
**Figure 7.1. Structure-activity relationships of BQCA.** The introduction of an azobenzene at the quinolone core and the top-moiety is predicted to be disadvantageous for cooperativity, modifications of the non-planar arm are plentiful though and allow introduction of further ring systems without affecting the essential function of the compound.

However, the absence of the hydrogen bond donor does not impair affinity, which had allowed us in a preceding project to design the photoswitchable subtype selective dualsteric ligand BQCAAI (**Figure 7.2**)<sup>28</sup>. Substitution at the quinolone-core (*e.g.*, fluorination) modulates the intrinsic efficacy of the allosteric ligands, a property which is today considered disadvantageous<sup>41-43</sup>.

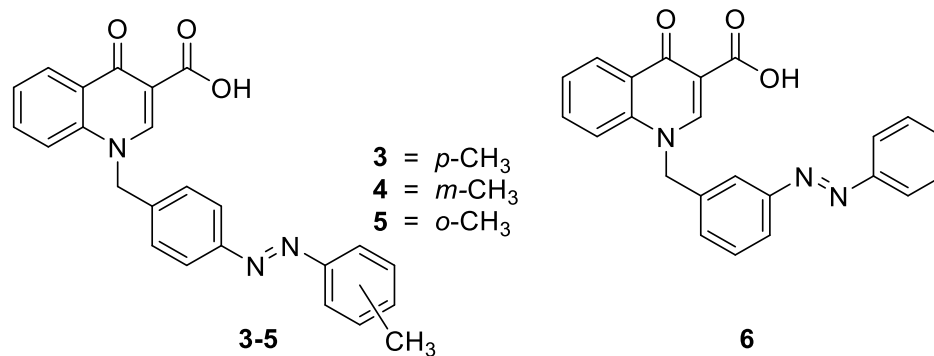
**0<sup>th</sup> Generation:**



**1<sup>st</sup> Generation:**



**2<sup>nd</sup> Generation:**



**3<sup>rd</sup> Generation:**

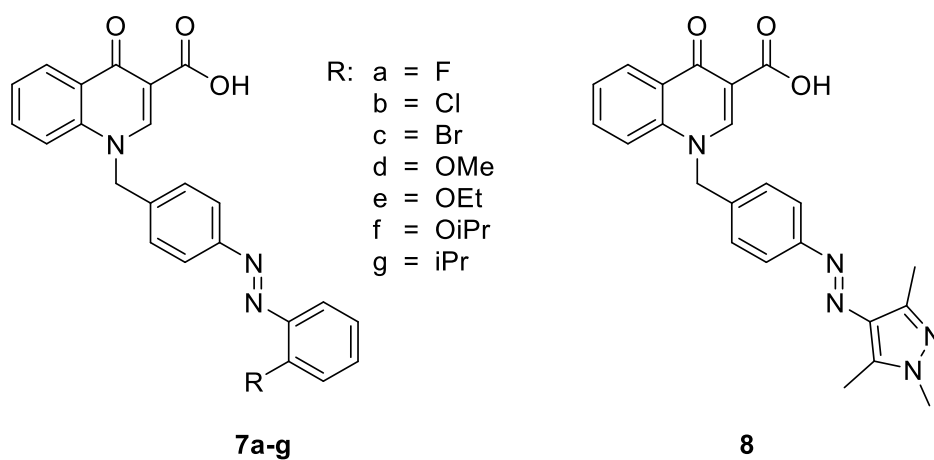


Figure 7.2. Overview over photoswitchable BQCA derivatives designed for optical control of M<sub>1</sub>R activation.

Moreover, none of the conducted SAR studies indicated that an “azo-substituent” at the core could be tolerated. In contrast to the former two positions, the non-planar arm has been shown to tolerate a huge variety of modifications and extensions with little impact on activity, hence, its SARs are often described as “flat”<sup>37,44</sup>.

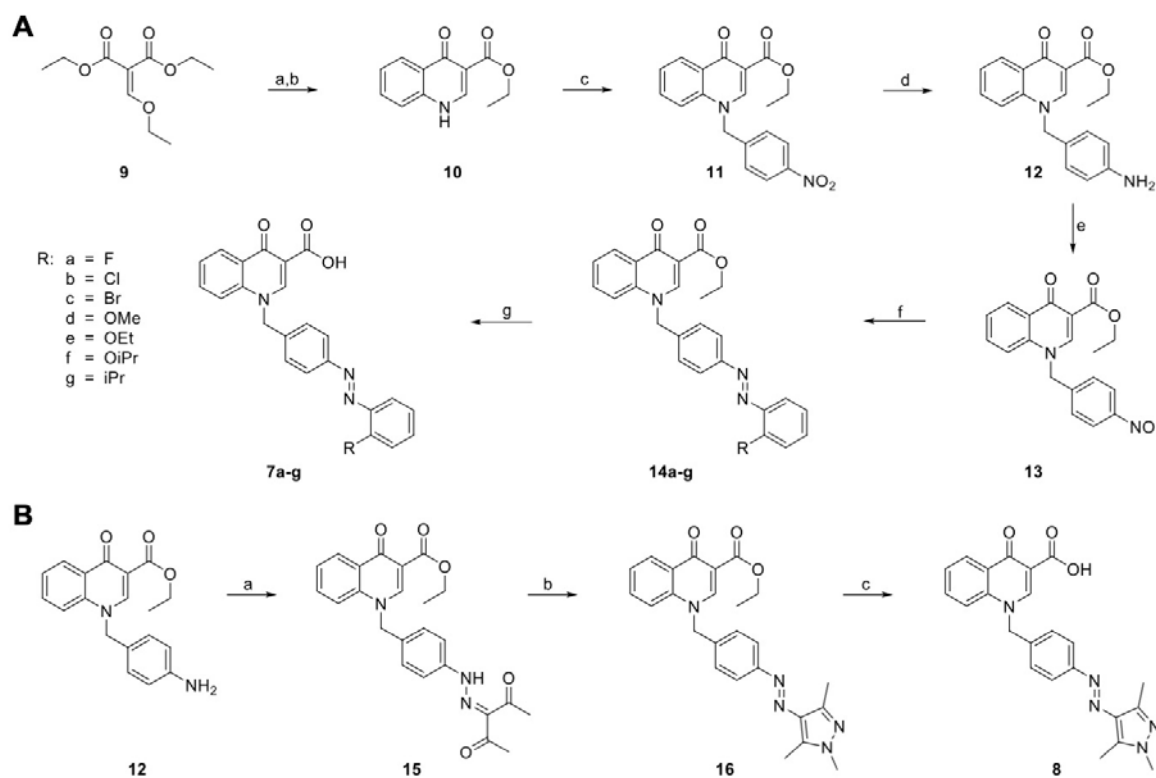
The reasoning was that these “flat-SARs” would prevent any change of the pharmacological properties induced upon isomerization of a non-planar photoswitchable arm. Consequently, this part of BQCA seems rather ill suited for the introduction of the photoswitchable moiety even if it is sterically tolerated. However, we deemed this an ideal starting point. The idea was, that in contrast to many other projects where introduction of the azobenzene itself already determines which photoform will be more active (*cis*-on or *trans*-on), we could in this case choose the preferred photopharmacological behavior.

Initially, two photoswitchable derivatives of 8-fluoro-BQCA (8F-BQCA) were synthesized to explore and validate the SAR landscape with photoswitchable moieties (8F substitution was afterwards omitted as it is reported to only increase the intrinsic agonistic efficacy without increasing the desired cooperativity)<sup>36</sup>. Starting with an azo-amidation of the carboxylic acid (**1**) and an azo-extension of the non-planar arm (**2**), the focus soon shifted on the development of BQCAs bearing photoswitchable non-planar arms with different substitution patterns (**Figure 7.2**).

Among the vast amount of non-planar arm modifications with little impact on activity, an interesting behavior towards C-ring methylation patterns can be found in the literature. Depending on the position on the C ring, methyl groups either have no impact or are detrimental for the compound’s potency<sup>37</sup>. Considered uninteresting for the optimization of BQCA itself, it provides a vulnerability, that a photoswitchable moiety might exploit. To examine whether C-ring methylation might be used as an impairing motive which could be switched in and out of the “weak spot”, a “methyl walk” on the distal azobenzene ring as 2<sup>nd</sup>-generation ligands was realized synthetically (**3-5**). (**Figure 7.2**). Simultaneously, it was also explored whether the quinolone core could be attached in *meta* position (*meta*-linked) with respect to the azo moiety (**6**).

Based on the results (*vide infra*) a 3<sup>rd</sup> series of photo-BQCAs was obtained, which exploited the *ortho* position of the distal benzene ring with substituents of varying electronic properties and steric demands (**7a-g**). Simultaneously, to demonstrate that the flat-SAR approach can be exploited to develop complementary photopharmacological behavior, a *trans*-on photo-BQCA

(**8**) was rationally designed based on recent insights into the nature of the (“cryptic”) allosteric binding pocket<sup>45</sup>. The synthesis of the 3<sup>rd</sup> generation of photo-BQCAs is described in the following **Scheme 7.1**, for synthetic schemes and details concerning photo-BQCAs **1-6** (see the **Supporting Information (SI)** for details, **Scheme S7.1-S7.3**).



**Scheme 7.1. Synthetic route to benzylazo-quinoline-carboxylic-acid derivatives of the 3<sup>rd</sup> generation.**

(A) Reagents and conditions: (a) Aniline, 130°C (86%); (b) Eaton’s reagent (Phosphorus pentoxide, 7.7 wt% in methanesulfonic acid), 130°C, 77%; (c) 1-(bromomethyl)-4-nitrobenzene, K<sub>2</sub>CO<sub>3</sub>, KI, DMF, RT, 89%; (d) Fe, NH<sub>4</sub>Cl, H<sub>2</sub>O, EtOH, 80°C, quant. (e) Oxone<sup>®</sup>, CH<sub>2</sub>Cl<sub>2</sub>, H<sub>2</sub>O, RT, 83%; (f) respective aniline, HOAc, RT, 53-92%; (g) 1N NaOH, THF, 50°C, 59-92%. (B) Synthetic route to the 1,3,5-trimethyl-pyrazole photoswitch. Reagents and conditions: (a) 1. NaNO<sub>2</sub>, H<sub>2</sub>O, AcOH, HCl, 0°C; 2. pentane-2,4-dione, NaOAc, EtOH, H<sub>2</sub>O, 0° to RT, 60%; (b) mono-methyl hydrazine, ethanol, 80°C, 71%; (c) 1N NaOH, THF, 50°C, 79%.

The quinolone-core (**10**) was synthesized as reported.<sup>36</sup> Instead of the typically employed, low yielding and laborious thermal cyclization of (phenylamino)methylene malonates in phenylether at over 200°C<sup>28,46</sup>, an improved cyclization using Eaton’s Reagent was employed to give compound **10** in good yields<sup>47,48</sup>. Subsequent *N*-benzylation with 1-(bromomethyl)-4-nitrobenzene followed by reduction of the *para*-nitro compound **11** yielded the corresponding aniline **12**. Aniline **12** was partially oxidized to the nitroso compound **13** using Oxone<sup>®</sup> in a heterogeneous H<sub>2</sub>O/CH<sub>2</sub>Cl<sub>2</sub> system. This gave access to derivatization by condensation of compound **13** with various commercially available anilines in a Baeyer-Mills reaction to the



corresponding azobenzenes (**14a-g**). Finally, the desired free carboxylic acids (**7a-g**) were obtained under basic hydrolysis of the ester moiety under standard conditions. The *trans*-on heteroarene photoswitch<sup>49</sup> (**8**) was synthesized branching from aniline **12** which was for this purpose converted into the corresponding diazonium salt and used *in situ* to form a phenylhydrazono moiety (**15**) by reaction with pentane-2,4-dione. Subsequent cyclization with mono-methyl hydrazine yielded the desired pyrazole/benzene photoswitch (**16**) which had to be hydrolyzed as described above to obtain the target carboxylic acid (**8**).

### 7.2.2 Photochemical characterization

Determination of photochemical properties of all synthesized ligands by UV-Vis spectroscopy revealed that all compounds can be maximally photo-isomerized to the *cis* configuration using light of 365 nm. Notably, all *ortho*-alkoxy substituted photo-BQCAs (**7d-f**) and the photoswitchable arylazopyrazole **8** can also be effectively *cis*-enriched using a higher wavelength of 385 nm. *Trans*-enrichment of all azobenzene based photo-BQCAs was achieved using 400 or 455 nm, while the photoswitchable pyrazole/benzene **8** was maximally *trans* isomerized using green or orange light (530/590 nm). However, irradiation with orange light needs a prolonged duration of irradiation (10 min), hence, 530 nm was used in all experiments. Concerning other relevant photochemical properties (ratios of photostationary states, resistance to photofatigue and thermal stability), all photo-BQCAs behaved as expected (see **SI** for the photochemical details).

### 7.2.3 Split luciferase complementation assay

All potential photoswitchable PAMs were evaluated *in vitro* at their maximally *cis/trans* enriched photo stationary states for their ability to increase the potency of the orthosteric muscarinic agonist carbachol (CCh) at the human M<sub>1</sub> muscarinic acetylcholine receptor (M<sub>1</sub>R). For this purpose, a concentration response curve of CCh was measured alone and in the presence of 1 μM pre-illuminated photo-BQCAs in either *cis*- or *trans*-enriched state. Human embryonic kidney (HEK) cells expressing the human M<sub>1</sub>R and a split luciferase-based probe for quantitative proximal determination of Gα<sub>q</sub> signaling in live cells were used. The probe detects interactions between Gα<sub>q</sub> and its effector phospholipase C-β<sub>3</sub> (PLC-β<sub>3</sub>) as a quantifiable parameter of receptor activation<sup>50</sup>. The wavelength emitted by the modified luciferase from click-beetle *Pyrophorus plagiophthalmus* (λ<sub>max</sub> = 613 nm) no interference with the compounds' photoisomerization (*i.e.*, biorthogonal wavelength)<sup>28,30</sup>.

As expected, the amide **1** showed no cooperativity with CCh in either of its configurations while the unsubstituted, *para*-linked photoswitchable non-planar arm (**2**) exhibited BQCA-like ( $EC_{50}(\text{CCh+BQCA}) = 55 \text{ nM}$ ) cooperativity which was independent of the conformation ( $EC_{50}(\text{CCh+}i\text{cis-2}) = 47 \text{ nM}$ ;  $EC_{50}(\text{CCh+}i\text{trans-2}) = 52 \text{ nM}$ ; **Figure 7.3A**). Evaluation of the 2<sup>nd</sup> generation of photo-BQCAs (**3-6**), **Figure 7.3B** and **SI**) showed that in fact positioning of the methyl could heavily influence the allosteric ligands. While the *para*-methyl compound (**3**) was devoid of any cooperativity in both configurations and behaved like compound **1**, the *meta*-methyl substituted photo-BQCA (**4**) showed some, however, reduced cooperativity with no *cis/trans* differences ( $EC_{50}(\text{CCh+}i\text{cis-4}) = 91 \text{ nM}$ ;  $EC_{50}(\text{CCh+}i\text{trans-4}) = 93 \text{ nM}$ ; **Figure 7.3B**, left panel). Strikingly, the *ortho*-methyl compound (**5**) exhibited BQCA-like cooperativity and additionally minor differences between the activity of the isomers favoring the *cis*-isomer ( $EC_{50}(\text{CCh+}i\text{cis-5}) = 47 \text{ nM}$ ;  $EC_{50}(\text{CCh+}i\text{trans-5}) = 75 \text{ nM}$ ; **Figure 7.3B**, right panel). Interestingly, *meta*-linked compound **6** also showed significant cooperation and a minor *cis*-on difference, however, the latter was considerably lower than that of compound **5** (see **SI**), thus the *ortho* position was focused on.

The results are in accordance with our expectations. The essential parameter to induce *cis/trans* activity differences is the size of the *ortho*-substituent at the distal benzene ring. This trend was observed for electron withdrawing substituents ( $\text{F} < \text{Cl} < \text{Br}$ ) as well as for electron donating substituents ( $\text{MeO} < \text{EtO} < \text{IPrO}$ ). The latter showed increased cooperativity in comparison to BQCA (**Table S7.1** for comprehensive overview). However, as optimization of the allosteric modulating capability was not the scope of this work, we did not further investigate which of the cooperativity parameters was increased.

The greatest separation between the *cis* and *trans* dose-response curves was achieved using the *ortho*-isopropyl compound (Photo-BQCisA, **7g**; ( $EC_{50}(\text{CCh+}i\text{cis-7g}) = 55 \text{ nM}$ ;  $EC_{50}(\text{CCh+}i\text{trans-7g}) = 152 \text{ nM}$ )) and the 1,3,5-trimethyl-pyrazole photoswitch (Photo-BQC*tr*Ans, **8**; ( $EC_{50}(\text{CCh+}i\text{cis-8}) = 156 \text{ nM}$ ;  $EC_{50}(\text{CCh+}i\text{trans-8}) = 56 \text{ nM}$ )). Both showed an approximately 3-fold increase upon irradiation with the correct wavelength. According to the prediction, the *cis/trans* activity difference is in each case induced by steric hindrance unilaterally affecting one of the two isomers. This is also reflected by the *in vitro* results, as both active isomers are identical to BQCA regarding their overall cooperativity, while the inactive conformation is almost identical to the CCh curve. While ligand **7g** is more active in its ultraviolet (UV) light (365 nm) induced, thermodynamically less stable *cis* configuration, compound **8** is more active in the thermodynamically more stable *trans* conformation which

can be enriched using green light (530 nm). In total, both ligands show complementing photopharmacological behavior.

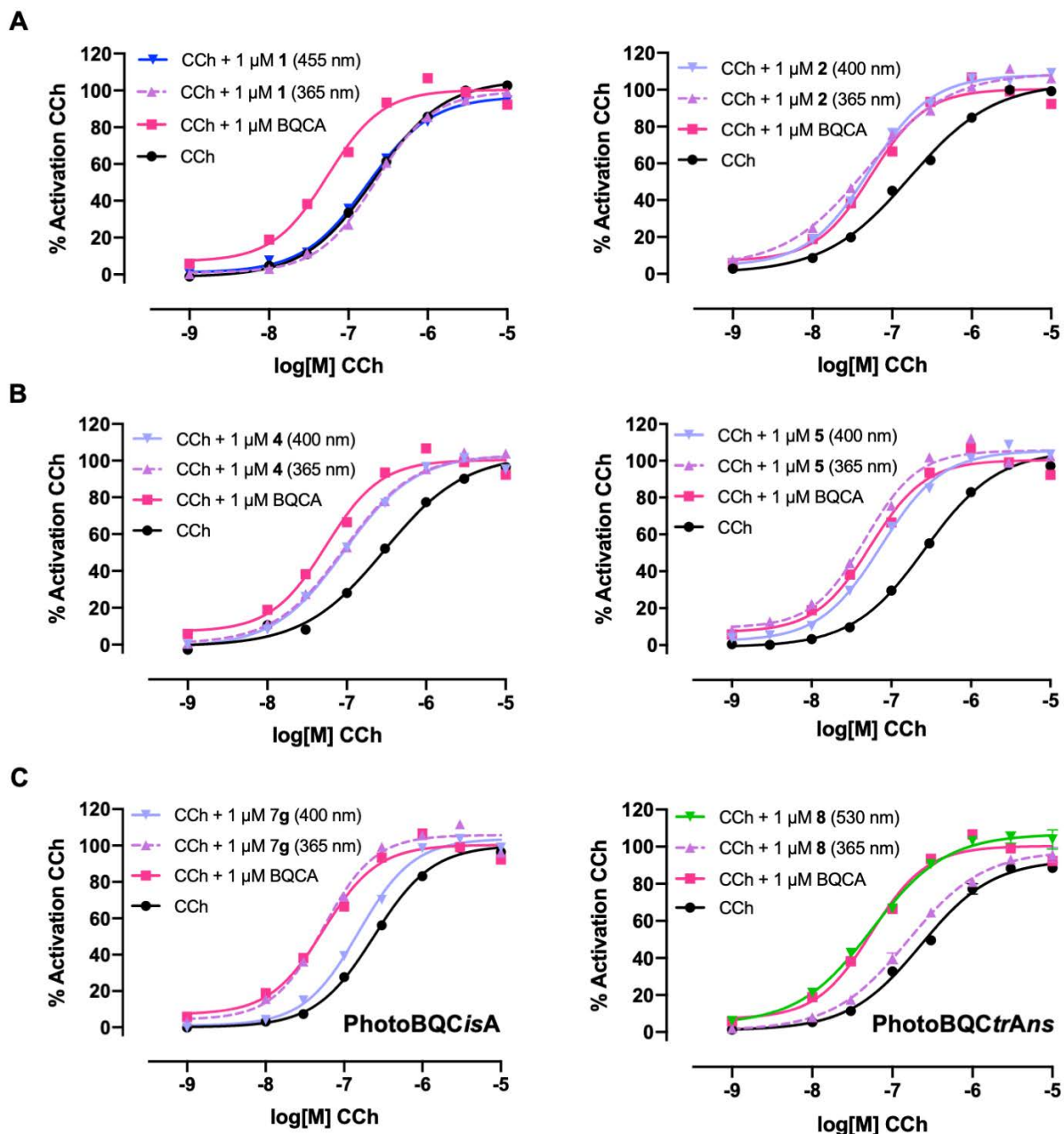


**Figure 7.3. Split luciferase complementation assay of potential photoswitchable mAChR<sub>1</sub> positive allosteric modulators.** Split luciferase assay of the most relevant BQCA derivatives from (A) 1<sup>st</sup>-, (B) 2<sup>nd</sup>- and (C) 3<sup>rd</sup>-generation. This assay detects the interaction between G $\alpha_q$  and its effector phospholipase C- $\beta_3$  (PLC- $\beta_3$ ), as a quantifiable parameter of receptor activation<sup>50</sup>. Concentration-response curves of muscarinic orthosteric agonist carbachol alone and in presence of 1  $\mu$ M pre-illuminated Photo-BQCAs in either *cis*- or *trans*-enriched state. BQCA (1  $\mu$ M) was included as reference. Data are given as the mean  $\pm$  standard error of mean (SEM) of 3 independent experiments performed in duplicate and normalized over the maximum and minimal response obtained by the concentration-response curve of carbachol.

## 7.2.4 Fluorescence-based plate reader assay

To validate the results, photo-BQCisA (**7g**) and photo-BQCtrAns (**8**) were further investigated using a plate reader-based fluorescence assay by measuring increases in intracellular calcium. The assay was performed in HEK cells co-expressing the human M<sub>1</sub>R and GCaMP6s (excitation 488 nm, emission 510 nm) as a genetically encoded calcium sensor. The calcium release upon receptor activation occurs only when the ligands **7g** or **8** are applied in their active configurations together with CCh as prestimulant (EC<sub>20</sub>) (**Figure 7.4**). These results confirm that both compound act as PAMs of M<sub>1</sub>R, with the ligand **7g** (**Figure 7.4A**) being more active in its *cis* and **8** (**Figure 7.4B**) in its *trans* form, respectively. As expected, no agonistic effect was observed, and no receptor response was caused by vehicle. CCh at saturation concentrations was used as positive control to normalize the data. No calcium responses were observed in HEK cells not expressing M<sub>1</sub>Rs (**Figure S7.7AB**).

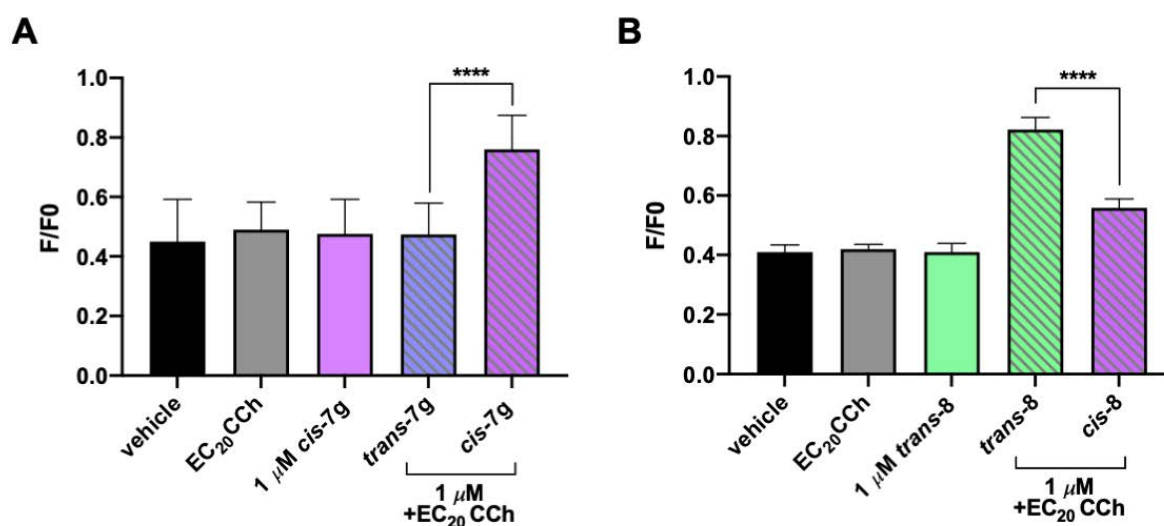


**Figure 7.4.** *In vitro* characterization of ligands **7g** and **8** using a plate reader-based fluorescence assay. The functional activity of the human M<sub>1</sub>R was measured by the increase of intracellular calcium in HEK cells co-expressing the receptor and the calcium indicator GCaMP6s. Only the application of (A) the *cis*-enriched **7g** or (B) *trans*-enriched **8** together with carbachol (CCh) at its EC<sub>20</sub> elicited significant calcium response. The amplitude of the response was quantified and compared by the one-way ANOVA with Tukey's multiple comparisons post-hoc test for compounds **7g** (1 μM) and **8** (1 μM): (*p*-value (\*\*\*\*) < 0.0001 for vehicle vs. active isomer + EC<sub>20</sub> CCh; *p*-value (\*\*\*\*) < 0.0001 for EC<sub>20</sub> CCh vs. active isomer + EC<sub>20</sub> CCh; *p*-value (\*\*\*\*) < 0.0001 for active isomer vs. active isomer + EC<sub>20</sub> CCh; *p*-value (\*\*\*\*) < 0.0001 for inactive isomer + EC<sub>20</sub> CCh vs. active isomer + EC<sub>20</sub> CCh). Data were normalized over the maximum response obtained with the saturation concentration of CCh (30 μM) and all statistical analyses were performed with GraphPad Prism 9. Error bars are ± SEM.

## 7.2.5 *In vitro* calcium imaging

Moreover, we were interested to evaluate Photo-BQ*CisA* and Photo-BQ*TrAns* in a downstream calcium imaging assay for their ability to allow reversible modulation of receptor signaling (Figure 7.5AB).

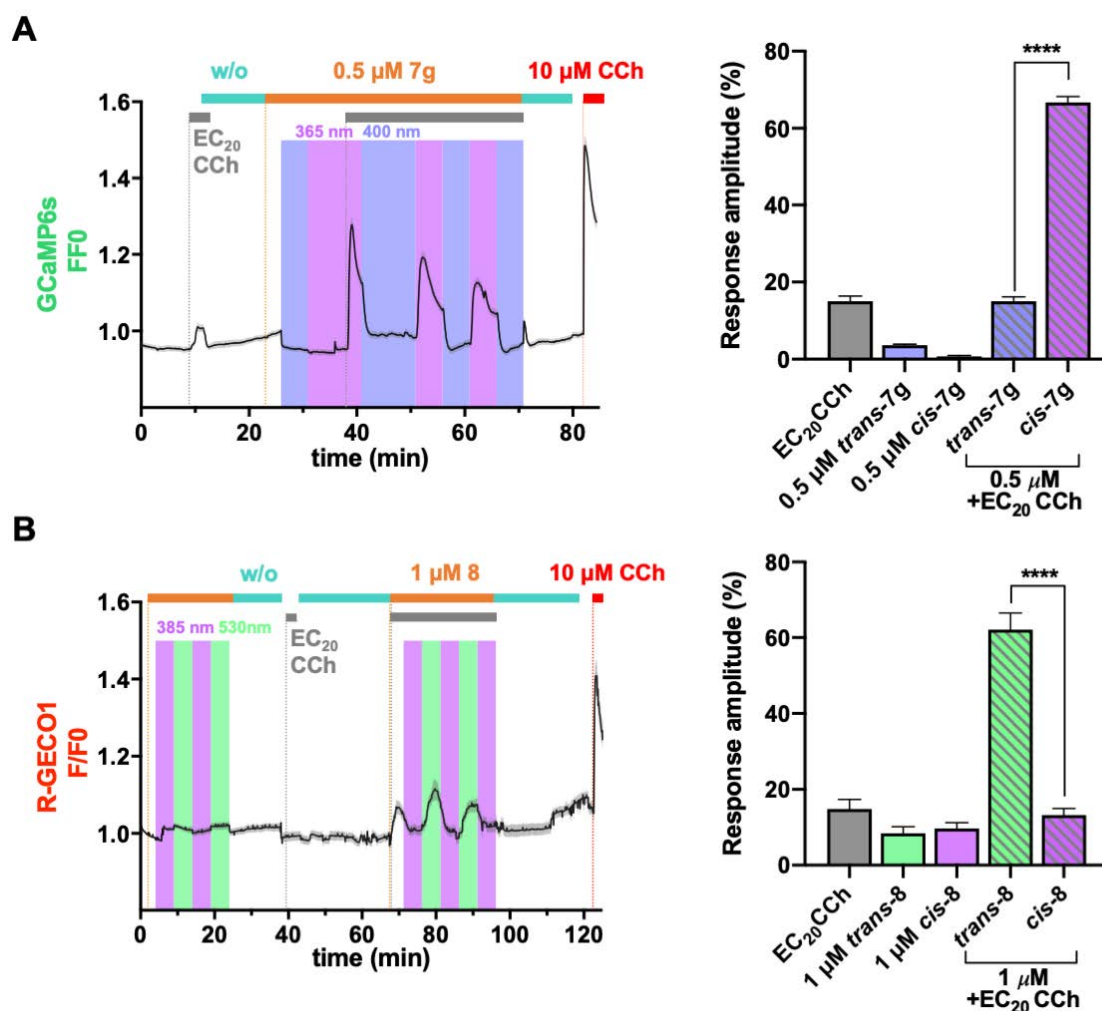


**Figure 7.5.** *In vitro* characterization of ligands **7g** and **8** using a live calcium imaging assay. Real time calcium imaging response (averaged traces on the left, black line, **A**,  $n = 116$  cells; **B**,  $n = 35$  cells) in HEK cells co-expressing human M<sub>1</sub>Rs and (**A**) GCaMP6s or (**B**) R-GECO1. Gray, orange and red bars indicate the application of vehicle (control); compounds **7g** (0.5 μM) or **8** (1 μM) and CCh (10 μM, reference agonist), respectively. Light blue bars indicate wash-out (w/o) periods. Violet, blue, and green rectangles represent periods of 365 nm, 400 nm and 530 nm illumination, respectively. Shadow represents  $\pm$  SEM. The quantification was made by calculating the amplitude of the response (right panel, **A**,  $n = 221$ ; **B**,  $n = 53$  cells). Data were normalized over the maximum response obtained with the saturation concentration of CCh (10 μM) and were analyzed using GraphPad Prism 9 by paired-sample Wilcoxon signed-rank test for compounds **7g** (0.5 μM) and **8** (1 μM): ( $p$ -value (\*\*\*\*)  $< 0.0001$  for vehicle vs. active isomer + EC<sub>20</sub> CCh;  $p$ -value (\*\*\*\*)  $< 0.0001$  for inactive isomer vs. active isomer + EC<sub>20</sub> CCh;  $p$ -value (\*\*\*\*)  $< 0.0001$  active isomer vs. active isomer + EC<sub>20</sub> CCh;  $p$ -value (\*\*\*\*)  $< 0.0001$  for inactive isomer + EC<sub>20</sub> CCh vs. active isomer + EC<sub>20</sub> CCh). Error bars are  $\pm$  SEM.

Fluorescence imaging was performed with calcium sensor GCaMP6s or R-GECO1 (excitation 562 nm, emission 600 nm) using CCh as pre-stimulant (EC<sub>20</sub>) and positive control (10 μM). First, the intrinsic agonistic activity of both compounds was assessed before and after isomerization into the active form and no increase in intracellular calcium was observed. Subsequently, cytosolic calcium oscillations on pre-stimulated cells were induced by addition of *cis*-enriched **7g**. Photoconversion of compound **7g** into its *trans* form resulted in a sharp decline of fluorescence response which could be switched on and off reversibly (**Figure 7.5A**, left panel). The same dynamic photomodulation of receptor activity was possible using compound **8** (**Figure 7.5B**, left panel). The responses under the application of the compounds and upon photoconversion with given wavelengths for the selected compounds were quantified by peak amplitude and the analysis showed an almost complete on/off switching (**Figure 7.5AB**, right panels). Fluorescence photoresponses were only observed in cells expressing human M<sub>1</sub> mAChRs (**Figure S7.7CD**).

### 7.2.6 Molecular docking

Based on recent insights into the nature of the (“cryptic”) allosteric binding pocket<sup>45</sup>, the behavior of the presented Photo-BQCAs can be nicely explained. Despite the flexible nature of this cryptic binding pocket, size and possibility to bind lipophilic building blocks is limited and therefore provide a rational way to design configuration-specific photoswitchable ligands (**Figure 7.6**). While the cryptic binding pocket can host an azobenzene moiety in *cis* and *trans* configuration, size and substitution pattern of the photoswitchable scaffold account for the specificity of the allosteric effect by distinct configurations. A plausible binding mode of PhotoBQCisA in its *trans* configuration could not be found without disturbing the placement of the quinolone moiety between W400 and Y179. PhotoBQCtrAns nicely fits cryptic binding pocket in its *trans* configuration. We surmise that the additional methyl groups might lead to a conformation of the *cis* configuration that is less favorable for binding within the cryptic binding pocket.

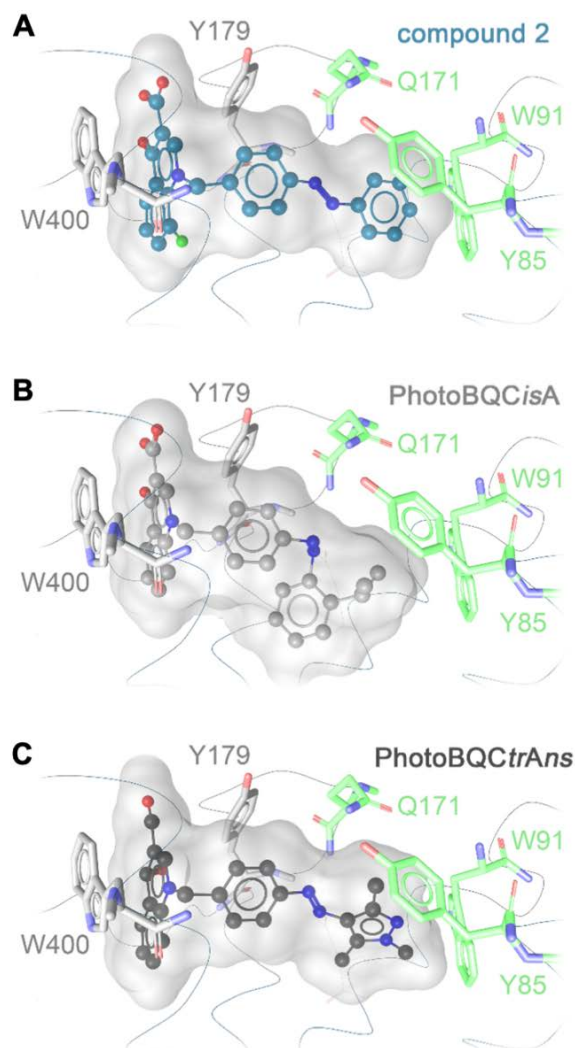


**Figure 7.6. Docking pose of *cis*- and *trans*- compound 2; PhotoBQCisA and PhotoBQCtrAns.** Proposed binding modes of (A) compound 2, (B) PhotoBQCisA and (C) PhotoBQCtrAns indicate a similar orientation in the extracellular receptor region. The quinolone core of all compounds is located between the allosteric key residues W400 and Y179 (light grey), and the photoswitchable building block is pointing in the previously reported cryptic binding pocket for which important residues are highlighted in green. Docking into the cryptic binding pocket was performed with Autodock 4.2 as implemented in LigandScout 4.4. with iterative side chain optimization to account for the flexibility of the cryptic binding pocket.

### 7.3 Conclusions

In summary, we have described the design, synthesis, and biological evaluation of the first reversibly photoswitchable allosteric modulators for class A GPCRs. According to their photopharmacological properties, the photoswitchable allosteric modulators termed photo-BQCisA and photo-BQCtrAns. At typical PAM concentrations, photo-BQCisA is inactive in the dark and can be activated using UV light (365 nm). Photo-BQCtrAns, at identical concentrations, is active in the dark-adapted *trans* state, which can also be enriched with green

light (530 nm). This allows activation of the preirradiated *cis*-isomers with light of deeper tissue penetrating capabilities than 365 nm. At BQCA like concentrations both compounds allow dynamic photomodulation of calcium oscillations induced by an EC<sub>20</sub> concentration of an orthosteric agonist. As such, we think that photo-BQC*is*A and photo-BQC*tr*Ans will follow the example of class B and C GPCR allosteric photoswitches constituting interesting and useful tool compounds in the ongoing efforts to understand complex signaling mechanism of GPCRs.



## References

- 1 Hauser, A. S., Attwood, M. M., Rask-Andersen, M., Schioth, H. B. & Gloriam, D. E. Trends in GPCR drug discovery: New agents, targets and indications. *Nat Rev Drug Discov* **16**, 829-842, doi:10.1038/nrd.2017.178 (2017).
- 2 Nickols, H. H. & Conn, P. J. Development of allosteric modulators of GPCRs for treatment of CNS disorders. *Neurobiol Dis* **61**, 55-71, doi:10.1016/j.nbd.2013.09.013 (2014).
- 3 Granier, S. & Kobilka, B. A new era of GPCR structural and chemical biology. *Nat Chem Biol* **8**, 670-673, doi:10.1038/nchembio.1025 (2012).
- 4 Hull, K., Morstein, J. & Trauner, D. *In vivo* photopharmacology. *Chem Rev* **118**, 10710-10747, doi:10.1021/acs.chemrev.8b00037 (2018).
- 5 Ricart-Ortega, M., Font, J. & Llebaria, A. GPCR photopharmacology. *Mol Cell Endocrinol* **488**, 36-51, doi:10.1016/j.mce.2019.03.003 (2019).
- 6 Gomez-Santacana, X. *et al.* Photoswitching the efficacy of a small-molecule ligand for a peptidergic GPCR: From antagonism to agonism. *Angew Chem Int Ed Engl* **57**, 11608-11612, doi:10.1002/anie.201804875 (2018).
- 7 Rustler, K., Pockes, S. & Konig, B. Light-switchable antagonists for the histamine H<sub>1</sub> receptor at the isolated guinea pig ileum. *ChemMedChem* **14**, 636-644, doi:10.1002/cmdc.201800815 (2019).
- 8 Lachmann, D., Konieczny, A., Keller, M. & Konig, B. Photochromic peptidic NPY Y<sub>4</sub> receptor ligands. *Org Biomol Chem* **17**, 2467-2478, doi:10.1039/c8ob03221a (2019).
- 9 Hauwert, N. J. *et al.* A Photoswitchable agonist for the histamine H<sub>3</sub> receptor, a prototypic family A G protein-coupled receptor. *Angew Chem Int Ed Engl* **58**, 4531-4535, doi:10.1002/anie.201813110 (2019).
- 10 Acosta-Ruiz, A. *et al.* Branched photoswitchable tethered ligands enable ultra-efficient optical control and detection of G protein-coupled receptors *in vivo*. *Neuron* **105**, 446-463 e413, doi:10.1016/j.neuron.2019.10.036 (2020).
- 11 Donthamsetti, P. *et al.* Cell specific photoswitchable agonist for reversible control of endogenous dopamine receptors. *Nat Commun* **12**, 4775, doi:10.1038/s41467-021-25003-w (2021).
- 12 Gutzeit, V. A. *et al.* A fine-tuned azobenzene for enhanced photopharmacology *in vivo*. *Cell Chem Biol* **28**, 1648-1663 e1616, doi:10.1016/j.chembiol.2021.02.020 (2021).
- 13 Riefolo, F. *et al.* Rational design of photochromic analogues of tricyclic drugs. *J Med Chem* **64**, 9259-9270, doi:10.1021/acs.jmedchem.1c00504 (2021).
- 14 Morstein, J. *et al.* Photoswitchable serotoninins for optical control of the 5-HT<sub>2A</sub> receptor. *Angew Chem Int Ed Engl* **61**, e202117094, doi:10.1002/anie.202117094 (2022).
- 15 Garrido-Charles, A. *et al.* Fast photoswitchable molecular prosthetics control neuronal activity in the cochlea. *J Am Chem Soc* **144**, 9229-9239, doi:10.1021/jacs.1c12314 (2022).
- 16 Gerwe, H., He, F., Pottie, E., Stove, C. & Decker, M. Enlightening the "spirit molecule": photomodulation of the 5-HT<sub>2A</sub> receptor by a light-controllable *N,N*-dimethyltryptamine derivative. *Angew Chem Int Ed Engl* **61**, e202203034, doi:10.1002/anie.202203034 (2022).
- 17 Bosma, R. *et al.* Optical control of the  $\beta_2$ -adrenergic receptor with opto-prop-2: A *cis*-active azobenzene analog of propranolol. *iScience* **25**, 104882, doi:10.1016/j.isci.2022.104882 (2022).
- 18 Lahmy, R. *et al.* Photochromic fentanyl derivatives for controlled  $\mu$ -opioid receptor activation. *Chemistry* **28**, e202201515, doi:10.1002/chem.202201515 (2022).

- 19 Matera, C. *et al.* Reversible photocontrol of dopaminergic transmission in wild-type animals. *Int J Mol Sci* **23**, doi:10.3390/ijms231710114 (2022).
- 20 Pittolo, S. *et al.* An allosteric modulator to control endogenous G protein-coupled receptors with light. *Nat Chem Biol* **10**, 813-815, doi:10.1038/nchembio.1612 (2014).
- 21 Broichhagen, J. *et al.* Allosteric optical control of a class B G protein-coupled receptor. *Angew Chem Int Ed Engl* **55**, 5865-5868, doi:10.1002/anie.201600957 (2016).
- 22 Jones, B. J. *et al.* Potent prearranged positive allosteric modulators of the glucagon-like peptide-1 receptor. *ChemistryOpen* **6**, 501-505, doi:10.1002/open.201700062 (2017).
- 23 Donthamsetti, P. *et al.* Selective photoswitchable allosteric agonist of a G protein-coupled Receptor. *J Am Chem Soc* **143**, 8951-8956, doi:10.1021/jacs.1c02586 (2021).
- 24 Gomez-Santacana, X., Panarello, S., Rovira, X. & Llebaria, A. Photoswitchable allosteric modulators for metabotropic glutamate receptors. *Curr Opin Pharmacol* **66**, 102266, doi:10.1016/j.coph.2022.102266 (2022).
- 25 Bossi, S. *et al.* A light-controlled allosteric modulator unveils a role for mGlu<sub>4</sub> receptors during early stages of ischemia in the rodent cerebellar cortex. *Front Cell Neurosci* **12**, 449, doi:10.3389/fncel.2018.00449 (2018).
- 26 Ricart-Ortega, M. *et al.* Mechanistic insights into light-driven allosteric control of GPCR biological activity. *ACS Pharmacol Transl Sci* **3**, 883-895, doi:10.1021/acspsci.0c00054 (2020).
- 27 Wijtmans, M., Josimovic, I., Vischer, H. F. & Leurs, R. Optical control of class A G protein-coupled receptors with photoswitchable ligands. *Curr Opin Pharmacol* **63**, 102192, doi:10.1016/j.coph.2022.102192 (2022).
- 28 Agnetta, L. *et al.* A photoswitchable dualsteric ligand controlling receptor efficacy. *Angew Chem Int Ed Engl* **56**, 7282-7287, doi:10.1002/anie.201701524 (2017).
- 29 Riefolo, F. *et al.* Optical control of cardiac function with a photoswitchable muscarinic agonist. *J Am Chem Soc* **141**, 7628-7636, doi:10.1021/jacs.9b03505 (2019).
- 30 Agnetta, L. *et al.* Fluorination of photoswitchable muscarinic agonists tunes receptor pharmacology and photochromic properties. *J Med Chem* **62**, 3009-3020, doi:10.1021/acs.jmedchem.8b01822 (2019).
- 31 Barbero-Castillo, A. *et al.* Control of brain state transitions with a photoswitchable muscarinic agonist. *Adv Sci (Weinh)* **8**, e2005027, doi:10.1002/advs.202005027 (2021).
- 32 Bock, A., Schrage, R. & Mohr, K. Allosteric modulators targeting CNS muscarinic receptors. *Neuropharmacology* **136**, 427-437, doi:10.1016/j.neuropharm.2017.09.024 (2018).
- 33 Jakubik, J. & El-Fakahany, E. E. Current advances in allosteric modulation of muscarinic receptors. *Biomolecules* **10**, doi:10.3390/biom10020325 (2020).
- 34 Ma, L. *et al.* Selective activation of the M<sub>1</sub> muscarinic acetylcholine receptor achieved by allosteric potentiation. *Proc Natl Acad Sci U S A* **106**, 15950-15955, doi:10.1073/pnas.0900903106 (2009).
- 35 Shirey, J. K. *et al.* A selective allosteric potentiator of the M<sub>1</sub> muscarinic acetylcholine receptor increases activity of medial prefrontal cortical neurons and restores impairments in reversal learning. *J Neurosci* **29**, 14271-14286, doi:10.1523/JNEUROSCI.3930-09.2009 (2009).
- 36 Mistry, S. N. *et al.* Synthesis and pharmacological profiling of analogues of benzyl quinolone carboxylic acid (BQCA) as allosteric modulators of the M<sub>1</sub> muscarinic receptor. *J Med Chem* **56**, 5151-5172, doi:10.1021/jm400540b (2013).
- 37 Kuduk, S. D. & Beshore, D. C. SAR studies on carboxylic acid series M<sub>1</sub> selective positive allosteric modulators (PAMs). *Curr Top Med Chem* **14**, 1738-1754, doi:10.2174/1568026614666140826120224 (2014).

- 38 Dallagnol, J. C. C. *et al.* Synthesis and pharmacological evaluation of heterocyclic carboxamides: Positive allosteric modulators of the M<sub>1</sub> muscarinic acetylcholine receptor with weak agonist activity and diverse modulatory profiles. *J Med Chem* **61**, 2875-2894, doi:10.1021/acs.jmedchem.7b01812 (2018).
- 39 Jorg, M. *et al.* 6-Phenylpyrimidin-4-ones as positive allosteric modulators at the M<sub>1</sub> mAChR: The determinants of allosteric activity. *ACS Chem Neurosci* **10**, 1099-1114, doi:10.1021/acschemneuro.8b00613 (2019).
- 40 Jorg, M. *et al.* Development of novel 4-arylpyridin-2-one and 6-arylpyrimidin-4-one positive allosteric modulators of the M<sub>1</sub> muscarinic acetylcholine receptor. *ChemMedChem* **16**, 216-233, doi:10.1002/cmdc.202000540 (2021).
- 41 Cruickshank, J. W., Brudzynski, S. M. & McLachlan, R. S. Involvement of M<sub>1</sub> muscarinic receptors in the initiation of cholinergically induced epileptic seizures in the rat brain. *Brain Res* **643**, 125-129, doi:10.1016/0006-8993(94)90017-5 (1994).
- 42 Alt, A. *et al.* Evidence for classical cholinergic toxicity associated with selective activation of M<sub>1</sub> muscarinic receptors. *J Pharmacol Exp Ther* **356**, 293-304, doi:10.1124/jpet.115.226910 (2016).
- 43 Rook, J. M. *et al.* Diverse effects on M<sub>1</sub> signaling and adverse effect liability within a series of M<sub>1</sub> ago-PAMs. *ACS Chem Neurosci* **8**, 866-883, doi:10.1021/acschemneuro.6b00429 (2017).
- 44 Johnstone, S. & Albert, J. S. Pharmacological property optimization for allosteric ligands: A medicinal chemistry perspective. *Bioorg Med Chem Lett* **27**, 2239-2258, doi:10.1016/j.bmcl.2017.03.084 (2017).
- 45 Hollingsworth, S. A. *et al.* Cryptic pocket formation underlies allosteric modulator selectivity at muscarinic GPCRs. *Nat Commun* **10**, 3289, doi:10.1038/s41467-019-11062-7 (2019).
- 46 Schramm, S. *et al.* Novel BQCA- and TBPB-derived M<sub>1</sub> receptor hybrid ligands: Orthosteric carbachol differentially regulates partial agonism. *ChemMedChem* **14**, 1349-1358, doi:10.1002/cmdc.201900283 (2019).
- 47 Eaton, P. E., Carlson, G. R. & Lee, J. T. Phosphorus pentoxide-methanesulfonic acid. Convenient alternative to polyphosphoric acid. *The Journal of Organic Chemistry* **38**, 4071-4073, doi:10.1021/jo00987a028 (1973).
- 48 Zewge, D., Chen, C. Y., Deer, C., Dormer, P. G. & Hughes, D. L. A mild and efficient synthesis of 4-quinolones and quinolone heterocycles. *J Org Chem* **72**, 4276-4279, doi:10.1021/jo070181o (2007).
- 49 Weston, C. E., Richardson, R. D., Haycock, P. R., White, A. J. & Fuchter, M. J. Arylazopyrazoles: Azoheteroarene photoswitches offering quantitative isomerization and long thermal half-lives. *J Am Chem Soc* **136**, 11878-11881, doi:10.1021/ja505444d (2014).
- 50 Littmann, T., Ozawa, T., Hoffmann, C., Buschauer, A. & Bernhardt, G. A split luciferase-based probe for quantitative proximal determination of Gα<sub>q</sub> signalling in live cells. *Sci Rep* **8**, 17179, doi:10.1038/s41598-018-35615-w (2018).

## Supporting Information (SI) of Chapter 7

### SI7.1 Chemical synthesis

#### SI7.1.1 Materials and methods

Common reagents and solvents were purchased from the following commercial suppliers: ABCR, Alfa Aesar, BLD-Pharm, Sigma-Aldrich, Merck, TCI Chemicals and used without further purification unless otherwise stated. Dry tetrahydrofuran (THF) was freshly distilled from sodium-benzophenone under an argon atmosphere. Reaction progress was monitored using analytical thin-layer chromatography (TLC) on precoated silica gel 60 GF254 plates (Macherey Nagel GmbH & Co). Detection was carried out by irradiation and consequent fluorescence quenching at 254 nm or excitation at 365 nm. Compounds were purified by column chromatography using silica gel 60 (60 Å pore size, 40-63 µm; Macherey Nagel GmbH & Co) as the stationary phase.

Reverse phase column chromatography was performed on an Interchim Puri Flash 430 (Ultra Performance Flash Purification) instrument connected to an Interchim Flash ELSD. FlashPure 4 g or 12 g C18 columns were used with gradients of H<sub>2</sub>O/MeOH as eluent systems. Nuclear magnetic resonance spectra were measured on a Bruker AV-400 NMR instrument (Bruker) in deuterated solvents (DMSO-*d*<sub>6</sub>, CDCl<sub>3</sub>, MeOD-*d*<sub>4</sub>, THF-*d*<sub>8</sub>). Chemical shifts are expressed in ppm relative to DMSO-*d*<sub>6</sub>, CDCl<sub>3</sub>, MeOD-*d*<sub>4</sub>, THF-*d*<sub>8</sub> (2.50; 7.26; 3.31; 3.58/1.73 for <sup>1</sup>H; 39.52; 77.16; 49.00; 67.57/25.37 for <sup>13</sup>C).

Measurements for verification and purity of the compounds were performed with a Shimadzu LC/MS system, comprising a DGU-20A3R controller, pump LC-20AB, degasser DGU-20A, and SPD-20A UV-Vis detector. Compounds were dissolved in MeOH and filtered through syringe filters prior to measurement. As a stationary phase, a Synergi 4U fusion-RP 80 Å (150 × 4.6 mm) column was used (Phenomenex). As a mobile phase, a gradient of H<sub>2</sub>O/MeOH (both containing 0.1% formic acid) was used.

Method: flow rate: 1.0 ml/min; detection: 254 nm; scan range: 60–1000 *m/z*; gradient: A: H<sub>2</sub>O (0.1% HCOOH); B: MeOH (0.1% HCOOH) 0–8 min 5%→90% B, 8–13 min 90% B, 13–14 min 90%→5% B, 14–18 min 5% B. The purity of all target compounds was found to be ≥ 95%. Purities were not tested at a particular photostationary state and therefore show an arbitrary *cis/trans* ratio (cf. chromatograms). ESI ionization was accomplished by a downstream

Shimadzu LCMS-2020 mass spectrometer. Data are reported as mass-to-charge ratio (*m/z*) of the corresponding positively charged molecular ions.

### SI7.1.2 Abbreviations

**Solvents:** EtOAc, ethyl acetate; CH<sub>2</sub>Cl<sub>2</sub>, dichloromethane; MeCN, acetonitrile; MeOH, methanol; EtOH, ethanol; THF, tetrahydrofuran; Et<sub>2</sub>O, diethyl ether; DMSO, dimethyl sulfoxide.

**Analytical characterizations:** NMR: d, doublet; dd, double doublet; ddd, double double doublet; dddd, doublet of doublet of doublet of doublets; dt, double triplet; m, multiplet; q, quartet; quin, quintet; s, singlet; t, triplet; m.p., melting point; R<sub>f</sub>, retention factor; rt, room temperature; RT, retention time.

### SI7.1.3 Synthetic routes

The respective benzyl quinolone carboxylic ethyl ester (1.0 equiv.) was suspended in THF (ca. 3 ml) and 1N NaOH (10 equiv.) was added. The mixture was stirred overnight at 50°C. Upon acidification of the reaction mixture with 6N HCl the respective benzyl quinolone carboxylic acid precipitated as a yellow to orange solid. Filtration of the product proved to be unfavorable, upon washing the fine precipitate slipped through most filters in significant quantities due to its colloidal properties. Thus, the precipitate was forced into the organic layer by the addition of brine/EtOAc, the layers were separated, and the solvent removed under reduced pressure. Purification was performed using either silica column chromatography (CH<sub>2</sub>Cl<sub>2</sub>/MeOH/AcOH) or recrystallization from THF yielding the respective product in moderate to excellent yields (60-91%).

**1-(4-((2-isopropylphenyl)diazenyl)benzyl)-4-oxo-1,4-dihydroquinoline-3-carboxylic acid (7g):** According to general method A ethyl 1-(4-((2-isopropylphenyl)diazenyl)benzyl)-4-oxo-1,4-dihydroquinoline-3-carboxylate (35 mg, 77.2 μmol, 1.0 equiv.) was saponified in a mixture of THF and 1N NaOH (800 μl, 0.80 mmol, 10 equiv.). Purification by silica column chromatography (CH<sub>2</sub>Cl<sub>2</sub>/MeOH/AcOH 50:1:0.1) yielded 1-(4-((2-isopropylphenyl)diazenyl)benzyl)-4-oxo-1,4-dihydroquinoline-3-carboxylic acid (23 mg, 54.1 μmol, 70%) as an orange solid.

<sup>1</sup>H NMR (400 MHz, THF-*d*<sub>8</sub>) δ 15.42 (s, 1H), 9.62 (s, 1H), 8.73 – 8.65 (m, 1H), 8.17 – 8.09 (m, 4H), 7.94 – 7.88 (m, 1H), 7.82 – 7.73 (m, 5H), 7.61 – 7.54 (m, 1H), 6.27 (s, 2H), 4.25 (hept, *J* = 6.9 Hz, 1H), 1.59 – 1.51 (m, 6H). <sup>13</sup>C NMR (101 MHz, THF-*d*<sub>8</sub>) δ 179.66, 166.34, 153.91,

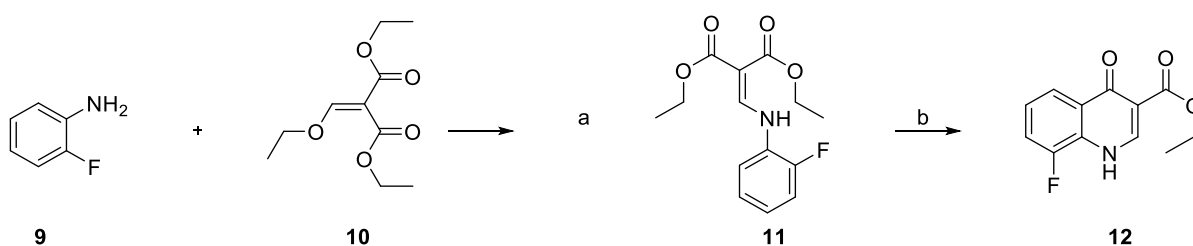
151.13, 150.44, 149.31, 141.09, 139.43, 134.61, 132.68, 128.27, 127.73, 127.42, 127.20, 126.74, 124.47, 122.22, 118.98, 116.02, 110.52, 57.78, 28.76, 24.31.

MS (ESI, positive):  $m/z$  calculated for [C<sub>26</sub>H<sub>24</sub>N<sub>3</sub>O<sub>3</sub>]<sup>+</sup>: 426.18, found: 426.15 [M + H]<sup>+</sup>. Purity (HPLC<sub>254nm</sub>) = 95%.

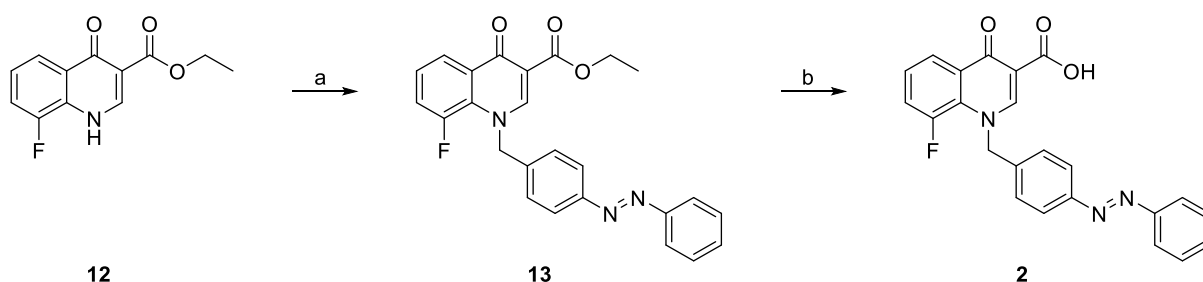
**4-oxo-1-(4-((1,3,5-trimethyl-1H-pyrazol-4-yl)diazenyl)benzyl)-1,4-dihydroquinoline-3-carboxylic acid (8):** According to general method A ethyl 4-oxo-1-(4-((1,3,5-trimethyl-1H-pyrazol-4-yl)diazenyl)benzyl)-1,4-dihydroquinoline-3-carboxylate (23 mg, 51.5 μmol, 1.0 equiv.) was saponified in a mixture of THF and 1N NaOH (520 μL, 0.52 mmol, 10 equiv.). Purification by silica column chromatography (CH<sub>2</sub>Cl<sub>2</sub>/MeOH/AcOH 20:1:0.1) and subsequent purification by reverse phase flash column chromatography (H<sub>2</sub>O/MeOH) yielded 4-oxo-1-(4-((1,3,5-trimethyl-1H-pyrazol-4-yl)diazenyl)benzyl)-1,4-dihydroquinoline-3-carboxylic acid (17 mg, 40.9 μmol, 79%) as a yellow solid.

<sup>1</sup>H NMR (400 MHz, DMSO-*d*<sub>6</sub>) δ 9.22 (s, 1H), 8.39 (s, 2H), 7.87 – 7.64 (m, 4H), 7.53 (s, 1H), 7.36 (s, 2H), 5.87 (s, 2H), 3.72 (s, 3H), 3.17 (s, 3H), 2.32 (s, 3H). <sup>13</sup>C NMR (101 MHz, DMSO-*d*<sub>6</sub>) δ 178.03, 166.06, 152.58, 150.60, 140.36, 139.71, 139.32, 135.43, 134.41, 127.44, 126.31, 126.22, 125.73, 125.05, 121.85, 118.69, 109.72, 58.64, 35.94, 13.69, 9.41.

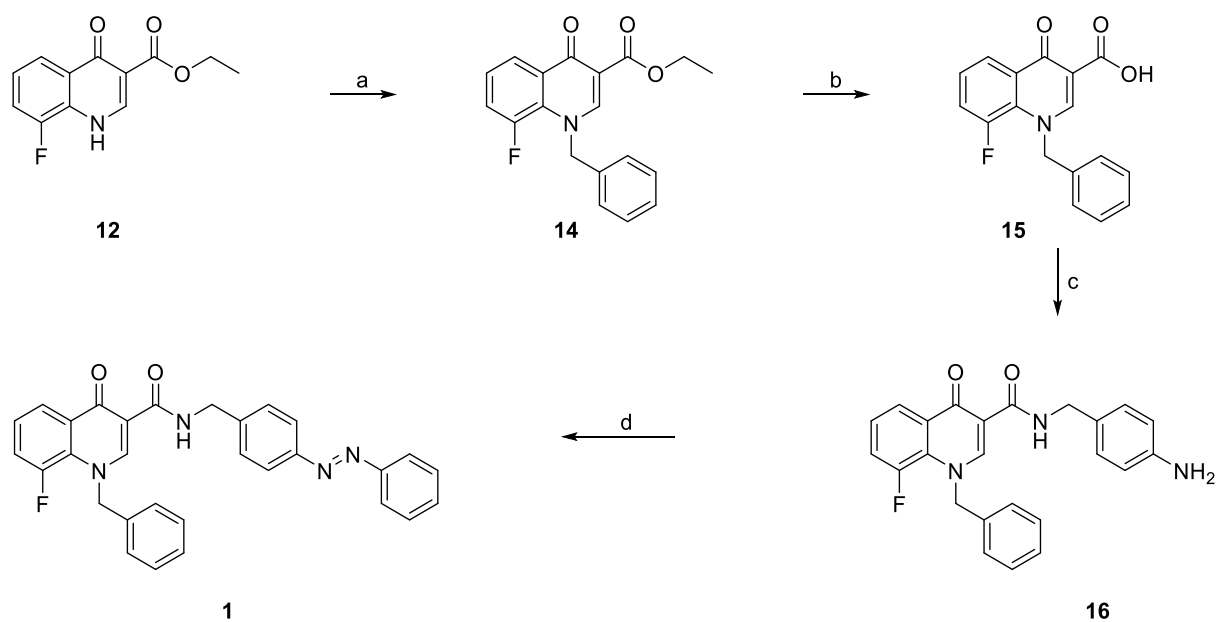
MS (ESI, positive):  $m/z$  calculated for [C<sub>23</sub>H<sub>22</sub>N<sub>5</sub>O<sub>3</sub>]<sup>+</sup>: 416.17, found: 416.15 [M + H]<sup>+</sup>. Purity (HPLC<sub>254nm</sub>) = 99%.



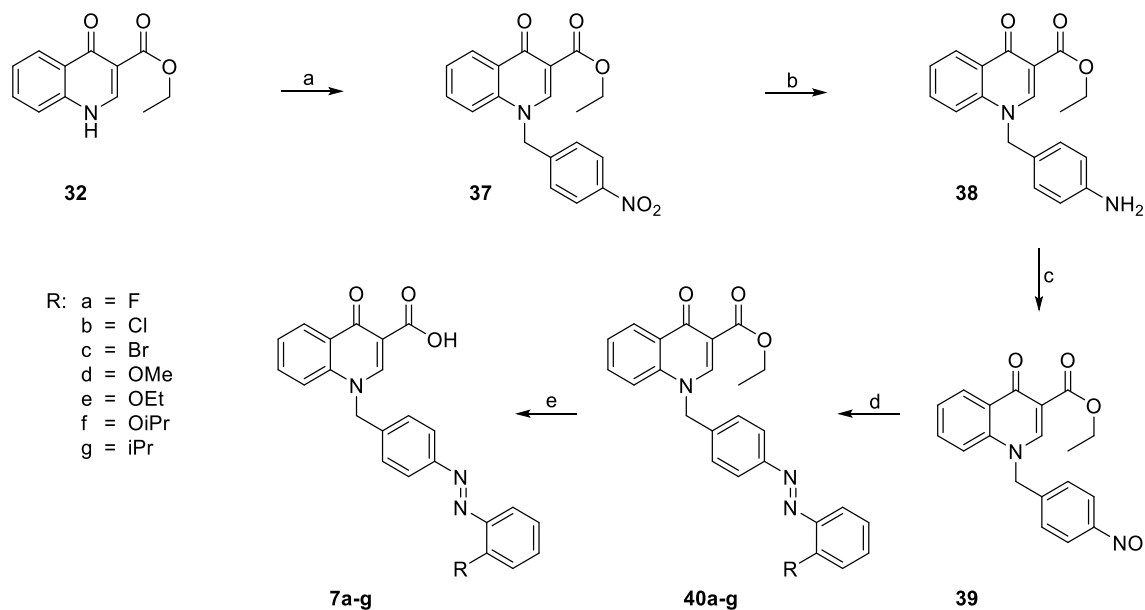
**Scheme S7.1. Synthetic route to the dihydroquinoline core fragment.** Reagents and conditions: (a) **9**, **10**, 120°C (96%); (b) Ph<sub>2</sub>O, microwave reactor (1200W) 210°C (26% of **12**).



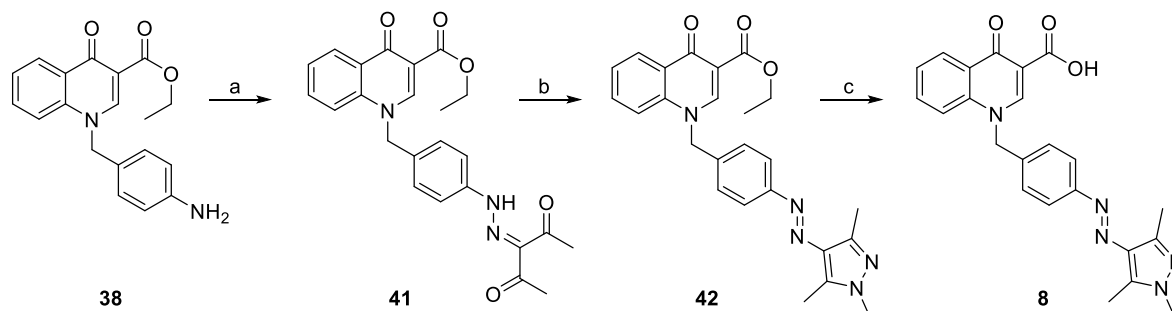
**Scheme S7.2. Synthetic route to azo-extended 8F-BQCA.** Reagents and conditions: (a) Azo-CH<sub>2</sub>-Br, K<sub>2</sub>CO<sub>3</sub>, DMF, 80°C (35%); (b) 3N NaOH, THF, 85°C (81%).



**Scheme S7.3. Synthetic route to the azo-amidation Photo-BQCA 1.** Reagents and conditions: (a) Bn-Br, K<sub>2</sub>CO<sub>3</sub>, KI, DMF, 80°C (65%); (b) 1N NaOH, THF, 50°C (98%); (c) 1) ethyl carbonochloridate, NEt<sub>3</sub>, DMF, 0°C, 4-(aminomethyl)aniline, 0°C to rt (82%); (d) nitrosobenzene (17), AcOH, rt (57%).



**Scheme S7.4. Synthetic route to benzylazo-quinoline-carboxylic-acid derivatives of the 3<sup>rd</sup> generation, optimized for quick derivatization at the distal benzene ring of the azo-moiety.** Reagents and conditions: (a) 1-(bromomethyl)-4-nitrobenzene, K<sub>2</sub>CO<sub>3</sub>, KI, DMF, rt (89%); (b) Fe, NH<sub>4</sub>Cl, H<sub>2</sub>O, EtOH, 80°C, quant. (c) Oxone<sup>®</sup>, CH<sub>2</sub>Cl<sub>2</sub>, H<sub>2</sub>O, rt (83%); (d) respective aniline, HOAc, RT, 53-92%; (e) 1N NaOH, THF, 50°C (59-92%).



**Scheme S7.5. Synthetic route to the 1,3,5-trimethyl-pyrazole photoswitch.** Reagents and conditions: (a) 1NaNO<sub>2</sub>, H<sub>2</sub>O, AcOH, HCl, 0°C; 2. pentane-2,4-dione, NaOAc, EtOH, H<sub>2</sub>O, 0°C to rt (60%); (b) mono-methyl hydrazine, ethanol, 80°C (71%); (c) 1N NaOH, THF, 50°C (79%).

## SI7.2 Photochemical characterization

UV-Vis spectra were recorded on a Varian Cary 50 Bio UV-Vis Spectrophotometer connected to a water bath for temperature control. Hellma (Type 100-QS) cuvettes (10mm light path) were used. Characterization was performed with 25 μM/50 μM solutions in DMSO/H<sub>2</sub>O 1:1 (v:v). Samples were irradiated using LEDs of Seoulviosys (UV Z5 series CUNx6A1B; 365nm), Roschwege (RSW-P01-385-2; 385 nm), LedEngin (LZ4-00UB00-U7, 400 nm), Osram (LD CQ7P-2U3U-W5-1-K, 455 nm; LT CP7P-KZLX-26, 530 nm; LY CP7P-JUKQ-36, 590 nm; LA CP7P-KQKS-W3, 617 nm), Cree (XPeBBL-L1-0000-00205, 475 nm) and Lumileds (LXML-PE01, 505 nm). LED modules were combined to a rated power of 4W and used with a forward current of I<sub>F</sub> = 350 mA. Irradiation of the solutions with the respective wavelengths were performed until the corresponding photostationary state (PSS) had equilibrated (1-2 min). Thermal relaxation was measured for a period over 2 h to determine whether the relaxation was significant with regards to the duration of the biological assays. For this purpose, the photochromic compounds were switched into the maximally *trans* enriched photostationary state. The absorption at the wavelength were the spectrum of the *cis*- and *trans*-isomer showed maximal difference (I<sub>Dmax</sub>) was measured for 15 min. Subsequently, the solutions were switched to the thermodynamically less stable *cis*-isomer using 365 nm light. The relaxation was recorded by monitoring the change of absorption at I<sub>Dmax</sub> for 2 h at 37°C. Afterwards, the solutions were switched to their maximally *trans* enriched PSS again. Percentage relaxation was calculated as  $D = (A_{cis \text{ enriched } t=2h} - A_{cis \text{ enriched } t=0}) * 100 / (A_{trans \text{ enriched}} - A_{cis \text{ enriched } t=0})$ . Absence of photo-fatigue was checked using either the described above Varian Cary UV-Vis Spectrophotometer plus Hellma (Type 100-QS) cuvettes or in case of characterization of multiple compounds at the same time, a 96-well plate and a Spectramax 250 absorbance microplate reader (molecular devices) were used. The compounds were irradiated alternatingly



with the indicated wavelengths and their absorbance at I<sub>Dmax</sub> was checked to be constant. The photostationary distributions (PSD) of the PSSs of interests were determined by HPLC. The amount of *cis*- and *trans*-isomer was quantified by integration of the respective peak. Absorption was measured at the respective isosbestic point.

Compound	Thermal relaxation @ 37°C	<i>cis/trans</i> ratio	EC <sub>50</sub> (CCh + 1 μM Cpd.)	EC <sub>50trans</sub> / EC <sub>50cis</sub>
<b>1</b>	7.3% (2 h)	PSS <sub>365</sub> : 74/26	218	0.8
		PSS <sub>400</sub> : 15/85	172	
<b>2</b>	5.6% (2 h)	PSS <sub>365</sub> : 80/20	45.1	1.16
		PSS <sub>455</sub> : 15/85	52.2	
<b>3</b>	6.9% (2 h)	PSS <sub>365</sub> : 88/12	187	1.10
		PSS <sub>400</sub> : 15/85	206	
<b>4</b>	10.9% (2 h)	PSS <sub>365</sub> : 84/16	91.5	1.01
		PSS <sub>400</sub> : 12/88	92.6	
<b>5</b>	13.8% (2 h)	PSS <sub>365</sub> : 91/9	47.0	1.59
		PSS <sub>400</sub> : 10/90	74.7	
<b>6</b>	4.4% (2 h)	PSS <sub>365</sub> : 63/37	36.5	1.45
		PSS <sub>455</sub> : 15/85	53.1	
<b>7a</b>	0.8% (2 h)	PSS <sub>365</sub> : 85/15	63.3	1.24
		PSS <sub>400</sub> : 21/79	78.5	
<b>7b</b>	0.4% (2 h)	PSS <sub>365</sub> : 92/8	74.8	1.49
		PSS <sub>400</sub> : 11/89	111	
<b>7c</b>	0.2% (2 h)	PSS <sub>365</sub> : 13/87	58.4	1.88
		PSS <sub>400</sub> : 20/80	110	
<b>7d</b>	5.7% (2 h)	PSS <sub>365</sub> : 95/5	38.4	1.60
		PSS <sub>455</sub> : 18/82	61.6	
<b>7e</b>	5.3% (2 h)	PSS <sub>365</sub> : 95/5	31.5	1.72
		PSS <sub>455</sub> : 33/67	54.2	
<b>7f</b>	4.4% (2 h)	PSS <sub>365</sub> : 94/6	39.8	1.56
		PSS <sub>455</sub> : 14/86	61.9	
<b>7g</b>	10.3% (2 h)	PSS <sub>365</sub> : 94/6	54.5	2.80
		PSS <sub>455</sub> : 14/86	152	
<b>8</b>	5.2% (2 h)	PSS <sub>365</sub> : 96/4	156	0.36
		PSS <sub>530</sub> : 8/92	55.5	
<b>BQCA</b>	-	-	54.8	-
-	-	-	213	-

**Table S7.1. Summary of thermal relaxation, *cis/trans* ratios and biological effects of the relevant photostationary states.**

### SI7.2.1 Compound 1

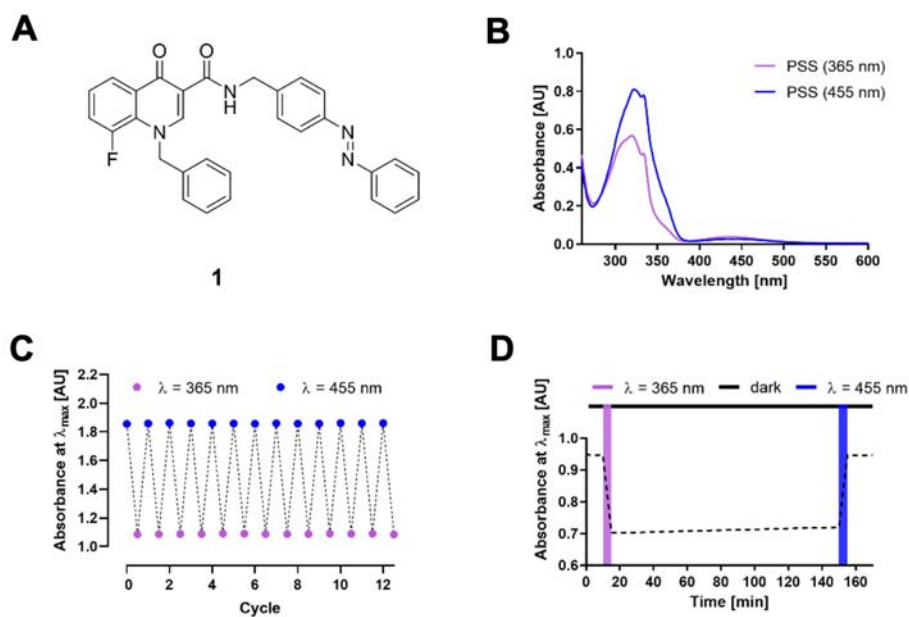


**Figure S7.1. Photochemical characterization of 1 (25  $\mu$ M, DMSO/H<sub>2</sub>O 1:1).** (A) Structure of 1 in its *trans* configuration. (B) Absorption spectra of maximally *cis/trans* enriched PSSs after irradiation with corresponding lights for 2 min. (C) Cycles of 365/455 nm irradiation (50  $\mu$ M, DMSO) showing no photodecomposition. (D) Thermal relaxation of the *cis*-isomer over a period of 2 h at 37°C.

### SI7.2.2 Compound 7g

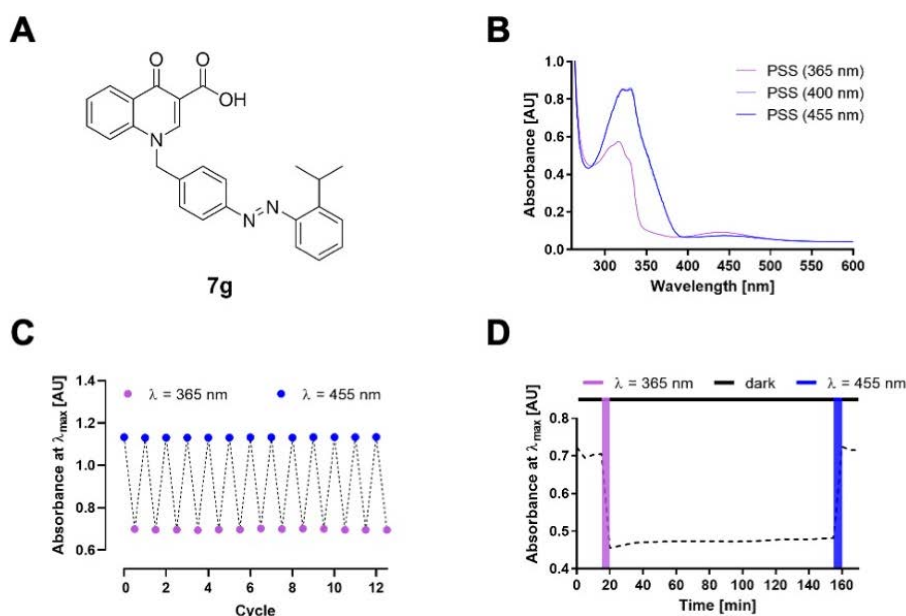


**Figure S7.2. Photochemical characterization of 7g (50  $\mu$ M, DMSO/H<sub>2</sub>O 1:1).** (A) Structure of 7g in its *trans* configuration. (B) Absorption spectra of maximally *cis/trans* enriched PSSs after irradiation with corresponding lights for 2 min. (C) Cycles of 365/455 nm irradiation (50  $\mu$ M, DMSO) showing no photodecomposition. (D) Thermal relaxation of the *cis*-isomer over a period of 2 h at 37°C.

### SI7.2.3 Compound 8

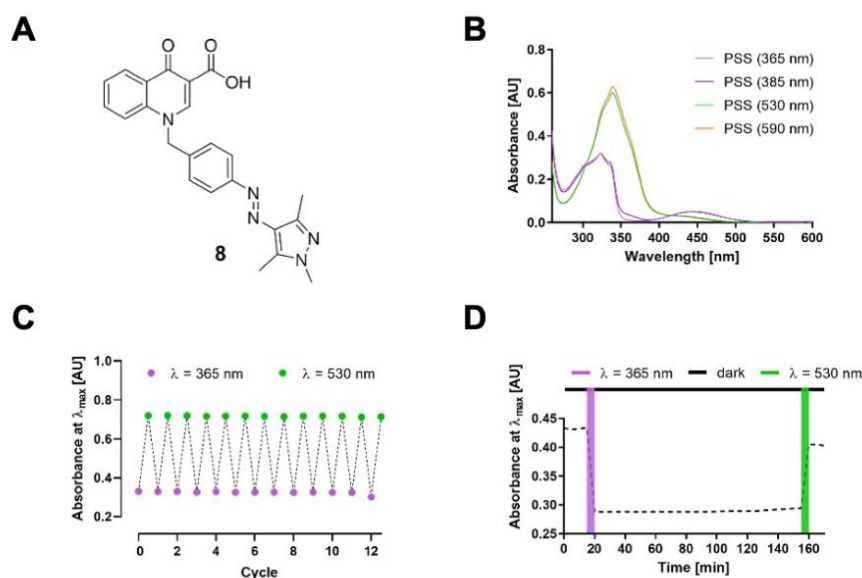


**Figure S7.3. Photochemical characterization of 8 (50  $\mu$ M, DMSO/H<sub>2</sub>O 1:1).** (A) Structure of 8 in its *trans* configuration. (B) Absorption spectra of maximally *cis/trans* enriched PSSs after irradiation with corresponding lights for 2 min. (C) Cycles of 365/530 nm irradiation (50  $\mu$ M, DMSO) showing no photodecomposition. (D) Thermal relaxation of the *cis*-isomer over a period of 2 h at 37°C.

### SI7.3 Split luciferase complementation assay

The activity of the photoswitchable allosteric modulators was determined by means of a Human Embryonic Kidney 293T (HEK 293T, American Type Culture Collection; ATCC) cell line, stably expressing the human muscarinic acetylcholine receptor 1 (M<sub>1</sub> mAChR or M<sub>1</sub>R) and a split luciferase complementation system: The G $\alpha_q$  subunit fused to a click-beetle luciferase fragment and the phospholipase C- $\beta_3$  (PLC- $\beta_3$ ) fused to the corresponding fragment<sup>1</sup>. Cells were routinely monitored for mycoplasma contamination and were negative. The cells were cultivated in Dulbecco's modified Eagle's medium (DMEM) containing 10% FCS (full medium), 0.6 mg/mL G418 and 0.001 mg/ml Puromycin, at 37°C in a water-saturated atmosphere containing 5% CO<sub>2</sub>. On the evening before the assay, the cells were detached from a 75-cm<sup>2</sup> flask by trypsinization and centrifuged. The pellet was resuspended in assay medium consisting of Leibovitz' L-15 (w/o phenol red) with 5% FCS and 10  $\mu$ M HEPES and the density of the suspension was adjusted to 1.25\*10<sup>6</sup> cells/ml. Then, 80  $\mu$ l of the cells were seeded in Nunc™ MicroWell™ 96 well plates (ThermoFisher Scientific: 136101) and incubated overnight in a humidified atmosphere at 37°C without additional CO<sub>2</sub>. For the assay, 10  $\mu$ l of 10 mM luciferin (ThermoFisher Scientific: 88293) in L-15 were added to each well and the cells were allowed to equilibrate for 10 min at 37°C.

For determination of the allosteric properties of the potential photoswitchable positive allosteric modulators (PAMs), a dilution series of carbachol (CCh) was combined with 20  $\mu$ M photo-PAM per concentration (1:1, v:v). This dilution series was then transferred to two clear V-profile 96-well plates (Hartenstein, Würzburg, Germany) which were irradiated separately with either *cis* or *trans* enriching wavelengths. Afterwards, 10  $\mu$ l per concentration of the irradiated CCh/photo-PAM dilution series was added to the equilibrated cells, yielding final in-well concentrations of CCh: 10  $\mu$ M – 3  $\mu$ M – 1  $\mu$ M – 300 nM – 100 nM – 30 nM – 10 nM – 1 nM with a fixed concentration of 1  $\mu$ M photo-PAM.

Additionally, a duplicate of the reference substance CCh and a negative control (L-15) was included in each individual experiment. Afterwards the plate was read in a pre-warmed Berthold Mithras LB 940. The luminescent signal was continuously monitored for 30 min after which a stable plateau had formed for every concentration. Each substance was measured in at least three independent experiments, in which each condition was tested in duplicate. Data were analyzed by taking the last 5 data points of each plateau and plotting them in GraphPad Prism 9. These values were normalized to the maximal response of reference agonist CCh (100%) and the negative control L-15 (0%). Afterwards, the values of the independent experiments were pooled to generate the overall concentration-response curves which were fitted using Prisms built-in log(agonist) vs. response equation. The *in vitro* characterization of the compounds of the 1<sup>st</sup>, 2<sup>nd</sup> and 3<sup>rd</sup> generation is shown in **Figure S7.4-S7.6**.

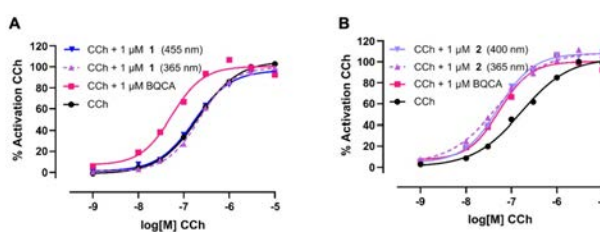


**Figure S7.4. Split luciferase complementation assay: 1<sup>st</sup> generation.**

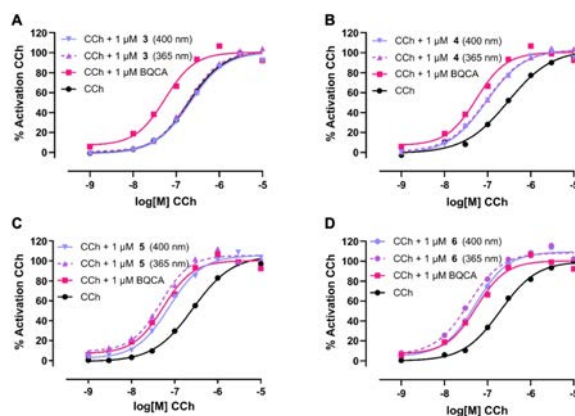


**Figure S7.5. Split luciferase complementation assay: 2<sup>nd</sup> generation.**

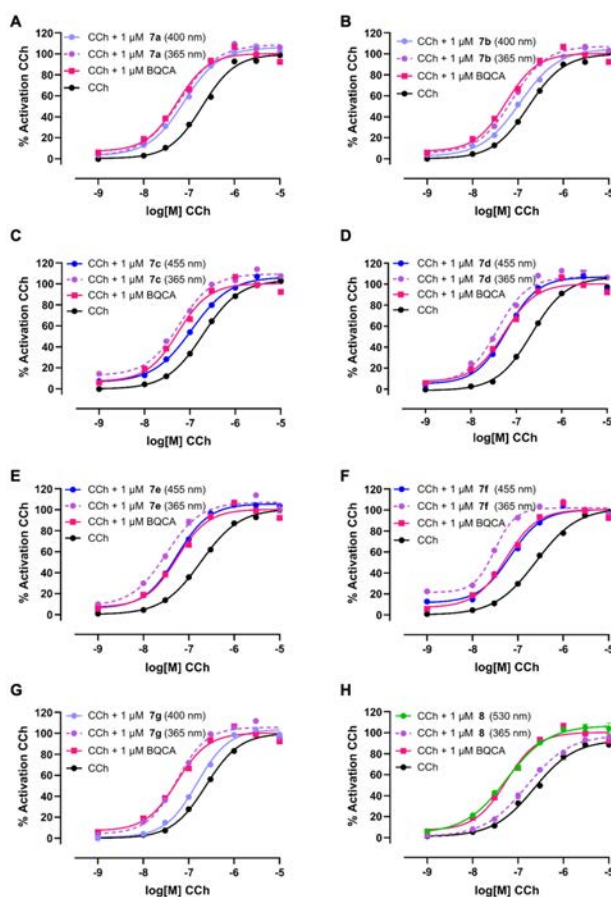


Figure S7.6. Split luciferase complementation assay: 3<sup>rd</sup> generation.

### SI7.3 Fluorescence-based plate reader assay

Human embryonic kidney tsA201 (HEK tsA201, American Type Culture Collection; ATCC) cells were maintained in Dulbecco's Modified Eagle's Medium/Nutrient Mixture F-12 Ham (DMEM/F12 1:1, Life Technologies) supplemented with 10% fetal bovine serum (FBS, Life Technologies), and 1% antibiotics (Penicillin/Streptomycin; Sigma-Aldrich, St. Louis, MO, USA) in a controlled environment (37°C, 98% humidity and 5% CO<sub>2</sub>). Human M<sub>1</sub> mAChR (Addgene), was transiently co-transfected with the calcium indicator Gcamp6s (ratio 1:1) through X-tremeGENE 9 DNA Transfection Reagent (Roche Applied Science) following the manufacturer's instructions. To determine changes in intracellular calcium concentrations upon receptor activation we have used a fluorescence plate reader assay. After 24 h, the cells were harvested with accutase (Sigma-Aldrich) and 80.000 cells/well were seeded onto a 96-well sterile polystyrene plate black with transparent bottom (dD, Biolab), which were pretreated with poly-L-Lysine (Sigma-Aldrich).

After 48 h the culture medium was aspirated and 100 µl of recording solution was added to each well. Subsequently, the signal was measured by the TECAN infinite 200 microplate reader

(Tecan Austria GmbH), which was controlled by i-Control software (Tecan Group Ltd., version 1.6). The microplate reader was set at 485 nm excitation wavelength and 535 nm emission wavelength, while applying empirically optimized parameters (temperature 37°C; integration time 40 μs; number of flashes 18; gain 120; number of cycles 25). Next, the blank or background signal was measured (*i.e.*, baseline reading). Later, 20 μl were taken from each well and 20 μl of the assay buffer, containing the compound or the control, were transferred to the cell plate and the changes in fluorescence intensity were recorded for 120 s. Positive and negative controls were included in the experiments. On one hand, CCh (30 μM), allowing to verify successful transfections and used as a reference to normalize our drugs. On the other hand, the vehicle (0.1% DMSO) resulted in a minimal fluorescence intensity to ensure that does not interfere with the receptors, was used as negative controls. All the experiments were performed under dark conditions to keep the compounds in their *trans* conformation. Further control experiments were performed in HEK cells without the transfection with M<sub>1</sub>R (**Figure S7.7**).

Test compounds were dissolved in DMSO (Sigma-Aldrich) and diluted with the assay buffer to a 2% concentration of DMSO in each well. Every compound was tested at 1 μM alone and together with the EC<sub>20</sub> of the agonist CCh (50 nM).

Photoisomerization of the compounds was achieved by pre-illuminating for 5 min with LEDs of Luminus (series SST-10-UV, part number LT-5242; 365 nm), (series SST-10-UV, part number LT-5245; 405 nm), Samsung (series LH351H, part number LT-5489), OSRAM Oslon (SSL 80-yellow, part number LT-2013, 530 nm). LED modules were combined to a rated power of 4W and used with a forward current of  $I_F = 350$  mA.

All data obtained with this assay were analyzed by using Excel (Microsoft, version 16.62) and GraphPad Prism (GraphPad Software, version 9). First, the raw data obtained by the Tecan were grouped in a single Excel sheet, because for each run the microplate reader produces a different sheet. The Relative Fluorescence (RF) was calculated through the ratio between the peak fluorescence and baseline for each well. Subsequently, the data were normalized with the maximal response to CCh (30 μM). Statistical differences were analyzed by one-way ANOVA followed by Tukey's post-hoc test, whereas a value of *p*-value (\*) < 0.05 was considered as significant. The data are expressed as the mean ± SEM for at least three independent experiments.

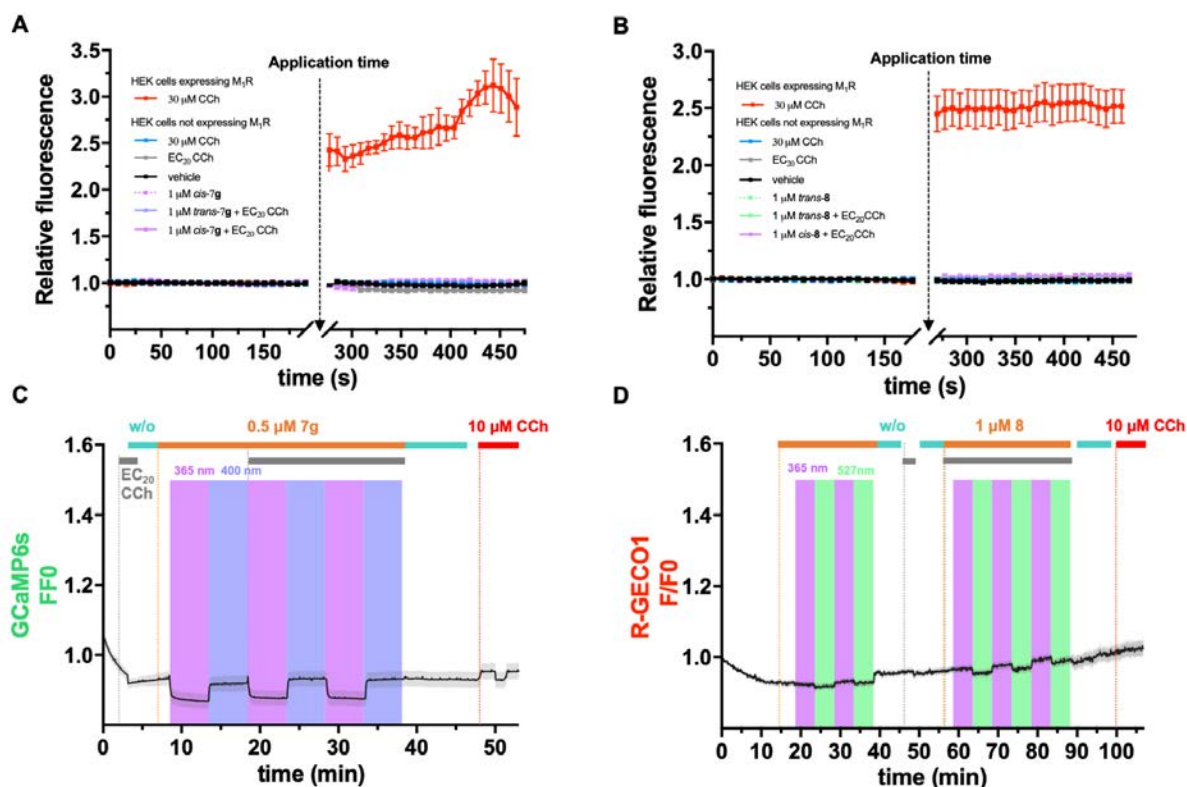


**Figure S7.7. Control experiments in HEK cells without the presence of human M<sub>1</sub> mAChR.** (A and B) The graphs plotting the relative fluorescence vs. time (s) showed no increase of intracellular calcium in plate reader-based calcium assay after application of agonist CCh (30 μM) or its EC<sub>20</sub> together with the pre-illuminated *trans* or *cis* form of the ligand **7g** (A, n=3 independent experiments) or **8** (B, n = 3 independent experiments). In contrary, the application of the CCh (30 μM) in cells expressing the M<sub>1</sub>R elicited a huge response. (C and D). No calcium oscillations were observed in live calcium imaging assay after application of agonist CCh (10 μM) or its EC<sub>20</sub> together with the active photoform of ligand **7g** (C, n = 40 cells) or **8** (D, n = 40 cells).

## SI7.4 *In vitro* calcium imaging

HEK tsA201 cells were transiently co-transfected with Human M<sub>1</sub> mAChR (Addgene) and GCaMP6s (ratio 1:1) to test the compound **7g** or R-GECO1 (ratio 1:1) to test the compound **8**. It was used the X-tremeGENE 9 DNA Transfection Reagent (see SI7.3). At 24 h after transfection, the cells harvested with accutase were seeded onto 16 mm glass coverslips (ThermoFisher Scientific) coated with poly-L-Lysine to allow cell adhesion. At 48 h after the transfection, the seeded cells were used for the experiments.

Prior to each experiment the cells were mounted on the recording chamber (Open Diamond Bath Imaging Chamber for Round Coverslips; Warner Instruments LLC) in recording solution (140 mM NaCl, 5.4 mM KCl, 1 mM MgCl<sub>2</sub>, 10 mM HEPES, 10 mM glucose and 2 mM CaCl<sub>2</sub>, with pH 7.40).

Then the recording chamber was placed on an IX71 inverted microscope with a 20x water immersion objective (XLUMPLFLN 20XW, 1 NA; Olympus).

GCaMP6s was excited during 50 ms at 488 nm by using a Polychrome V light source (Till Photonics GmbH) equipped with a Xenon Short Arc lamp (Ushio Europe B.V.) and a 505 nm dichroic beam splitter (Chroma Technology). The emission at 510 nm was filtered by a D535/540 nm emission filter (Chroma Technology) and collected by a C9100-13 EM-CCD camera (Hamamatsu Photonics). However, R-GECO1 was excited during 50 ms at 562 nm by using a Polychrome V light source (Till Photonics GmbH) equipped with a Xenon Short Arc lamp (Ushio Europe B.V.) and a 585 nm dichroic beam splitter (Chroma Technology). The emission at 600 nm was filtered by ET630/675nm emission filter (Chroma Technology) and collected by a C9100-13 EM-CCD camera (Hamamatsu Photonics).

Images were acquired with an imaging interval of 4 s with the SmartLux software (HEKA) at ambient temperature, where imaging analysis was done with Fiji (NIH, ImageJ). Of note, the CCh (10  $\mu$ M) was used as a positive control and as a reference to normalize the compounds. On the other hand, the vehicle was used to ensure that it did not induce the M<sub>1</sub>R. All the experiments were performed under dark conditions. Application of these compounds was performed by pipetting a small volume, during image acquisition, into the accessory pool of the recording chamber (approximately 1:1000 dilution). Compounds **7g** and **8** were dissolved in DMSO (Sigma-Aldrich) and diluted with the recording solution to a 0.1% final concentration of DMSO.

Photostimulation under 1 photon excitation (1PE) during the recordings was done by illuminating the entire focused field, using the Polychrome V connected to a computer. The shutter and wavelength were controlled using Patchmaster software (HEKA). For the photoisomerization of compound **7g** flashes of 365 nm (3.5 s duration for 5 min) and 400 nm (3.5 s duration for 5 min) whereas for compound **8** flashes of 385 nm (3.5 s duration) and 530 nm (3.5 s duration) were used. Each compound was applied together with the EC<sub>20</sub> of CCh. Numerical data were imported to GraphPad Prism version 9 (GraphPad Software). Statistical analysis was performed using the paired sample Wilcoxon signed rank test.



## Additional references

- 1 Littmann, T., Ozawa, T., Hoffmann, C., Buschauer, A. & Bernhardt, G. A split luciferase-based probe for quantitative proximal determination of G $\alpha_q$  signalling in live cells. *Sci Rep* **8**, 17179, doi:10.1038/s41598-018-35615-w (2018).

# Chapter 8

---

## Optical control of cardiac function with a photoswitchable muscarinic agonist

---

---

Fabio Riefolo, Carlo Matera, Aida Garrido-Charles, Alexandre M. J. Gomila, **Rosalba Sortino**, Luca Agnetta, Enrique Claro, Roser Masgrau, Ulrike Holzgrabe, Montserrat Batlle, Michael Decker, Eduard Guasch and Pau Gorostiza. **Optical control of cardiac function with a photoswitchable muscarinic agonist.** *J. Am. Chem. Soc.* 2019, 141, 7628-7636.



## Abstract

Light-triggered reversible modulation of physiological functions offers the promise of enabling on-demand spatiotemporally controlled therapeutic interventions. Optogenetics has been successfully implemented in the heart, but significant barriers to its use in the clinic remain, such as the need for genetic transfection. Herein, we present a method to modulate cardiac function with light through a photoswitchable compound and without genetic manipulation. The molecule, named **PAI**, was designed by introduction of a photoswitch into the molecular structure of an M<sub>2</sub> muscarinic acetylcholine receptors (M<sub>2</sub> mAChR or M<sub>2</sub>R) agonist. *In vitro* assays revealed that **PAI** enables light-dependent activation of M<sub>2</sub> mAChRs. To validate the method, we show that **PAI** photoisomers display different cardiac effects in a mammalian animal model, and demonstrate reversible, real-time photocontrol of cardiac function in translucent wild-type tadpoles. **PAI** can also effectively activate M<sub>2</sub>Rs using two-photon excitation with near-infrared light, which overcomes the scattering and low penetration of short-wavelength illumination and offers new opportunities for intravital imaging and control of cardiac function.



## 8.1 Introduction

Remote spatiotemporal control of physiological processes may provide novel treatment opportunities. Cardiopathies are paradigmatic in this regard, because of the rapid time course and complex integration of electrophysiological and molecular events in very specific areas of the heart. For instance, most cardiac rhythm control strategies rely on antiarrhythmic drugs (AADs) targeting ionic currents, whose effects cannot be regulated spatiotemporally. As a result, AADs often give rise to intolerable side effects, including ventricular proarrhythmogenicity, and are only partially effective. Overcoming the high failure and complication rates of current therapeutic strategies to treat these diseases will require both patient-personalized determination of the specific physiopathological mechanism and qualitative pharmacological breakthroughs<sup>1</sup>.

The application of light and optical techniques in medicine has had a profound impact over the past several decades, in diagnostics, surgery and therapy<sup>2</sup>. In particular, photoexcitation of intrinsic molecules or exogenous light-sensitive agents introduced in the body can affect the tissues and cells within in various ways, via the generation of heat (photothermal), chemical reactions (photochemical) and biological processes (photobiological/ photopharmacological or optogenetic)<sup>2</sup>. The potential of light as a therapeutic tool with high spatiotemporal resolution has been recently investigated in the cardiovascular field, particularly for arrhythmias, through optogenetics<sup>3-7</sup>. However, the application of such genetic techniques to human subjects with therapeutic purposes is still hampered by safety, regulatory and economic hurdles. Unlike optogenetics, photo-pharmacology relies on the use of exogenous light-regulated small molecules that can photocontrol native targets and that could be tested and approved using standard drug development procedures<sup>8-15</sup>. These molecules can be used in combination with devices that deliver light to specific locations in the body<sup>7,16-18</sup> in order to remotely control drug dosing and duration of action. Since the activity of drugs is structure-dependent, reversible photoresponsive drugs are obtained by the rational introduction of a molecular photoswitch into the structure of a bioactive compound<sup>8,14</sup>.

Cardiac function is controlled by the autonomic sympathetic and parasympathetic nervous systems, which act via adrenoceptors and muscarinic acetylcholine receptors (mAChRs), respectively<sup>19</sup>. In particular, the stimulation of  $\beta$ 1 and  $\beta$ 2 adrenergic receptors increases the heart rate (positive chronotropy) and contractility (positive inotropy), while stimulation of M<sub>2</sub> mAChRs decreases heart rate and prolongs the atrioventricular conduction time<sup>20,21</sup>. Thus,

adrenergic and muscarinic receptors constitute suitable target candidates to control cardiac function with light. The mAChRs belong to class A of G protein-coupled receptors (GPCRs) and are divided in five different subtypes ( $M_1R$ - $M_5R$ )<sup>22</sup>. The  $M_2$  mAChR is extensively expressed in the heart. All five mAChRs are characterized by a high sequence homology in the orthosteric site located in the transmembrane region. This fact limits the development of subtype-selective orthosteric agonists. On the other hand, the allosteric site located in the extracellular loop is less conserved; thus, muscarinic allosteric agents are commonly endowed with a more pronounced subtype-selectivity<sup>23</sup>. A chemical strategy commonly applied to overcome such limitation is the incorporation, within the same molecular structure, of two distinct pharmacophore elements belonging to (a) high-affinity orthosteric agonists and (b) highly selective allosteric ligands<sup>24-28</sup>. These hybrid compounds, termed “dualsteric” or “bitopic”, are capable of binding simultaneously to both the orthosteric and the allosteric sites of mAChRs and usually display valuable properties<sup>29</sup>, such as receptor subtype selectivity, functional selectivity<sup>26,30</sup> and higher tolerability *in vivo*<sup>31</sup>. Moreover, such ligands bear in their structure two permanently charged nitrogen atoms, which likely prevent them from crossing the blood-brain barrier, confining their effects to the periphery, which is advantageous for cardiovascular agents. Herein, we describe the first nongenetic method for the optical control of cardiac function with a photoswitchable agonist. The design and synthesis of this molecule and its pharmacological characterization under one-photon (1P) and two-photon (2P) excitation are reported.

## 8.2 Results and discussion

### 8.2.1 Rational design and chemical synthesis

Two novel putative photo-responsive muscarinic agents, named phthalimide-azo-iperoxo (**PAI**) and naphthalimide-azo-iperoxo (**NAI**), were designed by replacing the polymethylene spacer chain of known  $M_2$  mAChR dualsteric agonists (P-8-Iper and N-8-Iper)<sup>30-32</sup> with a molecular photoswitch, while conserving (a) the iperoxo-like orthosteric agonist moiety and (b) the  $M_2R$ -selective allosteric fragments derived from W84 and naphmethonium (**Figure 8.1**). The incorporation of a photoisomerizable unit into the structure of a dualsteric agonist should enable controlling with light the mutual position of the orthosteric and the allosteric moieties, presumably leading to differences between the two isomers in receptor affinity and efficacy. We chose an azobenzene core as photoresponsive component, because of the favorable characteristics that azobenzene-based photoswitches normally display for biological purposes

in comparison to other photoswitches, such as design flexibility, large changes in geometry upon isomerization, high photostationary states and fatigue resistance, fast photoisomerization rates, chemical stability, among others<sup>33</sup>. Moreover, the use of arylazo compounds has been proven safe in humans for some approved drugs and food colorants<sup>33</sup>.

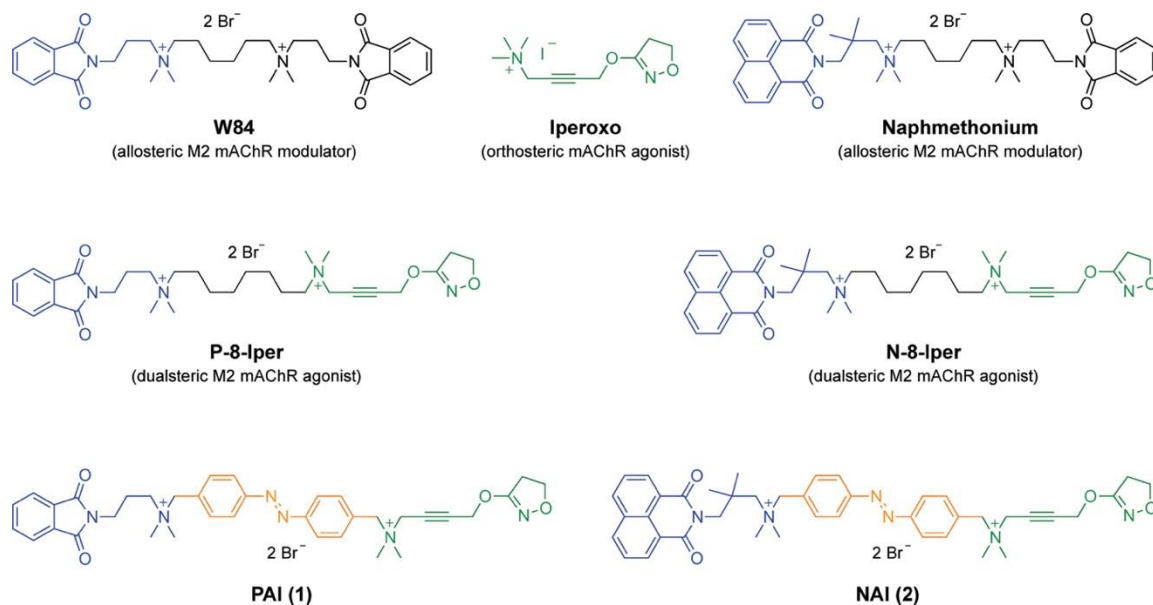
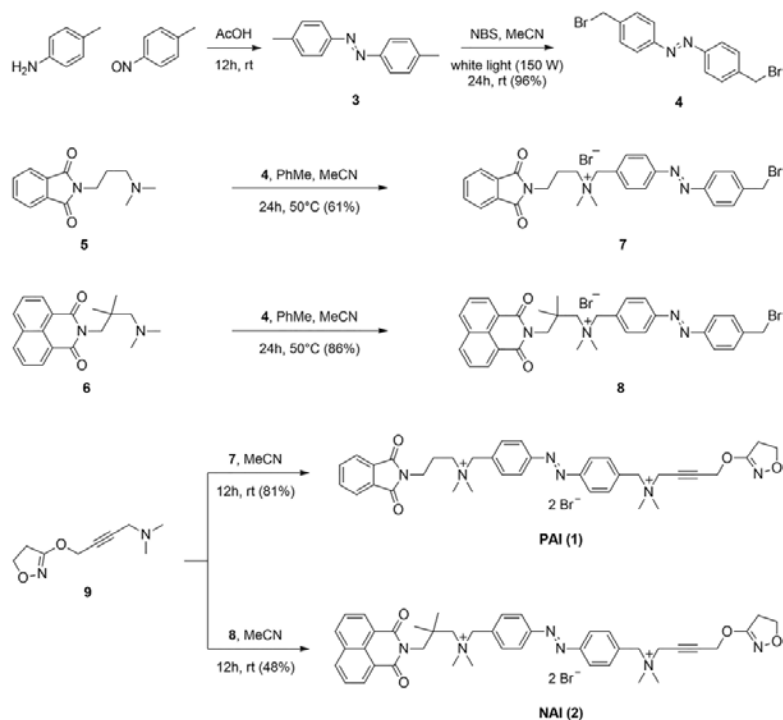


**Figure 8.1. Chemical structures of the muscarinic ligands.** The allosteric modulators W84 and Naphmethonium, the orthosteric agonist Iperoxo (IPX), the dualsteric agonists P-8-Iper and N-8-Iper, and the photoswitchable dualsteric ligands PAI and NAI.

**PAI (1)** and **NAI (2)** were prepared via two subsequent Menshutkin reactions between the azobenzene linker (**4**) and the corresponding allo- and orthosteric intermediates (**5** and **6**, **9**) (**Scheme 8.1**). Compound **3** was synthesized via the typical Mills reaction and successively brominated photochemically to afford the desired linker **4**. Notably, this photochemical reaction exempted us from using a radical initiator<sup>34</sup> and gave an excellent yield (96%), proving for the first time that light-induced benzylic halogenations can be conveniently used also for the preparation of such versatile photoswitchable linkers. Compounds **5**, **6**, and **9** were prepared as previously reported from commercially available starting materials (**Scheme 8.1** and **Supplementary Information; SI**)<sup>24-26,31</sup>. As a prerequisite for a reversible light-dependent control of their biological activity, **PAI** and **NAI** need to effectively behave as reversible photoswitches, which means that the photo-isomerization should be relatively fast and quantitatively significant in both directions.





Scheme 8.1. Chemical Synthesis of PAI and NAI.

## 8.2.2 Photochemical characterization

Ultraviolet-visible (UV-Vis) spectroscopy experiments showed that **PAI** and **NAI** have the typical absorption bands of conventional azobenzenes. **PAI** can be isomerized to the *cis* form (about 73% conversion) by applying 365 nm light, while it thermally relaxes back to the *trans* form in several hours at room temperature. It can be also effectively back-isomerized to the *trans* form by applying white or blue (460 nm) light (83% *trans*) (**Figure 8.2** and **Figure S8.3**). Surprisingly, **NAI** resulted refractory to photoisomerization (only 23% *cis* after 10 min at 365 nm, **Figure S8.3CD**), which shows that rational design of azobenzene-containing ligands does not always afford the expected results. We hypothesized that the absorption and emission properties of the naphthalimide moiety<sup>35</sup> could interfere with its photochromism. Given the unsatisfactorily photochromic behavior of **NAI**, we selected only **PAI** for further studies.

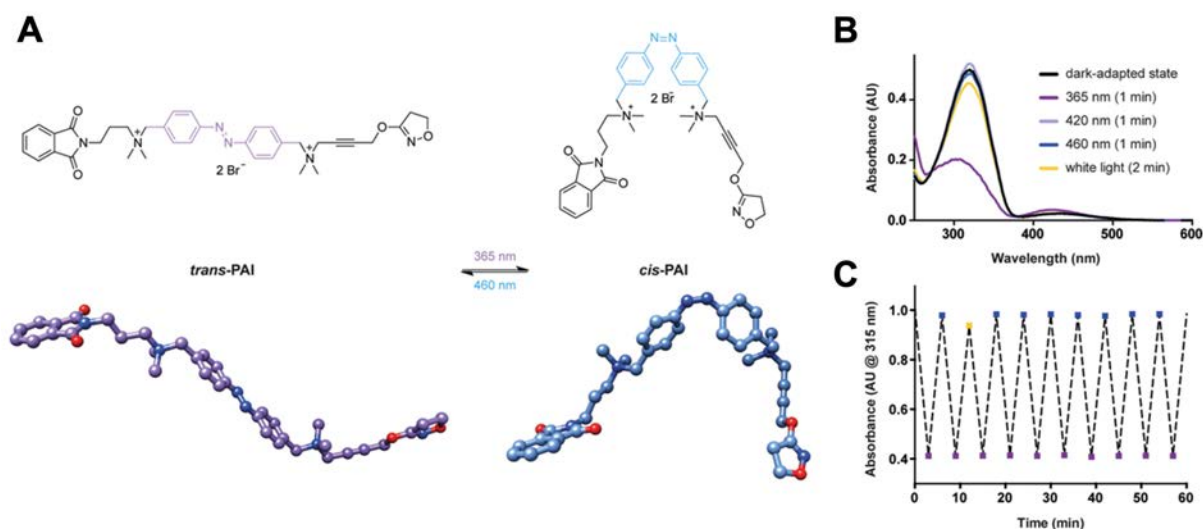


**Figure 8.2. Photochemical characterization.** (A) 2D and 3D representation of the chemical structures of *trans*- and *cis*-PAI. (B) Absorption spectra of PAI showing distinct photochromic behavior. (C) The photoswitching process can be repeated over several cycles without noticeable photofatigue.

### 8.2.3 *In vitro* calcium imaging

The photopharmacological properties of PAI were first assessed *in vitro* with real-time calcium imaging assays in transiently transfected HEK cells under 1P-illumination (Figure 8.3 and SI). We tested also the non-photoresponsive muscarinic agonist iperoxo (IPX)<sup>36</sup> as a control (Figure 8.3A). The application of *trans*-PAI (dark-adapted state) induced cytosolic calcium oscillations indicative of M<sub>2</sub> mAChR agonism, which were reduced by converting PAI to its *cis* form upon illumination with ultraviolet (UV) light (365 nm) (Figure 8.3BC). Calcium oscillations could be restored after back-isomerizing PAI to the *trans* configuration using blue light (460 nm). The time course of calcium responses during activation with *trans*-PAI displayed a diversity of behaviors in individual cells (Figure 8.3C), including oscillatory waves, transient peaks, and step responses as previously observed with PLC-activating GPCRs<sup>12</sup>. Quantification of photoresponses ( $\Delta F/F_0$ ) to PAI application and 365 nm illumination shows a reduction in the calcium signal induced by UV light pulses (Figure 8.3D). Intriguingly, PAI activated M<sub>2</sub>Rs in the range of picomolar concentrations, similarly to the superagonist IPX<sup>36</sup>. Thus, we demonstrated that PAI can effectively activate M<sub>2</sub> mAChRs *in vitro* in its dark-adapted (*trans*) form and its activity can be reversibly switched off and on with light.

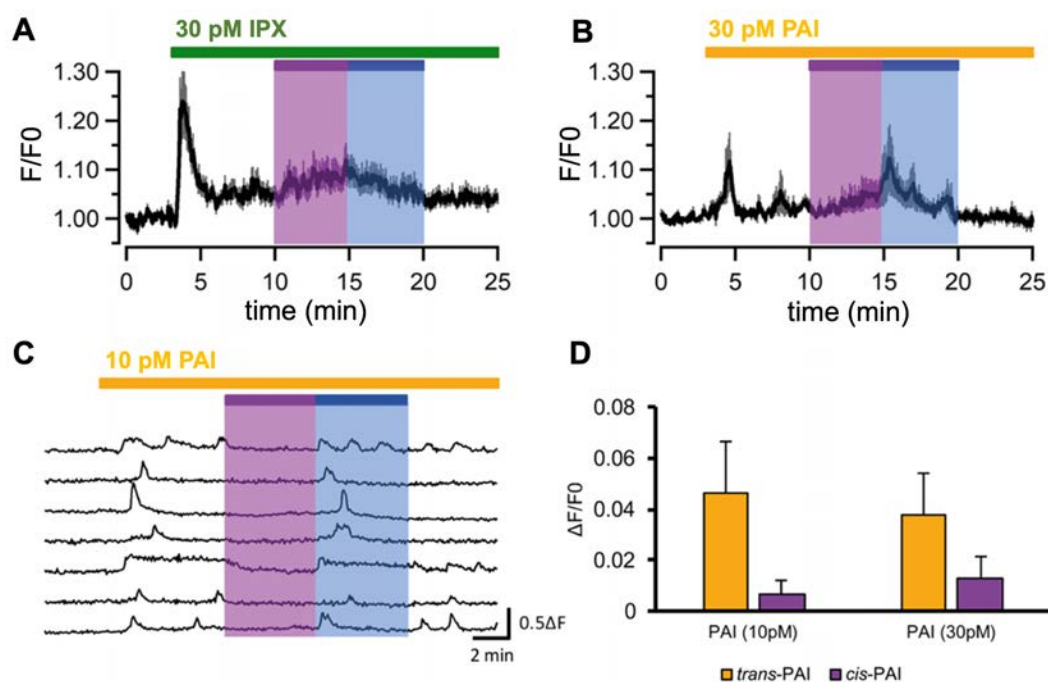


**Figure 8.3. PAI reversibly activates M<sub>2</sub> mAChRs with light in calcium imaging assays.** Real-time calcium imaging traces from HEK cells coexpressing M<sub>2</sub> mAChR and G $\alpha_{qTOP}$  loaded with 10  $\mu$ M of the calcium indicator OGB-1 AM. (A) Average trace of cell responses to 30 pM of non photoswitchable muscarinic agonist IPX (n = 130). Cells gave a sharp response to the application of IPX, but the concomitant application of pulses of UV or blue light did not alter calcium responses, as expected. (B) Average trace of cell responses to 30 pM of *trans*-PAI (n = 8). (C) Single cell calcium responses induced by the direct application of 10 pM of *trans*-PAI (yellow bar). Purple bars indicate illumination at 365 nm, blue bars indicate illumination at 460 nm. Gray shadow in the recordings represents  $\pm$  standard error of the mean (SEM). (D) Quantification of photoresponses to the application of PAI (yellow bar) at 10 pM (n = 356 cells from 5 different experiments) and 30 pM (n = 293 cells from 6 different experiments), and recovery after 365 nm illumination (purple bar). Error bars are  $\pm$  SEM.

## 8.2.4 Molecular docking

In order to account for the observed photoswitchable activity of PAI in M<sub>2</sub> mAChR, we looked for putative differences on the receptor level regarding binding efficacy of *cis*- and *trans*-PAI using molecular docking simulations (see the SI for details). PAI isomers were docked into their theoretical binding site at the human M<sub>2</sub> mAChR (PDB ID: 4MQT). Our results suggested that *trans*-PAI can bind to the M<sub>2</sub> mAChR in a typical dualsteric pose compatible with receptor activation (Figure S8.16A)<sup>37</sup>. In contrast, a flipped orientation is favored in the case of the *cis* form (Figure S8.16B). This binding pose is likely incompatible with receptor activation and provides a possible explanation for the light-dependent efficacy of PAI.

### 8.2.5 *In vivo* photocontrol of cardiac activity in rats

Once established that **PAI** allows light-dependent reversible activation of  $M_2$  mAChRs, we aimed at testing it as an agent to photocontrol cardiac function *in vivo*. We initially used Wistar rats for our experiments. The intraperitoneal administration of **PAI** induced progressive bradycardia and PR lengthening in a dose-dependent manner in both configurations (**Figure 8.4** and **Figure S8.17**). These effects were accompanied by variable degrees of systemic parasympathetic effects, such as salivation, urination and defecation. At low doses ( $\leq 3 \mu\text{M/kg}$ ), both isomers yielded a similar small effect, but remarkably differed at intermediate and high doses. At  $10 \mu\text{M/kg}$  **PAI** and higher doses, the PR interval was significantly more prolonged in *trans*; at  $30 \mu\text{M}$  and higher doses, heart rate was also lower in *trans*. The effects of **PAI** could not be photoswitched either with blue or with UV light, showing that the ability of light to penetrate murine cardiac tissue at those wavelengths is likely not sufficient to reach  $M_2$  mAChR location. Only the administration of atropine (2 mg) completely reverted bradycardia, PR lengthening and systemic parasympathetic effects in both groups (**Figure S8.17**). These results demonstrated an enhanced parasympathetic activity for the *trans*-isomer and confirmed in mammals the previous findings observed in cells.

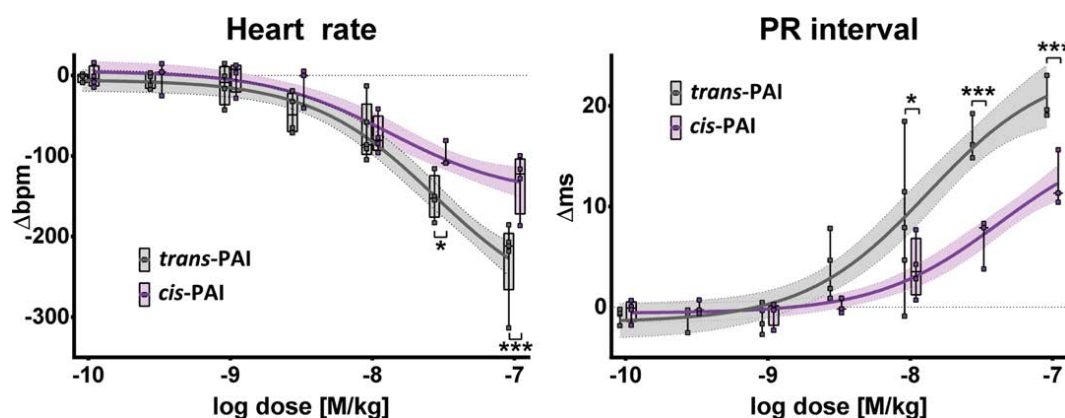


**Figure 8.4.** *In vivo* effect of *trans*- and *cis*-PAI on the cardiac activity of rats. The activity of dark-relaxed (*trans*, gray plots) and UV-illuminated **PAI** (*cis*, purple plots) administered intraperitoneally in anesthetized rats was tested by means of electrocardiography. The heart rate (left panel) and PR interval (right panel) are plotted as a function of increasing doses of both isomers, which induced progressive bradycardia and PR lengthening in a dose-dependent manner. Significant differences between the dark-relaxed and UV-treated **PAI** were found in the heart rate and PR interval at the higher doses ( $p$ -value (\*)  $< 0.05$ ;  $p$ -value (\*\*\*)  $< 0.001$  *trans* vs. *cis*), in agreement with the higher agonist activity of the *trans* form observed *in vitro* and in tadpoles. Three rats in the *trans*-group died, because of extreme bradycardia after the  $100 \mu\text{M/kg}$  dose. The effects of **PAI** were reversible only upon administration of the muscarinic antagonist atropine.

### 8.2.6 *In vivo* photocontrol of cardiac activity in frog tadpoles

As an alternative to demonstrate reversible control of cardiac function *in vivo*, we turned to an animal model in which light scattering is known to be low, thus allowing better light penetration. We selected *Xenopus tropicalis* tadpoles for this purpose since they are translucent and are recognized as an excellent model for studying the human cardiovascular system (**Figure 8.5**)<sup>38,39</sup>. Moreover, we had already successfully used video light microscopy to acquire real-time images of the developing beating heart by digitizing the expanding and contracting blood pool in early translucent hearts (**Figure 8.5A**)<sup>38,40</sup>.

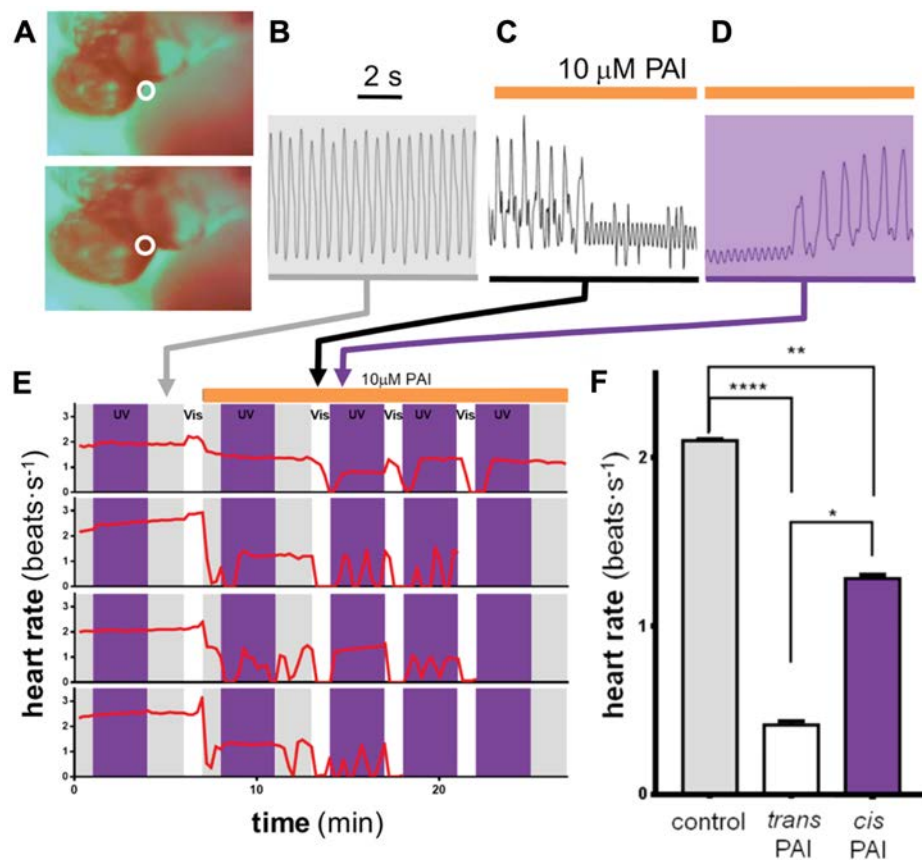


**Figure 8.5. Photoregulation of heart rate with PAI in frog tadpoles.** (A) Two video frames of a paralyzed tadpole heart indicating a region of interest (white circle) used to obtain the time course of heart beating movements (average of intensity vs. time). (B) Normal heartbeat recording obtained in control conditions (dim red light, indicated by a gray shade). Time scale: 2 s. (C) Adding 10  $\mu\text{M}$  *trans*-PAI under white light illumination reduces the heartbeat frequency, eventually causing cardiac arrest. (D) Under UV illumination (purple shade), *trans*-PAI is isomerized to *cis*-PAI and heartbeat is recovered. (E) Red traces indicate the heart rate (in  $\text{beats}\cdot\text{s}^{-1}$ , calculated every 15 s interval) as a function of time in 4 independent experiments with different animals. White, purple, and gray backgrounds indicate illumination with white, UV, and dim red light, respectively. Heart rate is not altered by illumination under control conditions (**Figure S8.19**). Adding 10  $\mu\text{M}$  *trans*-PAI under dim light reduces the heart rate in animals 2, 3, and 4. UV illumination isomerizes PAI to the *cis* form and the heart rate is partially recovered. Dim red light does not isomerize PAI (**Figure S8.18**) and heart rate is relatively stable. White light

converts **PAI** to the *trans*-isomer, causing cardiac arrest in all 4 animals. UV light restores heartbeat in all animals, some displaying an unstable rate. Several white/UV light cycles were repeated in some animals, showing similar effects. (F) Quantification of heart rate during the last minute of each period (beats·s<sup>-1</sup>, n = 4 tadpoles) in control conditions, under white light (*trans*-**PAI**) and under UV light (*cis*-**PAI**). Two-way for repeated measures ANOVA was performed with uncorrected Fisher's LSD test, significance values were established with a *p*-value = 0.05. Error bars represent standard error of the mean (SEM). The heart rate was significantly higher under UV illumination compared to visible light (*p*-value (\*) < 0.05). Both isomers produced a significant reduction of heart rate in comparison to controls (*p*-value (\*\*\*\*) < 0.001).

In the absence of **PAI**, the cardiac rate of tadpoles remained nearly constant at  $2.3 \pm 0.1$  beats·s<sup>-1</sup> during control illumination with UV light and at  $2.10 \pm 0.01$  beats·s<sup>-1</sup> in the dark. The variability score (V.S.) was  $7.97 \pm 0.07$ . Upon administration of 10 μM *trans*-**PAI**, heart rate decreased dramatically ( $0.41 \pm 0.02$  beats·s<sup>-1</sup> in the trace of **Figure 8.5E**) leading in some cases to cardiac arrest (**Figure 8.5C**). Heart beating recovered progressively upon UV illumination (*cis*-isomerization,  $1.28 \pm 0.02$  beats·s<sup>-1</sup>, **Figure 8.5F**), and was not altered in the dark since thermal relaxation is slow. Some animals displayed less stable cardiac rate during UV periods compared to controls (V.S. of  $17.4 \pm 0.2$  and  $8.30 \pm 0.02$ , respectively; **Figure S8.20**). Subsequent illumination of the animals with visible light (*cis*-to-*trans* isomerization) again reduced cardiac rate and eventually interrupted heart beating (V.S. of  $374 \pm 47.7$ , **Figure S8.20**). Cardiac activity was restored by later exposition to UV light, and further UV-Vis light cycles confirmed the reversibility of the pharmacological effects (see example **Supporting Movie S1**). Overall, these experiments demonstrated that **PAI** allows remote and reversible control of heart rate with light in living animals.

### 8.2.7 *In vitro* calcium imaging and two-photon stimulation

In order to overcome the scattering and low penetration of violet and visible illumination, we tested whether **PAI** could be used to activate M<sub>2</sub> mAChRs at longer wavelengths. In fact, a critical aspect that must be addressed to unleash the full potential of light-regulated drugs and favor their translation into clinic is their responsiveness to red or NIR radiation<sup>41,42</sup>, which enables higher penetration through tissue, abolishes photodamage and, in the case of 2P excitation, allows three-dimensional subcellular resolution<sup>42-46</sup>. **PAI** has an excellent thermal stability in both configurations (**Figure S8.5**) and is photochemically suited for *cis*-to-*trans* photoisomerization with NIR light under 2P-excitation, which encouraged us to test its effects in living cells in real-time calcium imaging assays using a confocal microscope equipped with a pulsed laser (**Figure 8.6**).

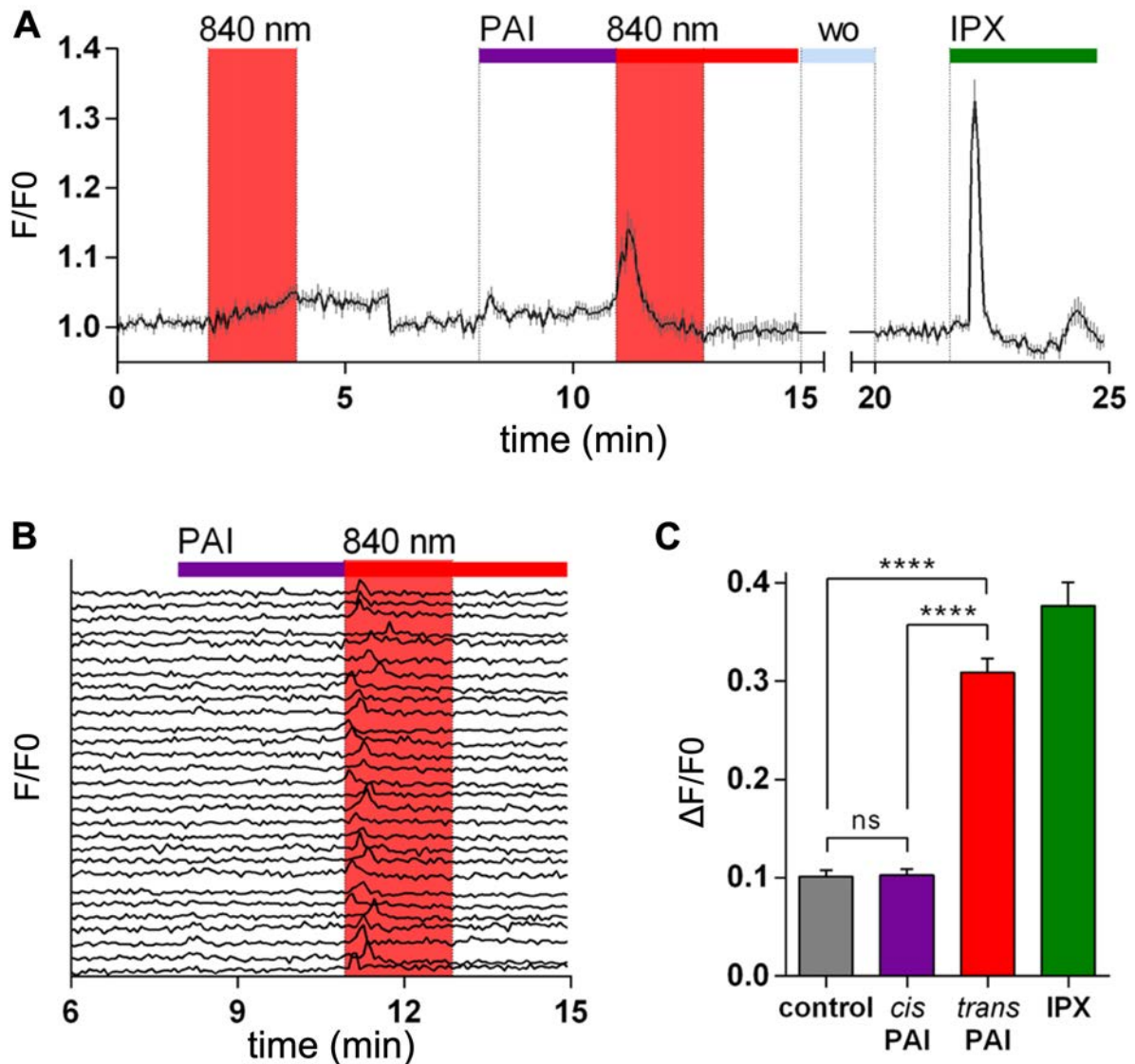


**Figure 8.6. Activation of PAI with NIR light under 2P excitation.** Real-time calcium imaging traces from HEK cells co-expressing M<sub>2</sub> mAChR and Gα<sub>qTOP</sub> loaded with 10 μM of the calcium indicator OGB-1 AM. (A) Average trace of cell responses to 30 pM *cis*-PAI preirradiated at 365 nm (purple bar), *trans*-enriched PAI obtained under 2P excitation at 840 nm (red bar), and the muscarinic agonist IPX (green bar) after wash-out (wo, light blue bar) (n = 29 cells). Neither 2P excitation alone (red panel) nor *cis*-PAI elicited calcium responses. Cells gave a sharp response upon application of pulsed NIR light (840 nm) in the presence of PAI due to its photoisomerization to the *trans*-active form. IPX was applied as a positive control. Gray shadow in the recordings represents ± SEM. (B) Single cell calcium responses induced by PAI under 2P-excitation at 840 nm (red panel) (n = 29 cells). Purple bar indicates application of preirradiated PAI (365 nm), red bar indicates illumination at 840 nm. (C) Quantification of photoresponses of 29 cells to the application of *cis*-PAI (purple bar) at 30 pM, after switching to *trans*-PAI using 2P-excitation at 840 nm (red bar), control under 2P-excitation at 840 nm (gray bar) and IPX (green bar). Error bars are ± SEM. Data were analyzed by using one-way ANOVA with Sidak post hoc test for multiple comparisons for statistical significance (p-value (\*\*\*\*) < 0.0001; GraphPad Prism 6).

**PAI** was initially applied in its *cis* (off) state, which as expected did not produce cytosolic calcium oscillations. Subsequent illumination at 840 nm induced robust calcium responses, as previously observed in calcium imaging experiments for *cis*-to-*trans* photoisomerization under 1P-excitation (**Figure 8.6A**). These results are quantified in **Figure 8.6C**. The responses ( $\Delta F/F_0$ ) obtained for *cis*-**PAI** (1P pre-irradiation at 365 nm) are comparable to controls, and 2P-induced isomerization to *trans*-**PAI** achieves calcium responses nearly as high as perfusion of IPX. It is worth noting that even under NIR excitation **PAI** maintains an outstanding potency (picomolar) to activate M<sub>2</sub>Rs, which is rarely observed in photoswitches<sup>11,42,47,48</sup>. Interestingly, 2P microscopy is extensively used for intravital imaging including cardiovascular imaging at subcellular resolution<sup>49,50</sup>. Thus, **PAI** has a bright future to control cardiac function with light.

### 8.3 Conclusions

The rapid and reversible control of cardiac activity is of particular interest in medicine, including the spatiotemporal manipulation of close anatomic structures bearing different electrophysiological functions in the heart. Light-activated cardiac drugs could be selectively enhanced in certain regions of the heart (*e.g.*, preventing undesired pro-arrhythmogenic ventricular effects when atria are targeted), or at certain times (on-demand, *i.e.*, active only during atrial fibrillation or bradycardia). For that purpose, cardiac patches with integrated electronics and electric stimulation<sup>46</sup> could be further equipped with optoelectronic devices for photostimulation. Drug-based cardiac photoregulation techniques offer potential advantages compared to electric stimulation of cardiac muscle, which produces inhomogeneous areas of de- and hyperpolarization, causes faradaic reactions that alter pH, and produces toxic gases (H<sub>2</sub>, O<sub>2</sub>, Cl<sub>2</sub>), all of which would be prevented by light-stimulation.

To this end, we have developed the first photoswitchable compound that enables control of cardiac activity with light in wild-type animals without genetic manipulation. To the best of our knowledge, **PAI** is also the first photoswitchable M<sub>2</sub> mAChR agonist to be reported. Despite the changes introduced in the ligand structure in order to photoregulate its activity, **PAI** retains the high potency of its parent compounds IPX and P-8-Iper<sup>31,36</sup>. **PAI** activates M<sub>2</sub>Rs in its *trans* configuration and can be reversibly photoswitched with different wavelengths including NIR light under 2P excitation. Future experiments will be addressed to demonstrate that **PAI** enables precise spatiotemporal control of cardiac function in mammals in combination with 2P cardiovascular imaging.



## References

- 1 Fabritz, L. *et al.* Expert consensus document: Defining the major health modifiers causing atrial fibrillation: A roadmap to underpin personalized prevention and treatment. *Nat Rev Cardiol* **13**, 230-237, doi:10.1038/nrcardio.2015.194 (2016).
- 2 Yun, S. H. & Kwok, S. J. J. Light in diagnosis, therapy and surgery. *Nat Biomed Eng* **1**, doi:10.1038/s41551-016-0008 (2017).
- 3 Pianca, N., Zaglia, T. & Mongillo, M. Will cardiac optogenetics find the way through the obscure angles of heart physiology? *Biochem Biophys Res Commun* **482**, 515-523, doi:10.1016/j.bbrc.2016.11.104 (2017).
- 4 Yu, L. *et al.* Optogenetic modulation of cardiac sympathetic nerve activity to prevent ventricular arrhythmias. *J Am Coll Cardiol* **70**, 2778-2790, doi:10.1016/j.jacc.2017.09.1107 (2017).
- 5 Bingen, B. O. *et al.* Light-induced termination of spiral wave arrhythmias by optogenetic engineering of atrial cardiomyocytes. *Cardiovasc Res* **104**, 194-205, doi:10.1093/cvr/cvu179 (2014).
- 6 Bruegmann, T. *et al.* Optogenetic defibrillation terminates ventricular arrhythmia in mouse hearts and human simulations. *J Clin Invest* **126**, 3894-3904, doi:10.1172/JCI88950 (2016).
- 7 Boyle, P. M., Karathanos, T. V. & Trayanova, N. A. "Beauty is a light in the heart": The transformative potential of optogenetics for clinical applications in cardiovascular medicine. *Trends Cardiovasc Med* **25**, 73-81, doi:10.1016/j.tcm.2014.10.004 (2015).
- 8 Lerch, M. M., Hansen, M. J., van Dam, G. M., Szymanski, W. & Feringa, B. L. Emerging targets in photopharmacology. *Angew Chem Int Ed Engl* **55**, 10978-10999, doi:10.1002/anie.201601931 (2016).
- 9 Izquierdo-Serra, M., Trauner, D., Llobet, A. & Gorostiza, P. Optical modulation of neurotransmission using calcium photocurrents through the ion channel LiGluR. *Front Mol Neurosci* **6**, 3, doi:10.3389/fnmol.2013.00003 (2013).
- 10 Nevola, L. *et al.* Light-regulated stapled peptides to inhibit protein-protein interactions involved in clathrin-mediated endocytosis. *Angew Chem Int Ed Engl* **52**, 7704-7708, doi:10.1002/anie.201303324 (2013).
- 11 Izquierdo-Serra, M. *et al.* Two-photon neuronal and astrocytic stimulation with azobenzene-based photoswitches. *J Am Chem Soc* **136**, 8693-8701, doi:10.1021/ja5026326 (2014).
- 12 Pittolo, S. *et al.* An allosteric modulator to control endogenous G protein-coupled receptors with light. *Nat Chem Biol* **10**, 813-815, doi:10.1038/nchembio.1612 (2014).
- 13 Izquierdo-Serra, M. *et al.* Optical control of endogenous receptors and cellular excitability using targeted covalent photoswitches. *Nat Commun* **7**, 12221, doi:10.1038/ncomms12221 (2016).
- 14 Velema, W. A., Szymanski, W. & Feringa, B. L. Photopharmacology: Beyond proof of principle. *J Am Chem Soc* **136**, 2178-2191, doi:10.1021/ja413063e (2014).
- 15 Matera, C. *et al.* Photoswitchable antimetabolite for targeted photoactivated chemotherapy. *J Am Chem Soc* **140**, 15764-15773, doi:10.1021/jacs.8b08249 (2018).
- 16 Hamaoka, T., McCully, K. K., Quaresima, V., Yamamoto, K. & Chance, B. Near-infrared spectroscopy/imaging for monitoring muscle oxygenation and oxidative metabolism in healthy and diseased humans. *J Biomed Opt* **12**, 062105, doi:10.1117/1.2805437 (2007).
- 17 Taub, A. F. Photodynamic therapy in dermatology: History and horizons. *J Drugs Dermatol* **3**, S8-25 (2004).

- 18 Kale, R. P., Kouzani, A. Z., Walder, K., Berk, M. & Tye, S. J. Evolution of optogenetic microdevices. *Neurophotonics* **2**, 031206, doi:10.1117/1.NPh.2.3.031206 (2015).
- 19 Brodde, O. E. & Michel, M. C. Adrenergic and muscarinic receptors in the human heart. *Pharmacol Rev* **51**, 651-690 (1999).
- 20 Brodde, O. E., Bruck, H., Leineweber, K. & Seyfarth, T. Presence, distribution and physiological function of adrenergic and muscarinic receptor subtypes in the human heart. *Basic Res Cardiol* **96**, 528-538, doi:10.1007/s003950170003 (2001).
- 21 Dhein, S., van Koppen, C. J. & Brodde, O. E. Muscarinic receptors in the mammalian heart. *Pharmacol Res* **44**, 161-182, doi:10.1006/phrs.2001.0835 (2001).
- 22 Caulfield, M. P. & Birdsall, N. J. International union of pharmacology. XVII. Classification of muscarinic acetylcholine receptors. *Pharmacol Rev* **50**, 279-290 (1998).
- 23 De Amici, M., Dallanocce, C., Holzgrabe, U., Trankle, C. & Mohr, K. Allosteric ligands for G protein-coupled receptors: A novel strategy with attractive therapeutic opportunities. *Med Res Rev* **30**, 463-549, doi:10.1002/med.20166 (2010).
- 24 Mohr, K. *et al.* Rational design of dualsteric GPCR ligands: Quests and promise. *Br J Pharmacol* **159**, 997-1008, doi:10.1111/j.1476-5381.2009.00601.x (2010).
- 25 Disingrini, T. *et al.* Design, synthesis, and action of oxotremorine-related hybrid-type allosteric modulators of muscarinic acetylcholine receptors. *J Med Chem* **49**, 366-372, doi:10.1021/jm050769s (2006).
- 26 Antony, J. *et al.* Dualsteric GPCR targeting: A novel route to binding and signaling pathway selectivity. *FASEB J* **23**, 442-450, doi:10.1096/fj.08-114751 (2009).
- 27 Matera, C. & Tata, A. M. Pharmacological approaches to targeting muscarinic acetylcholine receptors. *Recent Pat CNS Drug Discov* **9**, 85-100, doi:10.2174/1574889809666141120131238 (2014).
- 28 Agnetta, L. *et al.* A photoswitchable dualsteric ligand controlling receptor efficacy. *Angew Chem Int Ed Engl* **56**, 7282-7287, doi:10.1002/anie.201701524 (2017).
- 29 De Min, A. *et al.* A new molecular mechanism to engineer protean agonism at a G protein-coupled receptor. *Mol Pharmacol* **91**, 348-356, doi:10.1124/mol.116.107276 (2017).
- 30 Bock, A. *et al.* The allosteric vestibule of a seven transmembrane helical receptor controls G protein coupling. *Nat Commun* **3**, 1044, doi:10.1038/ncomms2028 (2012).
- 31 Matera, C. *et al.* Bis(ammonio)alkane-type agonists of muscarinic acetylcholine receptors: Synthesis, *in vitro* functional characterization, and *in vivo* evaluation of their analgesic activity. *Eur J Med Chem* **75**, 222-232, doi:10.1016/j.ejmech.2014.01.032 (2014).
- 32 Cristofaro, I. *et al.* Activation of M<sub>2</sub> muscarinic acetylcholine receptors by a hybrid agonist enhances cytotoxic effects in GB7 glioblastoma cancer stem cells. *Neurochem Int* **118**, 52-60, doi:10.1016/j.neuint.2018.04.010 (2018).
- 33 Broichhagen, J., Frank, J. A. & Trauner, D. A roadmap to success in photopharmacology. *Acc Chem Res* **48**, 1947-1960, doi:10.1021/acs.accounts.5b00129 (2015).
- 34 Tolosa, J., Kub, C. & Bunz, U. H. Hyperbranched: A universal conjugated polymer platform. *Angew Chem Int Ed Engl* **48**, 4610-4612, doi:10.1002/anie.200900980 (2009).
- 35 Jacquemin, D. P., E. A., Scalmani, G.; Ciofini, I.; Peltier, C.; Adamo, C. Absorption and emission spectra of 1,8-naphthalimide fluorophores: A PCM-TD-DFT investigation. *Chemical Physics* **372**, 61-66, doi:10.1016/j.chemphys.2010.04.032 (2010).

- 36 Schrage, R. *et al.* Agonists with supraphysiological efficacy at the muscarinic M<sub>2</sub> ACh receptor. *Br J Pharmacol* **169**, 357-370, doi:10.1111/bph.12003 (2013).
- 37 Bock, A. *et al.* Ligand binding ensembles determine graded agonist efficacies at a G protein-coupled receptor. *J Biol Chem* **291**, 16375-16389, doi:10.1074/jbc.M116.735431 (2016).
- 38 Bartlett, H. L., Scholz, T. D., Lamb, F. S. & Weeks, D. L. Characterization of embryonic cardiac pacemaker and atrioventricular conduction physiology in *Xenopus laevis* using noninvasive imaging. *Am J Physiol Heart Circ Physiol* **286**, H2035-2041, doi:10.1152/ajpheart.00807.2003 (2004).
- 39 Nieuwkoop, P. D. F., J. Normal table of *Xenopus laevis* (Daudin): A systematical and chronological survey of the development from the fertilized egg till the end of metamorphosis. *Garland Science*, 282 (1994).
- 40 Eckelt, K. M., H.; Llobet, A.; Gorostiza, P. Automated high-throughput measurement of bodymovements and cardiac activity of *Xenopus tropicalis* tadpoles. *Journal of Biological Methods* **1(2)**, e9, doi:10.14440/jbm.2014.29 (2014).
- 41 Dong, M., Babalhavaeji, A., Samanta, S., Beharry, A. A. & Woolley, G. A. Red-shifting azobenzene photoswitches for *in vivo* use. *Acc Chem Res* **48**, 2662-2670, doi:10.1021/acs.accounts.5b00270 (2015).
- 42 Cabre, G. *et al.* Rationally designed azobenzene photoswitches for efficient two-photon neuronal excitation. *Nat Commun* **10**, 907, doi:10.1038/s41467-019-08796-9 (2019).
- 43 Pawlicki, M., Collins, H. A., Denning, R. G. & Anderson, H. L. Two-photon absorption and the design of two-photon dyes. *Angew Chem Int Ed Engl* **48**, 3244-3266, doi:10.1002/anie.200805257 (2009).
- 44 Bort, G., Gallavardin, T., Ogden, D. & Dalko, P. I. From one-photon to two-photon probes: "caged" compounds, actuators, and photoswitches. *Angew Chem Int Ed Engl* **52**, 4526-4537, doi:10.1002/anie.201204203 (2013).
- 45 Pittolo, S. *et al.* Reversible silencing of endogenous receptors in intact brain tissue using 2-photon pharmacology. *Proc Natl Acad Sci U S A* **116**, 13680-13689, doi:10.1073/pnas.1900430116 (2019).
- 46 Feiner, R. *et al.* Engineered hybrid cardiac patches with multifunctional electronics for online monitoring and regulation of tissue function. *Nat Mater* **15**, 679-685, doi:10.1038/nmat4590 (2016).
- 47 Passlick, S., Richers, M. T. & Ellis-Davies, G. C. R. Thermodynamically stable, photoreversible pharmacology in neurons with one- and two-photon excitation. *Angew Chem Int Ed Engl* **57**, 12554-12557, doi:10.1002/anie.201807880 (2018).
- 48 Bartels, E., Wassermann, N. H. & Erlanger, B. F. Photochromic activators of the acetylcholine receptor. *Proc Natl Acad Sci U S A* **68**, 1820-1823, doi:10.1073/pnas.68.8.1820 (1971).
- 49 Scherschel, J. A. & Rubart, M. Cardiovascular imaging using two-photon microscopy. *Microsc Microanal* **14**, 492-506, doi:10.1017/S1431927608080835 (2008).
- 50 Matsuura, R. *et al.* Intravital imaging with two-photon microscopy reveals cellular dynamics in the ischemia-reperfused rat heart. *Sci Rep* **8**, 15991, doi:10.1038/s41598-018-34295-w (2018).

## Supporting Information (SI) of Chapter 8

### SI8.1 Chemical synthesis

#### SI8.1.1 Materials and methods

All reagents and solvents were purchased from Sigma-Aldrich and ServiQuimia and were used without any further purification. All reactions were performed under inert atmosphere of argon or nitrogen, unless differently stated. TLC analyses were performed on commercial silica gel 60 F<sub>254</sub> aluminium foils (Merck); spots were further evidenced by spraying with a dilute alkaline potassium permanganate solution or a phosphomolybdic acid solution 5% in ethanol and, for tertiary amines and quaternary ammonium compounds, with the Dragendorff reagent. Flash chromatography was performed on PanReac AppliChem silica gel 60 (40-63 microns) as stationary phase; mobile phases are specified for each compound. Ultraviolet-visible (UV-Vis) spectra and experiments were recorded with a Shimadzu UV-1800 UV-Vis Spectrophotometer with standard quartz cuvettes (10 mm light path).

<sup>1</sup>H-NMR, <sup>13</sup>C-NMR, COSY and HSQC spectra were registered with a Varian Mercury 400 MHz instrument (400 MHz for <sup>1</sup>H-NMR and 101 MHz for <sup>13</sup>C-NMR) in DMSO-*d*<sub>6</sub>, CDCl<sub>3</sub>, CD<sub>3</sub>OD. Residual signals of the deuterated solvents were used as an internal standard (DMSO-*d*<sub>6</sub>: <sup>1</sup>H 2.50 ppm, <sup>13</sup>C 39.52 ppm; CDCl<sub>3</sub>: <sup>1</sup>H 7.26 ppm, <sup>13</sup>C 77.16 ppm; CD<sub>3</sub>OD: <sup>1</sup>H 3.31 ppm, <sup>13</sup>C 49.00 ppm). Chemical shifts ( $\delta$ ) are expressed as parts-per-million (ppm) and coupling constants (*J*) as hertz (Hz).

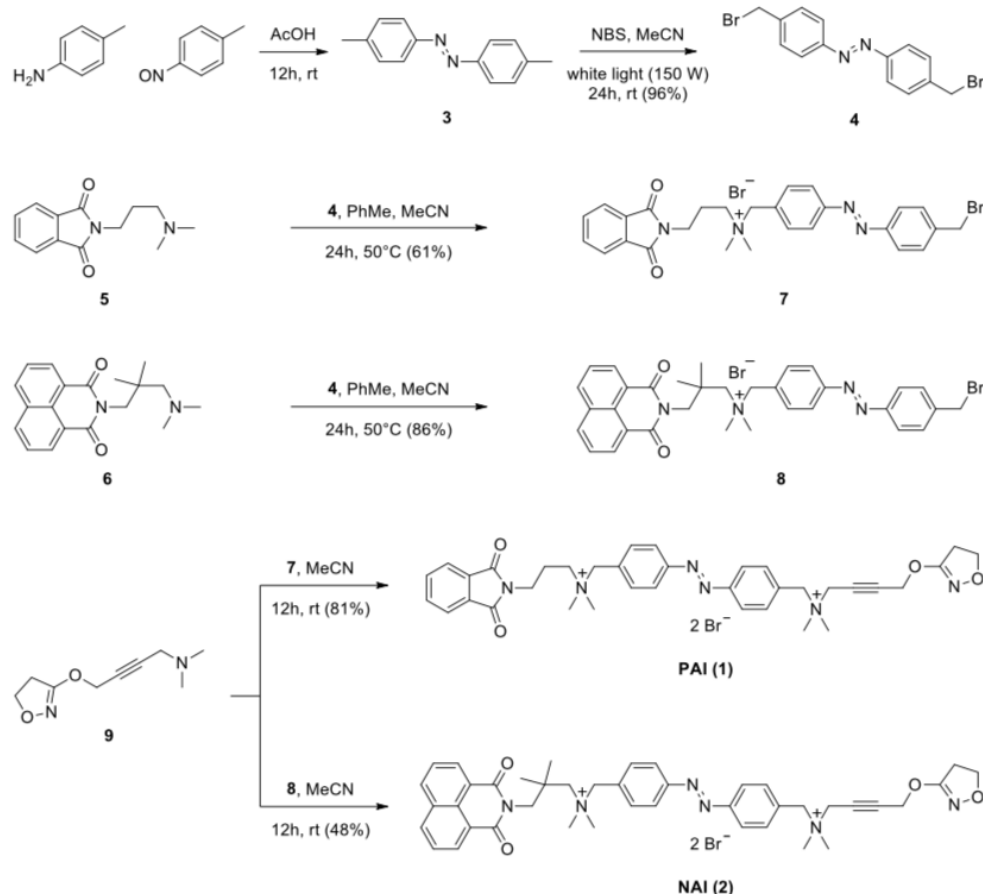
HPLC analyses and purification were performed with a Waters Alliance e2695 Separations Module, equipped with a Waters 2998 UV-Vis Photodiode Array Detector and a Waters ACQUITY QDa Mass Detector for detecting the analytes and a XSelect CSH C18 OBD Prep Column (130 Å, 5  $\mu$ m, 10 mm X 150 mm, 1/pkg, Waters). Water with 0.1% formic acid (v/v) and acetonitrile with 0.1% formic acid (v/v) were used as mobile phases (named A and B, respectively) with the following gradient: concentration phase B: 5→25% from 0 to 4 min; 25% from 4 to 7 min; 25→100% from 7 to 9 min; 100→5% from 9 to 11 min; 5% from 11 to 12 min. The flow rate was of 3 ml min<sup>-1</sup>. The purity of **PAI** compound was found to be  $\geq$  95%. High resolution mass spectroscopy measurements (ionization: NanoESI, positive ionization) were performed at the mass spectrometry core facility of the Institute for Research in Biomedicine (IRB, Barcelona, Spain) with an LTQ-FT Ultra (ThermoFisher Scientific) for direct infusion (Automated Nanoelectrospray) of the sample. The NanoMate

(AdvionBioSciences) aspirated the samples from a 384-well plate (protein Lobind) with disposable, conductive pipette tips, and infused the samples through the nanoESI Chip (which consists of 400 nozzles in a 20 x 20 array) towards the mass spectrometer. Spray voltage was 1.70 kV and delivery pressure was 0.50 psi. Data are reported as mass-to-charge ratio ( $m/z$ ) of the corresponding positively charged molecular ions.

### SI8.1.2 Abbreviations

**Solvents:** AcOEt: ethyl acetate; DCM: dichloromethane; MeCN: acetonitrile; MeOH: methanol; EtOH: ethanol; THF: tetrahydrofuran; Et<sub>2</sub>O: diethyl ether; iPr<sub>2</sub>O: diisopropyl ether; DMSO: dimethylsulfoxide.

**Analytical characterizations:** NMR: d: doublet; dd: double doublet; ddd: double double doublet; dt: double triplet; m: multiplet; q: quartet; quin: quintet; s: singlet; t: triplet; m.p.: melting point; R<sub>f</sub>: retention factor; rt: room temperature; RT: retention time.

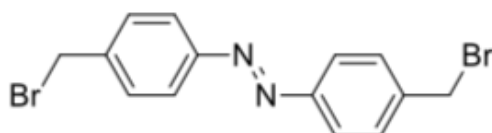


Scheme S8.1. Chemical synthesis of PAI and NAI.

### SI8.1.3 Synthetic routes

PAI and NAI were prepared by combining three different building blocks: (a) a photo-isomerizable spacer (**4**), (b) an allosteric fragment (**5** or **6**, respectively), and (c) an orthosteric iperoxo-like moiety (**9**) (**Scheme S8.1**). The intermediate compounds **5**, **6** and **9** and iperoxo (IPX) were all prepared by following synthetic procedures reported in the literature<sup>1-3</sup>.

#### 4,4'-Bis(bromomethyl)azobenzene (**4**)



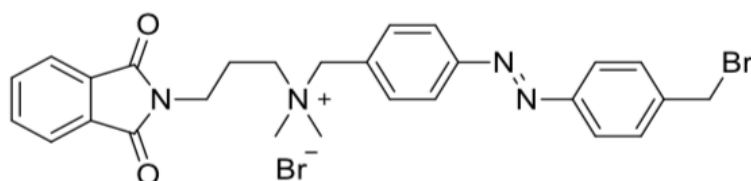
A solution 4,4'-dimethylazobenzene **3** (1.10 g, 5.23 mmol), prepared as reported by Velema *et al.*,<sup>4</sup> and *N*-bromosuccinimide (2.33 g, 13.08 mmol) in MeCN (200 ml) was stirred at room temperature under white light illumination (Dolan-Jenner Fiber-Lite Mi-150 Fiber Optic Illuminator, 150 W) for 24 h. Then, the mixture was concentrated, and the obtained orange solid was filtered and washed several times with MeOH. The resulting solid was dried under vacuum to afford **4** as an orange solid (1.34 g, 96% yield).

M.p.: 228-230°C

<sup>1</sup>H NMR (400 MHz, CDCl<sub>3</sub>): δ 7.90 (d, *J* = 8.4 Hz, 4H), 7.54 (d, *J* = 8.3 Hz, 4H), 4.56 (s, 4H).

<sup>13</sup>C NMR (101 MHz, CDCl<sub>3</sub>): δ 152.42, 140.93, 130.06, 123.51, 32.83.

#### *N*-(4-((4-(bromomethyl)phenyl)diazenyl)benzyl)-3-(1,3-dioxisoindolin-2-yl)-*N,N*-dimethylpropan-1-aminium bromide (**7**)

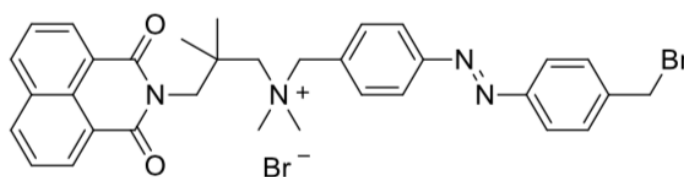


Azobenzene **4** (713 mg, 1.94 mmol) was completely dissolved in toluene (200 ml) at 70°C, and the resulting solution was left under stirring at 50°C. Then a solution of phthalimide **5** (50 mg, 0.22 mmol) in MeCN (50 ml) was slowly added dropwise. The reaction was left under stirring for 24 h at 50°C. Reaction progress was controlled by silica gel TLC to monitor the disappearance of the starting material **5** (eluent: DCM/MeOH, 95:5). At the end, the mixture was concentrated under reduced pressure and the resulting solid was washed several times with toluene in order to completely remove the excess azobenzene **4** and finally dried under reduced pressure to afford **7** as an orange solid (79 mg, 61%).

$^1\text{H}$  NMR (400 MHz,  $\text{CD}_3\text{OD}$ ):  $\delta$  7.98 – 7.89 (m,  $J = 8.8$  Hz, 4H), 7.87 (dd,  $J = 5.5, 3.1$  Hz, 2H), 7.80 (dd,  $J = 5.5, 3.1$  Hz, 2H), 7.74 (d,  $J = 8.5$  Hz, 2H), 7.64 (d,  $J = 8.4$  Hz, 2H), 4.68 (s, 2H), 4.67 (s, 2H), 3.83 (t,  $J = 6.3$  Hz, 2H), 3.48 – 3.40 (m, 2H), 3.14 (s, 6H), 2.37 – 2.25 (m, 2H).  $^{13}\text{C}$  NMR (101 MHz,  $\text{CD}_3\text{OD}$ ):  $\delta$  169.80, 154.98, 153.39, 143.78, 135.57, 135.15, 133.32, 131.29, 124.42, 124.35, 124.32, 68.52, 63.12, 50.81, 35.66, 33.00, 23.53.

LC-MS (QMS):  $m/z$  calculated for  $\text{C}_{27}\text{H}_{28}\text{BrN}_4\text{O}_2^+$ , 519.14 and 521.14; found 519.3 and 521.2  $[\text{M} + \text{H}]^+$ .

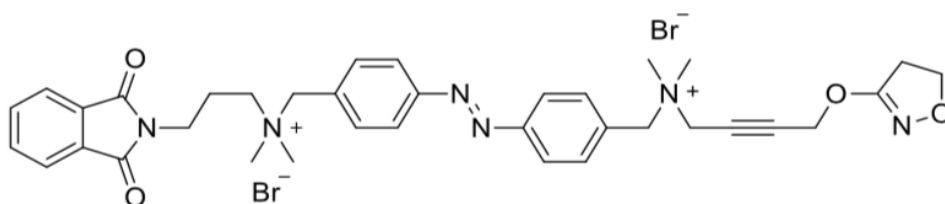
**(E)-N-(4-((4-(bromomethyl)phenyl)diazenyl)benzyl)-3-(1,3-dioxo-1H-benzo[de]isoquinolin-2(3H)-yl)-N,N,2,2-tetramethylpropan-1-aminium bromide (8)**



Azobenzene **4** (276 mg, 0.75 mmol) was completely dissolved in toluene (30 ml) at  $70^\circ\text{C}$ , and the resulting solution was left under stirring at  $50^\circ\text{C}$ . Then a solution of naphthalimide **6** (25 mg, 0.08 mmol) in MeCN (20 ml) was slowly added dropwise. The reaction was left under stirring for 24 h at  $50^\circ\text{C}$ . Reaction progress was controlled by silica gel TLC to monitor the disappearance of the starting material **6** (eluent: DCM/MeOH, 95:5). At the end, the mixture was concentrated under reduced pressure and the resulting solid was washed several times with toluene in order to completely remove the excess azobenzene **4** and finally dried under reduced pressure to afford **8** as an orange solid (10 mg, 86%).

$^1\text{H}$  NMR (400 MHz,  $\text{CD}_3\text{OD}$ ):  $\delta$  8.56 (dd,  $J = 7.3, 1.1$  Hz, 2H), 8.35 (dd,  $J = 8.5, 1.0$  Hz, 2H), 7.95 (dd,  $J = 8.4, 3.2$  Hz, 4H), 7.85 – 7.74 (m, 4H), 7.66 (d,  $J = 8.7$  Hz, 2H), 4.73 (s, 2H), 4.68 (s, 2H), 4.30 (s, 2H), 3.55 (s, 2H), 3.32 (s, 6H), 1.41 (s, 6H).  $^{13}\text{C}$  NMR (101 MHz,  $\text{CD}_3\text{OD}$ ):  $\delta$  165.21, 153.44, 151.99, 142.34, 134.31, 134.23, 131.73, 131.23, 130.17, 129.89, 127.85, 126.81, 122.99, 122.84, 122.10, 72.62, 71.92, 51.06, 49.04, 39.16, 31.60, 25.31.

**Phthalimide-Azo-Iperoxo, PAI (1)**

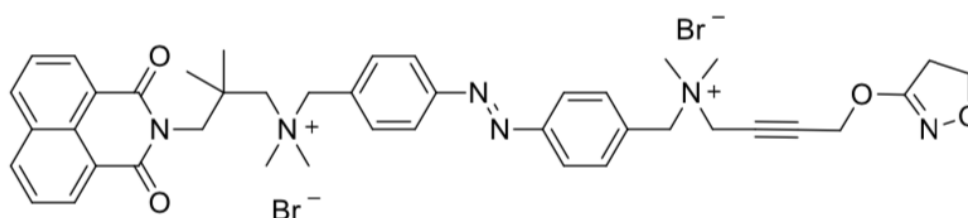


Compound **7** (50.4 mg, 0.08 mmol) and the isoxazoline **9** (30.6 mg, 0.17 mmol) were dissolved in MeCN (30 ml) and stirred at room temperature for 12 h. Reaction progress was controlled by silica gel TLC to monitor the disappearance of the starting material **7** (eluent: DCM/MeOH, 9:1). **PAI (1)** was then isolated from the resulting solution by precipitation after adding a few drops of Et<sub>2</sub>O to the reaction mixture, filtered, further washed with Et<sub>2</sub>O (20 ml x 3), and dried under reduced pressure (53 mg, 81%).

<sup>1</sup>H NMR (400 MHz, CD<sub>3</sub>OD) δ 8.10 (d, *J* = 8.5 Hz, 2H), 8.02 (d, *J* = 8.5 Hz, 2H), 7.90 (dd, *J* = 5.6, 3.0 Hz, 2H), 7.85 (d, *J* = 8.5 Hz, 2H), 7.82 (dd, *J* = 5.6, 3.0 Hz, 2H), 7.75 (d, *J* = 8.5 Hz, 2H), 4.99 (t, *J* = 1.6 Hz, 2H), 4.74 (s, 2H), 4.64 (s, 2H), 4.41 (t, *J* = 9.6 Hz, 2H), 4.35 (t, *J* = 1.7 Hz, 2H), 3.84 (t, *J* = 6.3 Hz, 2H), 3.47 – 3.38 (m, 2H), 3.22 (s, 6H), 3.11 (s, 6H), 3.07 (t, *J* = 9.6 Hz, 2H), 2.37 – 2.24 (m, 2H). <sup>13</sup>C NMR (101 MHz, CD<sub>3</sub>OD) δ 169.79, 168.80, 163.40, 163.05, 162.71, 154.99, 154.83, 135.56, 135.28, 124.70, 124.54, 124.31, 88.78, 76.82, 71.22, 68.47, 67.39, 63.24, 58.29, 54.94, 50.90, 50.76, 35.65, 33.66, 23.51.

RT (HPLC-PDA) = 6.24 min (*cis*-isomer), 6.67 min (*trans*-isomer); purity ≥ 95% (**Figure S8.1**). MS (ESI, positive): *m/z* calculated for C<sub>36</sub>H<sub>42</sub>N<sub>6</sub>O<sub>4</sub><sup>2+</sup>: 311.16, found 311.1625 [M + H]<sup>+</sup>(**Figure S8.2**).

**Naphthalimide-Azo-Iperoxo, NAI (2)**



Compound **8** (10 mg, 0.015 mmol) and the isoxazoline **9** (4.03 mg, 0.022 mmol) were dissolved in MeCN (10 ml) and stirred at room temperature for 12 h. Reaction progress was controlled by silica gel TLC to monitor the disappearance of the starting material **8** (eluent: DCM/MeOH, 9:1). **NAI (2)** was then isolated from the resulting solution by precipitation after adding a few drops of Et<sub>2</sub>O to the reaction mixture, filtered, further washed with Et<sub>2</sub>O (20 ml x 3), and dried under reduced pressure (6.10 mg, 48%).

<sup>1</sup>H NMR (400 MHz, CD<sub>3</sub>OD) δ 8.58 (dd, *J* = 7.3, 1.1 Hz, 2H), 8.37 (dd, *J* = 8.4, 1.1 Hz, 2H), 8.11 (d, *J* = 8.4 Hz, 2H), 8.01 (d, *J* = 8.4 Hz, 2H), 7.89 (d, *J* = 8.4 Hz, 2H), 7.86 – 7.77 (m, 4H), 4.99 (s, 2H), 4.79 (s, 2H), 4.76 (s, 2H), 4.48 – 4.38 (m, 4H), 4.31 (s, 2H), 3.58 (s, 2H), 3.33 (s, 6H), 3.25 (s, 6H), 3.07 (t, *J* = 9.6 Hz, 2H), 1.42 (s, 6H). <sup>13</sup>C NMR (101 MHz, CD<sub>3</sub>OD) δ 168.82, 166.66, 155.00, 154.76, 135.79, 135.75, 135.41, 133.18, 132.66, 132.20, 131.85, 129.31,



128.26, 124.68, 124.46, 123.57, 88.70, 76.94, 74.28, 73.17, 71.23, 67.39, 58.35, 55.01, 52.53, 50.96, 50.48, 40.63, 33.69, 26.73.

HR-MS (ESI, positive):  $m/z$  calculated for  $C_{36}H_{42}N_6O_4^{2+}$ : 350.18, found 350.18630  $[M + H]^+$ .

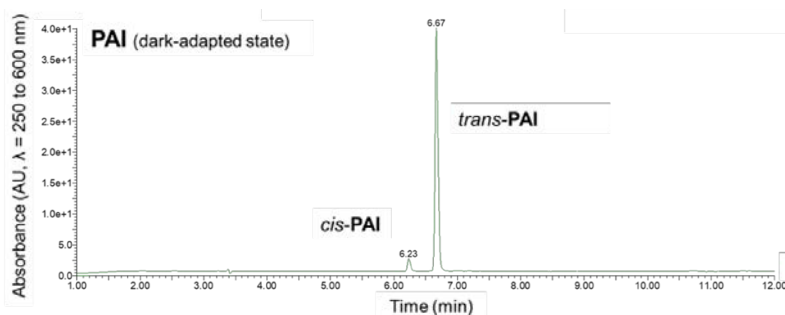


Figure S8.1. HPLC chromatogram of PAI as obtained under benchtop conditions (PDA detector from 250 to 600 nm; compound purity  $\geq 95\%$ ).

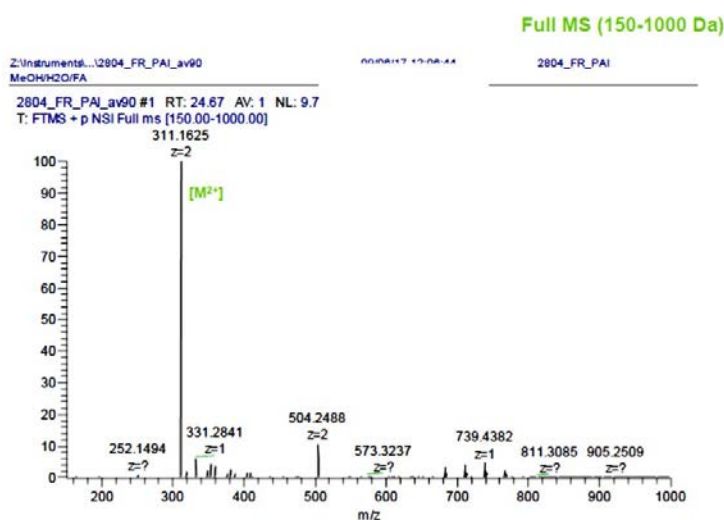


Figure S8.2. Full high-resolution mass spectrum of PAI (positive ionization).

## SI8.2 Photochemical characterization

An essential requirement for using **PAI** and **NAI** as light regulated  $M_2$  muscarinic acetylcholine receptor ( $M_2$  mAChR or  $M_2R$ ) agonists is that they effectively respond to light, which means that they can be quickly photoisomerized (from *trans*-to-*cis* and *vice versa*) between two different conformations with a relatively high degree of photoconversion (*trans/cis* ratio). To this end, we characterized **PAI** and **NAI** by UV-Vis spectroscopy.

**PAI** revealed a clear photochromic behavior with the typical absorption bands of azobenzenes. Maximum absorption peaks in aqueous solution were observed at around 315 nm and 430 nm and are due to the  $\pi-\pi^*$  and  $n-\pi^*$  transitions, respectively, which allows for distinct photoswitching between the *trans*- and *cis*-isomers (Figure S8.3A). **PAI** can be effectively

isomerized from *trans*-to-*cis* with ultraviolet (UV) light (365 nm), and back-isomerized from *cis*-to-*trans* with white or blue (460 nm) light. The process is reversible and can be repeated several times without any noticeable loss of photochromic behavior (**Figure S8.3B**).

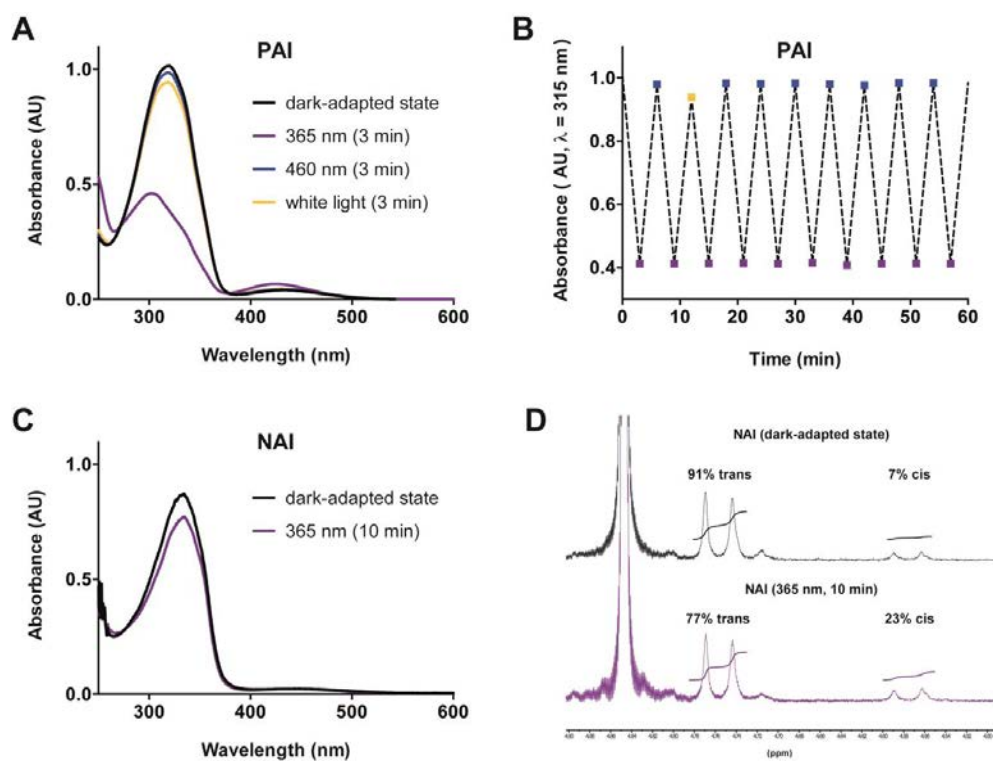


**Figure S8.3. Photochemical characterization of PAI and NAI.** (A) Absorption spectra of PAI in H<sub>2</sub>O (30 μM). (B) Reversibility and stability of the photochromic behavior of PAI over several cycles of isomerization. (C) Absorption spectra of NAI in H<sub>2</sub>O (30 μM). (D) Quantification of NAI photostationary state by <sup>1</sup>H-NMR analysis (800 μM in CD<sub>3</sub>OD), showing the ratio between the two isomers in the dark-adapted state and after illumination with 365 nm light (10 min).

Annoyingly, NAI resulted unusually refractory to photoisomerization than other azobenzene-containing compounds. We hypothesized that the absorption and emission properties of the naphthalimide moiety could interfere with the photoisomerization of the azobenzene unit (**Figure S8.3CD**).

We next quantified by <sup>1</sup>H-NMR and HPLC analysis the extent of photoisomerization for PAI (**Figure S8.4**). The amount of the thermodynamically less stable *cis*-isomer shifted from an initial value of 13% (as obtained under benchtop conditions) to 73% upon irradiation with 365 nm light for 10 min. Finally, we analyzed the thermal stability of the photostationary state (PSS) achieved after UV illumination. The PSS was relatively stable for at least 2 h in aqueous solution at 37°C in the dark. PAI could be rapidly reconverted to the *trans* state after

illumination with white light. Such thermal stability allowed us to conveniently study the two different photostationary states of PAI in a relatively large timescale (**Figure S8.5**).

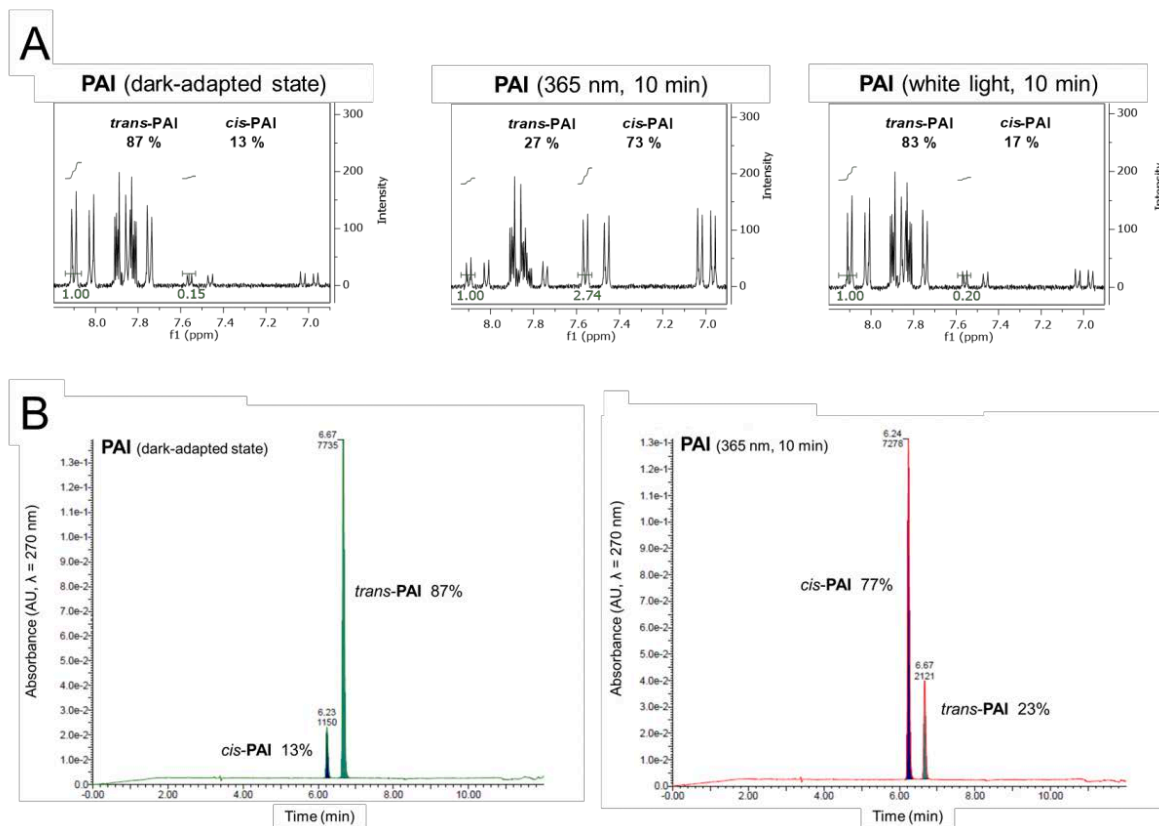


**Figure S8.4. Quantification of PAI photostationary state.** First by (A)  $^1\text{H-NMR}$  (800  $\mu\text{M}$  in  $\text{CD}_3\text{OD}$ ) and second by (B) HPLC analysis, showing the ratio between the two isomers as obtained under benchtop conditions and after 10 min of irradiation with 365 nm light and white light.

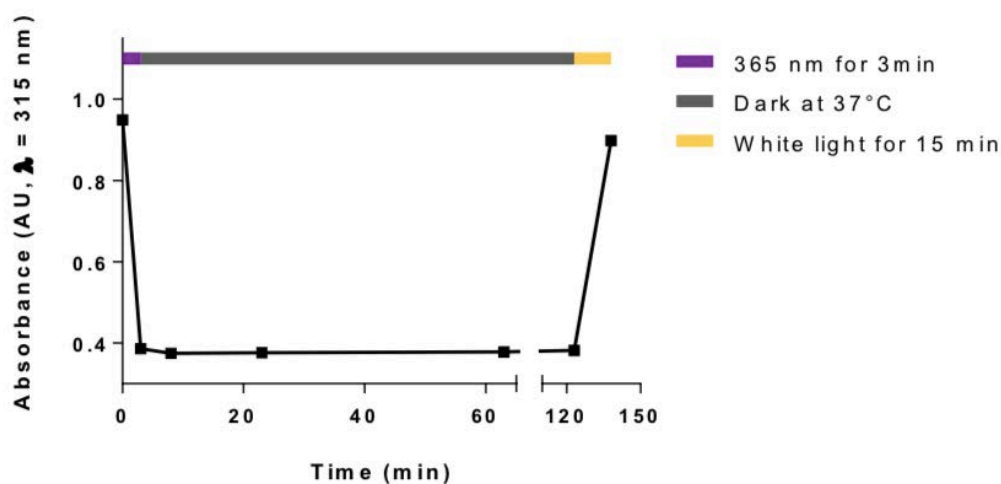


**Figure S8.5. Thermal stability of PAI.** The photostationary state achieved after irradiation with 365 nm light in aqueous solution (30  $\mu\text{M}$ ) is stable for more than 2 h at 37°C in the dark. Irradiation with white light allows to rapidly regain a PSS in favor of the *trans*-isomer.

## SI8.3 NMR spectroscopy

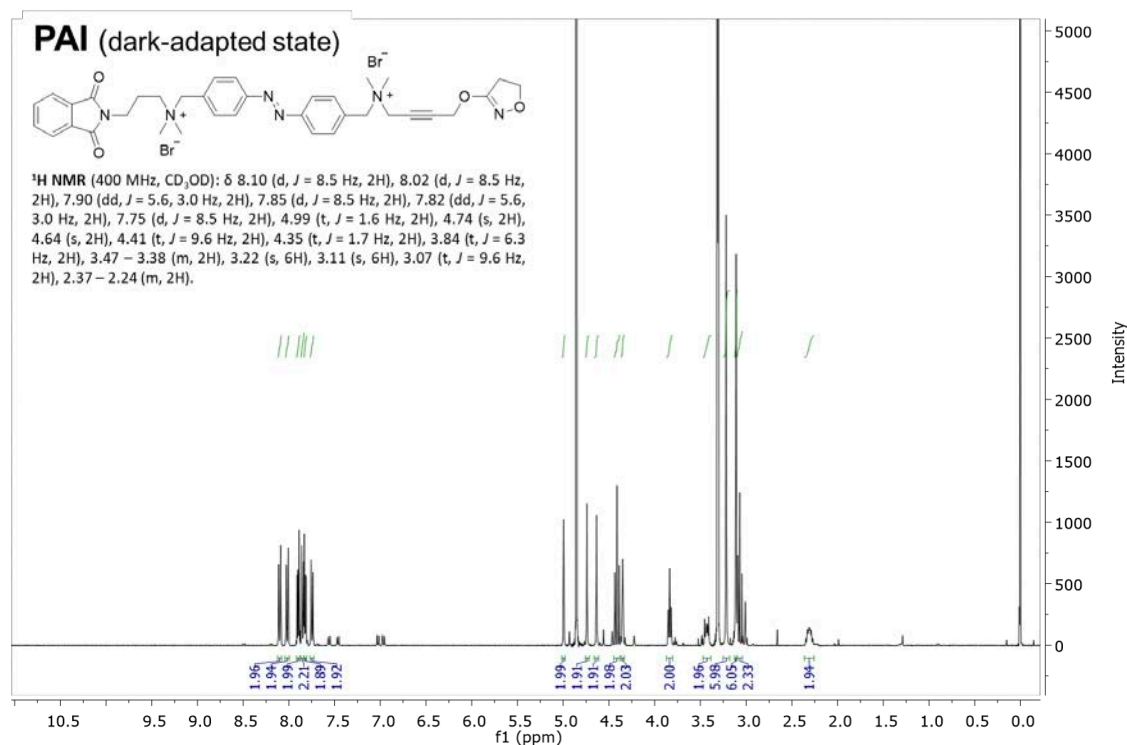


Figure S8.6. <sup>1</sup>H-NMR of PAI as obtained under benchtop conditions.

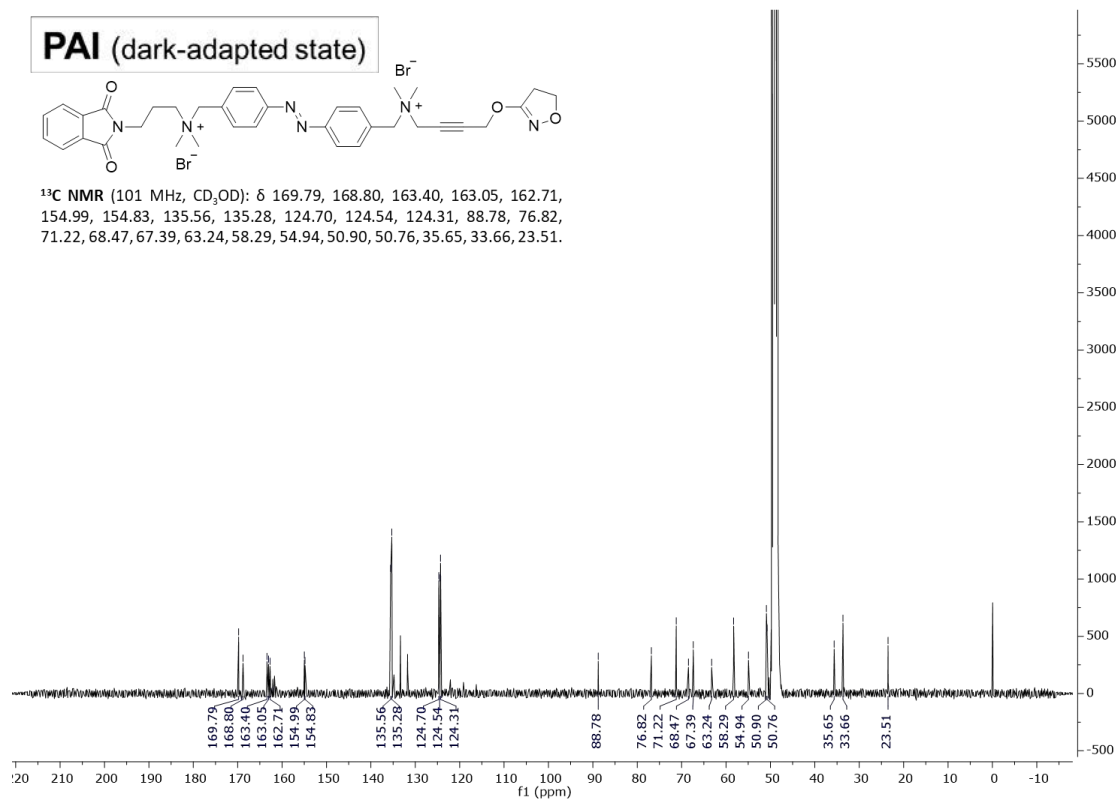


Figure S8.7. <sup>13</sup>C-NMR of PAI as obtained under benchtop conditions.

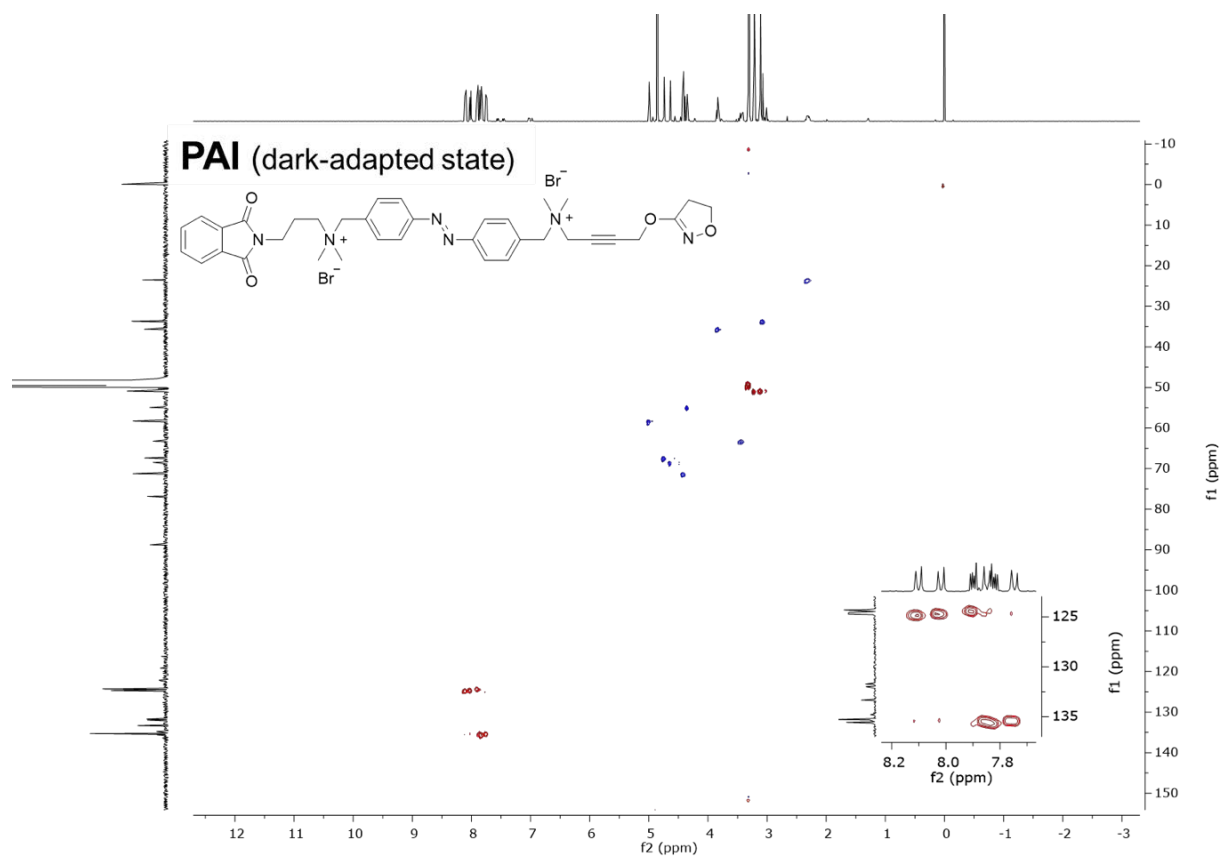


Figure S8.8. gCOSY of PAI as obtained under benchtop conditions.

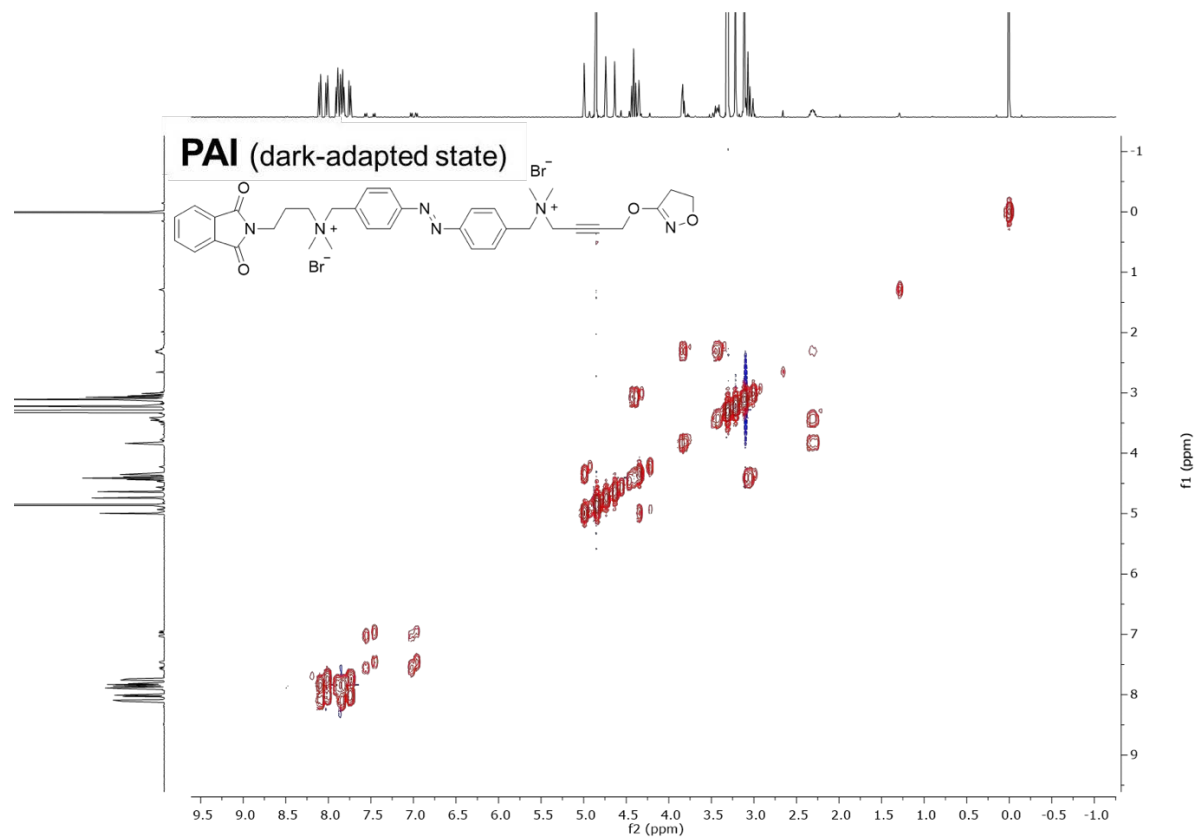


Figure S8.9. HSQC of PAI as obtained under benchtop conditions.

Supporting Information (SI) of Chapter 8: Optical control of cardiac function with photoswitchable muscarinic agonist

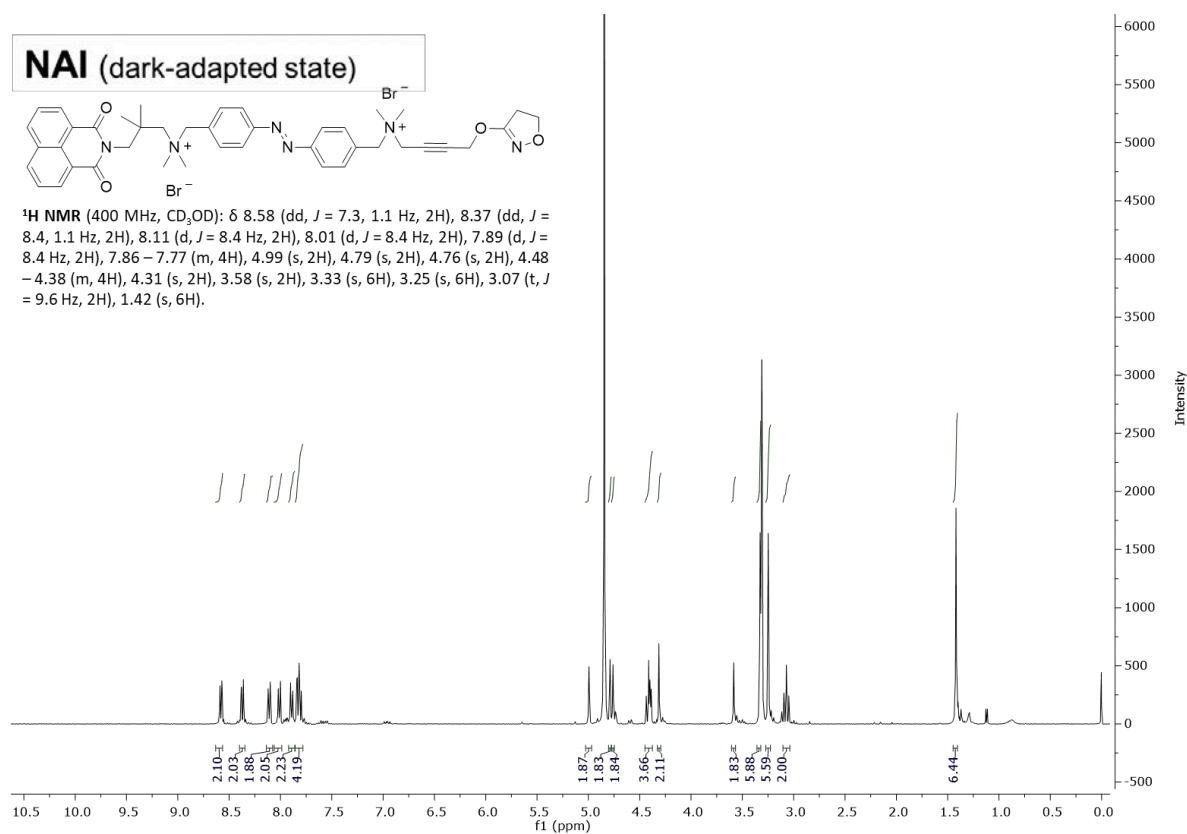


Figure S8.10. <sup>1</sup>H-NMR of NAI as obtained under benchtop conditions.

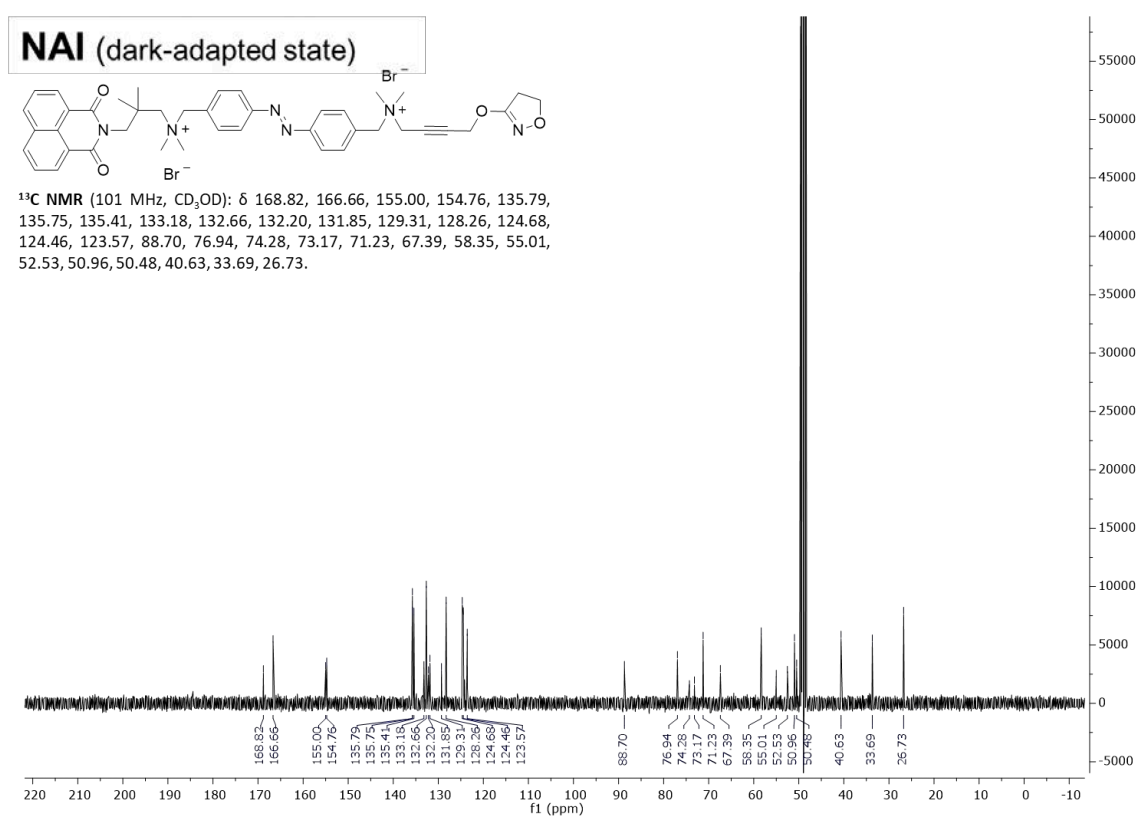


Figure S8.11. <sup>13</sup>C-NMR of NAI as obtained under benchtop conditions.

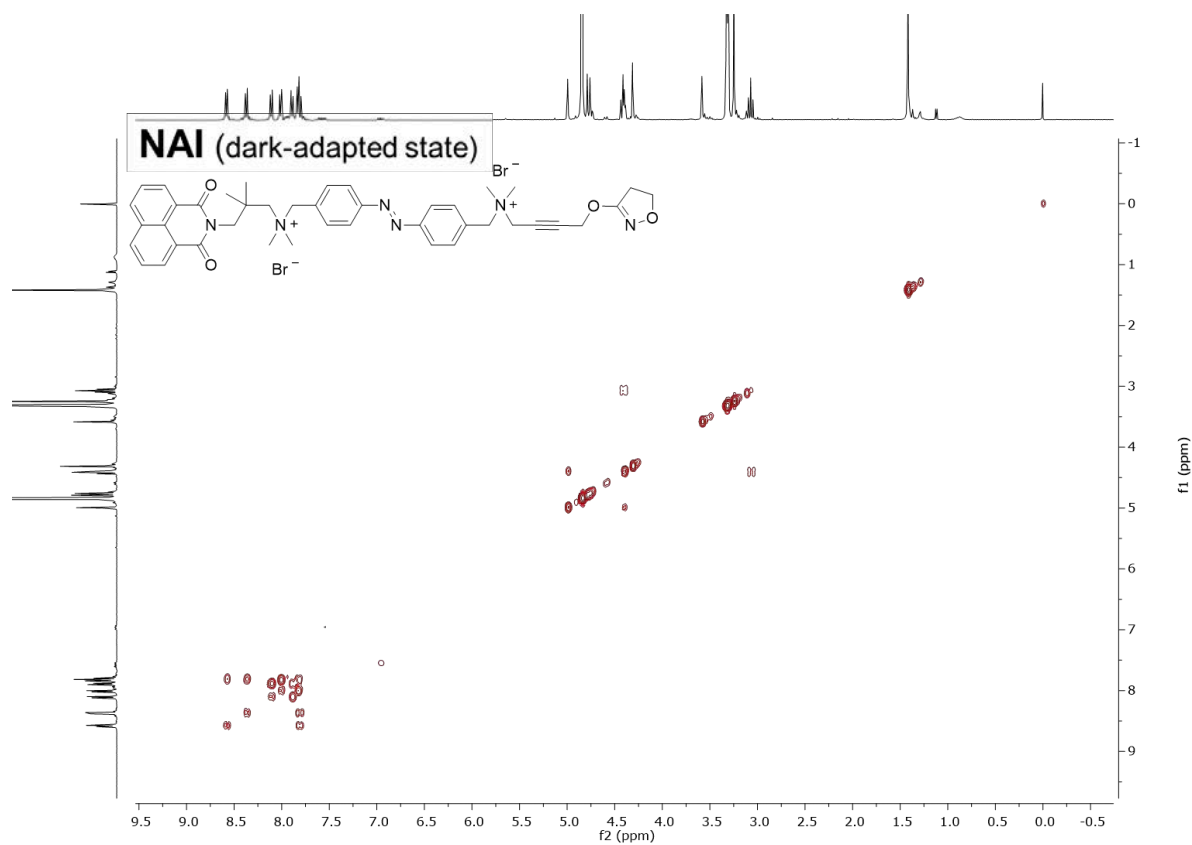


Figure S8.12. gCOSY of NAI as obtained under benchtop conditions.

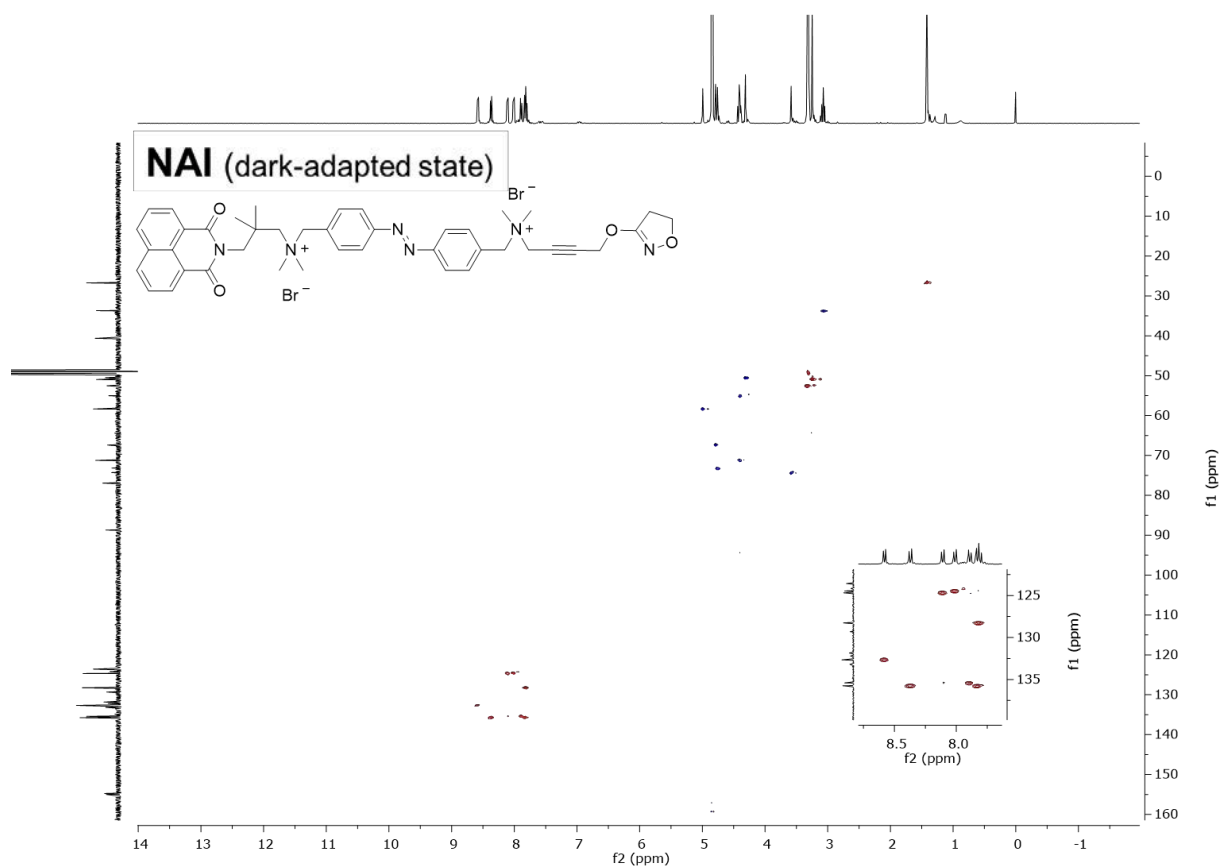


Figure S8.13. HSQC of NAI as obtained under benchtop conditions.

## **SI8.4 *In vitro* calcium imaging**

### **SI8.4.1 Materials and methods**

#### **SI8.4.1.1 Cell culture and transfection**

Human embryonic kidney tsA201 (HEK tsA201, American Type Culture Collection; ATCC) cells were maintained at 37°C in a humidified atmosphere with 5% CO<sub>2</sub> and grown in Dulbecco's Modified Eagle's Medium/Nutrient Mixture F-12 Ham (DMEM/F12 1:1, Life Technologies) medium, supplemented with 10% fetal bovine serum (FBS, Life Technologies) and antibiotics (1% penicillin/streptomycin, Sigma-Aldrich). Since M<sub>2</sub> mAChRs activate the G $\alpha_i$  protein subfamily, we co-transfected a chimeric G $\alpha_{q/i}$ -protein in order to couple M<sub>2</sub> mAChR activation to the phospholipase C pathway, thus inducing inositol 1,4,5-trisphosphate (IP<sub>3</sub>) production and subsequent intracellular calcium release from the endoplasmic reticulum. Co-expression of human M<sub>2</sub>R (Addgene) and chimeric G $\alpha_i$ /G $\alpha_q$  protein (G $\alpha_{qTOP}$ ) (ratio 1:1) was induced by plasmid transient transfection with X-tremeGENE 9 DNA Transfection Reagent (Roche Applied Science) following the manufacturer's instructions<sup>5</sup>. The day after transfection, cells were harvested with accutase (Sigma-Aldrich) and seeded onto 16-mm glass coverslips (ThermoFisher Scientific) pretreated with collagen (Sigma-Aldrich) to allow cell adhesion. Pre-confluent cultures were used for experiments between 48 h and 72 h after transfection.

#### **SI8.4.1.2 *In vitro* single-cell calcium imaging**

The bath solution used for single cell intracellular calcium recordings contained: 140 mM NaCl, 5.4 mM KCl, 1 mM MgCl<sub>2</sub>, 10 mM HEPES, 10 mM glucose and 2 mM CaCl<sub>2</sub>, and was adjusted to pH 7.4 with NaOH. Before each experiment, cells were mounted on the recording chamber (Open Diamond Bath Imaging Chamber for Round Coverslips from Warner Instruments) and loaded with the calcium indicator Oregon Green BAPTA-1 AM (OGB-1 AM; Life Technologies) for 30 min at 37°C and 5% CO<sub>2</sub>, at a final concentration of 10  $\mu$ M in Ca<sup>2+</sup>-free bath solution. Cells were rinsed with fresh solution, and the recording chamber was filled with 1 ml recording solution. Calcium imaging was performed on an IX71 inverted microscope (Olympus) with a XLUMPLFLN 20XW x20/1-NA water immersion objective (Olympus).

OGB-1 AM was excited during 8 ms at 488 nm using a Polychrome V monochromic light source (Till Photonics) equipped with a Xenon Short Arc lamp (Ushio Europe B.V.) and a 505 nm dichroic beam splitter (Chroma Technology). Emission at 526 nm was filtered by a



D535/40nm emission filter (Chroma Technology) and finally collected by a C9100-13 EM-CCD camera (Hamamatsu Photonics).

Images under 1P-illumination were acquired at room temperature with an imaging interval of 4 s with the SmartLux software (HEKA), and the imaging analysis was done with FIJI (NIH, ImageJ).

Images under 2P-illumination were acquired at room temperature with an inverted laser-scanning confocal microscope (TCS SP5, Leica Microsystems) equipped with a HCX PL APO 40×/1.25-0.75-NA oil objective for imaging cultured cells, and a HC PL APO 20×/0.7-NA CS air objective (Leica Microsystems). The imaging interval was of 4 s. Acquired image sequences were stored in the Leica image format and stacks for offline analysis with Fiji (NIH, ImageJ).

### SI8.4.1.3 Drug application and photoswitching assays

Addition of agonists was carried out by carefully pipetting 50 µl of the initial 200 pM solution of the compound directly into the accessory pool of the recording chamber for a final dilution of approximately 1:20.

IPX, a previously described muscarinic selective superagonist<sup>2</sup>, was used as a positive control to stimulate mAChRs in HEK tsA201 cells (30 pM).

Photostimulation under 1P-excitation during recordings was done by illumination of the entire focused field using the Polychrome V connected to a personal computer, and shutter and wavelength were controlled using Patchmaster software (HEKA). Light intervals lasted a total of 5 minutes for all the HEK cell experiments, with flashes of blue (460 nm, 3.5 s duration) and UV (365 nm, 3.5 s duration) light. The light power measured with a Newport 1916-C light meter placed after the objective was 16.48 W·m<sup>-2</sup> for 488 nm, 4.94 W·m<sup>-2</sup> for 365 nm, and 15.92 W·m<sup>-2</sup> for 460 nm.

2P-excitation experiments were performed in the Advanced Digital Microscopy Core Facility of IRB with a confocal multiphoton microscope equipped with a pulsed broadband Ti:Sapphire laser (Mai Tai, Spectra-Physics, Santa-Clara, CA-USA) which can be tuned from 710-990 nm (80 MHz repetition rate, 80 fs pulse, light power 2.8 mW µm<sup>-2</sup> at 720–840 nm).

## SI8.4.2 Control experiments

In order to assess the significance of PAI (photo)responses in M<sub>2</sub> mAChR expressing cells (Figure 8.3), further control experiments were performed in transfected cells in absence of PAI

(Figure S8.14). No responses were observed under illumination at 365 nm and 460 nm which excludes any response artifacts due to light stimuli alone.

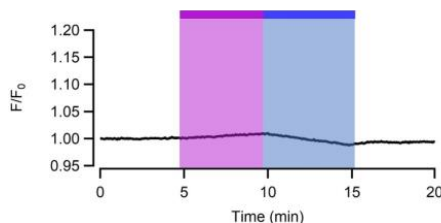


**Figure S8.14.** Real time calcium imaging traces from HEK cells incubated with 10  $\mu$ M of OGB-1AM for 30 min. The diagrams show the average trace of cells expressing M<sub>2</sub>R-G $\alpha$ <sub>qTOP</sub> in response to illumination at 365 nm (purple bar) and 460 nm (blue bar) ( $n = 34 \pm$  SEM).

### SI8.4.3 Receptor activation efficacy

Direct *cis*-PAI isomer application at 10 pM induce a response 50% lower than direct application of *trans*-PAI isomer. Application of the *cis*-isomer at 30 pM induced a response 10-fold lower compared to the *trans*-isomer response at the same concentration (Figure S8.15). Moreover, residual responses upon application of the *cis*-isomer can be attributed to the incomplete photoisomerization of the *trans*-isomer (*trans/cis* = 23:77 after 10 min at 365 nm).

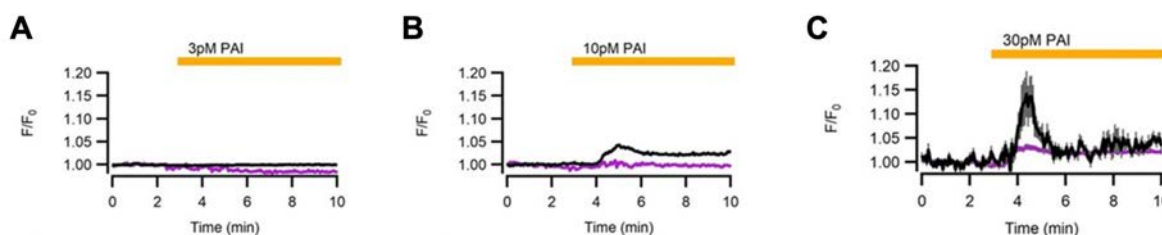


**Figure S8.15.** Real time calcium imaging traces from HEK cells expressing M<sub>2</sub>R-G $\alpha$ <sub>qTOP</sub> incubated with OGB-1 AM (10  $\mu$ M for 30 min). (A) Average trace of cell response induced by the direct application of 3 pM PAI (yellow bar) in its *trans* form (black line;  $n = 167$ ) or its *cis* form (purple line;  $n = 150$ ). (B) Average trace of cell response induced by the direct application of 10 pM PAI in its *trans* form (black line;  $n = 296$ ) or its *cis*-isoform (purple line;  $n = 150$ ). (C) Average trace of cell response to 30 pM PAI in its *trans* isoform (black line;  $n = 8$ ) or its *cis* form (purple line;  $n = 230$ ). Gray shadow in the recording represents  $\pm$  SEM.

### SI8.4.4 Receptor subtype selectivity

By comparing amplitude of calcium signal response of cells expressing M<sub>2</sub>R-G $\alpha$ <sub>qTOP</sub> or the M<sub>1</sub> muscarinic acetylcholine receptor (M<sub>1</sub> mAChR or M<sub>1</sub>R) in presence of *trans*-PAI (10 pM), the receptor subtype-selectivity of PAI (M<sub>2</sub>Rs against M<sub>1</sub>Rs) has been studied. Human M<sub>1</sub> mAChR (Addgene) was transfected as described in the Materials and methods section of the main text. M<sub>2</sub> mAChR transfected cells gave a significantly higher response than M<sub>1</sub> mAChR expressing cells (8% for M<sub>1</sub>R against 33% for M<sub>2</sub>R). Data were normalized over the maximum response

obtained with the nonselective orthosteric superagonist IPX at 30 pM. (*t*-test of two samples assuming equal variances *p*-value = 0.00158).

## SI8.5 Molecular docking simulations

### SI8.5.1 Materials and methods

Molecular docking simulations were performed using the crystal structure of the human M<sub>2</sub> mAChR retrieved from the Protein Data Bank (PDB ID: 4MQT, chain A)<sup>6</sup>. To allow the docking of the dualsteric ligands into the active M<sub>2</sub> mAChR structure, the so called “tyrosine lid”<sup>7,8</sup> was remodeled using rotamer libraries (UCSF Chimera)<sup>9</sup> of the tyrosine residues involved (Tyr-104, Tyr-403, Tyr-426). The protein pdb file was then prepared for docking by removing co-crystallized ligands, non-complexed ions and water molecules, and finally applying the Dock Prep tool available in the free software package UCSF Chimera. This involved the addition of hydrogens and assigning partial charges (AMBER ff14SB method). The structures of *trans*- and *cis*-PAI were built with standard bond length and angles using ChemDraw and then energy minimized with Chem3D by the MM2 method. The minimized compounds were further prepared for docking studies with UCSF Chimera by adding hydrogens and assigning partial charges (AMBER ff14SB method). The necessary pdbqt files of ligands and receptor were prepared using AutoDock 4.2 software. The docking studies were carried out using the standard docking protocol applied for AutoDock Vina in PyRx 0.8 virtual screening software. Autodock Vina has been reported to be an effective tool capable of quickly and accurately predicting bound conformations and binding energies of ligands with macromolecular targets<sup>10,11</sup>. A grid box of size 10.08 × 27.44 × 28.96 Å, with x, y and z coordinates of -2.98, -11.92 and -12.00, respectively, was fixed to cover the entire allosteric and orthosteric binding sites and accommodate the ligands to move freely. Docking studies were performed using an exhaustiveness value of 8 while all other parameters were maintained as defaults. All rotatable bonds within the ligands were allowed to rotate freely, and the receptor was considered rigid. The docking simulations were repeated three times for each ligand. The obtained poses were then ranked based on the predicted affinity docking scores (kcal/mol) and the best pose for each experiment was selected. The results were then analyzed using UCSF Chimera.

### SI8.5.2 Results and discussion

We used molecular docking simulations in an attempt to rationalize the photoswitchable efficacy of PAI. Both isomers of the ligand were docked into their putative allosteric and

orthosteric binding sites of the human M<sub>2</sub> mAChR in its active conformation (PDB ID: 4MQT, chain A). As previously reported<sup>7</sup>, molecular docking of dualsteric ligands into the M<sub>2</sub> mAChR required remodeling of the tyrosine lid (formed by Tyr-104, Tyr-403 and Tyr-426) which separates the orthosteric binding site from the allosteric binding site in the active conformation of the protein. To open this lid and put the two binding sites in communication, we selected different allowed conformers of each side chains while keeping all the other residues in their original position. Therefore, the only differences between the crystal structure and the obtained active-like receptor model were the side chain conformations of Tyr-104, Tyr-403 and Tyr-426. *Trans*-PAI and *cis*-PAI were docked at this receptor model using a standard docking protocol with AutoDock Vina in the PyRx 0.8 software with a suitable grid box. We ran three simulations for each ligand and selected the best pose obtained in each experiment based on the predicted binding affinity scores (kcal/mol). Best poses were superimposed into the M<sub>2</sub>R model in the presence of the reference agonist IPX (in its receptor-bound conformation) and analyzed using UCSF Chimera. The results of our *in silico* studies are presented in **Table S8.1** and **Figure S8.16**.

In IPX, key binding elements for agonist activity are (1) the positively charged nitrogen, which interacts with Asp-103 and displays  $\pi$ -cation interactions with Tyr-104, Tyr-403 and Tyr-426, (2) the triple bond, which exhibits hydrophobic contacts with Tyr-104, Trp-155 and Trp-400, and additionally (3) the oxygen of the 4,5-dihydroisoxazole moiety, which forms a hydrogen bond with Asn-404<sup>8</sup>. Our simulations revealed a dualsteric binding topography of PAI in both configurations. The IPX moiety of *trans*-PAI binds to the orthosteric binding site, with an orientation close to that observed for IPX in the receptor-bound crystal structure and the key elements for agonist activity lying in proximity of those of the reference agonist, whereas the phthalimide moiety protrudes toward extracellular domains, likely engaging residues of the common allosteric binding site (**Figure S8.16A**). In agreement with our results, *trans*-PAI could therefore bind to the M<sub>2</sub> mAChR in a dualsteric pose capable of inducing receptor activation. In contrast, *cis*-PAI appeared to bind preferentially in a flipped orientation, with the phthalimide group pointing out towards the orthosteric binding pocket and the 4,5-dihydroisoxazole moiety positioned in the allosteric binding site. Such a binding mode is not likely to form an active ligand-receptor complex and may justify the difference observed in terms of agonist efficacy between the two photo-isomers (**Figure S8.16B**).

Experiment number	Binding affinity (kcal/mol)	
	<i>trans</i> -PAI (best pose)	<i>cis</i> -PAI (best pose)
1	-11.6	-12.0
2	-11.6	-11.8
3	-11.3	-11.6

Table S8.1. Binding affinity scores of the best poses for each of the docking studies performed with *trans*- and *cis*-PAI.

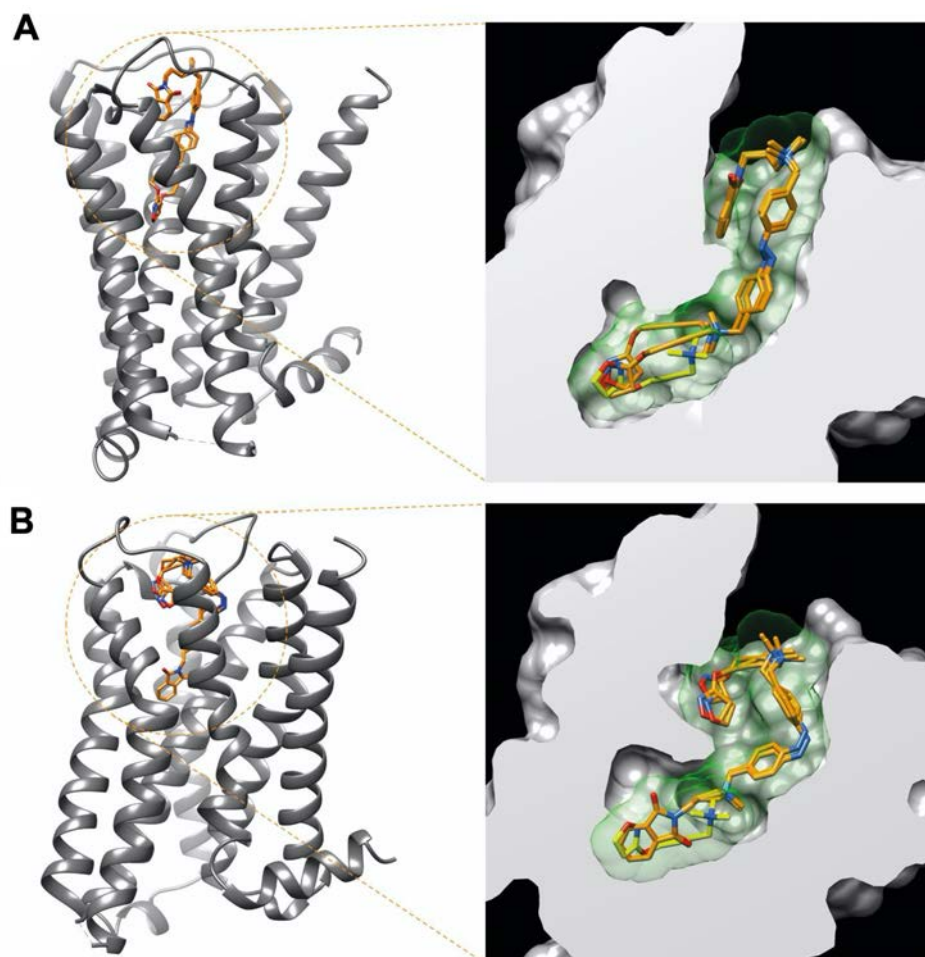


**Figure S8.16. Hypothetical binding mode of *trans*-PAI and *cis*-PAI to a M<sub>2</sub> mAChR model in its active state.** Panels (A) and (B) show a full view (left side, ribbon-style representation) and a zoomed view (right side, hydrophobicity surface representation with sectioning) of the simulated ligand-receptor complexes. The reference orthosteric agonist IPX, in yellow, appears in its receptor-bound conformation. *Trans*- and *cis*-PAI are represented in orange. Nitrogen and oxygen atoms of the ligands are colored in blue and red, respectively. Our simulations revealed a dualsteric binding topography of PAI for both configurations, but, while the *trans*-isomer seems to bind preferentially in an iperoxo-like binding pose (A), which is likely able to trigger receptor activation, the *cis*-isomer shows preference for a flipped orientation (B), which might be not compatible with the formation of active ligand-receptor complexes.

## SI8.6 *In vivo* experiments in rats

### SI8.6.1 Materials and methods

*In vivo* effects of **PAI** in both configurations (*trans* and *cis*) were further tested in male Wistar rats (400-500 g) under inhaled anesthesia (isoflurane 1.5%) and maintained at  $37 \pm 0.3^\circ\text{C}$  with a homothermic pad (Kent Scientific). All animals had a continuous electrocardiogram (ECG) obtained (lead II) and recorded for later offline analyses (PowerLab and LabChart v.8.1.2, ADInstruments). Analyses were performed in a blinded manner.

Nine rats were randomly assigned to receive cumulative doses of either predominantly *trans*- (“*trans*” group,  $n = 5$ ) or *cis*-isomer (“*cis*” group  $n = 4$ ) **PAI**. A single stock solution was used for all experiments, and dilutions were prepared just prior to each experiment. In the “*cis*” group, a vial containing 1 ml of **PAI** solution was irradiated with UV-light lamp (365 nm) in a custom-made closed chamber for 5 min, and thereafter administered intraperitoneally in dark conditions. Two animals (one for each “*cis*” and “*trans*” groups) were initially used to delimitate the effective dose range, which was found to be in the range of 100 nM/kg – 100  $\mu\text{M}/\text{kg}$  (results not shown). Subsequently, the following **PAI** doses were intraperitoneally administered at 7 min intervals in the remaining rats: 100 nM/kg; 300 nM/kg; 1  $\mu\text{M}/\text{kg}$ ; 3  $\mu\text{M}/\text{kg}$ ; 10  $\mu\text{M}/\text{kg}$ ; 30  $\mu\text{M}/\text{kg}$ ; 100  $\mu\text{M}/\text{kg}$ .

The heart rate ( $\text{beats}\cdot\text{min}^{-1}$ ) and the PR interval (ms) were measured offline to assess the parasympathetic effect of both **PAI** isomers (LabChart v.8.1.2, ADInstruments). A one-minute recording (from minute 5’30” to minute 6’30” after each dose administration) of stable ECG was analyzed. Heart rate and the PR interval were automatically determined, manually reviewed for accuracy, and modified if needed. Second degree Wenckebach atrio-ventricular block and subsequent complete block occurred in one rat receiving the 30  $\mu\text{M}/\text{kg}$  dose and one rat receiving the 100  $\mu\text{M}/\text{kg}$  dose, and were excluded from PR interval measurements. Results are shown as difference to the baseline value ( $\Delta$ ).

In order to test that parasympathetic activity was driving heart rate and PR-interval changes, and to assess its reversibility, atropine (two 1 mg doses separated by 5-7 min) was administered to one rat per group. A representative profile of a full experiment is shown in **Figure S8.17**.

### SI8.6.1.1 Data analysis and statistics

*In vivo* data is shown in boxplots, because some rats died after the administration of high doses of the active isomer *trans*-PAI, a maximum effect asymptotic value was not reached and a formal dose-response curve could not be built. Therefore, analyses were carried out with a two-way ANOVA in which two main factors (Isomer, Dose) and their interaction (Isomer x Dose) were included. In the case of a significant interaction, pairwise comparisons (Isomer effect at each Dose) were performed with the LSD test.

## SI8.7 *In vivo* experiments in *Xenopus tropicalis* tadpoles

### SI8.7.1 Materials and methods

African clawed frogs constitute an excellent animal model for behavioral, gene and electrophysiological studies<sup>12,13</sup>, and a powerful tool for drug discovery and preclinical animal testing<sup>14</sup>. In addition, they are especially suitable for heart monitoring since tadpoles are transparent until stages 48-50<sup>15</sup> and, in contrast to fish, their three-chamber heart is an excellent model for studying the human cardiovascular system<sup>16,17</sup>.

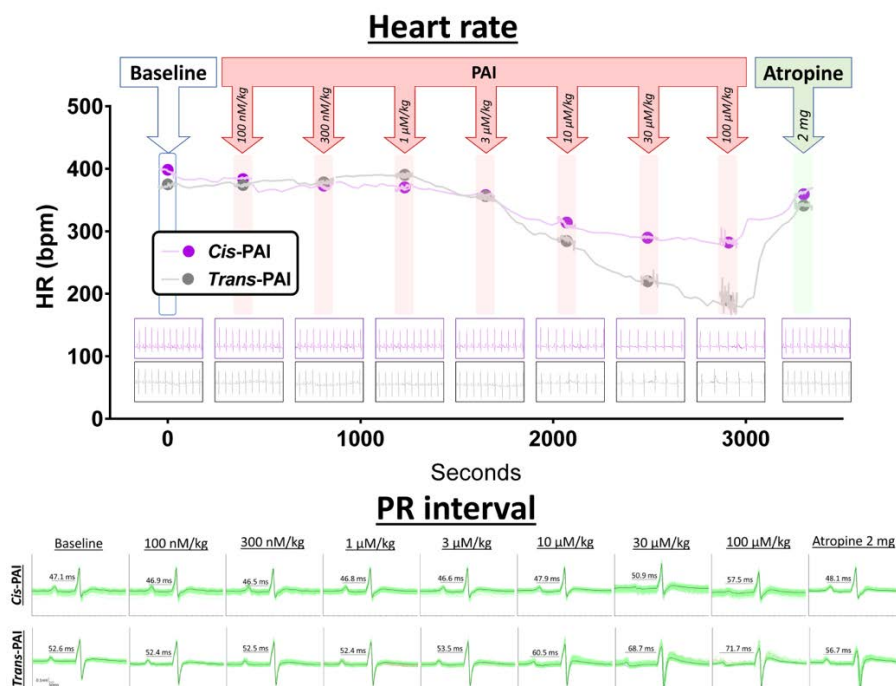


**Figure S8.17. Representative profile of the heart rate (upper panel) and the PR interval (lower panel) in two rats receiving increasing doses of PAI (*trans* or *cis* form), and atropine.** Heart rate is averaged every second in shadowed areas in the upper panel; in between doses, heart rate is averaged every 30 s.

### SI8.7.1.1 Animal housing

*Xenopus tropicalis* embryos (Nasco) were obtained by natural mating and maintained till 3-4 days post fertilization (dpf) in 0.1X Marc's modified Ringer's (MMR) solution in agarose coated petri dishes (10-15 cm diameter) in a dark incubator (24°C). Animals were transferred to tanks containing *Xenopus* water, which was prepared by adding 8 g of instant ocean salt (Instant Ocean) to 20 l of distilled water. Conductivity and pH were 700  $\mu\text{s}$  and 7.4-7.5, respectively. Tadpoles were kept at a density of 30-50 animals L<sup>-1</sup>, at 24°C and fed daily with spirulina. All procedures complied with the standards of the ethical commission of the University of Barcelona (UB, Barcelona, Spain). *Xenopus tropicalis* tadpoles (developmental stages 44-48 according to Nieuwkoop and Faber)<sup>15</sup> were paralyzed in 0.23 mM of Pancuronium dibromide solution (PCD) (Merck, Cat no. P1918) for 10 min and placed into a 48-well plate (Nunc™Microwell™) with 200  $\mu\text{l}$  of 0.1X solution of MMR-CaCl<sub>2</sub> (referred as BS from now on). PCD was preferred to tricaine because of its higher cardiac tolerability and non-UV dependent effects<sup>17</sup>.

### SI8.7.1.2 Cardiac activity measurements

Video recordings of tadpole hearts were performed using a Nikon Eclipse TS100 microscope equipped with an OptixCam Summit Series OCS-D3K2-5 camera, which substantially improved the resolution of the previously reported setup<sup>18</sup>. In order to prevent unintended *cis*-to-*trans* isomerisation of photoswitchable compounds, the microscope top-down light pathway was dimmed with a red plastic filter, which could be placed or removed during experimentation. Video recordings were acquired using the TouView software, enhancing visual contrast to improve cardiac imaging and video streams were converted to the AVI format. Recordings were briefly interrupted during compound addition and changes of illumination conditions. Video information and data analysis were extracted and executed with custom scripts based on ImageJ<sup>19</sup> for AVI files analysis and subsequently converted to the TXT format for R software analysis<sup>20</sup>.

The illumination protocol established for control and treatment video recordings applied the following procedure: one minute dimmed red light (650 nm, 34.0 W·m<sup>-2</sup>), 3 min under UV (365nm, 2.3 W·m<sup>-2</sup>) due to the required exposure time for a complete *trans*-to-*cis* isomerisation, 2 min dimmed red light and one minute under visible light (455 nm, 169.8 W·m<sup>-2</sup>) for *cis*-to-*trans* back isomerisation.



Tadpoles ( $n = 4$ ) were firstly paralyzed with PCD as previously described, placed in the BS and video recorded under the established protocol of illumination in the absence of PAI to monitor the effect of the light on cardiac activity and verify control conditions. Afterwards, animals were placed into a  $10 \mu\text{M}$  PAI solution and underwent the same protocol of illumination to observe the light-dependent effects of the drug.

### SI8.7.1.3 Data analysis and statistics

Heart beating movies were converted to a linear signal by selecting a region of interest displaying large periodic variations corresponding to heart movements and calculating the corresponding grey scale level as a function of time (Figure 8.5A-D). The cardiac rate ( $\text{beats} \cdot \text{s}^{-1}$ ) was calculated from this linear signal from the number of maxima every 15 s (red plots in Figure 8.5E). To statistically compare between different illumination periods and drug conditions, the cardiac rate was calculated from the last 30 s of every period. The stability of cardiac rhythm in each period was quantified with a unit-less variability score as the number of video frames between heartbeats. High scores correspond to longer periods with asynchronic or arrested cardiac activity. Perfectly steady rate in the absence of PAI yields a variability score of 8 (Figure S8.19).

Statistical analyses were carried out with a two-way repeated measures ANOVA with uncorrected Fisher's Least Significant Differences (LSD) test in which two main factors (heart beats per second,  $10 \mu\text{M}$  of PAI) and their interaction (heart beats per second  $\times$   $10 \mu\text{M}$  of PAI) were included (Figure 8.5F).

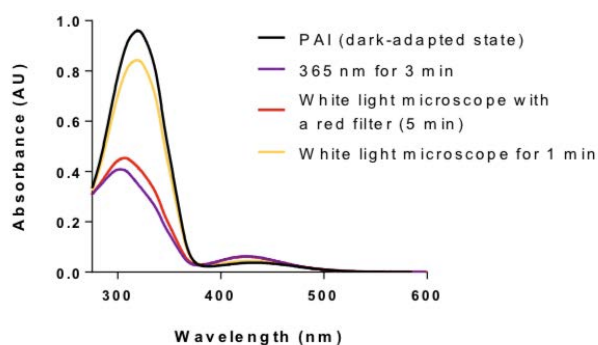


**Figure S8.18. Validation of the photochromic behavior of PAI under the illumination conditions used for our *in vivo* experiments in *Xenopus tropicalis* tadpoles.** PAI could be effectively isomerized to *cis* under illumination with 365 nm light (external source) and back-isomerized to *trans* using unfiltered microscope white light (100% intensity), whereas the *cis*-enriched photostationary state could be satisfactorily maintained when the microscope light was filtered with a common red polycarbonate filter.

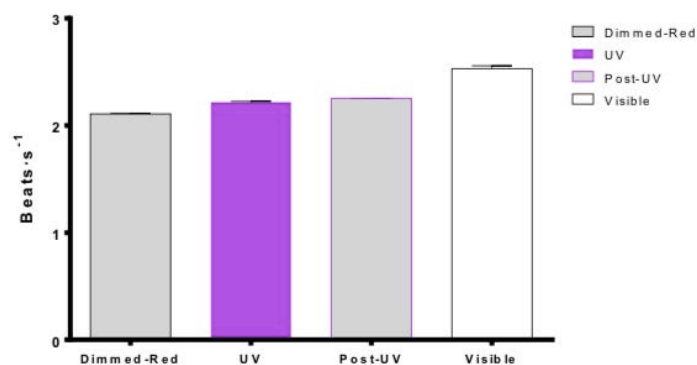


Figure S8.19. Cardiac activity (beats per second) recorded under different conditions of illumination in absence of PAI (control experiment). Error bars represent SEM (n = 4).

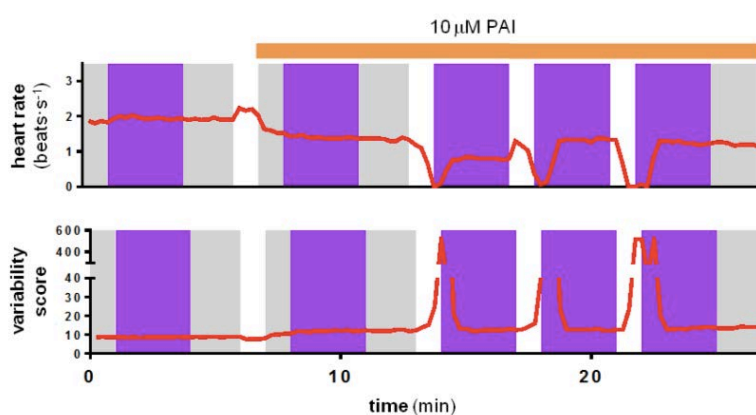


Figure S8.20. Example trace of cardiac rate from one animal in Figure 8.4 (top) and corresponding variability score calculated as the number of video frames between heartbeats (averaged every 15 s). Although the first exposure to 10 μM *trans*-PAI did not immediately reduce the heart rate of this animal, subsequent cycles of UV/white light in the presence of PAI reversibly switched the heartbeat on and off. Reduced heart rate was associated with longer periods displaying unstable, asynchronous cardiac activity and thus a higher variability score.

## Additional references

- 1 Dallanoce, C. *et al.* Synthesis and functional characterization of novel derivatives related to oxotremorine and oxotremorine-M. *Bioorg Med Chem* **7**, 1539-1547, doi:10.1016/s0968-0896(99)00107-8 (1999).
- 2 Kloeckner, J. S., J.; Holzgrabe, U. Convergent, short synthesis of the muscarinic superagonist iperoxo. *Tetrahedron Letters* **51**, 3470-3472, doi:10.1016/j.tetlet.2010.04.130. (2010).
- 3 Disingrini, T. *et al.* Design, synthesis, and action of oxotremorine-related hybrid-type allosteric modulators of muscarinic acetylcholine receptors. *J Med Chem* **49**, 366-372, doi:10.1021/jm050769s (2006).
- 4 Velema, W. A., van der Toorn, M., Szymanski, W. & Feringa, B. L. Design, synthesis, and inhibitory activity of potent, photoswitchable mast cell activation inhibitors. *J Med Chem* **56**, 4456-4464, doi:10.1021/jm400115k (2013).
- 5 Gomeza, J. *et al.* Coupling of metabotropic glutamate receptors 2 and 4 to G $\alpha_{15}$ , G $\alpha_{16}$ , and chimeric G $\alpha_{qi}$  proteins: Characterization of new antagonists. *Mol Pharmacol* **50**, 923-930 (1996).
- 6 Kruse, A. C. *et al.* Activation and allosteric modulation of a muscarinic acetylcholine receptor. *Nature* **504**, 101-106, doi:10.1038/nature12735 (2013).
- 7 Antony, J. *et al.* Dualsteric GPCR targeting: A novel route to binding and signaling pathway selectivity. *FASEB J* **23**, 442-450, doi:10.1096/fj.08-114751 (2009).
- 8 Bock, A. *et al.* Ligand binding ensembles determine graded agonist efficacies at a G protein-coupled receptor. *J Biol Chem* **291**, 16375-16389, doi:10.1074/jbc.M116.735431 (2016).
- 9 Pettersen, E. F. *et al.* UCSF Chimera--a visualization system for exploratory research and analysis. *J Comput Chem* **25**, 1605-1612, doi:10.1002/jcc.20084 (2004).
- 10 Morris, G. M. *et al.* AutoDock4 and AutoDockTools4: Automated docking with selective receptor flexibility. *J Comput Chem* **30**, 2785-2791, doi:10.1002/jcc.21256 (2009).
- 11 Dallakyan, S. & Olson, A. J. Small-molecule library screening by docking with PyRx. *Methods Mol Biol* **1263**, 243-250, doi:10.1007/978-1-4939-2269-7\_19 (2015).
- 12 Grainger, R. M. *Xenopus tropicalis* as a model organism for genetics and genomics: Past, present, and future. *Methods Mol Biol* **917**, 3-15, doi:10.1007/978-1-61779-992-1\_1 (2012).
- 13 Burggren, W. W. & Warburton, S. Amphibians as animal models for laboratory research in physiology. *ILAR J* **48**, 260-269, doi:10.1093/ilar.48.3.260 (2007).
- 14 Schmitt, S. M., Gull, M. & Brandli, A. W. Engineering *Xenopus* embryos for phenotypic drug discovery screening. *Adv Drug Deliv Rev* **69-70**, 225-246, doi:10.1016/j.addr.2014.02.004 (2014).
- 15 Nieuwkoop, P. D. F., J. Normal table of *Xenopus laevis* (Daudin): A systematical and chronological survey of the development from the fertilized egg till the end of metamorphosis. *Garland Science*, 282 (1994).
- 16 Boppart, S. A. *et al.* Noninvasive assessment of the developing *Xenopus* cardiovascular system using optical coherence tomography. *Proc Natl Acad Sci U S A* **94**, 4256-4261, doi:10.1073/pnas.94.9.4256 (1997).
- 17 Bartlett, H. L., Scholz, T. D., Lamb, F. S. & Weeks, D. L. Characterization of embryonic cardiac pacemaker and atrioventricular conduction physiology in *Xenopus laevis* using noninvasive imaging. *Am J Physiol Heart Circ Physiol* **286**, H2035-2041, doi:10.1152/ajpheart.00807.2003 (2004).

- 18 Eckelt, K. M., H.; Llobet, A.; Gorostiza, P. Automated high-throughput measurement of bodymovements and cardiac activity of *Xenopus tropicalis* tadpoles. *Journal of Biological Methods* **1(2)**, e9, doi:10.14440/jbm.2014.29 (2014).
- 19 Schindelin, J. *et al.* Fiji: An open-source platform for biological-image analysis. *Nat Methods* **9**, 676-682, doi:10.1038/nmeth.2019 (2012).
- 20 A language and environment for statistical computing (2016).



# Chapter 9

---

## Three-photon infrared stimulation of endogenous neuroreceptors *in vivo*

---

---

**Rosalba Sortino**, Marina Cunquero, Gustavo Castro-Olvera, Ricard Gelabert, Miquel Moreno, Fabio Riefolo, Carlo Matera, Noèlia Fernández-Castillo, José M. Lluch, Jordi Hernando, Pablo Loza-Alvarez and Pau Gorostiza. **Three-photon infrared stimulation of endogenous neuroreceptors *in vivo***. *Accepted for publication, Angewandte Chemie*, 2023.



## Abstract

To interrogate neural circuits and crack their codes, it is essential to combine *in vivo* brain activity imaging and spatiotemporally precise stimulation in three dimensions using genetic or pharmacological specificity. This challenge requires the deep penetration and focusing that can only be provided by infrared light and multiphoton excitation, which has led to a surge in methods for two-photon optogenetics and photopharmacology in recent years. However, three-photon brain stimulation *in vivo* remains to be demonstrated. Here, we report the regulation of neuronal activity in zebrafish larvae by three-photon excitation of a photoswitchable muscarinic agonist at 50 pM, a billion-fold lower concentration than used for uncaging, and with mid-infrared light of 1560 nm, the longest photostimulation wavelength reported so far. Photoresponses are robust, physiologically relevant, and offer an unprecedented way to modulate brain activity in wild-type animals with spatiotemporal resolution and pharmacological specificity. We also compute the multiphoton absorption probabilities and cross-sections of photoswitchable molecules, predicting that azobenzene-based ligands designed for one-photon excitation with ultraviolet and visible light have high three-photon absorption cross-section that can be used directly with pulsed infrared light. The wide application of three-photon pharmacology will deeply impact basic neurobiology and the progression of neuromodulation therapies based on light.





## 9.1 Introduction

To understand how (patho)physiological processes work, it is crucial to monitor activities of interest *in vivo* while manipulating specific molecular and cellular mechanisms and assessing their outcomes, including behavioral responses. For those purposes, *in vivo* and intravital microscopy technologies have proven virtually useful in every tissue and application from cancer<sup>1,2</sup> to infections<sup>3,4</sup>, including drug delivery<sup>5</sup>. These technologies have become particularly appealing for interrogating and manipulating brain activity<sup>6-9</sup>.

Several approaches have been reported for activity imaging and stimulating deep in the brain<sup>10</sup> *in vivo*: (a) microendoscopy with gradient refractive index lenses that are invasively introduced in the tissue<sup>11-13</sup>; (b) adaptive optics, wavefront shaping methods<sup>14-18</sup> and refinements to reduce aberrations, phase- and motion-dependence; and (c) multiphoton excitation (MPE) using pulsed infrared (IR) light, which is weakly absorbed and scattered by the tissue, allowing fluorescence imaging of chemical and genetically encoded indicators, thus affording deep penetration and sharp focusing. The nonlinear process of simultaneous absorption of multiple photons by a molecule to reach an electronic state whose energy equals the sum of the photon energies<sup>19</sup> requires a high intensity of light. The advent of pulsed lasers<sup>20,21</sup> enabled fluorescence microscopy in the visible range using two-photon excitation (2PE) of IR light<sup>22</sup> and led to 2PE calcium and sodium imaging of neuronal activity<sup>23</sup>.

Depths of several hundred micrometers can be achieved by 2PE at wavelengths between 700-900 nm (near-infrared NIR-I window)<sup>24</sup>. However, this still only constitutes a fraction of the cortical thickness of mice (~1 mm) and humans (up to ~5 mm). Longer wavelengths in the 1300-1700 nm range (extending into the NIR-II window) allow even lower light absorption and scattering, making them potentially compatible with the same fluorescent reporters using three-photon excitation (3PE). As a rule of thumb, a chromophore with 400 nm excitation wavelength under continuous wave illumination (one-photon excitation, 1PE) can also be excited at 800 nm by 2PE and at 1200 nm by 3PE if the corresponding absorption cross-sections are sufficiently high<sup>25</sup>. Over the last decade, 3PE has drawn growing interest in neuroscience, facilitating whole cortex imaging<sup>26,27</sup> and neuronal activity imaging<sup>28,29</sup>.

To interrogate neural circuits and crack their codes, activity imaging must be combined with spatiotemporally precise stimulation in three dimensions, which requires the focusing provided by MPE. Two-photon optogenetics<sup>30-32</sup> and photopharmacology including caged<sup>33,34</sup> and photoswitchable ligands<sup>35-39</sup> have been recently developed and reviewed<sup>40-44</sup>. However,

neuronal stimulation *in vivo* with 3PE has never been reported, either with optogenetics nor with photopharmacology.

In this study, we aimed at manipulating a physiological process using 3PE, which we achieved by photopharmacological activation of neuroreceptors. Specifically, we report that M<sub>2</sub> muscarinic acetylcholine receptors (M<sub>2</sub> mAChRs or M<sub>2</sub>Rs) can be selectively activated *in vitro* and *in vivo* using a photoswitchable dualsteric ligand (phthalimide-azobenzene-iperoxo, **PAI**) at picomolar concentrations in the bath and 1560 nm pulsed light, which is the longest photoactivation wavelength reported to date. These results demonstrate the applicability of three-photon pharmacology (3PP) applicability and set new uses for deep and focalized stimulation of cellular activity *in vivo*.

## 9.2 Results and discussion

In previous work, we have demonstrated that *cis*-**PAI** can be pharmacologically activated and deactivated. This through using continuous wave illumination under 1PE by the excitation of its  $n \rightarrow \pi^*$  transition at 420-460 nm, which promotes the formation of the active *trans*-isomer, while subsequent irradiation of its  $\pi \rightarrow \pi^*$  transition at 365 nm triggers photoisomerization towards the inactive *cis*-enriched configuration (**Figure 9.1**)<sup>38</sup>. In addition, we empirically applied 2PE to photoactivate **PAI** at approximately twice the wavelength of the 1PE  $n \rightarrow \pi^*$  transition (840 nm), which also induced its *cis*-to-*trans* isomerization and activated M<sub>2</sub> mAChR, thereby initiating intracellular calcium oscillations (**Figure 9.1** and **Figure S9.1**). We also noticed that such oscillations cannot be stopped with 730 nm pulsed light in the same range of peak power, suggesting that *trans*-to-*cis* isomerization by excitation of its  $\pi \rightarrow \pi^*$  transition is not an efficient process at 2PE (**Figure S9.1**).

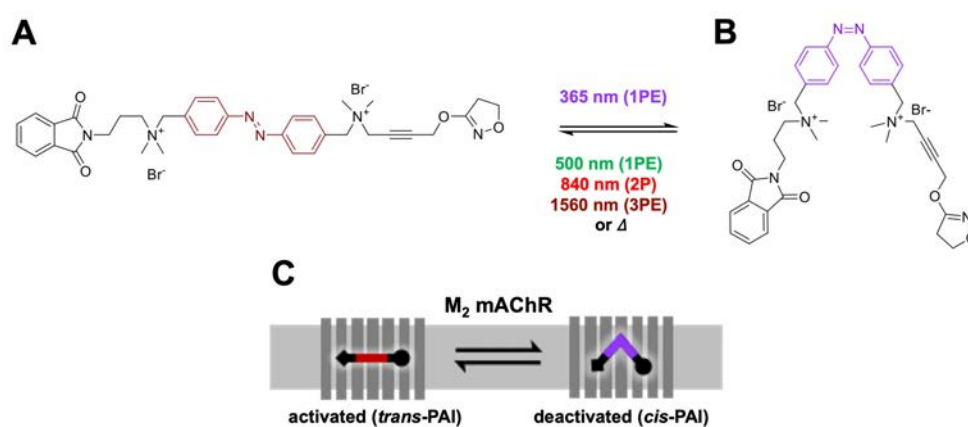


**Figure 9.1.** PAI (de)activates M<sub>2</sub> muscarinic acetylcholine receptors. 2D representation of the chemical structures of (A) *trans*-PAI and (B) *cis*-PAI. Photoisomerization between *trans* and *cis* can be achieved by 365 nm

(1PE) and between *cis* and *trans* by 420-460 nm (1PE), 840 nm (2PE)<sup>38</sup> and 1560 nm (3PE, this work). (C) Diagram depicting the 7 transmembrane receptor M<sub>2</sub> mAChR transitioning between the activated state in the presence of the ligand *trans*-PAI (left) and the deactivated state with *cis*-PAI (right). (Photo)activation of M<sub>2</sub> mAChR leads to cyclic (cAMP) decrease under physiological conditions. In this work, we have coupled M<sub>2</sub> mAChR activation to intracellular calcium release by means of the protein Gα<sub>qTOP</sub>, to take advantage of calcium imaging in cell populations<sup>38</sup>.

### 9.2.1 Theoretical calculations

To understand and improve the penetration and focusing of azo-based photoswitchable drugs using MPE, we have herein examined the 1PE, 2PE, and 3PE properties of PAI using theoretical calculations. As far as we know, only a previous computational study has been reported on the high-order multiphoton absorption cross-sections (2P-5P) of centrosymmetric *trans*-azobenzenes (*e.g.*, the azobenzene core of *trans*-PAI), which proposed different trends for the excitability of their odd- and even-order absorption processes. For *trans*-azo chromophores with an inversion center, the odd-photon absorption processes are largely determined by the one-photon absorption strength, whereas even-photon absorption processes are set by the two-photon absorption strength<sup>45</sup>. Based on this precedent and the lack of previous similar studies on *cis*-azobenzenes, we focused our attention on PAI and two other simpler azobenzene models (**Figure S9.2**), whose multiphoton absorption cross-sections were computed for both isomers using density functional calculations at the DFT/CAM-B3LYP level (**Tables S9.1-S9.6** and **Figures S9.3-S9.8**). The reliability of this method was validated by our calculations of their 2PE properties, which predicted that their *cis*-to-*trans* photoisomerization should be more favored than their *trans*-to-*cis* photoisomerization upon excitation with NIR-I radiation. Thus, larger two-photon excitability was computed for the lower energy  $n \rightarrow \pi^*$  ( $\sigma_{2,cis}/\sigma_{2,trans} = 11$ ) and  $\pi \rightarrow \pi^*$  ( $\sigma_{2,cis}/\sigma_{2,trans} = 1660$ ) transitions of *cis*-PAI in relation to *trans*-PAI, which agrees with our experimental results (**Table S9.5** and **Table S9.6**). Indeed, we have shown an efficient photoconversion of *cis*-PAI to the pharmacologically active *trans*-isomer using 2PE at 840 nm<sup>38</sup> and the difficulty to deactivate *trans*-PAI using 2PE at 730 nm (**Figure S9.1**). More interesting were our calculations of higher-order MPE of PAI like 3PE, which predict that its activation can be triggered using NIR-II wavelengths to achieve deeper distances into the tissues and even sharper focusing than 2PE<sup>27</sup>. In particular, the results of the molecular computations indicate that the *cis*-to-*trans* photoisomerization of the centrosymmetric azobenzene is favored under 3PE of their  $n \rightarrow \pi^*$  transition at around 1500 nm ( $\sigma_{3,cis}/\sigma_{3,trans} = 314$  for PAI; **Table S9.5** and **Table S9.6**). Overall, these data support the feasibility of 3PE to activate M<sub>2</sub> mAChRs.

To verify these predictions, we could not take advantage of the 2PE setup used in previous experiments<sup>35,37-39</sup>, as the SpectraPhysics Mai Tai Ti:sapphire laser tuning range only reaches 920 nm. Thus, we built a custom multiphoton stimulation and fluorescence imaging setup (**Figure S9.14**) based on an inverted microscope coupled to a femtosecond-pulsed laser beam (FFS, Toptica) that emits at a fixed wavelength of 1560 nm with a repetition rate of 100 MHz, a pulse duration of 120 fs, and allows a maximum peak power of 3.3 kW. Briefly, the optical system allows for imaging and tracking of the emitted fluorescence while photostimulating a region of interest.

### 9.2.2 *In vitro* calcium imaging and three-photon stimulation

In this setup, real-time calcium imaging assays were performed in transiently transfected human embryonic kidney (HEK) cells co-expressing M<sub>2</sub> mAChR and G $\alpha_{qTOP}$ <sup>46</sup> and loaded with the fluorescent calcium indicator Oregon Green BAPTA-1 AM (OGB-1 AM; see Supplementary Information). We performed calcium imaging at 1PE and manipulated the activity of M<sub>2</sub> mAChRs with the reference agonist iperoxo (IPX)<sup>47</sup> and with PAI under 3PE conditions (1560 nm at the maximum available peak power). Application of *cis*-PAI (50 pM *trans*-PAI, pre-illuminated with 365 nm, **Figure 9.1**) did not elicit cellular responses, as reported<sup>38</sup>. Remarkably, 3PE in the presence of *cis*-PAI induced a significant increase in intracellular calcium activity (**Figure 9.2A**), indicating that PAI was photoconverted to its *trans* form. The time course of calcium responses to 3PE of PAI displayed a diversity of behaviors in individual cells, such as oscillatory waves, transient peaks, and steps (**Figure 9.2B**). Similar intracellular responses have been previously observed in G $\alpha_q$ -coupled GPCRs like metabotropic glutamate 5 receptors<sup>48</sup> and depend on the ratio of endogenous G protein and receptor overexpression level in each cell<sup>37</sup>. M<sub>2</sub> mAChRs are naturally G $\alpha_i$ -coupled, but these effects can be attributed to the overexpression of G $\alpha_{qTOP}$  used in our calcium imaging assay.

To reduce deviations due to this temporal dependence, responses under control conditions, under the application of *cis*-PAI, and upon photoswitching with 3PE (*trans*-PAI enriched form), were quantified both by peak amplitude and area under the curve (AUC). The analysis of these parameters showed that 3PE of PAI significantly stimulated the release of intracellular calcium, as much as IPX, and that its effect is absent without illumination (*cis*-PAI) (**Figure 9.2CD**). 3PE alone did not produce any stimulation artifacts (n = 9, **Figure S9.9A**). Photoresponses were also absent in cells not expressing M<sub>2</sub> mAChRs (n = 40, **Figure S9.10**). All these experiments confirm that the calcium responses observed upon 3PE are elicited by

the specific interaction of the active isoform of PAI with M<sub>2</sub> mAChRs. Hence, *cis*-PAI can be photoswitched using 1560 nm light.

We further aimed to test the mechanism of PAI activation at this wavelength, and we studied the differences in cellular photoresponses concerning the photostimulation power, which is expected to follow a quadratic or cubic dependence for 2PE and 3PE, respectively. Using the same setup described above, the photoresponses were recorded at increasing laser power (63%,

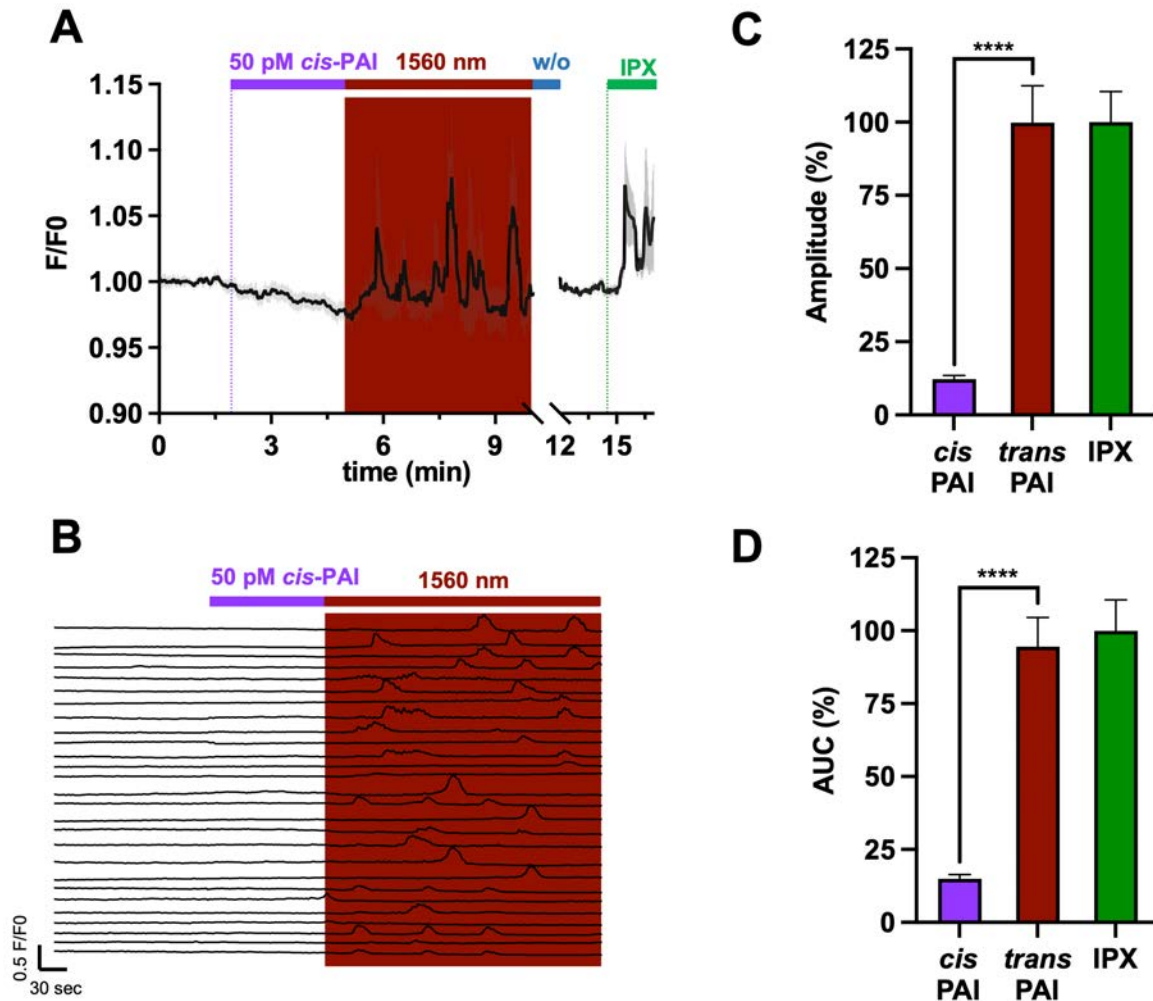


**Figure 9.2. Activation of PAI with near-infrared light under three-photon excitation.** Real-time calcium imaging traces from HEK cells co-expressing M<sub>2</sub> mAChR and Gα<sub>qTOP</sub>, which were loaded with the calcium indicator OGB-1 AM (10 μM). (A) Average trace of cell responses to the subsequent application of (1) *cis*-PAI (50 pM) pre-illuminated at 365 nm (purple bar), (2) *trans*-enriched PAI obtained under three-photon excitation (3PE) at 1560 nm maximum power (dark red bar), and (3) the muscarinic agonist iperoxo (IPX, green bar) after manual wash-out (w/o, blue bar) (n = 9 cells). Grey bands indicate the standard error of the mean (SEM). (B) Single cell calcium responses induced by PAI under 3PE at 1560 nm (dark red panel) (27 cells from 4 independent experiments). Purple bar indicates application of *cis*-PAI, dark red bar indicates illumination at 1560 nm. (C, D) The quantification is presented in the right graphs, where a significant response, in terms of area under the curve

(AUC) (C) and amplitude (D), is observed upon the application of a pulsed NIR light (1560 nm) in the presence of PAI due to its photoisomerization to the *trans*-active form ( $n = 27$  cells from 4 independent experiments). Data were normalized to the average cell response to the agonist IPX and statistical significance was inferred by the one-way ANOVA with Tukey's multiple comparisons post-hoc test  $p$ -value (\*\*\*\*)  $< 0.0001$ ; GraphPad Prism 9. Error bars are  $\pm$  SEM.

79%, 91%, and 100%, the latter corresponding to an average power of 42 mW at the back focal plane of the cells). Average and example traces from individual cells are shown in **Figure 9.3AB**. 3PE alone did not produce any artifacts ( $n = 10$ , **Figure S9.9B**). We quantified the responses by AUC, maximum amplitude, and percentage of photoresponsive cells (**Figure 9.3CD** and **Figure S9.11AB**). The power dependence of the AUC yields an exponential factor of 3.1 ( $R^2 = 0.996$ ), unambiguously confirming that PAI photoisomerization at 1560 nm follows a third-order non-linear process (3PE). The amplitude and fraction of responding cells display similar values but lower correlation, probably due to the transient nature of the  $M_2$ R-mediated cellular responses and the variable expression levels of  $M_2$  mAChRs and  $G\alpha_{qTOP}$  in individual cells.

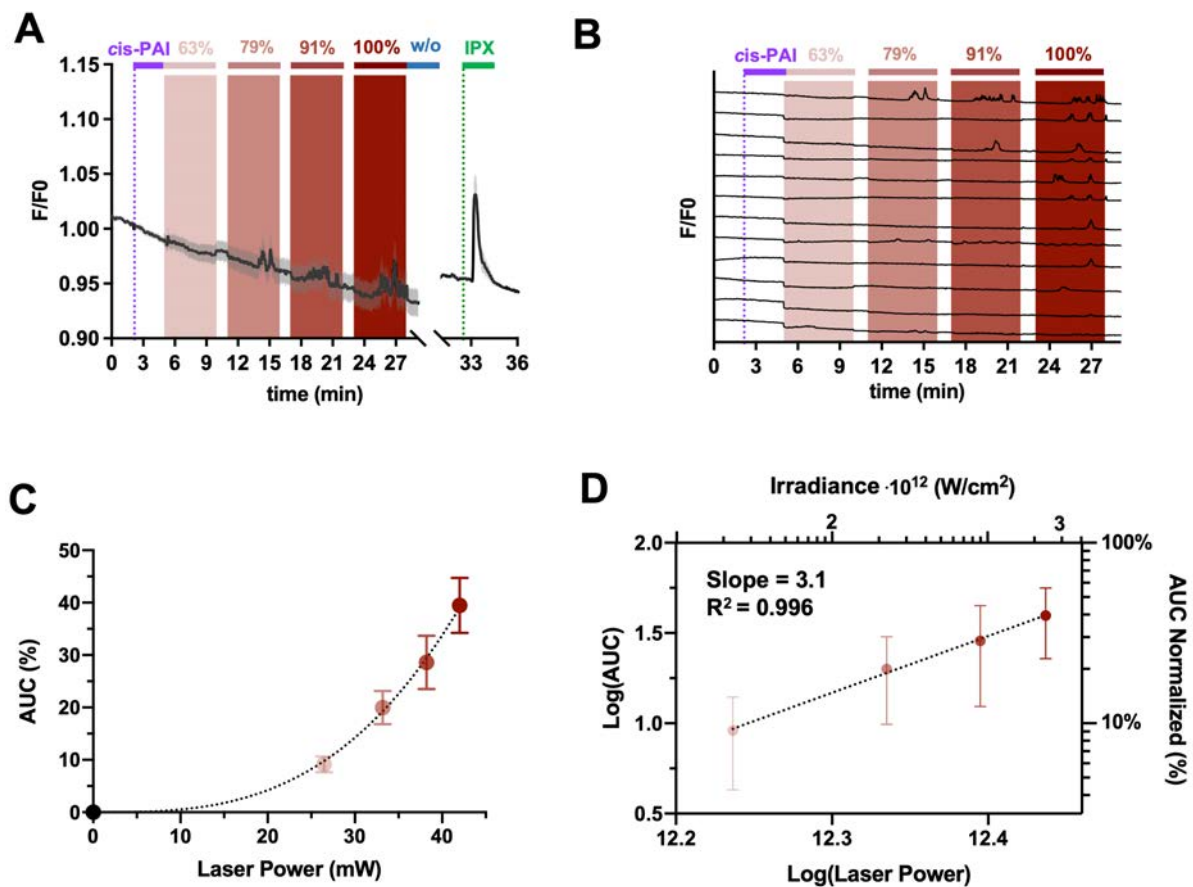


**Figure 9.3. Dependence of the multiphoton photoresponse on average laser power.** Real-time calcium imaging traces from HEK cells co-expressing  $M_2$  mAChR and  $G\alpha_{qTOP}$ , which were loaded with the calcium indicator OGB-1 AM (10  $\mu$ M). (A) Average trace of cell responses to *cis*-PAI (50 pM, purple bar), *trans*-enriched PAI

obtained under 3PE with different laser powers (63% light pink bar; 79% pink bar; 91% light red bar; 100% dark red bar, the latter corresponding to an average power of 42 mW at the back focal plane of the cells) and the muscarinic agonist iperoxo (IPX, green bar) after manual wash-out (w/o, blue bar) ( $n = 12$  cells). Grey band indicates SEM. **(B)** Single cell calcium responses induced by **PAI** (purple bar) under 3PE at 1560 nm with different laser power (63% light pink bar; 79% pink bar; 91% light red bar; 100% dark red bar,  $n = 12$  cells). **(C)** Photoresponse quantification as percent change of the area under the curve (AUC) as a function of average laser power at the back focal plane of the objective. Data have been normalized to the average cell response with IPX ( $n = 36$  cells from 4 independent experiments). The percentage of response vs. power can be fitted by a cubic function, indicating that the process is mediated by 3PE. **(D)** Linear regression model using logarithmically transformed data of the irradiance (in  $W \cdot cm^{-2}$ ). The  $R^2$  of the fit is 0.996 and the slope is 3.1.

We have previously shown that **PAI** can control cardiac function in tadpoles and rats<sup>38</sup>, and brain wave activity in mice<sup>49</sup> through the use of continuous wave illumination (1PE). Recently, we demonstrated *in vivo* photoswitching by 2PE in invertebrates<sup>39</sup>. To test 3PE in an animal model, we used zebrafish larvae expressing a genetically encoded calcium indicator, which made it possible to monitor brain activity (*i.e.*, GCaMP6s) and to study the changes in calcium concentration upon photostimulation with the customized optical set-up described above (see **Supplementary Information; SI**). **Figure 9.4A** shows an example of GCaMP6s fluorescence images, the zebrafish brain regions used for quantification, and the 3PE-stimulated region in the field of view. Spontaneous neuronal activity was observed throughout the experiment and was not significantly affected by 3PE or by the application of 50 pM *cis*-**PAI** in the bath (see example frames in **Figure 9.4B**). However, 3PE in the presence of *cis*-**PAI** produced large calcium responses in all regions of the brain, including the activation of well-defined structures that will be the subject of a dedicated study (see the rightmost frame in **Figure 9.4B**). A representative movie is available in the **SI (Figure S9.13)**. The time course of calcium activity in different brain regions is shown in **Figure 9.4C** and the corresponding quantifications (AUC and peak amplitude) are in **Figure 9.3D** and **Figure S9.12**. Overall, a fourfold increase in neuronal activity was elicited by **PAI** using 3PE *in vivo*.

### 9.2.3 *In vivo* neuronal photocontrol in zebrafish larvae and three-photon stimulation

These neuroexcitatory responses elicited by 3PE of **PAI** *in vivo* (**Figure 9.4**) are robust, physiologically relevant, and offer an unprecedented way to modulate brain activity in wild-type animals through  $M_2$ R<sub>s</sub> with high spatiotemporal resolution. In contrast, calcium responses *in vitro* (**Figures 9.2** and **Figure 9.3**) are weaker: 3PE responses are obtained from 25% of the cells expressing  $M_2$ R (**Figure 9.11A**) and reach 40% of IPX responses at the



maximum laser power (**Figure 9.11B**), probably due to the non-physiological coupling provided by  $G\alpha_{qTOP}$ . Nevertheless, these *in vitro* assays were convenient to set up and validate 3PE using high-throughput imaging rather than electrophysiological recordings in individual cells and may be useful to further refine the photoswitchable compounds and MPE optical system. Even the energy required to induce 3PE of PAI is orders of magnitude below the energy reported<sup>50</sup> in studies of optogenetic stimulation in cultured neurons (**Table S9.7**) (50 mW to fire an action potential, 64 mW to photodamage)<sup>51</sup>.

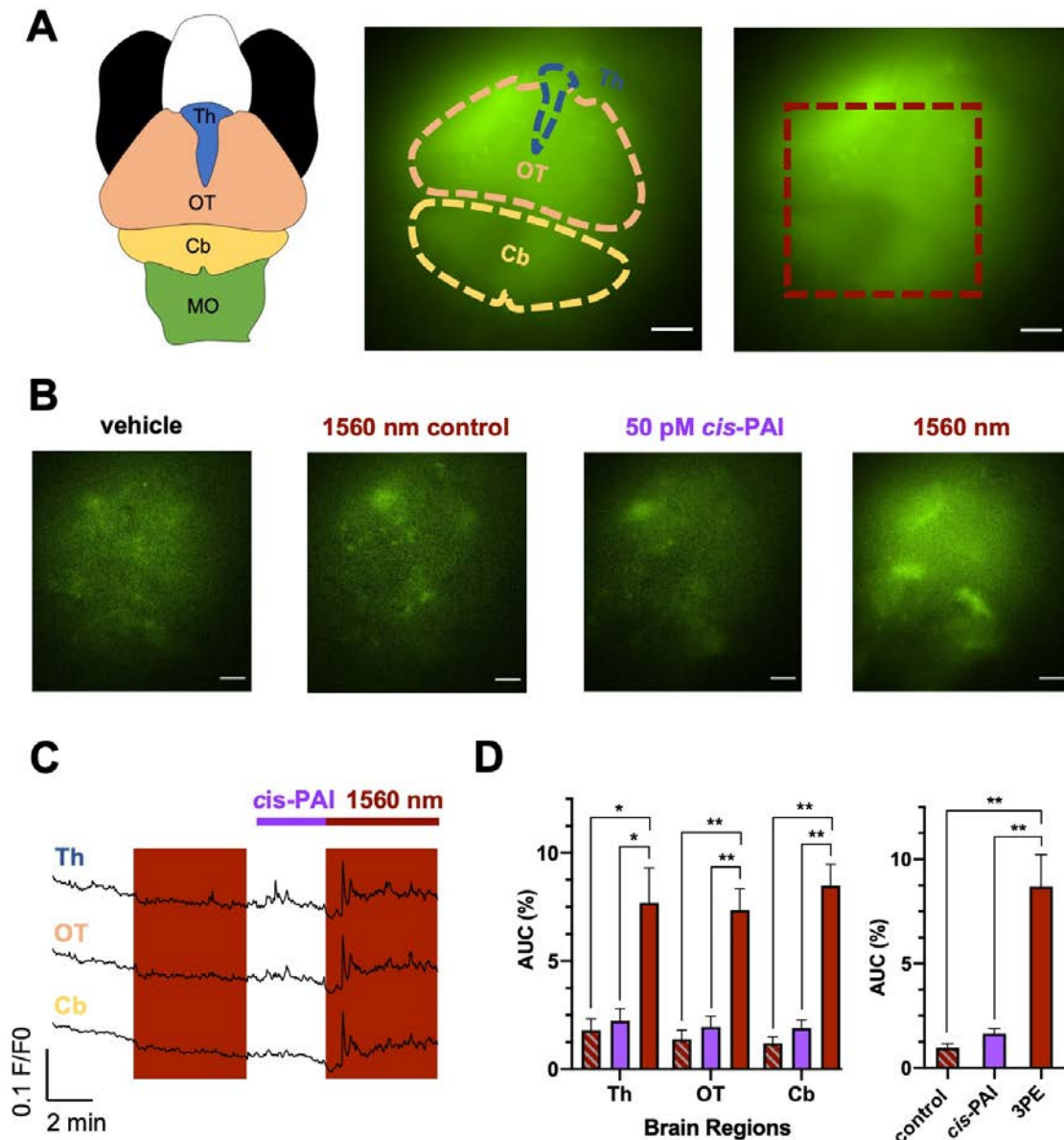


**Figure 9.4.** *In vivo* activation of PAI by three-photon excitation. Green fluorescence signal from GCaMP6s indicator upon different conditions. (A) Sketch of the main regions of the zebrafish larva brain (dorsal view): Th, thalamus; OT, optic tectum; Cb, cerebellum; MO, medulla oblongata. Among these regions, three were visible as shown in the middle figure from zebrafish larvae expressing the calcium indicator GCaMP6s. The region illuminated with the three-photon excitation (3PE) laser (red dashed line) is represented on the right. The scale bar

= 50  $\mu\text{m}$ . **(B)** Representative images of different experimental conditions. No effects were observed with the vehicle and with pulsed-laser irradiation (1560 nm) prior to adding the drugs. The application of 50 pM *cis*-PAI alone did not change neuronal activity, but upon pulsed-laser irradiation, large photoresponses were observed, presumably due to isomerization to the *trans*-PAI form. The scale bar represents 50  $\mu\text{m}$ . **(C)** Real-time fluorescence calcium imaging traces from different brain regions (Th, OT and Cb) under the conditions described in **(B)**. The transient and oscillatory response elicited by 3PE of PAI is observed in all regions. **(D)** Quantification of photoresponses in separate regions and averaged response over the whole brain ( $n = 5$ ). Striped bars indicate 3PE in the absence of drug, purple bars indicate the application of 50 pM *cis*-PAI, and dark red bars indicate photoresponses to 3PE (photoswitching to *trans*-PAI using 1560 nm light). Error bars are  $\pm$  SEM. Data were analyzed by paired t-test,  $p$ -value (\*\*) $< 0.01$  and  $p$ -value (\*) $< 0.05$  using GraphPad Prism 9.

The results obtained with 2PE (**Figure 9.5** in reference<sup>38</sup> and **Figure S9.1** in this work) agree with our calculations of the multiphotonic properties of PAI: the lower energy  $n \rightarrow \pi^*$  and  $\pi \rightarrow \pi^*$  transitions in *cis*-PAI are more favored than in *trans*-PAI under 2PE, elucidating why only *cis*-to-*trans* photoisomerization of PAI can be efficiently induced with 700-900 nm NIR-I radiation, whereas the reversible operation of the photoswitch within this spectral range is less encouraged. In contrast, our calculations for PAI and simpler azobenzenes predict a reversible behavior under 3PE. Their 3PE absorption cross-sections for the  $n \rightarrow \pi^*$  transition at around 1500 nm are much larger for the *cis*-isomer compared to the *trans* one, ensuring effective *cis*-to-*trans* photoisomerization, as conclusively demonstrated for PAI by our photopharmacology data in **Figures 9.2-9.4**. Here, this situation appears reversible for the  $\pi \rightarrow \pi^*$  transition with 3PE, which we computed to be more probable for the *trans*-isomer of these azo compounds compared to the corresponding 2PE transition ( $\sigma_{3P,trans}^{\pi \rightarrow \pi^*} / \sigma_{3P,cis}^{\pi \rightarrow \pi^*} = 122$  for PAI; **Table S9.5** and **Table S9.6**). This combined computational and experimental study raises hopes of strong and reversible responses for 3PE of all electronically-symmetric *trans*-azo-based photoswitchable drugs. In addition, it should enable reversible full-3PE operation of these compounds by orthogonally exciting their  $\pi \rightarrow \pi^*$  and  $n \rightarrow \pi^*$  transitions with NIR-II radiation to selectively trigger *trans*-to-*cis* and *cis*-to-*trans* photoconversion, respectively. Unfortunately, we have not yet tested this prediction experimentally due to the limited wavelength range of our pulsed lasers (700-900 nm tunable MaiTai and 1560 nm fixed wavelength Toptica).

Note that centrosymmetric azobenzenes make up a large portion of photochromic groups used in photopharmacology<sup>52</sup> and often display slow thermal relaxation and higher potency in *trans* configuration. Therefore, our results suggest that they could be used directly for 3PE with NIR-II light to take advantage of enhanced tissue penetration and focusing<sup>26-28,53</sup>. In addition, this behavior could be expanded to photopharmacological compounds based on electronically-asymmetric azobenzenes<sup>35,36,39</sup>, as asymmetric chromophores featuring electron donors and

acceptors also display high absorption cross-sections at 3PE<sup>54,55</sup>. Therefore, the wide application of 3PP would have a deep impact in the field as well as in chemical biology and phototherapies. These results may be relevant for multiphoton lithography<sup>56,57</sup> and polymerization<sup>58</sup> as well. A few 3PE studies have been reported for optogenetics<sup>50</sup> and caged compounds<sup>59</sup>. These potentially alternative 3PE methods would have advantages of their own (*e.g.*, genetic targeting and release of physiological ligands, respectively); however, they display relatively low 3PE efficacy. The 3P uncaging cross-section reported for these systems at 1064 nm ( $\sigma_{3P,uncaging} = 4.0 \cdot 10^{-85} \text{ cm}^6 \text{ s}^2 \text{ photon}^{-2}$ )<sup>59</sup> is several orders of magnitude lower than the 3P absorption cross-section computed for **PAI** at around 1500 nm ( $\sigma_{3P,cis} = 1.8 \cdot 10^{-77} \text{ cm}^6 \text{ s}^2 \text{ photon}^{-2}$ ), while the irradiance required for 3P optogenetic manipulation<sup>50</sup> is considerably larger than for 3P **PAI** photocontrol (**Table S9.7**). As a result, high overexpression levels or compound concentration may be required, leading to physiological disturbance (*e.g.*, altering the microstructure and composition of dendritic spines<sup>60</sup>) and unintended pharmacological effects (*e.g.*, GABA<sub>A</sub>R blockade in the case of caged glutamate prior to release<sup>61</sup>). As a reference, 2PE absorption cross-sections have been discussed for photopharmacology, including reversible photoswitches and caged compounds.

The multiphoton absorption cross-section of a photoswitchable ligand can be complemented by a figure of merit of its practical usability in 3PE: 50 pM *cis*-**PAI** (above its EC<sub>50</sub>)<sup>38</sup> allows, by 3PE photoactivation, nearly half of the maximal IPX responses at a power density that does not produce unspecific effects in neurons. This suggests that improving pharmacological potency (potentially reaching the femtomolar range) may be as beneficial as increasing the multiphoton cross-section to achieve highly sensitive photopharmacological compounds. Thus, when targeting endogenous receptors *in vivo* with 3PE, azobenzene photoswitches provide excellent performance. If optogenetic manipulation with 3PE<sup>50</sup> is of interest, genetically targeted azobenzene photoswitches like LiGluR<sup>62-65</sup> offer a convenient option. The concentration used in our 3PE assays with **PAI** (50 pM) is  $\sim 10^9$  times lower than that required for 2PE glutamate uncaging *in vivo* (20 mM)<sup>66</sup>.

The wavelength used in our experiments (1560 nm) allows effectively photoisomerizing **PAI** to the active form using 3PE. However, light is also strongly absorbed by water in this spectral range<sup>67</sup>, suggesting that wavelengths lying at lower absorption bands like 1300 nm or 1700 nm generally used for 3PE imaging may yield even better results, provided that the photoswitch absorption band for third-order processes is sufficiently wide.

### 9.3 Conclusions

In summary, we report the first method to control brain activity *in vivo* using 3PE and mid-IR light. It is based on the photopharmacological activation of mAChRs by means of the photoswitchable ligand **PAI** at 50 pM and 1560 nm light, which are respectively the lowest concentration and the longest photoactivation wavelength ever reported. In addition, we provide experimental assays to characterize their performance and theoretical guidelines for further optimization. Our calculations predict that most photoswitchable ligands used in 1PE photopharmacology with UV and visible light (symmetric and asymmetric azobenzenes) are suitable for 3PE with mid-IR light and can benefit from enhanced tissue penetration and focusing. The wide application of 3PP would be transformative for basic research in neurobiology and to progress advanced neuromodulation therapies based on light.

## References

- 1 Jain, R. K., Munn, L. L. & Fukumura, D. Dissecting tumour pathophysiology using intravital microscopy. *Nat Rev Cancer* **2**, 266-276, doi:10.1038/nrc778 (2002).
- 2 Perrin, L., Bayarmagnai, B. & Gligorijevic, B. Frontiers in intravital multiphoton microscopy of cancer. *Cancer Rep (Hoboken)* **3**, e1192, doi:10.1002/cnr2.1192 (2020).
- 3 Stolp, B. & Melican, K. Microbial pathogenesis revealed by intravital microscopy: Pros, cons and cautions. *FEBS Lett* **590**, 2014-2026, doi:10.1002/1873-3468.12122 (2016).
- 4 Sewald, X. Visualizing viral infection *in vivo* by multi-photon intravital microscopy. *Viruses* **10**, doi:10.3390/v10060337 (2018).
- 5 Amornphimoltham, P., Masedunskas, A. & Weigert, R. Intravital microscopy as a tool to study drug delivery in preclinical studies. *Adv Drug Deliv Rev* **63**, 119-128, doi:10.1016/j.addr.2010.09.009 (2011).
- 6 Grutzendler, J., Kasthuri, N. & Gan, W. B. Long-term dendritic spine stability in the adult cortex. *Nature* **420**, 812-816, doi:10.1038/nature01276 (2002).
- 7 Majewska, A. K., Newton, J. R. & Sur, M. Remodeling of synaptic structure in sensory cortical areas *in vivo*. *J Neurosci* **26**, 3021-3029, doi:10.1523/JNEUROSCI.4454-05.2006 (2006).
- 8 Yoder, E. J. & Kleinfeld, D. Cortical imaging through the intact mouse skull using two-photon excitation laser scanning microscopy. *Microsc Res Tech* **56**, 304-305, doi:10.1002/jemt.10002 (2002).
- 9 Stosiek, C., Garaschuk, O., Holthoff, K. & Konnerth, A. *In vivo* two-photon calcium imaging of neuronal networks. *Proc Natl Acad Sci U S A* **100**, 7319-7324, doi:10.1073/pnas.1232232100 (2003).
- 10 Abdelfattah, A. S. *et al.* Neurophotonic tools for microscopic measurements and manipulation: status report. *Neurophotonics* **9**, 013001, doi:10.1117/1.NPh.9.S1.013001 (2022).
- 11 Jung, J. C., Mehta, A. D., Aksay, E., Stepnoski, R. & Schnitzer, M. J. *In vivo* mammalian brain imaging using one- and two-photon fluorescence microendoscopy. *J Neurophysiol* **92**, 3121-3133, doi:10.1152/jn.00234.2004 (2004).
- 12 Murayama, M. & Larkum, M. E. *In vivo* dendritic calcium imaging with a fiberoptic periscope system. *Nat Protoc* **4**, 1551-1559, doi:10.1038/nprot.2009.142 (2009).
- 13 Bocarsly, M. E. *et al.* Minimally invasive microendoscopy system for *in vivo* functional imaging of deep nuclei in the mouse brain. *Biomed Opt Express* **6**, 4546-4556, doi:10.1364/BOE.6.004546 (2015).
- 14 Ji, N., Sato, T. R. & Betzig, E. Characterization and adaptive optical correction of aberrations during *in vivo* imaging in the mouse cortex. *Proc Natl Acad Sci U S A* **109**, 22-27, doi:10.1073/pnas.1109202108 (2012).
- 15 Ji, N. Adaptive optical fluorescence microscopy. *Nat Methods* **14**, 374-380, doi:10.1038/nmeth.4218 (2017).
- 16 Papagiakoumou, E. *et al.* Scanless two-photon excitation of channelrhodopsin-2. *Nat Methods* **7**, 848-854, doi:10.1038/nmeth.1505 (2010).
- 17 Papagiakoumou, E., Ronzitti, E. & Emiliani, V. Scanless two-photon excitation with temporal focusing. *Nat Methods* **17**, 571-581, doi:10.1038/s41592-020-0795-y (2020).
- 18 Aviles-Espinosa, R. *et al.* Measurement and correction of *in vivo* sample aberrations employing a nonlinear guide-star in two-photon excited fluorescence microscopy. *Biomed Opt Express* **2**, 3135-3149, doi:10.1364/BOE.2.003135 (2011).
- 19 Göppert-Mayer, M. Über elementarakte mit zwei quantensprüngen. *Annalen der Physik* **401**, 273-294, doi:10.1002/andp.19314010303 (1931).

- 20 Strickland, D. G., M. Compression of amplified chirped optical pulses. *Optics Communications* **56**, 219-221, doi:10.1016/0030-4018(85)90120-8 (1985).
- 21 Spence, D. E., Kean, P. N. & Sibbett, W. 60-fsec pulse generation from a self-mode-locked Ti:sapphire laser. *Opt Lett* **16**, 42-44, doi:10.1364/ol.16.000042 (1991).
- 22 Denk, W., Strickler, J. H. & Webb, W. W. Two-photon laser scanning fluorescence microscopy. *Science* **248**, 73-76, doi:10.1126/science.2321027 (1990).
- 23 Denk, W. *et al.* Anatomical and functional imaging of neurons using 2-photon laser scanning microscopy. *J Neurosci Methods* **54**, 151-162, doi:10.1016/0165-0270(94)90189-9 (1994).
- 24 Yaroslavsky, A. N. *et al.* Optical properties of selected native and coagulated human brain tissues *in vitro* in the visible and near infrared spectral range. *Phys Med Biol* **47**, 2059-2073, doi:10.1088/0031-9155/47/12/305 (2002).
- 25 Xu, C. W., W. in *Topics in fluorescence spectroscopy* Vol. 5 (ed J.R. Lakowicz) 471–540 (Springer, 2002).
- 26 Horton, N. G. *et al.* *In vivo* three-photon microscopy of subcortical structures within an intact mouse brain. *Nat Photonics* **7**, 205-209, doi:10.1038/nphoton.2012.336 (2013).
- 27 Guesmi, K. *et al.* Dual-color deep-tissue three-photon microscopy with a multiband infrared laser. *Light Sci Appl* **7**, 12, doi:10.1038/s41377-018-0012-2 (2018).
- 28 Ouzounov, D. G. *et al.* *In vivo* three-photon imaging of activity of GCaMP6-labeled neurons deep in intact mouse brain. *Nat Methods* **14**, 388-390, doi:10.1038/nmeth.4183 (2017).
- 29 Klioutchnikov, A. *et al.* A three-photon head-mounted microscope for imaging all layers of visual cortex in freely moving mice. *Nat Methods*, doi:10.1038/s41592-022-01688-9 (2022).
- 30 Rickgauer, J. P. & Tank, D. W. Two-photon excitation of channelrhodopsin-2 at saturation. *Proc Natl Acad Sci U S A* **106**, 15025-15030, doi:10.1073/pnas.0907084106 (2009).
- 31 Begue, A. *et al.* Two-photon excitation in scattering media by spatiotemporally shaped beams and their application in optogenetic stimulation. *Biomed Opt Express* **4**, 2869-2879, doi:10.1364/BOE.4.002869 (2013).
- 32 Klausen, M. B.-D., M. Two-photon uncaging of bioactive compounds: Starter guide to an efficient IR light switch. *Journal of Photochemistry and Photobiology C: Photochemistry Reviews* doi:10.1016/j.jphotochemrev.2021.100423 (2021).
- 33 Denk, W. Two-photon scanning photochemical microscopy: Mapping ligand-gated ion channel distributions. *Proc Natl Acad Sci U S A* **91**, 6629-6633, doi:10.1073/pnas.91.14.6629 (1994).
- 34 Ellis-Davies, G. C. R. Two-photon uncaging of glutamate. *Front Synaptic Neurosci* **10**, 48, doi:10.3389/fnsyn.2018.00048 (2018).
- 35 Izquierdo-Serra, M. *et al.* Two-photon neuronal and astrocytic stimulation with azobenzene-based photoswitches. *J Am Chem Soc* **136**, 8693-8701, doi:10.1021/ja5026326 (2014).
- 36 Carroll, E. C. *et al.* Two-photon brightness of azobenzene photoswitches designed for glutamate receptor optogenetics. *Proc Natl Acad Sci U S A* **112**, E776-785, doi:10.1073/pnas.1416942112 (2015).
- 37 Pittolo, S. *et al.* Reversible silencing of endogenous receptors in intact brain tissue using 2-photon pharmacology. *Proc Natl Acad Sci U S A* **116**, 13680-13689, doi:10.1073/pnas.1900430116 (2019).
- 38 Riefolo, F. *et al.* Optical control of cardiac function with a photoswitchable muscarinic agonist. *J Am Chem Soc* **141**, 7628-7636, doi:10.1021/jacs.9b03505 (2019).

- 39 Cabre, G. *et al.* Rationally designed azobenzene photoswitches for efficient two-photon neuronal excitation. *Nat Commun* **10**, 907, doi:10.1038/s41467-019-08796-9 (2019).
- 40 Chen, I. W., Papagiakoumou, E. & Emiliani, V. Towards circuit optogenetics. *Curr Opin Neurobiol* **50**, 179-189, doi:10.1016/j.conb.2018.03.008 (2018).
- 41 Adesnik, H. & Abdeladim, L. Probing neural codes with two-photon holographic optogenetics. *Nat Neurosci* **24**, 1356-1366, doi:10.1038/s41593-021-00902-9 (2021).
- 42 Dudek, M. *et al.* Two-photon absorption and two-photon-induced isomerization of azobenzene compounds. *RSC Adv* **10**, 40489-40507, doi:10.1039/d0ra07693g (2020).
- 43 Kellner, S. B., S. Two-photon excitation of azobenzene photoswitches for synthetic optogenetics. *Applied Sciences* **10**, 805, doi:doi.org/10.3390/app10030805 (2020).
- 44 Jerca, F. A. J., V.V.; Hoogenboom, R. Advances and opportunities in the exciting world of azobenzenes. *Nat Rev Chem* **6**, 51–69, doi:doi.org/10.1038/s41570-021-00334-w (2021).
- 45 Friese, D. H., Bast, R. & Ruud, K. Five-photon absorption and selective enhancement of multiphoton absorption processes. *ACS Photonics* **2**, 572-577, doi:10.1021/acsp Photonics.5b00053 (2015).
- 46 Gomeza, J. *et al.* Coupling of metabotropic glutamate receptors 2 and 4 to  $G\alpha_{15}$ ,  $G\alpha_{16}$ , and chimeric  $G\alpha_{q/i}$  proteins: characterization of new antagonists. *Mol Pharmacol* **50**, 923-930 (1996).
- 47 Schrage, R. *et al.* Agonists with supraphysiological efficacy at the muscarinic  $M_2$  ACh receptor. *Br J Pharmacol* **169**, 357-370, doi:10.1111/bph.12003 (2013).
- 48 Pittolo, S. *et al.* An allosteric modulator to control endogenous G protein-coupled receptors with light. *Nat Chem Biol* **10**, 813-815, doi:10.1038/nchembio.1612 (2014).
- 49 Barbero-Castillo, A. *et al.* Control of brain state transitions with a photoswitchable muscarinic agonist. *Adv Sci (Weinh)* **8**, e2005027, doi:10.1002/advs.202005027 (2021).
- 50 Rowlands, C. J. *et al.* Wide-field three-photon excitation in biological samples. *Light Sci Appl* **6**, e16255, doi:10.1038/lsa.2016.255 (2017).
- 51 Loza-Alvarez, P. A., D.; Aviles-Espinosa, R. *Semiconductor Lasers and Diode-based Light Sources for Biophotonics*. 472 (2018).
- 52 Wijtmans, M., Josimovic, I., Vischer, H. F. & Leurs, R. Optical control of class A G protein-coupled receptors with photoswitchable ligands. *Curr Opin Pharmacol* **63**, 102192, doi:10.1016/j.coph.2022.102192 (2022).
- 53 Klioutchnikov, A. *et al.* Three-photon head-mounted microscope for imaging deep cortical layers in freely moving rats. *Nat Methods* **17**, 509-513, doi:10.1038/s41592-020-0817-9 (2020).
- 54 Mandal, A. K. *et al.* Three-photon-excited luminescence from unsymmetrical cyanostilbene aggregates: morphology tuning and targeted bioimaging. *ACS Nano* **9**, 4796-4805, doi:10.1021/nn507072r (2015).
- 55 Cronstrand, P., Jansik, B., Jonsson, D., Luo, Y. & Agren, H. Density functional response theory calculations of three-photon absorption. *J Chem Phys* **121**, 9239-9246, doi:10.1063/1.1804175 (2004).
- 56 Juodkasis, S. M., V.; Seet, K.K.; Miwa, M. ; Misawa, H. Two-photon lithography of nanorods in SU-8 photoresist. *Nanotechnology* **16**, 846, doi:10.1088/0957-4484/16/6/039 (2005).
- 57 Markushyna, Y. S., A. Light as a tool in organic photocatalysis: Multi-photon excitation and chromoselective reactions. *European Journal of Organic Chemistry* doi:10.1002/ejoc.202200026 (2022).
- 58 Cumpston, B. H. A., S.P.; Barlow, S.; Marder, S.M.; Perry, J.W. Two-photon polymerization initiators for three-dimensional optical data storage and microfabrication. *Nature* **398**, 51–54, doi:10.1038/17989 (1999).

- 59 Tekeli, I. *et al.* Long-term *in vivo* single-cell lineage tracing of deep structures using three-photon activation. *Light Sci Appl* **5**, e16084, doi:10.1038/lsa.2016.84 (2016).
- 60 Allen, B. D., Singer, A. C. & Boyden, E. S. Principles of designing interpretable optogenetic behavior experiments. *Learn Mem* **22**, 232-238, doi:10.1101/lm.038026.114 (2015).
- 61 Maier, W., Corrie, J. E., Papageorgiou, G., Laube, B. & Grewer, C. Comparative analysis of inhibitory effects of caged ligands for the NMDA receptor. *J Neurosci Methods* **142**, 1-9, doi:10.1016/j.jneumeth.2004.07.006 (2005).
- 62 Volgraf, M. *et al.* Allosteric control of an ionotropic glutamate receptor with an optical switch. *Nat Chem Biol* **2**, 47-52, doi:10.1038/nchembio756 (2006).
- 63 Gorostiza, P. *et al.* Mechanisms of photoswitch conjugation and light activation of an ionotropic glutamate receptor. *Proc Natl Acad Sci U S A* **104**, 10865-10870, doi:10.1073/pnas.0701274104 (2007).
- 64 Szobota, S. *et al.* Remote control of neuronal activity with a light-gated glutamate receptor. *Neuron* **54**, 535-545, doi:10.1016/j.neuron.2007.05.010 (2007).
- 65 Numano, R. *et al.* Nanosculpting reversed wavelength sensitivity into a photoswitchable iGluR. *Proc Natl Acad Sci U S A* **106**, 6814-6819, doi:10.1073/pnas.0811899106 (2009).
- 66 Noguchi, J. *et al.* Bidirectional *in vivo* structural dendritic spine plasticity revealed by two-photon glutamate uncaging in the mouse neocortex. *Sci Rep* **9**, 13922, doi:10.1038/s41598-019-50445-0 (2019).
- 67 Wang, M. *et al.* Comparing the effective attenuation lengths for long wavelength *in vivo* imaging of the mouse brain. *Biomed Opt Express* **9**, 3534-3543, doi:10.1364/BOE.9.003534 (2018).



## Supporting Information (SI) of Chapter 9

### SI9.1 Cell culture and transfection

Human Embryonic Kidney tsA201 (HEK tsA201) cells were purchased from the European Collection of Authenticated Cell Culture. The cells were maintained at 37°C in a humidified atmosphere with 5% CO<sub>2</sub> and grown in Dulbecco's modified Eagle's medium/Nutrient Mixture F-12 Ham (DMEM/F12 1:1, Life Technologies) medium, supplemented with 10% fetal bovine serum (FBS, Life Technologies) and antibiotics (1% penicillin/streptomycin, Sigma-Aldrich). Since M<sub>2</sub> muscarinic acetylcholine receptor (mAChRs) activate the G $\alpha_i$  protein subfamily, we co-transfected chimeric G $\alpha_i$ /G $\alpha_q$  protein (G $\alpha_{qTOP}$ )<sup>1</sup> to couple M<sub>2</sub> mAChRs activation to the phospholipase C pathway, thus inducing inositol 1,4,5-trisphosphate (IP<sub>3</sub>) production and subsequent intracellular calcium release from the endoplasmic reticulum. Co-expression of human M<sub>2</sub> mAChRs (Addgene) and the G $\alpha_{qTOP}$  (ratio 1:1) was induced by plasmid transient transfection with X-tremeGENE 9 DNA Transfection Reagent (Roche Applied Science) following the manufacturer's instructions. The day after, cells were harvested with accutase (Sigma-Aldrich) and seeded onto 25 mm glass coverslips (ThermoFisher Scientific) coated with poly-L-Lysine (Sigma-Aldrich) to allow cell adhesion. Finally, the seeded cells were used for the experiments after 24 h.

### SI9.2 *In vitro* calcium imaging and two-photon excitation

The bath solution used for single cell intracellular calcium recordings contained: 140 mM NaCl, 5.4 mM KCl, 1 mM MgCl<sub>2</sub>, 10 mM HEPES, 10 mM glucose and 2 mM CaCl<sub>2</sub>, with pH 7.40. Before each experiment, cells were mounted on the recording chamber and loaded with the chemical calcium indicator Oregon Green 488 BAPTA-1, AM (OGB-1 AM, Life Technologies) for 30 min at 37°C and 5% CO<sub>2</sub>, at a final concentration of 10  $\mu$ M in Ca<sup>2+</sup>-free bath solution. Cells were rinsed with fresh solution, and the recording chamber was filled with 1 ml of the bath solution. In all the experiments PAI was applied in its *cis* conformation and the *trans*-to-*cis* photoisomerization was achieved by pre-illuminating the compound with a Vilber Lourmat UV Lamp (365 nm, 6 W) for 2 min before the application.

Two-photon excitation (2PE) experiments (**Figure S9.1**) were performed in the Advanced Digital Microscopy Core Facility of the Institut de Recerca Biomèdica de Barcelona (IRBB) using a confocal multiphoton microscope equipped with a pulsed broadband Ti:Sapphire laser (Mai Tai, Spectra- Physics), which can be tuned between 710-990 nm (80 MHz repetition rate,

80 fs pulse, light power  $2.8 \text{ mW} \cdot \mu\text{m}^{-2}$  at 720-840 nm). Images under 2PE were acquired at room temperature with an inverted laser-scanning confocal microscope (TCS SP5, Leica Microsystems) equipped with a HCX PL APO 40 $\times$ /1.25-0.75-NA oil objective for imaging cultured cells, and a HC PL APO 20 $\times$ /0.7-NA CS air objective (Leica Microsystems). The imaging interval was of 4 s. Acquired image sequences were stored in the Leica image format and stacks for offline analysis with Fiji (NIH, ImageJ).

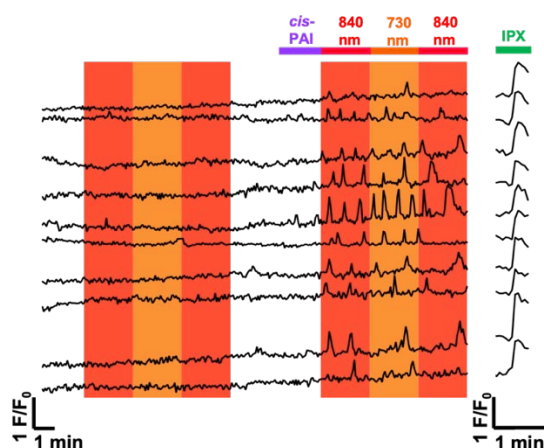


**Figure S9.1. The activation of PAI with near-infrared light under two-photon excitation is not reversible.** Real-time calcium imaging traces from HEK cells co-expressing M<sub>2</sub> mAChR and G $\alpha_{qTOP}$  loaded with 10  $\mu\text{M}$  of the fluorescent calcium indicator OGB-1 AM. Representative single cell calcium responses ( $n = 10$  cells) to 30 pM *cis*-PAI pre-illuminated at 365 nm (purple bar), to PAI under two-photon excitation (2PE) at 840 nm (red bar) and 730 nm (dark orange bar) and to the muscarinic superagonist iperoxo (IPX; green bar). Neither 2PE alone nor *cis*-PAI elicited calcium responses. Cells respond to application of pulsed near-infrared (NIR) light at 840 nm in the presence of PAI due to its photoisomerization to the *trans*-active form, but no switching to the *cis* isoform under 730 nm is observed, indicating that *trans*-to-*cis* isomerization is not a favorable process under 2PE.

### SI9.3 Molecular calculation of multiphotonic properties

Theoretical calculations were used to identify the lowest energy excited electronic state that leads to *cis*-to-*trans* isomerization of the N=N double bond of PAI and two model photoswitchable azocompounds (Figure S9.2). In the molecular orbital parlance, photoisomerization happens when one electron is promoted from an occupied molecular orbital to a molecular orbital with antibonding character and local  $\pi$  character in the azo group. This causes the bond order of the double bond to decrease, turning it into a single bond that can rotate freely leading to isomerization. The antibonding character is identified by the presence of a nodal plane perpendicular to the N—N bond in the azo group. The ground state geometry of PAI and the two model azocompounds were fully optimized at the DFT/CAM-B3LYP level<sup>2</sup> using the 6-311+G(d,p) basis set. The energies of the excited states (vertical excitations) and

the oscillator strengths were obtained using the time-dependent formalism (TD-DFT) with the 6-31G(d,p) basis set, whereas multiphotonic cross sections were calculated with the 6-31G(d) basis set. Gaussian09 suite of programs<sup>3</sup> was used for the optimization while the Dalton program<sup>4</sup> was chosen to perform the calculation and analysis of the multiphotonic properties.

Analysis of the one-, two- and three-photon optical transitions was conducted for the *trans*- and *cis*-isomers of the azobenzene derivatives depicted in **Figure S9.2**: (a) the parent azobenzene (**1**); (b) a simple model of the azo core of PAI (**2**); (c) and a PAI molecule.

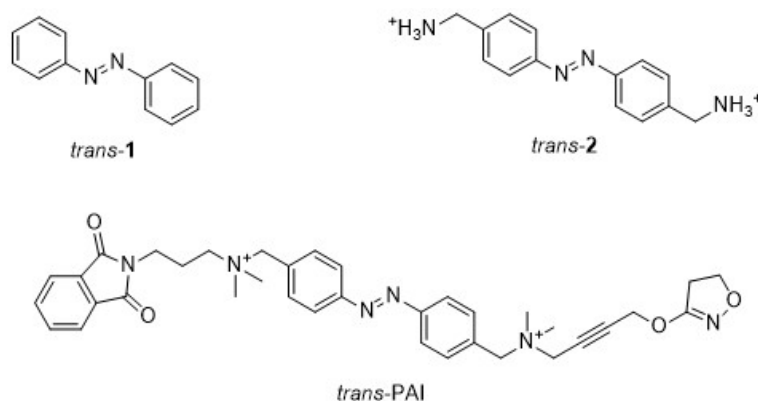


**Figure S9.2.** Molecular structures of the most stable *trans*-isomer of the three azo compounds theoretically analyzed.

### SI9.3.1 Azobenzene and PAI model results

**Tables S9.1-S9.4** report the main results obtained for azocompounds 1 and 2. Only singlet states were considered. The different singlet excited electronic states are labelled as usual:  $S_1$ ,  $S_2$ , ... , which refer to the first, second, ... singlet excited electronic state, respectively. For each possible transition, the oscillator strength ( $f$ ) determines its probability under one-photon excitation (1PE), while the cross-section ( $\sigma_i$ ) gives the same information for the two- and three-photon excitations (2PE and 3PE). The units of the cross-sections are Goeppert-Mayer (GM) for the two-photon cross section ( $1 \text{ GM} = 10^{-50} \text{ cm}^4 \cdot \text{s}/\text{photon}$ ) and atomic units (a.u.) for the three-photon cross section ( $1 \text{ a.u.} = 1.282 \cdot 10^{-83} \text{ cm}^6 \cdot \text{s}^2 \cdot \text{photon}^{-2}$ ). In both cases, the reported cross-sections are for a linear polarization and a full width at half maximum (FWHM) of 0.1 eV. The cross-sections for both two- and three-photon absorptions depend inversely on FWHM. Results given in **Tables S9.1-S9.4** were obtained with the 6-31G(d) basis set except when explicitly noted. Calculations included up to 20 singlet excited electronic states, though only transitions to the lowest five of these states are shown in the tables. The rest were found to occur at excitation energies well above the experimental values used herein.

State	E(eV)	f	$\sigma_2(\text{GM})$	$\sigma_3(\text{a.u.})$	Excitation <sup>a</sup>
S <sub>1</sub>	2.72	0.00	0.01	0.01	H-1 → L
S <sub>2</sub>	4.26	0.60	0.00	2.64·10 <sup>7</sup>	H → L
S <sub>3</sub>	4.85	0.03	0.00	5.59·10 <sup>5</sup>	H-2 → L
S <sub>4</sub>	4.86	0.00	3.30	2.17	H-3 → L
S <sub>5</sub>	5.59	0.00	3.28·10 <sup>2</sup>	0.15	H-4 → L

**Table S9.1. Energies, oscillator strengths (f) and cross-sections for the two- and three-photon absorption processes of *trans*-azobenzene (*trans*-1).** <sup>a</sup>Only the main contribution is shown. H and L stand for HOMO and LUMO, respectively.

State	E(eV)	f	$\sigma_2(\text{GM})$	$\sigma_3(\text{a.u.})$	Excitation <sup>a</sup>
S <sub>1</sub>	2.76	0.02	0.01	3.05·10 <sup>5</sup>	H → L
S <sub>2</sub>	4.85	0.16	4.07	4.38·10 <sup>6</sup>	H-1 → L
S <sub>3</sub>	4.92	0.02	74.70	8.48·10 <sup>5</sup>	H-2 → L
S <sub>4</sub>	5.13	0.07	2.29	2.34·10 <sup>6</sup>	H-4 → L
S <sub>5</sub>	5.17	0.00	25.40	5.19·10 <sup>4</sup>	H-3 → L

**Table S9.2. Energies, oscillator strengths (f) and cross-sections for the two- and three-photon absorption processes of *cis*-azobenzene (*cis*-1).** <sup>a</sup>Only the main contribution is shown. H and L stand for HOMO and LUMO, respectively.

State	E(eV) <sup>a</sup>	f <sup>a</sup>	$\sigma_2(\text{GM})$	$\sigma_3(\text{a.u.})$	Excitation <sup>b</sup>
S <sub>1</sub>	2.56 (2.61)	0.00 (0.00)	0.01	7.94·10 <sup>4</sup>	H → L
S <sub>2</sub>	4.29 (4.18)	0.79 (1.05)	0.00	8.57·10 <sup>7</sup>	H-1 → L
S <sub>3</sub>	4.80 (4.71)	0.04 (0.04)	0.00	8.66·10 <sup>5</sup>	H-2 → L
S <sub>4</sub>	4.80 (4.72)	0.00 (0.00)	3.30	1.49·10 <sup>4</sup>	H-3 → L
S <sub>5</sub>	5.62 (5.48)	0.00 (0.00)	3.28·10 <sup>2</sup>	8.08·10 <sup>3</sup>	H-4 → L

**Table S9.3. Energies, oscillator strengths (f) and cross-sections for the relevant two- and three-photon absorption processes of the *trans*-isomer 9 of the PAI azo model (*trans*-2).** <sup>a</sup>Numbers in parentheses are for the 6-311+G(d,p) basis set. <sup>b</sup>Only the main contribution is shown. H and L stand for HOMO and LUMO, respectively.

State	E(eV) <sup>a</sup>	f <sup>a</sup>	$\sigma_2(\text{GM})$	$\sigma_3(\text{a.u.})$	Excitation <sup>b</sup>
S <sub>1</sub>	2.76 (2.65)	0.04 (0.04)	0.12	1.95·10 <sup>6</sup>	H → L
S <sub>2</sub>	4.85 (4.79)	0.15 (0.11)	0.13	1.69·10 <sup>7</sup>	H-2 → L
S <sub>3</sub>	4.92 (4.83)	0.00 (0.01)	6.22·10 <sup>2</sup>	2.42·10 <sup>5</sup>	H → L+1
S <sub>4</sub>	5.13 (4.95)	0.03 (0.03)	1.42·10 <sup>2</sup>	2.20·10 <sup>6</sup>	H-1 → L
S <sub>5</sub>	5.17 (4.97)	0.44 (0.44)	2.32·10 <sup>2</sup>	5.53·10 <sup>7</sup>	H-1 → L+1

**Table S9.4. Energies, oscillator strengths (f) and cross-sections for the relevant two- and three-photon absorption processes of the *cis*-isomer of the PAI model (*cis*-2).** <sup>a</sup>Numbers in parentheses are for the 6-311 + G(d,p) basis set. <sup>b</sup>Only the main contribution is shown. H and L stand for HOMO and LUMO, respectively.

For the PAI model 2 the excited state energies and the oscillator strengths were also calculated with the larger 6-311 + G(d,p) basis set. At this higher computational level excitation energies are slightly lower than those calculated with the smaller 6-31G(d,p) used throughout. At any rate differences are small and well below the expected error of the TDDFT methodology (ca. 0.25 eV), so the use of the smaller basis set seems validated.

In the following **Figures S9.3-S9.6** the shape of the orbitals implied in the excitations to the lower excited states (those expected to be relevant in the study) are depicted. It is easy to discern  $n$  and  $\pi$  orbitals in the *trans*-isomers but in the *cis*-isomers this simple classification is not so crystalline as, due to steric repulsions, the more congested *cis* structures are no longer planar. No relevant differences are seen between the raw azobenzene and the **PAI** model as the added ammonium groups seem to play a very minor role in the relevant molecular orbitals. Almost all the reported electronic excitations involve the LUMO as the final destination of the excited electron. For both the *trans*- and *cis*-isomers this orbital is clearly  $\pi^*$  with a large antibonding character located in the azo group, so that it is expected that all the reported excitations to the LUMO may produce the isomerization of the substrate after irradiated with the corresponding frequency. The only exception is found in two of the reported excited electronic states of the *cis*-isomer of 2 that involve the LUMO+1. Due to the loss of planarity of the *cis*-isomer (already discussed), this orbital cannot be fully characterized as  $\pi^*$  though it clearly has local  $\pi$  antibonding character in the azo region.

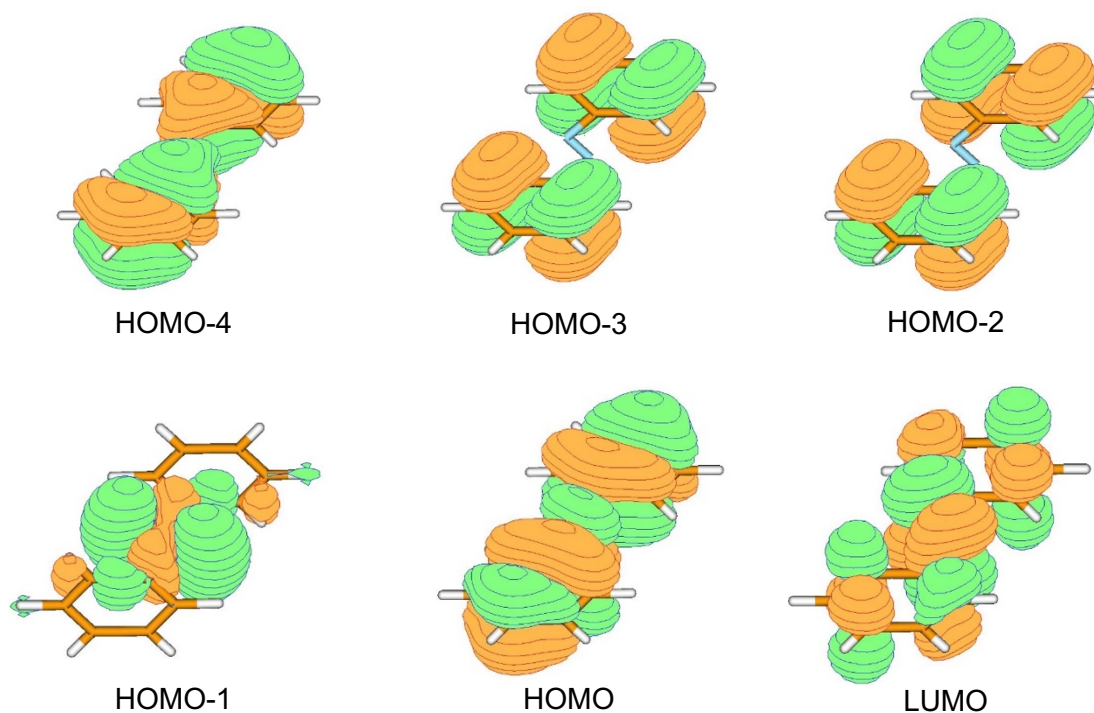


**Figure S9.3.** Shape of the molecular orbitals that participate in the 5 lowest excited electronic states of *trans*-azobenzene (*trans*-1).

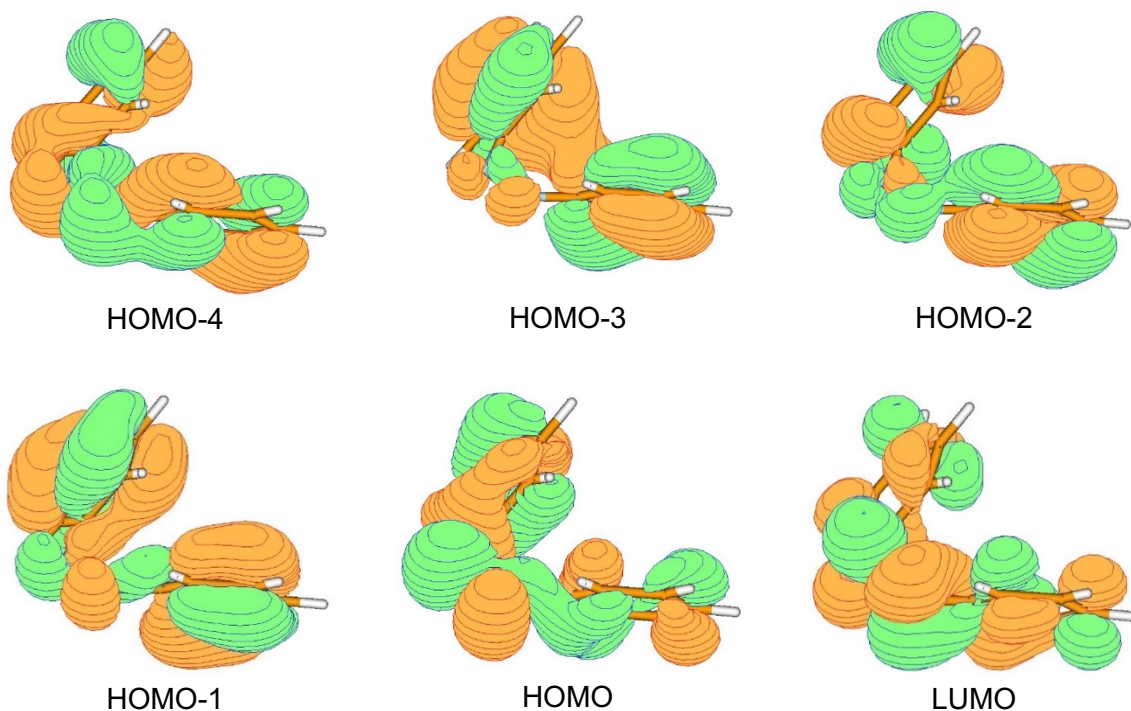


Figure S9.4. Shape of the molecular orbitals that participate in the 5 lowest excited electronic states of *cis*-azobenzene (*cis*-1).

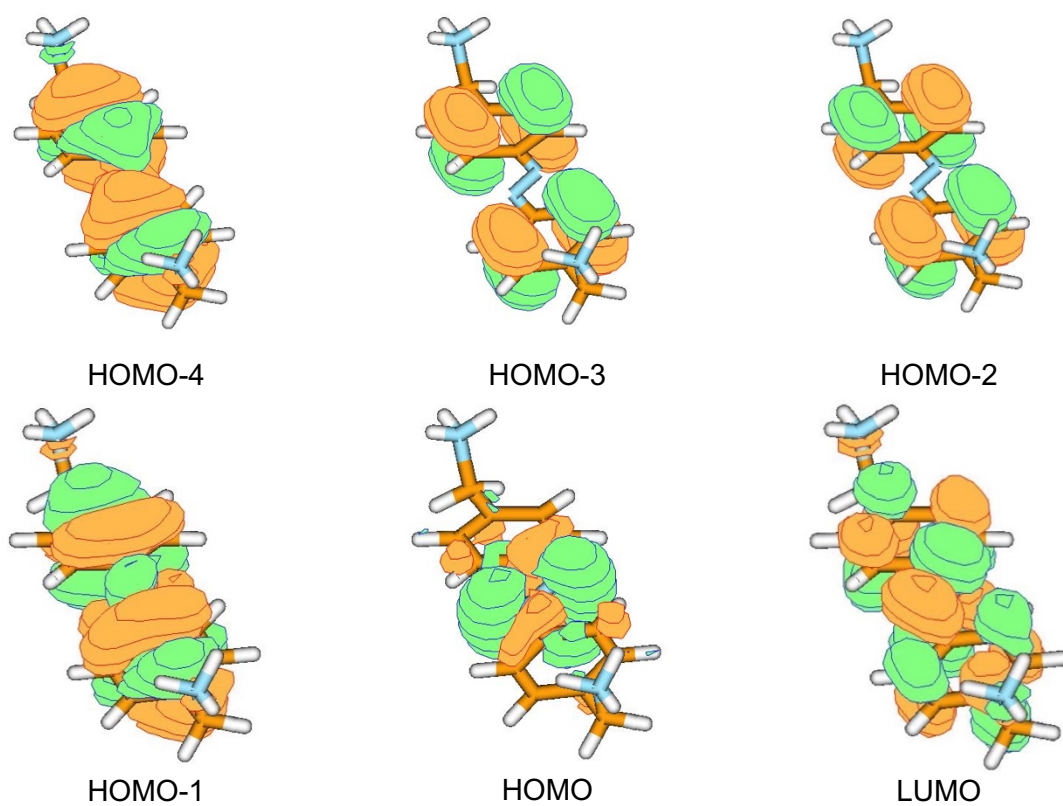


Figure S9.5. Shape of the molecular orbitals that participate in the 5 lowest excited electronic states of *trans*-PAI model (*trans*-2).

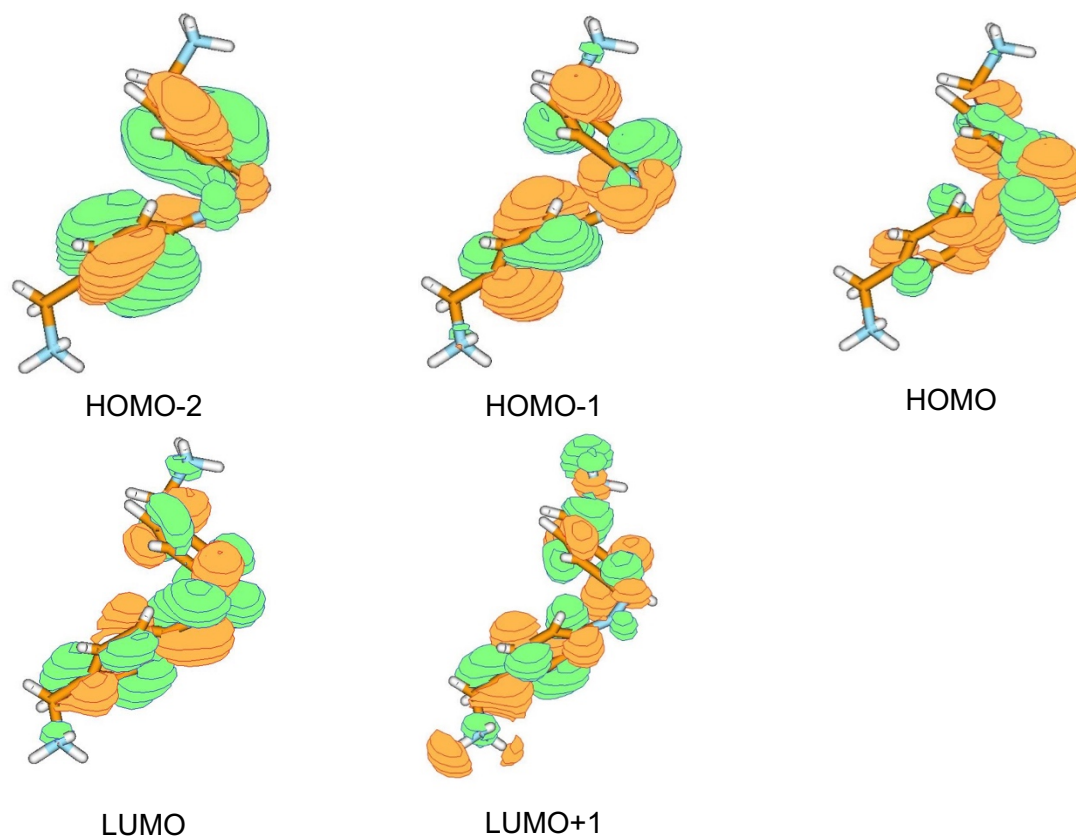


Figure S9.6. Shape of the molecular orbitals that participate in the 5 lowest excited electronic states of *cis*-PAI model (*cis*-2).

### SI9.3.2 PAI results

Similar calculations to those just reported for the smaller azo models 1 and 2 were finally performed for the full PAI molecule. The calculated excited states and their properties are presented in **Table S9.5** and **Table S9.6**, respectively, for the *trans*- and *cis*-isomers of PAI. These tables only report the excited states that imply electronic excitations localized in the azo unit so, even if only 5 excited states are included in the Tables (to coincide with the previous reported results for the smaller systems), as in the previous cases the calculation has extended up to 20 excited states. The excited states not reported in the tables imply excitations localized away of the azobenzene group, on the far side substituents (mainly, the aromatic condensed bicycle on the end of the molecule). Obviously, these states are irrelevant for the *cis*-to-*trans* isomerization process and have no equivalence in the PAI model 2, so they have not been included in the corresponding tables.

We can now compare the results of the full system presented in **Table S9.5** and **Table S9.6** with the ones for the PAI model 2 seen in **Tables S9.3** and **Table S9.4**. Because some excited electronic states of the full system are not involved in the isomerization process, as just discussed, the specific position of a given excited electronic state  $S_n$  is irrelevant and

comparison has to be made in the same order as the different states are presented in the corresponding tables. For instance,  $S_3$  of the *trans*-isomer of **PAI** presented in **Table S9.5** corresponds to  $S_2$  in the *trans*-isomer of **2** (**Table S9.3**), whereas  $S_2$  for the *cis*-isomer of **2** (**Table S9.4**) has to be related to  $S_6$  of the full **PAI** system (**Table S6**). Considering this equivalence, model **2** clearly provides results very similar to the ones for the full system; therefore, the use of the truncated **PAI** model in future work is legitimated by our calculations.

State	E(eV)	$\lambda_{1P}$ (nm)	$\lambda_{2P}$ (nm)	$\lambda_{3P}$ (nm)	f	$\sigma_2$ (GM)	$\sigma_3$ (a.u.)	Excitation <sup>a</sup>
$S_1$	2.62	473	946	1420	0.00	0.01	$4.36 \cdot 10^3$	H-6 $\rightarrow$ L
$S_3$	4.16	298	596	894	1.39	0.30	$1.67 \cdot 10^8$	H-4 $\rightarrow$ L
$S_6$	4.74	261	523	785	0.03	1.25	$8.55 \cdot 10^5$	H-9 $\rightarrow$ L
$S_7$	4.76	260	521	781	0.01	2.55	$3.57 \cdot 10^5$	H-10 $\rightarrow$ L
$S_{14}$	5.54	224	448	671	0.01	$7.88 \cdot 10^2$	$9.02 \cdot 10^5$	H-12 $\rightarrow$ L

**Table S9.5.** Energies, wavelengths of the one- two- and three-photon processes, oscillator strengths (f) and cross-sections for the relevant two- and three-photon absorption processes of the *trans*-isomer of the **PAI** molecule. <sup>a</sup>Only the main contribution is shown. H and L stand for HOMO and LUMO, respectively.

State	E(eV)	$\lambda_{1P}$ (nm)	$\lambda_{2P}$ (nm)	$\lambda_{3P}$ (nm)	f	$\sigma_2$ (GM)	$\sigma_3$ (a.u.)	Excitation <sup>a</sup>
$S_1$	2.64	470	939	1409	0.03	0.11	$1.37 \cdot 10^6$	H-1 $\rightarrow$ L
$S_6$	4.90	253	506	759	0.03	$4.98 \cdot 10^2$	$2.02 \cdot 10^6$	H-5 $\rightarrow$ L
$S_7$	4.98	249	498	747	0.04	20.8	$1.94 \cdot 10^6$	H-1 $\rightarrow$ L+2
$S_{11}$	5.06	245	490	735	0.30	3.39	$2.13 \cdot 10^7$	H-10 $\rightarrow$ L
$S_{13}$	5.43	228	457	685	0.04	$1.18 \cdot 10^2$	$3.37 \cdot 10^6$	H-1 $\rightarrow$ L+3

**Table S9.6.** Energies, wavelengths of the one- two- and three-photon processes, oscillator strengths (f) and cross-sections for the relevant two- and three-photon absorption processes of the *cis*-isomer of the **PAI** molecule. <sup>a</sup>Only the main contribution is shown. H and L stand for HOMO and LUMO, respectively.

Finally, **Figure S9.7** and **Figure S9.8** depict the shape of the molecular orbitals mainly involved in the relevant electronic excitations of the **PAI** full system in the *trans* and *cis* structures, respectively. As already discussed for the truncated **1** and **2** systems, all the excitations reported for *trans*-**PAI** lead to the  $\pi^*$  N-N antibonding LUMO, thus expecting to result in *trans*-to-*cis* isomerization. Again, due to the loss of planarity, symmetry assignments are not so clear for the *cis*-isomer. Accordingly, the different virtual orbitals involved in the relevant excited electronic states reported in **Table S6** are no longer strictly  $\pi^*$ , though it can be argued that all display some  $\pi$  antibonding character in the azo N-N region.



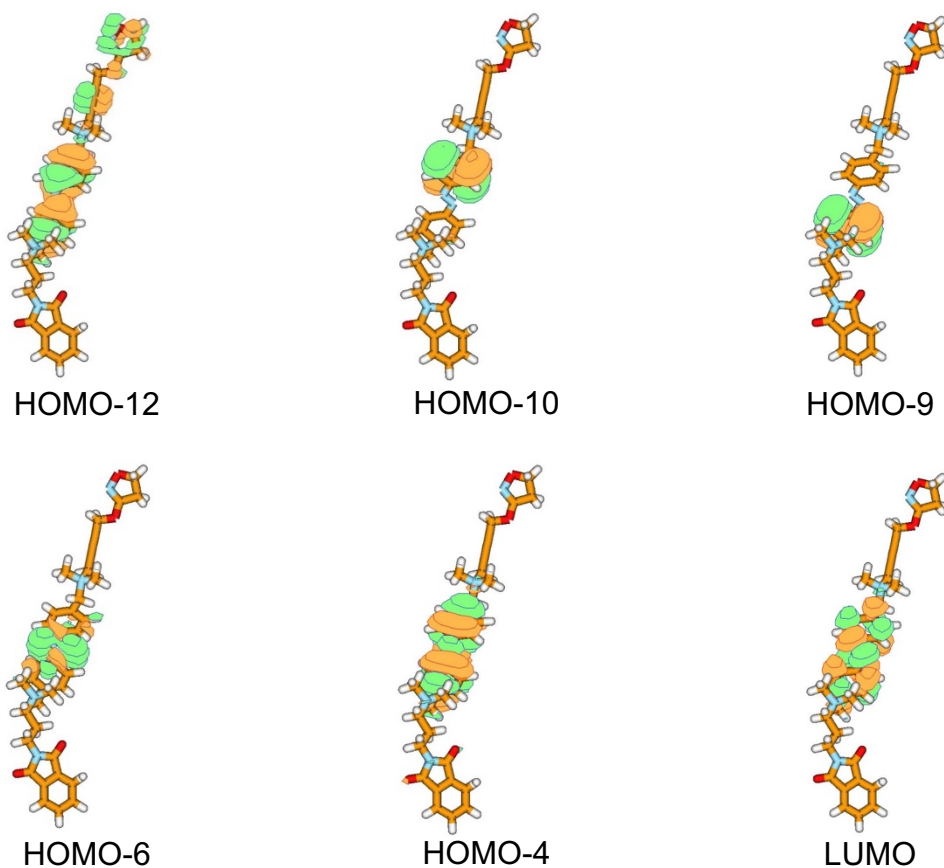


Figure S9.7. Shape of the molecular orbitals that participate in the relevant excited electronic states of *trans*-PAI full system.

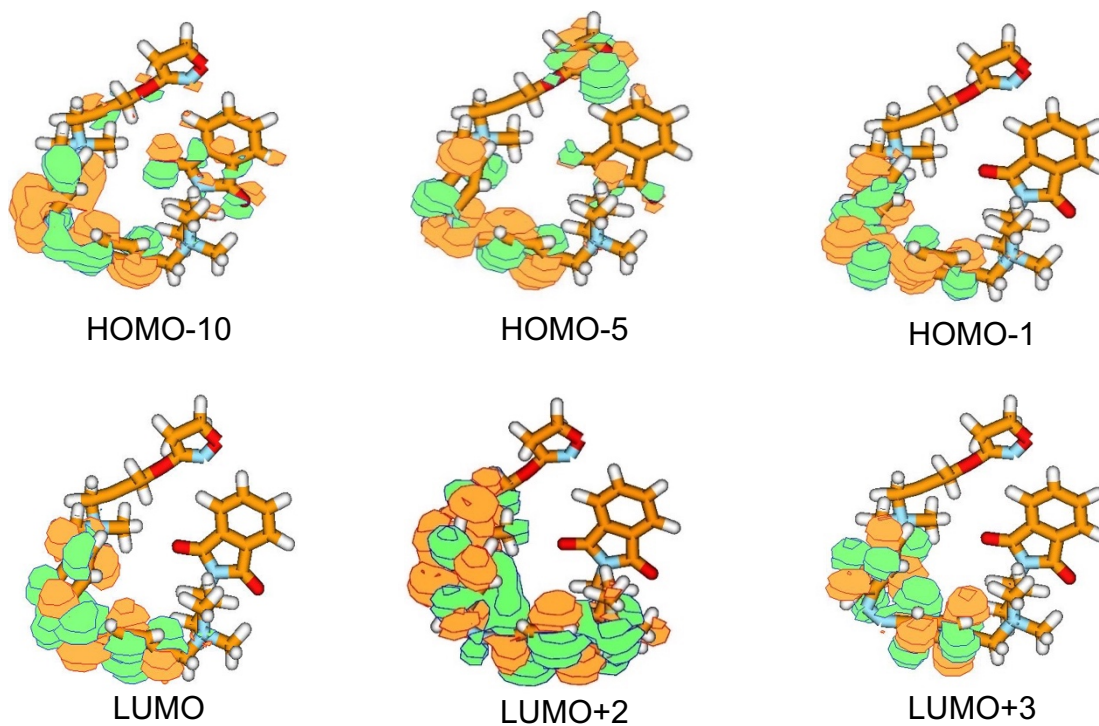


Figure S9.8. Shape of the molecular orbitals that participate in the relevant excited electronic states of *cis*-PAI full system.

### SI9.3 *In vitro* calcium imaging and three-photon excitation

The bath solution used for single cell intracellular calcium recordings contained: 140 mM NaCl, 5.4 mM KCl, 1 mM MgCl<sub>2</sub>, 10 mM HEPES, 10 mM glucose and 2 mM CaCl<sub>2</sub>, with pH 7.40. Before each experiment, cells were mounted on the recording chamber and loaded with the chemical calcium indicator OGB-1 AM (Life Technologies) for 30 min at 37°C and 5% CO<sub>2</sub>, at a final concentration of 10 μM in Ca<sup>2+</sup>-free bath solution. Cells were rinsed with fresh solution, and the recording chamber was filled with 1 ml of the bath solution.

Three-photon excitation (3PE) experiments were performed at the Institut de Ciències Fotòniques (ICFO). In all the experiments **PAI** was applied in its *cis* conformation and the photoisomerization was achieved by pre-illuminating the compound with a Vilber Lourmat UV Lamp (365 nm, 6 W) for 2 min before the application. The *cis*-to-*trans* photoisomerization was achieved by illuminating the specimen with a femtosecond-pulsed laser beam (FFS, Toptica) centered at 1560 nm used for the 3PE stimulation<sup>5</sup>. Cells were placed on an adapted inverted fluorescence microscope (Eclipse TE2000-U, Nikon) modified for performing nonlinear imaging experiments<sup>6</sup>. The coupling system for 3PE stimulation consisted of a pair of two galvanometric mirrors (Cambridge Technology) and a telescope arrangement followed with a dichroic mirror (DMSP1000R, Thorlabs) for sending the femtosecond-pulsed laser to a 40x NA 1.30 oil objective (Plan Fluor, Nikon). OGB-1 AM fluorescence was excited (1PE) with a mercury lamp (C-HGFI, Nikon) and fluorescence excitation/emission was filtered with a fluorescence cube centered at 480 nm for excitation and 535 nm for emission (FITC filter cube, Standard series, Nikon). 512 x 512 pixel images were acquired at room temperature every 2 s for 5 min with a sCMOS camera (Orca-Flash 4.0 v3, Hamamatsu) with NIS-Elements software (Nikon). For the power dependence experiments, we adjusted the laser power at the back sample plane of the objective to 26.5 mW (63%), 33.2 mW (79%), 38.2 mW (91%) and 42 mW (100%). Stock solutions of the agonists were stored at -20 °C in aqueous solution. Addition of agonists and vehicle was carried out by carefully pipetting directly into the recording chamber for a final concentration of 50 pM. Iperoxo (IPX), a previously described muscarinic selective superagonist, was used as a positive control to stimulate M<sub>2</sub> mAChRs in HEK tsA201 cells (30 pM).

Imaging data were extracted with Fiji (NIH, ImageJ). All data were analyzed by using Excel (Microsoft, version 16.62) and GraphPad Prism (GraphPad Software, version 9) and normalized with the maximal response to IPX (30 pM). Statistical differences were analyzed

by the one-way ANOVA with Tukey's multiple comparisons post-hoc test, whereas a value of  $p \leq 0.05$  was considered as significant. The data are expressed as the mean  $\pm$  SEM.

### SI9.3.1 Control experiments

Control experiments were performed in transfected HEK cells in absence of PAI to exclude any possible artifact due to the light stimuli alone (**Figure S9.9**). Further control experiments were performed in HEK cells without the transfection with M<sub>2</sub> mAChR and G $\alpha_{qTOP}$  (**Figure S9.10**).

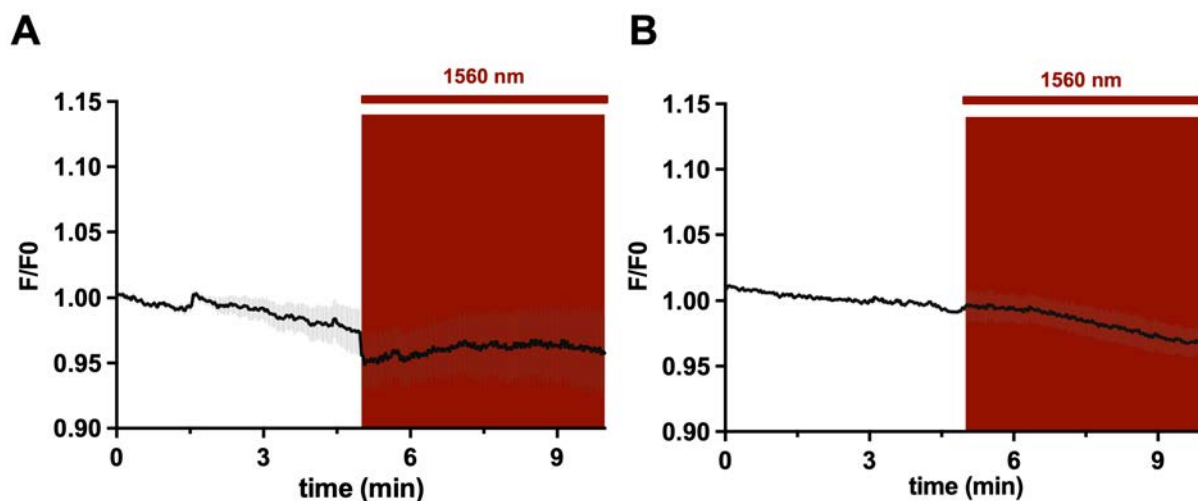


**Figure S9.9. Light control experiments.** Real-time calcium imaging traces from HEK cells co-expressing M<sub>2</sub> mAChR and G $\alpha_{qTOP}$ , which were loaded with the calcium indicator OGB-1 AM (10  $\mu$ M). **(A)** The graph shows the average trace of cells in response to illumination at 1560 nm using maximum laser power (dark red bar,  $n = 9$  cells). **(B)** The graph presents the average trace of cells in response to illumination at 1560 nm using maximum laser power for the power-dependence experiment shown in **Figure 9.3** (dark red bar,  $n = 10$  cells).

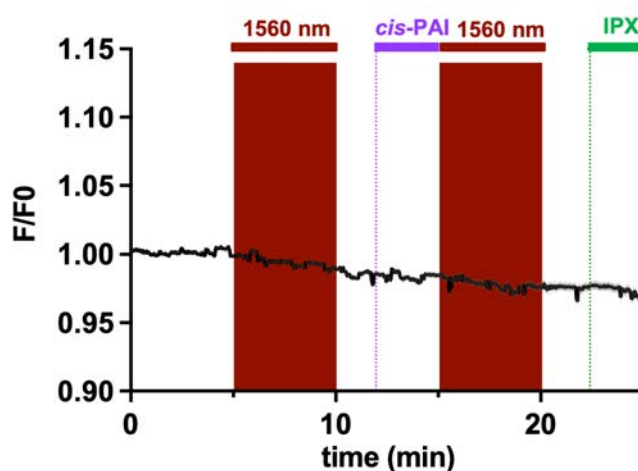


**Figure S9.10. Control experiments in HEK cells not expressing M<sub>2</sub> mAChR and G $\alpha_{qTOP}$ .** The cells were loaded with the calcium indicator OGB-1 AM (10  $\mu$ M). No calcium oscillations were observed after application of pre-irradiated *cis*-PAI (50 pM), *trans*-enriched PAI obtained under 3PE at 1560 nm using maximum laser power (dark red bar), and agonist iperoxo (IPX) ( $n = 40$  cells).

### SI9.3.2 Power dependence experiments

The photoresponses were quantified by percentage of photoresponsive cells and amplitude of the response (Figure S9.11).

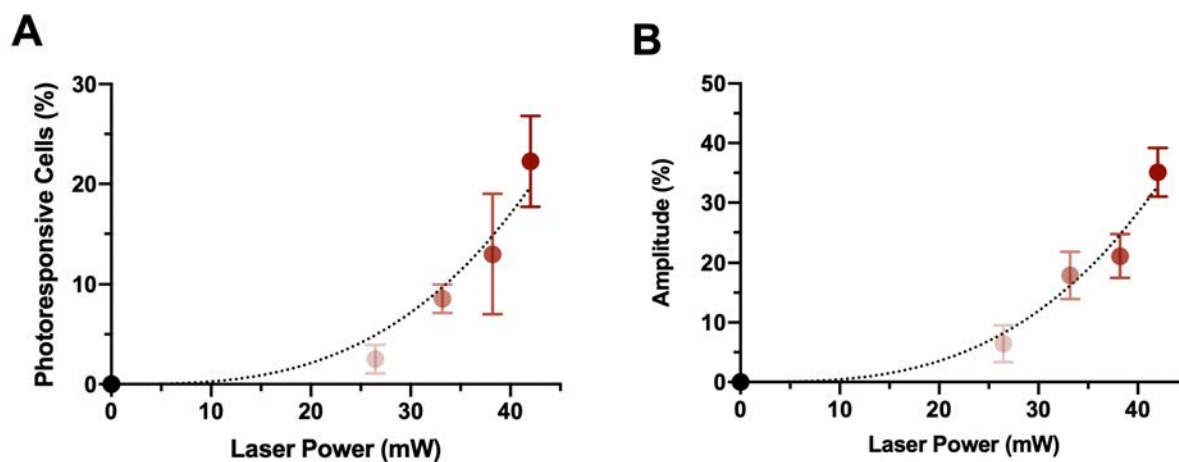


**Figure S9.11. Quantification of the power-dependence experiments.** (A) fraction (percentage) of photoresponsive cells ( $n = 36$  cells from 3 independent experiments) over the total number of cells activated by iperoxo (IPX;  $n = 145$  cells). ( $R^2 = 0.68$ , slope 4.6), and (B) fraction (percentage) of fluorescence photoresponse amplitude ( $R^2 = 0.79$ , slope 3.4) vs. different laser power intensities. Data have been normalized to the average cell response with IPX ( $n = 36$  cells from 4 independent experiments). The lower correlation observed in comparison to the quantification of AUC (Figure 9.3) may be due to the transient nature of the  $M_2R$ -mediated cellular responses and the variable expression levels of  $M_2$  mAChR and  $G\alpha_{qTOP}$  between individual cells.

### SI9.4 *In vivo* experiments with PAI under three-photon excitation

*In vivo* experiments were performed at ICFO with 5 days-post-fertilization (dpf) albino Tg(elavl3:GCaMP6s) zebrafish larvae. The experimental procedures were approved by a local Animal Welfare and Ethical Review board (Generalitat de Catalunya, ref #10716). All efforts were made to minimize animal suffering and the number of animals used in this study. Larvae were first anesthetized for 5 min in a 0.4% tricaine in E3 medium<sup>7</sup>. Then, they were mounted on 35 mm bottom-glass dishes (P35GC-1.5-10C, MatTek Corporation) and oriented with 1% low melting agarose (V2111, Promega Corporation). Subsequently, the plate was placed on an adapted inverted fluorescence microscope (Eclipse TE2000-U, Nikon) using a 25x NA 1.05 water immersion objective (XL Plan N, Olympus). An image in brightfield was taken as a reference and the imaging and photoisomerization experiments were done using the parameters as stated previously with the *in vitro* 3PE experiments. The imaging interval was of 1 s. 3PE experiments were carried out in a selected region of the field of view (Figure 9.4B) scanning

the femtosecond-pulsed laser at maximum power (100%, 42 mW). Neuronal activity movies were analyzed and quantified as described in the section Data analysis.

Drug/vehicle were applied directly to the ~200  $\mu$ l volume of the bath where the zebrafish larvae were immobilized.

Artifacts were induced by the mechanical application of the compounds, thereby the frames corresponding to each application were removed from the video used for the analysis. The representative images in **Figure 9.4B** were obtained by processing the video of each experimental condition to get the maximum intensity projection, and then subtracting the minimum intensity projection. Data were analyzed by paired-t-test, whereas a value of  $p \leq 0.05$  was considered as significant. The data are expressed as the mean  $\pm$  SEM.

The quantification of the AUC and amplitude of the response upon 3PE of PAI is shown in **Figure 9.4D** and **S9.12**.

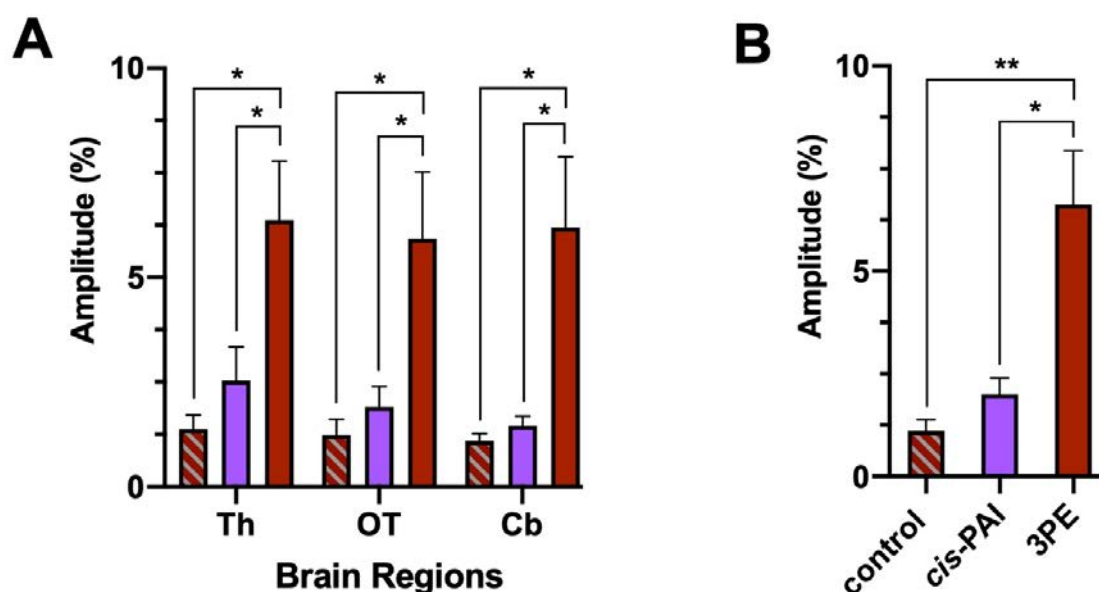


**Figure S9.12. *In vivo* activation of PAI by three-photon excitation.** Quantification of calcium imaging response as percent change of the amplitude upon three-photon excitation (3PE) of PAI in zebrafish brain. **(A)** Responses in three different brain regions (Th, thalamus; OT, optic tectum; Cb, cerebellum;  $n = 5$ ) to 3PE before drug application (striped bars), to *cis*-PAI application (violet bars), and to 3PE in the presence of *cis*-PAI (dark red bars). **(B)** Quantification of whole brain response, each column representing the mean  $\pm$  SEM of five independent experiment ( $n = 5$ ). Pre-illuminated *cis*-PAI (violet bar) was applied at 50 pM in the zebrafish bath. Upon switching to *trans*-PAI using 3PE at 1560 nm (dark red bar), large amplitude responses were observed. 3PE control at 1560 nm in the absence of *cis*-PAI did not elicit any effect (striped bar). Error bars indicate SEM. Data were analyzed by paired t-test,  $p$ -value (\*\*)  $< 0.01$  and  $p$ -value (\*)  $< 0.05$  using GraphPad Prism 9.

## SI9.5 Figure of merit applied to induce three-photon excitation (FOM<sub>3PE</sub>) of PAI molecule

	Output laser power [%]	P <sub>avg</sub> [mW]	FOM <sub>3PE</sub> [W <sup>3</sup> ]	FOM <sub>3PE</sub> /area [W <sup>3</sup> /mm <sup>2</sup> ]
<b>3P stimulation</b>	63	26.46	1.3 x10 <sup>5</sup>	6.6x10 <sup>10</sup>
	79	33.18	2.5x10 <sup>5</sup>	1.3x10 <sup>11</sup>
	91	38.22	3.8x10 <sup>5</sup>	1.9x10 <sup>11</sup>
	100	42	5.1x10 <sup>5</sup>	2.5x10 <sup>11</sup>
<b>3P optogenetic stimulation [8]</b>		50	≈7.4x10 <sup>13</sup>	≈2.2x10 <sup>16</sup>
<b>Damage threshold [8]</b>		62	≈1.4x10 <sup>14</sup>	≈4.3x10 <sup>16</sup>

**Table 9.7. Figure of merit applied to induce three-photon excitation (FOM<sub>3PE</sub>) of PAI molecule [W<sup>3</sup>].** The output laser power (%) used in this work with the corresponding power average at the sample plane (P<sub>avg</sub> [mW]), the figure of merit, FOM<sub>3PE</sub>=P<sub>avg</sub><sup>3</sup>/Δt<sup>2</sup>\*f<sup>2</sup>,<sup>9</sup> where Δt corresponds to the temporal width and f is the repetition rate of the excitation laser<sup>9</sup>. In this work, we use the FOM<sub>3PE</sub>/area [W<sup>3</sup>/mm<sup>2</sup>] as a comparative method. The area is calculated from the characteristics of the excitation objective used (NA = 1.3, λ = 1560 nm). The laser power required for 3P stimulation of PAI molecule is lower than that reported by Rowlands *et al.*, 2017<sup>8</sup>.

### SI9.6 3PE stimulation of cellular activity *in vivo*

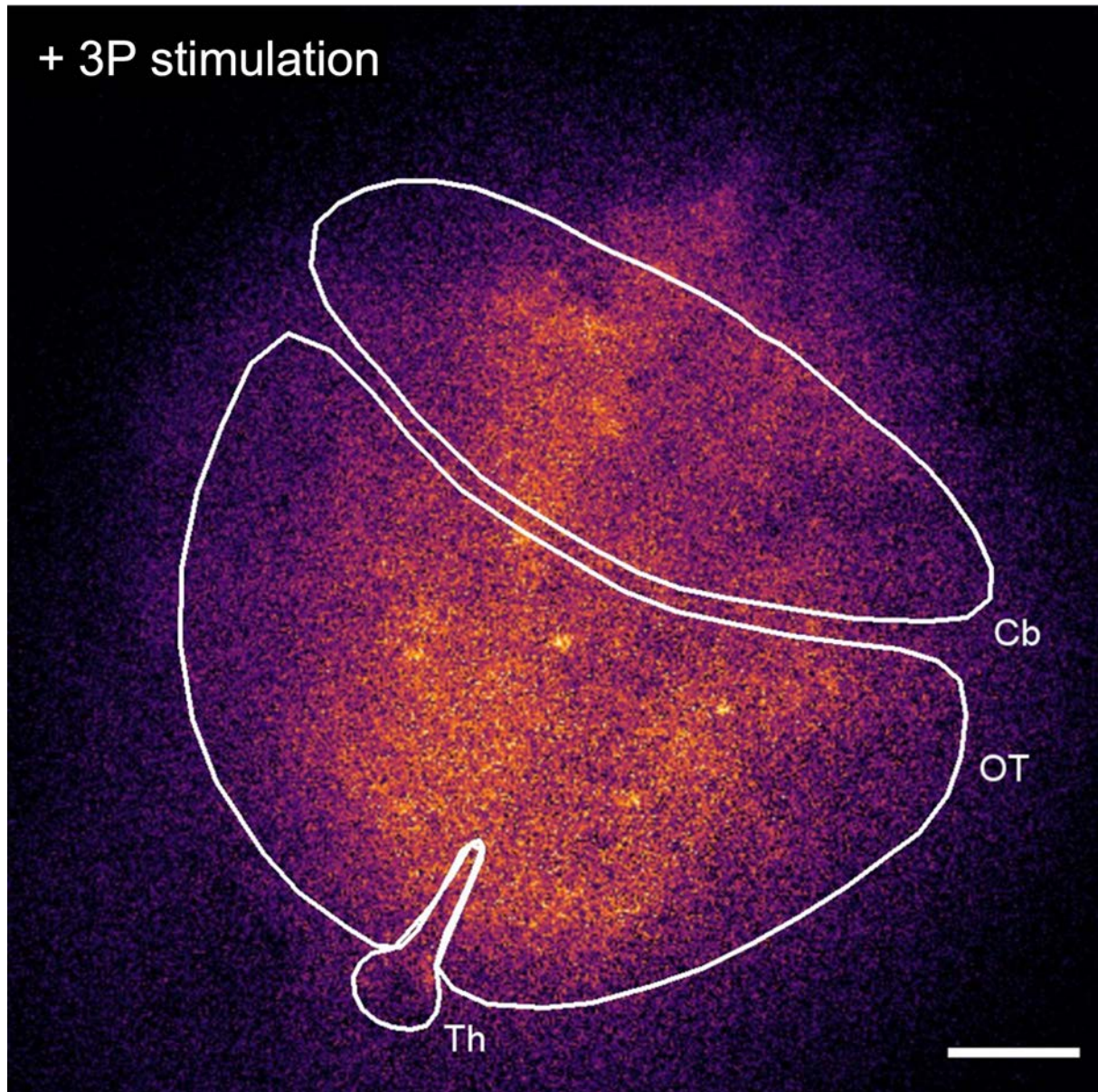


**Figure S9.13. Three-photon excitation of cellular activity *in vivo*.** Time-lapse images (1 s frame interval) of the fluorescence calcium signal from the zebrafish larvae brain (dorsal view) upon different conditions: (a) brain being irradiated with the pulsed-laser prior drug application, (b) application of 50 pM *cis*-PAI, (c) irradiation with the pulsed-laser in the presence of *cis*-PAI. Pulsed-laser irradiation in the absence of *cis*-PAI did not elicit visual changes in fluorescence intensity. Similarly, the application of *cis*-PAI without irradiating the pulsed-laser did not elicit major changes in the fluorescence signal. Upon laser effect, large changes in fluorescence intensity were observed due to the 3PE stimulation effect that photoconverts *cis*-to-*trans*-PAI. Th, thalamus; OT, optic tectum; Cb, cerebellum. Scale bar = 50  $\mu$ m.

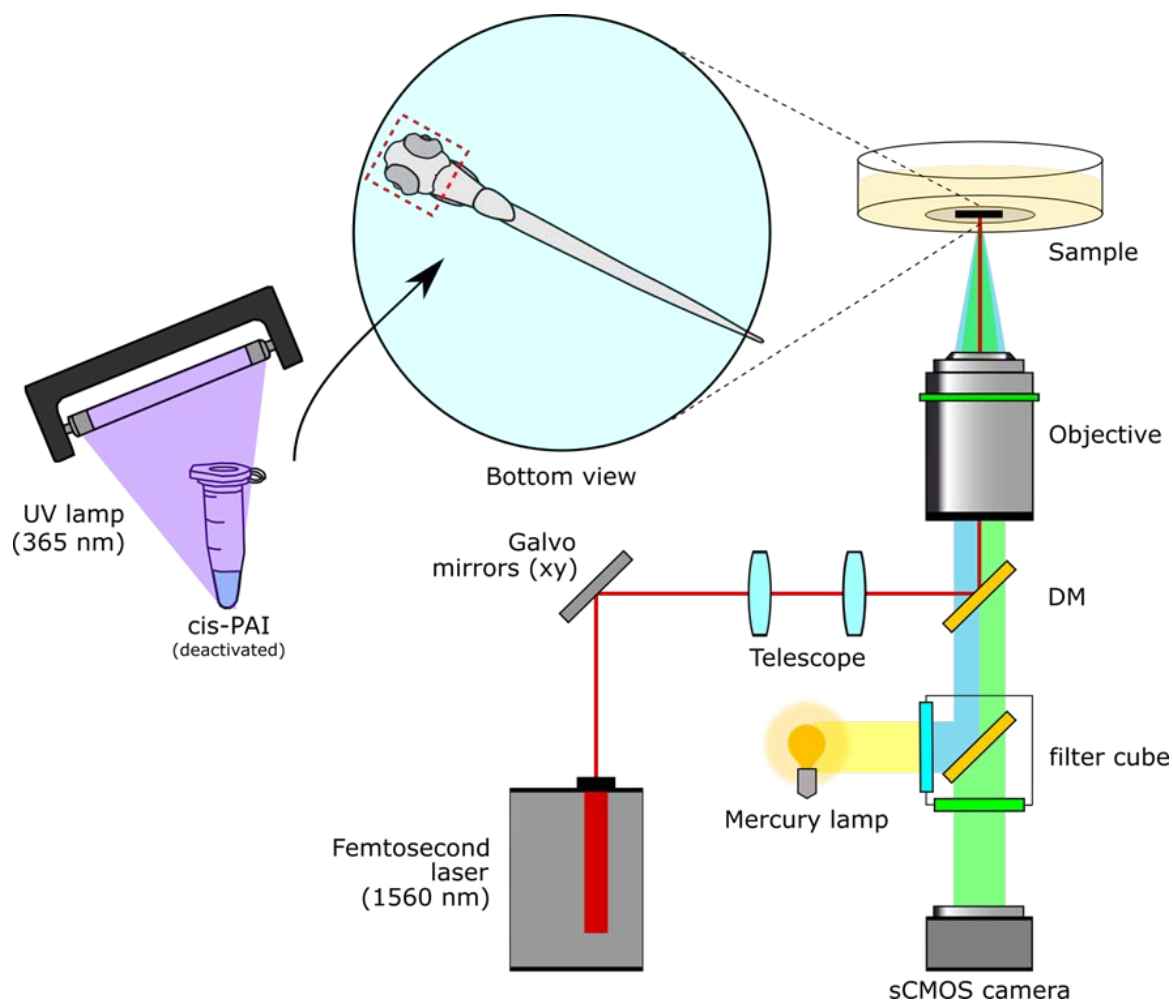


**Figure S9.14. Multiphoton stimulation imaging system used for three-photon excitation of cellular activity *in vivo*.** Tricaine-anesthetized zebrafish larvae [albino Tg(elavl3:GCaMP6s)] were mounted on bottom-glass dishes and oriented upside-down for proper visualization of the brain. The calcium activity was studied upon treatment with the previously deactivated form of PAI (*cis*-PAI) pre-irradiated with UV light (365 nm). The system consists of an adapted inverted fluorescence microscope modified for performing nonlinear imaging experiments. The coupling system for 3PE stimulation consisted of a femtosecond-pulsed laser (1560 nm) scanned with a pair of two galvanometric mirrors and a telescope arrangement followed with a dichroic mirror (DM) and a 25x NA 1.05 water immersion objective to focus the beam on the sample plane. GCaMP6s fluorescence was excited with a mercury lamp and fluorescence excitation/emission was filtered with a filter cube centered at 480 nm for excitation and 535 nm for emission. 512 x 512 pixel images were acquired every 1 s for 5 min with a sCMOS camera. 3PE stimulation was carried out in a selected region (represented with a dashed red square) scanning the femtosecond laser at maximum power (100%, 42 mW).



## Additional references

1. Gomeza, J. *et al.* Coupling of metabotropic glutamate receptors 2 and 4 to  $G\alpha_{15}$ ,  $G\alpha_{16}$ , and chimeric  $G\alpha_{q/i}$  proteins: characterization of new antagonists. *Mol Pharmacol* **50**, 923-930 (1996).
2. Handy, N.C. The molecular physics lecture 2004: (i) Density functional theory, (ii) Quantum Monte Carlo. *Molecular Physics* **102**, 2399-2409. 10.1080/00268970412331293848 (2004).
3. Frisch, M.J., Trucks, G.W., Schlegel, H.B., Scuseria, G.E., Robb, M.A., Cheeseman, J.R., Scalmani, G., Barone, V., Mennucci, B., and Petersson, G.A. Gaussian 09 (Gaussian, Inc.: Wallingford, CT, USA) (2009).
4. Olsen, J.M.H., Reine, S., Vahtras, O., Kjellgren, E., Reinholdt, P., Hjorth Dundas, K.O., Li, X., Cukras, J., Ringholm, M., Hedegård, E.D., et al. Dalton project: A python platform for molecular- and electronic-structure simulations of complex systems. *The Journal of Chemical Physics* **152**, 214115. 10.1063/1.5144298 (2020).
5. Aviles-Espinosa, R., Santos, S.I., Brodschelm, A., Kaenders, W.G., Alonso-Ortega, C., Artigas, D., and Loza-Alvarez, P. Third-harmonic generation for the study of *Caenorhabditis elegans* embryogenesis. *J Biomed Opt* **15**, 046020. 10.1117/1.3477535 (2010).
6. Santos, S.I., Mathew, M., Olarte, O.E., Psilodimitrakopoulos, S., and Loza-Alvarez, P. Femtosecond laser axotomy in *Caenorhabditis elegans* and collateral damage assessment using a combination of linear and nonlinear imaging techniques. *PLoS One* **8**, e58600. 10.1371/journal.pone.0058600 (2013).
7. Westerfield, M. The zebrafish book: A guide for the laboratory use of zebrafish (*Danio rerio*) (2000).
8. Rowlands, C. J. *et al.* Wide-field three-photon excitation in biological samples. *Light Sci Appl* **6**, e16255, doi:10.1038/lsa.2016.255 (2017).
9. Loza-Alvarez, P. A., D.; Aviles-Espinosa, R. *Semiconductor lasers and diode-based light sources for biophotonics* **472** (2018).

# Chapter 10

---

## Reversible photocontrol of dopaminergic transmission in wild-type animals

---

---

Carlo Matera, Pablo Calvé<sup>¶</sup>, Verònica Casadó-Anguera<sup>¶</sup>, **Rosalba Sortino<sup>¶</sup>**, Alexandre M. J. Gomila, Estefanía Moreno, Thomas Gener, Cristina Delgado-Sallent, Pau Nebot, Davide Costazza, Sara Conde-Berriozabal, Mercè Masana, Jordi Hernando, Vicent Casadó, Victoria Puig and Pau Gorostiza. **Reversible photocontrol of dopaminergic transmission in wild-type animals.** *Int. J. Mol. Sci.* 2022, 23, 10114. <sup>¶</sup>These authors contributed equally.



## Abstract

Understanding the dopaminergic system is a priority in neurobiology and neuropharmacology. Dopamine receptors are involved in the modulation of fundamental physiological functions, and dysregulation of dopaminergic transmission is associated with major neurological disorders. However, the available tools to dissect the endogenous dopaminergic circuits have limited specificity, reversibility, resolution, or require genetic manipulation. Here, we introduce **azodopa**, a novel photoswitchable ligand that enables reversible spatiotemporal control of dopaminergic transmission. We demonstrate that **azodopa** activates D<sub>1</sub>-like receptors *in vitro* in a light-dependent manner. Moreover, it enables reversibly photocontrolling zebrafish motility on a timescale of seconds and allows separating the retinal component of dopaminergic neurotransmission. **Azodopa** increases the overall neural activity in the cortex of anesthetized mice and displays illumination-dependent activity in individual cells. **Azodopa** is the first photoswitchable dopamine agonist with demonstrated efficacy in wild-type animals and opens the way to remotely controlling dopaminergic neurotransmission for fundamental and therapeutic purposes.



## 10.1 Introduction

Dopamine receptors (DARs) are members of the class A G protein-coupled receptor (GPCR) family and are prominent in the vertebrate central nervous system (CNS). Their primary endogenous ligand is the catecholaminergic neurotransmitter dopamine, a metabolite of the amino acid tyrosine. Among the many neuromodulators used by the mammalian brain to regulate circuit function and plasticity, dopamine (**Figure 10.1A**) stands out as one of the most behaviorally powerful<sup>1,2</sup>. Dopaminergic neurons are critically involved in diverse vital CNS functions, including voluntary movement, feeding, reward, motivation, sleep, attention, memory, and cognition. The extracellular concentration of components of dopamine oscillates following day/night cycles and plays important physiological roles in the regulation of olfaction, retinal function<sup>3</sup>, and circadian rhythms<sup>4</sup>. Disentangling these diverse components of DAR signaling and dopaminergic transmission is an unmet need both of basic research and medicine, because their abnormal function leads to complex medical conditions such as Parkinson's and Huntington's diseases, schizophrenia, attention deficit hyperactivity disorder, Tourette's syndrome, drug abuse, and addiction<sup>1</sup>. To date, five subtypes of DARs have been cloned: D<sub>1</sub>R, D<sub>2</sub>R, D<sub>3</sub>R, D<sub>4</sub>R, and D<sub>5</sub>R. Based on their coupling to either G $\alpha_{s/olf}$  proteins or G $\alpha_{i/o}$  proteins, which, respectively, stimulate or inhibit the production of the second messenger cAMP, DARs are classified as D<sub>1</sub>-like receptors (D<sub>1</sub>R, D<sub>5</sub>R) or D<sub>2</sub>-like receptors (D<sub>2</sub>R, D<sub>3</sub>R, D<sub>4</sub>R). However, both classes are known to signal through multiple pathways. Targeting these receptors using specific agonists and antagonists allows to modulate dopaminergic transmission and dopamine-dependent functions. Indeed, hundreds of compounds interfering with dopaminergic system have been developed, and many of them are clinically used to treat various disorders. They also constitute pharmacological tools to study the role of dopamine in synaptic and neural circuits<sup>5,6</sup> as well as the mechanisms underlying dopamine-related debilitating conditions<sup>7</sup>. However, conventional ligands cannot differentiate among specific neuronal sub-populations in heterogenous brain regions where multiple neuronal subtypes exist, thus potentially activating DARs that mediate distinct or even opposing physiological functions<sup>2</sup>. For this reason, the lack of circuit selectivity is a confounding element in basic research and likely cause of poor safety as well as efficacy of many dopaminergic drugs. Hence, methods to activate DARs noninvasively with high spatiotemporal resolution are required both for research and therapeutic purposes.

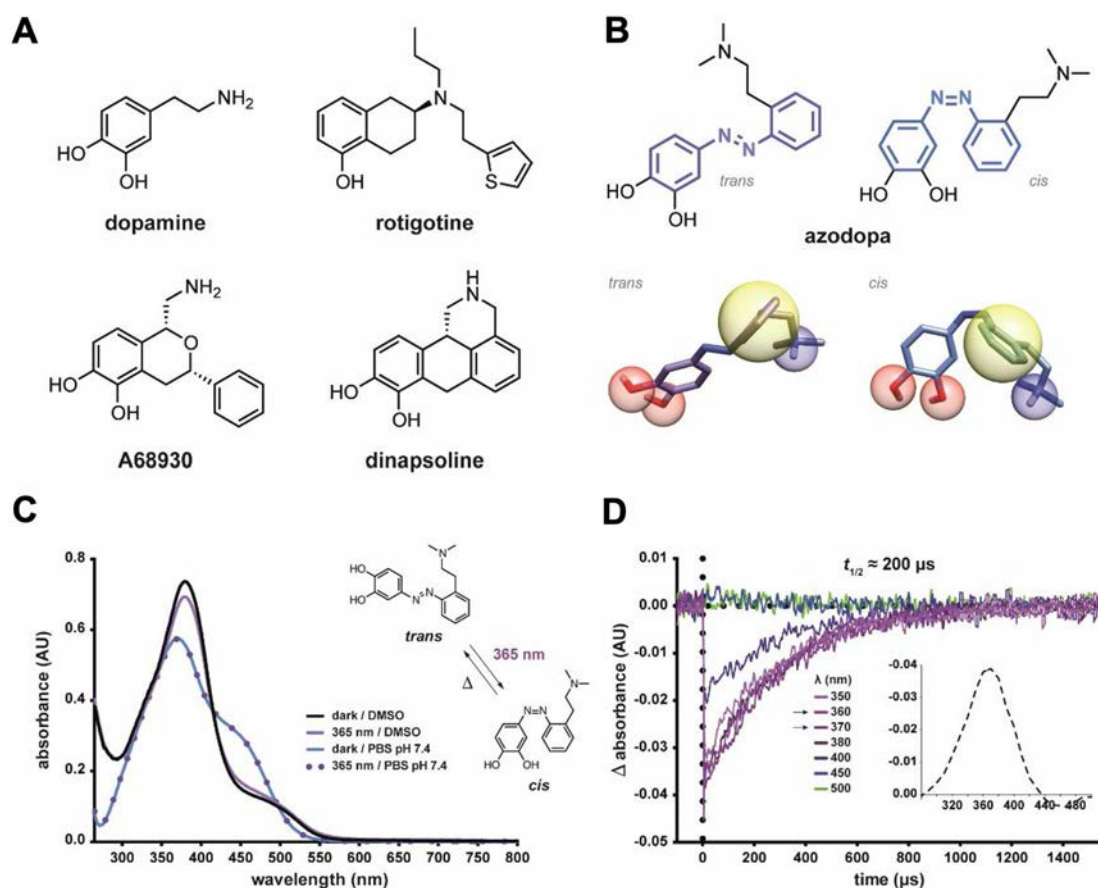


**Figure 10.1. Design, structure, and photochromism of azodopa.** (A) Chemical structure of dopamine and representative (semi)rigidified derivatives: rotigotine (nonselective agonist), A68930 (D<sub>1</sub>R agonist), and dinapsoline (D<sub>1</sub>R agonist). (B) 2D and 3D chemical structure of the photochromic dopamine ligand **azodopa** (*trans* and *cis*-isomers). Essential pharmacophoric features for D<sub>1</sub>R binding are highlighted: blue spheres represent cationic site points and H-bond donors, *i.e.*, the protonated amino function that can form a salt bridge and a hydrogen bond with Asp103 and Ser107, respectively; red spheres represent H-bond acceptors, *i.e.*, the hydroxyl groups of the catechol ring that can interact with Ser198, Ser199, and Ser202; yellow spheres represent hydrophobic elements, *i.e.*, the aromatic ring that can form  $\pi$ - $\pi$  interactions with Phe288 and Phe289. The mutual position and orientation of such pharmacophoric features in the receptor-bound conformation should affect binding affinity and efficacy of the ligands. (C) Photochromic behavior of **azodopa** (50  $\mu$ M) studied with steady-state spectroscopy in aqueous (PBS, pH 7.4) and organic (DMSO) solutions. As lifetimes of *cis*-hydroxyazobenzenes are very short in polar protic solvents, no changes in the absorption spectrum of aqueous solutions of **azodopa** could be observed after illumination with 365 nm light (3 min). (D) Photochromic behavior of **azodopa** (30  $\mu$ M) investigated by transient absorption spectroscopy in water (only representative traces are shown for the sake of clarity; see Figure S10.4 for the full experiment). Transient absorption time traces were measured at different wavelengths upon excitation of *trans*-**azodopa** with a 5 ns pulsed laser at  $\lambda = 355$  nm (3 mJ/pulse energy) and 25°C. Thermal relaxation half-life of the *cis*-isomer (200  $\mu$ s) was estimated by applying an exponential one-phase decay model (GraphPad Prism 6). Inset: Transient absorption spectrum of *trans*-**azodopa** upon pulsed irradiation at  $\lambda = 355$  nm recorded at  $t = 0$   $\mu$ s. X-values represent wavelength (nm), Y-values represent  $\Delta A$  (arbitrary units, AU).

Pursuing a traditional pharmacological approach would hardly pay off in such a physiological scenario, because a drug generally affects its target in multiple CNS regions at once and its effect is slowly reversible. Light is an unparalleled input signal to noninvasively manipulate biological systems in precisely designated patterns, and photopharmacology<sup>8-10</sup>, which relies on molecular photoswitches to regulate bioactive compounds, has already been successful in GPCRs<sup>11-16</sup>, ion channels<sup>17,18</sup>, and enzymes<sup>19,20</sup>. The possibility of using light as an external stimulus to manipulate specific populations of dopaminergic neurons has generated enormous interest in neurobiology since the invention of optogenetics<sup>21,22</sup>, in particular to elucidate the basis of complex behavioral and cognitive processes<sup>23,24</sup>. However, the achievements of optogenetics rely on the overexpression of exogenous proteins that lack critical aspects of endogenous GPCR signaling, including their native ligand binding sites, downstream molecular interactions, and other elements that can affect receptor dynamics. Thus, current optogenetic tools may provide partial, or sometimes inaccurate, insights into biological processes. In addition, the application of genetic manipulation techniques to human subjects is still importantly hampered by safety (possible immune responses against the gene transfer), regulatory, and economic issues. Complementary approaches to address some of these limitations have been proposed. Trauner, Isacoff, and collaborators developed light-gated DARs through a combined chemical–genetic method in which a weakly photoswitchable ligand was tethered via a maleimide–thiol conjugation to a genetically engineered cysteine residue at the target receptor in order to improve photocontrol<sup>25</sup>. They also used a genetically targeted membrane anchor to tether a dopaminergic ligand via SNAP-tag labeling<sup>15</sup>. Unlike the exogenous optogenetics tools described above, light-gated receptors bear a single-point mutation and provide a nearly physiological study system, but they still require gene delivery and overexpression. Genetics-free methods have also been described. For instance, Etchenique, Yuste, and collaborators developed a caged dopamine compound based on ruthenium–bipyridine chemistry and used it to activate dendritic spines with two-photon excitation<sup>26</sup>. More recently, Gienger *et al.*, 2020 described two caged DAR antagonists that can serve as valuable tools for light-controlled blocking of D<sub>2</sub>/D<sub>3</sub> receptors<sup>27</sup>. However, notwithstanding its virtues, uncaging is an irreversible chemical process, while a photopharmacological modulation based on reversible, byproduct-free molecular photoswitches has important advantages *in vivo*. Noteworthy in this regard is the work published by König and collaborators, who developed a set of photochromic small molecules by incorporation of dithienylethenes and fulgides into known dopamine receptor ligands<sup>28</sup>. Two of those compounds, named 29 and 52, showed an interesting isomer-dependent (open *vs.* closed form) efficacy at activating D<sub>2</sub> receptors,



although neither *in situ* photoswitching nor *in vivo* validation of their effects were reported. We present here the design, synthesis, and photopharmacological characterization of the first chemical tool that enables the reversible photocontrol of native dopamine receptors in wild-type (WT) animals. Notably, it can be used to separate the retinal component of dopaminergic neurotransmission in zebrafish and manipulate brain waves in mice.

## 10.2 Results

### 10.2.1 Rational design and chemical synthesis

Aryl azo compounds, especially azobenzenes, have emerged as the photoswitches of choice in photopharmacology because of their physical and chemical properties, which make them especially suitable for biological applications<sup>29,30</sup>. An elegant strategy for the incorporation of an azobenzene into a bioactive ligand<sup>11</sup> relies on the isosteric replacement of the two-atom linker between the two aromatic rings with a diazene unit ( $-N=N-$ )<sup>11,20,31-33</sup>, which entails minimal perturbation of pharmacophore and drug-like properties, thus accounting for the success of this so-called azologization approach<sup>31</sup>. However, to the best of our knowledge, this strategy is not applicable to any of the known dopamine agonists, since the scaffold of an isomerizable aryl azo compound is not directly conceivable in their structure.

In the quest for a freely diffusible drug-like dopaminergic photoswitch, we noticed that most agonists (especially to D<sub>1</sub>Rs, see **Figure 10.1A**) are rigid or semi-rigid, conformationally restrained structures in which essential pharmacophoric features are held in their mutual position<sup>34</sup>. Indeed, two main routes can be identified in the early development of dopamine agonists, namely, the rigidification of the dopamine molecule and the dissection of apomorphine, one of the first potent dopamine agonists to be found<sup>35</sup>. Dopamine rigidification led to the discovery of potent agonists, whereas the apomorphine de-rigidification generally reduced its efficacy<sup>36,37</sup>. It stands then to reason that governing the geometry of such structures would enable the control of their biological effects. This could be achieved by “building” upon a semi-rigid and photoisomerizable molecular frame the structural elements required for DAR activation and using light as external control signal. This approach can be likened to a “photoswitch decoration”, in which pharmacophore groups are introduced into the structure of a molecular photoswitch to design a light-controlled bioactive compound. Common features in the dopamine agonist pharmacophore model are the following: (a) a cationic site point (an amino group) that forms a salt bridge with an aspartic acid residue in the receptor’s third transmembrane (TM3) helix; (b) one or two hydrogen bond acceptor/donor sites (*e.g.*, hydroxy

groups), that interact with serine residues in TM5; and (c) an aromatic ring system that takes part in  $\pi$ - $\pi$  interactions with hydrophobic residues in TM6<sup>38-40</sup>. On these grounds, we devised a photo-switchable dopamine agonist by decorating an azobenzene molecule with two hydroxyl substituents (II) on one phenyl ring, and an amino group (I) connected through a short linker to the other phenyl ring (III) (**Figure 10.1B**). This molecule, that we named **azodopa**, carries the main DAR binding determinants and enables to change their relative position upon photoisomerization (**Figure 10.1B**). **Azodopa** was synthesized in two steps via an azo-coupling reaction between commercially available 2-(2-(dimethylamino)ethyl)aniline and 1,2-dihydroxybenzene (**Scheme S10.1** and **Supplementary Information, SI**, for detailed synthetic procedures and physicochemical characterization).

### 10.2.2 Photochemical characterization

An essential condition for **azodopa** to function as a photoswitchable dopamine ligand is that it photoisomerizes between two different configurations (*trans* and *cis*). We first characterized it by steady-state ultraviolet-visible (UV-Vis) absorption spectroscopy (**Figure 10.1C**), which revealed an absorption maximum at 370 nm in aqueous solution (PBS, pH 7.4) and at 380 nm in DMSO. It is known that the thermal *cis*-to-*trans* isomerization of 4-hydroxyazobenzenes follows a very fast kinetics in polar protic solvents via solvent-assisted proton transfer tautomerization, whereas it proceeds more slowly in aprotic and nonpolar solvents<sup>41</sup>. In agreement, no changes in the absorption spectrum of **azodopa** could be detected with a conventional UV-Vis spectrophotometer upon illumination at 365 nm in aqueous buffer because of the short lifetime of its *cis*-isomer in this medium, likely because of the presence of a non-negligible concentration of azonium cation at physiological pH and/or the formation of hydrogen-bonded complexes with the solvents that accelerate the thermal *cis*-to-*trans* isomerization via tautomerization, and only a small change could be recorded in a polar but aprotic solvent such as DMSO, where the tautomerization is still possible, although less pronounced (**Figure 10.1C**). No measurements were performed in nonpolar solvents (*e.g.*, toluene) because of the very poor solubility of our compound in this kind of media. We next determined the optimal isomerization wavelength and lifetime of *cis*-**azodopa** by means of transient-absorption spectroscopy with ns-time resolution. Upon pulsed excitation of **azodopa** in aqueous media with ultraviolet (UV) and violet light, an instantaneous and remarkable decrease of the absorption signal was detected, which can be ascribed to the depletion of the *trans* ground electronic state due to the photoinduced formation of the corresponding *cis*-isomer (**Figure 10.1D**)<sup>41,42</sup>. The initial absorption value was quickly recovered because of the fast

thermal *cis*-to-*trans* back-isomerization which restores the initial concentration of the *trans*-isomer with an estimated half-life of about 200  $\mu$ s (**Figure 10.1D**). Thus, since conversion to the *trans* form occurs almost immediately after turning the light off, we performed all biological experiments under continuous illumination. Overall, our absorption spectroscopy studies showed that **azodopa** undergoes *trans*-to-*cis* photoisomerization upon illumination with UV and violet light and it spontaneously reverts to its full *trans*-isomer in a fraction of a millisecond once the light is switched off. Other mechanisms, such as excited-state intramolecular proton transfer, could also play a role. In any case, **azodopa** should allow fast regulation of DAR activity using a single illumination source to induce *trans*-to-*cis* isomerization.

### 10.2.3 *In vitro* pharmacological characterization

We next tested the effects of **azodopa** on D<sub>1</sub>-like receptors, for which freely diffusible photoswitchable agonists have not been reported. First, we evaluated the binding affinity of **azodopa** in mammalian D<sub>1</sub>-like and D<sub>2</sub>-like receptors using competitive radioligand binding experiments performed either in the dark or under illumination at 365 nm (see **SI** for details)<sup>43,44</sup>. **Azodopa** displayed a good capacity to bind to D<sub>1</sub>-like and D<sub>2</sub>-like receptors, with higher affinity in the *trans* configuration in both cases. In particular, for D<sub>1</sub>-like receptors, we calculated an almost fourfold decrease in affinity at 365 nm ( $K_{d/\text{dark}} = 600$  nM,  $K_{d/365\text{ nm}} = 2200$  nM) (**Figure S10.5** and **Table S10.1**). Since the activation of D<sub>1</sub>-like receptors promotes cyclic adenosine monophosphate (cAMP) formation and phosphorylation by ERK1/2, we also investigated the ability of **azodopa** to behave as a D<sub>1</sub>-like receptor agonist by studying cAMP accumulation (**Figure 10.2A**) and ERK1/2 phosphorylation (**Figure 10.2B**) in cells overexpressing human D<sub>1</sub>Rs, both in the dark and under continuous illumination at 365 nm (to compare the “full *trans*” vs. the “*cis*-enriched” form, respectively). Intracellular cAMP accumulation was measured in human embryonic kidney 293T (HEK 293T) cells transiently transfected with D<sub>1</sub>Rs in a time-resolved fluorescence resonance energy transfer (TR-FRET) assay. We found that **azodopa** induced cAMP accumulation in a dose- and light-dependent manner (**Figure 10.2A**). In particular, we observed substantial differences between the two forms at 5  $\mu$ M and 10  $\mu$ M, with the *trans* form being significantly more effective at inducing cAMP production than the *cis*-enriched form at the same concentrations. When cells were co-treated with the D<sub>1</sub>-like antagonist SKF83566 (300 nM), the effect of **azodopa** was largely reduced or even disappeared, indicating that **azodopa** activates D<sub>1</sub>Rs. In cAMP assays performed in non-transfected HEK 293T cells used as negative control, **azodopa** (10  $\mu$ M), dopamine (1  $\mu$ M), and SKF38393 (300 nM) did not produce any effect (**Figure S10.6**). ERK1/2

phosphorylation was measured in HEK 293T cells transiently transfected with D<sub>1</sub>R by Western blot analysis using phosphor-ERK1/2 antibody. The application of **azodopa** (10 μM) promoted ERK1/2 phosphorylation to an extent that was significantly different between the two conditions (dark vs. light). The full *trans* form displayed an efficacy 3.6-fold greater than the *cis*-enriched form (**Figure 10.2B**), in agreement with the observations in cAMP accumulation assays. Again, co-treatment of the cells with SKF83566 abolished **azodopa** responses, showing that the effect observed were mediated by D<sub>1</sub>R. Although we did not thoroughly characterize the pharmacological activity profile, **azodopa** displayed D<sub>1</sub>R-mediated photoactivity (blocked by SKF83566) also in zebrafish (see later).

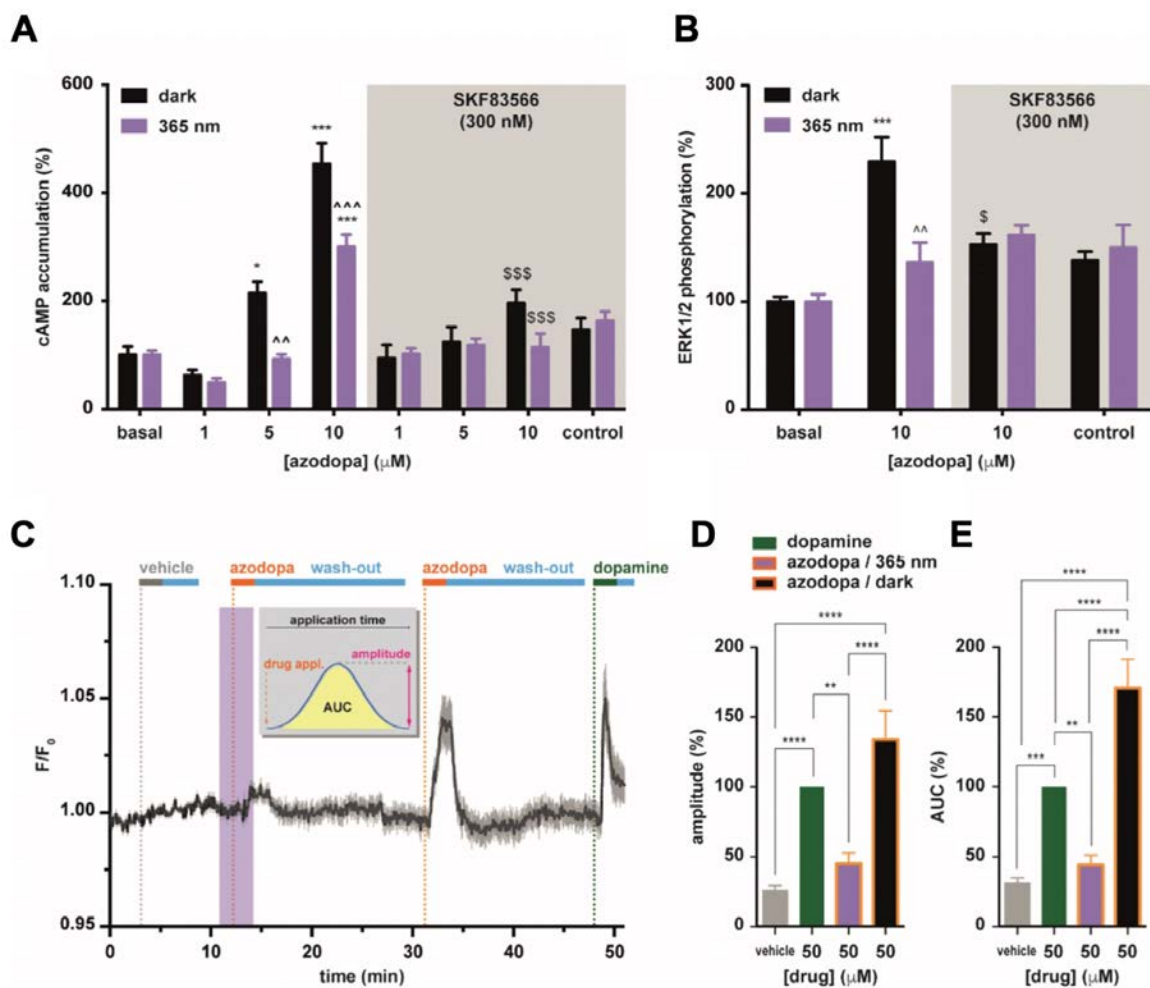


**Figure 10.2. *In vitro* pharmacological characterization of azodopa.** (A) Effect of D<sub>1</sub>R-mediated adenylyl cyclase activation. cAMP accumulation experiments in HEK 293T cells transiently transfected with D<sub>1</sub>R and treated with different concentrations of **azodopa**, in the dark (black bars) or under illumination (purple bars), in the presence (gray area) or not (white area) of a D<sub>1</sub>-like receptor antagonist (SKF83566). Values are represented in percentage vs. basal levels of cAMP. Data are mean ± SEM. (6 experiments performed in quadruplicate). Statistical differences were analyzed by the two-way ANOVA followed by Tukey's post-hoc test (*p*-value (\*\*\*) < 0.001 vs. basal; *p*-value (\*) < 0.05 vs. basal; *p*-value (^^) < 0.001 vs. dark; *p*-value (^) < 0.01 vs. dark; *p*-value

(\$\$\$) < 0.001 vs. controls non-pretreated with the antagonist). **(B)** Effect on D<sub>1</sub>R-mediated ERK1/2 activation. ERK1/2 phosphorylation was determined in HEK 293T cells transiently transfected with D<sub>1</sub>R and treated with different concentrations of **azodopa**, in the dark (black bars) or under illumination (purple bars), in the presence (grey area) or not (white area) of a D<sub>1</sub>-like receptor antagonist (SKF83566). Values are represented in percentage vs. basal levels of ERK1/2 phosphorylation. Data are mean ± SEM (3 or 4 experiments performed in triplicate or quadruplicate). Statistical differences were analyzed by two-way ANOVA followed by Tukey's post hoc test (*p*-value (\*\*\*) < 0.001 vs. basal; *p*-value (^) < 0.01 vs. dark; *p*-value (\$) < 0.05 vs. controls non-pretreated with the antagonist). **(C-E)** Effect on D<sub>1</sub>R-mediated intracellular calcium release compared to dopamine. **(C)** Real-time calcium imaging response (averaged traces, black line, n = 24 cells) in HEK 293T cells co-expressing D<sub>1</sub>Rs and R-GECO1 as calcium indicator. Traces were recorded upon direct application of **azodopa** (50 μM), orange bars) in the dark (white area) and under illumination (purple area). Shadow represents "± SEM". Gray and green bars indicate the application of vehicle (control) and dopamine (reference agonist), respectively. Light blue bars indicate wash-out periods. See example frames and raw data traces of individual cells in Figure S10.8, and Video S10.1 for the entire movie. Two values of the calcium responses generated by **azodopa** were calculated (Origin 8 software) and compared: the peak amplitude ΔF/F<sub>0</sub> **(D)**, calculated as the difference between the maximal and the minimal intensity of each response (*p*-value (\*\*\*\*) < 0.0001 for vehicle vs. dopamine; *p*-value (\*\*\*\*) < 0.0001 for vehicle vs. **azodopa**/dark; *p*-value (\*\*\*\*) < 0.0001 for **azodopa**/365 nm vs. **azodopa**/dark; *p*-value (\*\*) = 0.035 for dopamine vs. **azodopa**/365 nm), and the area under the curve (AUC) **(E)**, calculated as the integral over the entire application time of vehicle or drugs (*p*-value (\*\*\*\*) < 0.0001 vehicle vs. dopamine; *p*-value (\*\*\*\*) < 0.0001 for vehicle vs. **azodopa**/dark; *p*-value (\*\*\*\*) < 0.0001 for dopamine vs. **azodopa**/dark; *p*-value (\*\*\*\*) < 0.0001 for **azodopa**/365 nm vs. **azodopa**/dark; *p*-value (\*\*\*) = 0.001 for vehicle vs. dopamine; *p*-value (\*\*) = 0.0025 for dopamine vs. **azodopa**/365 nm). Data are mean ± SEM (n = 40 cells from 3 independent experiments). Data were normalized over the maximum response obtained with the saturating concentration of dopamine (50 μM) and were analyzed by one-way ANOVA followed by Tukey's post hoc test for statistical significance. All statistical analyses (panels **A**, **B**, **D** and **E**) were performed with GraphPad Prism 6.

It is known that D<sub>1</sub>Rs are also linked to other second messenger systems. These include receptor-mediated activation of phospholipase C (Gα<sub>q</sub> coupling) to generate inositol 1,4,5-trisphosphate (IP<sub>3</sub>) which participates in phosphoinositide turnover and calcium-regulated signaling pathways in the brain<sup>45</sup>. IP<sub>3</sub> receptors are mainly located in the endoplasmic reticular membrane where IP<sub>3</sub> can mobilize Ca<sup>2+</sup> from intracellular stores<sup>45</sup>. Thus, as a complementary method to characterize **azodopa** *in vitro*, we performed calcium-imaging experiments in HEK 293T cells co-expressing D<sub>1</sub>Rs and R-GECO1 as calcium indicator and used dopamine as a control (**Figure 10.2C–E**, **Figure S10.8**, **Figure S10.7** and **Video S10.1**). **Azodopa** (50 μM) was applied to the cells both in the dark and under illumination with UV light. Dopamine (50 μM) was tested as reference agonist. Robust increases of intracellular calcium were observed by the application of **azodopa** in the dark (pure *trans*-isomer), whereas only weak increases were recorded when **azodopa** was applied under illumination (**Figure 10.2C** and **Figure S10.8**). Calcium responses were quantified and compared by peak amplitude and area under the

curve (AUC). The analysis of these parameters showed that *trans-azodopa* stimulates the release of intracellular calcium (similar to dopamine) and this effect is abolished under illumination. In this experiment, *trans-azodopa* displayed significantly higher efficacy than dopamine (**Figure 10.2DE**). No responses were observed in control experiments in HEK cells ( $n = 25$ ) not expressing D<sub>1</sub>R, thus confirming that the calcium oscillations were elicited by a specific interaction at this receptor (**Figure S10.7**). Moreover, we verified that *trans-azodopa* fully recovers its efficacy after long (60 min) exposure to 365 nm light, demonstrating that its effects are reversibly photodependent and are not due to an irreversible photodegradation of the molecule (**Figure S10.17** and **Figure S10.18**). Our results in calcium imaging experiments suggest that *trans-azodopa* activates the G $\alpha_q$ /phospholipase C pathway, in addition to the canonical G $\alpha_s$ /adenylyl cyclase pathway already investigated. Such intriguing behavior has been described also for other dopamine agonists<sup>45</sup>.

Taken as a whole, the results from our *in vitro* experiments illustrated in **Figure 10.2** show that *trans-azodopa* is a full agonist at D<sub>1</sub>-like receptors and that its effects can be partially or completely switched off with light. The reduction of *azodopa* efficacy under illumination can be attributed to the photoisomerization process which decreases the partial concentration of the *trans*-isomer at the target receptor and/or disrupts the ligand interaction(s) at the binding pocket.

#### 10.2.4 Behavioral effects in zebrafish larvae

The promising photopharmacological profile of *azodopa* prompted to use it *in vivo* to modulate dopaminergic neurotransmission. For that purpose, we designed a behavioral assay to record and quantify the locomotor activity of living animals as a function of drug concentration and illumination. It is known that dopamine plays a pivotal role in motor control in humans, as it activates striatal direct pathway neurons that directly project to the output nuclei of the basal ganglia through D<sub>1</sub>Rs, whereas it inhibits striatal indirect pathway neurons that project to the external pallidum through D<sub>2</sub>Rs<sup>46</sup>. We chose zebrafish larvae (*Danio rerio*) as animal model for our experiments because of their transparency, which facilitates the delivery of light, and their morphological, genetic, and behavioral similarity to higher vertebrates<sup>10,47-52</sup>. Indeed, a functional nervous system is established after only 4-5 days of embryonic development in zebrafish, enabling them to perform complex behaviors such as swimming and exploratory activity. In particular, the major dopaminergic pathways in mammals are also represented in the zebrafish brain, and homologous receptors for most of the mammalian subtypes have been identified in these animals. Humans and zebrafish share 100% of the amino acids in the binding site for D<sub>1</sub>Rs and D<sub>3</sub>Rs, and 85-95% for D<sub>2</sub>Rs and D<sub>4</sub>Rs, and generally similar effects are

observed for dopaminergic ligands in zebrafish and in mammals<sup>51</sup>. As a rule of thumb, dopamine receptor agonists increase the locomotor activity, whereas antagonists decrease it<sup>53</sup>. However, disentangling the action of drugs on the multiple components of dopaminergic transmission (including different brain regions<sup>2</sup>, the regulation of retinal function<sup>3</sup>, and of circadian rhythms<sup>4</sup>) constitutes an unmet need of pharmacology and medicine. Therefore, we set to test **azodopa** *in vivo* and to take advantage of photocontrolling dopaminergic responses.

Zebrafish larval movements were tracked using a ZebraBox device for automated behavioral recording. Zebrafish larvae at 6 days post-fertilization (6 dpf) were randomly divided into control (vehicle) and treatment groups (with **azodopa** added to water). Each individual was placed in a separate well of a 96-well plate. Our setup allowed exposing the animal to controlled cycles of dark and 365 nm UV illumination, using the following protocol: dark (20 min, for adaptation), UV light (30 s), dark (20 min), and then four cycles of UV light (30 s) and dark (5 min) (see **SI** for details and **Video S10.2**). In order to identify alterations in behavior, we measured multiple properties of locomotor activity to determine the activity level<sup>54</sup>. In particular, we focused on fast movements and measured swimming distances and duration of fast swimming, defined as speed  $\geq 6 \text{ mm}\cdot\text{s}^{-1}$ .

We first studied a wide concentration range (spanning from 1 nM to 1 mM **azodopa**) to determine if behavioral effects could be observed without signs of acute toxicity. No significant differences in locomotor activity were observed between the control group and the treatment groups up to a concentration of 10  $\mu\text{M}$ , neither in the dark nor upon illumination (**Figure S10.9**). A strong increase in swimming activity was recorded at 1 mM, but the effect ceased after 30 min, possibly because the fish were exhausted. We observed the most interesting alterations of the behavioral profile at 100  $\mu\text{M}$  (**Figure 10.3A-D** and **Figure S10.12**). The changes in the swimming activity over time for this group and the control group are plotted in **Figure 10.3A** (full experiment represented in **Figure S10.9** and see also **Video S10.2**). We detected a progressive increase in activity for 30-40 min and relatively small photoresponses (*e.g.*, at 20 min in **Figure 10.3A**) which is often due to the slow uptake of the drug in the fish<sup>14</sup>. After this period, animals treated with 100  $\mu\text{M}$  **azodopa** displayed a high swimming activity in the dark that was sustained for the whole duration of the experiment, and that was abolished during each period of UV illumination (30 s bouts between minute 40 and 60 in **Figure 10.3A**).

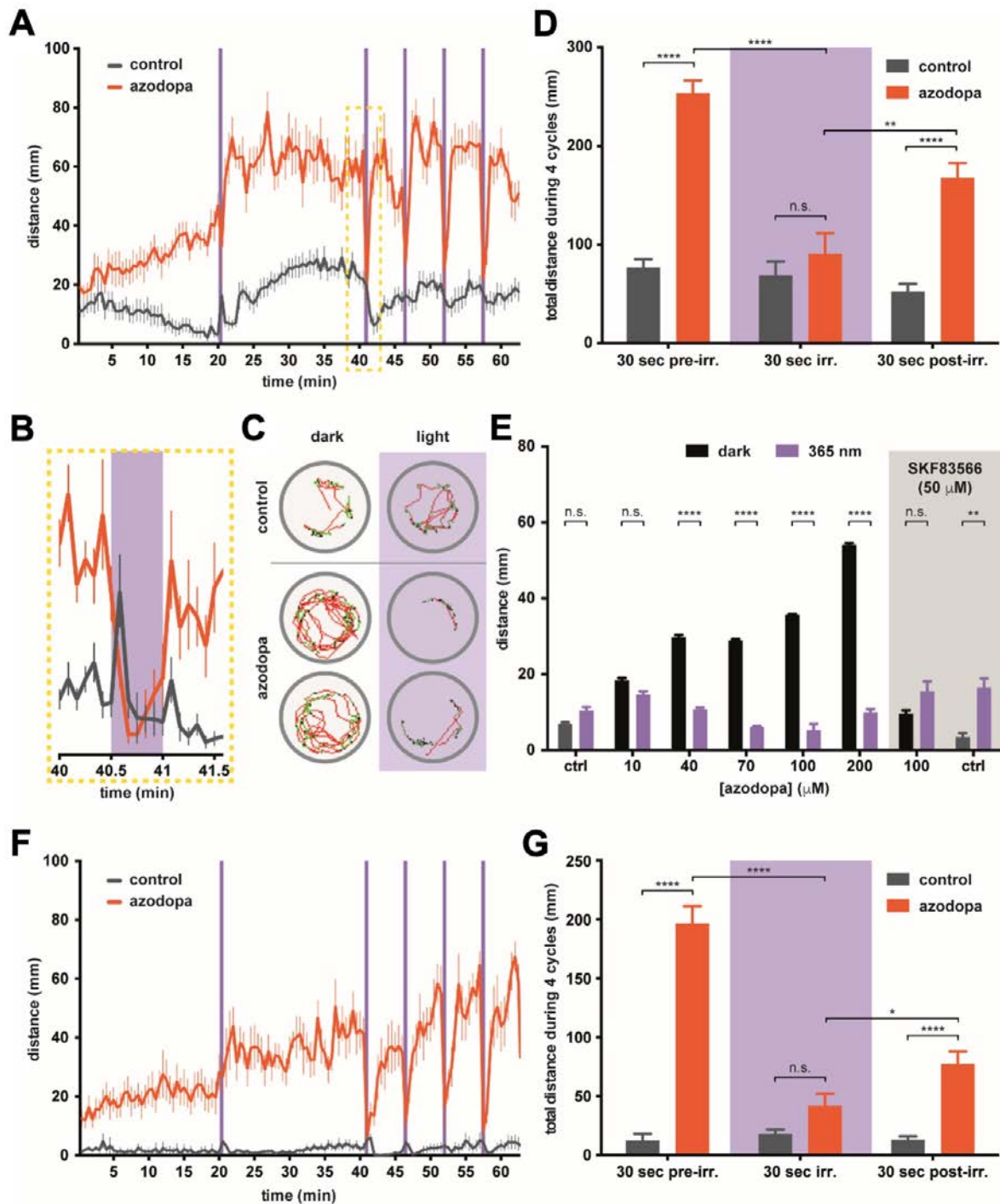


**Figure 10.3. Behavioral effects of azodopa in zebrafish.** (A-E) Experiments with normal zebrafish. (A) Swimming activity (distance/time) in larvae exposed to vehicle (control, grey line) or 100  $\mu\text{M}$  **azodopa** (treatment, orange line) in the dark (white areas) or under illumination with 365 nm light (purple bars). Data are mean  $\pm$  SEM. ( $n = 11-12$  individuals/group). (B) Representative time frame (40-41.5 min) of the swimming activity integrated every 5 s, showing how the effect of **azodopa** can be completely shut down upon illumination. The spike of activity observed for the control group upon illumination represents the startle response to the light stimulus. (C) Exemplary trajectories of individual larvae in one well containing the vehicle and two wells containing 100  $\mu\text{M}$  **azodopa** in the dark (40-40.5 min) and under illumination (40.5-41 min). Green lines and red lines indicate slow and fast swimming periods, respectively. The remarkable and light-dependent difference in behavior between



untreated and **azodopa**-treated fish can be appreciated by observing these trajectories and the Video S10.2. **(D)** Quantification of the total distances swum by the control group (vehicle) and the treatment group (100  $\mu\text{M}$  **azodopa**) during 4 consecutive cycles of illumination (30 s) and dark (30 s before and after illumination). Data are mean  $\pm$  SEM. (n = 11-12 individuals/group) and were analyzed by two-way ANOVA followed by Tukey's post hoc test ( $p$ -value (\*\*\*\*)  $< 0.0001$ ;  $p$ -value (\*\*) = 0.0037). **(E)** Dose-response study of **azodopa** (white area) and effect of a co-administered  $\text{D}_1$ -like receptor antagonist (gray box). Different groups of larvae were exposed to increasing concentrations of **azodopa**. For quantification, the average distance swum by each group during the last 4 consecutive dark-light cycles (30 s integration) was considered. The graph shows that *trans*-**azodopa** (black bars) increases the fish locomotor activity in a dose-dependent manner, but its effects are abolished by the co-administration of a potent and selective  $\text{D}_1$ -like receptor antagonist (SKF83566, 50  $\mu\text{M}$ ). Data are mean  $\pm$  SEM (n = 12 individuals/group) and were analyzed by two-way ANOVA followed by Sidak's post hoc test ( $p$ -value (\*\*\*\*)  $< 0.0001$ ;  $p$ -value (\*\*\*) = 0.0063). **(F, G)** Experiments with blinded zebrafish. **(F)** Swimming activity (distance/time) in larvae exposed to vehicle (control, gray line) or 100  $\mu\text{M}$  **azodopa** (treatment, orange line) in the dark (white areas) or under illumination with 365 nm light (purple bars). Data are mean  $\pm$  SEM (n = 12 individuals/group). **(G)** Quantification of the total distances swum by the control group (vehicle) and the treatment group (100  $\mu\text{M}$  **azodopa**) during 4 consecutive cycles of illumination (30 s) and dark (30 s before and after illumination). Data are mean  $\pm$  SEM (n = 12 individuals/group) and were analyzed by two-way ANOVA followed by Tukey's post hoc test ( $p$ -value (\*\*\*\*)  $< 0.0001$ ;  $p$ -value (\*) = 0.0232). All statistical analyses (**D, E** and **G**) were performed with GraphPad Prism 6.

These results agree with the intracellular signaling photoresponses observed *in vitro* and confirm a *trans*-on/*cis*-off dopamine agonist profile. An averaged time course (between 40-41.5 min, integrated every 5 s) of the swimming activity is magnified in **Figure 10.3B**. Representative trajectories of individual fish in wells containing the vehicle or 100  $\mu\text{M}$  **azodopa** in the dark (40-40.5 min) and under illumination (40.5-41 min) are shown in **Figure 10.3C**, where green and red lines indicate slow ( $< 6 \text{ mm}\cdot\text{s}^{-1}$ ) and fast ( $\geq 6 \text{ mm}\cdot\text{s}^{-1}$ ) swimming periods, respectively (see **Figure S10.13** for the entire plate and SM for experimental details and analysis). **Figure 10.3D** shows the quantification and statistical analysis of the total distances swum by the control group and the treatment group (100  $\mu\text{M}$  **azodopa**) during the last four cycles, namely, once the maximum effect of the drug was reached and maintained (30 s pre-illumination, 30 s illumination, and 30 s post-illumination periods).

Fish treated with **azodopa** covered a distance three times longer than the control group during the same dark periods, and this effect was blocked under illumination. Interestingly, we also noticed a reduction in swimming activity during the first 30 s of dark after each illumination pulse in the treatment group, likely because the fish needed some time to recover the maximum level of activity. The differences between the total distances swum by the treatment group

during the 30 s periods of dark (pre- or post-illumination) and the 30 s periods of illumination were also statistically significant (**Figure 10.3D**).

Next, we sought to verify whether the effect of **azodopa** on zebrafish locomotor activity is dose-dependent by testing a range of concentrations around 100  $\mu\text{M}$ . For our analysis, we averaged the distance swum by each group during the last four consecutive dark-light cycles (30 s integration). We observed that **azodopa** increased the swimming activity in the dark in a dose-dependent manner, while the effect under 365 nm illumination was smaller at all concentrations and yielded a weak dose dependence (**Figure 10.3E**; see also **Figure S10.10** for a representation of the activity profile at all concentrations). Moreover, we observed that co-application of the D<sub>1</sub>-like antagonist SKF83566 (50  $\mu\text{M}$ ) abolished the behavioral effects produced by **azodopa** at 100  $\mu\text{M}$  in the dark, and restored zebrafish activity to control levels (**Figure 10.3E** and **Figure S10.11**). These experiments allow to exclude the participation of adrenergic receptors in the photoresponses *in vivo*<sup>14</sup> and support the hypothesis that they are mediated by D<sub>1</sub>-like rather than D<sub>2</sub>-like receptors (SKF83566 is 1000-fold more potent in the formers). However, they cannot rule out the involvement of 5-HT<sub>2</sub> receptors, as the antagonist binds them with only 20-fold weaker potency.

To distinguish between the contribution of visual responses to (a) the changes in fish locomotion and (b) the dopaminergic modulation with **azodopa**, we repeated the experiments with blinded zebrafish larvae. The zebrafish retina contains four different cone photoreceptor subtypes (UV, S, M, L), each one defined by the expression of specific opsins that confer a particular wavelength-sensitivity. UV cones express SWS1, an opsin with peak sensitivity in the UV range ( $\lambda_{\text{max}} = 354 \text{ nm}$ )<sup>55</sup>; therefore, the removal of functional UV cones can be used to suppress UV-dependent behaviors<sup>56</sup>. Blinded zebrafish larvae were obtained via a noninvasive blinding technique that induces photoreceptor apoptosis while preserving the rest of the retina (see **SI** for details)<sup>57</sup>. They were remarkably inactive and unresponsive to illumination (**Figure 10.3FG**). The activity profile of **azodopa**-treated blinded zebrafish was qualitatively like the one observed with **azodopa**-treated normal zebrafish (**Figure 10.3A and F**, respectively). **Azodopa** (100  $\mu\text{M}$ ) produced a remarkable increase of the swimming activity of blind larvae for the entire experiment during the dark periods, and this effect was abolished upon illumination. Quantification of the total distances swum by the control group and the treatment group (100  $\mu\text{M}$  **azodopa**) during the last four dark-light cycles confirmed our observations: the locomotion of blinded animals could be significantly photoswitched with **azodopa**. The overall decrease in swimming activity of blinded zebrafish (**Figure 10.3FG**)

compared to normal zebrafish (**Figure 10.3A-E**) is due to the induced blindness, which reduces their exploratory tendencies. This phenomenon is more pronounced in the control-blinded group, which is almost immobile, and makes the effect of **azodopa** on locomotion appear even stronger: **azodopa**-treated blinded larvae covered a total distance 16 times longer (during pre-illumination periods) and 6 times longer (during post-illumination periods) than the one swum by control animals (**Figure 10.3G**).

The fact that **azodopa** can elicit behavioral photoresponses in blinded zebrafish and that they have similar magnitude to those in normal fish show that retinal photoreceptors are not directly involved in the observed change in locomotion upon illumination. Instead, photoresponses must be attributed to other dopaminergic circuits in the CNS (present both in blinded and normal larvae) that are effectively placed under the control of light with **azodopa**. Interestingly, the time course of photoresponses does display differences between blinded and normal larvae, and these must be ascribed to the presence of visual inputs in normal animals. The most outstanding one is the recovery of locomotion after turning off UV light in the presence of **azodopa**, which is significantly faster in normal zebrafish larvae than in blinded ones (see four cycles in **Figure 10.3A and F** and quantification in **Figure S10.12**). Thus, **azodopa** enables time-resolved behavioral experiments that contain unique information about the dopaminergic modulation of retinal function<sup>3</sup>, and that will be further investigated with spatially resolved neuronal activity maps.

Overall, behavioral responses in zebrafish larvae agree with our previous findings *in vitro* and confirm that **azodopa** is a reversible photoswitchable dopaminergic agonist displaying dose-dependent locomotor effects. In addition, we demonstrated that zebrafish larvae, previously exposed to azodopa and dark-light cycles, recovered normal swimming behavior after washout (see **Figure S10.19 and SI**), and were still alive about 48 h after the experiment. The robust photocontrol of behavior and the apparent absence of acute toxicity encouraged us to test the potential of **azodopa** in a mammalian model.

### 10.2.5 Electrophysiological recordings in anesthetized mice

We studied whether **azodopa** modulates neural activity in the cortex of mice. For such experiments, we developed a custom setup that combined *in vivo* electrophysiological recordings and the possibility to illuminate with 365 nm LEDs. The Open Ephys data acquisition system was used to record neural activity via an octrode (four two-wire stereotrode

array) inserted in the superficial layers of the secondary motor cortex (M2) with a large craniotomy that allowed exposure of cortical tissue (**Figure 10.4A**).

We first investigated the effects of **azodopa** in the absence of light in two mice anesthetized with isoflurane (Mouse 1 and Mouse 2, **Figure 10.4B-E**). In each animal, we recorded spiking activity of individual neurons (single unit activity, SUA) and local field potentials (LFPs) in M2 before and after the administration of *trans*-**azodopa**. We quantified mean firing rates (spikes per second) and LFP power from 1 to 10 Hz. Transient oscillatory signals observed in LFPs reflect the summed synchronized activity of neural networks and are also called neural oscillations. Neural oscillations between 1 and 10 Hz have been associated with cognitive processing during alertness and slow waves during slow wave sleep and anesthesia (*i.e.*, UP and DOWN states). The experiments started after cortical activity was stable for at least 10 min. Then, we recorded baseline neural activity for 10 more minutes. During this period, slow fluctuations of neural activity were observed both at the single-neuron and LFP levels that were associated with UP and DOWN states typically observed during anesthesia (**Figure 10.4B**). Later, 10  $\mu$ l of *trans*-**azodopa** at 3  $\mu$ M concentration were administered manually on the surface of the cortex with a standard pipette. **Azodopa** increased neural activity few seconds after its administration. The effects were transient in many neurons and the general activity remained elevated for at least 5 min (**Figure 10.4C**). There was a boost in the firing rate of individual neurons that no longer followed the UP and DOWN cycles. In addition, more neurons could be identified after *trans*-**azodopa** administration (21 neurons during baseline and 33 neurons after **azodopa** in mouse 1; see also **Figure S10.14**). In fact, in mouse 2, we isolated 23 neurons during baseline and only 10 neurons after *trans*-**azodopa** because spiking activity was so elevated that spikes from different neurons co-occurred altering the shape of the waveforms and thus prevented their classification. Corresponding with the increased spiking activity of neurons, the power of oscillatory activities augmented, although moderately compared to changes in firing rate (**Figure 10.4C**, bottom panel). Statistical analyses confirmed significant increases of firing rate and 1-10 Hz power when combining the two animals (**Figure 10.4DE**).

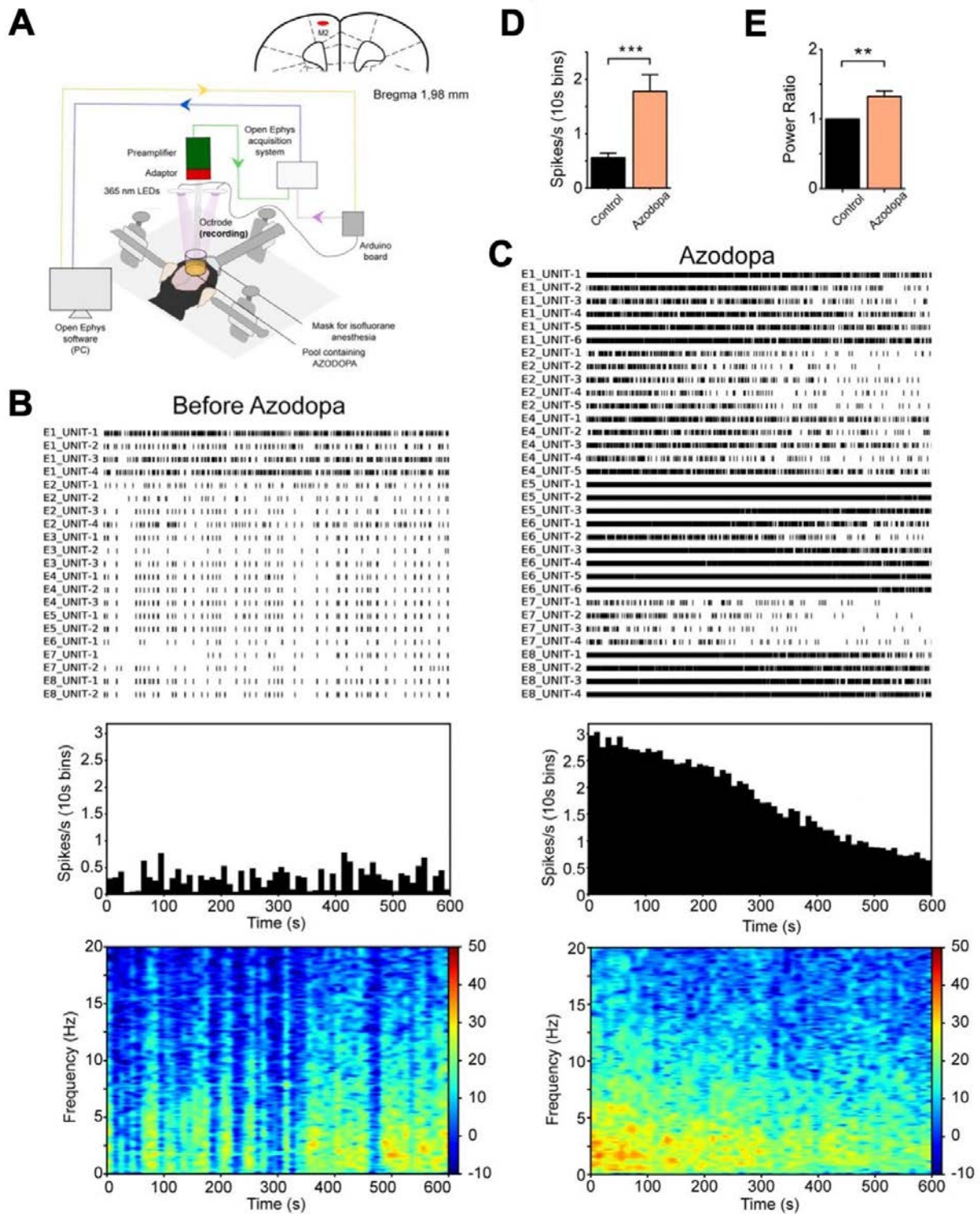


**Figure 10.4. Effect of cortical administration of *trans*-azodopa on electrophysiological recordings in anesthetized mice.** (A) Animals were anesthetized with isoflurane and placed in a stereotaxic apparatus. A craniotomy was drilled above the secondary motor cortex (M2) and an octrode was inserted in the superficial layers. Analogic signals were bandpass filtered and digitized by a preamplifier, amplified by an Open Ephys data acquisition system (green arrow), and finally visualized and recorded in a PC (blue arrow). Neural activity was recorded during baseline conditions and after administration of *trans*-azodopa on the cortical surface (3  $\mu$ M concentration in 10  $\mu$ l volume). See the Supplementary Information for further details of the setup and Figures

S10.17–S10.19 for the effect of illumination on **azodopa**. **(B)** Neural activity during baseline conditions in Mouse 1. Raster plot of spiking activity in the cortex of one mouse for 10 min. Each row depicts the spiking activity of a single neuron (unit), each tick representing an action potential. We used arrays of 8 electrodes (octrodes) in each animal, from which several units could be recorded. Neurons are labeled by their electrode number (E1 to E8). Firing rates were stable and followed the UP and DOWN slow fluctuations typical of anesthesia. The quantification of firing rates and average time–frequency spectrogram of the power of neural oscillations ( $n = 8$  electrodes) are shown below. **(C)** Neural activity after the administration of  $3 \mu\text{M}$  *trans*-**azodopa** in Mouse 1 (zero indicates the time of administration). **Azodopa** boosted the firing rate of neurons and increased the power of neural oscillations. **(D)** **Azodopa** increased spiking activity of cortical neurons. Mean firing rate of neurons before and after the administration of *trans*-**azodopa**. Data are mean  $\pm$  SEM ( $n = 44$  neurons during baseline vs. 43 neurons after **azodopa** in two mice) and were analyzed with an unpaired t-test ( $p$ -value (\*\*\*) = 0.0002). **(E)** **Azodopa** increased the power (1–10 Hz) of neural oscillations in the two animals. Due to the large differences in the baseline power of the two mice, we normalized the power to its baseline for visualization purposes only. Data are mean  $\pm$  SEM ( $n = 16$  channels per condition from two mice) and were analyzed with a paired t-test ( $p$ -value (\*\*)) = 0.0011).

We next investigated the effects of **azodopa** under 365 nm illumination in two more mice anesthetized with isoflurane (Mouse 3 and Mouse 4, **Figures S10.14–S10.16**). In each mouse, we first injected 0.5 ml of saline and later 0.5 ml  $3 \mu\text{M}$  **azodopa** in consecutive experiments. Solutions were administered with an infusion pump over the course of one minute to avoid environmental noise and to allow electrophysiological recordings during the administration. Moreover, drug administration was conducted under illumination so that **azodopa** penetrated cortical tissue in an inactive form. Then, we illuminated the motor cortex with five consecutive cycles of one minute of darkness (OFF) and one minute of light (ON) (**Figure S10.14**). Here, we focused on differential spiking activity during light and dark cycles because **azodopa** displayed a stronger effect than on the power of neural oscillations in the previous experiments (**Figure 10.4**).

After the injection of saline, the mean firing rate of neurons remained like baseline levels, and neural activity slightly increased during the light cycles compared to the dark cycles (**Figure S10.14**). In the presence of **azodopa**, neural activity increased as in direct application experiments (**Figure 10.4**) and some neurons showed rapid and reversible changes in their firing patterns during the ON and OFF light cycles. Interestingly, some of these neurons decreased their spiking activity during the light periods (DARK-ON) and others increased it (LIGHT-ON; **Figure S10.15** and **Figure S10.16**). Although these heterogeneous effects of light cancelled each other out in the global average (**Figure S10.14C**), manual pooling of single unit recordings yielded significant differences in neural activity between dark and light conditions (**Figure S10.16**). Since DARs are expressed both in excitatory and inhibitory neurons of the

frontal cortex, we hypothesize that DARK-ON neurons may correspond to those expressing D<sub>1</sub>-like receptors, which decrease their firing rates when **azodopa** is deactivated by light, and LIGHT-ON neurons may be cells affected indirectly by network effects driven by DARK-ON neurons.

Overall, our first *in vivo* studies in anesthetized mice indicate that *trans*-**azodopa** exerts excitatory actions on brain cortical microcircuits, as reflected by the increased spiking and oscillatory activities. The effects of **azodopa** were transient; the firing rate of many neurons was increased for few minutes, while in others the elevated firing lasted more than 10 min. This could be due to the diffusion (and therefore dilution) of **azodopa** within cortical tissue over time, and possibly to its metabolic washout and reuptake by synaptic terminals<sup>58</sup>. The increase of cortical activity by *trans*-**azodopa** is consistent with our results from functional studies in cell cultures and suggests that *trans*-**azodopa** may also act as a dopamine agonist in the mouse brain<sup>59</sup>. The general excitatory action of **azodopa** was modulated by UV light in individual neurons, some of which revealed a decrease in spiking activity while others increased it. These heterogeneous responses to D<sub>1</sub>-like receptor activation in WT animals bear physiological relevance and are currently being studied.

### 10.3 Discussion and conclusions

Understanding the dopaminergic system dynamics is a central question in neurobiology and neuropharmacology. In fact, DARs are involved in the modulation of fundamental physiological functions such as voluntary movement, motivation, cognition, emotion, reward, and neuroendocrine secretion, among others, and a dysregulation of the dopaminergic transmission is unavoidably associated with major psychiatric and neurological disorders. However, the available techniques to dissect neuronal circuits and their role in pathological conditions have several shortcomings. Electrical stimulation lacks cellular specificity and conventional pharmacological manipulation lacks temporal and spatial resolution<sup>60</sup>. Optogenetic tools allow the modulation of specific neural circuit elements with millisecond precision, but are limited by non-uniform expression of the optogenetic actuators and generation of non-physiological patterns of activity throughout the targeted population of neurons. Here, we introduce a novel photopharmacological agonist that enables reversible spatiotemporal control of intact dopaminergic pathways *in vivo*. We show that **azodopa** triggers DAR-mediated cAMP accumulation and ERK1/2 phosphorylation as well as phospholipase C activation in its *trans* configuration, and its efficacy can be reduced or switched off under

illumination. Accordingly, **azodopa** allows the reversible photocontrol of zebrafish motility on a timescale of seconds, increasing the swimming activity exclusively in the *trans* active state. **Azodopa** can be bath-applied, does not require microinjection or genetic manipulation, and is compatible with high-throughput behavioral screening in WT or transgenic fish, and with other treatments including pharmacological ones. For instance, the inactivity of blinded larvae under control conditions can be risen to levels comparable to normal (untreated) animals by adding *trans-azodopa* in the water without illumination. In addition, locomotion is reduced to control levels upon photoisomerization to the *cis* form, which suggests that **azodopa** might be used to interfere with extracellular dopamine/melatonin cycles in the retina involved in circadian rhythms<sup>3</sup>. Furthermore, the intriguing observation that DAR activation by **azodopa** *cis*-to-*trans* isomerization (dark relaxation) produces faster behavioral responses in normal fish than in blinded ones offers new opportunities to interrogate the dopaminergic modulation of retinal circuits with spatiotemporal, pharmacological, and cell-type specificity<sup>61</sup>. Our results thus complement recently reported genetic–photopharmacological agonists<sup>15</sup> and photopharmacological antagonists<sup>25</sup> and open the way to dissect dopaminergic neurotransmission in intact animals. Characterizing in detail the pharmacological profile and safety of **azodopa** was not the aim of this work, but experiments with zebrafish in the presence of a selective antagonist suggested that D<sub>1</sub>-like receptors are the main mediators of the photocontrolled behavior.

*Trans-azodopa* also exerts excitatory actions on brain cortical microcircuits at firing rates and frequency bands relevant for behavior in mice<sup>62</sup>. In agreement with our *in vitro* studies, **azodopa** induced a general increase in neural excitability, although the time course and light dependence of the responses was heterogeneous in individual neurons. We identified cortical neurons with LIGHT-ON and DARK-ON patterns, which is expected when administering in the intact brain an agonist of dopamine receptors that are expressed both in excitatory and inhibitory neurons. These responses must be characterized further, but it must be noted that isoflurane anesthesia produces profound inhibitory effects on brain activity. The activity of neural networks may be more difficult to modulate under anesthesia than during alertness, which prompts to evaluate the effects of **azodopa** under light-dark regimes in awake mice.

From a photochromic point of view, **azodopa** displays a short half-life of thermal relaxation, which is useful in neurobiology since a single wavelength of light allows to rapidly toggle the photoswitch between its two isomers. However, **azodopa** requires UV light for deactivation, which is normally undesired in photopharmacology due to poor tissue penetration and potential



phototoxicity. Moreover, **azodopa** is active in the most thermodynamically stable configuration (*trans*). Although there are clinical conditions that might take advantage of a dark-active drug that can be deactivated on demand (*e.g.*, to reduce levodopa-induced dyskinesia in Parkinson's disease)<sup>63</sup>, light-activatable compounds are generally preferred for research and therapeutic purposes. Hence, new dopaminergic photoswitches must be developed that are active in the less thermodynamically stable configuration<sup>64</sup> and photoisomerize with visible<sup>65</sup> or infrared light<sup>66,67</sup> in order to unleash their full potential as photopharmacological tools.

In summary, **azodopa** is a photochromic activator of endogenous dopamine receptors that does not require genetic manipulation and is the first photoswitchable dopaminergic agonist with demonstrated efficacy *in vivo* in intact WT animals, including mammals. This ligand allows analyzing the different components of the dopaminergic circuitry and is a breakthrough in developing novel photoswitchable drugs potentially useful to manage neurological conditions, including movement disorders and addiction.

## References

- 1 Beaulieu, J. M. & Gainetdinov, R. R. The physiology, signaling, and pharmacology of dopamine receptors. *Pharmacol Rev* **63**, 182-217, doi:10.1124/pr.110.002642 (2011).
- 2 Tritsch, N. X. & Sabatini, B. L. Dopaminergic modulation of synaptic transmission in cortex and striatum. *Neuron* **76**, 33-50, doi:10.1016/j.neuron.2012.09.023 (2012).
- 3 Firsov, M. L. A., L.A. The role of dopamine in controlling retinal photoreceptor function in vertebrates. *Neurosci Behav Physi* **46**, 138–145 doi:10.1007/s11055-015-0210-9 (2016).
- 4 Korshunov, K. S., Blakemore, L. J. & Trombley, P. Q. Dopamine: A modulator of circadian rhythms in the central nervous system. *Front Cell Neurosci* **11**, 91, doi:10.3389/fncel.2017.00091 (2017).
- 5 Puig, M. V. & Miller, E. K. The role of prefrontal dopamine D<sub>1</sub> receptors in the neural mechanisms of associative learning. *Neuron* **74**, 874-886, doi:10.1016/j.neuron.2012.04.018 (2012).
- 6 Puig, M. V. & Miller, E. K. Neural substrates of dopamine D<sub>2</sub> receptor modulated executive functions in the monkey prefrontal cortex. *Cereb Cortex* **25**, 2980-2987, doi:10.1093/cercor/bhu096 (2015).
- 7 Beaulieu, J. M., Espinoza, S. & Gainetdinov, R. R. Dopamine receptors - IUPHAR Review 13. *Br J Pharmacol* **172**, 1-23, doi:10.1111/bph.12906 (2015).
- 8 Lerch, M. M., Hansen, M. J., van Dam, G. M., Szymanski, W. & Feringa, B. L. Emerging targets in photopharmacology. *Angew Chem Int Ed Engl* **55**, 10978-10999, doi:10.1002/anie.201601931 (2016).
- 9 Hull, K., Morstein, J. & Trauner, D. *In vivo* photopharmacology. *Chem Rev* **118**, 10710-10747, doi:10.1021/acs.chemrev.8b00037 (2018).
- 10 Pianowski, Z. L. *Molecular photoswitches: Chemistry, properties, and applications*. 1152 (Wiley-VCH, Weinheim, 2022).
- 11 Pittolo, S. *et al.* An allosteric modulator to control endogenous G protein-coupled receptors with light. *Nat Chem Biol* **10**, 813-815, doi:10.1038/nchembio.1612 (2014).
- 12 Agnetta, L. *et al.* Fluorination of photoswitchable muscarinic agonists tunes receptor pharmacology and photochromic properties. *J Med Chem* **62**, 3009-3020, doi:10.1021/acs.jmedchem.8b01822 (2019).
- 13 Riefolo, F. *et al.* Optical control of cardiac function with a photoswitchable muscarinic agonist. *J Am Chem Soc* **141**, 7628-7636, doi:10.1021/jacs.9b03505 (2019).
- 14 Prischich, D. *et al.* Adrenergic modulation with photochromic ligands. *Angew Chem Int Ed Engl* **60**, 3625-3631, doi:10.1002/anie.202010553 (2021).
- 15 Donthamsetti, P. *et al.* Cell specific photoswitchable agonist for reversible control of endogenous dopamine receptors. *Nat Commun* **12**, 4775, doi:10.1038/s41467-021-25003-w (2021).
- 16 Berizzi, A. E. & Goudet, C. Strategies and considerations of G protein-coupled receptor photopharmacology. *Adv Pharmacol* **88**, 143-172, doi:10.1016/bs.apha.2019.12.001 (2020).
- 17 Bregestovski, P., Maleeva, G. & Gorostiza, P. Light-induced regulation of ligand-gated channel activity. *Br J Pharmacol* **175**, 1892-1902, doi:10.1111/bph.14022 (2018).
- 18 Izquierdo-Serra, M. *et al.* Optical control of endogenous receptors and cellular excitability using targeted covalent photoswitches. *Nat Commun* **7**, 12221, doi:10.1038/ncomms12221 (2016).
- 19 Szymanski, W., Ourailidou, M. E., Velema, W. A., Dekker, F. J. & Feringa, B. L. Light-controlled histone deacetylase (HDAC) inhibitors: Towards photopharmacological chemotherapy. *Chemistry* **21**, 16517-16524, doi:10.1002/chem.201502809 (2015).

- 20 Matera, C. *et al.* Photoswitchable antimetabolite for targeted photoactivated chemotherapy. *J Am Chem Soc* **140**, 15764-15773, doi:10.1021/jacs.8b08249 (2018).
- 21 Steinberg, E. E. & Janak, P. H. Establishing causality for dopamine in neural function and behavior with optogenetics. *Brain Res* **1511**, 46-64, doi:10.1016/j.brainres.2012.09.036 (2013).
- 22 Stauffer, W. R. *et al.* Dopamine neuron-specific optogenetic stimulation in rhesus macaques. *Cell* **166**, 1564-1571 e1566, doi:10.1016/j.cell.2016.08.024 (2016).
- 23 Chang, C. Y. *et al.* Brief optogenetic inhibition of dopamine neurons mimics endogenous negative reward prediction errors. *Nat Neurosci* **19**, 111-116, doi:10.1038/nn.4191 (2016).
- 24 Hare, B. D. *et al.* Optogenetic stimulation of medial prefrontal cortex D<sub>1</sub>R neurons produces rapid and long-lasting antidepressant effects. *Nat Commun* **10**, 223, doi:10.1038/s41467-018-08168-9 (2019).
- 25 Donthamsetti, P. C. *et al.* Optical control of dopamine receptors using photoswitchable tethered inverse agonist. *J Am Chem Soc* **139**, 18522-18535, doi:10.1021/jacs.7b07659 (2017).
- 26 Araya, R., Andino-Pavlovsky, V., Yuste, R. & Etchenique, R. Two-photon optical interrogation of individual dendritic spines with caged dopamine. *ACS Chem Neurosci* **4**, 1163-1167, doi:10.1021/cn4000692 (2013).
- 27 Gienger, M., Hubner, H., Lober, S., Konig, B. & Gmeiner, P. Structure-based development of caged dopamine D<sub>2</sub>/D<sub>3</sub> receptor antagonists. *Sci Rep* **10**, 829, doi:10.1038/s41598-020-57770-9 (2020).
- 28 Lachmann, D. *et al.* Photochromic dopamine receptor ligands based on dithienylethenes and fulgides. *Chemistry* **23**, 13423-13434, doi:10.1002/chem.201702147 (2017).
- 29 Szymanski, W., Beierle, J. M., Kistemaker, H. A., Velema, W. A. & Feringa, B. L. Reversible photocontrol of biological systems by the incorporation of molecular photoswitches. *Chem Rev* **113**, 6114-6178, doi:10.1021/cr300179f (2013).
- 30 Broichhagen, J., Frank, J. A. & Trauner, D. A roadmap to success in photopharmacology. *Acc Chem Res* **48**, 1947-1960, doi:10.1021/acs.accounts.5b00129 (2015).
- 31 Schoenberger, M., Damijonaitis, A., Zhang, Z., Nagel, D. & Trauner, D. Development of a new photochromic ion channel blocker via azologization of fomicaine. *ACS Chem Neurosci* **5**, 514-518, doi:10.1021/cn500070w (2014).
- 32 Borowiak, M. *et al.* Photoswitchable inhibitors of microtubule dynamics optically control mitosis and cell death. *Cell* **162**, 403-411, doi:10.1016/j.cell.2015.06.049 (2015).
- 33 Morstein, J., Awale, M., Reymond, J. L. & Trauner, D. Mapping the azolog space enables the optical control of new biological targets. *ACS Cent Sci* **5**, 607-618, doi:10.1021/acscentsci.8b00881 (2019).
- 34 Casagrande, C. B., G. Perspectives in the design and application of dopamine receptor agonists. *Pharmacochemistry Library* **24**, 67-84, doi:org/10.1016/S0165-7208(96)80008-0 (1996).
- 35 Rodenhuis, N. *Centrally acting dopaminergic agents with an improved oral bioavailability: Synthesis and pharmacological evaluation*. PhD thesis, University of Groningen, (2000).
- 36 Pettersson, I. & Liljefors, T. Structure-activity relationships for apomorphine congeners. Conformational energies vs. biological activities. *J Comput Aided Mol Des* **1**, 143-152, doi:10.1007/BF01676958 (1987).

- 37 Cannon, J. G., Borgman, R. J., Aleem, M. A. & Long, J. P. Centrally acting emetics. 7. Hofmann and Emde degradation products of apomorphine. *J Med Chem* **16**, 219-224, doi:10.1021/jm00261a011 (1973).
- 38 Malo, M., Brive, L., Luthman, K. & Svensson, P. Investigation of D<sub>2</sub> receptor-agonist interactions using a combination of pharmacophore and receptor homology modeling. *ChemMedChem* **7**, 471-482, 338, doi:10.1002/cmhc.201100545 (2012).
- 39 Malo, M., Brive, L., Luthman, K. & Svensson, P. Investigation of D<sub>1</sub> receptor-agonist interactions and D<sub>1</sub>/D<sub>2</sub> agonist selectivity using a combination of pharmacophore and receptor homology modeling. *ChemMedChem* **7**, 483-494, 338, doi:10.1002/cmhc.201100546 (2012).
- 40 Kolaczkowski, M., Bucki, A., Feder, M. & Pawlowski, M. Ligand-optimized homology models of D<sub>1</sub> and D<sub>2</sub> dopamine receptors: application for virtual screening. *J Chem Inf Model* **53**, 638-648, doi:10.1021/ci300413h (2013).
- 41 Garcia-Amoros, J., Sanchez-Ferrer, A., Massad, W. A., Nonell, S. & Velasco, D. Kinetic study of the fast thermal *cis-to-trans* isomerisation of *para*-, *ortho*- and polyhydroxyazobenzenes. *Phys Chem Chem Phys* **12**, 13238-13242, doi:10.1039/c004340k (2010).
- 42 Izquierdo-Serra, M. *et al.* Two-photon neuronal and astrocytic stimulation with azobenzene-based photoswitches. *J Am Chem Soc* **136**, 8693-8701, doi:10.1021/ja5026326 (2014).
- 43 Ferre, S. *et al.* G protein-coupled receptor oligomerization revisited: Functional and pharmacological perspectives. *Pharmacol Rev* **66**, 413-434, doi:10.1124/pr.113.008052 (2014).
- 44 Casado, V. *et al.* Useful pharmacological parameters for G protein-coupled receptor homodimers obtained from competition experiments. Agonist-antagonist binding modulation. *Biochem Pharmacol* **78**, 1456-1463, doi:10.1016/j.bcp.2009.07.012 (2009).
- 45 Jin, L. Q., Wang, H. Y. & Friedman, E. Stimulated D<sub>1</sub> dopamine receptors couple to multiple G $\alpha$  proteins in different brain regions. *J Neurochem* **78**, 981-990, doi:10.1046/j.1471-4159.2001.00470.x (2001).
- 46 Chiken, S. *et al.* Dopamine D<sub>1</sub> receptor-mediated transmission maintains information flow through the cortico-striato-entopeduncular direct pathway to release movements. *Cereb Cortex* **25**, 4885-4897, doi:10.1093/cercor/bhv209 (2015).
- 47 Basnet, R. M., Zizioli, D., Taweedet, S., Finazzi, D. & Memo, M. Zebrafish larvae as a behavioral model in neuropharmacology. *Biomedicines* **7**, doi:10.3390/biomedicines7010023 (2019).
- 48 Howe, K. *et al.* The zebrafish reference genome sequence and its relationship to the human genome. *Nature* **496**, 498-503, doi:10.1038/nature12111 (2013).
- 49 Kalueff, A. V., Stewart, A. M. & Gerlai, R. Zebrafish as an emerging model for studying complex brain disorders. *Trends Pharmacol Sci* **35**, 63-75, doi:10.1016/j.tips.2013.12.002 (2014).
- 50 Lange, M. *et al.* The ADHD-susceptibility gene *lphn3.1* modulates dopaminergic neuron formation and locomotor activity during zebrafish development. *Mol Psychiatry* **17**, 946-954, doi:10.1038/mp.2012.29 (2012).
- 51 Ek, F. *et al.* Behavioral analysis of dopaminergic activation in zebrafish and rats reveals similar phenotypes. *ACS Chem Neurosci* **7**, 633-646, doi:10.1021/acschemneuro.6b00014 (2016).
- 52 Levitas-Djerbi, T. & Appelbaum, L. Modeling sleep and neuropsychiatric disorders in zebrafish. *Curr Opin Neurobiol* **44**, 89-93, doi:10.1016/j.conb.2017.02.017 (2017).

- 53 Irons, T. D., Kelly, P. E., Hunter, D. L., Macphail, R. C. & Padilla, S. Acute administration of dopaminergic drugs has differential effects on locomotion in larval zebrafish. *Pharmacol Biochem Behav* **103**, 792-813, doi:10.1016/j.pbb.2012.12.010 (2013).
- 54 Ingebretson, J. J. & Masino, M. A. Quantification of locomotor activity in larval zebrafish: considerations for the design of high-throughput behavioral studies. *Front Neural Circuits* **7**, 109, doi:10.3389/fncir.2013.00109 (2013).
- 55 Raymond, P. A., Barthel, L. K. & Curran, G. A. Developmental patterning of rod and cone photoreceptors in embryonic zebrafish. *J Comp Neurol* **359**, 537-550, doi:10.1002/cne.903590403 (1995).
- 56 Guggiana-Nilo, D. A. & Engert, F. Properties of the visible light phototaxis and UV avoidance behaviors in the larval zebrafish. *Front Behav Neurosci* **10**, 160, doi:10.3389/fnbeh.2016.00160 (2016).
- 57 Taylor, S., Chen, J., Luo, J. & Hitchcock, P. Light-induced photoreceptor degeneration in the retina of the zebrafish. *Methods Mol Biol* **884**, 247-254, doi:10.1007/978-1-61779-848-1\_17 (2012).
- 58 Kaufman, D. M. M., M. J. in *Kaufman's clinical neurology for psychiatrists (seventh edition)* (ed D. M.; Milstein Kaufman, M. J.) Ch. 21, 501-525 (W.B. Saunders, 2013).
- 59 Roffman, J. L. *et al.* Dopamine D<sub>1</sub> signaling organizes network dynamics underlying working memory. *Sci Adv* **2**, e1501672, doi:10.1126/sciadv.1501672 (2016).
- 60 Nieh, E. H., Kim, S. Y., Namburi, P. & Tye, K. M. Optogenetic dissection of neural circuits underlying emotional valence and motivated behaviors. *Brain Res* **1511**, 73-92, doi:10.1016/j.brainres.2012.11.001 (2013).
- 61 Roy, S. & Field, G. D. Dopaminergic modulation of retinal processing from starlight to sunlight. *J Pharmacol Sci* **140**, 86-93, doi:10.1016/j.jphs.2019.03.006 (2019).
- 62 Alemany-Gonzalez, M. *et al.* Prefrontal-hippocampal functional connectivity encodes recognition memory and is impaired in intellectual disability. *Proc Natl Acad Sci U S A* **117**, 11788-11798, doi:10.1073/pnas.1921314117 (2020).
- 63 Aubert, I. *et al.* Increased D<sub>1</sub> dopamine receptor signaling in levodopa-induced dyskinesia. *Ann Neurol* **57**, 17-26, doi:10.1002/ana.20296 (2005).
- 64 Cabre, G. *et al.* Synthetic photoswitchable neurotransmitters based on bridged azobenzenes. *Org Lett* **21**, 3780-3784, doi:10.1021/acs.orglett.9b01222 (2019).
- 65 Garrido-Charles, A. *et al.* Fast photoswitchable molecular prosthetics control neuronal activity in the cochlea. *J Am Chem Soc* **144**, 9229-9239, doi:10.1021/jacs.1c12314 (2022).
- 66 Pittolo, S. *et al.* Reversible silencing of endogenous receptors in intact brain tissue using 2-photon pharmacology. *Proc Natl Acad Sci U S A* **116**, 13680-13689, doi:10.1073/pnas.1900430116 (2019).
- 67 Cabre, G. *et al.* Rationally designed azobenzene photoswitches for efficient two-photon neuronal excitation. *Nat Commun* **10**, 907, doi:10.1038/s41467-019-08796-9 (2019).

## Supporting Information (SI) of Chapter 10

### SI10.1 Chemical synthesis

#### SI10.1.1 Materials and methods

All chemicals and solvents are from commercial suppliers and used without purification. Reactions were monitored by thin layer chromatography (TLC: EMD/Millipore, silica gel 60 on aluminium support, layer thickness: 200  $\mu\text{m}$ , particle size: 10-12  $\mu\text{m}$ ) by visualization under 254 and/or 365 nm lamp. Nuclear magnetic resonance spectrometry (NMR): Varian-Mercury 400 MHz. Chemical shifts ( $\delta$ ) are reported in parts per million (*ppm*) against the reference compound tetramethylsilane using the signal of the residual non-deuterated solvent [methanol- $d_4$   $\delta = 3.31$  ppm (1H),  $\delta = 49.00$  ppm ( $^{13}\text{C}$ )]. High-performance Liquid Chromatography (HPLC) apparatus: Waters Alliance 2695 separation module coupled to Waters 2996 photodiode detector (PDA) with MassLynx 4.1 software for data acquisition; XSelect CSH C18 OBD Preparative Column (130  $\text{\AA}$ , 5  $\mu\text{m}$ , 10 mm x 150 mm); mobile phase: water w/0.1% formic acid (solvent A) and acetonitrile w/0.1% formic acid (solvent B); elution method: flow 3 ml/min, gradient 0.0–1.0 min, 0% B; 1.0–7.0 min, 0–100% B; 7.0–8.0min, 100% B; 8.0–9.0 min, 100–0% B; 9.0–10.0 min, 0% B; runtime 10 min. Mass spectroscopy (MS) apparatus: Waters ACQUITY QDa detector (single quad mass detector) equipped with an electrospray ionization (ESI) interface. Spectra have been scanned between 100 and 1000 Da with values every 0.1 s and peaks are given as mass/charge (*m/z*) ratio. High resolution mass spectrometry analyses were performed with an LTQ-FT Ultra Mass Spectrometer (ThermoFisher Scientific) with NanoESI positive ionization. A sample of the final compound was reconstituted in 100  $\mu\text{l}$  of MeOH and diluted 1/100 with  $\text{CH}_3\text{CN}/\text{H}_2\text{O}/\text{formic acid}$  (50:50:1) for MS analysis. The sample was introduced by direct infusion (Automated Nanoelectrospray). The NanoMate (Advion BioSciences) aspirated the samples from a 384-well plate (protein Lobind) with disposable, conductive pipette tips, and infused the samples through the nanoESI Chip (which consists of 400 nozzles in a 20 x 20 array) towards the mass spectrometer. Spray voltage was 1.70 kV, delivery pressure 0.50 psi and *m/z* range 50-2000 Da. Data were acquired with Xcalibur software, vs.2.0SR2 (ThermoFisher Scientific). Elemental composition from experimental exact mass monoisotopic value was obtained with a dedicated algorithm integrated in Xcalibur software. Data are reported as mass-to-charge ratio (*m/z*) of the corresponding positively charged molecular ion.

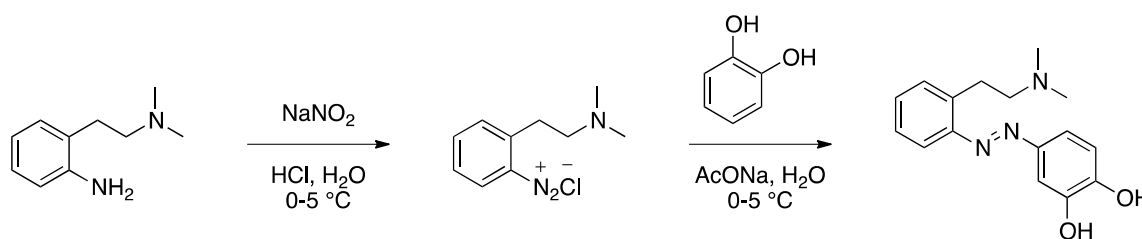
## SI10.1.2 Abbreviations

**Solvents:** EtOAc, ethyl acetate; CH<sub>2</sub>Cl<sub>2</sub>, dichloromethane; MeCN, acetonitrile; MeOH, methanol; EtOH, ethanol; THF, tetrahydrofuran; Et<sub>2</sub>O, diethyl ether; DMSO, dimethyl sulfoxide.

**Analytical characterizations:** NMR: d, doublet; dd, double doublet; ddd, double double doublet; dddd, doublet of doublet of doublet of doublets; dt, double triplet; m, multiplet; q, quartet; quin, quintet; s, singlet; t, triplet; m.p., melting point; R<sub>f</sub>, retention factor; rt, room temperature; RT, retention time.

## SI10.1.3 Synthetic routes

**Azodopa** was prepared in fair yield (about 63%) via an azo coupling reaction between freshly diazotized 2-(2-(dimethylamino)ethyl)aniline and 1,2-dihydroxybenzene (**Scheme S10.1**).



**Scheme S1.** Chemical synthesis of azodopa.

### **Scheme S10.1. Chemical synthesis of azodopa.**

**4-((2-(2-(dimethylamino)ethyl)phenyl)diazenyl)benzene-1,2-diol [azodopa]:** In a round-bottom flask, to a mixture of 2-(2-(dimethylamino)ethyl)aniline (165 mg, 1.00 mmol) in water (3 ml) was added concentrated HCl (0.4 ml), and the obtained solution was cooled to 0-5°C. A pre-cooled solution (0-5°C) of NaNO<sub>2</sub> (76 mg, 1.10 mmol) in water (0.5 ml) was added dropwise to the first solution under vigorous stirring and the resulting mixture was stirred for 30 min at 0-5°C. The so-obtained yellowish aqueous solution of 2-(2-(dimethylamino)ethyl)benzenediazonium chloride was then added dropwise into a second round-bottom flask containing a mixture of 1,2-dihydroxybenzene (332 mg, 3.00 mmol) and sodium acetate (907 mg, 11.00 mmol) in water (3 ml) at 0-5°C under vigorous stirring. This final mixture was then allowed to slowly warm up to room temperature and stirred for 12 h (reaction color turned from yellow to dark orange/red). The reaction crude was filtered and then directly purified by reverse-phase HPLC (see the general section above for details) to provide **azodopa** as a dark orange formate salt (63% yield; purity ≥ 98% as determined by HPLC-PDA analysis).

$^1\text{H}$  NMR (400 MHz, methanol- $d_4$ )  $\delta$  8.54 (s, 1H), 7.65 (dd,  $J = 7.9, 1.3$  Hz, 1H), 7.48 – 7.38 (m, 4H), 7.35 (ddd,  $J = 7.9, 6.7, 2.1$  Hz, 1H), 6.93 (d,  $J = 8.4$  Hz, 1H), 3.51 – 3.40 (m, 2H), 3.15 – 3.05 (m, 2H), 2.71 (s, 6H).  $^{13}\text{C}$  NMR (101 MHz, methanol- $d_4$ )  $\delta$  169.95, 151.61, 151.08, 148.20, 147.30, 136.53, 131.92, 131.84, 129.31, 121.15, 116.78, 116.01, 107.52, 60.08, 43.61, 27.83. RT (HPLC-PDA) = 6.53 min (*trans*).

HR-MS (ESI, positive): calculated for  $\text{C}_{16}\text{H}_{20}\text{N}_3\text{O}_2^+$ : 286.1550, found 286.1546 ( $\Delta\text{ppm} = -1.41$ )  $[\text{M} + \text{H}]^+$ .

## SI10.2 HPLC analyses and mass spectra

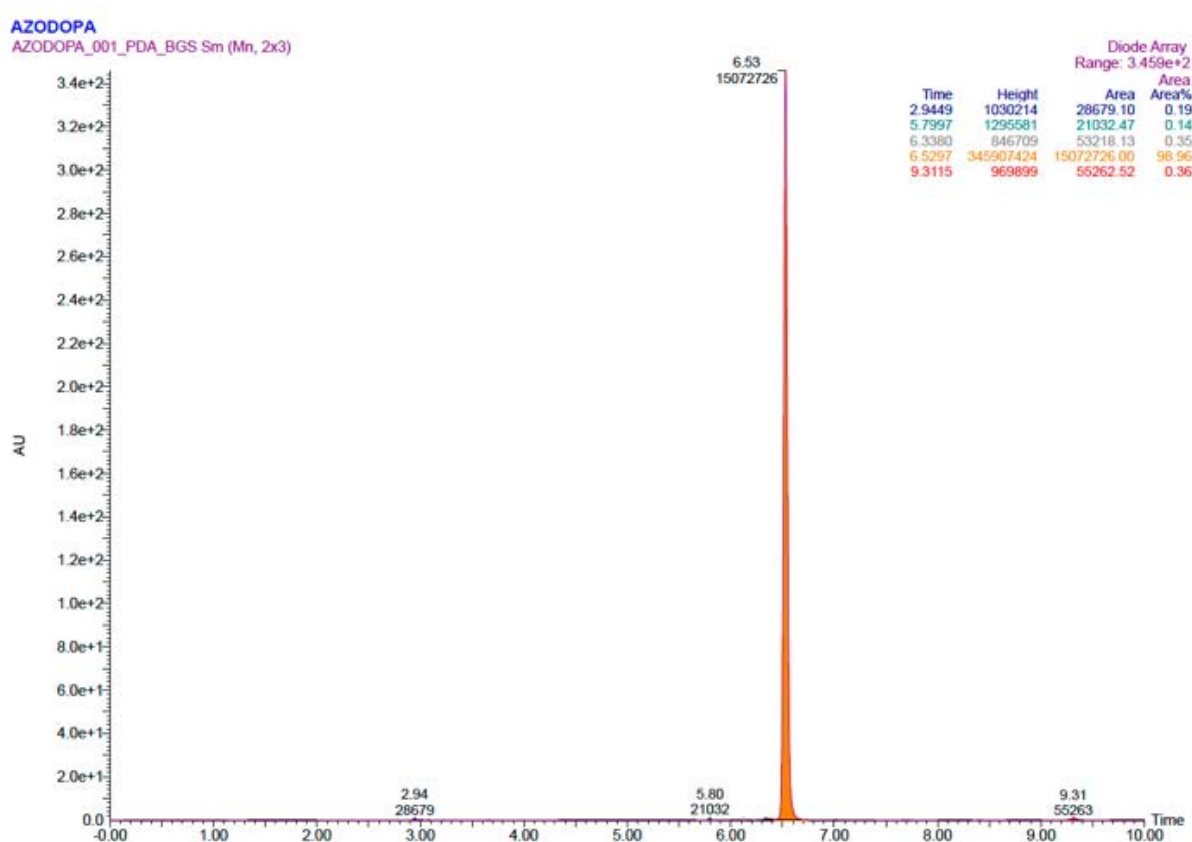


Figure S10.1. HPLC-PDA chromatogram of azodopa.



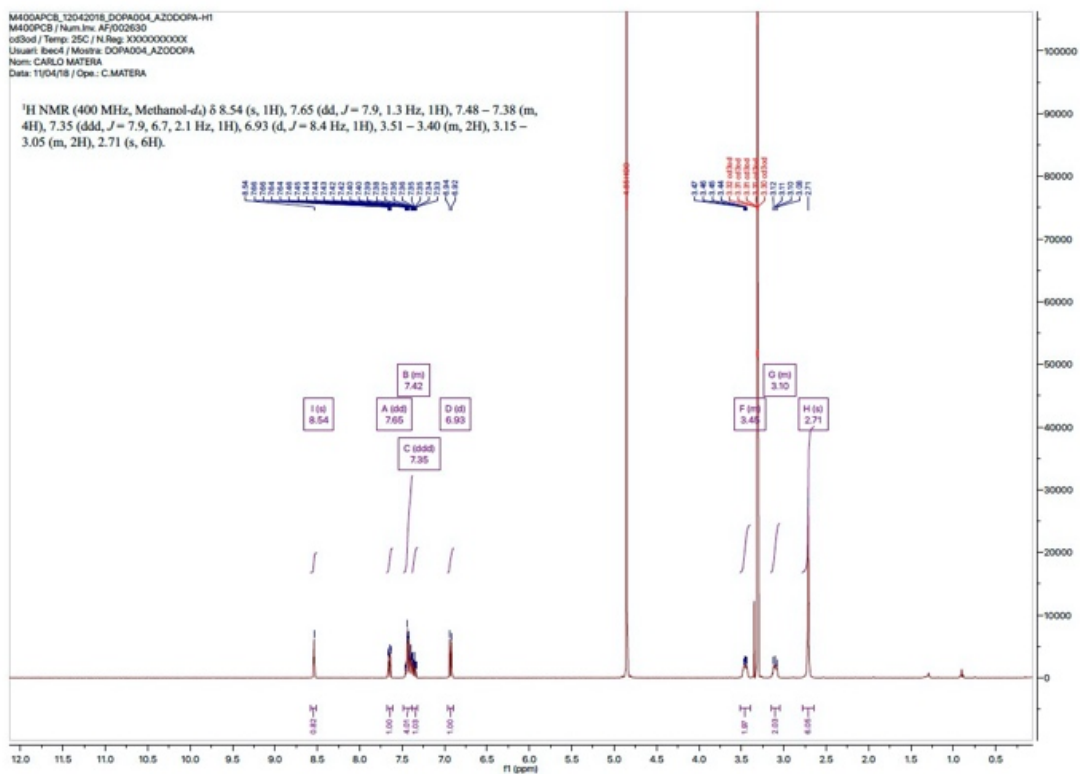


Figure S10.2.  $^1\text{H}$ -NMR spectrum of azodopa.

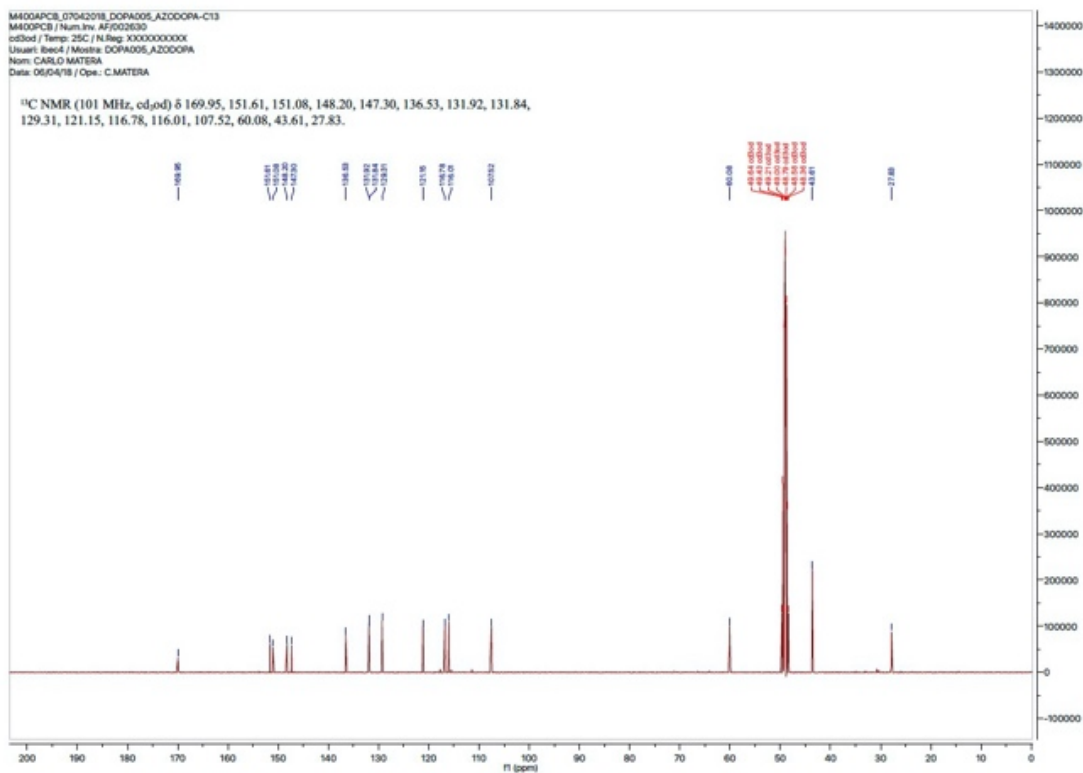
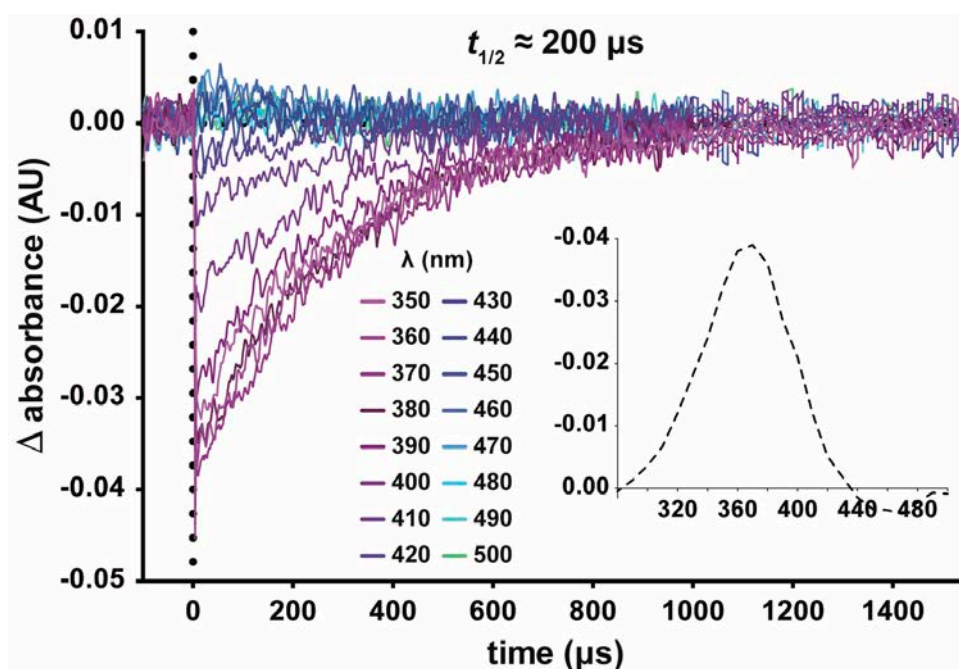


Figure S10.3.  $^{13}\text{C}$ -NMR spectrum of azodopa.

### SI10.3 Photochemical characterization

Steady-state ultraviolet-visible (UV-Vis) spectra were recorded with a Shimadzu UV-1800 UV-Vis Spectrophotometer using standard quartz cuvettes (10 mm optical path). Photoisomerization was accomplished by irradiating **azodopa** with a Vilber Lourmat ultraviolet (UV) Lamp (365 nm, 6 W) for 1-3 min. Transient absorption measurements were recorded with a nanosecond laser flash photolysis system (LKII, Applied Photophysics) equipped with a Nd:YAG laser (Brilliant, Quantel) as pump source ( $\lambda_{\text{ex}} = 355 \text{ nm}$ ), a Xe lamp as probe source, and a photomultiplier tube (PMT, R928, Hamamatsu) coupled to a spectrograph as detector. Thermal relaxation half-life was estimated applying an exponential one-phase decay model (GraphPad Prism 6).

The thermal relaxation half-life of the *cis*-isomer is about 200  $\mu\text{s}$  and thus conversion to the *trans* form occurs almost immediately after turning the light off. For this reason, all biological experiments were performed under continuous illumination.



**Figure S10.4. Photochromic behavior of azodopa investigated by transient absorption spectroscopy in water.** Transient absorption time traces were measured at different wavelengths upon excitation of *trans*-azodopa (30  $\mu\text{M}$ ) with a 5 ns pulsed laser at  $\lambda = 355 \text{ nm}$  (3 mJ/pulse energy) and 25°C. Thermal relaxation half-life of the *cis*-isomer (200  $\mu\text{s}$ ) was estimated applying an exponential one-phase decay model (GraphPad Prism 6). Inset: Transient absorption spectrum of *trans*-azodopa upon pulsed irradiation at  $\lambda = 355 \text{ nm}$  recorded at  $t = 0 \mu\text{s}$ . X-values represent wavelength (nm), Y-values represent  $\Delta A$  (arbitrary units, AU).

## SI10.4 Radioligand binding assay

Brains of male and female sheep of 4-6 months old were freshly obtained from the local slaughterhouse. Brain striatum was disrupted with a Polytron homogenizer (PTA 20 TS rotor, setting 3; Kinematica) for two 5 s periods in 10 volumes of 50 mM Tris-HCl buffer, pH 7.4, containing a proteinase inhibitor cocktail (Sigma-Aldrich). Membranes were obtained by centrifugation twice at  $105.000 \times g$  for 45 min at 4°C. The pellet was stored at -80 °C, washed once more as described above and resuspended in 50 mM Tris-HCl buffer for immediate use. Membrane protein was quantified by the bicinchoninic acid method (Pierce Chemical Co) using bovine serum albumin (BSA) dilutions as standard. Binding experiments were performed with membrane suspensions at room temperature in 50 mM Tris-HCl buffer, pH 7.4, containing 10 mM MgCl<sub>2</sub>.

**Figure S10.5** for D<sub>1</sub>-like receptor competition-binding assays, membrane suspensions (0.2 mg of protein/ml) were incubated for 90 min with a constant free concentration of 1 nM (non-irradiated curve) or 3 nM (irradiated curve) of the D<sub>1</sub>-like receptor antagonist [<sup>3</sup>H]SCH23390 (PerkinElmer) and increasing concentrations of **azodopa** (from 1 nM to 100 μM). For saturation-binding assays, membrane suspensions (0.2 mg of protein/ml) were incubated for 2 h at room temperature in 50 mM Tris-HCl buffer, pH 7.4, containing 10 mM MgCl<sub>2</sub> with increasing concentrations of the D<sub>1</sub>-like receptor antagonist [<sup>3</sup>H]SCH23390 (from 0.08 to 7.5 nM of free radioligand concentration for the irradiated curve and from 0.02 to 2.3 nM of free radioligand concentration for the non-irradiated curve) ( $K_{DA1}(\text{dark}): 0.3 \pm 0.1 \times \text{nM}$ ,  $K_{DA1}(\text{UV}): 1.6 \pm 0.6 \text{ nM}$ ,  $p\text{-value} (*) < 0.05$  vs. UV, unpaired t-test,  $n = 5$ ). Non-specific binding was determined in the presence of 20 μM of non-labeled SCH23390. Even though both competition curves appear similar, due to the lower affinity of the radioligand upon illumination (**Figure S10.5A**), we calculated an almost 4-fold decrease in affinity at 365 nm (see **Table S10.1**).

For D<sub>2</sub>-like receptor competition-binding assays, membrane suspensions (0.2 mg of protein/ml) were incubated for 2 h with a constant free concentration of 0.8 nM of the D<sub>2</sub>R antagonist [<sup>3</sup>H]YM-09151-2 ( $K_{DA1} = 0.30 \text{ nM}$ ) and increasing concentrations of **azodopa**. Nonspecific binding was determined in the presence of 30 μM of dopamine because at this concentration dopamine does not displace the radioligand from sigma receptors.

During the incubation period, incubates were irradiated or not with UV light. Experiments under illumination were performed by continuously irradiating with a Vilber Lourmat transilluminator (model ECX-F20.L, 365 nm, 6 x 8 W). In both binding assays, free and

membrane-bound ligands were separated by rapid filtration of 500  $\mu\text{l}$  aliquots in a cell harvester (Brandel) through Whatman GF/C filters embedded in 0.3% polyethylenimine (PEI) that were subsequently washed for 5 s with 5 ml of ice-cold 50 mM Tris-HCl buffer. The filters were incubated with 10 ml of Ultima Gold MV scintillation cocktail (PerkinElmer) overnight at room temperature and radioactivity counts were determined using a Tri-Carb 2800 TR scintillation counter (PerkinElmer) with an efficiency of 62%. Data were analyzed according to the “dimer model” developed by Casadó *et al.*, 2007<sup>1</sup>. Radioligand competition and saturation curves were analyzed by nonlinear regression using the commercial Grafit curve-fitting software (Erithacus Software), by fitting the binding data to the mechanistic dimer receptor model, as described in detail elsewhere<sup>2</sup>.

In conclusion, we found that **azodopa** has 3-fold greater affinity for D<sub>2</sub>-like than D<sub>1</sub>-like receptors, and in both cases the affinity is higher in the dark (*trans*-isomer).

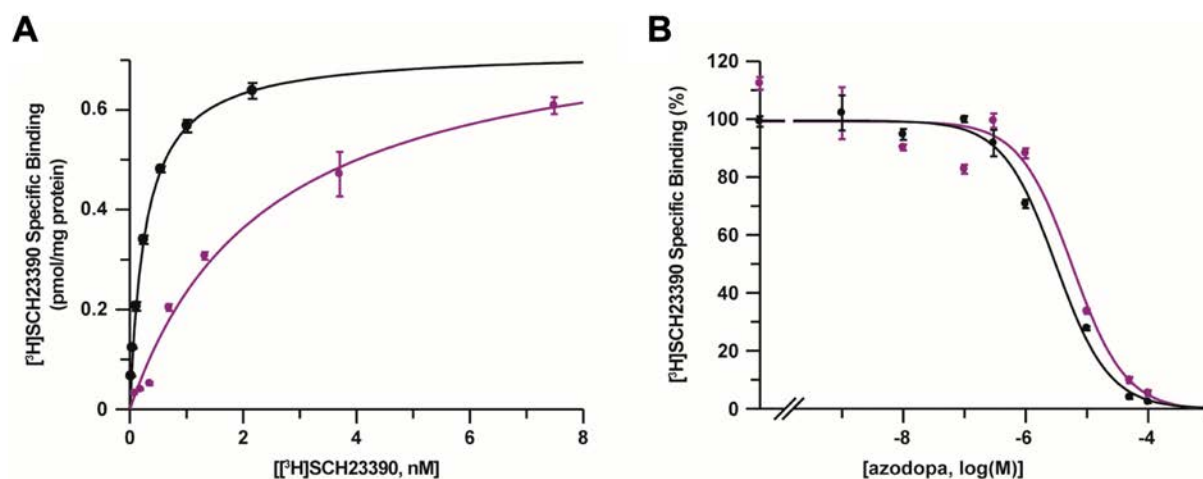


**Figure S10.5. Radioligand saturation binding experiments.** (A) Saturation experiments for D<sub>1</sub>R in sheep brain striatum membranes. Saturation assays (0.2 mg protein/ml) were performed, and data were fitted as indicated above. These experiments were performed with increasing concentrations of the D<sub>1</sub>R antagonist [<sup>3</sup>H]SCH23390 in the presence (purple) or absence (black) of UV irradiation during the incubation period of 1 h. Data are mean  $\pm$  SEM values from a representative experiment performed in triplicate. Affinity values of [<sup>3</sup>H]SCH23390 appear in Table S10.1. (B) Radioligand competition binding experiments. Competition experiments for D<sub>1</sub>R in sheep brain striatum membranes. Competition assays (0.2 mg protein/ml) were performed, and data were fitted as indicated above. The D<sub>1</sub>R antagonist [<sup>3</sup>H]SCH23390 at 1 nM was displaced with increasing concentrations of **azodopa** in the presence (purple) or absence (black) of UV irradiation during the incubation period. Data are mean  $\pm$  SEM values from a representative experiment performed in triplicate. 100% of [<sup>3</sup>H]SCH23390 specific binding =  $1.1 \pm 0.1$  pmol/mg protein ( $n = 9$  experiments performed in triplicate). Affinity values of **azodopa** ( $K_{DB}$ ) appear in Table S10.1.

Compound	D <sub>1</sub> R (*)	D <sub>2</sub> R (*)
Dark	K <sub>DB</sub> : 600 ± 100 nM	K <sub>DB</sub> : 210 ± 30 nM
UV light	K <sub>DB</sub> : 2200 ± 600 nM	K <sub>DB</sub> : 900 ± 300 nM

**Table S10.1. Binding affinity of azodopa for D<sub>1</sub>R and D<sub>2</sub>R in the dark and under illumination.** Affinity values obtained by fitting data from competition experiments of [<sup>3</sup>H]SCH23390 and [<sup>3</sup>H]YM-09151-2 vs. **azodopa** to the dimer receptor model. Data are mean ± SEM from 3-5 experiments performed with different striatal homogenates of 3-4 animals. Statistical differences between the values obtained were calculated by an unpaired t-test. *p*-value (\*) < 0.05 for affinity under UV vs. in dark.

## SI10.5 cAMP accumulation assay

For cAMP determinations, the human receptor construct of dopamine receptor D<sub>1</sub> (D<sub>1</sub>R) fused to full-length yellow variant of green fluorescent protein (EYFP) was used<sup>3</sup>. 2 µg of plasmid cDNA was transfected into Human embryonic kidney 293T (HEK 293T, American Type Culture Collection; ATCC) cells using PEI (Sigma-Aldrich) in 25-cm<sup>2</sup> cell culture flasks. Cells were maintained in culture with Dulbecco's modified Eagle's medium (DMEM; Sigma-Aldrich) supplemented with 2 mM L-glutamine, MEM nonessential amino acid solution (1/100), 100 U/ml penicillin/streptomycin, and 5% (v/v) of heat-inactivated fetal bovine serum (FBS) and kept in an incubator at 37°C and 5% CO<sub>2</sub>. All experiments were performed approximately 48 h after transfection.

Homogeneous time-resolved fluorescence energy transfer (HTRF) assays were performed using the Lance Ultra cAMP kit (PerkinElmer), based on competitive displacement of a europium chelate-labelled cAMP tracer bound to a specific antibody conjugated to acceptor beads. We first established the optimal cell density which provides a response that covers most of the dynamic range of the cAMP standard curve. Thus, 1200 cells in growing in medium containing 30 µM zardaverine were put into each well of a white ProxiPlate 384-well microplate (PerkinElmer). Cells were pretreated or not with the D<sub>1</sub>-like receptor antagonists SKF83566 (Tocris) for 5 min before the activation with **azodopa** for 15 min. During these 15 min, cells were irradiated or not with UV light to induce the *trans/cis* isomerization of the compound. Experiments under illumination were performed by continuously irradiating with a Vilber Lourmat transilluminator (model ECX-F20.L, 365 nm, 6 x 8 W). Fluorescence at 665 nm was analyzed on a PHERAstar Flagship microplate reader equipped with an HTRF optical module (BMGLab technologies). cAMP assays were also performed in non-transfected HEK 293T cells (**Figure S10.6**). In these cells, the effect of **azodopa** at 10 µM, dopamine at 1 µM and the D<sub>1</sub>-like receptor agonist SKF38393 at 300 nM was tested to ensure that all the effects observed

were D<sub>1</sub> receptor (D<sub>1</sub>R)-dependent. Statistical differences were analyzed by two-way ANOVA followed by Tukey's post-hoc test (GraphPad Prism 6).

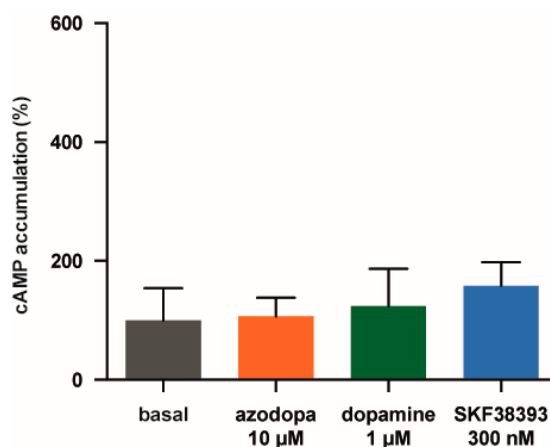


**Figure S10.6. Effect of D<sub>1</sub>R agonists on the adenylyl cyclase activity in non-transfected HEK 293T cells.** As a negative control experiment, cAMP accumulation was determined in non-transfected HEK 293T cells activated with the D<sub>1</sub>R agonists **azodopa** (10 µM, orange), dopamine (1 µM, green) or SKF38393 (300 nM, blue) for 15 min. Values are represented in % vs. basal levels (gray) of cAMP. Data are mean ± SEM of 3 experiments performed in quadruplicate.

## SI10.6 ERK phosphorylation assay

For ERK1/2 phosphorylation determinations, the human receptor construct of D<sub>1</sub>R fused to EYFP was used. 2 µg of plasmid cDNA was transfected into HEK 293T cells using PEI (Sigma-Aldrich) in 25 cm<sup>2</sup> cell culture flasks. Cells were maintained in culture with DMEM (Sigma-Aldrich) supplemented with 2 mM L-glutamine, MEM nonessential amino acid solution (1/100), 100U/ml penicillin/streptomycin, and 5% (v/v) of heat-inactivated FBS and kept in an incubator at 37°C and 5% CO<sub>2</sub>. All experiments were performed approximately 48 h after transfection.

The day of the experiment, cells were starved by treating them with serum free media for 3-4 h at 37°C. After that, cells were incubated with the indicated antagonist for 5 min and then, with **azodopa** for 7 min at 37°C. As for cAMP assays, cells were irradiated or not with UV light during the **azodopa** incubation. Experiments under illumination were performed by continuously irradiating with a Vilber Lourmat transilluminator (model ECX-F20.L, 365 nm, 6 x 8 W). Then, cells were rinsed with ice-cold phosphate-buffered saline and lysed by adding 200 µl ice-cold lysis buffer (50 mM Tris-HCl [pH 7.4], 50 mM NaF, 150 mM NaCl, 45 mM β-glycerophosphate, 1% Triton X-100, 20 mM phenyl-arsine oxide, 0.4 mM NaVO<sub>4</sub>, and protease inhibitor cocktail). The cellular debris was removed by centrifugation at 13.000 x g

for 5 min at 4°C, and the protein was quantified. To determine the level of ERK1/2 phosphorylation, equivalent amounts of protein were separated by electrophoresis on a denaturing 10% SDS polyacrylamide gel and transferred onto polyvinylidene difluoride membranes. Odyssey blocking buffer (LI-COR Biosciences) was then added, and the membrane was rocked for 90 min. The membranes were then probed with a mixture of a mouse anti-phospho-ERK1/2 antibody (1:2500; Sigma-Aldrich) and rabbit anti-ERK1/2 antibody that recognizes both phosphorylated and nonphosphorylated ERK1/2 (1:40000; Sigma-Aldrich) overnight at 4°C. The 42- and 44-kDa bands corresponding to ERK1 and ERK2 were visualized by the addition of a mixture of IRDye 800 (anti-mouse) antibody (1:10000; Sigma-Aldrich) and IRDye 680 (anti-rabbit) antibody (1:10000; Sigma-Aldrich) for 2 h and scanned by the Odyssey infrared scanner (LICOR Biosciences). Band densities were quantified using the scanner software and exported to Excel (Microsoft). The level of phosphorylated ERK1/2 isoforms was normalized for differences in loading using the total ERK1/2 protein band intensities. Statistical differences were analyzed by two-way ANOVA followed by Tukey's post-hoc test (GraphPad Prism 6).

### **SI10.7 Calcium imaging assay**

Human embryonic kidney tsA201 (HEK tsA201) cells were purchased from the European Collection of Authenticated Cell Culture. Cells were maintained at 37°C in a humidified atmosphere with 5% CO<sub>2</sub> and grown in DMEM and Ham's F-12 Nutrient Mixture (DMEM/F12 1:1, Life Technologies), supplemented with 10% fetal bovine serum (Life Technologies) and antibiotics (1% penicillin/streptomycin, Sigma-Aldrich). Plasmid pcDNA 3.1 (+) encoding human D<sub>1</sub>R was obtained as a kind gift from Ewa Błasiak (Department of Physical Biochemistry, Jagiellonian University, Kraków, Poland). Transient expression of the human D<sub>1</sub>R and the genetically encoded calcium indicator Red-Genetically Encoded Calcium 1 (RGECO-1; Addgene, ratio1:1) was induced by using the X-tremeGENE 9 DNA Transfection Reagent (Roche Applied Science) following the manufacturer's instructions. The day after, cells were harvested with Accutase (Sigma-Aldrich) and seeded onto 16 mm glass coverslips (ThermoFisher Scientific) pretreated with poly-L-Lysine (Sigma-Aldrich) to favor cell adhesion. Pre-confluent cultures were used for experiments at 48-72 h after transfection. The bath solution used for single cell intracellular calcium recordings contained: 140 mM NaCl, 5.4 mM KCl, 1 mM MgCl<sub>2</sub>, 10 mM HEPES, 10 mM glucose and 2 mM CaCl<sub>2</sub>, and was adjusted to pH 7.40 with aqueous NaOH. Before each experiment, cells were mounted on the recording chamber (Open Diamond Bath Imaging Chamber for Round Coverslips from Warner

Instruments). Cells were rinsed with fresh solution, and the recording chamber was filled with 1 ml recording solution and placed on an IX71 inverted microscope (Olympus) with a XLUMPLFLN 20XW x 20/1 water immersion objective (Olympus). R-GECO1 was excited during 50 ms at 562 nm by using a Polychrome V light source (Till Photonics) equipped with a Xenon Short Arc lamp (Ushio Europe B.V.) and a 585 nm dichroic beam splitter (Chroma Technology). Emission at 600 nm was filtered by ET630/675nm emission filter (Chroma Technology) and finally collected by a C9100-13 EM-CCD camera (Hamamatsu Photonics). Images were acquired at room temperature with an imaging interval of 4 s with the SmartLux software (HEKA). Imaging analysis was performed with FIJI (ImageJ).

Dopamine (50  $\mu$ M, Sigma-Aldrich) was used as agonist to stimulate D<sub>1</sub>Rs expressed in HEK tsA201 cells. Addition of dopamine, **azodopa** or vehicle (0.1% DMSO) was carried out by carefully pipetting a small volume during image acquisition into the accessory pool of the recording chamber to assure a good mixing of the solution. Photoisomerization of **azodopa** was achieved by continuously irradiating with a Vilber Lourmat UV Lamp (365 nm, 6 W) for 3 min before application. R-GECO1 is a red-shifted Ca<sup>2+</sup> fluorescent indicator and it was chosen because imaging at longer wavelength minimizes the effect of the unwanted fluorescence generated by continuously illuminating the specimen with 365 nm light. Data were normalized over the maximum response obtained with dopamine at 50  $\mu$ M. Control experiments were also performed to validate the effect of azodopa in D<sub>1</sub>R expressing HEK cells (**Figure S10.7**). Differently, when D<sub>1</sub>R is expressed, the effect of azodopa is evident (**Figure S10.8**) The Origin 8 software was used to calculate the values of the peak amplitude and the values of the area under the curve (AUC). AUC values correspond to the integral of the curves over each drug application interval. Statistical differences were analyzed by one-way ANOVA followed by Tukey's post-hoc test (GraphPad Prism 6).

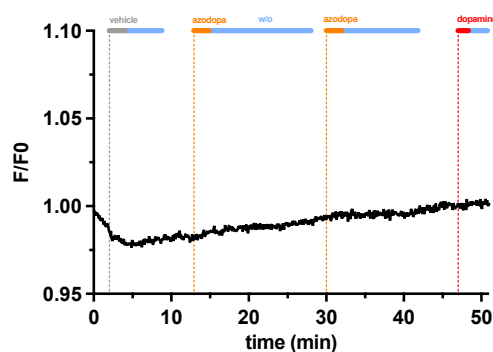


**Figure S10.7. Calcium imaging experiments in control cells.** Real-time calcium imaging in HEK tsA201 cells (n = 25) expressing R-GECO1, but not D<sub>1</sub>R. No calcium oscillations were recorded upon the application of vehicle (gray), **azodopa** (orange) under illumination and in the dark, or dopamine (green). Data are mean  $\pm$  SEM.



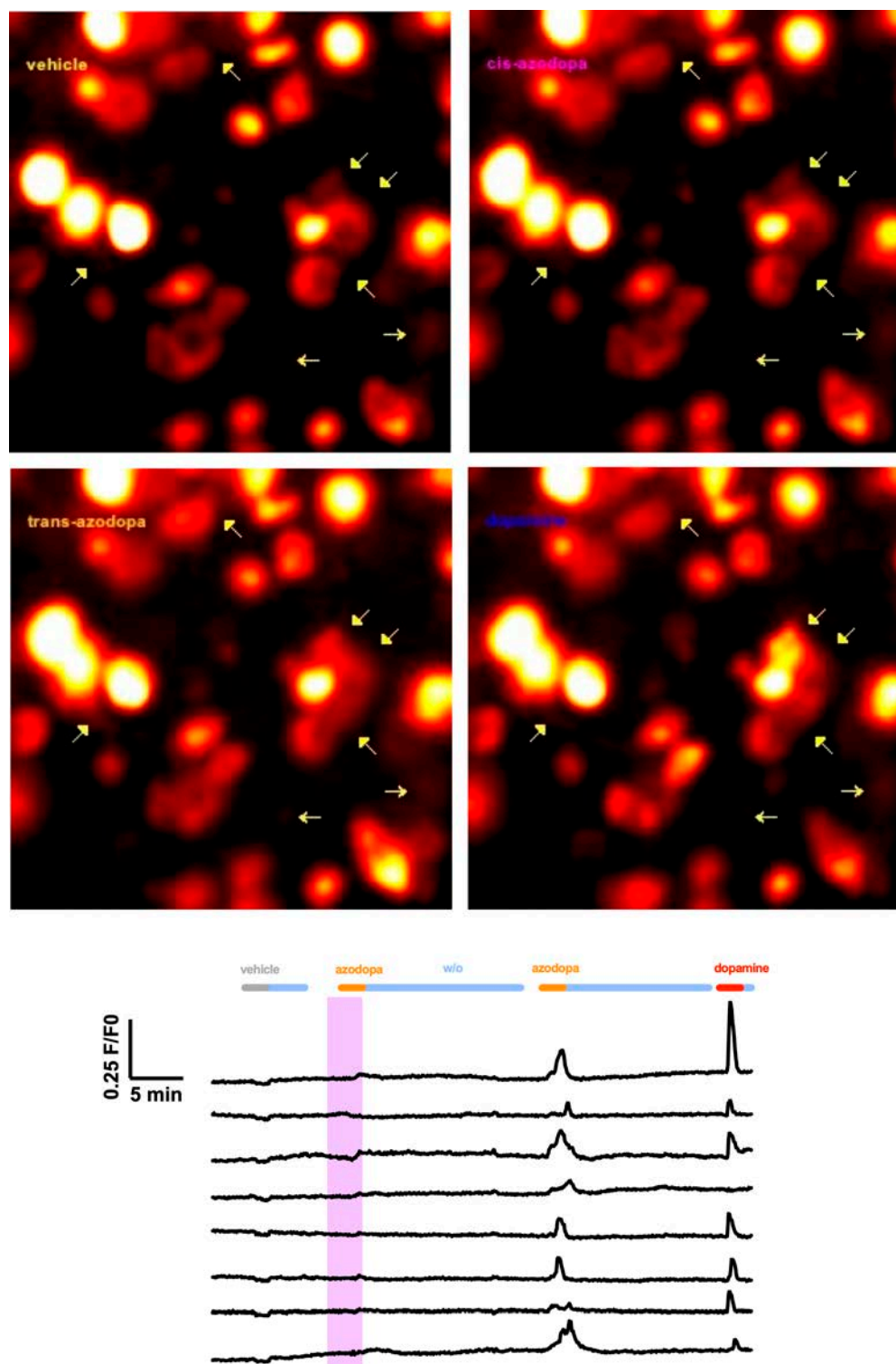


**Figure S10.8. Effect of azodopa on D<sub>1</sub>R-mediated intracellular calcium release.** Example frames from SI Movie 2 (top images; arrows indicating cells responding to *trans*-azodopa and dopamine over the time course of the experiment) and real-time calcium imaging response traces (bottom panel) in HEK tsA201 cells co-expressing D<sub>1</sub>R<sub>s</sub> and R-GECO1 as calcium indicator. Single-cell calcium traces for 8 representative cells are shown. Traces were recorded upon direct application of **azodopa** (50  $\mu$ M, orange bars) in the dark (white area) and under illumination (purple area). Shadow represents  $\pm$  SEM'. Gray and green bars indicate the application of vehicle (control) and dopamine (reference agonist), respectively. Light blue bars indicate wash-out periods.

## SI10.8 Behavioral assay in zebrafish

Wild-type (WT) zebrafish embryos (Tüpfel long-fin strain) were purchased from the animal facility of the Barcelona Biomedical Research Park (PRBB, Barcelona, Spain) and raised in darkness for 6 days at 28.5°C in UV filtered tap water in Petri dishes (daily cleaned and refilled). Animal development was checked every 24 hours. Unhealthy or abnormal embryos and larvae were removed and euthanatized in tricaine methanesulfonate 0.02%. All experiments and procedures were conducted according to the European Directive 2010/63/EU.

For the experiments with blinded zebrafish, larvae underwent a non-invasive and highly specific blinding technique that induces photoreceptor apoptosis in the dorsal and central retina<sup>4</sup>. The light-lesioning procedure was performed in a thermostatic and well-ventilated room equipped with small fans for air circulation and heat dissipation. Larvae at 5 days post-fertilization (dpf) were placed inside a 25 mm petri dish containing 20 ml of UV filtered tap water, inserted in a closed mirrored chamber, and then exposed to 135.000 lux light emitted by a mercury lamp (model Olympus U-LH100HG) for 30 min. Temperature was monitored throughout the whole procedure.

Behavioral studies were conducted on WT zebrafish larvae at 6 dpf. Vehicle and compounds were added with a multichannel pipette to exclude differences related to a delay in the application of each solution. Movements were recorded and analyzed using the ZebraBox tracking system (**Figure S10.13**) and the ZebraLab software (ViewPoint Life Science). On the morning of the test, 6 dpf larvae were moved into a new batch of fresh water and checked for motility capabilities and possible physical mutations. Larvae were then randomly divided into control and treatment groups. Every individual was placed in a separate well of a 96 well plate, each containing 200 µl of fresh UV filtered water and left undisturbed in the dark for 30 min to get acquainted with the new setting (habituation time). Afterwards, 100 µl of water were removed from each well and replaced with 100 µl of a double concentrated vehicle or treatment solution. At this point, the plate was inserted into the ZebraBox and the recording period started. Activity was recorded for a total of 62.5 min. Animals were exposed to controlled cycles of dark and 365 nm UV light, using the following protocol of illumination: dark (20 min, for adaptation), UV light (30 s), dark (20 min), and then four cycles of UV light (30 s) and dark (5 min). Illumination at 365 nm was performed with a built-in array of 12 LEDs placed 12 cm away from the multi-well plate. Light intensity, measured with a Newport 1916-C-2 optical

powermeter coupled to a Newport 918D-SL-OD3R detector, was 5.9 mW·cm. All experiments were conducted at 12.00 pm (UTC+01:00).

Alterations of locomotor activity were determined by monitoring and measuring fast movements, swimming distances and duration of high-speed swimming. In particular, the dependent variables measured included: total distance travelled, distance travelled at  $\leq 2 \text{ mm}\cdot\text{s}^{-1}$ , distance travelled at  $2\text{--}6 \text{ mm}\cdot\text{s}^{-1}$ , distance travelled at  $\geq 6 \text{ mm}\cdot\text{s}^{-1}$ , time spent moving, time spent freezing, and number of bursts. The arbitrary cut-off for motility ( $6 \text{ mm}\cdot\text{s}^{-1}$ ) was chosen because no variance was found among the groups at lower speeds. Total movements were not considered to limit the error of the video recording on minimal movements. Data were analyzed by two-way ANOVA with Tukey's post-hoc test or uncorrected Fisher's least significant difference test for statistical significance (GraphPad Prism 6).

Additional experiments showing the effect on azodopa on the locomotor activity of zebrafish larvae with or without the presence of  $D_1R$  antagonist are shown in **Figures S10.9-10.11** while its effect in normal vs. blinded fishes is shown in **Figure S10.12**.

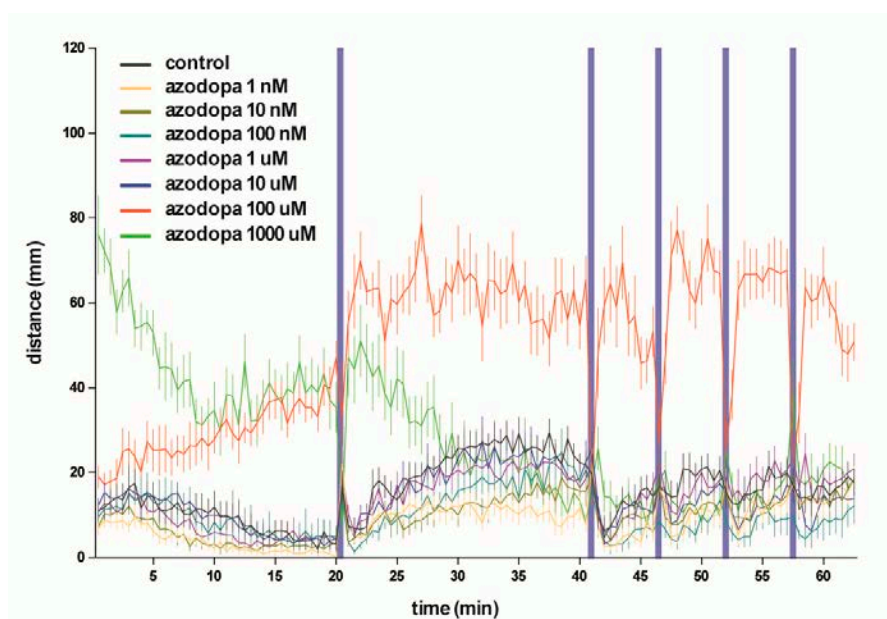


**Figure S10.9. Effects of azodopa on the locomotor activity of zebrafish larvae.** Swimming activity (distance moved over time) in larvae exposed to vehicle (control group) or **azodopa** in a wide range of concentrations (from 1 nM to 1 mM) in the dark (white areas) or under illumination with 365 nm light (purple bars). Up to a concentration of 10  $\mu\text{M}$  **azodopa**, no significant differences in the locomotor activity were detected in comparison with the control group. A great increase of the swimming activity was recorded at 1 mM (green line), but the effect eventually disappeared in about 30 min, when fish were possibly exhausted. The most interesting and representative alterations of the behavioral profile were observed at 100  $\mu\text{M}$ . Only fast movements (speed  $\geq 6 \text{ mm}\cdot\text{s}^{-1}$ ) were considered and integrated every 30 s. Data are mean  $\pm$  SEM (n = 11-12 individuals/condition).

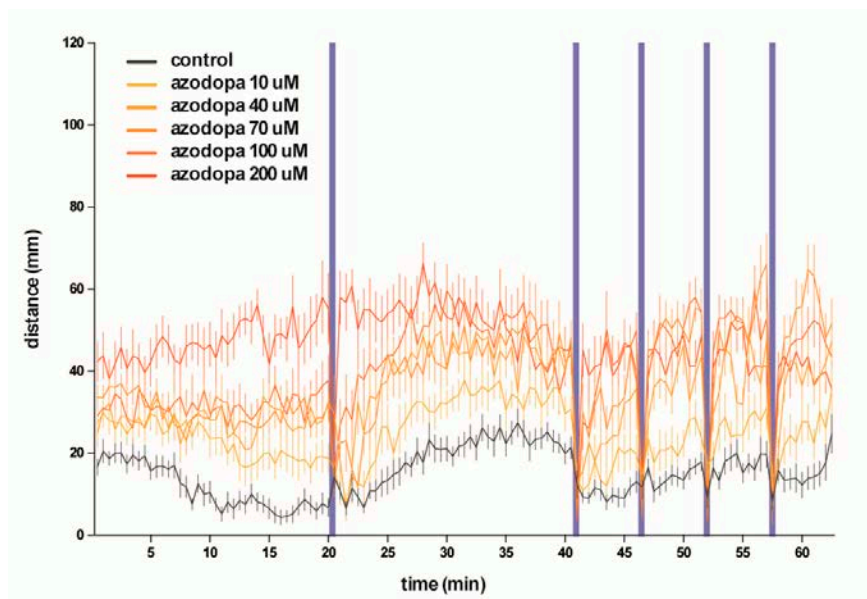


**Figure S10.10. Effects of azodopa on the locomotor activity of zebrafish larvae.** Swimming activity (distance moved over time) in larvae exposed to vehicle (control group) or **azodopa** in a small range of concentrations (from 10  $\mu\text{M}$  to 200  $\mu\text{M}$ ) in the dark (white areas) or under illumination with 365 nm light (purple bars). **Azodopa** induced a dose-dependent increase of the swimming activity in the dark. Only fast movements (speed  $\geq 6 \text{ mm}\cdot\text{s}^{-1}$ ) were considered and integrated every 30 s. Data are mean  $\pm$  SEM (n = 12 individuals/condition).

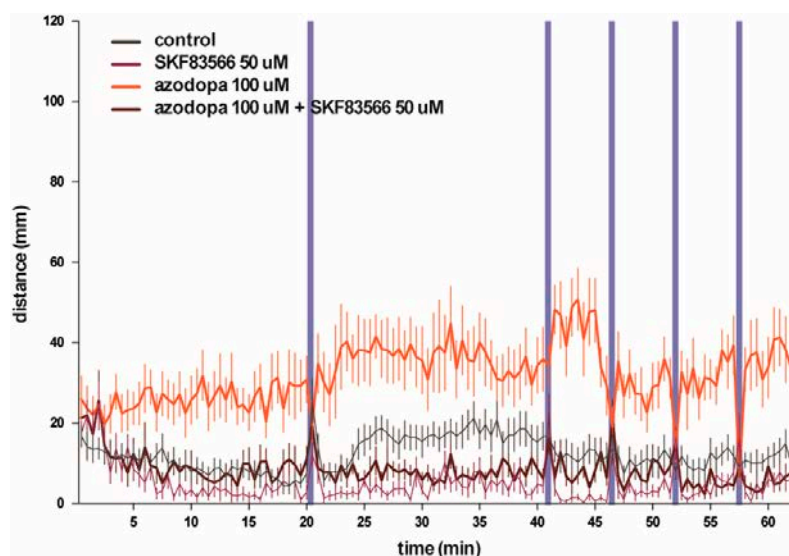


**Figure S10.11. The effects of azodopa on zebrafish locomotor activity are counteracted by a  $D_1R$  antagonist.** Swimming activity (distance moved over time) in larvae exposed to vehicle (control group), **azodopa** (100  $\mu\text{M}$ ), SKF83566 (50  $\mu\text{M}$ ,  $D_1R$ -selective antagonist), or **azodopa** + SKF83566 (100  $\mu\text{M}$  and 50  $\mu\text{M}$ , respectively), in the dark (white areas) or under illumination with 365 nm light (purple bars). The co-application of a  $D_1R$  antagonist abolished the behavioral effects produced by **azodopa**, restoring a more basal level of activity (brown line), and suggesting that **azodopa** locomotor effects are  $D_1R$ -mediated. Only fast movements (speed  $\geq 6 \text{ mm}\cdot\text{s}^{-1}$ ) were considered and integrated every 30 s. Data are mean  $\pm$  SEM (n = 12 individuals/condition).

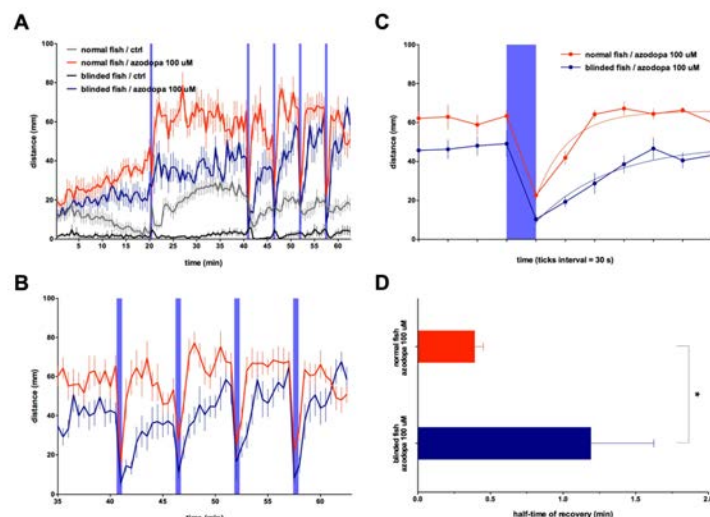


**Figure S10.12. Azodopa produces faster behavioral responses in normal fish than in blinded fish upon *cis-to-trans* isomerization.** (A) Swimming activity (distance moved over time) in normal and blinded zebrafish larvae exposed to vehicle (control group) or **azodopa** (100  $\mu$ M) in the dark (white areas) or under illumination with 365 nm light (purple bars). (B) Zoomed view of the last 4 dark-light cycles from panel 'A' to compare the kinetics of photoresponse in normal fish versus blinded fish. (C) Average of swimming activity (distance moved over time) in normal and blinded zebrafish larvae exposed to **azodopa** ( $n = 11-12$  individuals/condition, 4 last consecutive dark-light-dark periods). Blinded zebrafish needed more time to recover the maximum level of activity when the light was switched off, likely because of the absence of visual response. The recovery of activity in normal and blinded fish fitted a pseudo- first-order model (non-linear regression based on one-phase association kinetics;  $R^2_{\text{normal}} = 0.8553$ ,  $R^2_{\text{blinded}} = 0.7168$ ; solid curves in orange and blue), with statistically different rate constants ( $K_{\text{normal}} = 1.83 \pm 0.39$ ,  $K_{\text{blinded}} = 0.80 \pm 0.35$ ; F test,  $p$ -value (\*) < 0.05). (D) In order to statistically compare the half-times of recovery, data points from each dark-light-dark period were analyzed independently by nonlinear regression and refitted to a one-phase association curve. The four half-times from either the normal group or the blinded group curves were then averaged and analyzed by an unpaired two-tailed t-test ( $p$ -value (\*) < 0.05). All analyses were performed with GraphPad Prism 6.

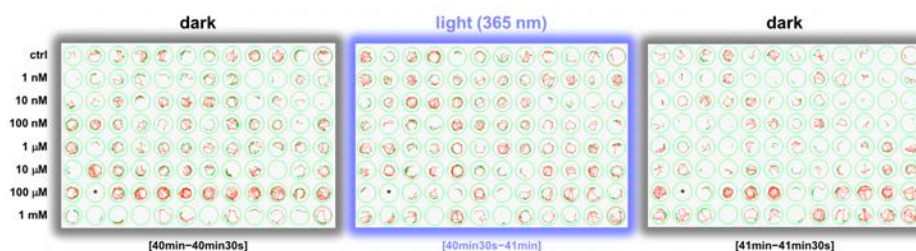


**Figure S10.13. Tracking of zebrafish larvae movement in a 96-well plate.** Trajectories of individual larvae treated with the vehicle (control group) or **azodopa** (from 1 nM to 1 mM) in different lighting conditions. Green lines and red lines indicate slow and fast swimming periods, respectively. Larvae treated with 100  $\mu$ M **azodopa** show higher activity in the dark in comparison with the controls, while they returned to control levels of activity under illumination. Trajectories were extrapolated from the same experiment represented in Figure 3A-D and Figure S12. (\*) Dead larvae excluded from the analysis.

## SI10.9 Electrophysiological recordings in mice

Young adult C57BL/6 male mice ( $n = 4$ , Charles River Laboratories) were obtained from the local colony at the PRBB Animal Facility. Mice were 3 months old and weighed 20-25 g at the time of the experiments. All procedures were conducted in compliance with EU directive 2010/63/EU and Spanish guidelines (Laws 32/2007, 6/2013 and Real Decreto 53/2013) and were authorized by the local Animal Research Ethics Committee and the local government (Generalitat de Catalunya).

Mice were anesthetized with isoflurane at 0.5-2% and placed in a stereotaxic apparatus. A heating pad was placed between the animal and the stereotaxic frame to maintain body temperature. The level of anesthesia was regularly tested by tail-pinching, retraction of the hind paws and changes in body temperature. A craniotomy was unilaterally drilled above the secondary motor cortex (M2: AP +2.0 mm, L 0.8 mm from bregma). Dental cement was used to build a small pool around the craniotomy that contained the saline or **azodopa** solutions. One custom-made octrode with 8 independent electrodes (4 two-wire stereotrodes) was inserted approximately 200  $\mu\text{m}$  deep into the superficial layers of the M2. The stereotrodes were made by twisting a strand of tungsten wire of 25  $\mu\text{m}$  of diameter (Advent) and had impedances that ranged from 100 to 400  $\text{k}\Omega$ .

Neural signals were recorded with the multi-channel Open Ephys system at a sampling rate of 30 kHz. The electrode wires were pinned to an adaptor to facilitate their connection to an Intan RHD2132 preamplifier that bandpass filtered (0.1-6 kHz) and digitized the analogic signals. These were later amplified and processed by the Open Ephys data acquisition system and finally visualized and stored in a PC via the Open Ephys GUI software. During the recordings, the exposed electrophysiological parts (octrode, adaptor, amplifier, LEDs) were shielded with aluminum foil to prevent environmental and electrical noise to interfere with the recordings. Experiments started when the anesthesia level and the electrophysiological signals were stable for 10 minutes. We recorded neural signals for 10 minutes under baseline conditions. Then, **azodopa** was administered with a standard 20  $\mu\text{l}$  pipette at a 3  $\mu\text{M}$  concentration in 10  $\mu\text{l}$  volume. After the administration, the recordings started again and continued for 10 more minutes. After the experiments ended, the mice were euthanized.

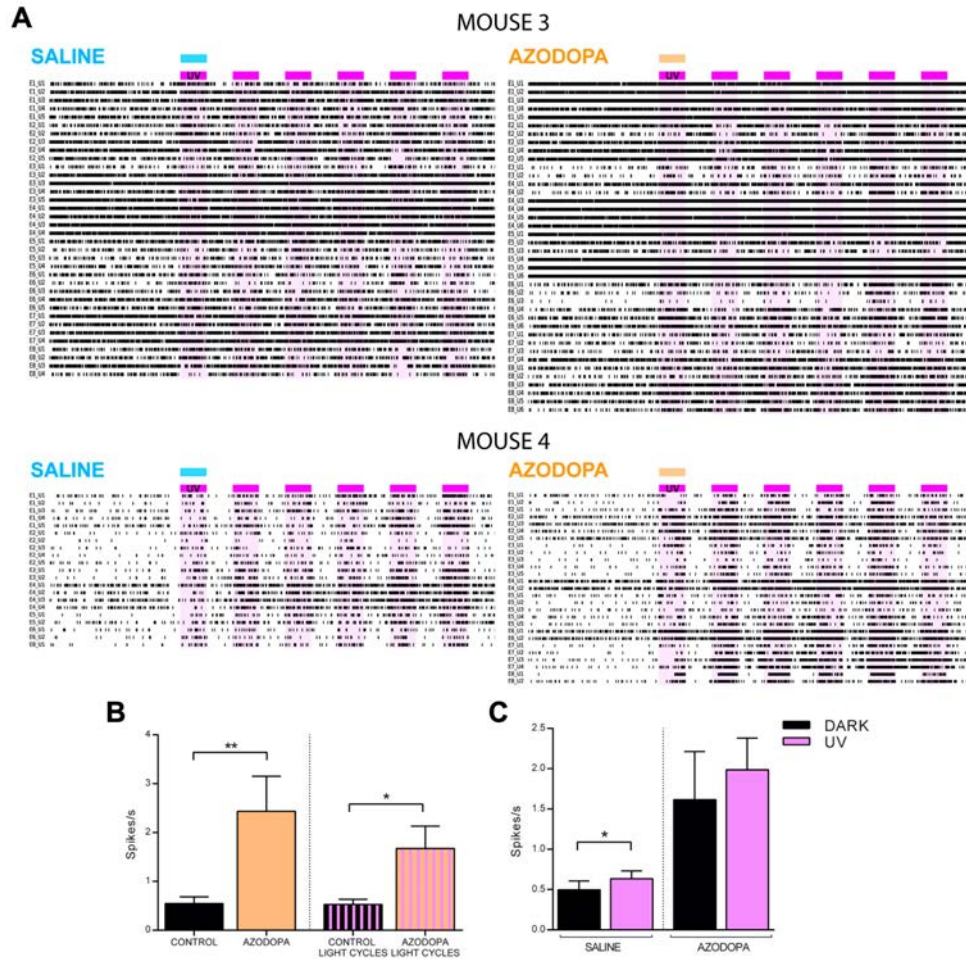
**Azodopa** was photoswitched with 365 nm light from two LEDs controlled by the computer via an Arduino board (yellow arrow, **Figure 10.4A** in the main article). This allowed a precise control of the illumination periods (one-minute ON cycles) that were timestamped to the Open

Ephys recording file (purple arrow, **Figure 10.4A** in the main article; results of illumination in **Figures S10.14-S10.16**). In two mice, the two LEDs were placed on top of their heads so that light was directed towards the craniotomy for illumination with 365 nm light. The Arduino UNO board turned on and off the two LEDs and sent analogical triggers to the Open Ephys data acquisition system that included them as timestamps in the electrophysiological recordings. The illumination patterns consisted in one-minute ON one-minute OFF cycles. In these experiments, we first performed controls with saline, where 0.5 ml of saline were administered into the pool via an infusion pump at 0.5 ml per minute. Subsequently, the experiment was repeated with 0.5 ml 3  $\mu$ M **azodopa**. We conducted continuous recordings that included a 5 min baseline and 12 min epochs after saline or **azodopa** administration with ON/OFF illumination cycles of UV light. The first illumination cycle started simultaneously to the drug administration (1 min period). The goal was to inactivate **azodopa**, while it accumulated in the pool. After the experiments ended, the mice were euthanized.

Recorded signals from each electrode were filtered offline to extract spiking activity and local field potentials (LFPs). Spiking activity was estimated by first subtracting the raw signal from each electrode with the mean signal of the 8 electrodes, which removed artifacts present in all the electrodes. Then, continuous signals were filtered between 450-6000 Hz with Python (Butterworth bandpass filter, order 2) and saved as NEX files. Spike sorting was performed with the Offline Sorter v4 software (Plexon Inc.). We first thresholded the signal and removed noise artifacts manually. Then, the K-means algorithm was used for automatic sorting of spikes to minimize any bias in the analyses. To obtain LFPs, signals were detrended and decimated to 1 kHz with custom-written scripts in Python. Spectrograms were constructed using the spectrogram function of the SciPy package (10 s windows, no overlap) and power was quantified with the multitaper power method of the spectral\_connectivity package in Python. The taper parameters chosen for the analyses were: time-half-bandwidth product = 5, 9 tapers.

The firing rate of individual neurons was compared between baseline and **azodopa** and between saline and **azodopa** with an unpaired t-test (baseline vs. **azodopa**,  $n = 44$  vs. 43 neurons; saline vs. **azodopa**,  $n = 57$  vs. 67 neurons). For each electrode, the mean firing rate of all neurons and LFP power (1 to 10 Hz) were compared between conditions with a paired t-test ( $n = 2$  mice, 8 electrodes per mouse). In the photoswitching experiments, the firing rates of individual neurons and LFP power were compared between the light and dark cycles with a paired t-test. We omitted the first light cycle (when saline or **azodopa** were injected) and compared the following 5 light cycles with the prior 5 dark cycles. We identified neurons that fired more in the dark

than during light cycles (DARK-ON neurons) and neurons with the opposite pattern (LIGHT-ON neurons) in Mouse 3. Statistical analyses were conducted with the GraphPad Prism 6 statistical package.





**azodopa** application this tendency in the averaged firing rate was maintained but not significant differences were obtained due to the cancellation of the opposing responses to light and darkness of individual neurons (see selected traces in Figure S10.15).

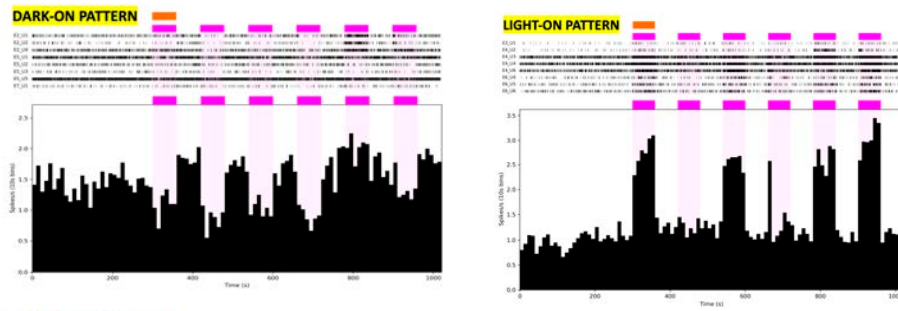


**Figure S10.15. Individual neurons in the same mouse display opposite photoswitching patterns of spiking activity with azodopa.** In Mouse 3, upon application of **azodopa** neurons can respond to light with opposite firing patterns, some decreasing their spiking activity during the light cycles (DARK-ON pattern, 8 pooled recordings) and others increasing it during the same cycles (LIGHT-ON pattern, 8 pooled recordings).

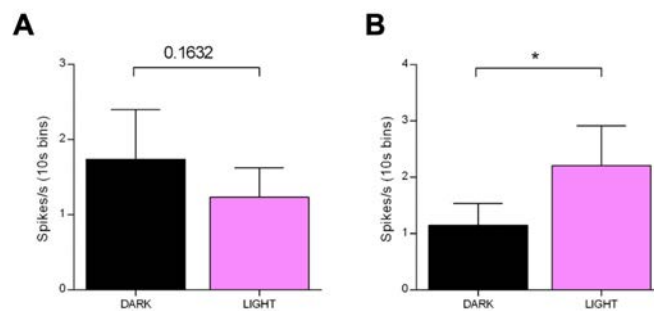


**Figure S10.16. Photoswitching of spiking activity *in vivo* with azodopa.** Quantification of the firing rate of (A) 8 neurons that decrease their spiking activity during the light cycles (dark-ON pattern) and (B) 8 neurons that increase their spiking activity during the light cycles (light-ON pattern). All neurons were recorded in Mouse 3. We compared the average spiking activity during the first 5 cycles of illumination (omitting the first cycle when **azodopa** was injected) with their previous 5 dark cycles (paired t-test;  $p$ -value (\*) = 0.013).

## SI10.10 Azodopa resistance to photodegradation

We verified in two ways that **azodopa** does not undergo significant irreversible photodegradation under the assay conditions, *i.e.*, that the efficacy of the *trans*-isomer can be maintained unaltered even after prolonged exposure to 365 nm light: (a) we analyzed a sample of **azodopa** by HPLC-PDA-MS before and after illumination (3 min and 60 min) (Figure S10.17), and (b) we compared in calcium imaging experiments the efficacy in the dark of a sample of **azodopa** that was pre-illuminated with 365 nm light for 60 min (named **azodopa-60** for simplicity) with another sample of **azodopa** from the same batch but never exposed to light (Figure S10.18).

We did not detect any significant variation in the composition of the sample by HPLC-PDA-MS. Moreover, the efficacy in the dark of **azodopa-60** was statistically not different from the efficacy of the non-illuminated sample.

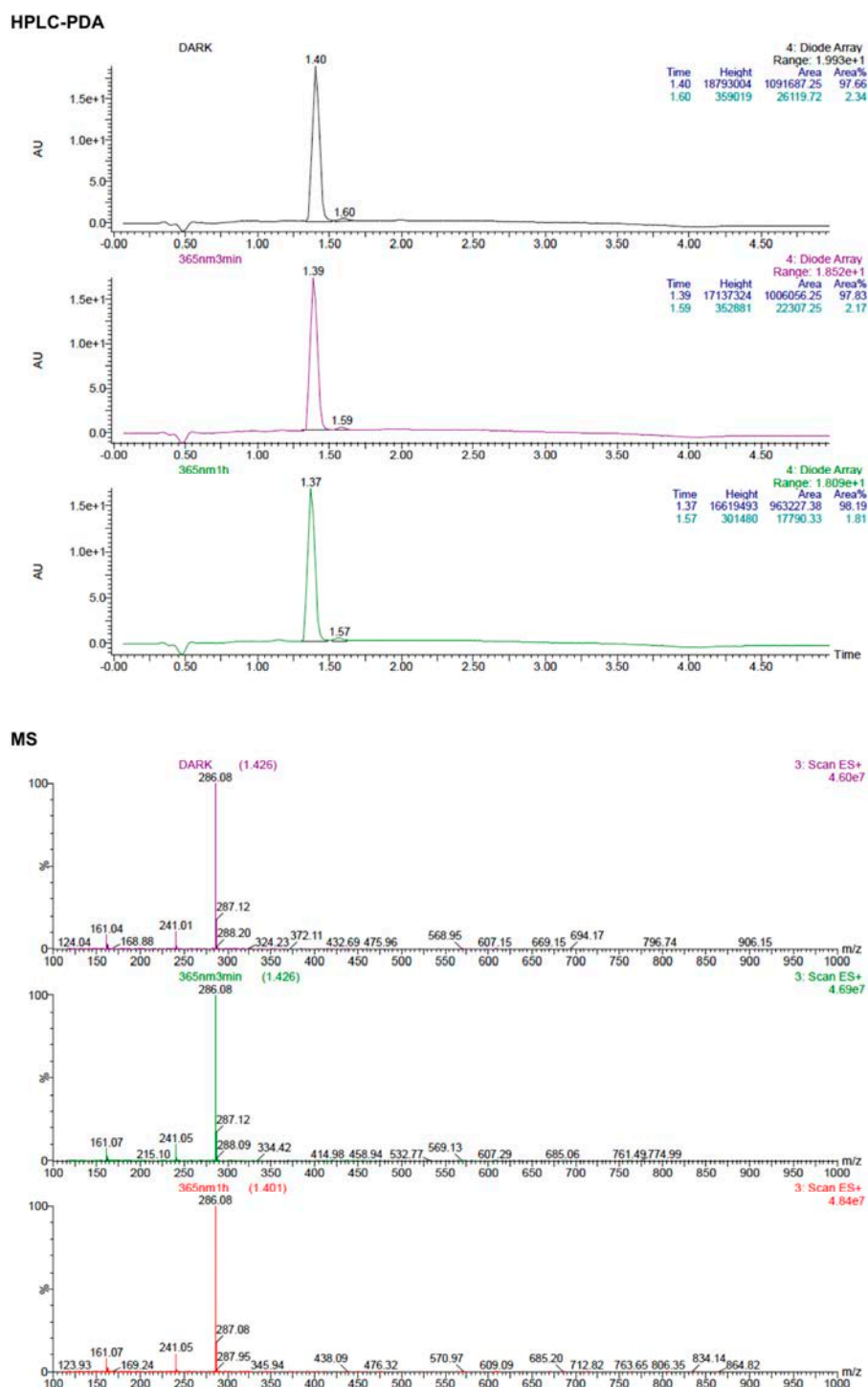


**Figure S10.17. HPLC-PDA chromatograms.** These were corresponding mass spectra of **azodopa** (50 μM) before and after illumination with a Vilber Lourmat UV Lamp (365 nm, 6 W) for 3 min and 60 min (top: dark; middle: 365 nm, 3 min; bottom: 365 nm, 60 min). No significant variations in the composition of the sample were detected.

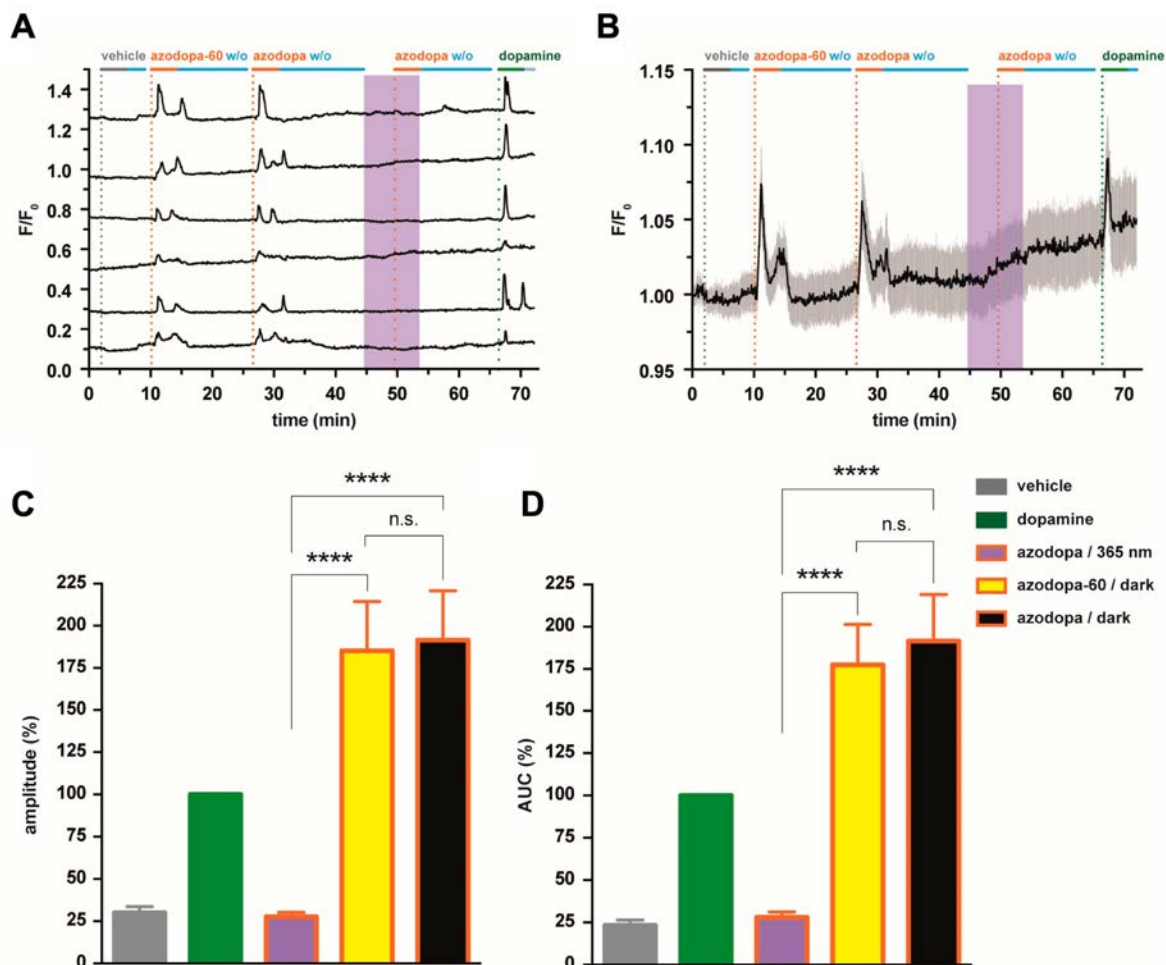


**Figure S10.18. *trans*-Azodopa maintains its efficacy in calcium imaging experiments also after prolonged pre-exposure to ultraviolet light.** Real-time calcium imaging response in HEK tsA201 cells co-expressing D<sub>1</sub>Rs and R-GECO1 as calcium indicator. **(A)** Single traces from 6 representative cells. **(B)** Averaged traces from 21 cells. Shadow represents ‘± SEM’. Traces were recorded upon direct application of **azodopa** (200 μM, orange bars) in the dark (white areas) and under illumination (purple area). **Azodopa-60** stands for “pre-irradiated **azodopa**” (Vilber Lourmat UV Lamp, 365 nm, 6 W, 60 min). Gray and green bars indicate the application of vehicle (control) and dopamine (reference agonist, 50 μM), respectively. Light blue bars indicate wash-out periods. Two values of the calcium responses generated by **azodopa** were calculated (Origin 8 software) and compared: the peak amplitude  $\Delta F/F_0$  **(C)**, calculated as the difference between the maximal and the minimal intensity of each response ( $p$ -value (\*\*\*\*) < 0.0001 for **azodopa**/365 nm vs. **azodopa-60**/dark;  $p$ -value (\*\*\*\*) < 0.0001 for **azodopa**/365 nm vs. **azodopa**/dark), and the area under the curve (AUC) **(D)**, calculated as the integral over the entire application time of vehicle or drugs ( $p$ -value (\*\*\*\*) < 0.0001 **azodopa**/365 nm vs. **azodopa-60**/dark;  $p$ -value (\*\*\*\*) < 0.0001 for **azodopa**/365 nm vs. **azodopa**/dark). Data are mean ± S.E.M. (n = 34 cells from 3 independent experiments). Data were normalized over the maximum response obtained with the saturating concentration of dopamine (50 μM) and were analyzed by one-way ANOVA followed by Tukey’s post-hoc test for statistical significance. All statistical analyses were performed with GraphPad Prism 6. As shown, no statistical difference was observed between **azodopa** and **azodopa-60** neither in amplitude nor in AUC of the calcium responses generated.

## SI10.11 Recovery of normal swimming behavior of zebrafish larvae after washout

We demonstrated that zebrafish larvae, previously treated with **azodopa** 100  $\mu\text{M}$  and exposed to dark-light cycles, recover normal swimming behavior after washout (**Figure S10.19**, see caption for details). After the first experiment (**Figure S10.19A**), the fish were transferred and maintained in fresh water for more than 1 h, and the motility experiment was repeated using the same protocol of illumination (**Figure S10.19B**). As shown in the figure, the two groups of fish displayed comparable swimming activity and reactivity to illumination after washout (**Figure S10.19B**), independently if they had been previously exposed to **azodopa** or control solution. Moreover, all the larvae, kept in fresh water, were still alive after about 48 h.

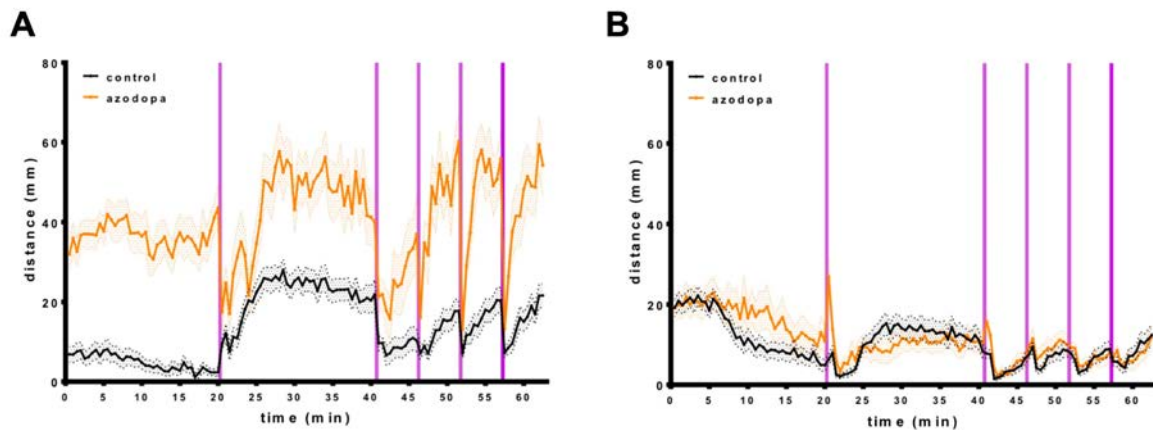


**Figure S10.19. Recovery of normal swimming behavior of zebrafish larvae after washout.** (A) Swimming activity (distance/time) in larvae exposed to vehicle (control, gray line) or 100  $\mu\text{M}$  **azodopa** (treatment, orange line) in the dark (white areas) or under illumination with 365 nm light (purple bars), following the same experimental procedure and illumination protocol shown in Figure 10.3. (B) Swimming activity (distance/time) in larvae previously exposed to vehicle (control, gray line) or 100  $\mu\text{M}$  **azodopa** (treatment, orange line) after washout. Washout procedure: fish were washed in fresh water (5 ml  $\times$  5 times, in a period of > 1 h) and then added to a new 96-well plate; each individual was placed into the same well position as in the first experiment; before starting the second experiment, all larvae were disturbed by adding 100  $\mu\text{l}$  of water to each well in order to reproduce the same distress as in the first experiment (vehicle or treatment solution addition). Data are mean  $\pm$  SEM (n = 24 individuals/group).

## Additional references

- 1 Casado, V. *et al.* Old and new ways to calculate the affinity of agonists and antagonists interacting with G protein-coupled monomeric and dimeric receptors: The receptor-dimer cooperativity index. *Pharmacol Ther* **116**, 343-354, doi:10.1016/j.pharmthera.2007.05.010 (2007).
- 2 Casado, V. *et al.* Useful pharmacological parameters for G protein-coupled receptor homodimers obtained from competition experiments. Agonist-antagonist binding modulation. *Biochem Pharmacol* **78**, 1456-1463, doi:10.1016/j.bcp.2009.07.012 (2009).
- 3 Ferrada, C. *et al.* Marked changes in signal transduction upon heteromerization of dopamine D<sub>1</sub> and histamine H<sub>3</sub> receptors. *Br J Pharmacol* **157**, 64-75, doi:10.1111/j.1476-5381.2009.00152.x (2009).
- 4 Taylor, S., Chen, J., Luo, J. & Hitchcock, P. Light-induced photoreceptor degeneration in the retina of the zebrafish. *Methods Mol Biol* **884**, 247-254, doi:10.1007/978-1-61779-848-1\_17 (2012).

# Chapter 11

---

*In vivo* restoration of visual acuity with  
upstream-targeted photopharmacology

---

---

**Rosalba Sortino**, Aleix González Díez, Santiago Milla Navarro, Pablo Calvé, Joaquín Martínez Tambella, Victor Paleo-García, Alexandre Gomila Juaneda, Nuria Camarero Palau and Xavier Rovira. ***In vivo* restoration of visual acuity with upstream-targeted photopharmacology**. All the indicated authors contributed experimentally to this work.



## Abstract

Blinding diseases that are caused by the degeneration of rods and cones (*e.g.*, retinitis pigmentosa) leave the rest of the retinal circuitry largely intact, although it is no longer able to respond to light. Photopharmacology has developed compounds to potentially restore impairments in vision by conferring light sensitivity to the remaining inner retinal neurons. Here, we report a library of fifteen novel compounds acting as agonist and positive allosteric modulators (ago-PAM) that photocontrol metabotropic glutamate 6 (mGlu<sub>6</sub>) receptors, which are located solely postsynaptic of the photoreceptors (PhRs) at the dendrites of ON bipolar cells (OBCs). Therefore, mGlu<sub>6</sub> receptors are upstream targets in the retinal circuitry, located next to where physiological photoresponses are generated (*i.e.*, in PhRs). These photoswitchable ligands thus act as “molecular prostheses”, that restore the light input to the retina *via* upstream-targeted control of the circuit after PhRs degeneration. *In vitro* results show that two compounds (**1492** and **1495**) have outstanding properties for this purpose, including nanomolar *trans*-on activity, fast relaxation in the dark, and switching with blue and white light. These photochromic ligands provide for the first time rapid and full recovery of the visual acuity in blind zebrafish larvae and restore visually guided behavior in blind mice by topical application. Altogether, compounds **1492** and **1495** display favorable properties and constitute potential drug candidates for sight restoration in patients of degenerative blinding diseases.





## 11.1 Introduction

Inherited retinal degenerative diseases (*e.g.*, retinitis pigmentosa; RP and age-related macular degeneration) are caused by the progressive loss of rod and cone photoreceptors (PhRs), ultimately leading to blindness. In those disorders the downstream neurons of the inner retina are spared<sup>1</sup> and undergo slow remodeling<sup>2,3</sup>. Visual impairment is one of the ten most prevalent causes of disability that affect approximately 295 million people with 43 million being blind around the world<sup>4</sup>. Several approaches have been developed to restore visual functions. First, retinal chips (*e.g.*, Argus I, Argus II, Alpha IMS and Alpha ANS)<sup>5</sup> can be implanted into the eye to electrically stimulate the remaining neurons of the inner retina. Second, embryonic stem cells can be differentiated into PhRs progenitors *in vitro*. The transplantation of these stem cell-derived progenitors in the retina of blind animals leads to the restoration of retinal light responses<sup>6,7</sup>. Third, viral expression of optogenetic tools (*e.g.*, microbial, human opsins or engineered constructs) restore visual responses, or in some cases visual acuity, in blind mouse models for RP<sup>8-14</sup>. Recently, a few of these approaches that employ variants of channelrhodopsin (ChR) have reached clinical trials. Although each of these strategies have shown potential for restoring visual functions, they all have limitations. Retinal implants pose high surgical risks and costs and they were recently discontinued due to limited restoration of visual acuity. Stem cells require invasive surgery and represent an irreversible treatment involving serious risks that may not be managed by a qualified care team (*e.g.*, teratoma)<sup>15</sup>. All the optogenetic approaches involve invasive and irreversible gene therapy<sup>16</sup>, arising safety and ethical concerns, beside regulatory complexities. In fact, the impact of the treatment is unknown, regarding the potential phototoxic effects to tissues, cancer formation, transfer of genes to future progeny and immune response against overexpressed microbial proteins. These drawbacks could be overcome by a photopharmacological approach based on small photochromic ligands (PCLs). PCLs are freely diffusible compounds that can be reversibly toggled between two configurations using different wavelengths of light that favor each of the isomers. They are subject to specific pharmacokinetics and could be replaced by new molecules as they become available. They do not require permanent genetic manipulation or invasive interventions. The developed PCLs generally bestow light sensitivity into retinal ganglion cells (RGCs), restoring light driven behavior in blind mice<sup>17-21</sup>. However, conferring light-sensitivity to retinal neuron upstream of RGCs may enable more complex retinal signal processing<sup>2,22</sup>. Moreover, the abovementioned PCLs target ubiquitous proteins (*e.g.*, potassium channels) and, thereby, might show a poor safety profile and potentially cause severe side effects.

In this study, we propose a novel strategy to restore vision which involves a new molecular target, allowing upstream signaling control of the retinal circuit. **Prosthe6** (*i.e.*, optogluram) is a positive allosteric modulator (PAM) of metabotropic glutamate 6 (mGlu<sub>6</sub>) and 4 (mGlu<sub>4</sub>) receptors and it was the reference compound to design of a library with fifteen novel allosteric modulators. These compounds represent a toolset together with a combination of photochemical properties that target mGlu<sub>6</sub> receptors. The localization of the mGlu<sub>6</sub> receptor at ON bipolar cells (OBCs) dendrites postsynaptic to PhRs<sup>23</sup> (**Figure 11.1B**) offers a highly selective retinal response. Endowing OBCs with light sensitivity is expected to take full advantage of the surviving retinal circuitry, including signal amplification and encoding, thereby allowing high photosensitivity, edge detection, and dominance.

Under physiological conditions, glutamate (*i.e.*, the endogenous agonist) continuously activates OBCs through the mGlu<sub>6</sub> receptor in the dark, resulting with the closure of the transient receptor potential melastatin 1 (TRPM1) channel and cells' hyperpolarization<sup>24-27</sup> (**Figure 11.1C, top left diagram**). In contrast, PhRs do not release glutamate under illumination, leading to an inactivity of mGlu<sub>6</sub> receptor, while the TRPM1 is opened and OBCs are depolarized<sup>25,26,28</sup> (**Figure 11.1C, bottom left diagram**). These novel photoswitchable allosteric ligands (*i.e.*, **1492** and **1495**) act as “molecular prostheses” that functionally replace the PhRs by activating the mGlu<sub>6</sub> receptors in a light-dependent manner in the absence of glutamate, which is depleted when PhRs are degenerated (**Figure 11.1C, top right diagram**). Interestingly, they possess intrinsic agonistic activity (ago-PAM)<sup>29</sup> in their *trans* configuration without requiring co-application of an agonist, and they do not activate mGlu<sub>6</sub> receptor in their *cis* configurations, under blue and white illumination (**Figure 11.1C, bottom right diagram**). Thus, they closely mimic the physiological action of light on the retinal circuit.

In this study, the two best performing compounds (*i.e.*, **1492** and **1495**) are shown to display ago-PAM activity, nanomolar potency, fast-relaxation, and blue light-switching. They photoswitch mGlu<sub>6</sub> activity *in vitro*, and they are capable of restoring visual acuity in zebrafish larvae and light driven behavior in blind mice through intravitreal and topical applications.

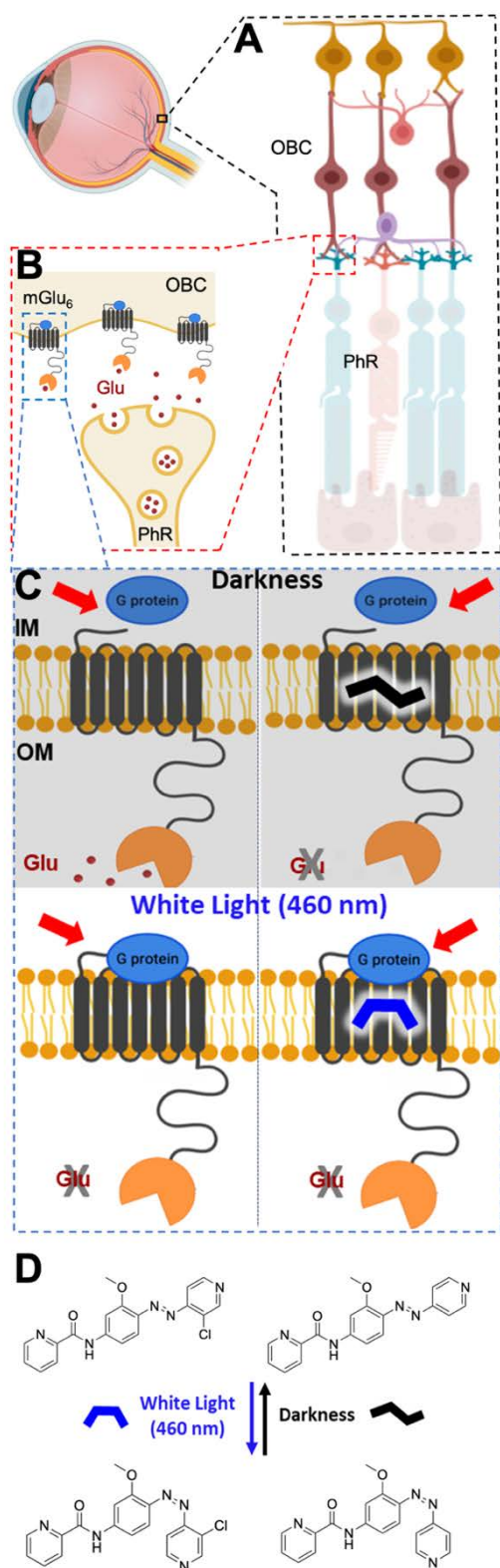


**Figure 11.1. Rationale of vision restoration targeting upstream retinal stimulation with photoswitchable allosteric modulators of mGlu<sub>6</sub> receptor.**

(A) Cellular structure of the human retina indicating the rod and cone photoreceptor (PhR) cells at the bottom, which lose functionality or die during retinal degeneration, and their postsynaptic neurons (*e.g.*, ON bipolar cells; OBCs) which are spared by the process. In particular, OBCs receive input from rods and are thus located “upstream” at the top of the neuronal circuit of the retina. Endowing them with light sensitivity is expected to take full advantage of the surviving retinal circuitry, including signal amplification and encoding, thereby allowing high photosensitivity, edge detection, dominance, etc. (B) The topmost transducer of PhR signals is the mGlu<sub>6</sub> receptor located postsynaptic of rods in OBC. It is activated by glutamate released by PhRs synaptic terminals. (C) In the dark (top left diagram), PhRs release glutamate (*i.e.*, endogenous agonist) at the outer membrane (OM) side of OBCs, which activates mGlu<sub>6</sub> receptor and releases its G $\alpha_o$  protein at the inner membrane (IM) side, with the consequent closure of the transient receptor potential melastatin 1 (TRPM1) channel and the OBCs are kept at rest. Under illumination (bottom left diagram) PhRs do not release glutamate, mGlu<sub>6</sub> receptors and their G $\alpha_o$  protein remains inactive and bound respectively, TRPM1 remains open and eventually causing the neurons to fire action potential. The strategy to functionally replace PhRs by photosensitive molecular prostheses requires compounds that activate mGlu<sub>6</sub> receptors in a light-dependent manner and in the absence of the glutamate, which is absent at the OM of RBCs when PhRs are degenerated. In the dark (top right diagram) the compound should activate mGlu<sub>6</sub> receptor in the absence of glutamate. Under illumination at different wavelengths (*e.g.*, blue in the bottom right diagram) the compound should not activate mGlu<sub>6</sub> receptor. In this way, the compound would retain physiological signal flow in the circuit and act as a “molecular prosthesis” for

upstream-targeted functional restoration of retinal function. (D) Photoswitchable allosteric modulators of group III mGluRs may serve this purpose, if they display mGlu<sub>6</sub> receptor agonism and potentiation in the *trans* form (*i.e.*, mimicking the physiological activation of the receptor in the dark) and weaker activity in the *cis* form under 460 nm light (*i.e.*, corresponding to the physiological deactivation of mGlu<sub>6</sub> receptor under illumination). The structures and photoisomerization of the best performing compounds 1492 and 1495 are shown.

## 11.2 Results

### 11.2.1 *In vitro* calcium imaging

We first investigated whether a reported PAM of mGlu<sub>6</sub> and mGlu<sub>4</sub> receptors named **prosthe6**<sup>30,31</sup> (*i.e.*, optogluram) was able to exert its effect on mGlu<sub>6</sub> receptor and (de)activate it in the absence of glutamate (ago-PAM activity)<sup>29</sup> (**Figure S11.1**). We performed a calcium fluorescence imaging in human embryonic kidney (HEK) cells expressing the receptor and we monitored the intracellular calcium concentrations. The genetically encoded calcium indicator GCaMP6s was mainly used in the experiments. L-2-amino-4-phosphonobutyric acid (L-AP4) is a selective agonist of group III mGlu receptors that was used as a control for the experiments and a reference to normalize our compounds' response amplitudes. The application of L-AP4 elicited reproducible calcium responses indicative of mGlu<sub>6</sub> receptor activation (**Figure 11.2A and Figure S11.2A**) and allowed building dose-response curves (**Figure S11.2B**).

The induced calcium oscillations through the application of *trans*-**prosthe6** are terminated by the photoconversion to *cis*-**prosthe6** under 380 nm light. Green light (500 nm) restored the receptor activity, leading to sustained or oscillatory calcium responses (**Figure 11.2B**). Averaged time course of WT mGlu<sub>6</sub> receptor responses in the presence of **prosthe6** (representative single cells in **Figure S11.3A**) under different illumination conditions, is presented in **Figure 11.2C**. Of note, 30 minutes before performing the experiment with the WT mGlu<sub>6</sub> receptor the medium was changed to glutamate-free DMEM GlutaMAX-1 to avoid the influence of extracellular glutamate. Calcium oscillations were observed upon application of the *trans* isomers of the compounds, which were reduced by the photoconversion to the *cis* isomers under 380 nm light. Subsequent *cis*-to-*trans* isomerization under 500 nm light rapidly reactivated the mGlu<sub>6</sub> receptor, leading to oscillatory calcium responses. Therefore, **prosthe6** is an ago-PAM which reversibly photocontrols the mGlu<sub>6</sub> receptors. Neither the application of vehicle nor illumination alone evoked calcium responses. Quantification of the results showed that *trans*-**prosthe6** isomer produced significantly larger responses than the *cis*-isomer for all the concentrations used (**Figure 11.2E**). Therefore, we decided to further characterize **prosthe6** and dose-response curves of this compound were calculated under *trans*- and *cis*-enriched illumination conditions (green and violet respectively, **Figure S11.4AB**). Next, to validate the ago-PAM activity of **prosthe6**, we performed real-time calcium imaging assays in HEK cells expressing the mGlu<sub>6</sub> mutant T148A receptor, which is not activated by orthosteric ligands<sup>32</sup>. No responses were elicited by vehicle, orthosteric agonists L-AP4 or glutamate. Robust photoswitching of T148A mGlu<sub>6</sub> receptor responses by **prosthe6** is shown in **Figure 11.2D**

**and Figure S11.3B.** Quantification of the T148A mGlu<sub>6</sub> receptor photoresponses by **prosthe6** showed a nearly four-fold difference between the *trans* and *cis* isomers, demonstrating the ago-PAM activity of the compound, in addition to its positive allosteric modulation (**Figure 11.2F**).

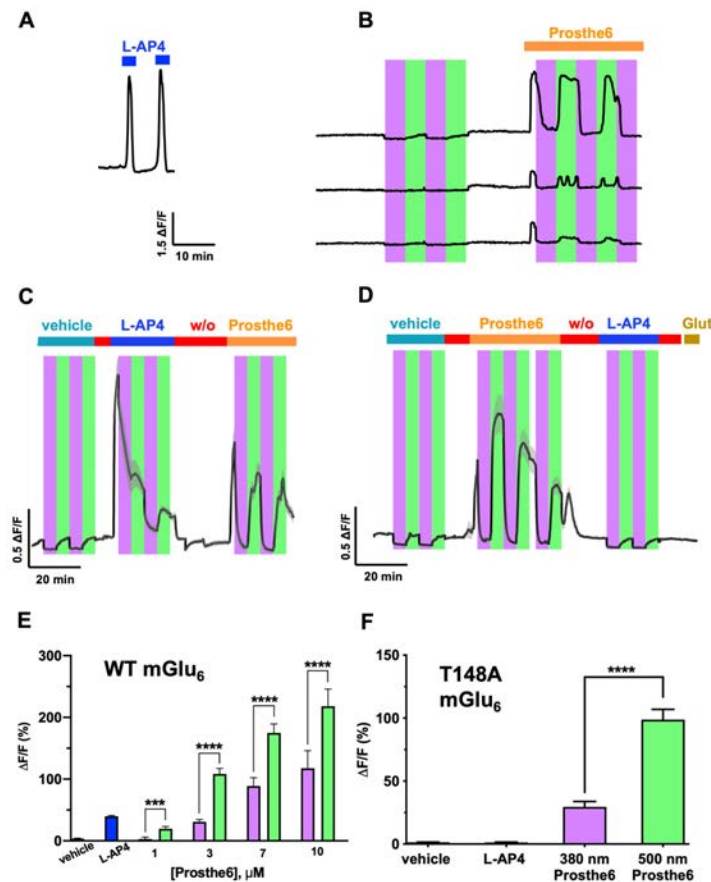


**Figure 11.2. Prosthe6 allows reversibly photoswitching mGlu<sub>6</sub> receptor activity without glutamate *in vitro*.** (A) Cellular responses mediated by mGlu<sub>6</sub> receptor can be recorded using calcium fluorescence imaging and co-expression of mouse mGlu<sub>6</sub> receptor, G $\alpha_{q\text{TOP}}$ , and GCaMP6s in HEK cells. In this assay, the perfusion of 1  $\mu\text{M}$  L-AP4 (a selective agonist of group III mGlu receptors) elicited reproducible calcium responses indicative of mGlu<sub>6</sub> receptor activation. (B) Example traces of calcium activity ( $\Delta\text{F}/\text{F}$ ) under alternating 380 nm and 500 nm illumination alone (control) and in the presence of 3  $\mu\text{M}$  **prosthe6** without adding glutamate. Responses are observed upon the application of *trans*-**prosthe6** in the dark and are terminated by photoconversion to *cis*-**prosthe6** under 380 nm light. Subsequent *cis*-to-*trans* isomerization under 500 nm light rapidly reactivated mGlu<sub>6</sub> receptors, leading to sustained or oscillatory calcium responses. (C) Time course of mGlu<sub>6</sub> receptor  $\Delta\text{F}/\text{F}$  responses (black trace indicates the average of  $n = 20$  cells and grey band corresponds to the standard error of the mean, SEM) in the presence of vehicle, 15  $\mu\text{M}$  L-AP4, and 3  $\mu\text{M}$  **prosthe6** under alternating 380 and 500 nm illumination. (D) Averaged time course ( $n = 21$  cells) of calcium responses of the mGlu<sub>6</sub> mutant T148A receptor, which is not activated by orthosteric ligands<sup>32</sup>. No responses were elicited by vehicle, 15  $\mu\text{M}$  L-AP4 or 10  $\mu\text{M}$  glutamate orthosteric agonists. Robust photoswitching of T148A mGlu<sub>6</sub> receptor responses by 3  $\mu\text{M}$  **prosthe6** demonstrated intrinsic agonist activity of the compound in addition to positive allosteric modulation (PAM). Thus, **prosthe6** is a photoswitchable ago-PAM. (E) Dose-response of 1  $\mu\text{M}$  ( $n = 11$  cells), 3  $\mu\text{M}$  ( $n = 166$  cells), 7  $\mu\text{M}$  ( $n = 118$  cells), and 10  $\mu\text{M}$  ( $n = 144$  cells) **prosthe6**. *Trans*-**prosthe6** produced significantly larger responses than

the *cis*-isomer at all the concentrations used. The data were normalized to the maximum response obtained with 15  $\mu\text{M}$  L-AP4. (F) Quantification of T148A mGlu<sub>6</sub> receptor photoresponses by 3  $\mu\text{M}$  **prosthe6** yielded significant differences between 380 nm and 500 nm illumination. Statistical analysis of panels E and F were performed by the paired sample Wilcoxon signed rank test, *p*-value (\*\*\*) < 0.001 and *p*-value (\*\*\*\*) < 0.0001 with GraphPad Prism 6. Error bars indicate  $\pm$  SEM.

Furthermore, we aimed to verify these results with different fluorescent indicators (chemical or genetically encoded) and *in vitro* expression conditions of the receptors. Therefore, we performed calcium imaging assay using three different fluorescent transducers of intracellular calcium concentrations (*i.e.*, GCaMP6s, R-GECO1, OGB-1AM) in WT mGlu<sub>6</sub> or T148A mGlu<sub>6</sub> receptor (Figure S11.5). The results confirmed that **prosthe6** is an ago-PAM of mGlu<sub>6</sub> receptors, which is independent of the *in vitro* expression conditions of the receptor, oscillatory or steady responses, and calcium imaging conditions. Photoresponses were absent in cells not expressing mGlu<sub>6</sub> receptor (Figure S11.6). Thus, **prosthe6** meets the photopharmacological requirements (*trans*-on ago-PAM) to emulate the physiological action of light on mGlu<sub>6</sub> receptors mediated by PhRs. Overall, in the absence of illumination (or under visible light) the *trans*-isomer activates the receptors even without glutamate, and under violet light, the *cis*-isomer potentiates them less, akin to illumination in physiological conditions (Figure 11.1C).

### 11.2.2 *In vivo* optokinetic assay in zebrafish larvae and behavioral assay in mice with prosthe 6

The *in vitro* profile of the **prosthe6** compound matched the molecular requirements to restore vision *via* mGlu<sub>6</sub> in OBCs, as described in Figure S11.1. Hence, we were encouraged to carry out *in vivo* assays in zebrafish larvae (*Danio rerio*). Zebrafish is a well-established animal model especially for neurobehavioural studies<sup>33</sup> and the transparency of their larvae makes them convenient for photopharmacological applications<sup>34-37</sup>. To determine visual-dependent behaviors, we first set up an acute model of blindness and then we validated the model using an optokinetic response (OKR) assay. To overcome the lack of 380 nm light emission from commercial display screens, an OKR device was custom-built to create a visual stimulus, consisting of a stripe pattern using 500 nm and 380 nm light-emitting diodes (LEDs), located at 90° and 0° respectively (Figure 11.3A). The conic carousel is internally mirrored and presents open vertical windows. The different wavelengths of light pass through these windows and converge to the center of the carousel (where larvae are immobilised into 7% of methylcellulose), forming a moving striped pattern. The larvae respond to the stimulus by

moving their eyes in the direction of the rotating stripes until it reaches the limit of the vision field. This results in an eye saccade (quick movement) in the opposed direction for positional resetting of the eye (**Figure 11.3A**). The tracking of the saccades allows to measure the visual acuity of the animals, which constitutes a potential benefit of upstream-targeted photoswitches. The OKR setup allowed to determine the experimental time window, to optimize the blinding protocol and the time course of recovery. The results showed that visual acuity is strongly reduced after 15 hours (h) of blindness photoinduction but is recovered during the following 9 h. Therefore, all vision restoration experiments were performed after 15 h from the treatment. Larvae saccades were recorded with a camera through a binocular lens and quantified in response to rotating bands of 380 and 500 nm, which were projected to the center of the dish. As represented in **Figure 11.3B**, the blinded larvae do not display saccadic responses to the rotating light pattern, and they recover this reflex few seconds after adding 3  $\mu$ M **prosthe6**. Quantification of the OKR assay results (expressed in saccades/min) demonstrated a full recovery of visual acuity with **prosthe6** at 3  $\mu$ M (**Figure 11.3C**). The OKR assay thus provides a proof of concept of vision restoration based on photoswitchable allosteric modulators of mGlu<sub>6</sub> receptors. Moreover, this technique is convenient for early screening of photoswitchable candidates for vision restoration.

Furthermore, **prosthe6** was tested to restore visually guided behavior in blind mice. Initial experiments with *rd10* mice were difficult to reproduce, due to dispersion in the time course of degeneration and partial blindness of these mice at early life stages. This model might mask potential photoresponses of the compound. Thus, we turned to *Opn4<sup>-/-</sup>* mice that lack photosensitive melanopsinic cells, although having functional retinas<sup>38</sup> and we chemically induced PhR damage (*i.e.*, intraperitoneal injection of sodium iodate, 40 mg/kg). Iodate causes PhR cell damage and leaves mice unresponsive to illumination<sup>39</sup>. Evaluation of vision loss and restoration by injection of 30  $\mu$ M **prosthe6** were carried out at least 3 weeks after a single iodate injection. To assess the visual performance of the mice, their light avoidance behavior (innate preference for darkness) was quantified using a transition test (**Figure 11.3DE**). In this test, two boxes are connected by a door and illuminated with light of controlled intensity and wavelength (**Figure 11.3D**); in one box we applied 500 nm light (which favors isomerization of **prosthe6** to the *trans* active form, green box) and in the other box we used 380 nm light (which favors isomerization of **prosthe6** to the *cis* inactive form, purple box). The compound was administered through unilateral and intravitreal injection and in a single dose without supplementation. The time spent in each box (**Figure 11.3E**) was measured and indicated as



the percentage of the total time of the experiment in each condition: (a) evaluation of vision loss (“post damage control”) and (b) light-avoidance test after 2 h (c) light-avoidance test after 48 h from the injection of **prosthe6**.

After damage, animals displayed slight preference for the dimmer 380 nm room, or no preference. 3 animals out of 6 spent significantly less time in the 380 nm room than in the 500 nm room upon **prosthe6** injection. This reversal of preference indicates that the 380 nm room was perceived as “illuminated” and the 500 nm as “dark” after drug injection, in agreement with the molecular design of **Figure S11.1** and the *in vitro* results of **Figure 11.2**. This behavior was observed 2 h after **prosthe6** injection and was consistently maintained after 48 h. Topical bilateral application of 30  $\mu$ M **prosthe6** in separate experiments did not significantly change the visually guided behavior. There were no signs of pain or distress observed in the animals, using either administration routes.

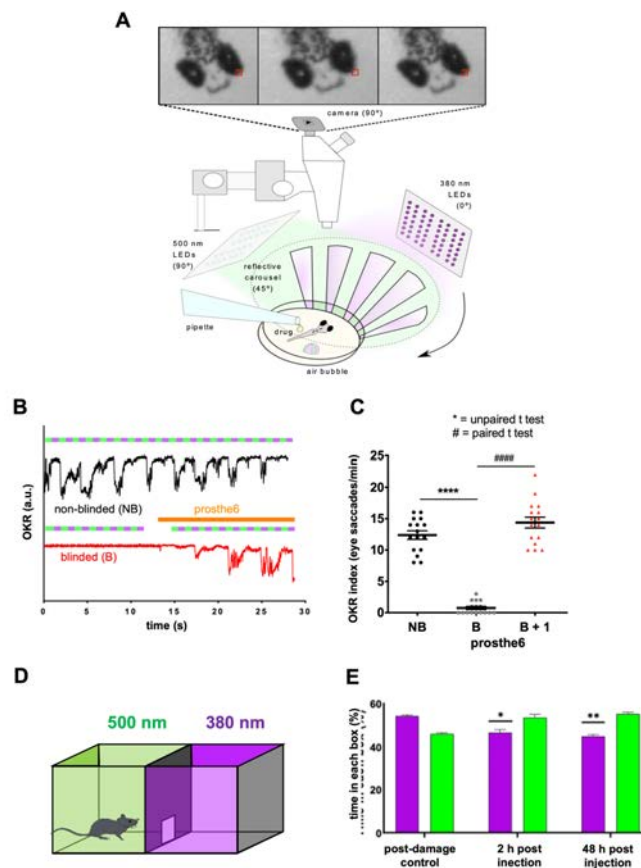


**Figure 11.3. Prosthe6 restores visual acuity in blind zebrafish larvae and light-driven behavior in blind mice.** (A) Larvae were acutely blinded with bright light as reported<sup>9</sup> and immobilized in a petri dish with 8% methylcellulose medium. Their visual acuity was evaluated individually using an optokinetic reflex (OKR) assay to measure eye movements (saccades) before (non-blinded, NB), after the blinding procedure (blinded, B), and upon adding 3  $\mu$ M **prosthe6** to the medium. To project the light pattern on the larvae, a 45° truncated conic carousel made of reflective plastic was used to reflect 500 nm light from a LED lamp located above (90°) and to pass 380

nm light from another LED lamp located horizontally ( $0^\circ$ ) through windows perforated vertically in the carousel. An air bubble deposited on the petri dish near each larva at the center of the carousel was utilized to reflect the vertical 380/500 nm light pattern and to monitor its rotation at 15.5 revolutions per minute (rpm). **(B)** Larvae saccades were recorded with a camera through a binocular lens and quantified in response to rotating bands of 380 and 500 nm projected to the center of the dish. Dark and red plots represent eye movements *vs.* the time course of the intensity in the red box indicated in (A) for NB and B zebrafish larvae, respectively. Blinded larvae did not display saccadic responses to the rotating light pattern but recover this reflex few seconds after adding 3  $\mu\text{M}$  **prosthe6** (orange stripe) on top of the larva in the petri dish. **(C)** Quantification and statistical analysis of the OKR assay (saccades/min,  $n = 16$  animals per group) showed that 3  $\mu\text{M}$  **prosthe6** afforded full recovery of visual acuity. Statistical differences between B *vs.* NB were determined by the unpaired t-test,  $p$ -value (\*\*\*\*)  $< 0.0001$ , and between NB *vs.* B treated with **prosthe6** by the paired test,  $p$ -value (####)  $< 0.0001$ . Data are presented as mean  $\pm$  SEM. **(D)** Representation of the light-avoidance box, where each compartment is illuminated with a different light source: in one box we applied 500 nm light (to favor the *trans* active form, green box) and in the other box we used 380 nm light (to favor the *cis* inactive form, purple box). **(E)** Behavioral assay in *Opn4<sup>-/-</sup>* mice 3 weeks after the treatment with sodium iodate. The time spent in each box was measured and indicated as the mean of percentage of the total time of the experiment (3 min, 3 replicates per animal) in each condition: (a) evaluation of vision loss (“post damage control”) and (b) light-avoidance test after 2 h (c) light-avoidance test after 48 h from the injection of **prosthe6**. No preference or slight preference for the dimmer 380 nm room was displayed after the damage. After the unilateral intravitreal injection of **prosthe6** (30  $\mu\text{M}$ ), 3 out of 6 animals spent significantly less time in the 380 nm room perceived as illuminated than in the 500 nm room perceived as dark. This behavior was observed 2 h and 48 h after **prosthe6** injection. Statistical differences were determined by the paired t-test,  $p$ -value (\*\*)  $< 0.01$ ,  $p$ -value (\*)  $< 0.05$ . Experiments in blinded zebrafish were carried out by Pablo Calvé, Alexandre Gomila-Juaneda, and Xavier Rovira at IBEC. Experiments in mice were carried out by Santiago Milla and Victor Paleo-García at UAH.

### 11.2.3 Fluorescence-based plate reader assay

Despite the breakthrough proof of concept of **prosthe6** to restore visual acuity and visually guided behavior with upstream targeted photopharmacology, it has certain shortcomings for practical use (*e.g.*, micromolar activity, slow thermal relaxation, the need of UV light for photoswitching, and cross activity with mGlu<sub>4</sub> receptor, as reported). To circumvent these limitations, we designed fast-relaxing and blue light-switched compounds that were synthesized by Aleix González-Díaz in collaboration with the laboratory of Dr. Amadeu Llebaria at IQAC (**Figure S11.7**). This library of fifteen derivatives represents a complete photopharmacological toolset with diverse properties. We set up a protocol to perform a high-throughput screening of the 15 photoswitchable allosteric ligands using a microplate reader (**Figure S11.8**) in HEK cells overexpressing mouse WT or mouse mutant T148A mGlu<sub>6</sub>. The results showed that all the 15 compounds possess intrinsic agonistic activity (ago-PAM) and display higher efficacy and potency than **prosthe6**. Among them, the 7 best performing compounds were selected for

efficacy tests in HEK cells overexpressing human WT mGlu<sub>6</sub> receptor (**Figure S11.8**), which validated the previous results. To further characterize these 7 compounds, dose response curves were generated from experiments in HEK cells overexpressing human WT (**Figure S11.9**), mouse WT (**Figure S11.10**) or mutant T148A mouse (**Figure S11.11**) mGlu<sub>6</sub> receptor. These compounds displayed nanomolar potency (**Figure S11.12**) and were able to photoswitch mGlu<sub>6</sub> activity (**Figures S11.10**, blue plots and **S11.13**). Overall, the *in vitro* characterization was key to select the 2 best-performing compounds (*i.e.*, **1492** and **1495**) in terms of efficacy, potency, and functional switching for *in vivo* applications. The chemical structures and the dose response curves in mouse mutant T148A mGlu<sub>6</sub> receptors are shown in **Figure 11.4**.

These optimized compounds fully meet the photopharmacological requirements needed for the vision restoration purposes (**Figure 11.1**), including *trans*-ago-PAM activity in the dark, deactivation with visible light ( $\geq 460$  nm including white light), nanomolar potency, and a very fast thermal relaxation, allowing to operate with one wavelength.

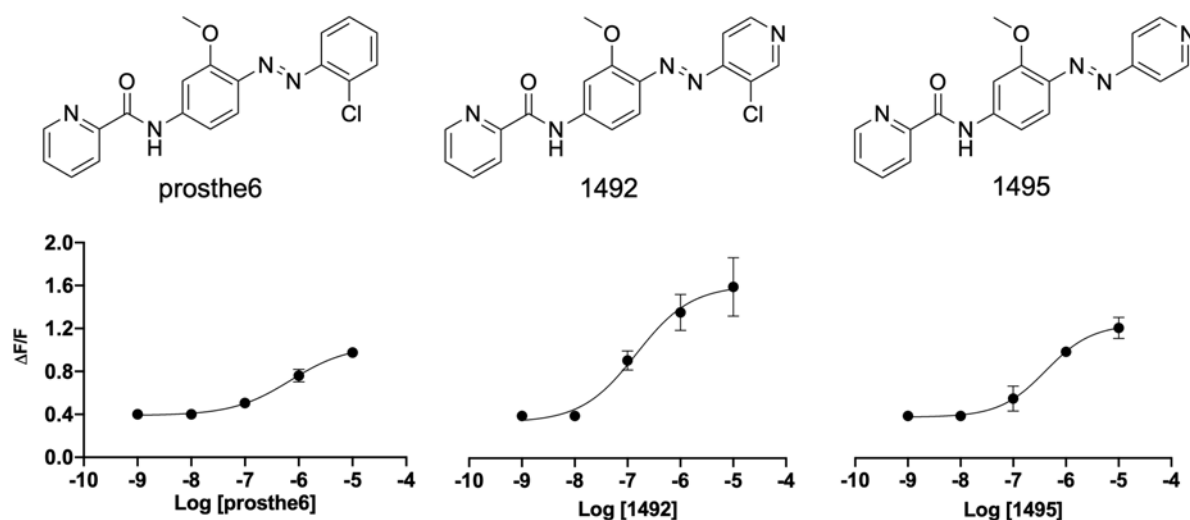


**Figure 11.4.** Chemical structures and dose-response curves of photoswitchable ligands prosth6 (left), 1493 (middle) and 1495 (right). These compounds were synthesized by Aleix González-Díaz at IQAC.

#### 11.2.4 *In vivo* optokinetic assay in zebrafish larvae and behavioral assay in mice with 1492 and 1495

The outstanding results *in vitro* prompted further evaluation of the promising compounds **1492** and **1495** through *in vivo* behavioral assays. As previously described for **prosth6**, the aim was to go beyond photosensitivity and obtain a measure of visual acuity. To achieve this purpose, we used the OKR setup described above with one modification. Since **prosth6** is a slow relaxing compound, two different wavelengths are needed and stripes of two different colors

must be projected. Compounds **1492** and **1495** are both fast relaxing and only require one wavelength to isomerize (in our case white light). Strikingly, both compounds significantly restored visual acuity in blinded larvae, with compound **1492** inducing greater recovery (*i.e.*, higher number of saccades/min; **Figure 11.5A**) and at lower concentration than **1495** (**Figure 11.5B**). These results agree with the *in vitro* characterization.

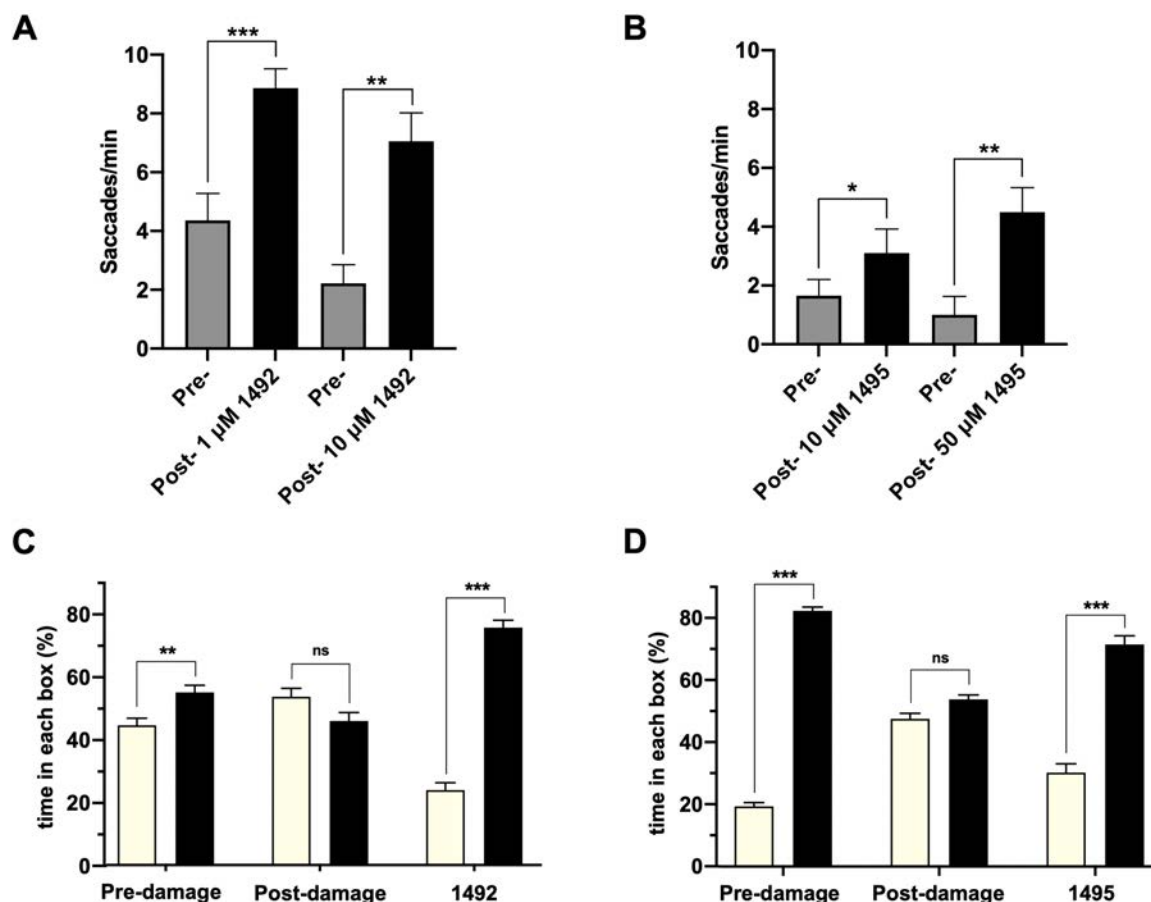


**Figure 11.5. 1492 and 1495 restore visual acuity in blind zebrafish larvae and light-driven behavior in blind mice.** (A) Quantification and statistical analysis of the OKR assay in blind zebrafish larvae (saccades/min) show that compound **1492** allows significant recovery of visual acuity at all the concentrations used (1  $\mu$ M,  $n = 13$ ; 10  $\mu$ M,  $n = 8$ ). Data are presented as mean  $\pm$  SEM. (B) Quantification and statistical analysis show that **1495** enables significant recovery of visual acuity at all concentrations used (10  $\mu$ M,  $n = 10$ ; 50  $\mu$ M,  $n = 8$ ). Data are presented as mean  $\pm$  SEM. (C) Behavioral assays in *Opn4<sup>-/-</sup>* mice, blinded by chemical damage to the PhRs. The topical administration of 30  $\mu$ M **1492** restores the light-avoidance behavior in 6 out of 6 blind mice, which display a preference for the dark room as previous to the retinal damage. (D) Topical application of 30  $\mu$ M **1495** recovers the dark room preference in blind mice (6 out of 9). Statistical differences in all the panels are determined by the paired t-test,  $p$ -value (\*\*\*)  $< 0.001$ ,  $p$ -value (\*\*)  $< 0.01$  and  $p$ -value (\*)  $< 0.05$ . Data are presented as mean  $\pm$  SEM. Experiments in blinded zebrafish were carried out by Joaquín Martínez-Tambella, Rosalba Sortino and Alexandre Gomila-Juaneda at IBEC. Experiments in mice were carried out by Santiago Milla and Victor Paleo-García at UAH.

We next investigated whether light-avoidance behavior could be restored in *Opn4*<sup>-/-</sup> mice, blinded by chemical damage to the PhRs, as shown above. Behavioral assays were carried (a) before photoreceptor damage, (b) after photoreceptor damage, and (c) after topical drug application. Cool white LEDs (emission centered at 460 nm) were used to favor *trans*-to-*cis* isomerization of both compounds. The results demonstrated that both **1492 (Figure 11.5C)** and **1495 (Figure 11.5D)** robustly restored preference for the dark room (*trans* active isomer) 2 h after topical application, without showing signs of pain or distress.

### 11.3 Discussion

A decade ago, the restoration of visual function seemed a difficult goal to accomplish, if not unachievable. Progresses on various fronts (*e.g.*, retinal implants, stem cell transplantation, optogenetic tools) have been made and some of these technologies have produced promising clinical results and good reasons for optimism. However, each of these strategies presents several drawbacks. Prosthetic electronic implants require invasive surgery and have been discontinued, due to reduced visual resolution provided<sup>40</sup>. Stem cells-derived photoreceptors require highly invasive and irreversible intervention and are prone to neoplastic changes<sup>41</sup>.

Optogenetic approaches introduce microbial opsins (*e.g.*, ChR and its variants, such as Halorhodopsin) with viral vectors to turn light-responsive the neurons that are spared in degenerative retinal diseases (*e.g.*, OBCs or RGCs)<sup>8,10,42-47</sup>. Three clinical trials are currently underway to test them (<https://clinicaltrials.gov>; Identifier: NCT03326336, NCT02556736 and NCT04278131). One of these pioneer studies (*i.e.*, NCT03326336) tests the administration of the adeno-associated viral vector encoding a red shifted variant of ChR (*i.e.*, ChrimsonR)<sup>48</sup>. Notably, following this treatment, partial functional recovery was observed in a blind patient. However, microbial opsins are not as sensitive to light as mammalian opsins and the patient who participates the trial must use goggles that deliver a high-intensity image to the retina<sup>16</sup>. This also implies the risk of damaging the remaining PhRs in RP patients. Moreover, microbial opsins are prone to cause immune responses to foreign proteins. Optogenetic strategies that use opsins of mammalian origin and higher photosensitivity (*e.g.*, melanopsin) have also been developed<sup>12,49-51</sup>. They are 1000-fold more light sensitive than ChR, due to G protein amplification signal and, as native proteins, minimize the potential for immunogenic adverse effects. Nonetheless, they show slow kinetics in terms of (de)activation which is only sufficient for basic perception, but do not support vision during motion. Therefore, it performs poorly for high-resolution vision associated to human disorders<sup>52</sup>. The development of melanopsin-mGlu<sub>6</sub>

chimeras (*i.e.*, Opto-mGlu<sub>6</sub>) overcame this shortfall by optimizing the activation of the native mGlu<sub>6</sub> pathway G $\alpha_6$ -mediated<sup>14,53</sup>. The Opto-mGlu<sub>6</sub> consists of the light sensing domain of melanopsin and the intracellular domain of mGlu<sub>6</sub> receptor. Ectopic expression of this engineered construct in the OBCs of blind mice recovered their visual acuity. Importantly, all the OBC-targeted optogenetic approaches (*e.g.*, Opto-mGlu<sub>6</sub>) were doable thanks to the development of modified adeno-associated virus (AAV) capsids and OBC-specific promoters<sup>14,54,55</sup>. Other melanopsin-mGlu<sub>6</sub> chimeras (*e.g.*, Mela(CTmGlu<sub>6</sub>) or Mela(CT+IL3mGlu<sub>6</sub>), where the C-terminal domain alone or together with the intracellular loop 3 are replaced with the ones of mGlu<sub>6</sub> receptor, have recently been developed, showing promising results for Mela(CTmGlu<sub>6</sub>). However, the engineered opsins approach inevitably requires transgenic animals to restore visual functions or behavior, and it would be a more feasible therapeutic option for humans to pursue also non-transgenic routes. Thus, despite the immense potential of optogenetics approaches for sight restoration, they raise moral, regulatory, safety, and tolerability issues. In fact, the long-term impact of this irreversible treatment is unknown and, if needed, attempts to revert the treatment may lead to severe harm.

A tethered photoswitch based strategy (*i.e.*, SNAG-mGlu<sub>2</sub>) provides high specificity and has shown to enhance visual acuity in an animal model of retinal degeneration, but it also involves an irreversible manipulation<sup>56</sup>. Akin to optogenetic approaches, this strategy would be very difficult, if not impossible, to reverse in case that complications arise.

Alternatively, PCLs are reversible and represent a one-component system which is simpler, and potentially less immunogenic than two-component systems used by optogenetic strategies<sup>57,58</sup>. These compounds have the same advantages as small molecules drugs, including the ease of application and the fast distribution into tissues. Once photoswitches have proven to be clinically successful, they will be highly affordable and more widely applicable than any other alternative. In 2022, one of these compounds (BENAQ)<sup>21</sup> has entered a clinical trial in humans for the first time (*i.e.*, NCT05282953). This compound and other reported PCLs have shown efficacy for vision restoration in animal models of outer retinal degeneration, but target proteins that are widely expressed throughout the central nervous system (*e.g.*, kainate and AMPA receptors, potassium channels)<sup>20,59-62</sup>. Therefore, these PCLs might display a poor safety profile and cause undesired effects. Nevertheless, the excitement in the field of photopharmacology for these advancements is sure to spark new and improved developments.

In this work we report novel photoswitchable allosteric modulators that target mGlu<sub>6</sub> receptors which are exclusively expressed in OBCs and are postsynaptic to PhRs in physiological

conditions. Therefore, the drugs that photocontrol mGlu<sub>6</sub> receptors can be envisaged as “synthetic photoreceptors” or “molecular prostheses”, allowing to retain the physiological signal flow in the circuit when PhRs are degenerated. Moreover, these compounds bind to sites that are less preserved across receptor subtype families (*i.e.*, allosteric sites) which can confer them advantages compared to orthosteric ligands, including subtype-selectivity<sup>63</sup>.

The goal of sight restoration strategies is to recover high-level of vision and not only basic perception. Hitherto, no reported PCL has provided visual acuity. Here, we demonstrated for the first time that these compounds enhanced visual acuity (*i.e.*, the ability to track moving lines) in zebrafish larvae, demonstrating a proof of concept of vision restoration based on photoswitchable allosteric modulators of mGlu<sub>6</sub> receptors. This was probably possible with a target and compounds that make the strategy of upstream-targeted photopharmacology a reality<sup>2,57</sup>. In fact, image processing, including encoding of orientation, motion, and contrast occurs at the top of the retinal circuitry (*i.e.*, upstream to RGCs)<sup>2,4</sup>. The OBCs are the first interneurons of the retina that receive direct input from PhRs. In retinal degenerative disease (where PhRs are degenerated) OBCs become the first surviving cells at the top of the retinal hierarchy. Therefore, conferring light sensitivity to the OBC can generate a more complex and native-like output signal which maintains the inner retinal processing and, thus, preserve the RGC-receptive fields<sup>2,22</sup>. This enables to restore higher quality vision compared to the PCLs that target the RGCs.

## 11.4 Conclusions

In summary, we have shown the development of a library of ago-PAMs that achieve nanomolar potency and photocontrol of mGlu<sub>6</sub> receptors which are exclusively expressed at OBCs. This offers a unique specific response, while providing an upstream-signaling control of the retinal circuit by using photopharmacology. Importantly, we have initially identified two compounds (*i.e.*, **1492** and **1495**) that are fast relaxing, blue light switching, and allow *in vivo* restoration of visual acuity for the first time. Moreover, they restore light-avoidance behavior in blind mice by topical administration. These properties make **1492** and **1495** excellent candidates for further preclinical studies and a potential drug-based therapy for vision restoration in humans. Upon suitable formulation to cross the human cornea and to make their effects long-lasting, we envision that these compounds could give rise to an unprecedented therapy that is highly efficacious, noninvasive, safe, user-friendly and topically self-administered.

## References

- 1 Santos, A. *et al.* Preservation of the inner retina in retinitis pigmentosa. A morphometric analysis. *Arch Ophthalmol* **115**, 511-515, doi:10.1001/archophth.1997.01100150513011 (1997).
- 2 Marc, R., Pfeiffer, R. & Jones, B. Retinal prosthetics, optogenetics, and chemical photoswitches. *ACS Chem Neurosci* **5**, 895-901, doi:10.1021/cn5001233 (2014).
- 3 Marc, R. E. *et al.* Extreme retinal remodeling triggered by light damage: Implications for age related macular degeneration. *Mol Vis* **14**, 782-806 (2008).
- 4 Van Gelder, R. N. *et al.* Regenerative and restorative medicine for eye disease. *Nat Med* **28**, 1149-1156, doi:10.1038/s41591-022-01862-8 (2022).
- 5 Ayton, L. N. *et al.* An update on retinal prostheses. *Clin Neurophysiol* **131**, 1383-1398, doi:10.1016/j.clinph.2019.11.029 (2020).
- 6 Jayakody, S. A., Gonzalez-Cordero, A., Ali, R. R. & Pearson, R. A. Cellular strategies for retinal repair by photoreceptor replacement. *Prog Retin Eye Res* **46**, 31-66, doi:10.1016/j.preteyeres.2015.01.003 (2015).
- 7 Lamba, D. A., Gust, J. & Reh, T. A. Transplantation of human embryonic stem cell-derived photoreceptors restores some visual function in Crx-deficient mice. *Cell Stem Cell* **4**, 73-79, doi:10.1016/j.stem.2008.10.015 (2009).
- 8 Busskamp, V. *et al.* Genetic reactivation of cone photoreceptors restores visual responses in retinitis pigmentosa. *Science* **329**, 413-417, doi:10.1126/science.1190897 (2010).
- 9 Thyagarajan, S. *et al.* Visual function in mice with photoreceptor degeneration and transgenic expression of channelrhodopsin-2 in ganglion cells. *J Neurosci* **30**, 8745-8758, doi:10.1523/jneurosci.4417-09.2010 (2010).
- 10 Lagali, P. S. *et al.* Light-activated channels targeted to ON bipolar cells restore visual function in retinal degeneration. *Nat Neurosci* **11**, 667-675, doi:10.1038/nn.2117 (2008).
- 11 Caporale, N. *et al.* LiGluR restores visual responses in rodent models of inherited blindness. *Mol Ther* **19**, 1212-1219, doi:10.1038/mt.2011.103 (2011).
- 12 Cehajic-Kapetanovic, J. *et al.* Restoration of vision with ectopic expression of human rod opsin. *Curr Biol* **25**, 2111-2122, doi:10.1016/j.cub.2015.07.029 (2015).
- 13 Berry, M. H. *et al.* Restoration of high-sensitivity and adapting vision with a cone opsin. *Nat Commun* **10**, 1221, doi:10.1038/s41467-019-09124-x (2019).
- 14 van Wyk, M., Pielecka-Fortuna, J., Lowel, S. & Kleinlogel, S. Restoring the ON switch in blind retinas: Opto-mGlu<sub>6</sub>, a next-generation, cell-tailored optogenetic tool. *PLoS Biol* **13**, e1002143, doi:10.1371/journal.pbio.1002143 (2015).
- 15 Chaudhry, G. R. *et al.* Fate of embryonic stem cell derivatives implanted into the vitreous of a slow retinal degenerative mouse model. *Stem cells and development* **18** **2**, 247-258 (2009).
- 16 Harris, A. R. & Gilbert, F. Restoring vision using optogenetics without being blind to the risks. *Graefes Arch Clin Exp Ophthalmol* **260**, 41-45, doi:10.1007/s00417-021-05477-6 (2022).
- 17 Polosukhina, A. *et al.* Photochemical restoration of visual responses in blind mice. *Neuron* **75**, 271-282, doi:10.1016/j.neuron.2012.05.022 (2012).
- 18 Tochitsky, I. *et al.* Restoring visual function to blind mice with a photoswitch that exploits electrophysiological remodeling of retinal ganglion cells. *Neuron* **81**, 800-813, doi:10.1016/j.neuron.2014.01.003 (2014).
- 19 Klapper, Simon D. & Busskamp, V. Vision restoration becomes druggable. *Neuron* **92**, 3-5, doi:https://doi.org/10.1016/j.neuron.2016.09.030 (2016).



- 20 Tochitsky, I., Kienzler, M. A., Isacoff, E. & Kramer, R. H. Restoring vision to the blind with chemical photoswitches. *Chem Rev* **118**, 10748-10773, doi:10.1021/acs.chemrev.7b00723 (2018).
- 21 Tochitsky, I., Trautman, J., Gallerani, N., Malis, J. G. & Kramer, R. H. Restoring visual function to the blind retina with a potent, safe and long-lasting photoswitch. *Sci Rep* **7**, 45487, doi:10.1038/srep45487 (2017).
- 22 Kralik, J., van Wyk, M., Stocker, N. & Kleinlogel, S. Bipolar cell targeted optogenetic gene therapy restores parallel retinal signaling and high-level vision in the degenerated retina. *Communications Biology* **5**, 1116, doi:10.1038/s42003-022-04016-1 (2022).
- 23 Vardi, N., Duvoisin, R., Wu, G. & Sterling, P. Localization of mGlu<sub>6</sub> to dendrites of ON bipolar cells in primate retina. *J Comp Neurol* **423**, 402-412, doi:10.1002/1096-9861(20000731)423:3<402::aid-cne4>3.0.co;2-e (2000).
- 24 Morgans, C. W., Brown, R. L. & Duvoisin, R. M. TRPM1: The endpoint of the mGlu<sub>6</sub> signal transduction cascade in retinal ON bipolar cells. *Bioessays* **32**, 609-614, doi:10.1002/bies.200900198 (2010).
- 25 Morgans, C. W. *et al.* TRPM1 is required for the depolarizing light response in retinal ON bipolar cells. *Proc Natl Acad Sci U S A* **106**, 19174-19178, doi:10.1073/pnas.0908711106 (2009).
- 26 Shen, Y., Rampino, M. A., Carroll, R. C. & Nawy, S. G protein-mediated inhibition of the Trp channel TRPM1 requires the G $\beta\gamma$  dimer. *Proc Natl Acad Sci U S A* **109**, 8752-8757, doi:10.1073/pnas.1117433109 (2012).
- 27 Xu, Y. *et al.* The TRPM1 channel in ON bipolar cells is gated by both the  $\alpha$  and the  $\beta\gamma$  subunits of the G protein Ga $\alpha$ . *Scientific Reports* **6**, 20940, doi:10.1038/srep20940 (2016).
- 28 Koike, C., Numata, T., Ueda, H., Mori, Y. & Furukawa, T. TRPM1: A vertebrate TRP channel responsible for retinal ON bipolar function. *Cell Calcium* **48**, 95-101, doi:10.1016/j.ceca.2010.08.004 (2010).
- 29 Conn, P. J., Christopoulos, A. & Lindsley, C. W. Allosteric modulators of GPCRs: A novel approach for the treatment of CNS disorders. *Nat Rev Drug Discov* **8**, 41-54, doi:10.1038/nrd2760 (2009).
- 30 Zussy, C. *et al.* Dynamic modulation of inflammatory pain-related affective and sensory symptoms by optical control of amygdala metabotropic glutamate receptor 4. *Mol Psychiatry* **23**, 509-520, doi:10.1038/mp.2016.223 (2018).
- 31 Pittolo, S. *et al.* An allosteric modulator to control endogenous G protein-coupled receptors with light. *Nat Chem Biol* **10**, 813-815, doi:10.1038/nchembio.1612 (2014).
- 32 Rovira, X. *et al.* Overlapping binding sites drive allosteric agonism and positive cooperativity in type 4 metabotropic glutamate receptors. *FASEB J* **29**, 116-130, doi:10.1096/fj.14-257287 (2015).
- 33 Kokel, D. *et al.* Rapid behavior-based identification of neuroactive small molecules in the zebrafish. *Nat Chem Biol* **6**, 231-237, doi:10.1038/nchembio.307 (2010).
- 34 Prischich, D. *et al.* Adrenergic modulation with photochromic ligands. *Angew Chem Int Ed Engl* **60**, 3625-3631, doi:10.1002/anie.202010553 (2021).
- 35 Matera, C. *et al.* Photoswitchable antimetabolite for targeted photoactivated chemotherapy. *J Am Chem Soc* **140**, 15764-15773, doi:10.1021/jacs.8b08249 (2018).
- 36 Matera, C. *et al.* Reversible photocontrol of dopaminergic transmission in wild-type animals. *Int J Mol Sci* **23**, doi:10.3390/ijms231710114 (2022).
- 37 Rustler, K. *et al.* Optical control of GABA<sub>A</sub> receptors with a fulgimide-based potentiator. *Chemistry* **26**, 12722-12727, doi:10.1002/chem.202000710 (2020).

- 38 Milla-Navarro, S., Pazo-Gonzalez, M., Germain, F. & de la Villa, P. Phenotype characterization of a mice genetic model of absolute blindness. *Int J Mol Sci* **23**, doi:10.3390/ijms23158152 (2022).
- 39 Kiuchi, K., Yoshizawa, K., Shikata, N., Moriguchi, K. & Tsubura, A. Morphologic characteristics of retinal degeneration induced by sodium iodate in mice. *Curr Eye Res* **25**, 373-379, doi:10.1076/ceyr.25.6.373.14227 (2002).
- 40 Kleinlogel, S., Vogl, C., Jeschke, M., Neef, J. & Moser, T. Emerging approaches for restoration of hearing and vision. *Physiol Rev* **100**, 1467-1525, doi:10.1152/physrev.00035.2019 (2020).
- 41 Wood, E. H. *et al.* Stem cell therapies, gene-based therapies, optogenetics and retinal prosthetics: Current state and implications for the future. *Retina* **39**, 820-835, doi:10.1097/IAE.0000000000002449 (2019).
- 42 Sengupta, A. *et al.* Red-shifted channelrhodopsin stimulation restores light responses in blind mice, macaque retina and human retina. *EMBO Mol Med* **8**, 1248-1264, doi:10.15252/emmm.201505699 (2016).
- 43 Sato, M. *et al.* Visual responses of photoreceptor-degenerated rats expressing two different types of channelrhodopsin genes. *Scientific Reports* **7**, 41210, doi:10.1038/srep41210 (2017).
- 44 Bi, A. *et al.* Ectopic expression of a microbial-type rhodopsin restores visual responses in mice with photoreceptor degeneration. *Neuron* **50**, 23-33, doi:10.1016/j.neuron.2006.02.026 (2006).
- 45 Kleinlogel, S. *et al.* Ultra light-sensitive and fast neuronal activation with the Ca<sup>2+</sup>-permeable channelrhodopsin CatCh. *Nat Neurosci* **14**, 513-518, doi:10.1038/nn.2776 (2011).
- 46 Lin, J. Y., Knutsen, P. M., Muller, A., Kleinfeld, D. & Tsien, R. Y. ReaChR: A red-shifted variant of channelrhodopsin enables deep transcranial optogenetic excitation. *Nature Neuroscience* **16**, 1499-1508, doi:10.1038/nn.3502 (2013).
- 47 Klapoetke, N. C. *et al.* Independent optical excitation of distinct neural populations. *Nature Methods* **11**, 338-346, doi:10.1038/nmeth.2836 (2014).
- 48 Sahel, J. A. *et al.* Partial recovery of visual function in a blind patient after optogenetic therapy. *Nat Med* **27**, 1223-1229, doi:10.1038/s41591-021-01351-4 (2021).
- 49 Lin, B., Koizumi, A., Tanaka, N., Panda, S. & Masland, R. H. Restoration of visual function in retinal degeneration mice by ectopic expression of melanopsin. *Proceedings of the National Academy of Sciences* **105**, 16009-16014, doi:doi:10.1073/pnas.0806114105 (2008).
- 50 Gaub, B. M., Berry, M. H., Holt, A. E., Isacoff, E. Y. & Flannery, J. G. Optogenetic vision restoration using rhodopsin for enhanced sensitivity. *Mol Ther* **23**, 1562-1571, doi:10.1038/mt.2015.121 (2015).
- 51 De Silva, S. R. *et al.* Long-term restoration of visual function in end-stage retinal degeneration using subretinal human melanopsin gene therapy. *Proc Natl Acad Sci U S A* **114**, 11211-11216, doi:10.1073/pnas.1701589114 (2017).
- 52 Baker, C. K. & Flannery, J. G. Innovative optogenetic strategies for vision restoration. *Front Cell Neurosci* **12**, 316, doi:10.3389/fncel.2018.00316 (2018).
- 53 Dhingra, A., Faurobert, E., Dascal, N., Sterling, P. & Vardi, N. A retinal-specific regulator of G protein signaling interacts with G $\alpha_o$  and accelerates an expressed metabotropic glutamate receptor 6 cascade. *J Neurosci* **24**, 5684-5693, doi:10.1523/jneurosci.0492-04.2004 (2004).
- 54 Hulliger, E. C., Hostettler, S. M. & Kleinlogel, S. Empowering retinal gene therapy with a specific promoter for human rod and cone ON bipolar cells. *Mol Ther Methods Clin Dev* **17**, 505-519, doi:10.1016/j.omtm.2020.03.003 (2020).

- 55 Cronin, T. *et al.* Efficient transduction and optogenetic stimulation of retinal bipolar cells by a synthetic adeno-associated virus capsid and promoter. *EMBO Mol Med* **6**, 1175-1190, doi:10.15252/emmm.201404077 (2014).
- 56 Berry, M. H. *et al.* Restoration of patterned vision with an engineered photoactivatable G protein-coupled receptor. *Nat Commun* **8**, 1862, doi:10.1038/s41467-017-01990-7 (2017).
- 57 Van Gelder, R. N. Photochemical approaches to vision restoration. *Vision Res* **111**, 134-141, doi:10.1016/j.visres.2015.02.001 (2015).
- 58 Berry, M. H. *et al.* Photopharmacology for vision restoration. *Current Opinion in Pharmacology* **65**, 102259, doi:https://doi.org/10.1016/j.coph.2022.102259 (2022).
- 59 Tochitsky, I. & Kramer, R. H. Optopharmacological tools for restoring visual function in degenerative retinal diseases. *Curr Opin Neurobiol* **34**, 74-78, doi:10.1016/j.conb.2015.01.018 (2015).
- 60 Izquierdo-Serra, M. *et al.* Optical control of endogenous receptors and cellular excitability using targeted covalent photoswitches. *Nat Commun* **7**, 12221, doi:10.1038/ncomms12221 (2016).
- 61 Laprell, L. *et al.* Photopharmacological control of bipolar cells restores visual function in blind mice. *J Clin Invest* **127**, 2598-2611, doi:10.1172/JCI92156 (2017).
- 62 Hüll, K. *et al.* Photopharmacologic vision restoration reduces pathological rhythmic field potentials in blind mouse retina. *Sci Rep* **9**, 13561, doi:10.1038/s41598-019-49999-w (2019).
- 63 Lane, J. R., Abdul-Ridha, A. & Canals, M. Regulation of G protein-coupled receptors by allosteric ligands. *ACS Chem Neurosci* **4**, 527-534, doi:10.1021/cn400005t (2013).

## Supporting Information (SI) of Chapter 11

### SI11.1 Plasmid construction

The mouse mutant (T148A) mGlu<sub>6</sub> receptor was created and had a punctiform mutation (*i.e.*, a threonine to alanine exchange at position 148) in the “Venus flytrap” domain (VFD), resulting in a receptor that is insensitive to its orthosteric ligands<sup>1</sup>. This site-directed mutagenesis was accomplished through a PCR-driven overlap extension by using the KOD Hot Start Master Mix kit (Sigma-Aldrich). The final product (around 800 bp) containing the mutation of interest was loaded on an agarose gel, purified by a gel extraction kit (Qiagen) and inserted in an expression vector (PGEM-T Easy Vector systems; Promega) to transform bacteria (One Shot™ MAX Efficiency™ DH5α-T1<sup>R</sup>; ThermoFisher Scientific). Subsequently, the DNA from positively screened colonies was sequenced to verify the correctly established mutation. Then the insert and the vector were digested with the EcoRI (New England Biolabs), a restriction enzyme, whereas the digested vector backbone was treated with the Antarctic phosphatase (New England Biolabs) prior to ligation, preventing the two ends of the vector to re-circularize. The cut insert was ligated into the vector and the complete insert + vector construct was transformed into the DH5α bacteria. Successful creation of the plasmid was screened through mini-prepping (#740588.50, NucleoSpin Plasmid, Mini kit for plasmid DNA) and Sanger sequencing of random colonies.

### SI11.2 *In vitro* calcium imaging

Human embryonic kidney tsA201 (HEK tsA201, American Type Culture Collection; ATCC) cells were maintained in Dulbecco’s Modified Eagle’s Medium/Nutrient Mixture F-12 Ham (DMEM/F12 1:1, Life Technologies) supplemented with 10% fetal bovine serum (FBS, Life Technologies), and 1% antibiotics (Penicillin/Streptomycin; Sigma-Aldrich) in a controlled environment (37°C, 98% humidity and 5% CO<sub>2</sub>). Mouse wild type (WT) mGlu<sub>6</sub> or mutant (T148A), where the mutant receptor is devoid to be activated by orthosteric ligands, were transiently co-transfected with Gα<sub>qTOP</sub> and the calcium indicator GCaMP6s (ratio 1:0.25:0.6) through X-tremeGENE 9 DNA Transfection Reagent (Roche Applied Science) following the manufacturer’s instructions. The genetically encoded GCaMP6s calcium indicator was prevalently used in the experiments. However, in a set of experiments the red genetically encoded R-GECO1 and the chemical indicator Oregon Green BAPTA-1 AM (OGB-1 AM; Life Technologies) were applied to validate previous results. The mouse mGlu<sub>6</sub> receptor plasmid

was a kind gift from Prof. Takahisa Furukawa (Institute for Protein Research, Osaka University, Osaka, Japan). The day after, cells were harvested with accutase (Sigma-Aldrich) and seeded onto 16 mm glass coverslips (ThermoFisher Scientific) coated with poly-L-Lysine (Sigma-Aldrich) to allow cell adhesion. The seeded cells were used for calcium imaging assay (*i.e.*, to determine changes in intracellular calcium concentrations upon receptor activation) after 24 h. The bath solution used for single cell intracellular calcium recordings contained: 140 mM NaCl, 5.4 mM KCl, 1 mM MgCl<sub>2</sub>, 10 mM HEPES, 10 mM glucose and 2 mM CaCl<sub>2</sub>, with pH 7.40. Prior to each experiment, cells were mounted on the recording chamber (Open Diamond Bath Imaging Chamber for Round Coverslips from Warner Instruments LLC) and placed in the recording solution. Although the cells loaded with 10 μM OGB-1AM were placed in a Ca<sup>2+</sup>-free bath solution at 37°C and 5% CO<sub>2</sub> for 30 min. Of note, co-transfected HEK tsA201 cells with WT mGlu<sub>6</sub> receptor were pre-incubated for 30 min with GlutaMAX (ThermoFisher Scientific), ensuring that the calcium response was solely induced by the **prosthe6** alone. Next, cells were rinsed with fresh recording solution, the recording chamber was filled with 1 ml recording solution and placed on an IX71 inverted microscope with a 20x water immersion objective (XLUMPLFLN 20XW, 1 NA; Olympus).

GCaMP6s or OGB-1 AM were excited during 50 ms at 488 nm by using a Polychrome V light source (Till Photonics GmbH) equipped with a Xenon Short Arc lamp (Ushio Europe B.V.) and a 505 nm dichroic beam splitter (Chroma Technology). The emission at 510 nm was filtered by a D535/40 nm emission filter (Chroma Technology) and collected by a C9100-13 EM-CCD camera (Hamamatsu Photonics). However, R-GECO1 was excited during 50 ms at 562 nm by using a Polychrome V light source (Till Photonics GmbH) equipped with a Xenon Short Arc lamp (Ushio Europe B.V.) and a 585 nm dichroic beam splitter (Chroma Technology). The emission at 600 nm was filtered by ET630/75nm emission filter (Chroma Technology) and collected by a C9100-13 EM-CCD camera (Hamamatsu Photonics).

Images were acquired with an imaging interval of 2 s with the SmartLux software (HEKA) at ambient temperature, where imaging analysis was done with Fiji (NIH, ImageJ).

Of note, the L-2-amino-4-phosphonobutyric acid (L-AP4, Tocris Biosciences) was used as a positive control in combination with the mouse WT mGlu<sub>6</sub> receptor and used as a reference to normalize **prosthe6**. On the other hand, the vehicle was used to ensure that it did not induce the WT or T148A mGlu<sub>6</sub> receptor. The L-AP4 and glutamate (Sigma-Aldrich) were used as a negative control with the mutant T148A mGlu<sub>6</sub> receptor.

All the experiments were performed under dark conditions to hold **prosthe6** in its *trans* conformation. Application of **prosthe6** (*i.e.*, optogluram) was performed by pipetting a small volume, during image acquisition, into the accessory pool of the recording chamber (approximately 1:1000 dilution). **Prosthe6** was dissolved in dimethyl sulfoxide (DMSO; Sigma-Aldrich) and diluted with the recording solution to a 0.1% final concentration of DMSO.

### SI11.2.1 Rationale of vision restoration targeting mGlu<sub>6</sub> receptor with prosthe6

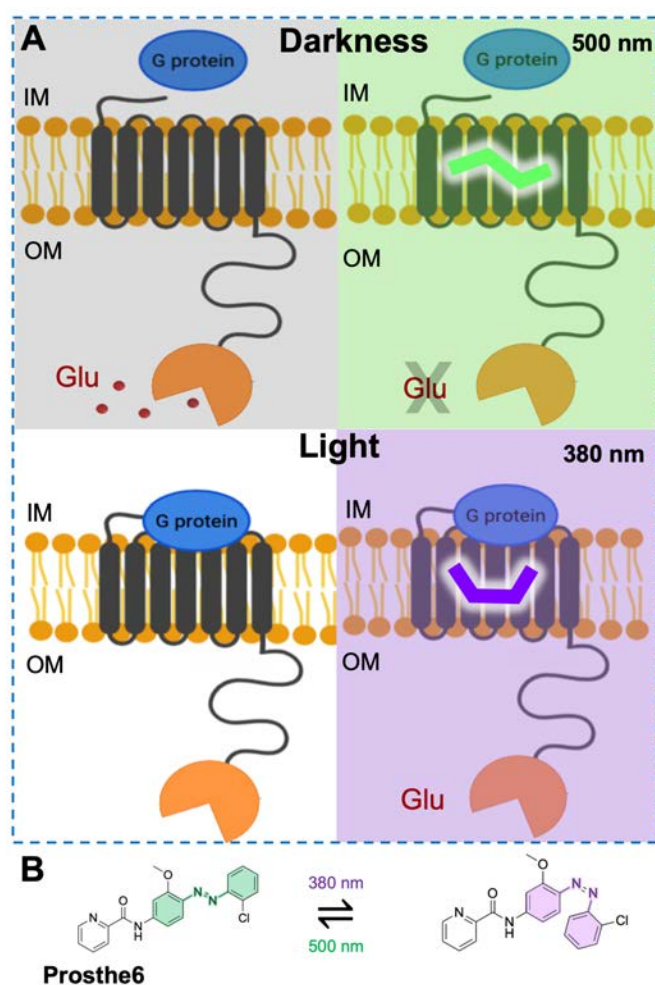


**Figure S11.1. Rationale of vision restoration targeting upstream retinal stimulation with photoswitchable allosteric modulators of mGlu<sub>6</sub> receptor.** (A) In the dark (top left diagram), PhRs tonically release glutamate, which activates mGlu<sub>6</sub> receptor that is negatively couple to the TRPM1 channel. Under illumination (bottom left diagram) PhRs do not release glutamate, mGlu<sub>6</sub> receptor is inactive with the consequent opening of the TRPM1. In the dark (or under green illumination, top right diagram) the compound should activate mGlu<sub>6</sub> receptor in the absence of glutamate. Under illumination at a different wavelength (violet in the bottom right diagram) the compound should not activate mGlu<sub>6</sub> receptor. In this way, the compound would retain physiological signal flow in the circuit and act as a "molecular prosthesis" for upstream-targeted functional restoration of retinal function. (B) The structure and photoisomerization of **prosthe6** are shown in panel B.

### SI11.2.2 Dose response curve of the orthosteric agonist L-AP4

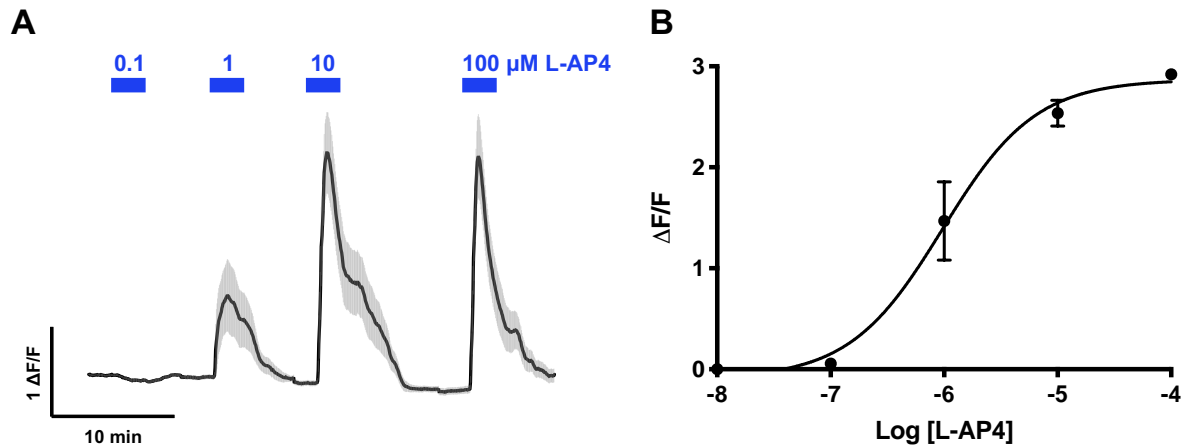


**Figure S11.2. Validation of *in vitro* assay to quantify mGlu<sub>6</sub> receptor activity.** (A) time course of calcium response ( $n = 20$  cells) of WT mGlu<sub>6</sub> receptor to several concentrations of the orthosteric agonist L-AP4 (0.1, 1, 10 and 100  $\mu\text{M}$ ) and (B) the corresponding dose-response plot. The determined  $\text{EC}_{50}$  value is 0.96  $\mu\text{M}$ . The dose-response curve was obtained from GraphPad Prism using a sigmoidal dose-response curve model with variable slope. Results are shown as the mean of two independent experiments  $\pm$  SEM.

### SI11.2.3 Calcium imaging activity in presence of prosthe6 from WT and T148A mGlu<sub>6</sub> receptors

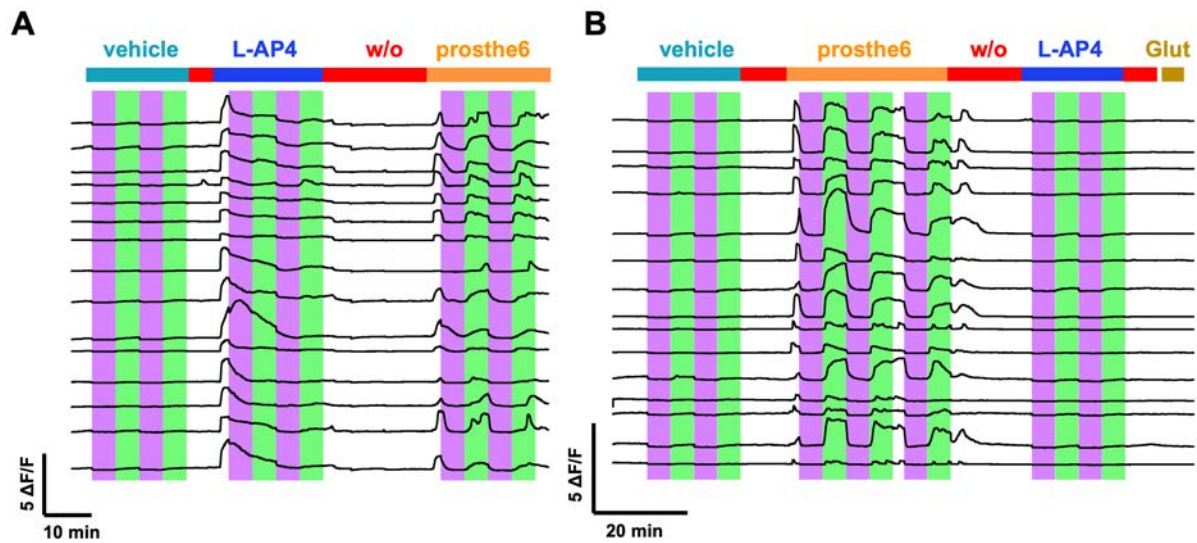


**Figure S11.3. Representative single cells of calcium activity in presence of prosthe6 from WT and T148A mGlu<sub>6</sub> receptors.** (A) Representative traces ( $n = 15$  cells) of calcium activity under 380 nm/500 nm illumination alone (control) and in the presence of 3  $\mu$ M prosthe6 without glutamate addition from WT mGlu<sub>6</sub> (B) Representative traces ( $n = 15$  cells) of calcium activity under 380/500 nm illumination alone (control) and in the presence of 3  $\mu$ M prosthe6 from T148A mGlu<sub>6</sub> receptors.

### SI11.2.4 Dose response curve of prosthe6

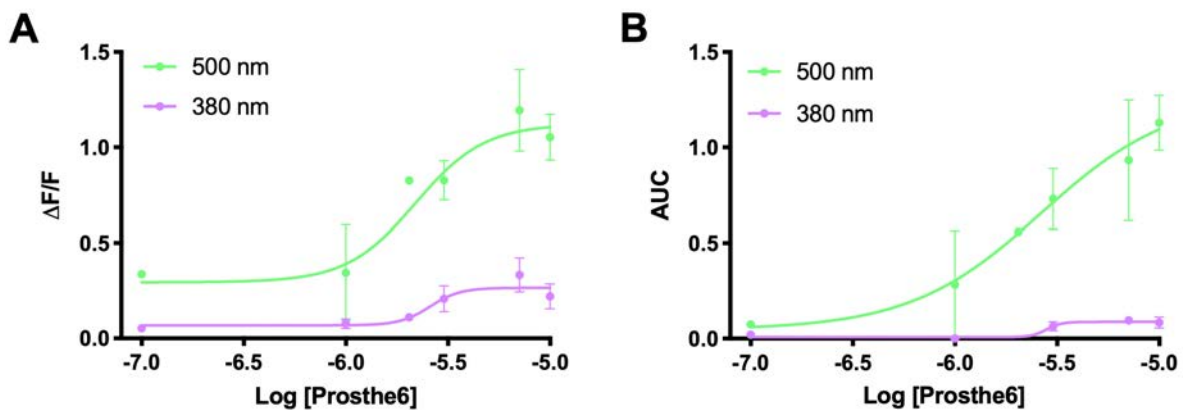


**Figure S11.4. Dose-response curve of prosthe6 upon activating the WT mGlu<sub>6</sub> receptor.** The data were plotted as (A)  $\Delta F/F$  or (B) area under the curve (AUC) and normalized to the maximal response of L-AP4 (15  $\mu$ M). The *trans*-prosthe6 was slightly more potent than the *cis*-isomer (the  $EC_{50}$  values determined for *trans*- and *cis*-prosthe6 are 2.4  $\mu$ M and 2.7  $\mu$ M, respectively) and showed a maximal efficacy of 110% vs. 10% for the *cis*-isomer. The dose-response curves were obtained with GraphPad Prism using a sigmoidal dose-response curve model with variable slope. Each concentration is shown as the mean of two or three independent experiments  $\pm$  SEM.



### SI11.2.5 Dose response curve of prosthe6

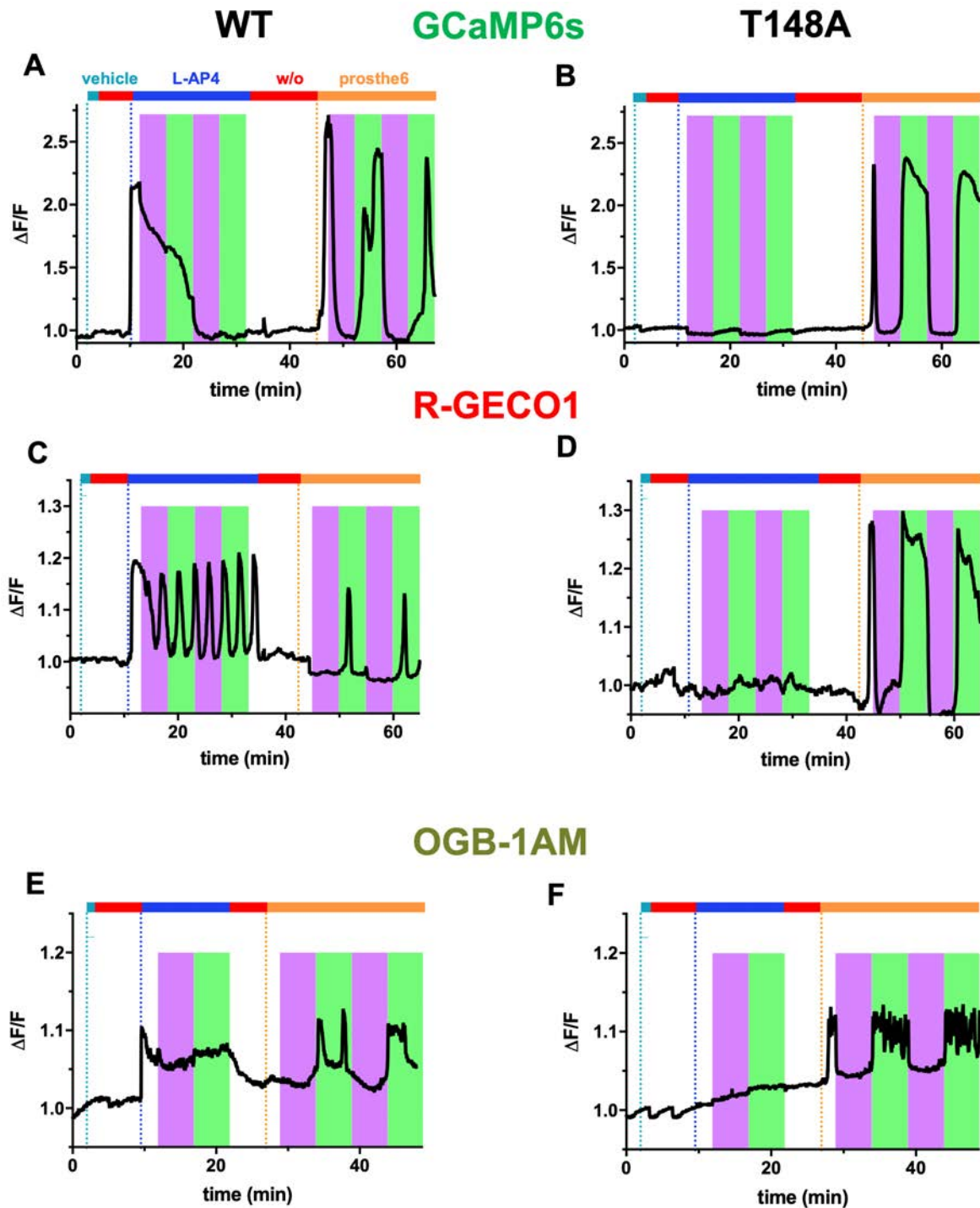
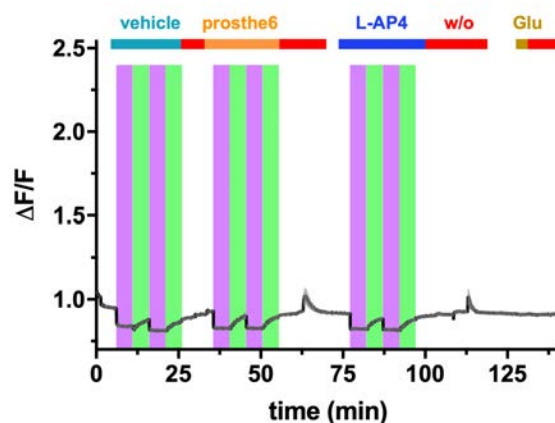


Figure S11.5. Calcium imaging responses of WT and T148A mGlu<sub>6</sub> receptors to the orthosteric agonists L-AP4 and to the allosteric modulator prosthe6. Three different fluorescent transducers of intracellular calcium concentration were employed genetically encoded GCaMP6s (excitation 488 nm, emission 510 nm) and R-GECO1 (excitation 562 nm, emission 600 nm); chemical Oregon Green BAPTA-1 acetoxy methyl ester (OGB-1AM, excitation 488 nm, emission 510 nm). The results confirmed that **prosthe6** is an ago-PAM for the mGlu<sub>6</sub> receptor, regardless of the *in vitro* expression conditions for the receptor, oscillatory or steady responses, and calcium imaging conditions.

### SI11.2.6 Control experiments



**Figure S11.6.** Control experiments of *prothe6* using *in vitro* calcium imaging experiments in HEK cells in the absence of mGlu<sub>6</sub> receptor expression. After application of 3  $\mu$ M *prothe6* in the dark-adapted state (*trans*) and under 380 nm/500 nm illumination cycles (n = 40 cells), 15  $\mu$ M L-AP4 and 10  $\mu$ M glutamate orthosteric agonists, calcium responses were ten-fold weaker than in mGlu<sub>6</sub> receptor-expressing cells (**Figure 11.2**). Error bars indicate  $\pm$  SEM.

### SI11.3 Chemical structures of the new library of photoswitches

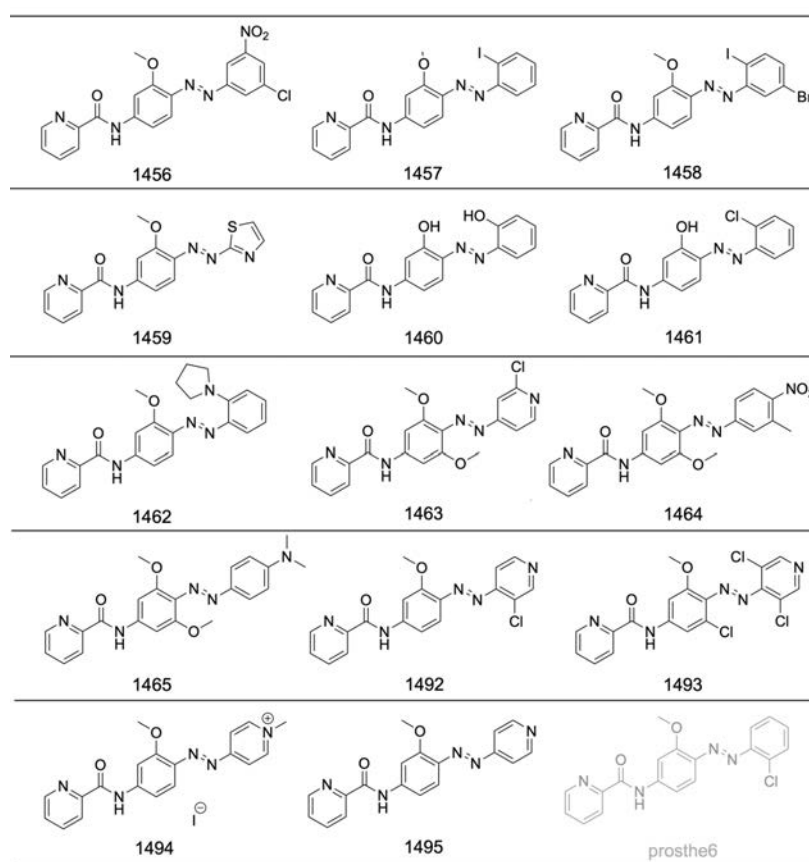


**Figure S11.7.** Chemical structures of the new library of photoswitches (in black) and the reported *prothe6* (in grey).

## SI11.4 Fluorescence-based plate reader assay

The fluorescence-based calcium mobilization assay was performed in the HEK tsA201 cell line which were transfected with human wild type (WT), mouse WT mGlu<sub>6</sub> or mutant (T148A), Gα<sub>qTOP</sub> and the calcium indicator GCaMP6s (see SI11.2). At 24 h post-transfection, the cells were harvested with accutase (Sigma-Aldrich) and 80.000 cells/well were seeded onto a 96-well sterile polystyrene plate black with transparent bottom (dD, Biolab), which were pretreated with poly-L-Lysine (Sigma-Aldrich). At 48 h the assay was performed, determining changes in intracellular calcium concentrations upon receptor activation.

In general, the culture medium was aspirated and 100 µl of recording solution was added to each well. Subsequently, the signal was measured by the TECAN infinite 200 microplate reader (Tecan Austria GmbH), which was controlled by i-Control software (Tecan Group Ltd., version 1.6). The microplate reader was set at 485 nm excitation wavelength and 535 nm emission wavelength, while applying empirically optimized parameters (temperature 37°C; integration time 40 µs; number of flashes 18; gain 120; number of cycles 25). Next, the blank or background signal was measured (*i.e.*, baseline reading). Later, 20 µl were taken from each well and 20 µl of the assay buffer, containing the compound or the control, were transferred to the cell plate and the changes in fluorescence intensity were recorded for 120 s.

Positive and negative controls were included in the experiments. In cell overexpressing the human WT or mouse WT mGlu<sub>6</sub> receptor, L-AP4 allowed to verify successful transfections. In cell overexpressing the mutant T148A mGlu<sub>6</sub> receptor the compound **prosthe6** was used to verify successful transfections and used as a reference to normalize our drugs in all the experiments. The vehicle (0.1% DMSO) resulted in a minimal fluorescence intensity to ensure that does not interfere with the receptors, was used as negative controls. All the experiments were performed under dark conditions to keep the compounds in their *trans* conformation. Test compounds were dissolved in DMSO (Sigma-Aldrich) and diluted with the assay buffer to a 2% concentration of DMSO in each well. Every compound was tested at 100 nM, 1 µM and 10 µM alone. Photoisomerization of the compounds was achieved by pre-illuminating for 3 min. To study the effect of the compounds in the *cis* conformation, they were illuminated with light with 460 nm wavelength for 3 min, and then were added to the cells as soon as possible because are fast-relaxing molecules.

All data obtained with this assay were analyzed by using Excel (Microsoft, version 16.62) and GraphPad Prism (GraphPad Software, version 9). First, the raw data obtained by the Tecan

were grouped in a single Excel sheet, because for each run the microplate reader produces a different sheet. The Relative Fluorescence (RF) was calculated through the ratio between the peak fluorescence and baseline for each well. Subsequently, the data were normalized with the maximal response to **prosthe6** (10  $\mu$ M). Statistical differences were analyzed by one-way ANOVA followed by Tukey's post-hoc test, whereas a value of *p*-value (\*) < 0.05 was considered as significant. The data are expressed as the mean  $\pm$  SEM for at least three independent experiments.

### SI11.4.1 Screening of the photoswitchable allosteric modulators

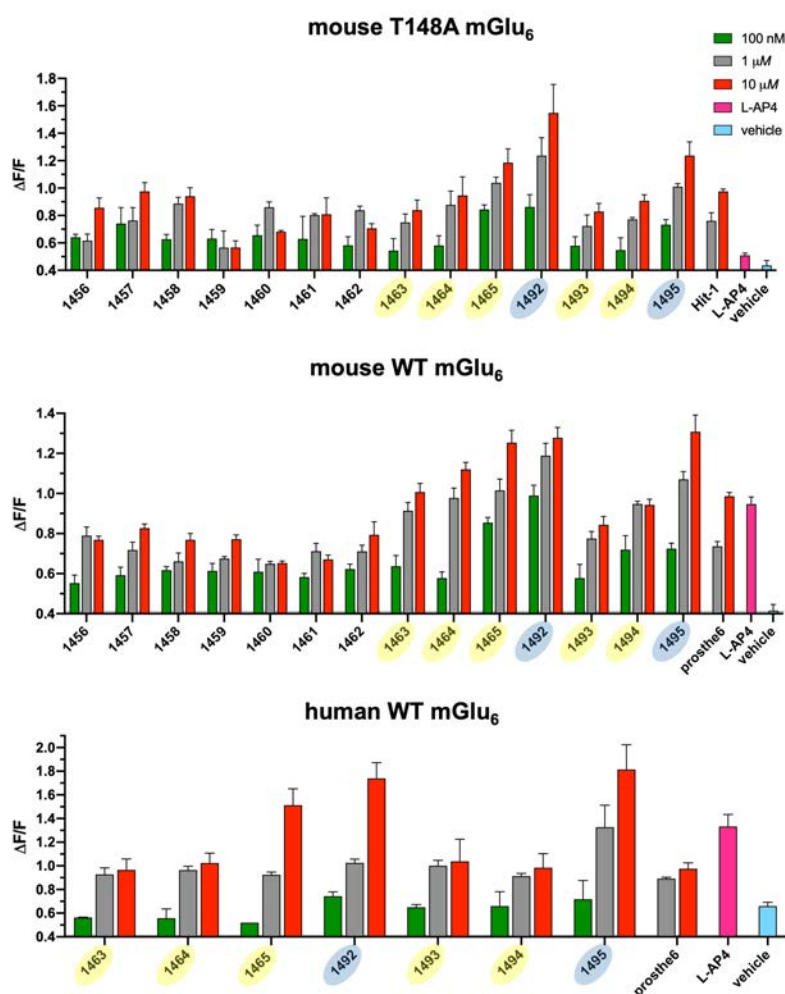


**Figure S11.8. *In vitro* screening of the novel photoswitches in HEK cells expressing mouse mutant T148A, mouse WT and human WT mGlu<sub>6</sub> receptor.** The fluorescence-based calcium mobilization assay was performed in HEK cells tsA201 co-transfected with human WT, mouse WT or mouse T148A mutant mGlu<sub>6</sub> receptor, G $\alpha_{qTOP}$  and GCaMP6s. The library of photoswitchable compounds was tested at three concentration (0.1, 1 and 10  $\mu$ M). Data were normalized with the maximal response to prosthe6. The vehicle was used as negative control. L-AP4 was used as positive control in experiments with human and mouse WT mGlu<sub>6</sub>, whereas it was used as negative control in experiments with mutant T148A mGlu<sub>6</sub>. The seven selected compounds are highlighted with blue ovals, while the two best performing compounds are highlighted with yellow ovals.

### SI11.4.2 Dose response curve of the seven selected compound in human wild-type mGlu<sub>6</sub> receptor

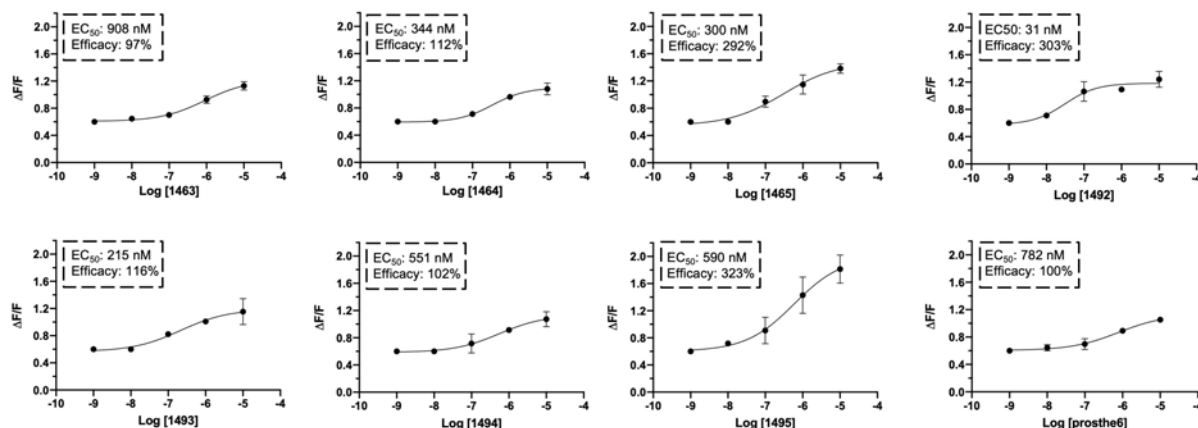


**Figure S11.9. Dose response relationship in human wild-type mGlu<sub>6</sub> receptor.** Dose-response curves to determine the EC<sub>50</sub> for each compound in its *trans*-isomer (black solid line). The concentration-dependent dose-curve data were plotted as  $\Delta F/F$  and normalized to 10  $\mu\text{M}$  **prosth6**. Curves were calculated from GraphPad using a sigmoidal dose-response curve model with variable slope. Results are shown as the mean of at least three independent experiments  $\pm$  SEM. The EC<sub>50</sub> values determined are 908 nM for the compound 1463; 344 nM for the compound 1464; 300 nM for the compound 1465; 31 nM for the compound **1492**; 215 nM for the compound 1493; 551 nM for the compound 1494 and 590 nM for the compound **1495**. The efficacy values compared to **prosth6** (100%) are 97% for compound 1463; 112% for compound 1464; 292% for compound 1465; 303% for the compound **1492**; 116% for the compound 1493; 102% for the compound 1494 and 323% for the compound **1495**.

### SI11.4.3 Dose response curve of the seven selected compound in mouse wild-type mGlu<sub>6</sub> receptor

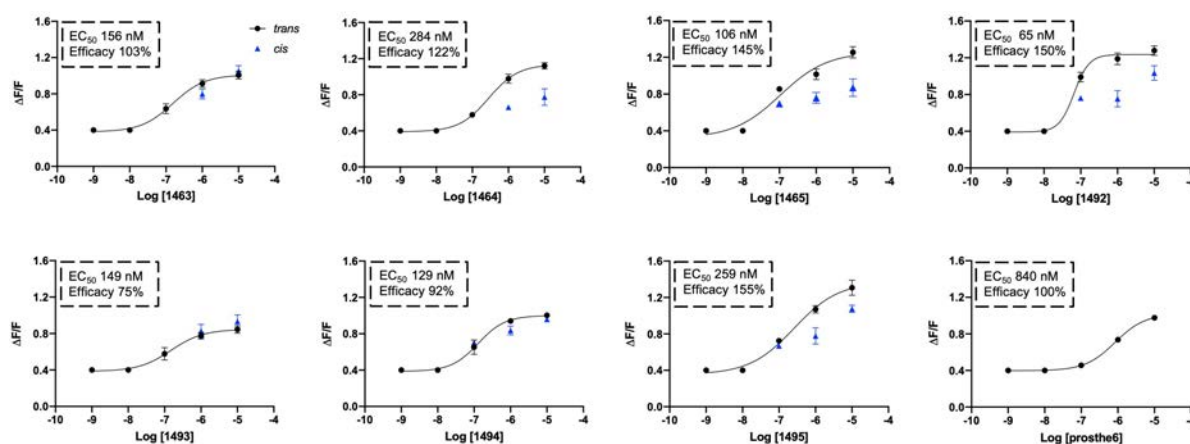


**Figure S11.10. Dose response relationship in mouse WT mGlu<sub>6</sub> receptor.** Dose-response curves to determine the EC<sub>50</sub> for each compound in its *trans*-isomer (black solid line). The concentration-dependent dose-curve data were plotted as  $\Delta F/F$  and normalized to 10  $\mu\text{M}$  **prosth6**. Curves were calculated from GraphPad using a sigmoidal dose-response curve model with variable slope. Results are shown as the mean of at least three independent

experiments  $\pm$  SEM. For the *cis*-isomers of the compounds 1463, 1464, 1493 two points are shown at 1  $\mu$ M and 10  $\mu$ M and for the compounds 1465, **1492**, 1494 and **1495** three points are shown at 100 nM, 1  $\mu$ M and 10  $\mu$ M. The EC<sub>50</sub> values determined for the *trans*-isomers are 156 for compound 1463; 284 nM for compound 1464; 106 nM for the compound 1465; 65 nM for the compound **1492**; 149 nM for compound 1493; 129 nM for the compound 1494 and 259 nM for the compound **1495**. The efficacy values compared to **prosthe6** (100%) are 145% for compound 1465; 150% for compound **1492**; 92% for compound 1494 and 154% for compound **1495**. Shortlisted compounds **1492** and **1495** display the most favorable properties and are highlighted in blue ovals.

### SI11.4.4 Dose response curve of the seven selected compound in mutant T148A mouse mGlu<sub>6</sub> receptor

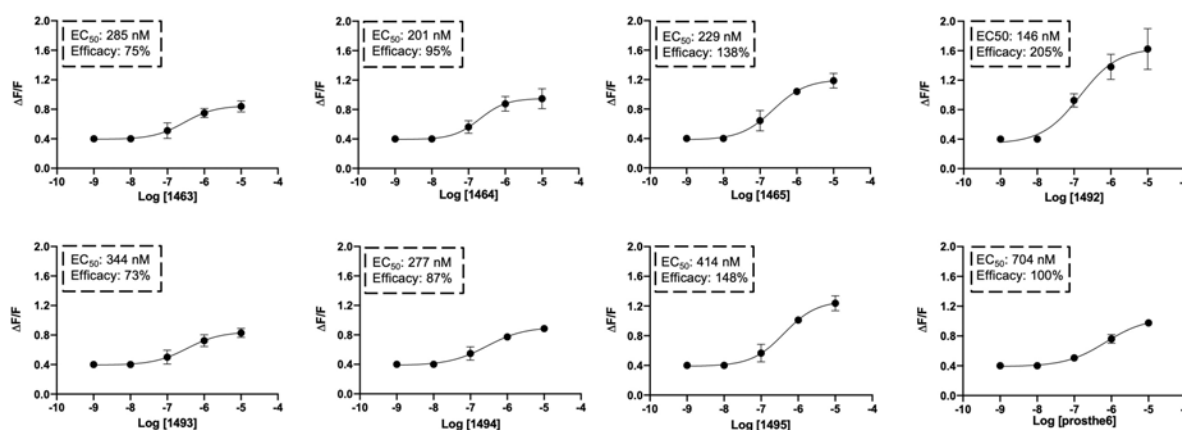


**Figure S11.11. Dose response relationship in mutant T148A mouse mGlu<sub>6</sub> receptor.** In the case of the mutant T138A mGlu<sub>6</sub> receptor, the efficacy values compared to **prosthe6** (100%) were 75% for compound 1463, 95% for 1464, 138% for 1465, 205% for **1492**, 73% for 1493, 87% for 1494 and 148% for **1495**. The EC<sub>50</sub> values determined for the *trans* form were on the nanomolar range for all compounds tested (285 nM for compound 1463, 201 nM for 1464, 229 nM for 1465, 146 nM for **1492**, 344 nM for 1493, 277 nM for 1494 and 259 nM for **1495**).

### SI11.4.5 EC<sub>50</sub> values of the seven selected compounds

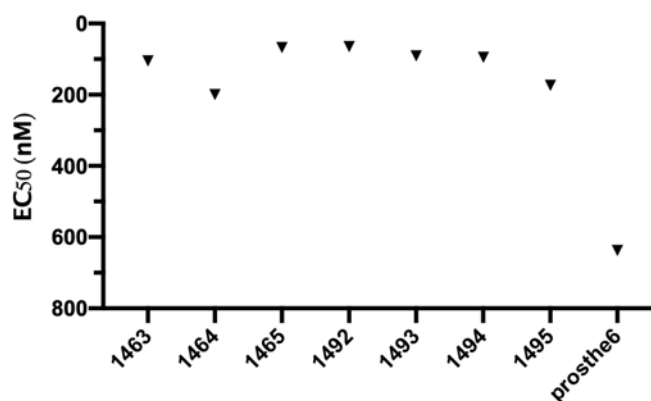


**Figure S11.12. EC<sub>50</sub> values of the 7 best performing photoswitches in mouse mutant T148A mGlu<sub>6</sub> receptor.**

## SI11.4.6 Photoswitching activity of the seven selected compounds

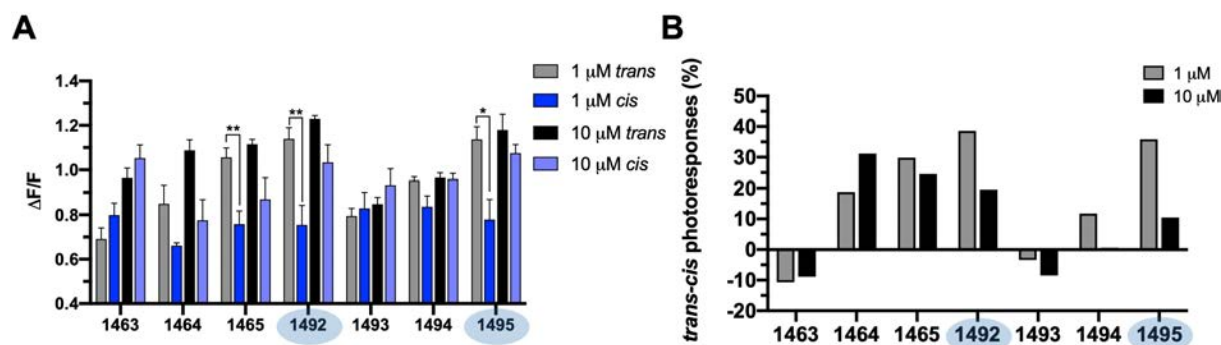


**Figure S11.13. The novel photoswitchable allosteric modulators allow reversible photoswitching of mGlu<sub>6</sub> activity** (A) Each compound allows reversible photoswitching mGlu<sub>6</sub> receptor activity without glutamate *in vitro*. The *cis*-isomers were obtained by illuminating the compounds for 2 min at 460 nm. The compounds 1463 and 1493 seems to be *cis*-active, while the other compounds are *trans*-active. The compounds 1465, 1492 and 1492 show significant photoswitching at 1  $\mu\text{M}$ , with the *trans*-isomer to be the active one. The data were analyzed by the unpaired Mann-Whitney test ( $p$ -value (\*\*) $< 0.01$ ,  $p$ -value (\*) $< 0.05$ ; GraphPad Prism 6). Error bars are  $\pm$  SEM. (B) Histogram showing the differences in photoresponses ( $\Delta F/F$ )*trans*- ( $\Delta F/F$ )*cis*, expressed in %.

## SI11.5 Animals

### SI11.5.1 Acute induction of blindness in zebrafish larvae

Tüpfel-Lon Danio rerio embryos were developed in constant darkness and maintained in 95 mm petri dishes containing UV filtered tap water at 28°C. Zebrafish larvae were not fed and UV filtered tap water was daily cleaned and refilled. Animal development (larval growth, morphology, and behavior) was checked every 24 h and unhealthy larvae were removed for euthanasia in tricaine methanesulfonate 0.02%. Zebrafish were purchased at the animal facility of the Barcelona Biomedical Research Park (PRBB). The experimental research on animals was approved by the European Communities council directive 2010/63.

Zebrafish larvae at 6 days post fertilization (dpf) were used for the ultrahigh intense light treatment which consists of the exposure of the animals to a 135.000 lux light emitted by a mercury lamp (model Olympus U-LH100HG) for 33 min. Blindness photoinduction was realized in a closed handmade chamber whose inside is completely covered of mirrors to allow an extensive photoreceptor apoptosis in the dorsal and central retina<sup>2</sup>. Light lesioning was performed in a ventilated room using a fan to avoid water heating. Ambient chamber and water temperatures were measured at the beginning and at the end of the procedure. Experiments were completed 15 h after blinding induction.

The custom-built optokinetic response machine was used. To test **prosthe6**, the light stripe pattern was generated using 500 and 380 nm LEDs placed above and in front of zebrafish larvae, respectively. To test the compounds **1492** and **1495** only white light was used as they are both fast relaxing. The turning drum was made with reflective plastic and its rotation speed can be controlled with a potentiometer. OKR experiments were optimized and completed with a rotating drum speed of 15.5 rpm. Testing was performed at 6 or 7 dpf and larvae were immobilized in a 25 mm petri dish containing 8% methylcellulose that was placed on a central platform situated in the inner zone of the drum. Larvae responses were analyzed in 1 min videos recorded with a microscope camera (model OCS-D3K2-5) incorporated to the binocular boom arm stereo microscope (model OM99 GRS-ACRO). The microscope camera needs an external intense white light for good quality videos recordings. To avoid the influence of the white light in **prosthe6**'s isomerization, recordings were performed under a red filter that preserved intact **prosthe6**'s action spectrum. Data were analyzed manually and expressed as the mean  $\pm$  SEM, with n indicating the number of animals per group.

### SI11.5.2 Chemical induced blindness in *Opn4*<sup>-/-</sup> mice

All procedures were carried out according to European (Directive 86/609/CEE) and national (Royal Decree 53/2013, February 1st) regulations in force on the protection of animals that are used for experimentation and other scientific purposes, and Law 32/2007 for the care of animals in their exploitation, transport, experimentation, and sacrifice; in addition, the guidelines of the association for research in vision and ophthalmology were followed (the Association for Research in Vision and Ophthalmology, ARVO). The mice were housed in ventilated racks with ultrafiltration cages of air through HEPA filters (high-efficiency particulate air filters) with a ventilation rate of more than 30 atmospheric changes per hour. The room had an ambient temperature of  $21 \pm 1^\circ\text{C}$  and a relative humidity of  $55 \pm 10\%$ . The animals were fed A04 feed pellets (Panlab SL, Spain) and allowed to eat and drink ad libitum. The bed of the cages was made of absorbent sawdust. Weekly cleanings were performed. Circadian cycles were established with an alternation of 12:12 h of light/dark and with an average of 20 lux in each cage during the day phase and total darkness during the night phase.

The *Opn4*<sup>-/-</sup> mice were used subjected to the light/dark transition test, where the experimental groups consisted of a variable number of animals, irrespective of sex. The *Opn4*<sup>-/-</sup> mice have a mutation for a gene responsible for the synthesis of melanopsin. Hence, the intrinsically photosensitive RGCs or melanopsin cells lack melanopsin photopigment and are unable to



respond to visual stimuli. Blindness induction was performed by administrating NaIO<sub>3</sub> systemic in mice. After control tests, a dose of 65 mg/kg was administered by intraperitoneal (i.p.) injection with a 25 G needle. The animals were not anaesthetized during intraperitoneal administration of NaIO<sub>3</sub>.

Animals (*Opn4<sup>-/-</sup>*) were subjected to the Light/Dark transition test prior to i.p. administration of NaIO<sub>3</sub>. With this test we can measure the light sensitivity of an animal. A wooden experimental set was built, consisting of two compartments, each 59 cm high and 28.5 cm on each side, and connected by a small opening in the wall. The lighting in each compartment was adapted according to the photoswitch studied.

<b>Illumination</b>	<b>Wavelength</b>	<b>Light intensity (lx)</b>	<b>Reference</b>
<b>White light</b>		39	Ledflexi Inspire, Leroy Merlin, Spain
<b>UV light</b>	380 nm	9.7	RS Components, 137-1322, VCC
<b>Green light</b>	500 nm	22.6	RS Components, 769-3551, Broadcom

**Table S11.1. Light intensities**

The light intensities used were (A.W. Sperry – SLM-110, A.W. Sperry Instruments): white light, 39 lx (Ledflexi Inspire, Leroy Merlin, Spain); 380 nm, 9.7 lx (RS Components, 137-1322, VCC); 500 nm, 22.6 lx (RS Components, 769-3551, Broadcom). Animals are allowed to explore both compartments, and the time spent in each compartment is being timed. The animals were introduced first into the darkest compartment (the one with the minimum light intensity for each study), while the opening between the two compartments remained blocked, thus preventing the escape reflex of the animals. After 3 s, the passage between the two compartments was cleared and the animal was allowed to explore freely for 3 min, with the time spent in each compartment being timed. During the experimental time, the room was kept in total darkness and any noise or external influence from the operator was kept to a minimum to create the least stressful environment possible and to allow the animal to feel free to explore. When it was found that the animals did not show any visual alteration, NaIO<sub>3</sub> was administered systemically. The animals were returned to their respective cages and allowed to rest for 3 or more weeks. Prior to administration of the photoswitches, a new Light/Dark transition test was performed, checking that the animals did not show rejection of the compartments with higher light intensity. Subsequently, the animals were gaseously anaesthetised using vaporised isoflurane (Isoflo<sup>®</sup>, Zoetis S.L.). For this purpose, a TEC 3 isoflurane vaporiser (MSS International Ltd) was used. A constant flow of 0.4 l/min of O<sub>2</sub> was maintained during the procedures. To induce anaesthesia, the animal was placed in an airtight box and vaporised with a flow of 5% isoflurane. After induction, the isoflurane flow was reduced to 2% for the duration

of the procedure, and the animal was switched to a mask holder adapted for mice. The animal, anaesthetised with isoflurane, was placed under the magnifying glass (Wild Heerbrugg) to proceed with the unilateral intravitreal injection of the various photosensitive molecules, which was performed in the nasal area of the eyeball, behind the sclero-corneal limbus. It was used a 10 µl syringe (NanofilTm, World Precision Instruments) with a 34 G needle (NanofilTm, NF35BV-2, World Precision Instruments). In all cases the injection was performed in the right eye of the animals. For the topical application 10 µl drop were applied on the ocular surface of both eyes. The animals were allowed to rest for 2 h and 30 min and then re-introduced to the Light/Dark transition test. All animals were placed in the darkest compartment in all cases. The test was repeated three times for each animal, each time cleaning each compartment to avoid falsification of the results. All experimental procedures were carried out following very similar schedules, during the night phase of the animals, to ensure a higher activity of the animals, as well as a higher reproducibility.

## Additional references

- 1 Rovira, X. *et al.* Overlapping binding sites drive allosteric agonism and positive cooperativity in type 4 metabotropic glutamate receptors. *FASEB J* **29**, 116-130, doi:10.1096/fj.14-257287 (2015).
- 2 Taylor, S., Chen, J., Luo, J. & Hitchcock, P. Light-induced photoreceptor degeneration in the retina of the zebrafish. *Methods Mol Biol* **884**, 247-254, doi:10.1007/978-1-61779-848-1\_17 (2012).

# Chapter 12

---

## Discussion

---



G protein-coupled receptors (GPCRs) are widely expressed throughout the human brain and are involved in numerous neurotransmission systems. These receptors bind to a large variety of messenger molecules and mediate the action of these messengers, which are key modulators of multiple physiological functions<sup>1</sup>. They are classified into several major families based on shared sequences and structural features. Due to their diversity, specificity, and involvement in human diseases, GPCRs have been a central focus of drug discovery. Indeed, nearly a third of the total market share of therapeutics targets GPCRs<sup>2</sup>. More specific, over 500 GPCR drugs that are designed to target GPCRs are binding a receptor of the class A or rhodopsin-like family, while only a few drugs target the class C GPCRs or metabotropic glutamate/pheromone receptors. Interestingly, the muscarinic acetylcholine receptors (mAChRs or MRs) and the

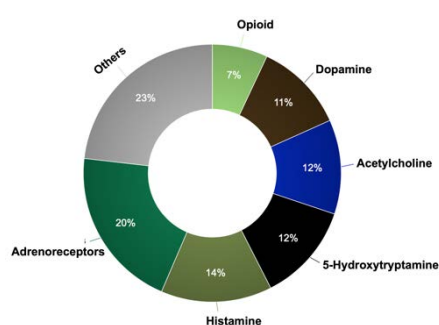


**Figure 12.1. GPCRs target by drug**

Adapted from Hauser *et al.*, 2017<sup>2</sup>.

dopamine receptors (DARs) are among the most targeted GPCRs by currently FDA-approved drugs (**Figure 12.1**)<sup>2</sup>. The thesis focuses on the mAChRs, subtype 1 and subtype 2 (M<sub>1</sub> mAChRs and M<sub>2</sub> mAChRs; **Chapters 3-9**), DARs (**Chapter 10**) and on the metabotropic glutamate 6 receptor (mGlu<sub>6</sub> receptor, **Chapter 11**). The mAChRs and DARs belong to the GPCRs of class A, whereas the mGlu<sub>6</sub> receptor is a class C GPCR.

The advances in X-ray crystallography, cryo-EM, *in silico* computational modeling and the development of high-throughput screening of GPCRs have facilitated the discovery of novel ligands. Nevertheless, these drugs face many hurdles, such as sub-optimal pharmacokinetic properties, limited target selectivity and efficacy, but also lack temporal and spatial resolution. In fact, there is a high rate of failure during the clinical drug development, while only a limited number of drugs that target GPCRs are reaching the market<sup>2</sup>.

These drawbacks that coincide with traditional pharmacology can be overcome by photopharmacology, a growing area of endeavor, which enables the control of endogenous receptors with high spatiotemporal precision by using photoswitchable molecules. One of the photopharmacological modalities implies the use of photochromic ligands (PCLs). These small diffusible molecules contain a photochromic moiety that reversibly switches between two isomers with different chemical, physical and pharmacological properties. Therefore, these two isomers of a PCL may display distinct affinity and/or efficacy for the target receptor<sup>3-6</sup>. This photopharmacological approach allows to bidirectionally control biological functions and offer the possibility to precisely investigate drug targets (*e.g.*, GPCRs).

Azobenzene has emerged as one of the most popular photochromic moieties due to multiple reasons, such as photostability, design versatility, reversibility, biocompatibility, synthetic accessibility. In fact, these compounds are intensively used for a plethora of applications in the field of neurobiology<sup>7</sup>. Most of the azobenzene-based photoswitches require the use of ultraviolet (UV) light for photoisomerization. UV light is strongly scattered by organic matter, which impedes the penetration through cells or tissues and may cause damage to living cells<sup>8,9</sup>. Therefore, its *in vivo* application in mammals is hindered. On the contrary, near-infrared (NIR) light penetrates deeper into the tissues with reduced scattering and reduced photodamaging, resulting as the foremost candidate for various *in vivo* applications (**Figure 12.3AB** and **Figure 2.30C**).

By changing the nature and number of substituents in *ortho*, *meta*, and *para* positions of the azobenzene (**Figure 12.2**), several characteristics of the photochromic moiety (*e.g.*, stability in water, thermal relaxation, operational wavelength, stability to reduction by thiols, etc.) could be fine-tuned<sup>10</sup>. In fact, fluorination of azobenzene at an *ortho* position generally enhances the nonlinear properties (*i.e.*, high two-photon (2P) absorption cross-section), while providing a bistable character (*i.e.*, stability in both *cis* and *trans* conformation)<sup>11</sup>. For instance, this allows the xanoswitches-**18a** and -**18b** (**Chapter 5**) to be photoactivated with 2P NIR light. Introducing substituents at all four *ortho* positions leads to azobenzene-based photoswitches with unusual properties useful for biological applications<sup>10,12,13</sup>.

An example is represented by the tetra-*ortho*-fluoro substituted compounds; those molecular photoswitches show high bistability, with a slow thermal *cis*-to-*trans* relaxation rate in the order of minutes/hours/days and an almost complete *trans*-to-*cis* photoconversion (*e.g.*, 90:10 *trans/cis* for xanoswitch-**4**, **Chapter 6**). Moreover, tetra-*ortho* chlorinated photoswitches generally have a remarkable shift in absorption. This occurred for instance for xanoswitch-**5** that switches from *trans*-to-*cis* with 590 nm orange light at one-photon (1P) excitation and relaxes back to *trans* thermally or with 455 nm blue light (**Chapter 6**)<sup>10</sup>. The push-pull systems are characterized by (at least) an electron-donating group on one side of the azo unit and an electron-withdrawing group on the other side. The strongest effects on absorption and relaxation of these substitutions are often found in *para*. They are commonly used to decrease

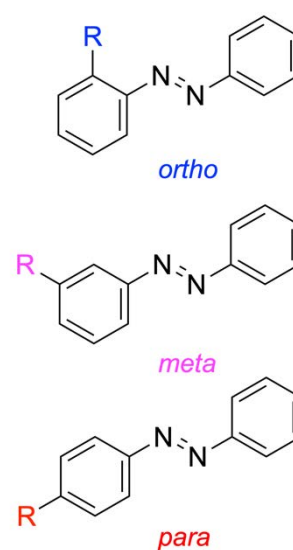


**Figure 12.2. *Ortho*, *meta* and *para* substitutions in the azobenzene.**

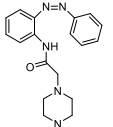
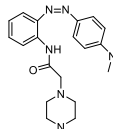
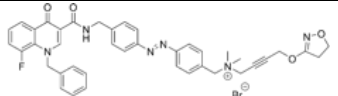
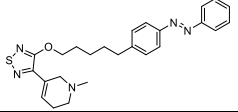
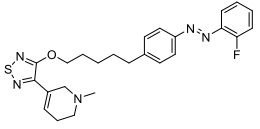
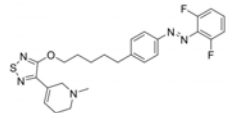
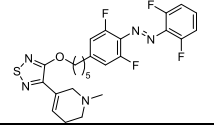
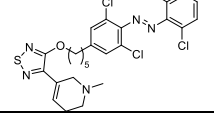
the thermal stability of the *cis*-isomer (*e.g.*, cryptozepine-3, **Chapter 3**; azodopa, **Chapter 10**; compounds **1492** and **1495**, **Chapter 11**). Furthermore, azoheterocyclic photoswitches (*e.g.*, arylazopyrazoles) represent another strategy to increase the duration of the thermal half-life of the *cis*-isomer (*e.g.*, days) and the separation of the absorption maxima of the *trans*- and *cis*-isomers (*e.g.*, compound **7g**, **Chapter 7**). This chemical functionalization may be crucial for the successful use of these PCLs to overcome potential limitations in physiological systems. However, it is important to consider that those adjustments could alter the photophysical properties of the photoswitches (*e.g.*, absorption spectrum and isomerization quantum yield) as well as their pharmacological properties, if the overall molecular dipole or specific interactions with the protein target binding pocket are affected.

This thesis aimed to characterize an array of PCLs that were designed to interact with different targets and to have different properties (*e.g.*, PSS distribution, activation wavelength, half-life, biological activity, etc.). The nature of the substituents will dictate the *modus operandi* of a photoswitch, but there is not a favored combination of properties *a priori*. Hence, the choice of the photoswitch strictly depends on the desired biological application<sup>14</sup>.

As previously mentioned, the PCLs investigated during my project can target different endogenous receptors, thus, responding to distinct unmet clinical needs. The properties and applications of these compounds are summarized in **Table 12.1**. They act as agonists, antagonists or modulators and present different mechanisms of action, including (a) orthosteric (cryptozepine-2 and -3, **Chapters 3** and **4**; xanoswitches-16e, -18a, and -18b, **Chapters 5**; xanoswitches-4 and -5, **Chapter 6**; azodopa, **Chapter 10**); (b) allosteric (compounds **7g** and **8**, **Chapter 7**; prosthe6, **1492** and **1495**, **Chapter 11**) or (c) dualsteric or bitopic interactions (**BAI**, **Chapter 4**; **PAI**, **Chapters 8** and **9**).

The main part of the thesis is based on the development and application of PCLs, which target the M<sub>1</sub> and M<sub>2</sub> subtypes of mAChRs. It is well known that M<sub>1</sub> and M<sub>2</sub> mAChRs are both involved in (patho)physiological functions of the central nervous system (CNS), as the distribution of these subtypes is abundant in the brain<sup>15</sup>. The repertoire of photoswitchable ligands developed within the frame of this thesis were mainly targeted to the M<sub>1</sub>R (*i.e.*, agonists, antagonists, and modulators) and are outlined in **Table 12.1**, which includes only the outstanding compounds.



GPCR class	GPCR target	Compound name	Compound structure	Compound activity	Active isoform	Wavelengths	Thermal stability	Applications	References
A	M <sub>1</sub> R	Cryptozepine-2		Antagonist	<i>cis</i>	365/460 nm	Slow-relaxing	<i>in vitro</i> calcium (HEK cells) <i>ex vivo</i> mouse atria <i>ex vivo</i> brain waves (mice)	Riefolo <i>et al.</i> Chapters 3-4
A	M <sub>1</sub> R	Cryptozepine-3		Antagonist	<i>cis</i>	460 nm	Fast-relaxing	<i>in vitro</i> calcium (HEK cells)	Riefolo <i>et al.</i> Chapter 3
A	M <sub>1</sub> R	BAI		Dualsteric agonist	<i>trans</i>	365/455 nm	Slow-relaxing	<i>in vitro</i> calcium (HEK cells) <i>ex vivo</i> brain waves (mice) <i>in vivo</i> brain waves (mice)	Agnetta <i>et al.</i> Chapter 3
A	M <sub>1</sub> R	Xanoswitch-16e		Agonist	<i>cis</i>	365/455 nm	Slow-relaxing	<i>in vitro</i> calcium (HEK cells)	Chapter 5
A	M <sub>1</sub> R	Xanoswitch-18a		Agonist	<i>cis</i>	365/455 nm	Slow-relaxing	<i>in vitro</i> calcium 1P & 2P (HEK cells) <i>in vitro</i> calcium (hippocampal neurons) <i>in vivo</i> calcium 2P (mice)	Chapter 5
A	M <sub>1</sub> R	Xanoswitch-18b		Agonist	<i>cis</i>	365/400 nm	Slow-relaxing	<i>in vitro</i> calcium (HEK cells & hippocampal neurons)	Chapter 5
A	M <sub>1</sub> R	Xanoswitch-4		Agonist	<i>cis</i>	530/405 nm	Slow-relaxing	<i>in vitro</i> calcium (HEK cells)	Chapter 6
A	M <sub>1</sub> R	Xanoswitch-5		Agonist	<i>cis</i>	590/405 nm	Slow-relaxing	<i>in vitro</i> calcium (HEK cells) <i>in vivo</i> locomotion (zebrafish)	Chapter 6

Continued on the next page →

GPCR class	GPCR target	Compound name	Compound structure	Compound activity	Active isoform	Wavelengths	Thermal stability	Applications	References
A	M <sub>1</sub> R	BQCisA/7g		PAM	<i>cis</i>	365/455 nm	Slow-relaxing	<i>in vitro</i> calcium (HEK cells)	Chapter 7
A	M <sub>1</sub> R	BQTrAns/8		PAM	<i>trans</i>	365/530 nm	Slow-relaxing	<i>in vitro</i> calcium (HEK cells)	Chapter 7
A	M <sub>2</sub> R	PAI		Dualsteric agonist	<i>trans</i>	365/460 nm	Slow-relaxing	<i>in vitro</i> calcium 1P, 2P & 3P (HEK cells) <i>in vivo</i> heart (zebrafish) <i>in vivo</i> brain waves (mice) <i>in vivo</i> calcium 3P (zebrafish)	Riefolo <i>et al.</i> , Barbero-Castillo <i>et al.</i> , Chapters 8-9
A	D <sub>1</sub> R	Azodopa		Agonist	<i>trans</i>	365 nm	Fast-relaxing	<i>in vitro</i> calcium (HEK cells) <i>in vivo</i> locomotion (zebrafish) <i>in vivo</i> electrophysiological recordings (mice)	Matera <i>et al.</i> , Chapter 10
C	mGlu <sub>6</sub>	Prosthe6/ Optogluram		Ago-PAM	<i>trans</i>	380/500 nm	Slow-relaxing	<i>in vitro</i> calcium (HEK cells) <i>in vivo</i> OKR (zebrafish) <i>in vivo</i> light avoidance test (mice)	Pittolo <i>et al.</i> , Zussy <i>et al.</i> , Chapter 11
C	mGlu <sub>6</sub>	1492		Ago-PAM	<i>trans</i>	470 nm	Fast-relaxing	<i>in vitro</i> calcium (HEK cells) <i>in vivo</i> OKR (zebrafish) <i>in vivo</i> light avoidance test (mice)	Chapter 11
C	mGlu <sub>6</sub>	1495		Ago-PAM	<i>trans</i>	470 nm	Fast-relaxing	<i>in vitro</i> calcium (HEK cells) <i>in vivo</i> OKR (zebrafish) <i>in vivo</i> light avoidance test (mice)	Chapter 11

Table 12.1. A summary of the properties and applications of the compounds used in this thesis.

**Chapter 3** is focused on the development of light-regulated M<sub>1</sub>R antagonists using the new strategy of azologization that was developed and dubbed as “crypto-azologization”. Pirenzepine (PNZ) is an M<sub>1</sub>R selective muscarinic antagonist used to treat peptic ulcer disease and its scaffold was used as a model due to its “privileged” structure, which contain a fused three-ringed system (tricyclic structure). Importantly, this strategy could be extended to many other compounds that belong to the important class of tricyclic drugs (*e.g.*, antidepressants) and are used to treat a diversity of clinical conditions. However, these compounds show a low selectivity, causing undesirable side effects and toxicity. This has progressively reduced their appeal in human therapies<sup>15-17</sup>, which could be regained if their activity could be constrained spatiotemporally to reduce systemic (adverse) effects.

By using an azologization strategy, we have developed novel light switching derivatives of PNZ, named “crypto-azologs”. Despite the structural dissimilarity with the parent compound, the crypto-azologs retain micromolar binding and an antagonist character. These photoswitches were characterized through a calcium imaging assay in HEK cells overexpressing the M<sub>1</sub>R. In general, this assay allows fast detection of GPCR-induced responses in living cells and is used to show (non-)dynamic optical modulation. Remarkably, cryptozepine-**2** and -**3** are both more active in their *cis* conformation, which was intended by design. For therapeutic purposes, it is generally preferred that photopharmacological agents are active in *cis* (but not always; see **Chapter 11**), which means that they are inactive under dark conditions and must be activated by light (*i.e.*, 365 nm for cryptozepine-**2** and 460 nm for cryptozepine-**3**). So far, only a few GPCR-targeting *cis*-active compounds have been described, which makes this work even more eminent. Moreover, the difference in antagonistic activity between the *trans*- and *cis*-isomers *in vitro* was amplified in different physiological context (*i.e.*, mouse atria and cerebral cortex; **Chapter 4**), where lower concentrations were used. This happens when a target protein is part of a signaling cascade, which could produce an enhancement of the *in vivo* effect<sup>18,19</sup>. Cryptozepine-**2** showed a stronger inhibitory activity compared to cryptozepine-**3** and modest selectivity towards M<sub>1</sub>R over M<sub>2</sub>R. Therefore, the cryptozepine-**2** was tested in mouse atria, where the *cis*-isomer inhibited the M<sub>1</sub>R.

Afterwards, the effect of this compound was studied in cortical networks (*ex vivo*) by our collaborators (María Victoria Sánchez-Vives, MD, PhD) at the August Pi i Sunyer Biomedical Research Institute (IDIBAPS, Barcelona, Spain). Interestingly, cortical slices of the ferret (*Mustela furo*) robustly reproduce electrophysiologically-detected slow oscillations (SO), compared with other animal models (**Chapter 4**). The SO consists of alternating periods of

high neuronal firing (Up states) and periods of near silence (Down states), which are generated during unconsciousness (*e.g.*, deep sleep, anesthesia, or brain lesions)<sup>20-26</sup> and are, thus, associated to a characteristic cortical state. In separate *ex vivo* experiments, the isomers of cryptozepine-**2** were co-applied with carbachol (CCh), a non-selective muscarinic agonist. The muscarinic activation of SO by CCh was blocked only through the co-application of the pre-illuminated active *cis* form together with CCh, whereas the *trans*-isomer with CCh did not alter the muscarinic activation. Therefore, cryptozepine-**2** was able to reversibly modulate the SO activity.

In a study of Barbero-Castillo *et al.*, 2021, the non-selective muscarinic agonist iperoxo (IPX) increased the excitability of the network in a seizure-like manner<sup>27</sup>. Subsequently, we aimed to investigate whether the photoswitchable antagonistic cryptozepine-**2** was able to modulate the muscarinic-induced seizure-like activity. Importantly, we demonstrated that the application of the *trans*-isomer of the cryptozepine-**2** did not alter seizure-like activity, while its isomerization to the *cis*-isomer by UV light inhibited the epileptiform discharges *ex vivo*.

Therewithal, we studied the effect of the M<sub>1</sub>R dualsteric photoswitchable agonist BQCAAI, (**BAI** for simplicity) on SO, which was synthesized as described in Agnetta *et al.*, 2017<sup>28</sup>. First, this compound was pharmacologically characterized and its selectivity for M<sub>1</sub> vs. M<sub>2</sub> mAChRs determined through a calcium imaging assay, where HEK cells were overexpressing the M<sub>1</sub>R or M<sub>2</sub>R. Next, **BAI** was applied in both conformations to cortical slices as well as in intact mouse brain. The results showed that **BAI** in its *trans* active form was able to increase the SO in cortical networks (*i.e.*, *ex vivo* and *in vivo*). However, high concentrations of **BAI** were epileptogenic (*e.g.*, IPX), whereas this effect was not observed for **PAI** in Barbero-Castillo *et al.*, 2021<sup>27</sup>. The latter is also a dualsteric compound based on IPX, but it targets the M<sub>2</sub>R and is active in its *trans* configuration (**Chapter 8**). This result points to a different role of M<sub>1</sub>R and M<sub>2</sub>R in epileptogenesis (see below). Importantly, the application of *trans*-**PAI** made it possible to manipulate the brain waves in isolated cortical slices as well as in anesthetized mice. The activation of M<sub>1</sub>R by **BAI** led to an increase of SO with the emergence of seizure-like activity, which is missing in M<sub>2</sub>R-mediated signals. This was probably due to the activation of different intracellular pathways by these subtypes. Overall, these findings allowed to gain more insights on the modulation of the network excitability mediated by M<sub>1</sub>R and M<sub>2</sub>R. Currently, there is a limited knowledge about the roles of muscarinic receptors in cortical dynamics, while our photoswitchable M<sub>1</sub> and M<sub>2</sub> mAChRs ligands provide a unique tool to investigate neuronal pathways with a high spatiotemporal precision. Another aspect to be considered is that **BAI**,

akin to **PAI**, is a dualsteric compound that bears a high affinity/low selectivity orthosteric moiety (*i.e.*, IPX) connected through a linker with a selective allosteric building block (*i.e.*, BQCA and phthal for **BAI** and **PAI**, respectively). Altogether, this infers that **BAI** and **PAI** have both the advantages of orthosteric and allosteric ligands. However, the effect of these molecules cannot be “switched off” *in vivo*, as UV light has a low penetration depth in brain tissue where is required for their transition into the *cis* inactive state. They are also dark-active compounds (*trans*-on). We successfully addressed these important limitations identified critical for the *in vivo* applications, in the subsequent chapters (**Chapters 5, 6 and 9**).

The previously observed shortcomings of **BAI** could be solved by using NIR with other optimized photoswitchable compounds, which respond to two-photon excitation (2PE). In fact, NIR is divided in NIR-I (700-900 nm) and NIR-II windows (900-1700 nm) (**Figure 12.3A**), both of which can penetrate tissues and the skull (**Figure 12.3B**). **Chapter 5** focuses on the synthesis and applications of photopharmacological muscarinic agonists (*i.e.*, xanoswitches). Given the key role of M<sub>1</sub>Rs in learning and memory processes, agonists have been developed for the treatment of cognitive impairments. More than 25 years ago xanomeline, an M<sub>1</sub>R agonist, was developed and showed to alleviate the negative symptoms of patients suffering from Alzheimer’s disease (AD) and schizophrenia (SZ)<sup>29-32</sup>. Despite these advances, the clinical utility of xanomeline is restricted by dose-limiting adverse effects, mediated by the activation of peripheral mAChRs upon systemic administration. This hampered the clinical application of this compound. Up to date, xanomeline has completed a phase III clinical trial for treatment of SZ in combination with trospium chloride, a brain-impermeant muscarinic antagonist to reduce peripheral side effects<sup>33</sup>. Therefore, the spatiotemporal control of xanomeline would endow the therapeutic selectivity that is required to be effective and safe *per se*. A set of photoswitchable xanomeline derivatives, xanoswitches, were developed in collaboration with the laboratory of Prof. Dr. Michael Decker (Institute of Pharmacy and Food Chemistry, University of Wuerzburg; JMU, Wuerzburg, Germany). The compounds were obtained by introducing an azobenzene at the aliphatic chain of the xanomeline, while a variable linker length was placed in between the azobenzene and the thiadiazole core. First, a split luciferase complementation assay (SCLA) was performed to screen the novel compounds based on their efficacy, potency, and degree of functional 1P switching. Remarkably, all xanoswitches displayed “*cis*-on” activity, which is a desirable characteristic in photopharmacology. In addition, most compounds retained the nanomolar potency of their parent compound. The xanoswitches bearing a linker length of 4 or 5 carbon atoms (compounds **16d** and **16e**) showed the best efficacy and potency.

These “first-in-class” compounds were further optimized for 2PE in order to achieve a breakthrough in 2P pharmacology, namely the demonstration of photoreversible (bidirectional) control of neuronal activity *in vivo* with infrared (IR) light and a dark-inactive, drug-like molecule.

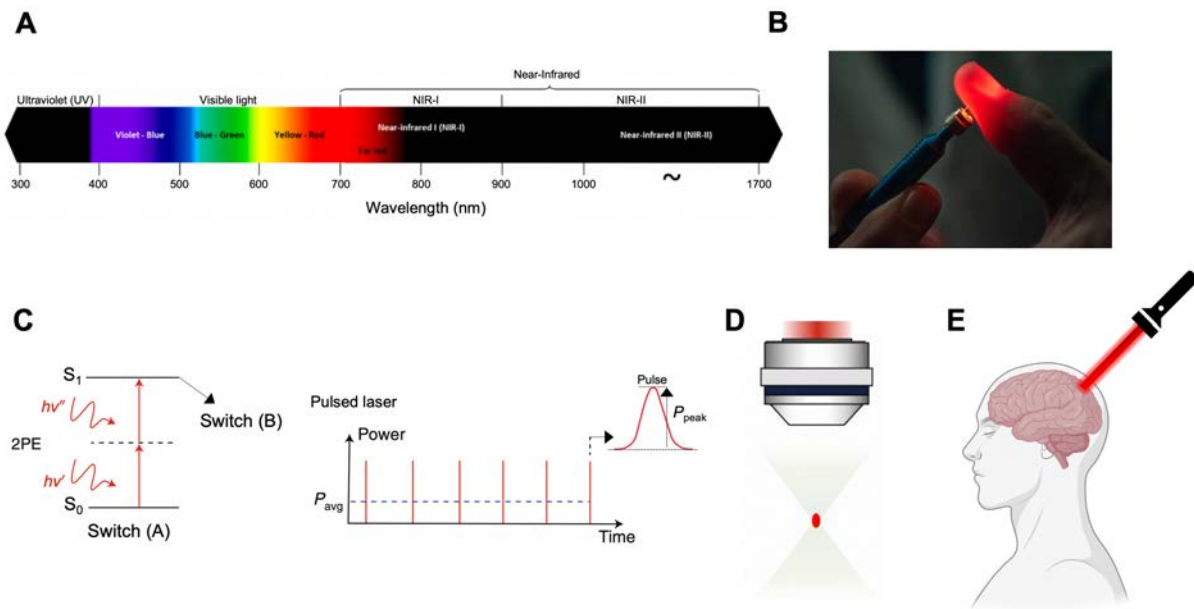


**Figure 12.3. Infrared light for biological applications.** (A) The electromagnetic spectrum ranging from ultraviolet (UV) to near infrared (NIR) light. NIR consists of NIR-I (700-900 nm) and NIR-II (900-1700 nm) regions. (B) Photo showing red light transmitted through the finger, due to its capability to penetrate through tissues and bones. (C) Jablonski energy diagrams representing the two-photon (2P) induced isomerization which is a consequence of the 2P absorption process and the representation of a pulsed laser, where each pulse is characterized by the peak power. (D) The 2PE process is restricted to the focal point of the laser beam. (E) Transcranial activation of the photoswitchable ligand by application of infrared (IR) light from an external device, allowing reversible and noninvasive control of a specific neurotransmission pathways or to restore altered slow oscillation patterns. Adapted from Dudek *et al.*, 2020 and Papagiakoumou *et al.*, 2020<sup>11,34</sup>.

Over the last few years, the use of the 2PE technique together with the development of IR, femtosecond-pulsed lasers have driven the application of the photoswitches in a biological context, which has been pioneered at the Institute for Bioengineering of Catalonia (IBEC, Barcelona, Spain)<sup>35-38</sup>. A photoswitchable moiety that is a strong 2P absorber isomerizes from its *trans* to its *cis* conformation, when 2Ps of low-energy IR light (*i.e.*, each with half of the energy needed) from a pulsed laser are absorbed simultaneously (**Figure 12.3C**). The wavelengths needed for multiphoton absorption can be estimated by multiplying the wavelength used for 1P absorption by the number of photons (*i.e.*, 400 nm x 2  $\rightarrow$  800 nm). The 2P absorption process depends on the square of the intensity of light combined with tightly focused beams, exciting a very small volume (femtoliters) (**Figure 12.3D**). Together, the IR

light and focused excitation give rise to many advantages, including better tissue penetration than visible light (up to mm), reduced scattering, reduced phototoxicity, three-dimensional submicrometric spatial resolution and patterned illumination<sup>39-44</sup>.

A potential limitation of the xanoswitches presented in **Chapter 5** is that they are based on azobenzene. It is generally known that the unsubstituted azobenzene displays a very low 2P absorption cross-section. In addition, the evaluation of the 2P absorption spectrum of small molecule photoswitches is quite laborious, requiring complex computational simulations and experimental examinations<sup>45</sup>.

Especially for photochromic tethered ligands (PTLs), different strategies have been employed to enhance the 2PE properties, such as (a) indirectly by tethering a 2P-absorbing antenna to the ligand or (b) directly through introducing functional groups to increase the electronic asymmetry of the azobenzene itself (*e.g.*, push-pull system)<sup>35,37</sup>. The first method is the most used with the photoswitch bearing an antenna (*e.g.*, naphthalene or pyrene) linked through a spacer to the photoswitchable moiety<sup>35,46</sup>. Although both approaches improve the 2P induced isomerization, while the first generally results in low aqueous solubility and the second produces low thermal stability of the *cis*-isomer, which makes it difficult to reach a high percentage of *cis* populations in the photostationary state. Moreover, the PTL-based approach generates a high selectivity for the target receptor, but often requires genetic manipulations by the anchoring either to a membrane-embedded element (*e.g.*, membrane anchored PORTL) or to a genetically modified receptor (*e.g.*, LiGluR). The second method cannot be directly translated to the PCLs, where the azobenzene is itself interacting with the binding site of the GPCR. Therefore, it is more challenging in the PCL-based approach to add chemical modifications at the photoswitch that do not hinder the interaction with the binding site.

Of note, previous studies at IBEC reported that isosteric, single atom modifications (addition of a fluorine) are required to turn 1P switches into 2P switches<sup>37</sup>. In general, enhanced nonlinear optical properties (*e.g.*, by push-pull modifications) come along with simultaneous reduction of the thermal stability of the *cis*-isomer<sup>35</sup>. In our case, the mono- and di-fluorinated derivatives of the compound **16e** (*i.e.*, **18a** and **18b**, respectively), approximately retained the potency and functional switching of the parent compound, while the thermal stability of the *cis*-isomer was not altered. In contrast, the di-fluorinated derivatives of the compound **16d** showed a complete loss of functional photoswitching, underlying the importance of finding minimal changes that enable 2P switching. The compounds **18a** and **18b** bidirectionally manipulated M<sub>1</sub>R *in vitro* under 2PE. Notably, xanoswitch-**18b** allowed for the first time photoreversible control of

cortical activity with two different NIR wavelengths *in vivo*. Thus, these photoswitches improved qualitatively the properties of **PAI**, which switches *in vitro* from the inactive *cis* to the active *trans* isoform under 840 nm light (**Chapter 8**). However, the 2P switching of **PAI** was not reversible, as demonstrated in **Chapter 9 (Figure S9.1)**. In addition, xanoswitch-**18a** and **-18b** offer more drug-like properties than **PAI** and constitute better candidates for potential clinical use.

2PE has been successfully applied by another photopharmacological strategy, such as the photouncaging. The first study using 2P uncaging was carried out by Denk *et al.*, 1994 and, since then, many caged neurotransmitters (*e.g.*, caged glutamate or caged dopamine) for 2P uncaging have been synthesized<sup>47-49</sup>. However, the intrinsic irreversibility of this method limits its use to basic research purposes (*e.g.*, studying neurotransmission pathways and neuroplasticity)<sup>47,50,51</sup>. Important work has also been carried out to precisely control neural activity *in vitro* and *in vivo* by 2P optogenetic tools<sup>43,52-57</sup>. However, notwithstanding its virtues, optogenetic involves genetic manipulation, which raises some safety concerns (*e.g.*, possible immune response against microbial opsins) that hamper its therapeutic applications in humans, among other regulatory and economic issues<sup>58,59</sup>.

In contrast, xanoswitches are PCLs, which display reversibility and do not require genetic manipulation. These compounds possess suitable characteristics (*e.g.*, enhanced 2PE and *cis*-on) for *in vivo* applications. In fact, the systemic administration of inactive drug and transcranial activation, by using tissue penetrating IR light from an external device, would allow reversible and noninvasive modulation of muscarinic neurotransmission at the desired locations (**Figure 1E**). These methods could be used as a potential treatment of pathological conditions. For instance, to alleviate or recover altered SO patterns, such as in sleep disorders, coma, and cognitive disorders (*e.g.*, Down syndrome, Williams syndrome, early aging, and AD)<sup>24,26,60-62</sup>. In addition, aberrant SO also emerge due to stroke or traumatic brain injury (TBI)<sup>22,23,25,63-66</sup>. The only disadvantage is the limited portability of the pulsed laser, optical setup and head-fixed device, which are large and heavy equipment. Interestingly, miniscopes coupled to fiber laser have been developed for multiphoton brain activity imaging in freely moving mice<sup>67-70</sup>.

The use of portable and inexpensive illumination devices would be allowed by compounds that can be directly photoswitched by orange-red light at one-photon excitation (1PE). Obtaining photoswitches that isomerize in the red and IR spectrum has proven difficult<sup>71</sup>. Together with the laboratory of Prof. Dr. Michael Decker, we obtained an orange-absorbing photoswitchable M<sub>1</sub>R agonist and its development and applications are described in **Chapter 6**.



Based on the knowledge acquired to develop 2PE *cis*-on xanowitches and on structure-activity relationships (SAR) studies, the molecular library was expanded by synthesizing the tetra *ortho*-fluorinated compounds (*i.e.*, xanowitches-**3** and **-4**). These novel compounds operate with blue (450 nm *cis*-to-*trans*) and green light (530 nm *trans*-to-*cis*). In addition, a tetra-*ortho*-chlorinated compound (*i.e.*, xanowitch-**5**) can be switched with orange/red light (590 nm *trans*-to-*cis*) and blue light (450 nm *cis*-to-*trans*). After initial *in vitro* screening with the SCLA, xanowitches-**4** and **-5** were evaluated by calcium imaging assay, where both compounds allowed reversible and dynamic photocontrol of the M<sub>1</sub>R-based calcium release.

The performance of xanowitch-**5**, which has great potential for biological applications, was also evaluated in a small animal model, the zebrafish (*Danio rerio*) larvae. It is well known that muscarinic receptors are involved in a variety of central processes, including locomotion. In a more physiological context, the activation of the M<sub>1</sub>Rs by the *cis*-xanowitch-**5** seems to inhibit the locomotor activity, whereas *trans*-xanowitch-**5** significantly increased it. The mechanism underlying the outcome of these observed motor response might be associated to the well-known interplay between dopaminergic and cholinergic systems. Indeed, several basal ganglia nuclei containing cholinergic interneurons are heavily innervated by dopaminergic terminals (*i.e.*, striatum, nucleus accumbens and olfactory bulb), playing a crucial role in the motor circuits of the brain<sup>72</sup>. In fact, different muscarinic receptor subtypes at interneurons and medium spiny neurons could be activated or suppressed, resulting in the diversification of motor activity responses<sup>73,74</sup>.

The achievements of this thesis set the path for future developments and unexplored therapeutic opportunities. Novel compounds, like xanowitch-**5**, could also be evaluated in other more complex animal models (*e.g.*, pigs and mice) of cortical microlesions and concussions (*e.g.*, stroke or TBI)<sup>75-77</sup>. We envisage that a stroke or TBI mouse model may provide a robust experimental setting to produce an increase of the SO frequency using xanowitch-**5** and continuous external illumination. It should be possible to use lightweight devices, such as conventional light emitting diodes (LEDs), compact continuous-wave diode lasers or CE-marked medical lamps. These could be integrated as headset devices, such as those used for electroencephalography or NIR spectroscopy.

Another strategy that was explored in this thesis implied the development of photoswitchable allosteric modulators to increase the target specificity. In fact, allosteric modulators could be used to fine-tune the GPCR activity (see **Chapter 2**, section 2.1.2). These molecules have the advantage of binding to the non-conserved receptor binding sites (allosteric sites), which

increase the probability to selectively interact with a specific receptor subtype. Unlike agonist and antagonists, allosteric modulators generally do not influence receptor functions in the absence of an endogenous ligand<sup>78</sup>, although compounds of **Chapter 11** act both as agonists and allosteric modulators. The majority of reported photoswitchable ligands are agonists or antagonists of class A GPCR<sup>79</sup>. Hitherto, photoswitchable allosteric modulators have been developed for class B and class C<sup>80-82</sup>. Mainly the latter target the mGlu receptor family, but up to now no photoswitchable allosteric modulators were reported for class A GPCRs<sup>79</sup>.

**Chapter 7** describes the design, synthesis, and biological characterization of the first reversibly positive allosteric modulators (PAMs) reported for class A GPCRs. These compounds were named as photo-**BQCisA/7g** and photo-**BQCtrAns/8** because they are derivatives of BQCA. In addition, they showed complementary pharmacological properties as the first is a *cis*-on PAM, while the second is a *trans*-on PAM. These compounds were selected after an *in vitro* screening by the SCLA. Next, the results were validated by two different calcium assays: (a) a plate reader-based fluorescence assay and (b) a live calcium imaging assay. The latter showed that both compounds in their active isomer allowed the dynamic and reversible modulation of the receptor signaling, together with CCh as a pre-stimulant agonist.

Depending on the required biological application, it could be more convenient to use one or the other compound. Photo-**BQCisA/7g** is inactive in the dark-adapted state and activated using UV light, whereas photo-**BQCtrAns/8** is active in the dark-adapted state or enriched with green light and inactivated by UV light. These compounds could be useful tools to understand the complexity of GPCRs signaling mechanisms. Moreover, the library of these compounds could be expanded to further red-shift the switching wavelengths of 1PE or 2PE compounds.

In **Chapters 8** and **9**, we complete the applications of photoswitches directed to muscarinic receptors. **PAI** has not only been used to modulate SO in the brain cortex, but cardiac function *in vivo* as well (**Chapter 8**). Note that this photoswitch was chronologically developed and reported earlier than the xanoswitches. To characterize **PAI** *in vitro*, we co-transfected the HEK cells with M<sub>2</sub> mAChR and a G $\alpha_{q/i}$  protein (G $\alpha_{qTOP}$ ). The G $\alpha_{qTOP}$  is a chimeric protein, where a few residues are exchanged to make the G $\alpha_q$  protein recognize and bind to the intracellular loop of a G $\alpha_{i/o}$  coupled receptors (*e.g.*, M<sub>2</sub> mAChR). Therefore, the receptor stayed unaltered as well as the binding to PLC<sup>83</sup>. This strategy was later also applied to detect mGlu<sub>6</sub> receptor activation as well, as this receptor is coupled to G $\alpha_{i/o}$  protein under physiological conditions (**Chapter 11**).

The complex multidisciplinary challenge described in **Chapter 9** was to ameliorate the tissue penetration and three-dimensional focusing of azobenzene-based photoswitches, such as **PAI** (which switches under UV illumination) by means of multiphoton excitation and IR light. This project has been developed in collaboration with the laboratories of Dr. Pablo Loza-Alvarez (Institut de Ciències Fotòniques; ICFO, Castelldefels, Spain). First, theoretical computational calculations were performed to examine the 1PE, 2PE and three-photon excitation (3PE) properties of **PAI**. These *in silico* data predicted that azobenzene-based ligands designed for 1PE with UV and visible light have high three photon (3P) absorption cross-sections. Thereby, supporting the feasibility of 3PE to activate the M<sub>2</sub>R. The 3PE implies wavelengths of the NIR-II (900-1700 nm) window, which provides increased tissue penetration, decreased light scattering and reduced photodamage. This has enormous advantages over 2PE (NIR-I, 700-900 nm), as showed in **Figure 12.2A**. In **Chapter 9**, the activation of **PAI** by 3PE was demonstrated in HEK cells as well as in zebrafish larvae, representing the first proof-of concept for photoactivation of a photoswitchable compound by 3PE. More specifically, this study aimed to stimulate neuroreceptors *in vivo* using 3PE with mid-infrared light of 1560 nm, which is the longest photoactivation wavelength used so far. Hitherto, neuronal stimulation *in vivo* with 3PE had never been reported, neither with optogenetic nor by photopharmacology. This method could significantly enhance the effectiveness of photopharmacology and would be a major driver for 3PE applications in basic neurobiological research and in noninvasive neuromodulation therapies based on light.

**Chapter 10** reports the development of a PCL to reversibly control dopaminergic neurotransmission. Impairments of the dopaminergic system are related to psychiatric and neurological pathologies, including Parkinson's disease (PD), SZ, and addictions<sup>84-86</sup>. Before our report on the photoswitchable dopaminergic agonist azodopa, several compounds had been developed to photocontrol DARs, aiming to contribute to a better understanding of the mechanism underlying the dopaminergic circuits. In fact, in a combined optogenetic-photopharmacological approach, a PTL named maleimide-azobenzene-PPHT (MAP) was synthesized from 2-(*N*-phenethyl-*N*-propyl)amino-5-hydroxytetralin (PPHT), which is a well-known DAR ligand<sup>87</sup>. The covalently binding of MAP to an engineered cysteine at the orthosteric binding site of D<sub>1</sub>R and D<sub>2</sub>R reversibly blocked the receptors' activation. Interestingly, MAP behaved as an antagonist or inverse agonist, depending on the conjugation site. The untethered analog of MAP (*i.e.*, azobenzene-PPHT; AP) allowed reversible control of D<sub>1</sub>R and D<sub>2</sub>R, although, like MAP, it was characterized only *in vitro*. Later, MP-D<sub>1</sub>R<sub>ago</sub> was

developed to selectively photocontrol D<sub>1</sub>R *in vivo* within a specific class of neurons. It is composed of a membrane anchor (M), consisting of a SNAP-tag and a transmembrane segment and a PORT ligand (P)<sup>88</sup>. However, M must be virally delivered, which involves a genetic manipulation that may affect physiological neural properties. Alternatively, to this photopharmacological-genetic approach, the photouncaging strategy provided (a) caged antagonists, which block *in vitro* D<sub>2</sub>R/D<sub>3</sub>R in a light dependent manner, and (b) caged dopamine compounds sensitive to 2PE (*e.g.*, RuBi-Dopa), which have been used for functional mapping of the dopaminergic neurotransmission pathway. As mentioned above, the photouncaging and the PCL-based approach are both photopharmacological genetic-free strategies. Importantly, the PCL has unique advantages over the irreversible release by photouncaging, as it allows to reversibly control the target receptor that is relevant for biological applications.

With these precedents, in **Chapter 10** we present the first PCL, (*i.e.*, **azodopa**), allowing reversible control of endogenous DARs in wild-type (WT) animals. After the photochemical characterization, we tested the effects of **azodopa** in a cell line overexpressing D<sub>1</sub>R through evaluating the canonical (G $\alpha_s$ /AC) and non-canonical (G $\alpha_q$ /PLC) pathways. This study indicated the compound as a *trans*-on full agonist of D<sub>1</sub>R, whereas it activated both signaling pathways. Interestingly, **azodopa** is a fast-relaxing PCL with a half-life about 200 microseconds, which is useful in neurobiology to rapidly toggle the photoswitch between the two conformations with a single wavelength of light (one-wavelength photoswitch). Due to the fast thermal relaxation of the *cis*-isomer, all the biological experiments either with **azodopa** and other fast-relaxing compounds (*i.e.*, cryptozepine-3, **Chapter 3**) were performed using a continuous illumination to sustain a population of *cis*-isomers. After the *in vitro* characterization, the behavioral effect of **azodopa** was investigated both in zebrafish larvae and in anesthetized mice. The experiments with the zebrafish larvae showed that **azodopa** enables to robustly photocontrol the locomotor activity in a reversible manner. Of note, the experiments were repeated in blinded animals, allowing to separate the retinal component from the dopaminergic neurotransmission. This simple experiment opens exciting avenues to study dopaminergic signaling in the retina. Moreover, in anesthetized mice the electrophysiological recordings showed the excitatory effects of *trans*-**azodopa** on brain cortical microcircuits. In general, a *cis*-on activity is preferred in photopharmacology, although several clinical conditions may take advantage of a dark-active drug (*e.g.*, to diminish levodopa-induced dyskinesia in PD<sup>89</sup> or the **prosthe6** for vision restoration as described in **Chapter 11**). The main drawback of **azodopa** is the need to use UV light to deactivate it. Nevertheless, this could be

overcome by refining its chemical design with suitable substituents, allowing to photoisomerize the molecule with visible or IR light and to be active in its *cis* form. In a follow-up project sparked by the results of this thesis, several **azodopa** analogs have been developed in collaboration with the laboratory of Dr. Carlo Matera (University of Milan; UNIMI, Milan, Italy), which displayed outstanding activities *in vivo*. Overall, our findings pave the way to remotely control the dopaminergic neurotransmission for research and therapeutic purposes.

The final chapter (**Chapter 11**) of this thesis focuses on the applications of reported (*i.e.*, **prosthe6/optogluram**) and novel (*i.e.*, **1492** and **1495**) PCLs that activate and deactivate mGlu<sub>6</sub> receptors in a light dependent manner. This project has been developed in collaboration with the laboratories of Prof. Dr. Pedro de la Villa (Alcalá University; UAH, Alcalá de Henares, Spain) and of Dr. Amadeu Llebaria (Institute of Advanced Chemistry of Catalonia; IQAC-CSIC, Barcelona, Spain). An essential element and motivation in this project to restore vision with small molecules is that mGlu<sub>6</sub> receptor is the topmost transducer of photoreceptors (PhRs) signals in the retinal circuit. In retinal degenerative diseases, (*e.g.*, retinitis pigmentosa; RP), PhR cells (*i.e.*, rods and cones) are progressively lost, leading to blindness. However, downstream neurons of the inner retina (*e.g.*, ON bipolar cells; OBCs) are spared, which could be photosensitized by using light-regulated drugs. Moreover, the eye is easily accessible to drug application, post-administration monitoring and it is relatively privileged from an immunological point of view, which may help reducing adverse responses to the administered drug<sup>90,91</sup>.

As previously mentioned, the PCLs characterized in **Chapter 11** target mGlu<sub>6</sub> receptors that are located solely postsynaptic to the OBC dendrites<sup>92,93</sup>. Other photoswitches for vision restoration target ubiquitous retinal proteins like potassium channels. In contrast, our compounds are designed to retain the physiological signal flow in the circuit even in the absence of glutamate (*i.e.*, the endogenous agonist), which is lacking after the PhRs are degenerated (**Figure 11.1, Chapter 11**). This approach offers an unparalleled opportunity to induce highly selective retinal responses with a favorable safety profile, while targeting upstream-signaling of the retinal circuit.

The **prosthe6** was previously reported to be a PAM of the metabotropic glutamate 4 (mGlu<sub>4</sub>) receptor<sup>94,95</sup>. In this thesis, it was investigated whether **prosthe6** could manipulate mGlu<sub>6</sub> receptor activity, by activating the receptor in absence of the orthosteric agonist (ago-PAM)<sup>96</sup>. The compound was tested in a calcium imaging assay in a cell line overexpressing the WT or the mutant T148A mGlu<sub>6</sub> receptor and the chimeric G $\alpha_{q/i}$  protein. The T148A punctiform

mutation was made in the venus flytrap domain (VFD), resulting in a receptor that is insensitive to its orthosteric ligands and thereby, suitable for our purpose<sup>97</sup>. These results showed that the compound acts as an ago-PAM, enabling to reversibly switch the mGlu<sub>6</sub> receptor activity in the absence of a pre-stimulating orthosteric agonist (*e.g.*, L-AP4) and demonstrating the feasibility of a single-component, drug-based approach to vision restoration. These findings prompted *in vivo* experiments to measure visual acuity, which constitutes the major promise of an upstream-targeted photoswitch in an induced model for blindness (*e.g.*, zebrafish larvae). An optokinetic reflex (OKR) device developed at IBEC was used to track eye movements (*i.e.*, saccades), allowing to evaluate the visual acuity of the blinded animals<sup>98</sup>. Remarkably, the blinded larvae recover this reflex in few seconds after adding **prosthe6** in the water, which indicates that this compound enables full recovery of visual acuity. Then, experiments with blind mice were performed in collaboration with the laboratory of Prof. Dr. Pedro de la Villa. Blindness was chemically induced by damaging the PhRs of *Opn4*<sup>-/-</sup> mice. Although this mouse model lacks photosensitive melanopsinic cells, they have a functional retina in physiological conditions. After blindness was established, the visual performance of these *Opn4*<sup>-/-</sup> mice was assessed through a light avoidance test. A moderate preference was observed for the area that was perceived by the blind animal as a dark environment (active, *trans*-isomer) compared to the area that was perceived as “illuminated” area (inactive, *cis*-isomer). Altogether, these results confirmed the restoration of the light avoidance behavior.

After demonstrating a proof of concept of vision restoration based on photoswitchable allosteric modulators of mGlu<sub>6</sub> receptor, we aimed at overcoming the limitations of **prosthe6** (*e.g.*, micromolar activity, slow thermal relaxation, the need of alternating UV and green light for photoswitching, cross activity with mGlu<sub>4</sub> receptor) as previously reported. To reach this purpose, we designed fast-relaxing and blue light-switched compounds that were synthesized as a library of fifteen derivatives in collaboration with the laboratory of Dr. Amadeu Llebaria. This library represents a photopharmacological toolbox with a variety of photochemical properties. Then, a protocol was optimized to perform high-throughput screening in a microplate reader, which was extremely important to select the two best-performing compounds (*i.e.*, **1492** and **1495**) for *in vivo* applications. These optimized compounds fulfill the photopharmacological requirements needed for vision restoration purposes, including *trans*-ago-PAM activity, the use of visible light ( $\geq 460\text{nm}$ ), nanomolar potency, and fast thermal relaxation, allowing to operate it with a single wavelength. These two PCLs have demonstrated the ability to restore for the first time the visual acuity in blind zebrafish larvae. In addition, a

full restoration was observed of their visually guided behavior in blind mice, both through intravitreal and topical applications. The latter result was outstanding and would especially be suitable for patient self-administration and compliance.

Other approaches for vision restoration include electronic retinal implant, which can be epiretinal (*e.g.*, Argus I, Argus II) or subretinal (*e.g.*, Alpha IMS, Alpha AMS). However, these implants have a high surgical risks and costs and have recently been discontinued due to the low restoration of visual functions<sup>90</sup>. In addition, gene therapy is highly invasive and may trigger immune response or retinal detachment. Currently, there are several optogenetic clinical trials ongoing (*i.e.*, NCT03326336, NCT02556736, NCT04278131), relying on the introduction of channelrhodopsin (ChR) variants as prosthetic light sensor to the retinal ganglion cells (RGCs). However, extreme bright light and gene therapy are required. Moreover, bestowing light-sensitivity to RGCs bypasses the processing of visual information, which occurs upstream of the RGCs. In contrast, endowing light-sensitivity to neuronal cells which are localized at the top of the retinal circuit (*e.g.*, OBCs), offers signal amplification and image processing, and, thus, the preservation of the RGC-receptive fields<sup>99,100</sup>. This enables to restore higher quality vision compared to the approaches that target the RGCs. Recently, animal opsins (*e.g.*, medium wave cone opsin) and engineered opsins (*e.g.*, Opto-mGlu<sub>6</sub> receptor) have also been explored<sup>101,102</sup>. Interestingly, the development of synthetic adeno-associated viruses (AAVs) and promoters that are OBC specific allowed OBC-targeted optogenetic approaches<sup>101,103,104</sup>. The application of GPCR opsins enables signal amplifications, as they are around 1000-fold more light sensitive than ChRs. Nevertheless, they show slow kinetics in terms of (de)activation and is only sufficient for basic perception, making it a poor tool for the high visual acuity that is associated in human disorders<sup>105</sup>. This limit was overcome by optimizing the activation of the OBC's G $\alpha_o$  signaling pathway through the development of melanopsin-mGlu<sub>6</sub> chimeras (*i.e.*, Opto-mGlu<sub>6</sub> receptor), where the intracellular domain was replaced with the ones of mGlu<sub>6</sub> receptor<sup>101,106</sup>. The ectopic expression of the Opto-mGlu<sub>6</sub> receptor allowed to restore the visual acuity in blind mice. In addition, other melanopsin-mGlu<sub>6</sub> chimeras (*e.g.*, Mela(CTmGlu<sub>6</sub> receptor) or Mela(CT+IL3mGlu<sub>6</sub> receptor) have recently been developed, where the C-terminal domain alone or together with the intracellular loop 3 are replaced with the ones of mGlu<sub>6</sub> receptor, with promising results for Mela(CTmGlu<sub>6</sub> receptor). However, by using engineered opsins, transgenic animals are needed to show any function or behavior, but to make it a feasible option for therapies in humans, non-transgenic routes should also be pursued. Although a tethered photoswitch based strategy has shown to enhance visual

acuity in an animal model of retinal degeneration, it involves an irreversible manipulation<sup>107</sup>. This kind of strategy would be very difficult, if not impossible, to reverse in case that complications occur.

In contrast, therapeutical approaches with small molecule represent a simpler and reversible strategies, allowing an optimal adjusted dose to maximize the efficacy and minimize toxicity as it is done with drug-based therapies. Furthermore, PCLs could be added, removed or replaced with improved compounds and the technology advances<sup>108</sup>. In 2022, one of these molecules (*i.e.*, BENAQ) has entered a clinical trial in humans for the first time (NCT05282953)<sup>109</sup>. Although several reported PCLs have shown efficacy *in vivo*, they displayed low potency and low selectivity as they target proteins that are broadly expressed throughout the CNS (*e.g.*, kainate and AMPA receptors, potassium channels)<sup>108,110,111</sup>. Therefore, these PCLs might have a poor safety profile and potentially cause adverse effects.

In this Chapter, we have shown the development of photoswitches that achieve nanomolar potency and target the mGlu<sub>6</sub> receptors expressed only at OBCs. This offers a unique response specificity, while providing upstream-signaling control of the retinal circuit. Importantly, we have identified the first PCLs to allow restoration of visual acuity *in vivo*. These features make **1492** and **1495** favorable candidates for further preclinical development and a potential therapy for humans. Upon suitable formulation to cross the human cornea, we envision that those compounds could be topically applied, giving rise to a highly advantageous therapy that is non-invasive, safe, user-friendly, and self-administered.

Overall, the work presented in this thesis shows the development and applications of an extended array of PCLs to regulate GPCRs in their native environment with a high spatiotemporal control. These PCLs provide different combinations of photochromic properties and *modus operandi* to be chosen, depending on the intended biomedical application. Each of them provides novel conceptual and/or methodological contributions. The presented findings broaden the availability of photopharmacological tools, not only to investigate a biological target with a high spatial and temporal resolution, but also for innovative and noninvasive treatments of different pathologies with light.



## References

- 1 Yang, D. *et al.* G protein-coupled receptors: Structure- and function-based drug discovery. *Signal Transduct Target Ther* **6**, 7, doi:10.1038/s41392-020-00435-w (2021).
- 2 Hauser, A. S., Attwood, M. M., Rask-Andersen, M., Schioth, H. B. & Gloriam, D. E. Trends in GPCR drug discovery: New agents, targets and indications. *Nat Rev Drug Discov* **16**, 829-842, doi:10.1038/nrd.2017.178 (2017).
- 3 Broichhagen, J., Frank, J. A. & Trauner, D. A roadmap to success in photopharmacology. *Acc Chem Res* **48**, 1947-1960, doi:10.1021/acs.accounts.5b00129 (2015).
- 4 Velema, W. A., Szymanski, W. & Feringa, B. L. Photopharmacology: Beyond proof of principle. *J Am Chem Soc* **136**, 2178-2191, doi:10.1021/ja413063e (2014).
- 5 Gorostiza, P. & Isacoff, E. Y. Optical switches for remote and noninvasive control of cell signaling. *Science* **322**, 395-399, doi:10.1126/science.1166022 (2008).
- 6 Lerch, M. M., Hansen, M. J., van Dam, G. M., Szymanski, W. & Feringa, B. L. Emerging targets in photopharmacology. *Angewandte Chemie International Edition* **55**, 10978-10999, doi:https://doi.org/10.1002/anie.201601931 (2016).
- 7 Beharry, A. A. & Woolley, G. A. Azobenzene photoswitches for biomolecules. *Chem Soc Rev* **40**, 4422-4437, doi:10.1039/c1cs15023e (2011).
- 8 Banerjee, G., Gupta, N., Kapoor, A. & Raman, G. UV induced bystander signaling leading to apoptosis. *Cancer Letters* **223**, 275-284, doi:https://doi.org/10.1016/j.canlet.2004.09.035 (2005).
- 9 Bachelor, M. A. & Bowden, G. T. UVA-mediated activation of signaling pathways involved in skin tumor promotion and progression. *Semin Cancer Biol* **14**, 131-138, doi:10.1016/j.semcancer.2003.09.017 (2004).
- 10 Dong, M., Babalhavaeji, A., Samanta, S., Beharry, A. A. & Woolley, G. A. Red-shifting azobenzene photoswitches for *in vivo* use. *Accounts of Chemical Research* **48**, 2662-2670, doi:10.1021/acs.accounts.5b00270 (2015).
- 11 Dudek, M. *et al.* Two-photon absorption and two-photon-induced isomerization of azobenzene compounds. *RSC Advances* **10**, 40489-40507, doi:10.1039/D0RA07693G (2020).
- 12 Bleger, D. & Hecht, S. Visible-light-activated molecular switches. *Angew Chem Int Ed Engl* **54**, 11338-11349, doi:10.1002/anie.201500628 (2015).
- 13 Samanta, S. *et al.* Photoswitching azo compounds *in vivo* with red light. *Journal of the American Chemical Society* **135**, 9777-9784, doi:10.1021/ja402220t (2013).
- 14 Welleman, I. M., Hoorens, M. W. H., Feringa, B. L., Boersma, H. H. & Szymański, W. Photoresponsive molecular tools for emerging applications of light in medicine. *Chemical Science* **11**, 11672 - 11691 (2020).
- 15 Scarr, E. Muscarinic receptors: Their roles in disorders of the central nervous system and potential as therapeutic targets. *CNS Neurosci Ther* **18**, 369-379, doi:10.1111/j.1755-5949.2011.00249.x (2012).
- 16 Eglen, R. M. Muscarinic receptor subtype pharmacology and physiology. *Prog Med Chem* **43**, 105-136, doi:10.1016/S0079-6468(05)43004-0 (2005).
- 17 Kruse, A. C. *et al.* Muscarinic acetylcholine receptors: Novel opportunities for drug development. *Nat Rev Drug Discov* **13**, 549-560, doi:10.1038/nrd4295 (2014).
- 18 Hull, K., Morstein, J. & Trauner, D. *In vivo* photopharmacology. *Chem Rev* **118**, 10710-10747, doi:10.1021/acs.chemrev.8b00037 (2018).
- 19 Kneuttinger, A. C. A guide to designing photocontrol in proteins: Methods, strategies and applications. *Biol Chem* **403**, 573-613, doi:10.1515/hsz-2021-0417 (2022).

- 20 Sanchez-Vives, M. V., Massimini, M. & Mattia, M. Shaping the default activity pattern of the cortical network. *Neuron* **94**, 993-1001, doi:10.1016/j.neuron.2017.05.015 (2017).
- 21 Mattia, M. & Sanchez-Vives, M. V. Exploring the spectrum of dynamical regimes and timescales in spontaneous cortical activity. *Cogn Neurodyn* **6**, 239-250, doi:10.1007/s11571-011-9179-4 (2012).
- 22 Modarres, M. H., Kuzma, N. N., Kretzmer, T., Pack, A. I. & Lim, M. M. EEG slow waves in traumatic brain injury: Convergent findings in mouse and man. *Neurobiol Sleep Circadian Rhythms* **2**, 59-70, doi:10.1016/j.nbscr.2016.06.001 (2017).
- 23 Cassidy, J. M. *et al.* Low-frequency oscillations are a biomarker of injury and recovery after stroke. *Stroke* **51**, 1442-1450, doi:doi:10.1161/STROKEAHA.120.028932 (2020).
- 24 Russo, S. *et al.* Focal lesions induce large-scale percolation of sleep-like intracerebral activity in awake humans. *Neuroimage* **234**, 117964, doi:10.1016/j.neuroimage.2021.117964 (2021).
- 25 Butz, M. *et al.* Perilesional pathological oscillatory activity in the magnetoencephalogram of patients with cortical brain lesions. *Neuroscience Letters* **355**, 93-96, doi:https://doi.org/10.1016/j.neulet.2003.10.065 (2004).
- 26 Sarasso, S. *et al.* Local sleep-like cortical reactivity in the awake brain after focal injury. *Brain* **143**, 3672-3684, doi:10.1093/brain/awaa338 (2020).
- 27 Barbero-Castillo, A. *et al.* Control of brain state transitions with a photoswitchable muscarinic agonist. *Adv Sci (Weinh)* **8**, e2005027, doi:10.1002/advs.202005027 (2021).
- 28 Agnetta, L. *et al.* A photoswitchable dualsteric ligand controlling receptor efficacy. *Angew Chem Int Ed Engl* **56**, 7282-7287, doi:10.1002/anie.201701524 (2017).
- 29 Bymaster, F. P. *et al.* Xanomeline: A selective muscarinic agonist for the treatment of Alzheimer's disease. *Drug Development Research* **40**, 158-170, doi:https://doi.org/10.1002/(SICI)1098-2299(199702)40:2<158::AID-DDR6>3.0.CO;2-K (1997).
- 30 Bodick, N. C. *et al.* Effects of xanomeline, a selective muscarinic receptor agonist, on cognitive function and behavioral symptoms in Alzheimer disease. *Arch Neurol* **54**, 465-473, doi:10.1001/archneur.1997.00550160091022 (1997).
- 31 Shekhar, A. *et al.* Selective muscarinic receptor agonist xanomeline as a novel treatment approach for schizophrenia. *Am J Psychiatry* **165**, 1033-1039, doi:10.1176/appi.ajp.2008.06091591 (2008).
- 32 Bender, A. M., Jones, C. K. & Lindsley, C. W. Classics in chemical neuroscience: Xanomeline. *ACS Chemical Neuroscience* **8**, 435-443, doi:10.1021/acschemneuro.7b00001 (2017).
- 33 Brannan, S. K. *et al.* Muscarinic cholinergic receptor agonist and peripheral antagonist for schizophrenia. *New England Journal of Medicine* **384**, 717-726, doi:10.1056/NEJMoa2017015 (2021).
- 34 Papagiakoumou, E., Ronzitti, E. & Emiliani, V. Scanless two-photon excitation with temporal focusing. *Nature Methods* **17**, 571-581, doi:10.1038/s41592-020-0795-y (2020).
- 35 Izquierdo-Serra, M. *et al.* Two-photon neuronal and astrocytic stimulation with azobenzene-based photoswitches. *J Am Chem Soc* **136**, 8693-8701, doi:10.1021/ja5026326 (2014).
- 36 Pittolo, S. *et al.* Reversible silencing of endogenous receptors in intact brain tissue using 2-photon pharmacology. *Proc Natl Acad Sci U S A* **116**, 13680-13689, doi:10.1073/pnas.1900430116 (2019).
- 37 Cabre, G. *et al.* Rationally designed azobenzene photoswitches for efficient two-photon neuronal excitation. *Nat Commun* **10**, 907, doi:10.1038/s41467-019-08796-9 (2019).

- 38 Riefolo, F. *et al.* Optical control of cardiac function with a photoswitchable muscarinic agonist. *J Am Chem Soc* **141**, 7628-7636, doi:10.1021/jacs.9b03505 (2019).
- 39 Pawlicki, M., Collins, H. A., Denning, R. G. & Anderson, H. L. Two-photon absorption and the design of two-photon dyes. *Angewandte Chemie International Edition* **48**, 3244-3266, doi:https://doi.org/10.1002/anie.200805257 (2009).
- 40 Bort, G., Gallavardin, T., Ogden, D. & Dalko, P. I. From one-photon to two-photon probes: “Caged” compounds, actuators, and photoswitches. *Angewandte Chemie International Edition* **52**, 4526-4537, doi:https://doi.org/10.1002/anie.201204203 (2013).
- 41 Denk, W., Strickler, J. H. & Webb, W. W. Two-photon laser scanning fluorescence microscopy. *Science* **248**, 73-76, doi:10.1126/science.2321027 (1990).
- 42 Papagiakoumou, E. *et al.* Functional patterned multiphoton excitation deep inside scattering tissue. *Nature Photonics* **7**, 274-278, doi:10.1038/nphoton.2013.9 (2013).
- 43 Oron, D., Papagiakoumou, E., Anselmi, F. & Emiliani, V. Two-photon optogenetics. *Prog Brain Res* **196**, 119-143, doi:10.1016/b978-0-444-59426-6.00007-0 (2012).
- 44 Watson, B. O., Nikolenko, V. & Yuste, R. Two-photon imaging with diffractive optical elements. *Front Neural Circuits* **3**, 6, doi:10.3389/neuro.04.006.2009 (2009).
- 45 Carmi, I. *et al.* Holographic two-photon activation for synthetic optogenetics. *Nat Protoc* **14**, 864-900, doi:10.1038/s41596-018-0118-2 (2019).
- 46 Gascón-Moya, M. *et al.* An optimized glutamate receptor photoswitch with sensitized azobenzene isomerization. *The Journal of Organic Chemistry* **80**, 9915-9925, doi:10.1021/acs.joc.5b01402 (2015).
- 47 Ellis-Davies, G. C. R. Two-photon uncaging of glutamate. *Front Synaptic Neurosci* **10**, 48, doi:10.3389/fnsyn.2018.00048 (2018).
- 48 Passlick, S. & Ellis-Davies, G. C. R. Comparative one- and two-photon uncaging of MNI-glutamate and MNI-kainate on hippocampal CA1 neurons. *J Neurosci Methods* **293**, 321-328, doi:10.1016/j.jneumeth.2017.10.013 (2018).
- 49 Denk, W. Two-photon scanning photochemical microscopy: mapping ligand-gated ion channel distributions. *Proc Natl Acad Sci U S A* **91**, 6629-6633, doi:10.1073/pnas.91.14.6629 (1994).
- 50 Abrahamsson, T., Cathala, L., Matsui, K., Shigemoto, R. & Digregorio, D. A. Thin dendrites of cerebellar interneurons confer sublinear synaptic integration and a gradient of short-term plasticity. *Neuron* **73**, 1159-1172, doi:10.1016/j.neuron.2012.01.027 (2012).
- 51 Araya, R., Andino-Pavlovsky, V., Yuste, R. & Etchenique, R. Two-photon optical interrogation of individual dendritic spines with caged dopamine. *ACS Chem Neurosci* **4**, 1163-1167, doi:10.1021/cn4000692 (2013).
- 52 Packer, A. M., Russell, L. E., Dalgleish, H. W. & Hausser, M. Simultaneous all-optical manipulation and recording of neural circuit activity with cellular resolution *in vivo*. *Nat Methods* **12**, 140-146, doi:10.1038/nmeth.3217 (2015).
- 53 Chen, I. W., Papagiakoumou, E. & Emiliani, V. Towards circuit optogenetics. *Curr Opin Neurobiol* **50**, 179-189, doi:10.1016/j.conb.2018.03.008 (2018).
- 54 Adesnik, H. & Abdeladim, L. Probing neural codes with two-photon holographic optogenetics. *Nat Neurosci* **24**, 1356-1366, doi:10.1038/s41593-021-00902-9 (2021).
- 55 Yang, W., Carrillo-Reid, L., Bando, Y., Peterka, D. S. & Yuste, R. Simultaneous two-photon imaging and two-photon optogenetics of cortical circuits in three dimensions. *eLife* **7**, e32671, doi:10.7554/eLife.32671 (2018).
- 56 Rickgauer, J. P. & Tank, D. W. Two-photon excitation of channelrhodopsin-2 at saturation. *Proc Natl Acad Sci U S A* **106**, 15025-15030, doi:10.1073/pnas.0907084106 (2009).

- 57 Begue, A. *et al.* Two-photon excitation in scattering media by spatiotemporally shaped beams and their application in optogenetic stimulation. *Biomed Opt Express* **4**, 2869-2879, doi:10.1364/BOE.4.002869 (2013).
- 58 Packer, A. M., Roska, B. & Hausser, M. Targeting neurons and photons for optogenetics. *Nat Neurosci* **16**, 805-815, doi:10.1038/nn.3427 (2013).
- 59 Allen, B. D., Singer, A. C. & Boyden, E. S. Principles of designing interpretable optogenetic behavior experiments. *Learn Mem* **22**, 232-238, doi:10.1101/lm.038026.114 (2015).
- 60 Ruiz-Mejias, M. *et al.* Overexpression of Dyrk1A, a Down syndrome candidate, decreases excitability and impairs gamma oscillations in the prefrontal Cortex. *The Journal of Neuroscience* **36**, 3648-3659, doi:10.1523/jneurosci.2517-15.2016 (2016).
- 61 Castano-Prat, P. *et al.* Altered slow (<1 Hz) and fast (beta and gamma) neocortical oscillations in the 3xTg-AD mouse model of Alzheimer's disease under anesthesia. *Neurobiology of Aging* **79**, 142-151, doi:https://doi.org/10.1016/j.neurobiolaging.2019.02.009 (2019).
- 62 Kaada, B. R., Harkmark, W. & Stokke, O. Deep coma associated with desynchronization in EEG. *Electroencephalography and Clinical Neurophysiology* **13**, 785-789, doi:https://doi.org/10.1016/0013-4694(61)90111-0 (1961).
- 63 Kaltiainen, H., Helle, L., Liljeström, M., Renvall, H. & Forss, N. Theta-band oscillations as an indicator of mild traumatic brain injury. *Brain Topogr* **31**, 1037-1046, doi:10.1007/s10548-018-0667-2 (2018).
- 64 Robb Swan, A. *et al.* Magnetoencephalography slow-wave detection in patients with mild traumatic brain injury and ongoing symptoms correlated with long-term neuropsychological outcome. *J Neurotrauma* **32**, 1510-1521, doi:10.1089/neu.2014.3654 (2015).
- 65 Allen, C. M. *et al.* Magnetoencephalography abnormalities in adult mild traumatic brain injury: A systematic review. *NeuroImage: Clinical* **31**, 102697, doi:https://doi.org/10.1016/j.nicl.2021.102697 (2021).
- 66 Huang, M.-X. *et al.* An automatic MEG low-frequency source imaging approach for detecting injuries in mild and moderate TBI patients with blast and non-blast causes. *NeuroImage* **61**, 1067-1082, doi:https://doi.org/10.1016/j.neuroimage.2012.04.029 (2012).
- 67 Zong, W. *et al.* Fast high-resolution miniature two-photon microscopy for brain imaging in freely behaving mice. *Nature Methods* **14**, 713-719, doi:10.1038/nmeth.4305 (2017).
- 68 Zong, W. *et al.* Miniature two-photon microscopy for enlarged field-of-view, multi-plane and long-term brain imaging. *Nature Methods* **18**, 46-49, doi:10.1038/s41592-020-01024-z (2021).
- 69 Zong, W. *et al.* Large-scale two-photon calcium imaging in freely moving mice. *Cell* **185**, 1240-1256.e1230, doi:https://doi.org/10.1016/j.cell.2022.02.017 (2022).
- 70 Klioutchnikov, A. *et al.* A three-photon head-mounted microscope for imaging all layers of visual cortex in freely moving mice. *Nature Methods* **20**, 610-616, doi:10.1038/s41592-022-01688-9 (2023).
- 71 Dong, M. *et al.* Near-infrared photoswitching of azobenzenes under physiological conditions. *J Am Chem Soc* **139**, 13483-13486, doi:10.1021/jacs.7b06471 (2017).
- 72 Crans, R. A. J. *et al.* Striatal dopamine D<sub>2</sub>-muscarinic acetylcholine M<sub>1</sub> receptor-receptor interaction in a model of movement disorders. *Front Pharmacol* **11**, 194, doi:10.3389/fphar.2020.00194 (2020).
- 73 Gerber, D. J. *et al.* Hyperactivity, elevated dopaminergic transmission, and response to amphetamine in M<sub>1</sub> muscarinic acetylcholine receptor-deficient mice. *Proc Natl Acad Sci U S A* **98**, 15312-15317, doi:10.1073/pnas.261583798 (2001).

- 74 Crans, R. A. J. & Ciruela, F. Dopaminergic-cholinergic imbalance in movement disorders: A role for the novel striatal dopamine D<sub>2</sub>-muscarinic acetylcholine M<sub>1</sub> receptor heteromer. *Neural Regen Res* **16**, 1406-1408, doi:10.4103/1673-5374.300988 (2021).
- 75 Xiong, Y., Mahmood, A. & Chopp, M. Animal models of traumatic brain injury. *Nat Rev Neurosci* **14**, 128-142, doi:10.1038/nrn3407 (2013).
- 76 Chen, C. *et al.* A novel simple traumatic brain injury mouse model. *Chinese Neurosurgical Journal* **8**, 8, doi:10.1186/s41016-022-00273-5 (2022).
- 77 Kinder, H. A., Baker, E. W. & West, F. D. The pig as a preclinical traumatic brain injury model: Current models, functional outcome measures, and translational detection strategies. *Neural Regen Res* **14**, 413-424, doi:10.4103/1673-5374.245334 (2019).
- 78 Wacker, D., Stevens, R. C. & Roth, B. L. How ligands illuminate GPCR molecular pharmacology. *Cell* **170**, 414-427, doi:10.1016/j.cell.2017.07.009 (2017).
- 79 Wijtmans, M., Josimovic, I., Vischer, H. F. & Leurs, R. Optical control of class A G protein-coupled receptors with photoswitchable ligands. *Curr Opin Pharmacol* **63**, 102192, doi:10.1016/j.coph.2022.102192 (2022).
- 80 Gomez-Santacana, X., Panarello, S., Rovira, X. & Llebaria, A. Photoswitchable allosteric modulators for metabotropic glutamate receptors. *Curr Opin Pharmacol* **66**, 102266, doi:10.1016/j.coph.2022.102266 (2022).
- 81 Donthamsetti, P. *et al.* Selective photoswitchable allosteric agonist of a G protein-coupled receptor. *J Am Chem Soc* **143**, 8951-8956, doi:10.1021/jacs.1c02586 (2021).
- 82 Broichhagen, J. *et al.* Allosteric optical control of a class B G protein-coupled receptor. *Angewandte Chemie International Edition* **55**, 5865-5868, doi:https://doi.org/10.1002/anie.201600957 (2016).
- 83 Gomeza, J. *et al.* Coupling of metabotropic glutamate receptors 2 and 4 to G $\alpha_{15}$ , G $\alpha_{16}$ , and chimeric G $\alpha_{qi}$  proteins: Characterization of new antagonists. *Mol Pharmacol* **50**, 923-930 (1996).
- 84 Beaulieu, J. M. & Gainetdinov, R. R. The physiology, signaling, and pharmacology of dopamine receptors. *Pharmacol Rev* **63**, 182-217, doi:10.1124/pr.110.002642 (2011).
- 85 Kienast, T. & Heinz, A. Dopamine and the diseased brain. *CNS Neurol Disord Drug Targets* **5**, 109-131, doi:10.2174/187152706784111560 (2006).
- 86 Eyles, D., Feldon, J. & Meyer, U. Schizophrenia: Do all roads lead to dopamine or is this where they start? Evidence from two epidemiologically informed developmental rodent models. *Transl Psychiatry* **2**, e81, doi:10.1038/tp.2012.6 (2012).
- 87 Donthamsetti, P. C. *et al.* Optical control of dopamine receptors using a photoswitchable tethered inverse agonist. *J Am Chem Soc* **139**, 18522-18535, doi:10.1021/jacs.7b07659 (2017).
- 88 Donthamsetti, P. *et al.* Cell specific photoswitchable agonist for reversible control of endogenous dopamine receptors. *Nat Commun* **12**, 4775, doi:10.1038/s41467-021-25003-w (2021).
- 89 Aubert, I. *et al.* Increased D<sub>1</sub> dopamine receptor signaling in levodopa-induced dyskinesia. *Ann Neurol* **57**, 17-26, doi:10.1002/ana.20296 (2005).
- 90 Kleinlogel, S., Vogl, C., Jeschke, M., Neef, J. & Moser, T. Emerging approaches for restoration of hearing and vision. *Physiol Rev* **100**, 1467-1525, doi:10.1152/physrev.00035.2019 (2020).
- 91 Sahel, J. A., Bennett, J. & Roska, B. Depicting brighter possibilities for treating blindness. *Sci Transl Med* **11**, doi:10.1126/scitranslmed.aax2324 (2019).
- 92 Nakajima, Y. *et al.* Molecular characterization of a novel retinal metabotropic glutamate receptor mGlu<sub>6</sub> with a high agonist selectivity for L-2-amino-4-phosphonobutyrate. *J Biol Chem* **268**, 11868-11873 (1993).

- 93 Vardi, N., Duvoisin, R., Wu, G. & Sterling, P. Localization of mGlu<sub>6</sub> to dendrites of ON bipolar cells in primate retina. *J Comp Neurol* **423**, 402-412, doi:10.1002/1096-9861(20000731)423:3<402::aid-cne4>3.0.co;2-e (2000).
- 94 Pittolo, S. *et al.* An allosteric modulator to control endogenous G protein-coupled receptors with light. *Nat Chem Biol* **10**, 813-815, doi:10.1038/nchembio.1612 (2014).
- 95 Zussy, C. *et al.* Dynamic modulation of inflammatory pain-related affective and sensory symptoms by optical control of amygdala metabotropic glutamate receptor 4. *Mol Psychiatry* **23**, 509-520, doi:10.1038/mp.2016.223 (2018).
- 96 Conn, P. J., Christopoulos, A. & Lindsley, C. W. Allosteric modulators of GPCRs: A novel approach for the treatment of CNS disorders. *Nat Rev Drug Discov* **8**, 41-54, doi:10.1038/nrd2760 (2009).
- 97 Rovira, X. *et al.* Overlapping binding sites drive allosteric agonism and positive cooperativity in type 4 metabotropic glutamate receptors. *The FASEB Journal* **29**, 116-130, doi:https://doi.org/10.1096/fj.14-257287 (2015).
- 98 Brockerhoff, S. E. Measuring the optokinetic response of zebrafish larvae. *Nat Protoc* **1**, 2448-2451, doi:10.1038/nprot.2006.255 (2006).
- 99 Marc, R., Pfeiffer, R. & Jones, B. Retinal prosthetics, optogenetics, and chemical photoswitches. *ACS Chem Neurosci* **5**, 895-901, doi:10.1021/cn5001233 (2014).
- 100 Kralik, J., van Wyk, M., Stocker, N. & Kleinlogel, S. Bipolar cell targeted optogenetic gene therapy restores parallel retinal signaling and high-level vision in the degenerated retina. *Communications Biology* **5**, 1116, doi:10.1038/s42003-022-04016-1 (2022).
- 101 van Wyk, M., Pielecka-Fortuna, J., Löwel, S. & Kleinlogel, S. Restoring the ON switch in blind retinas: Opto-mGlu<sub>6</sub> receptor, a next-generation, cell-tailored optogenetic tool. *PLoS Biol* **13**, e1002143, doi:10.1371/journal.pbio.1002143 (2015).
- 102 Berry, M. H. *et al.* Restoration of high-sensitivity and adapting vision with a cone opsin. *Nat Commun* **10**, 1221, doi:10.1038/s41467-019-09124-x (2019).
- 103 Hulliger, E. C., Hostettler, S. M. & Kleinlogel, S. Empowering retinal gene therapy with a specific promoter for human rod and cone ON bipolar cells. *Mol Ther Methods Clin Dev* **17**, 505-519, doi:10.1016/j.omtm.2020.03.003 (2020).
- 104 Cronin, T. *et al.* Efficient transduction and optogenetic stimulation of retinal bipolar cells by a synthetic adeno-associated virus capsid and promoter. *EMBO Mol Med* **6**, 1175-1190, doi:10.15252/emmm.201404077 (2014).
- 105 Baker, C. K. & Flannery, J. G. Innovative optogenetic strategies for vision restoration. *Front Cell Neurosci* **12**, 316, doi:10.3389/fncel.2018.00316 (2018).
- 106 Dhingra, A., Faurobert, E., Dascal, N., Sterling, P. & Vardi, N. A retinal-specific regulator of G protein signaling interacts with G $\alpha_o$  and accelerates an expressed metabotropic glutamate receptor 6 cascade. *J Neurosci* **24**, 5684-5693, doi:10.1523/jneurosci.0492-04.2004 (2004).
- 107 Berry, M. H. *et al.* Restoration of patterned vision with an engineered photoactivatable G protein-coupled receptor. *Nat Commun* **8**, 1862, doi:10.1038/s41467-017-01990-7 (2017).
- 108 Tochitsky, I. & Kramer, R. H. Optopharmacological tools for restoring visual function in degenerative retinal diseases. *Curr Opin Neurobiol* **34**, 74-78, doi:10.1016/j.conb.2015.01.018 (2015).
- 109 Tochitsky, I., Trautman, J., Gallerani, N., Malis, J. G. & Kramer, R. H. Restoring visual function to the blind retina with a potent, safe and long-lasting photoswitch. *Sci Rep* **7**, 45487, doi:10.1038/srep45487 (2017).
- 110 Izquierdo-Serra, M. *et al.* Optical control of endogenous receptors and cellular excitability using targeted covalent photoswitches. *Nat Commun* **7**, 12221, doi:10.1038/ncomms12221 (2016).

- 111 Tochitsky, I., Kienzler, M. A., Isacoff, E. & Kramer, R. H. Restoring vision to the blind with chemical photoswitches. *Chem Rev* **118**, 10748-10773, doi:10.1021/acs.chemrev.7b00723 (2018).

# Chapter 13

---

## Conclusions

---





The main conclusions drawn from this thesis are summarized as follows:

- We have developed and characterized four M<sub>1</sub>R-selective photoswitchable antagonists based on the new “cryptoazologization” strategy by using a pirenzepine scaffold. Therefore, we expanded the rational design of photochromic ligands to tricyclic drugs (**Objective 1, Chapter 3**).
- One of the cryptoazolog derivatives named cryptozepine-2 inhibits M<sub>1</sub>R in its *cis* conformation both *in vitro* and in cardiac atria *ex vivo*, allowing the administration of inactive drugs, which is a desirable feature in photopharmacology to reduce systemic adverse effects (**Objective 1, Chapter 3**).
- We have also shown that cryptozepine-2 regulates both physiological slow oscillations and pathological epileptic discharges in the cortex (**Objective 1, Chapter 4**), offering a powerful tool to investigate cortical dynamics and to explore potential antiseizure therapies.
- We have characterized an M<sub>1</sub>R-selective photoswitchable dualsteric ligand named **BAI** (**Objective 1, Chapter 4**), which allows to study the pathophysiological roles of muscarinic subtypes in cholinergic neurotransmission.
- We have designed and characterized a library of photoswitchable *cis*-on M<sub>1</sub>R agonists based on the xanomeline structure, referred to as “xanoswitches”. These compounds are activated by orange-red or infrared light, enabling deep tissue penetration. They pave the way to further advance towards *in vivo* applications of photopharmacology (**Objective 2, Chapter 5 and Chapter 6**).
- Xanoswitches-**18a** and -**18b** reversibly activate and deactivate M<sub>1</sub>R *in vitro* by one-photon and by two-photon excitation (2PE) (**Objective 2, Chapter 5**).
- Xanoswitch-**18a** enables bidirectionally controlling cortical activity in live mice by 2PE (**Objective 2, Chapter 5**).
- Xanoswitches-**4** and -**5** reversibly photocontrol M<sub>1</sub>R activity *in vitro* and are respectively activated by green and orange-red light (**Objective 2, Chapter 6**).
- Xanoswitch-**5** reversibly controls the locomotory activity of blinded zebrafish larvae (**Objective 2, Chapter 6**).

- We have characterized the first reversibly photoswitchable allosteric modulators for class A GPCRs, which represents a unique tool to comprehend the complex signaling mechanism of GPCRs (**Objective 3, Chapter 7**).
- We have developed the first M<sub>2</sub>R-selective photoswitchable dualsteric ligand (**PAI**) which enables photocontrolling cardiac activity in wild-type animals (**Objective 4, Chapter 8**).
- **PAI** activates M<sub>2</sub>Rs in its *trans* configuration and can be activated with near infrared light using 2PE (**Objective 5, Chapter 8**).
- We have developed the first method to regulate brain activity *in vivo* using three-photon excitation (3PE) (**Objective 5, Chapter 9**). The wide application of three-photon pharmacology will revolutionize basic research of neurobiology and the progression of noninvasive neuromodulation therapies based on light.
- We have developed the first photoswitchable dopaminergic agonist (**azodopa**) that displays efficacy in intact wild-type animals, including mammals. This compound will contribute to a better understanding of the mechanism underlying dopaminergic circuits (**Objective 6, Chapter 10**).
- We have developed a molecular library of photoswitchable agonist and positive allosteric modulators of mGlu<sub>6</sub> receptors. These “molecular prostheses” for vision restoration retain the physiological signal flow in retinal circuits affected by photoreceptor degeneration (**Objective 7, Chapter 11**).
- Compounds **1492** and **1495** restore light-driven behavior in a mouse model of blindness by topical application, enabling potential therapies that are noninvasive, safe, user-friendly, and self-administered (**Objective 7, Chapter 11**).
- Photoswitchable mGlu<sub>6</sub> ago-PAMs **1492** and **1495** and their parent molecule **prosth6** can fully restore visual acuity in blind zebrafish larvae, demonstrating a proof-of-concept of vision restoration based on small molecules that are targeted upstream in the retinal circuit (**Objective 8, Chapter 11**).

---

# Summary

---



G protein-coupled receptors (GPCRs) modulate diverse cellular responses to the majority of neurotransmitters and hormones within the human body. They exhibit much structural and functional diversity and are responsive to a plethora of ligands and stimuli including both endogenous (*e.g.*, biogenic amines, cations, lipids, peptides, and glycoproteins) and exogenous (*e.g.*, therapeutic drugs, photons, tastants, and odorants). Due to the key roles of GPCRs in a myriad of physiological processes, signaling pathways associated with GPCRs are implicated in the pathophysiology of various diseases, ranging from metabolic, immunological, and neurodegenerative disorders to cancer and infectious diseases. Approximately 40% of clinically approved drugs mediate their effects by modulating GPCR signaling pathways, which makes them attractive targets for drug screening and discovery. In this work, we focus on distinct GPCRs which are involved in vital pathways, such as the muscarinic acetylcholine receptors, subtype -1 and subtype -2 ( $M_1$  and  $M_2$  mAChRs; class A); the dopamine receptor 1 ( $D_1$ R; class A), and the metabotropic glutamate 6 receptor (mGlu<sub>6</sub> receptor; class C). Both  $M_1$  receptor ( $M_1$ R) and  $M_2$  receptor ( $M_2$ R) are important drug targets for several diseases that affect the central nervous system (CNS), including Alzheimer's disease, Parkinson's disease (PD), schizophrenia, sleep disorders, and acute brain diseases.  $M_2$ R also represent a target for cardiac disfunctions; the  $D_1$ R for hypertension and PD, and mGlu<sub>6</sub> receptor for retinal degenerative diseases, like retinitis pigmentosa.

Traditional pharmacological approaches for the modulation of the GPCRs activity are still limited since precise spatiotemporal control of a ligand is lost as soon it is administered. Photopharmacology proposes the use of small diffusible molecules called photochromic ligands (PCLs) (or photoswitches) to overcome this shortfall, since their activity can be reversibly controlled by light with high precision. In this thesis, we combined photochromic, cell-based (calcium fluorescence assays), and *in vivo* photopharmacological approaches to characterize several photoswitches either agonists, antagonists, dualsteric ligands or allosteric modulators.

In **Chapter 3** we introduce a novel method of photoswitch design named “cryptoazologization”, which replaces the tricyclic core of “privileged” drugs with different azobenzenes as molecular photoswitches. This strategy offers the advantage of producing photoswitchable compounds that are inactive in the *trans* configuration, the most thermodynamically stable. The *cis* isomer can be obtained upon illumination with the appropriate wavelength, mimicking the tricyclic geometry of the parent drug and its effect. The potential of the “cryptoazologization” has been demonstrated by the development of four pirenzepine derivatives, termed “cryptozepines”. We have characterized these new compounds

for mAChRs through a calcium imaging assay in HEK (human embryonic kidney) cells overexpressing the M<sub>1</sub>R. The cryptozepine-2 that showed a stronger inhibitory activity was studied *ex vivo* in cardiac atria as well as in cortical network. The latter study is the focus of **Chapter 4** in which the antagonistic effect of cryptozepine-2 is observed in ferret slices where it blocks muscarinic activation of slow oscillations. In addition, we found that cryptozepine-2 suppresses M<sub>1</sub>R-mediated epileptiform seizures in its *cis* active form. In parallel, the ability of the reported dualsteric agonist benzyl quinolone carboxylic acid-azo-iperoxo (**BAI**) was demonstrated to increase the frequency of slow oscillatory activity in cortical networks both *ex vivo* and *in vivo* in its *trans* configuration. Phthalimide-azo-iperoxo (**PAI**) is another dualsteric photoswitchable compound which is also active in its *trans* form (**Chapter 8**). Differently from **BAI**, **PAI** targets the M<sub>2</sub>Rs, being the first photoswitchable M<sub>2</sub> mAChR agonist to be reported. This compound enables the control of cardiac activity with light in wild-type animals without genetic manipulation. However, the limitation of **PAI** and **BAI** is that both *trans*-to-*cis* isomerize under UV light. Consequently, the property of noninvasiveness of light, a key advantage of pharmacological agents, is lost. We managed to activate **PAI** with longer, tissue-penetrating wavelengths such as 840 nm under two-photon excitation (2PE) (**Chapter 9**).

In this thesis, thereby, we also aimed at further expanding the photopharmacological toolset with the development of compounds or the optimization of methods that can resolve different shortcomings that we have identified as critical for *in vivo* applications. In principle, the tissue penetration depth limitation can be overcome by shifting the operational wavelengths into the “biological window” (650-1100 nm). Besides the operational wavelength, another shortcoming is represented by the large excitation volume caused by the linear dependence of one-photon excitation (1PE). In contrast, the nonlinearity of multiphoton excitation at the focal point affords subcellular resolution in three dimensions. To meet both requirements of deep tissue penetration and focalized photoswitching, multiphoton pharmacology takes advantage of near-infrared (NIR) pulsed lasers and nonlinear absorption of certain photochromic moieties.

In **Chapter 5**, we developed a set of *cis*-on xanomeline (*i.e.*, muscarinic agonist) derivatives named “xanoswitches”. The best-in-class compounds were selected based on their responses to an *in vitro* assay and these photoswitches were chemically modified to allow photoisomerization by two-photon excitation (2PE) using a pulsed NIR light laser. This was done using single point, bio-isosteric modifications at the azobenzene. These **2PE xanoswitches** afforded photocontrol of calcium oscillation in various settings, including *in vitro* and, for the first time, bidirectional, reversible photomodulation of neuronal activity *in*

*in vivo* using NIR-light. In **Chapter 9** we have presented the first proof of concept for photoactivation of a photoswitchable compound (*i.e.*, **PAI**) by three-photon excitation (3PE) *in vitro* and *in vivo*. The wide application of two-photon and three-photon pharmacology would be transformative for research and development in chemical biology and to progress with advanced phototherapies.

Depending on the biological application, the three-dimensional micrometric spatial resolution obtained by 2PE might not be necessary or desired. Instead, 1PE possesses significant advantages to activate larger areas of tissue. **Chapter 6** describes the development of **1PE xanowitches** through the introduction into the molecular structure of a tetra-*ortho* chlorinated azobenzene. These compounds allowed reversible modulation of calcium oscillation *in vitro* with orange light and photocontrol of zebrafish motility. This would also allow using standard “off-the-shelf” light emitting diodes (LEDs) which are lightweight and widely accessible, simplifying its applicability for photopharmacological therapies for the PNS and CNS.

Another goal of this work was to develop the first reversibly photoswitchable allosteric modulators for class A GPCRs, described in **Chapter 7**. Using the prototypical M<sub>1</sub>R positive allosteric modulator benzyl quinolone carboxylic acid (BQCA), a set of **Photo-BQCA**s was developed. These compounds exhibit complementary photopharmacological properties, one being *cis*- and one being *trans*-on. Biological characterization demonstrated their ability to modulate receptor activation in presence of an orthosteric agonist in a light dependent manner. These photoswitches represent interesting and useful tools in the ongoing efforts to understand complex signaling mechanism of GPCRs.

Moreover, this work presents the development and application of **azodopa**, a photopharmacological agent that is aimed at light-regulation of dopaminergic system (**Chapter 10**). We demonstrated that this compound activates D<sub>1</sub>-like receptors *in vitro* in a light-dependent manner and it enables reversibly photocontrolling zebrafish motility on a time scale of seconds. Moreover, it increases the overall neural activity in the cortex of anesthetized mice. **Azodopa** is the first photoswitchable dopamine agonist with demonstrated efficacy in wild-type animals, opening the way to remotely control dopaminergic neurotransmission for fundamental and therapeutic purposes.

In **Chapter 11**, we describe the development and application of a photoswitchable compound library targeting metabotropic glutamate 6 (mGlu<sub>6</sub>) receptors and acting as agonist and positive allosteric modulators (ago-PAM) with nanomolar potency. We performed a high-throughput



## Summary

screening of 15 photoswitchable allosteric ligands using a microplate reader and we identified two compounds (*i.e.*, **1492** and **1495**) that are fast relaxing, blue light switching, and allow *in vivo* restoration of visual acuity for the first time. Moreover, they restore light-avoidance behavior in blind mice by topical administration. The characteristics of these compounds make them excellent candidates for further preclinical studies and a potential drug-based therapy for sight restoration in humans.

The presented findings broaden the availability of photopharmacological tools not only to investigate complex signaling pathways that underlie many (patho)physiological processes but also for innovative and noninvasive treatments of different pathologies with light.

---

# Resumen

---



Los receptores acoplados a proteínas G (GPCR) modulan diversas respuestas celulares a la mayoría de los neurotransmisores y hormonas del cuerpo humano. Presentan una gran diversidad estructural y funcional y responden a una plétora de ligandos y estímulos endógenos (aminas biógenas, cationes, lípidos, péptidos y glicoproteínas) y exógenos (fármacos terapéuticos, fotones, sustancias gustativas y odorantes). Debido a las funciones clave de los GPCR en una miríada de procesos fisiológicos, las vías de señalización asociadas a los GPCR están implicadas en la fisiopatología de diversas enfermedades, desde trastornos metabólicos, inmunológicos y neurodegenerativos hasta cáncer y enfermedades infecciosas. Aproximadamente el 40% de los fármacos aprobados clínicamente median sus efectos modulando las vías de señalización de los GPCRs, lo que los convierte en dianas atractivas para el cribado y descubrimiento de fármacos. En este trabajo, nos centramos en distintos GPCR que intervienen en vías vitales, como los receptores muscarínicos de acetilcolina, subtipo-1 y subtipo-2 ( $M_1$  y  $M_2$  mAChR; clase A); el receptor de dopamina 1 ( $D_1$ R; clase A) y el receptor metabotrópico de glutamato 6 (receptor mGlu<sub>6</sub>; clase C). Tanto el receptor  $M_1$  ( $M_1$ R) como el receptor  $M_2$  ( $M_2$ R) son importantes dianas farmacológicas para varias enfermedades que afectan al sistema nervioso central (SNC), como la enfermedad de Alzheimer, la enfermedad de Parkinson, la esquizofrenia, los trastornos del sueño y las enfermedades cerebrales agudas. Los  $M_2$ R también representan una diana para disfunciones cardíacas; los  $D_1$ R para la hipertensión y la enfermedad de Parkinson y el receptor mGlu<sub>6</sub> para enfermedades degenerativas de la retina, como la retinosis pigmentaria.

Los enfoques farmacológicos tradicionales para la modulación de la actividad de los GPCR siguen siendo limitados, ya que el control espaciotemporal preciso de un ligando se pierde en cuanto se administra. La fotofarmacología propone el uso de pequeñas moléculas difusibles llamadas ligandos fotocromicos (PCLs) (o fotoconmutadores) para superar este déficit, ya que su actividad puede ser controlada reversiblemente por la luz con alta precisión. En esta tesis, hemos combinado enfoques fotoquímicos, celulares (ensayos de fluorescencia del calcio) y fotofarmacológicos *in vivo* para caracterizar varios fotoconmutadores, ya sean agonistas, antagonistas, ligandos dualstéricos o moduladores alostéricos.

En el **Capítulo 3** se muestra el desarrollo de un método novedoso denominado "criptoazologuización", que sustituye el núcleo tricíclico de fármacos "privilegiados" por diferentes azobencenos como fotoconmutadores moleculares. Esta estrategia ofrece la ventaja de producir compuestos fotoactivables que son inactivos en la configuración *trans*, la más estable termodinámicamente. El isómero *cis* puede obtenerse tras iluminar con la longitud de

onda adecuada, imitando la geometría tricíclica del fármaco original y su efecto. El potencial de la "criptoazologuización" se ha demostrado con el desarrollo de cuatro derivados de pirenzepina, denominados "criptozepinas". Hemos caracterizado estos nuevos compuestos para los mAChR mediante un ensayo de imagen de calcio en células HEK que sobreexpresan el M<sub>1</sub>R. La criptozepina-2, que mostró una mayor actividad inhibidora, se estudió *ex vivo* en aurículas cardíacas, así como en la red cortical. Este último estudio es el tema central del **Capítulo 4**, donde se muestra el efecto antagonista de la criptozepina-2 en rodajas de hurón, donde bloquea la activación muscarínica en las oscilaciones lentas. Además, descubrimos que la criptozepina-2 suprime las convulsiones epileptiformes mediadas por M<sub>1</sub>R en su forma *cis* activa. Paralelamente, también se demostró la capacidad del agonista benzil quinolona carboxílico-azo-iperóxido (**BAI**) para aumentar la frecuencia de la actividad oscilatoria lenta en redes corticales tanto *ex vivo* como *in vivo* en su configuración *trans*. La ftalimida-azo-iperóxido (**PAI**) es otro compuesto fotoisomerizable dualstérico que también es activo en su forma *trans* (**Capítulo 8**). A diferencia del **BAI**, el **PAI** se dirige a los M<sub>2</sub>R, siendo el primer agonista fotoconmutable de los mAChR M<sub>2</sub> que se ha descrito. Este compuesto permite controlar la actividad cardíaca con luz en animales silvestres sin manipulación genética. Sin embargo, la limitación de **PAI** y **BAI** es que ambos isomerizan de *trans* a *cis* con luz UV, que presenta baja penetración en el tejido. En consecuencia, se pierde la propiedad de no invasividad de la luz, una ventaja clave del agente farmacológico. Hemos conseguido activar el **PAI** con longitudes de onda más largas, como 840 nm, bajo excitación de dos fotones (2PE) (**Capítulo 9**).

En esta tesis, por tanto, también pretendemos ampliar el conjunto de herramientas fotofarmacológicas con el desarrollo de compuestos o la optimización de métodos que puedan resolver diferentes deficiencias que hemos identificado como críticas para las aplicaciones *in vivo*. En principio, la limitación de la profundidad de penetración en los tejidos puede superarse desplazando las longitudes de onda operativas a la "ventana biológica" (650-1100 nm). Además de la longitud de onda operativa, otra deficiencia está representada por el gran volumen de excitación causado por la dependencia lineal de la excitación monofotónica (1PE). Por el contrario, la no linealidad de la excitación en el punto focal permite una resolución subcelular en tres dimensiones. Para cumplir ambos requisitos de penetración tisular profunda y de fotoconmutación focalizada, la farmacología multifotónica aprovecha los láseres pulsados NIR y la absorción no lineal de ciertas moléculas fotocromáticas.

En el **Capítulo 5** se desarrolló un conjunto de derivados de xanomelina (es decir, agonista muscarínico) *cis-on* denominados "xanoconmutadores". Se seleccionaron los mejores

compuestos de su clase mediante un ensayo *in vitro* y estos fotoconmutadores se modificaron químicamente para permitir la fotoisomerización mediante excitación de dos fotones (2PE) utilizando un láser pulsado de luz NIR. Para ello se utilizaron modificaciones bioisostéricas de un solo punto en el azobenceno. Con estos **xanoconmutadores** activados mediante **2PE**, logramos fotocontrolar las oscilaciones de calcio en varios escenarios *in vitro* y, por primera vez, la fotomodulación bidireccional y reversible de la actividad neuronal *in vivo* con luz NIR. En el **Capítulo 9** hemos presentado la primera prueba de concepto de fotoactivación de un compuesto fotosensible (es decir, **PAI**) mediante excitación trifotónica (3PE) *in vitro* e *in vivo*. La aplicación generalizada de la farmacología de dos fotones y tres fotones puede transformar la investigación y el desarrollo en biología química y promover las fototerapias avanzadas.

Dependiendo de la aplicación biológica, la estimulación a escala micrométrica con 2PE puede conllevar limitaciones. En su lugar, la 1PE posee ventajas significativas para activar áreas más extensas de tejido. El **Capítulo 6** describe el desarrollo de **xanoconmutadores** activados con **1PE** mediante la introducción en la estructura molecular de un azobenceno tetra-*orto* clorado. Estos compuestos permitieron la modulación reversible de las oscilaciones de calcio *in vitro* con luz naranja y el fotocontrol de la motilidad de peces cebra. Ello permitiría también utilizar diodos emisores de luz (LED) convencionales, ligeros y fácilmente disponibles, lo que simplificaría su aplicabilidad en terapias fotofarmacológicas para el SNP y el SNC.

Otro de los objetivos de este trabajo fue el desarrollo de los primeros moduladores alostéricos reversibles y fotosensibles para GPCR de clase A, descritos en el **Capítulo 7**. Utilizando el M<sub>1</sub> prototípico, se desarrolló un modulador alostérico reversible para GPCR de clase B. A partir del modulador alostérico positivo prototípico del M<sub>1</sub>R, el ácido bencil quinolona carboxílico (BQCA), se desarrolló un conjunto de **Photo-BQCA**s. Estos compuestos presentan propiedades fotofarmacológicas complementarias, una *cis* y otra *trans*. La caracterización biológica demostró su capacidad para modular la activación del receptor en presencia de un agonista ortostérico de forma dependiente de la luz. Estos fotoconmutadores representan compuestos interesantes y útiles en los esfuerzos que se están realizando para comprender el complejo mecanismo de señalización de los GPCRs.

Además, este trabajo presenta el desarrollo y la aplicación de la **azodopa**, un agente fotofarmacológico dirigido a la regulación lumínica del sistema dopaminérgico (**Capítulo 10**). Demostramos que este compuesto activa los receptores D<sub>1</sub>R *in vitro* de forma dependiente de la luz y permite fotocontrolar de forma reversible la motilidad de peces cebra en una escala temporal de segundos. Además, aumenta la actividad neuronal global en la corteza de ratones

anestesiados. La **azodopa** es el primer agonista dopaminérgico fotoconmutable con eficacia demostrada en animales silvestres, lo que abre el camino al control remoto de la neurotransmisión dopaminérgica con fines fundamentales y terapéuticos.

En el **Capítulo 11**, describimos el desarrollo y la aplicación de una biblioteca de compuestos nuevos que actúan como agonistas y moduladores alostéricos positivos (ago-PAM) con potencia nanomolar y que se dirigen a los receptores metabotrópicos de glutamato 6 (mGlu<sub>6</sub>). Realizamos un cribado de alto rendimiento de 15 ligandos alostéricos fotosensibles utilizando un lector de microplacas e identificamos dos compuestos (es decir, **1492** y **1495**) que son de relajación rápida, conmutan con luz azul y permiten por primera vez la restauración *in vivo* de la agudeza visual. Además, restauran el comportamiento de evitación de la luz en ratones ciegos mediante administración tópica. Las características de estos compuestos los convierten en excelentes candidatos para nuevos estudios preclínicos y en una posible terapia farmacológica para la restauración de la vista en humanos.

Los hallazgos presentados amplían la disponibilidad de herramientas fotofarmacológicas no sólo para investigar vías de señalización complejas que subyacen a muchos procesos (pato) fisiológicos, sino también para tratamientos innovadores y no invasivos de diferentes patologías mediante luz.

---

## Acknowledgements

---





“The important thing is not to stop questioning. Curiosity has its own reason for existence. One cannot help but be in awe when he contemplates the mysteries of eternity, of life, of the marvelous structure of reality. It is enough if one tries merely to comprehend a little of this mystery each day.”

*Old Man's Advice to Youth: 'Never Lose a Holy Curiosity.'*

Albert Einstein, 2 May 1955

I am pretty sure this part of my thesis will probably be the most popular one 😊.

I guess, I could tell you I never encountered any problems. I guess, I could tell you that I never had a failed experiment and that it all went off without a hitch. I guess, I could LIE..... In reality, I would better describe the process of obtaining my PhD as a roller coaster ride, full of curves, twists, and falls. All this significantly correlated with my confidence levels over the years, which took a serious hit several times. Many times, I believed that I would not make it and the thought of throwing the towel into the ring crossed my mind. It's during these times that I relied the most on the people I wish to thank in this section. They always encouraged me and made me see “the glass half full”. I have no doubt that I would not have been able to accomplish any of this without them and for this I will be eternally grateful.

First of all, I sincerely thank Pau for the opportunity to work on such interesting and inspiring projects. You believed in me from the start of my PhD and continued to do so until now. You are an amazing person and a great mentor, always supportive, optimistic, and inspiring. No matter if it was a day off or 23:00 o'clock you have always been there. Thank you for pushing me to reach a high quality in every aspect of my projects and to teach me to be proud of what I achieved! Your guidance and never-ending support have been invaluable, and I cannot thank you enough.

I wish to thank my past and present group members for the friendly, open, and welcoming atmosphere in the lab.

I started my PhD in Bellvitge's lab, where I have nice memories of that period, except when I felt sick for several days. Nuri I will always remember you bringing me sushi at the hospital. This is just one of the many friendly and helpful gestures (inside and outside the lab) you did towards me during these years, which show what a caring and nice person you are!

## Acknowledgements

Alexinooo the first day we met you already started with your annoying jokes :P and with your fake theories, like about the origin of the pizza! After many discussions, I hope you finally agree that pizza is Italian!!! You try your best to appear super pesadooo, but deep deep deep inside you have a lovely heart. Thank you for always providing a positive note, when I was feeling down, and for making me laugh at my own insecurities.

Aida, we shared some painful moments praying the Olympus to work. I learned to be patient and give to it time, especially on Mondays! It was nice to share part of my journey with you and to discuss the manyyy problems of everyday lab life. Miquel you are a cheerful and positive person and a great scientist! Thank you for all the advice you have given to me! Clarita, we talked a lot and support each other. It was very important for me, and I wish we cross our paths again! Pablitooo, I hope you learned how to cook properly pasta. Watching your weird mixes during lunch time almost killed me. It was nice to have you around even for a short time. I wish you all the best for the future and hopefully we will meet again! Xavi thank you for your guidance at the beginning of my PhD and your precious advice. Sadly, it was only for a couple of months, but I learned a lot from you! Luca, I enjoyed working with you and not only because your molecules did not disappoint me! You are a pleasant and ironic person and I would love to meet you again!

Francinoo pinguino mio when we first met it was love at first sight (sorry René)! The experiments did not make our life easy, we had to work hard and to read lot of papers to understand the source of the problems and many times it was very frustrated! Luckily, I could always count on you to provide a lively atmosphere with lots of laughter to lift my spirit. You did not stay long in the lab, but I'm very happy our friendship lasted through many years. I feel grateful to have you in my life. Ti voglio bene!!!

Galinkyyy you have brought to the lab not only your knowledge and expertise, but also a gust of enthusiasm! It took me some time to remember that you are from Ukraine and not from Poland but, believe me, I will never forget what you have done since I met you! You are a colleague and a friend, who is always supportive and helpful! Your understanding and encouragement meant a lot to me especially during the difficult times. You even came to cook in my place your famous quiche, when me and René needed some help. And especially in the last months before the thesis's submission you have been my personal motivator eheh. I can't thank you enough and I'm glad you are part of my Barcelona's family.

## Acknowledgements

A big thanks goes to my pesadito culiadito Morita. I met you as a colleague and then you also became a flatmate and of course an important friend! We talked for hours and hours about topics of any sort and never get tired of each other (at least I hope so eheh). You have been my confident and my point of reference and I will always keep in mind your precious advice! Thank you to introduce me to the pisolita that is a witness of many funny moments in our beloved balcony! Through you I met also Alecita that became part of the crazy family bringing her optimism and positive energy. We shared unforgettable moments, and it was difficult for me when you decided to return to Chile. I miss you guys a lot and of course I miss the fruit of your love, our gordito Vicente. I wish you all the best with all my heart and I really hope to meet you again!! <3

During the time in Bellvitge's lab I have also had the pleasure of meeting people of other labs. A special thanks goes to Anita who definitely contributed to my mental well-being by listening to my whining when I was stressed and demotivated. You provided me with the necessary dose of motivation to carry on. You are a genuine and loving person, and I am glad to be your friend! Thanks also for forcing me to join the "Mojitada", where I met my viking, René. I wish to thank also Nerea, Marta, Alba and Santi. You guys contribute to the pleasant working environment, and I could always rely on you for help (especially the precious advice from Santi for the PCR) and words of encouragement. Pep it was stimulating to work for several days with you! I got to know you better and you are a very nice person!

I left in Bellvitge a part of my heart, but it was also nice to reunite with the rest of our group at IBEC. In this way, I had the opportunity to spend more time with Manolito and really you are the most active person that I ever met! You have million hobbies, million activities and you make me feel olddd eheheh. You always update me about the last technology and I always learn something new by talking to you! Thank you for being always nice and encouraging!! Marina your positive energy is contagious!! I always enjoy chatting with you and please go more often to Argentina... I want to taste again those delicious biscuits!! Ekin Ekin you are a lovely, dedicated and kind-hearted person, who is always available to help everybody in the group. I appreciate a lot what you have done for me, and I enjoyed working with you! I am sure we will always be in touch, and I wish you the very best!! Nayeli thank you for your collaborative spirit and enthusiasm! It was stimulating to discuss about one of the projects and I hope we will have more chances in the future! Joaquin you are incredible! Thank you for teaching me how to manipulate and perform experiments with our lovely "pescaditos" and for all the tips about

## Acknowledgements

software, plugins and all your valuable advices! Your insights and point of view are very valuable, and I think you are an important point of reference for all the lab!

I want to thank also my Bachelor and Master students (mis pollitos) Marta, Eric, Paula, Claudio, Jose, Xevi, and Alvar. You were all amazing students and I hope I was a good supervisor eheh.

I move to the ChemSpace now. Luisa, I wish you a huge, huge, huge luck for everything. I want to hear from now on only about beautiful experiences!!! Ramssss, I always have a great time with you!! If I'm stressed, you do or say something that make me laugh and relax! And of course thanks for your help and support especially in these last months!! You have a beautiful soul and a kind heart, and you deserve all the best!! Daviaa, it was a pleasure to have you in the lab and to collaborate for the orexin project! Thank you also for encouraging me, when the paperwork for the thesis's deposit made me crazyyy! I wish you all the best for your career and I hope you can update me soon about everything!!

Hubert thank you for the amazing work you have done, for synthetizing compounds that worked super good and for being always available to discuss any problem and making me discover a new music world...Rammstein eheh. It was also nice to meet you in person and perform some experiment together!! Hopefully we can meet again soon! Wish you the best!!

Aleix you are a very kind and friendly person and of course a great chemist as well! Thank you for being always available for meetings, chats, calls and for your reassuring words!!!

Thank you, Marina and Gus, for an unforgettable time at ICFO. I will always remember that me and Marina were the only people left inside the building when the lockdown started. It was confusing but also kind of hilarious. Thank you, guys, for such an amazing time with you laughing, enjoying the PAI PAI song (as an auspicious ritual) during the experiments and many good and rememberable conversations. You made my day even when it was stressful, and experiments didn't work!

Thank you to Dr. Pedro de la Vila, Dr. Pablo Loza-Alvarez, Dr. Michael Decker, Dr. Amadeu Llebaria and Dr. María Victoria Sánchez for sharing your immense knowledge and expertise, for all those interesting meetings and the productive collaboration. Pedro thank you for your lovely welcome when I came to Alcalá de Henares! It was an honor and a pleasure to perform experiments with you!

And now it's the turn of Fabinssss the "father" of manyyy molecules that made me work a lot, but also gave me a lot of satisfaction!! I remember in my first group meeting I saw one of your presentations and I already thought that you were a very capable and hard-working person. With

## Acknowledgements

time I confirmed my first impression, but I also got to know you better and I feel lucky to be your friend!! You bend over backwards to help, you find the right words to encourage and make it look easier. You were there when I was lost and confused, and you literally guide me and push me Forza Rosinaa scrivi scrivi scrivi!! Dai che ce la fai!! Thank you will never be enough! Ti voglio bene!! A bit thanks also to Maria!!! You are an amazing, positive, and caring person, that's why my son is in love with you eheheh. I feel always better after I talk to you!!

Carlinooo, I was extremelyyyy sad when you went back to Italy!! Actually, I started crying already before you left (from one of Fabio's jokes) but at the same point it became real ☹. You have shown me what it entails to be a good scientist, to have confidence that it will work out, and to never give up. Your hard work and quality of seeing the good in everything are truly inspiring!! You are not just an example as a scientist... you are a wonderful friend and I want to thank you for having such a positive impact on my life. But you did something that made me suffer...azodopaaaaa!!!! Not sure if I will ever forgive you for that ahahah. Ti voglio bene!!

Rossina miaaaa it's your turn!! We did not share the same project, but we always share thoughts, opinions, advice and for some time also your flat! When my apartment was literally on fire, and I did not have where to go at 02:00 in the night... I knew I could count on you!! And on Giorgio too!!! Thank you for supporting me in so many occasions, for listening to my complains, for cheering me up when experiments did not work, to teach me how to hand knit, to be always available to go and try different sushi restaurant ahahh. In fact, since you left Barcelona I only order sushi take away ☹ Ti voglio bene!!

Thank you Khashayar for helping me with the cover of my thesis and sorry if I was very heavy and perfectionist about that eheheh. I promise you will eat soon my anelletti al forno eheheh.

Muchísimas gracias Pilar!! Your encouragement and help with all the paperwork meant a lot to me!! Listening to your relaxing voice helped as well eheh and when I came to deposit my bible and we finally met in person it was for me a great pleasure! Thank you to the coordinator of my PhD program, Dr. Josefa Badia for your constant support over the years!

A big thanks to my Dutch family starting with my parents in law Gonny and Han for your endless support. Gonny without you there wouldn't be a thesis. When I asked you for help you came to Barcelona twice without second thoughts. In this way, I could focus on the writing and being able to deposit on time. Your words of encouragement and your kindness, when I was extremely stressed gave me the strength to go forward! Thank you for everything!! Han not sure if I'm completely ready for all your questions, but I promise I will try to reply and explain

## Acknowledgements

in the best way I can! Thank you for making me always laugh! Love you both! Dankjewel to my brothers and sisters in law Brenda, Bus, Claire and Koen and my beautiful niece Lenita and my handsome nephews: Toninjo, Eric, Casper and Hugo. You all made me feel from the beginning welcome in the family and you are so important for me!!

Grazie alla mia comunità a Barcellona..a partire dalla mia amica Martinaaa!! Ti sei beccata audio infiniti spesso pieni di sfoghi di ogni tipo e tu mi hai ascoltata, consigliata, capita!! La mia vita qui non sarebbe la stessa senza di te! Sei preziosa ed insostituibile!! Grazie di tutto!! Ti voglio bene!

Alla mia C-Squad: Antonella, Alessandra, Alessia, Silvia & Lea!! Sono fortunata ad avervi incontrate!!! I nostri venerdì non li cambierei per niente al mondo! Grazie grazie grazie!! Mi avete sempre tirata su il morale quando mi avete vista giù e superrr stressata! Vi lovvooo!!!

Thank you to my friend Dieghitoooo!!! You are one of the first person I met in Barcelona..I'm glad we always are in contact and still friends after so many years!! You make me always laugh with your crazy stories. So happy you are back in Barcelona!! Janiniii I love to spend time with you..I get affected by your positive vibes..that helped me even in my down days. Os quiero!

Una grande fetta di ringraziamenti va alla mia famiglia siciliana a cominciare da mia nonna Michela, la mia roccia ed il mio porto sicuro. Mi hai insegnato cos'è il bene incondizionato e che si dimostra lasciando all'altro la libertà di scegliere, anche se questo comporta il rischio di poter sbagliare. Mi hai lasciata libera di scoprire il mondo, di studiare all'estero e di vivere nella città che più mi facesse stare bene, anche se lontano da te. Essere distanti ci ha fatto soffrire ma i legami quelli veri, indissolubili non vengono scalfiti. Anche quando la vita non è stata clemente con noi, hai sofferto in silenzio e mi hai sempre dato la forza per andare avanti e rendere orgogliosi chi ci ha lasciato. Ed io spero che oggi i miei angeli custodi siano fieri dei miei traguardi e gioiscano nel vedermi realizzata e felice. Ti amo con tutta me stessa!

Non ci sono parole per ringraziare mio fratello Calogero! Hai sempre creduto in me anche quando ero la prima a non crederci. E anche se sono la sorella maggiore devo ammettere che a volte sei stato tu a mostrare più maturità. Mi hai sostenuta anche quando pensavi che stessi sbagliando e mi hai aiutata a rialzarmi tutte le volte che sono caduta. Sei stato la mia luce nei momenti bui e la mia ancora di salvezza. Il nostro legame è raro e prezioso e spero che anche i nostri figli possano crescere uniti così come lo siamo noi. Ti voglio infinitamente bene! Ringrazio con tutto il cuore mia cognata Giuliana che per me è come una sorella. Da quando sei entrata nella mia vita hai portato gioia, buon'umore ed entusiasmo. Ci sentiamo

continuamente e ho sempre bisogno del tuo parere prima di prendere qualsiasi decisione eheheh Sei indispensabile e preziosa e sono fortunata ad averti nella mia vita! Non ti saró mai abbastanza grata per aver dato alla luce i miei splendidi nipoti Giovanni e Giusy che riempiono le mie giornate di allegria e risate e mi rendono una zia orgogliosa. Ringrazio anche Francesca, Mimí, Gemma, Giambartolo e la meravigliosa Ginevra per il vostro affetto e supporto. In particolare Francesca per la sua gentilezza, disponibilità ed il suo prezioso aiuto.

Un grazie particolare alle mie Butty, Lia e Luisa, che si sono state, ci sono e so che ci saranno sempre. Sono innumerevoli le volte in cui avete ascoltato i miei sfoghi, soprattutto quando lo stress e la demotivazione hanno preso il sopravvento. Mi avete calmata, mi avete fatto riflettere e consigliata. Siete delle amiche encomiabili e vi voglio un bene dell'anima! Ringrazio anche Giovanni e Giuseppe per aver accettato e compreso che non possono competere con la nostra relazione ahah Giuseppe grazie per i consigli preziosi che mi dai da sempre! Non possono mancare nei miei ringraziamenti la nostra miniBú Beatrice e Dariuzzo. Solo vedere le vostre foto e video mi riempie il cuore di gioia!

Un grazie immenso va alla mia Aironcello...grazie perché ci sei sempre!!! Sei un'amica leale, sincera e affettuosa. Mi sento libera di esprimere ogni mia paura e fragilità sapendo di ricevere la comprensione, il sostegno e l'incoraggiamento di cui ho bisogno per affrontare ogni situazione difficile. Sei una certezza nella mia vita e sai che ti voglio infinitamente bene. Ringrazio anche Aleee motherfather e Brillo.

Un grazie speciale alla mia figlioccia del cuore Giovina verso cui nutro un affetto particolare. Gio sai quanto siamo legate e quanto ti voglio bene! Pinuzza ci siamo sempre capite con uno sguardo e sei un riferimento importante nella mia vita, grazie per tutto quello che hai sempre fatto per me e per il tuo affetto sincero. Al mio caro Giovanni Aiello grazie di cuore per l'affetto incondizionato e sincero che mi hai sempre dimostrato, ti voglio bene!

Francesco e Maria Antonietta grazie grazie grazie!!! Da voi ho sempre ricevuto tanta forza e incoraggiamento. Non posso non ringraziare i miei padrini Viviana e Ivan, Giuseppe e Carmela perché ho sempre potuto contare su di voi.

Le mie amiche freshhhh Annalisa e Giusy che mi hanno sempre sostenutooo...da quando siete venute a trovarmi qui a Barcellona ne é passato di tempo e molte cose sono cambiate...ma la nostra amicizia é rimasta invariata! sono sicura che i nostri figli saranno amici sinceri così come lo siamo noi!



## Acknowledgements

Last but not less important the loves of my life...**Massimo ♥** and **René ♥!!** Massi mio, vita mia, cuore mio you are such a blessing to my life! I love watching you grow. You are the sunshine of my days and you spread kindness like wildfire! Of course, being a parent isn't just flowers and romance. It is the hardest job. It means also no sleep, no rest, more responsibilities, more worries....and adding up writing a PhD thesis in the meanwhile can be veryyy challenging and consuming! Just the way you are always smiling, happy, friendly with everybody helped me immensely! When you were only 5-month-old you adapted easily at the kindergarten.. you never cried. And when you started sleeping all night long... Ohh God, it was such a relief!! You are more perfect than I could have ever dreamed when I found out I was pregnant, and I love you more deeply than I ever thought was possible!! And finally, my other cuoreee, my René!!! I'm happy with my choice to start this PhD... otherwise I would never have met you!! No words will never be enough to thank you for your endless love, help and support...for always being there for me and for providing a comforting atmosphere at home. You kept me motivated, focused; you handled my stress and my bursts; you took care of Massi a lottt... even cookingg much more than before... always trying to let me have as much time as possible to concentrate on writing. I appreciate and rely on your advice. Sorryy if sometimes I said that you are too critical or too pesado... I know you do for me... to make me reach always the best results... to be as you usually say "always consistent"!! I feel extremely happy to share my life with you, to be your wife and I can't wait to see what the future holds for our little family.

**Hou immens veel van jullie allebei ♥ ♥ ♥**

## Acknowledgements



